Hee-Jin Kim
Kwan-Hyun Youn
Ji-Soo Kim
You Soo Kim
Sung Ok Hong
Jongju Na

Ultrasonographic Anatomy of the Face and Neck for Minimally Invasive Procedures

An Anatomic Guideline for Ultrasonographic-Guided Procedures

Springer

Ultrasonographic Anatomy of the Face and Neck for Minimally Invasive Procedures

Hee-Jin Kim • Kwan-Hyun Youn
Ji-Soo Kim • You Soo Kim
Sung Ok Hong • Jongju Na

Ultrasonographic Anatomy of the Face and Neck for Minimally Invasive Procedures

An Anatomic Guideline for Ultrasonographic-Guided Procedures

Springer

Hee-Jin Kim
Division in Anatomy and Development Biology
Department of Oral Biology
Yonsei University College of Dentistry
Seoul, Korea (Republic of)

Ji-Soo Kim
Dr Youth Clinic
Seoul, Korea (Republic of)

Sung Ok Hong
Department of Oral and Maxillofacial Surgery
Kyung Hee University Hospital at Gangdong
Seoul, Korea (Republic of)

Kwan-Hyun Youn
Department of Fine Arts, Bio Medical Art
Incheon Catholic University
Incheon, Korea (Republic of)

You Soo Kim
YSBio Co., Ltd.
Seoul, Korea (Republic of)

Jongju Na
Viol Co. Ltd.
Seongnam-si, Korea (Republic of)

ISBN 978-981-15-6559-5 ISBN 978-981-15-6560-1 (eBook)
https://doi.org/10.1007/978-981-15-6560-1

Preface

There has never been a book like this.

This is the very first book to describe the superficial anatomical structure of the face and neck by detailed ultrasonography. The reason is this structure is very complicated, and anatomical structures such as fat, blood vessels, and nerves of the face and neck are intermingled together. Therefore, it was difficult to explain the three-dimensional superficial structures instead of the two-dimensional anatomical descriptions shown through the classical anatomical studies.

This book is written based on the results of our ultrasonographic studies over the past 5 years. Though I have been doing anatomical studies in this field for the past 25 years, it was difficult to describe the anatomical structures from ultrasonographic images at the start of our research project. However, the ultrasonographic facial anatomy has been clarified one by one by the passionate research of the faculty of my lab. The data obtained from our ultrasonographic studies have already been published or are being published in many papers; it is intended to be released in a visible atlas format. The first words of a salesperson who set up the ultrasonography device in our laboratory were very impressive and unforgettable. "If you would open your mind, and the ultrasonographic images will be visible." Because of all these factors, ultrasonographic imaging has a large academic characteristic along with a big learning curve.

Ultrasonography has recently been utilized in various diagnoses, monitoring, and treatments of skin diseases. The generalized application of ultrasonography in musculoskeletal areas has been developed in the last 15 years. However, aesthetic medicine is in its nascent stage, and it is speculated that its utilization will soon be broadened. Limitedly, many clinicians use US as an adjunctive tool during minimally invasive procedures, and patients' expectations have been raised.

Ultrasonography allows clinicians to use less amounts of botulinum toxin to achieve optimal outcomes by precisely targeting the exact muscle. In addition, ultrasonography allows one to find the accurate layer during filler injections and thread lifting procedures to minimize various complications. Conventional blind techniques without the use of ultrasonography may cause vascular complications such as bleeding, hematoma, bruising, and skin atrophy. These so-called minimally invasive procedures have relied on the clinicians' understanding of the anatomy and skills to minimize vascular complications. Only ultrasonography can help clinicians detect the anatomical variations of the muscles and vessels for satisfying procedural results; we believe that the role of ultrasonography in aesthetic procedures will be strengthened. The authors would like to strongly provide a basic guidance for US-guided aesthetic procedures.

Based on these backgrounds, this book consists of ten chapters with 537 illustrations and US images, integrating both the basic and clinical sciences. The basics are explained in the introductory Chapters 1 and 2, entitled the basic principles of US and general clinical anatomy. Chapters 3 through 7 describe in detail the interpretation of US images for each part based on the clinical anatomy of the face and neck. The reference lines and points used in this book were based on our research projects that have been conducted in our lab, and the points used in this book have been published in many articles. In fact, the US anatomy of the superficial face and

neck is difficult to understand without a detailed anatomical knowledge. For this reason, a detailed knowledge of the anatomy and an understanding of many anatomical variations are required. The last three chapters consist of the US anatomy conjoined with minimally invasive procedures. Basic clinical procedures and US interpretations and the novel techniques of US-guided procedures for safe botulinum toxin, filler injection, and threading insertion are described and illustrated. Detailed items related to US-guided clinical procedures will be described in depth in our upcoming publications.

I would like to acknowledge the authors who had a crucial role in the making of this book. First, I would like to give infinite thanks to Prof. Kwan-Hyun Youn for providing all of the visuals for this book. I believe that Prof. Youn has raised the field of medical illustration to that of world-class standards. Many thanks to the effort of the MedArt team. Many clear, simple, and creative visual contents in this book are made possible by Ms. Hyewon Hu and Mr. Hyeong-Seok Choi led by Prof. Youn. I also wish to thank Dr. Ji-Soo Kim for organizing all the critically important clinical information and tips. Without his own novel US-guided injection techniques and enormous clinical experiences, the clinical chapters could not be disclosed in this book. Likewise, I thank Dr. You Soo Kim for his insightful inquisitions and questions that made coming up with creative contents possible. In addition, I appreciate Prof. Sung Ok Hong for editing and arranging the manuscript. I would like to express my respect and appreciation to Dr. Jongju Na, an aesthetic physician and a CEO of Viol Co. Ltd., for his brilliant idea on US applications and for providing full support to our authors and illustration team. Without the efforts and enthusiasm of the aforementioned co-authors in providing clinical manuscripts and in revising all of the visuals despite their busy clinical schedules, this book's text and artwork would not be possible.

In addition, I would like to thank Mr. Young Cheol Hwang, a managing director of Alpinion Medical Systems and Iljin Holdings Co. Ltd, and Mr. Eui Chul Kwon, a team manager of Alpinion Medical System Co. Ltd, for their US equipment and technical supports.

Above all, I also thank our staff, Professor Kyung-Seok Hu and You-Jin Choi, and my PhD and graduate students, Hyung-Jin Lee, Ji-Hyun Lee, Kang-Woo Lee, Hyungkyu Bae, Kyu-Lim Lee, Hyun Jin Park, Hyo-Sang Ahn, Jin-Won Kim, and Alonso Hormazabal-Peralta, from Yonsei University College of Dentistry who actively helped create the anatomical visual contents and aided in revising works for this book. Special thanks to Kyu-Ho Yi who helped us in overseeing the general architecture of the book. Also, big thanks to my beloved daughter Soyeon Kim who revised the English language of this book.

Great anatomy will be forever …

Seoul, Korea (Republic of)
March, 2020

Hee-Jin Kim
On behalf of the authors

Contents

Basic Principles of Ultrasonographic Imaging

1

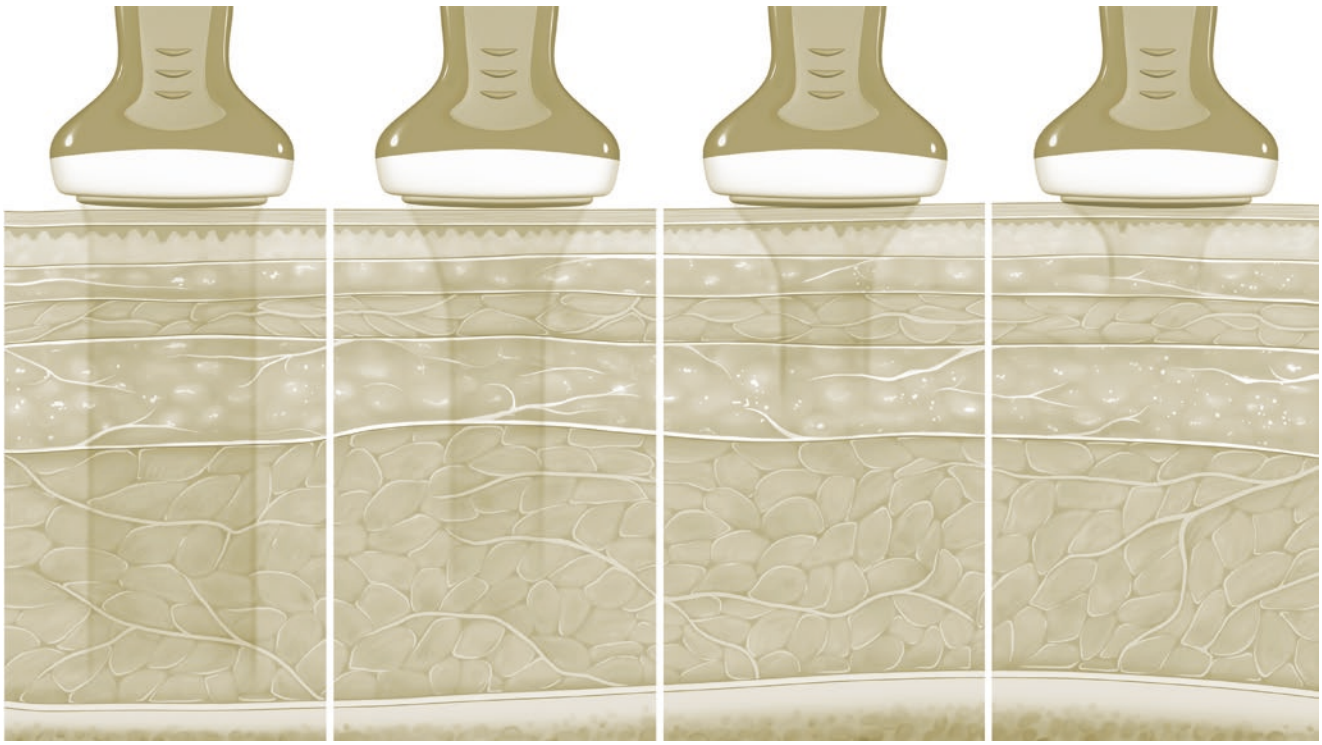

H.-J. Kim et al., *Ultrasonographic Anatomy of the Face and Neck for Minimally Invasive Procedures*,
https://doi.org/10.1007/978-981-15-6560-1_1

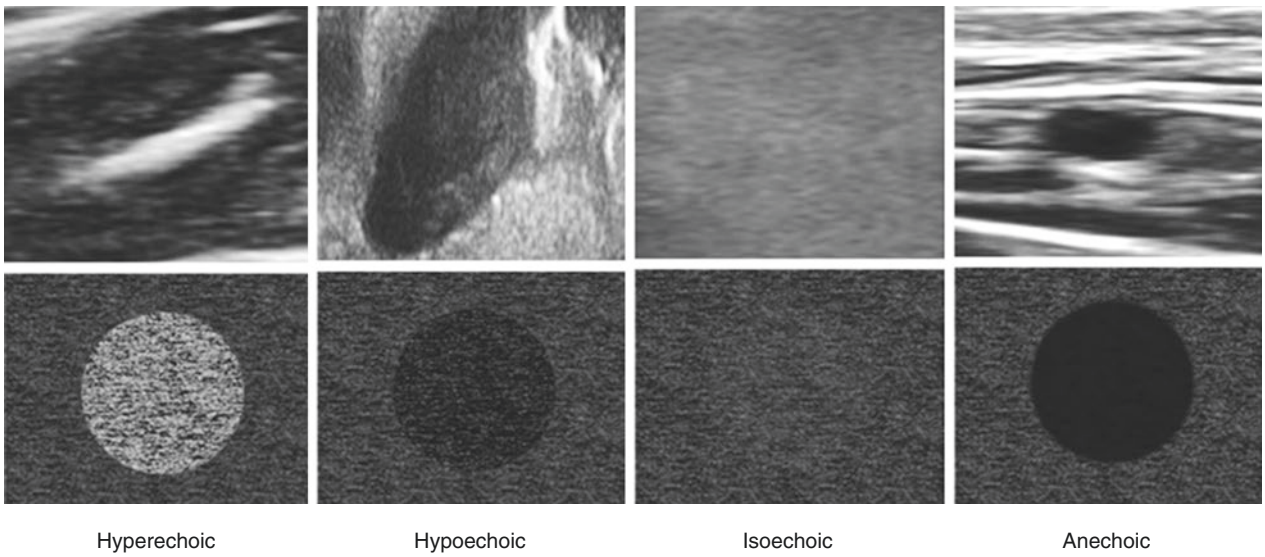

Fig. 1.1 Types of echogenicity. Echogenicity means the ability to reflect or transmit the ultrasonographic waves in the context of the surrounding tissue. The images show hyperechoic in white, hypoechoic in gray, and anechoic in black. (Published with kind permission of © Hee-Jin Kim 2020. All Rights Reserved)

Imaging by ultrasonography (US) utilizes the interaction of sound waves with tissue to produce an image or to determine the velocity of moving contents such as blood in the Doppler image. Furthermore, US has been used in many different fields to detect objects and measure distances. US waves are produced by a transducer, which can both emit US waves and detect reflected US echoes.

The US is a frequently used device in hospital settings; however, in the field of aesthetics, it is not commonly used. This chapter starts off by focusing on the basics of the US for the face and neck aesthetic procedures.

1.1 Physics and Techniques of US Imaging

1.1.1 Echogenicity

The principle theory of US imaging is that the transducer emits US waves from 3 to 25 MHz and receives reflected sound from the acoustic interface and then is digitally visualized. When the probed tissues produce similar images as the surrounding structures, they are referred to as isoechoic. When no echoes are reflected from the tissue, they are dark images called anechoic. Vessels and filler materials are shown as anechoic images. Hypoechoic images are weak echoes demonstrated as dark gray color in muscles and cartilages. On the contrary, hyperechoic structures are strong echoes that appear white such as ligaments, fasciae, and the surface of the bone (Fig. 1.1).

1.1.2 Optimized Images

To acquire the optimal image, a transducer with an adequate frequency that reflects in proper resolution and penetration is necessary. When the US wave frequency is high, the spatial resolution is bigger, and the depth of penetration is smaller. Conversely, when the frequency is low, the depth of penetration is bigger, and the spatial resolution is smaller. The 10–15 MHz linear transducer penetrates 2–5 cm, which is generally recommended in the facial area. Wave frequencies over 22 MHz are usually used for skin diagnosis (Fig. 1.2).

The ability to differentiate between two structures with disparate depths is called time resolution or depth resolution. Differentiation between two adjacent structures is called lateral resolution. The focal zone has the highest axial resolution, which is formed in the area where the sound beam is the narrowest. As the wave shoots away from the transducer, the region where wave diameter decreases is called the near field and where it increases is called the far field, respectively. The resolution is best at the focal zone (point) and decreases at the far-field area where resolution artifacts are seen (Fig. 1.3).

The focal zone (point) is more superficial when the frequency is higher, deeper when the frequency is lower. The US image shown in Fig. 1.4 is the masseter m. at 7.5 MHz and 15 MHz frequency, respectively. At 7.5 MHz, the masseter m. appears slightly blurry, but using the 15 MHz frequency, it is shown in higher resolution (Fig. 1.4).

Adjustment of the gain changes the brightness of the images. By increasing the gain value, electrical signals are amplified, which increases the brightness of the entire image. However, an increase in background noise can also potentially raise artifacts and lower the lateral resolution (Fig. 1.5).

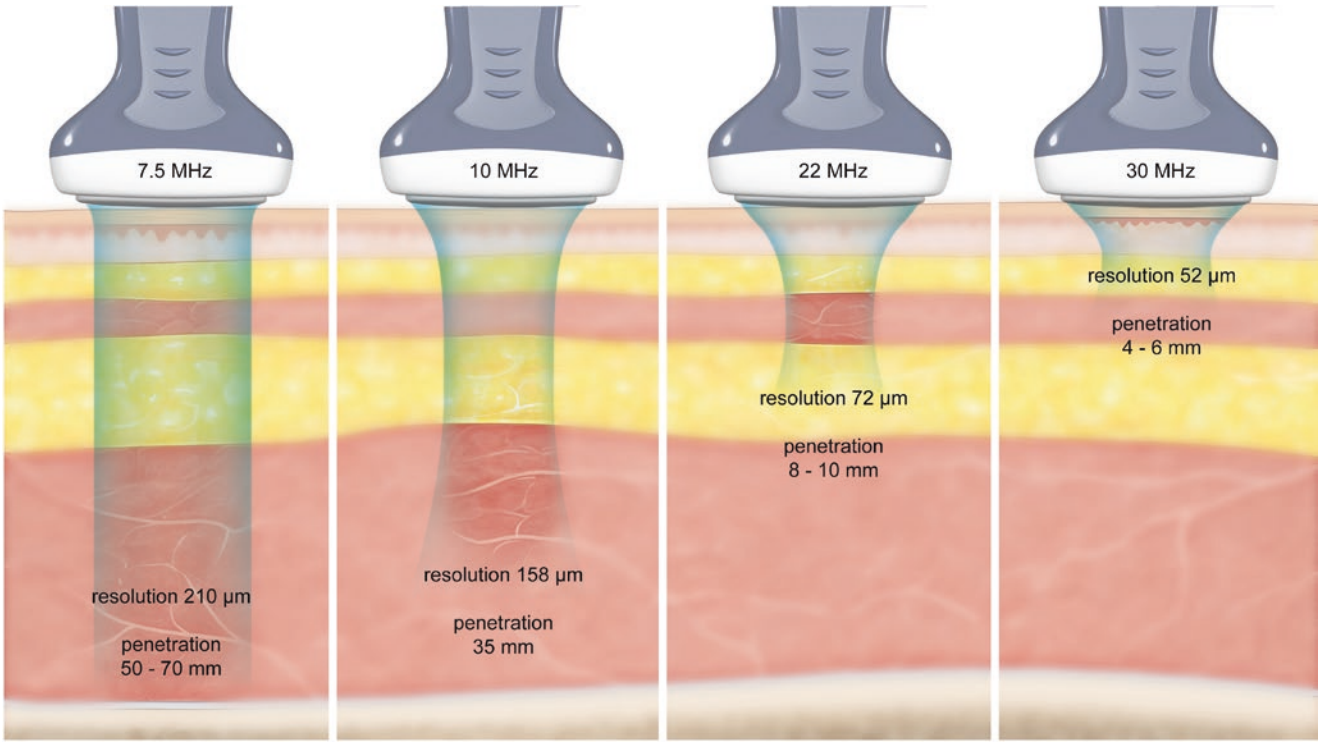

Fig. 1.2 Selections of optimal ultrasonographic wave frequency. Transducers with higher frequency show less penetration depth, which is better to observe superficial structures. (Published with kind permission of © Kwan-Hyun Youn 2020. All Rights Reserved)

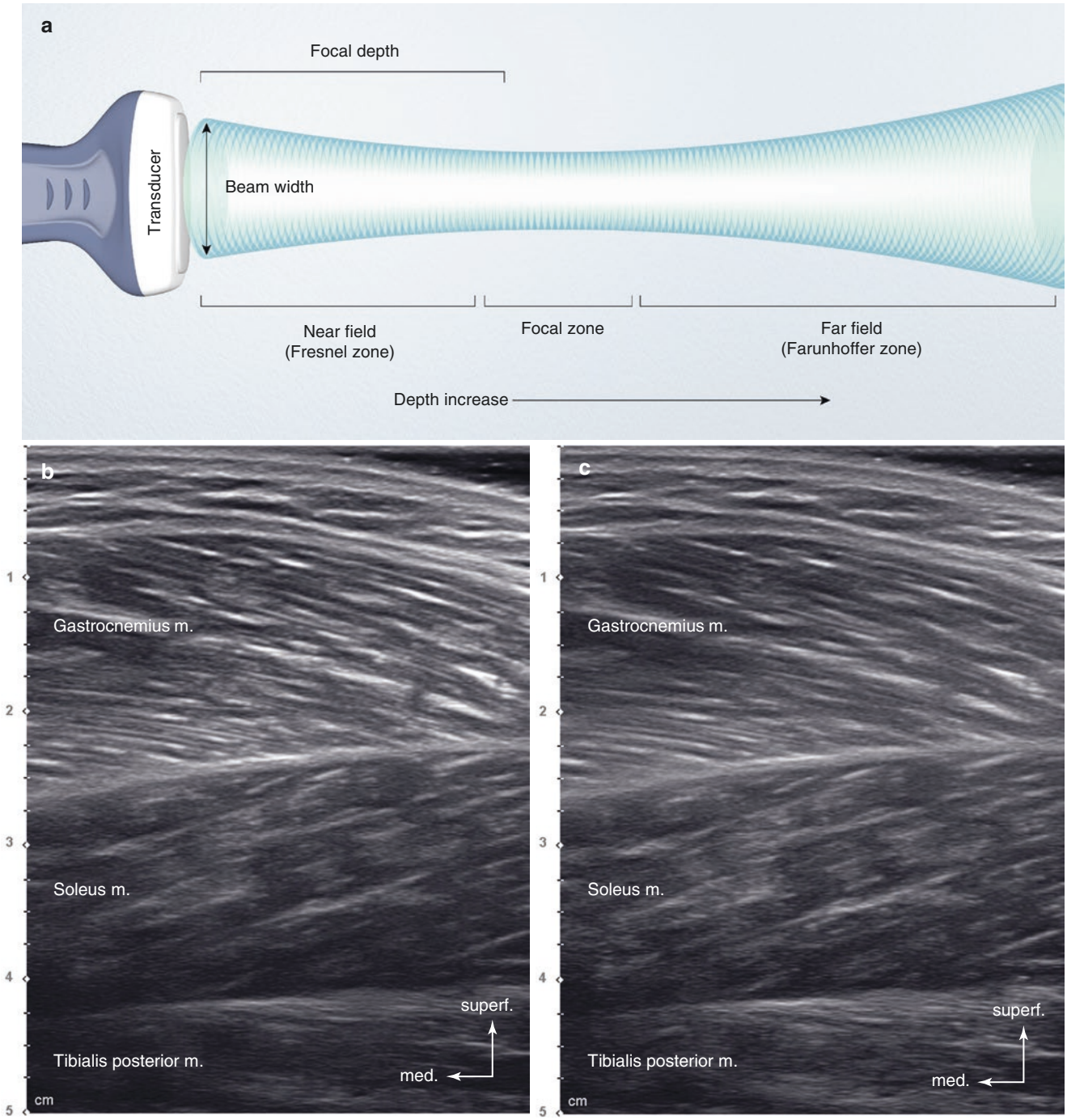

Fig. 1.3 Adjusting the focal zone and focus. (**a**) Illustration representing the stream of the ultrasonographic wave, (**b**) ultrasonographic image focused superficially (2 cm in depth), and (**c**) ultrasonographic image focused deeply (4 cm in depth). (Published with kind permission of © Hee-Jin Kim and Kwan-Hyun Youn 2020. All Rights Reserved)

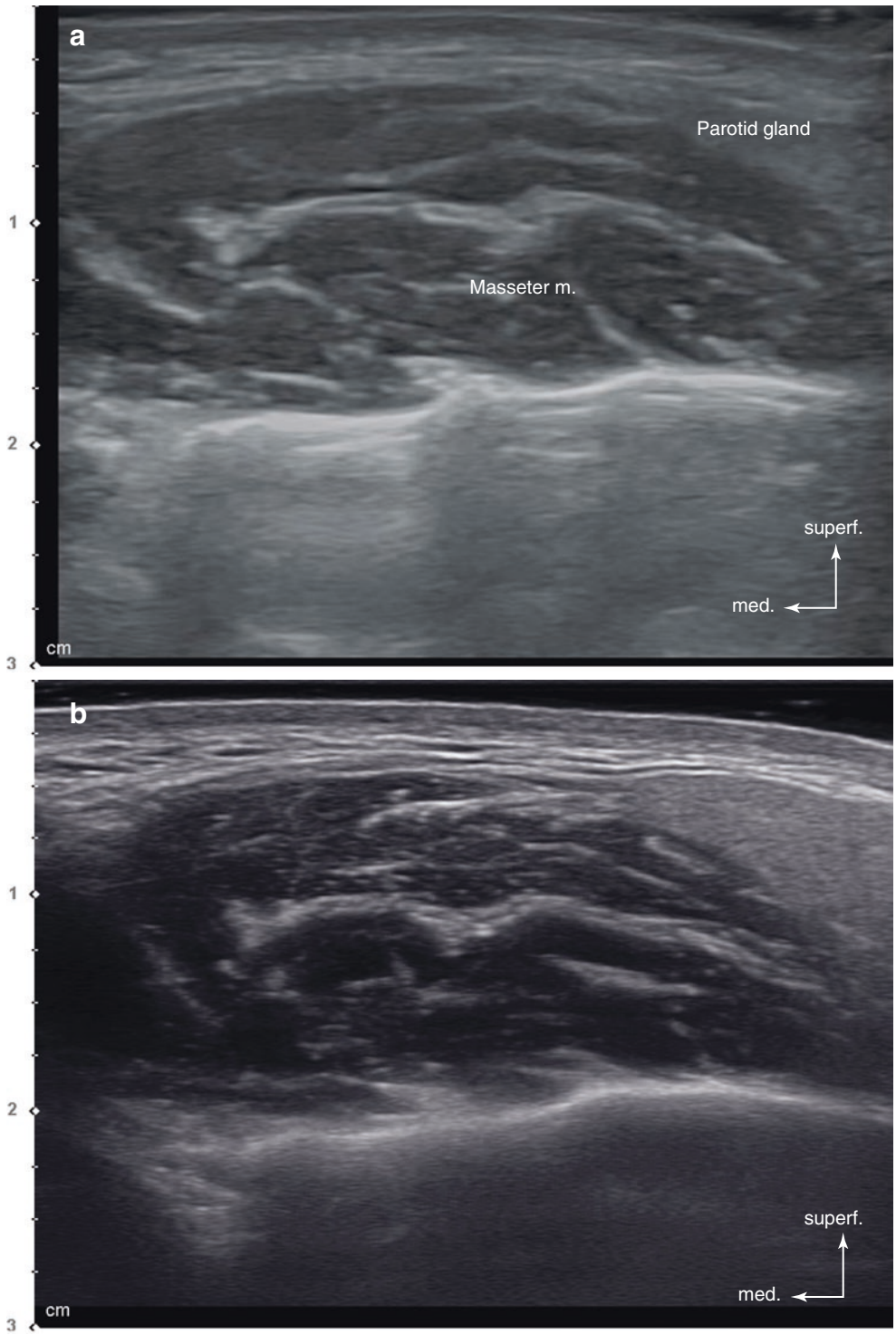

Fig. 1.4 Selection of optimal transducer frequency (MHz). (**a**) 7.5 MHz frequency and (**b**) 15 MHz frequency. (Published with kind permission of © Hee-Jin Kim 2020. All Rights Reserved)

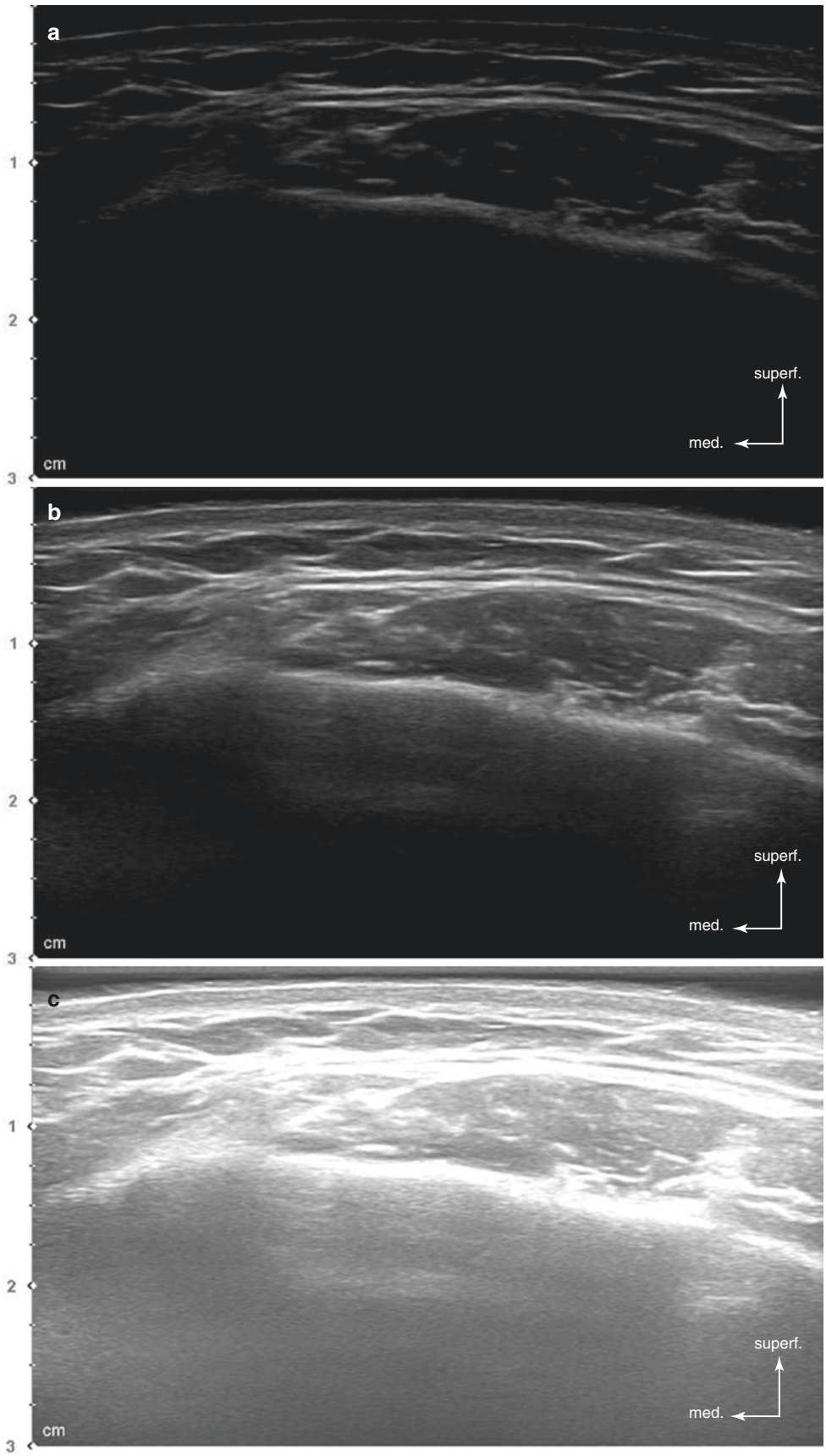

Fig. 1.5 Selection of optimal gain value. (**a**) Dark image with too low gain, (**b**) optimal image with correct gain, and (**c**) bright image with too high gain. (Published with kind permission of © Hee-Jin Kim 2020. All Rights Reserved)

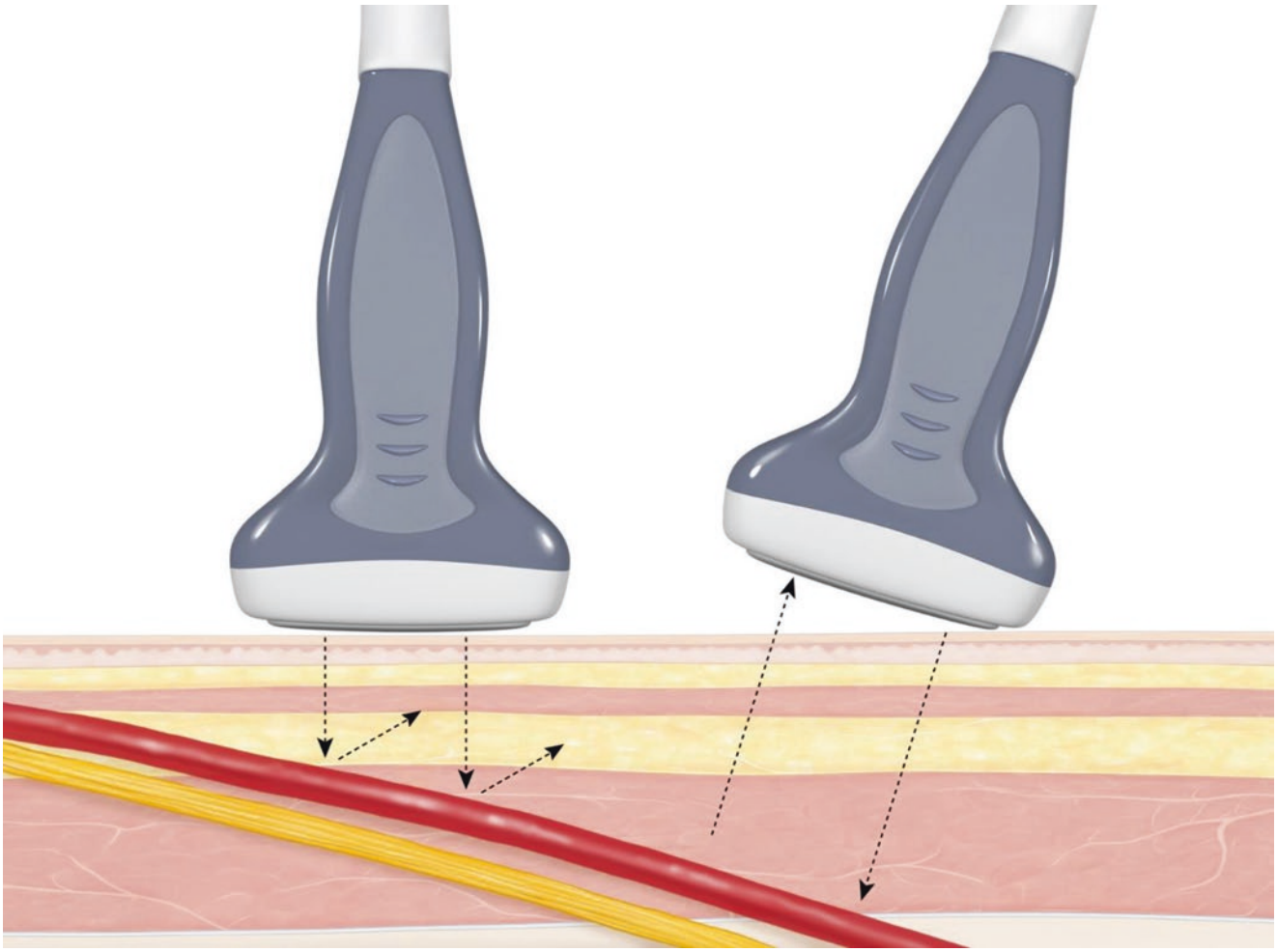

Fig. 1.6 The insonating angle in long-axis view. Vessels and nerves are shown clearly when the transducer is located parallel to these structures with heel-toe maneuver. (Published with kind permission of © Kwan-Hyun Youn 2020. All Rights Reserved)

1.1.3 Angle of Incidence

Penetration and reflection are greatest when the US's insonating angle is 90° of the surface of the anatomical structure. If the insonating angle is oblique and not at the right angle, the resolution decreases. The resolution can be improved using the heel-to-toe maneuver that accesses at 90° of the structure (Fig. 1.6). When observing the vessel and nerve of an area, an oblique insonating angle will make the artery appear in an oval shape and obstruct the visibility of nerves. A 90° insonating angle will reveal the distinct honeycomb appearance of the nerve and round shape of the artery (Fig. 1.7).

1.1.4 Transducer Manipulation

Several transducer manipulation techniques are required to attain appropriate images of the target structure. The pressure technique puts the target structure in place by applying vertical pressure to the transducer. The alignment (sliding) technique moves the transducer antero-posteriorly and laterally aligning the sonic window to the target structure.

Rotation of the transducer will procure an image along the long axis when placed parallel, and along the short axis when rotated at a 90° angle of the target structure. Tilting the transducer will place the insonating angle at 90° and will increase the resolution. These four techniques are the basic and essential transducer manipulation techniques and are called PART, abbreviated by the first letters of each technique (Figs. 1.8 and 1.9).

When observing a specific anatomical structure, the transducer is placed longitudinally to obtain an image along the axis while moving in a proximal and distal direction using the alignment technique. Then, the transducer is shifted 90° using the rotation technique to gain a short-axis view. These images are similar to the AP view and lateral view of an X-ray. Overall, the vessel pathway, shape and location of the target structure, and adjacent anatomical boundaries can be precisely evaluated (Fig. 1.10).

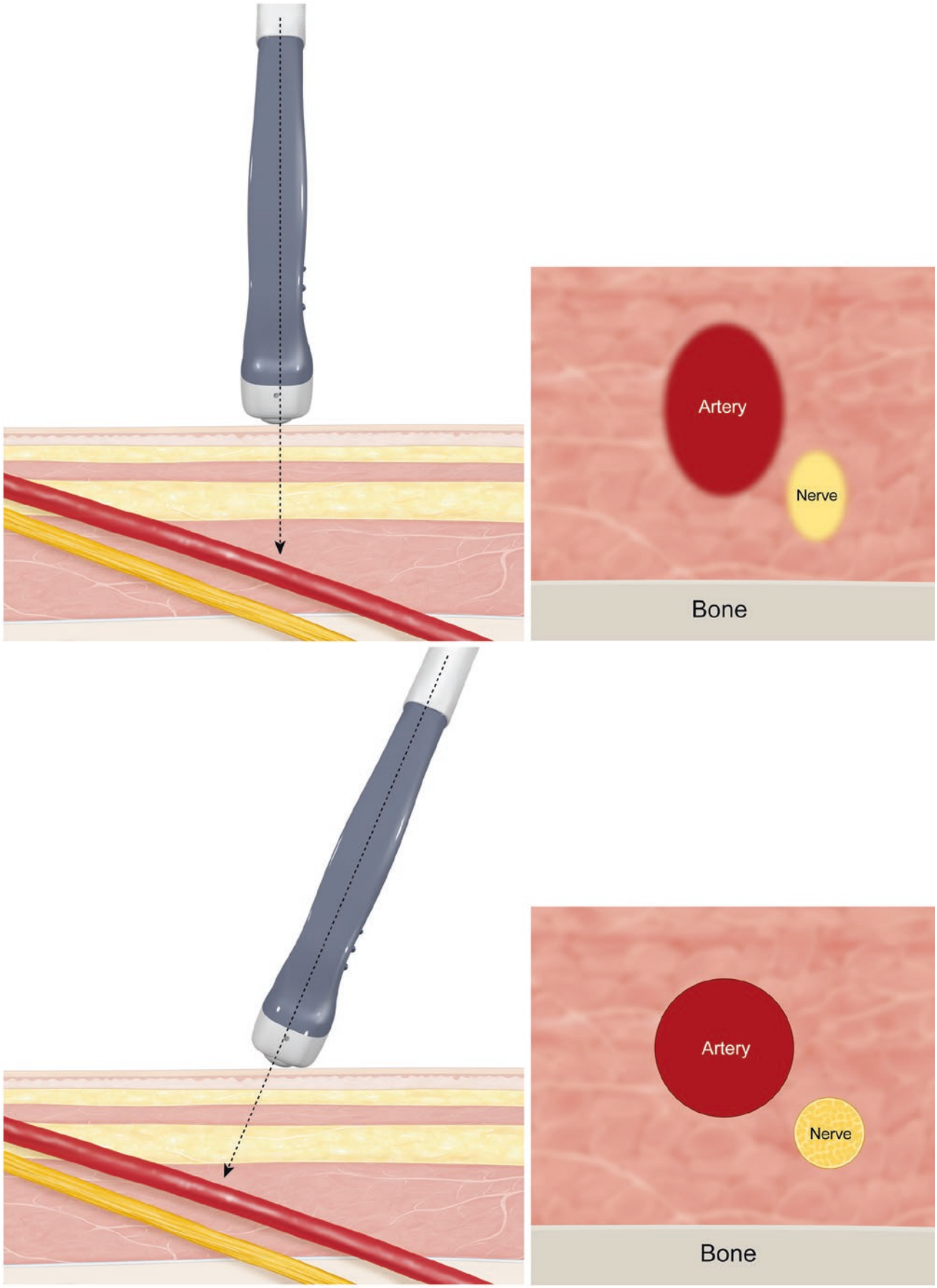

Fig. 1.7 The insonating angle in short-axis view. Vessels and nerves are shown round, not oval when the transducer is located perpendicular to these structures. (Published with kind permission of © Kwan-Hyun Youn 2020. All Rights Reserved)

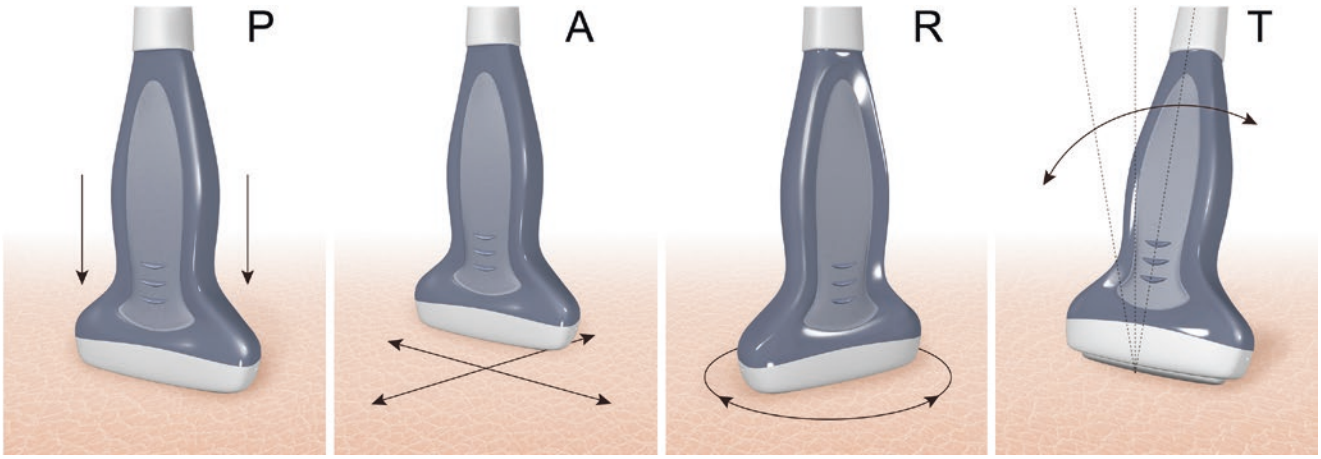

Fig. 1.8 Transducer movement. *P*, pressure; *A*, alignment; *R*, rotation; *T*, tilting. (Published with kind permission of © Kwan-Hyun Youn 2020. All Rights Reserved)

Fig. 1.9 Correct postures for holding the transducer. Transducer should be firmly supported by other fingers that are not holding the transducer. (Published with kind permission of © Kwan-Hyun Youn 2020. All Rights Reserved)

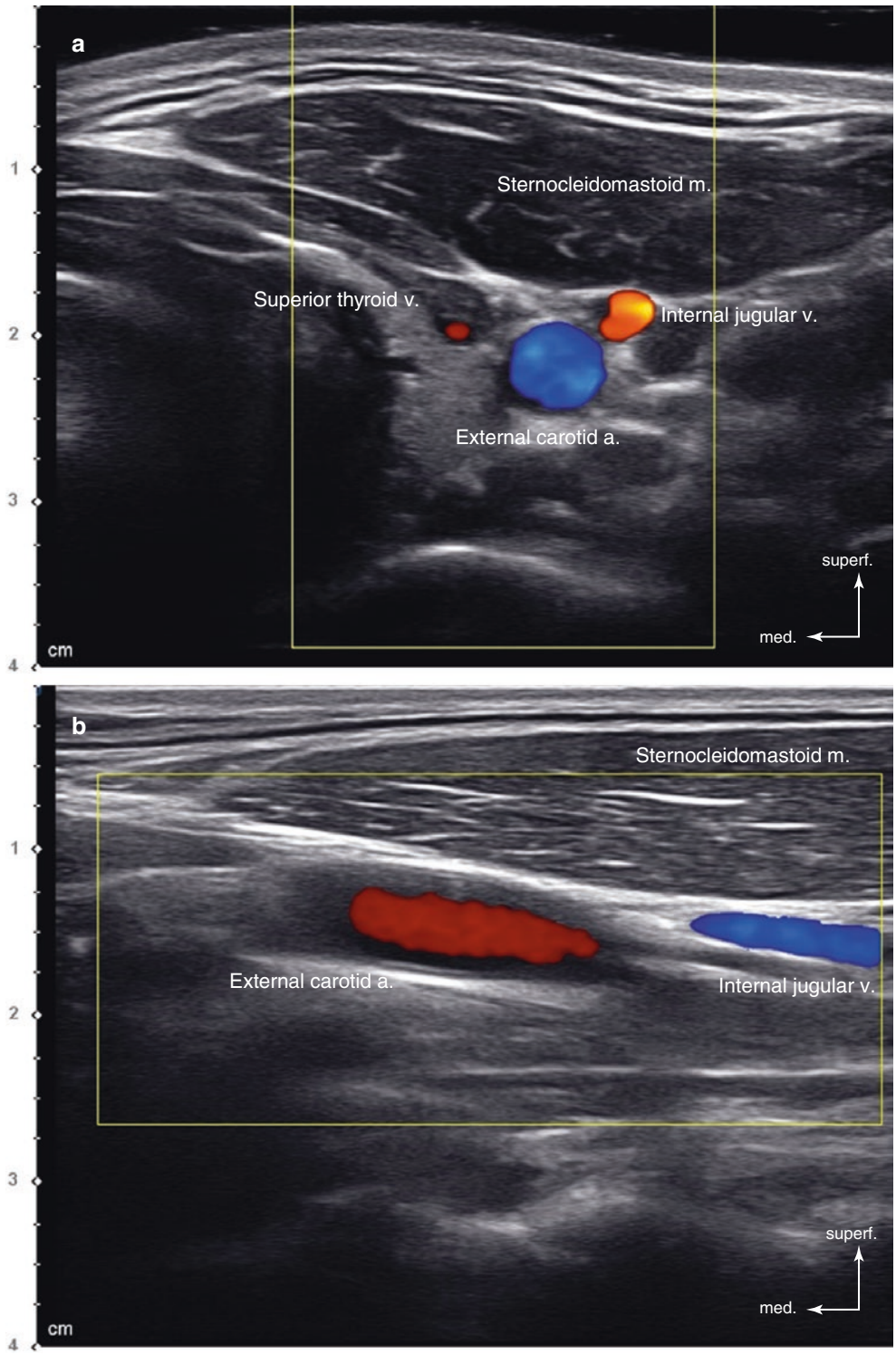

Fig. 1.10 The Doppler image of the carotid triangle. (**a**) Short-axis view and (**b**) long-axis view. (Published with kind permission of © Hee-Jin Kim 2020. All Rights Reserved)

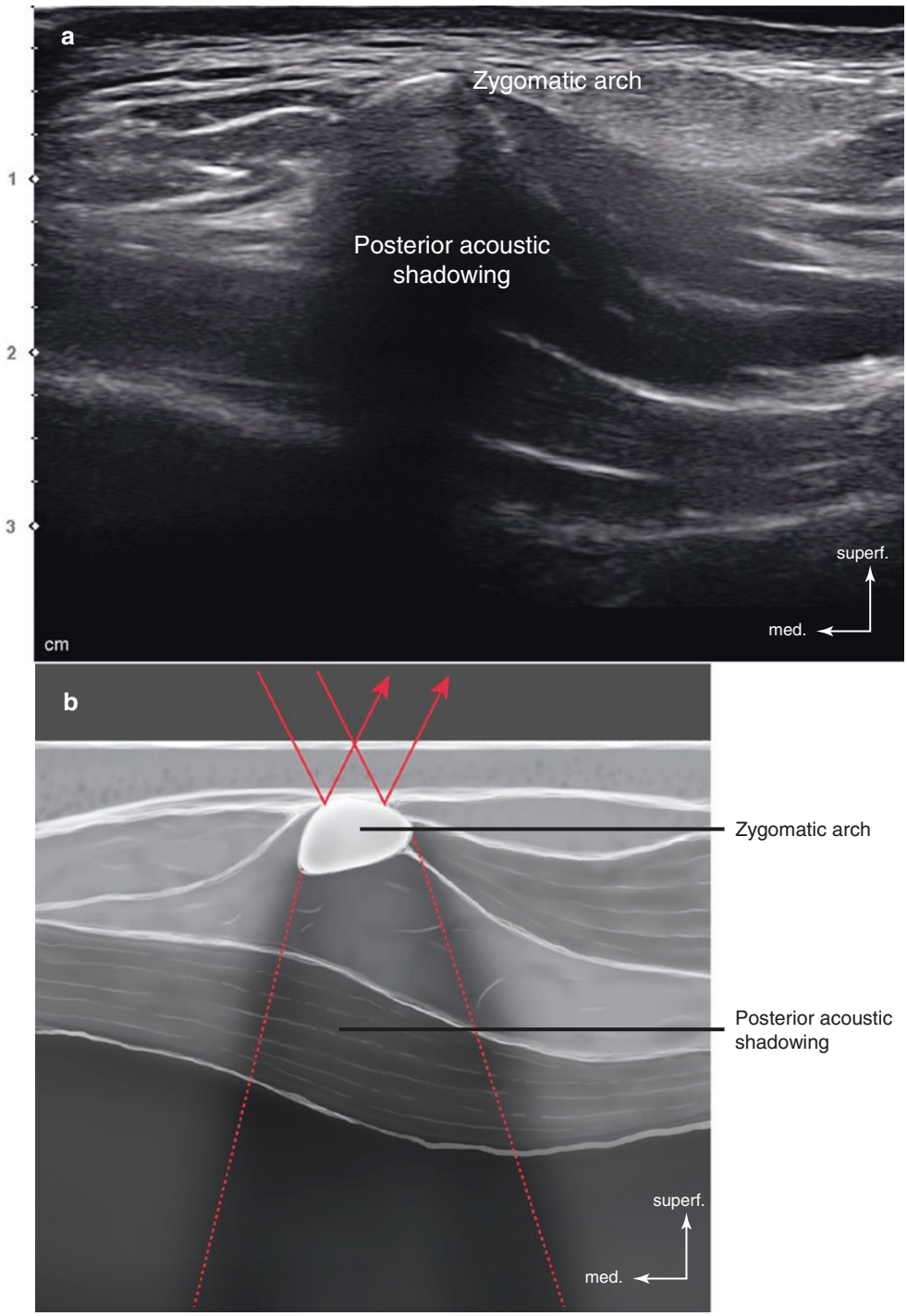

Fig. 1.11 Posterior acoustic shadowing. (**a**) Image of the zygomatic arch shows shadowing deep to the bone structure and (**b**) illustration representing the mechanism of the posterior acoustic shadowing. (Published with kind permission of © Hee-Jin Kim and Kwan-Hyun Youn 2020. All Rights Reserved)

1.1.5 Artifacts

An artifact or a false image in the US can manifest a nonexisting structure or hide an existing structure. This is because the location, size, or echo of the structure can distort the image. In some cases, the artifact can bring confusion to the interpretation of the results and change the diagnosis. Therefore, a comprehension of the artifacts produced by the physical and mechanical mechanisms of the US and adjustment of such artifacts to increase the image quality are required.

The following are some artifacts that may develop in the facial area during US.

1.1.5.1 Posterior Acoustic Shadowing

Shadow artifacts are formed due to either a nonechoic area near the bone or due to a calcified material, or high echo foreign bodies, which are all relatively bright (Fig. 1.11). Air bubbles may also produce a shadow artifact (Fig. 1.12).

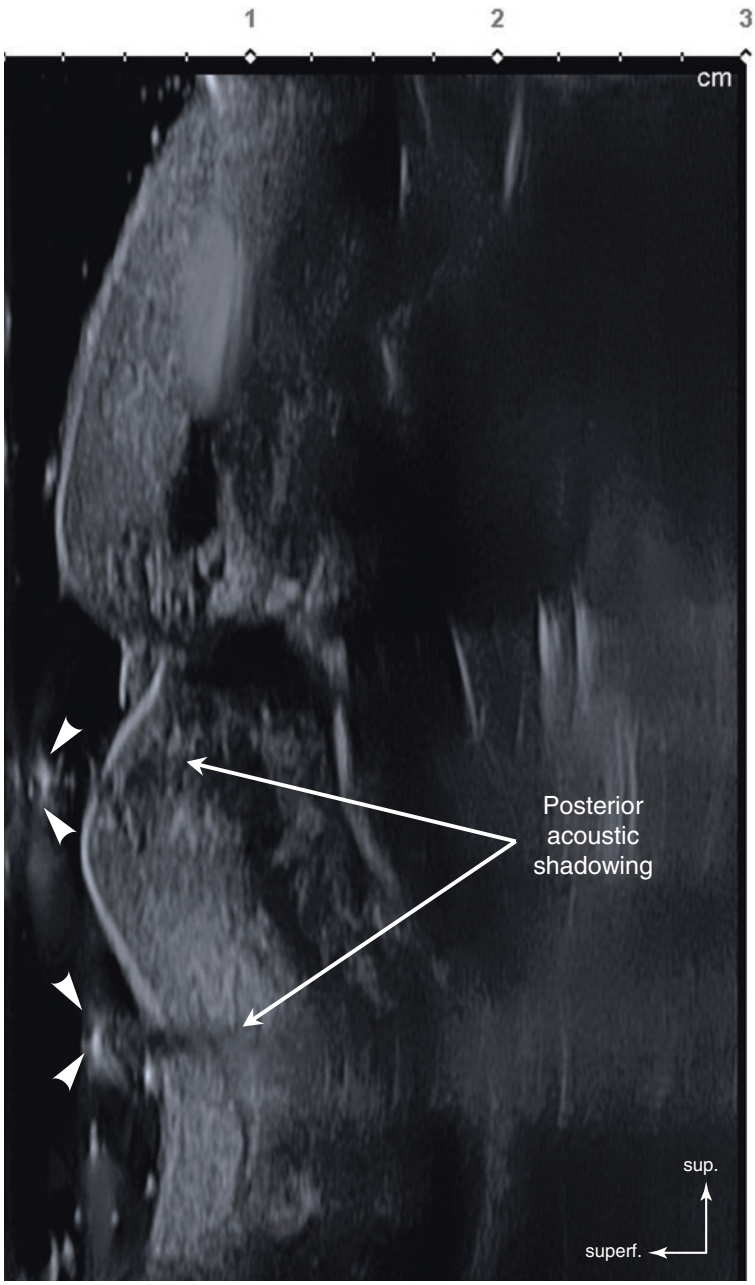

Fig. 1.12 Posterior acoustic shadowing (arrows) are formed by air bubbles (arrowheads) in the gel. (Published with kind permission of © Hee-Jin Kim 2020. All Rights Reserved)

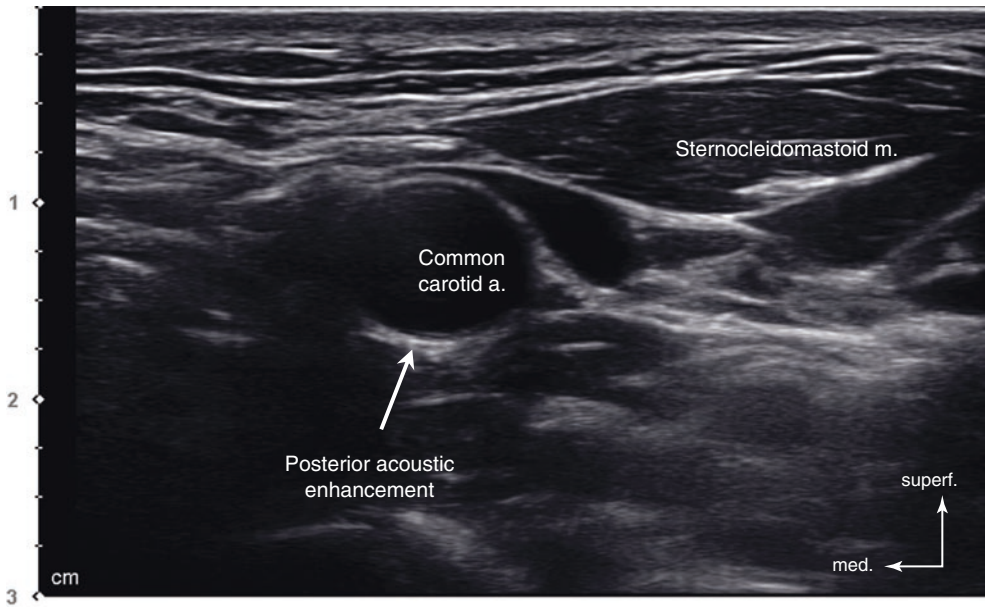

Fig. 1.13 Posterior acoustic enhancement. Image posterior to the common carotid artery shows the increased echogenicity (arrow). (Published with kind permission of © Hee-Jin Kim 2020. All Rights Reserved)

1.1.5.2 Posterior Acoustic Enhancement

This enhancement artifact is formed when the tissues appear hyperechoic relative to the upper adjacent fluid-filled structure. This can occur because of relatively less reflecting echoes from cysts, vessels, and solid soft tissue tumors (Fig. 1.13).

1.1.5.3 Reverberation Artifact

This artifact is made when vertically parallel structures reflect multiple echoes of uniform intervals, which can generally be seen in metallic needle tip reflections (Fig. 1.14).

1.1.5.4 Bayonet Artifact

The needle may also look bent due to the varying speed of ultrasound waves penetrating through different soft tissue such as muscle and adipose tissue.

1.2 Brightness Mode (B Mode)

The brightness mode (B mode) converts reflection echoes into bright dot images, which are utilized in most US diagnostic machines. The brightness of the dots is proportionate to the frequency of the reflected sounds. Anatomical structures and movement are digitalized in real time.

1.3 Doppler Effect Mode

The Doppler effect mode in US is used to find vessels in the body. The received US frequency changes when the transducer reflects echoes that have hit a moving structure such as blood. The differences between the transmitted US waves and received echoes are called frequency shift. The Doppler effect describes the change that occurs between the transducer and reflected structure. Higher frequency can be seen when the reflected structure is nearby. On the contrary, frequency decreases when further away from the transducer (Fig. 1.15).

There are several types of Doppler imaging. The color Doppler displays the vascular flow in red and blue. The vascular flow towards the transducer is in red and towards the opposite direction in blue. This color Doppler image is made by superimposition of the grayscale US images. Color saturation depicts the speed of the vascular flow and is brighter when the flow is faster and darker when the flow is slower. The spectral Doppler analyzes the periodic waveform and provides the quantitative data for vascular flow direction, speed, and amount (Fig. 1.16).

Fig. 1.17a represents anechoic vessels of the neck. The color Doppler represents vessels distinctively (Fig. 1.17b). Distinguishing artery and vein should be evaluated by the anatomical relationship, not by the color. If the anatomy of the targeted area is ambiguous, the compression technique can be used to differentiate between the collapsible vein and noncollapsible artery. The medially located artery is round and pulsatile while the laterally located vein is slightly distorted with no pulse (Fig. 1.17c).

The power Doppler mode presents all Doppler echoes as one uniform color regardless of its direction and speed. The power Doppler is more sensitive to smaller and lower flow vessels since all vascular flow data are reported. It has advantages in analyzing the inflammation and infectious lesions while detecting dilated small vessels. However, it cannot be used to measure the vascular flow and speed due to its high sensitivity (Fig. 1.18).

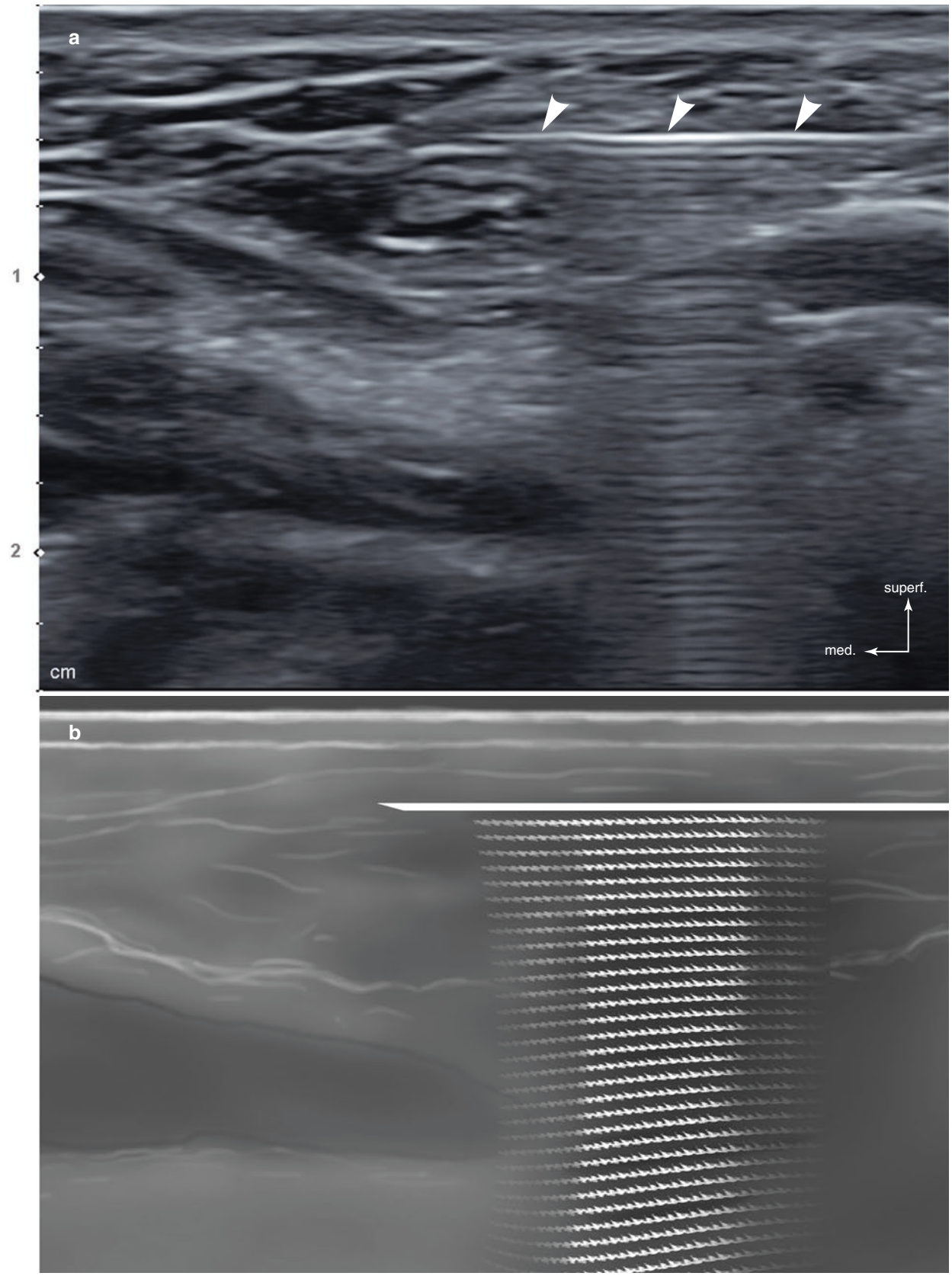

Fig. 1.14 Reverberation artifact. (**a**) Series of linear reflective echoes deep to the needle (arrowheads) are seen at subcutaneous tissue of the neck and (**b**) illustration representing the reverberation artifact.

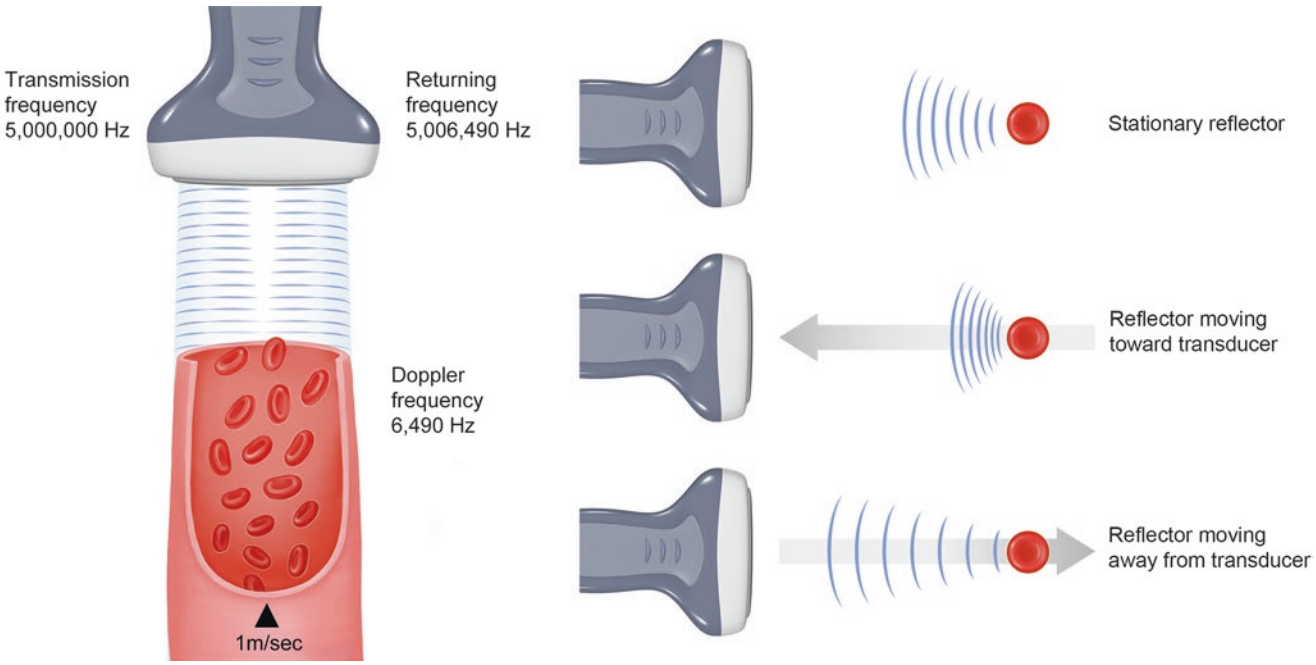

Fig. 1.15 Mechanism of Doppler effect. As the blood cell moves toward transducer, frequency of reflected ultrasound increases. On the contrary, frequency decreases as it moves away from transducer. (Published with kind permission of © Kwan-Hyun Youn 2020. All Rights Reserved)

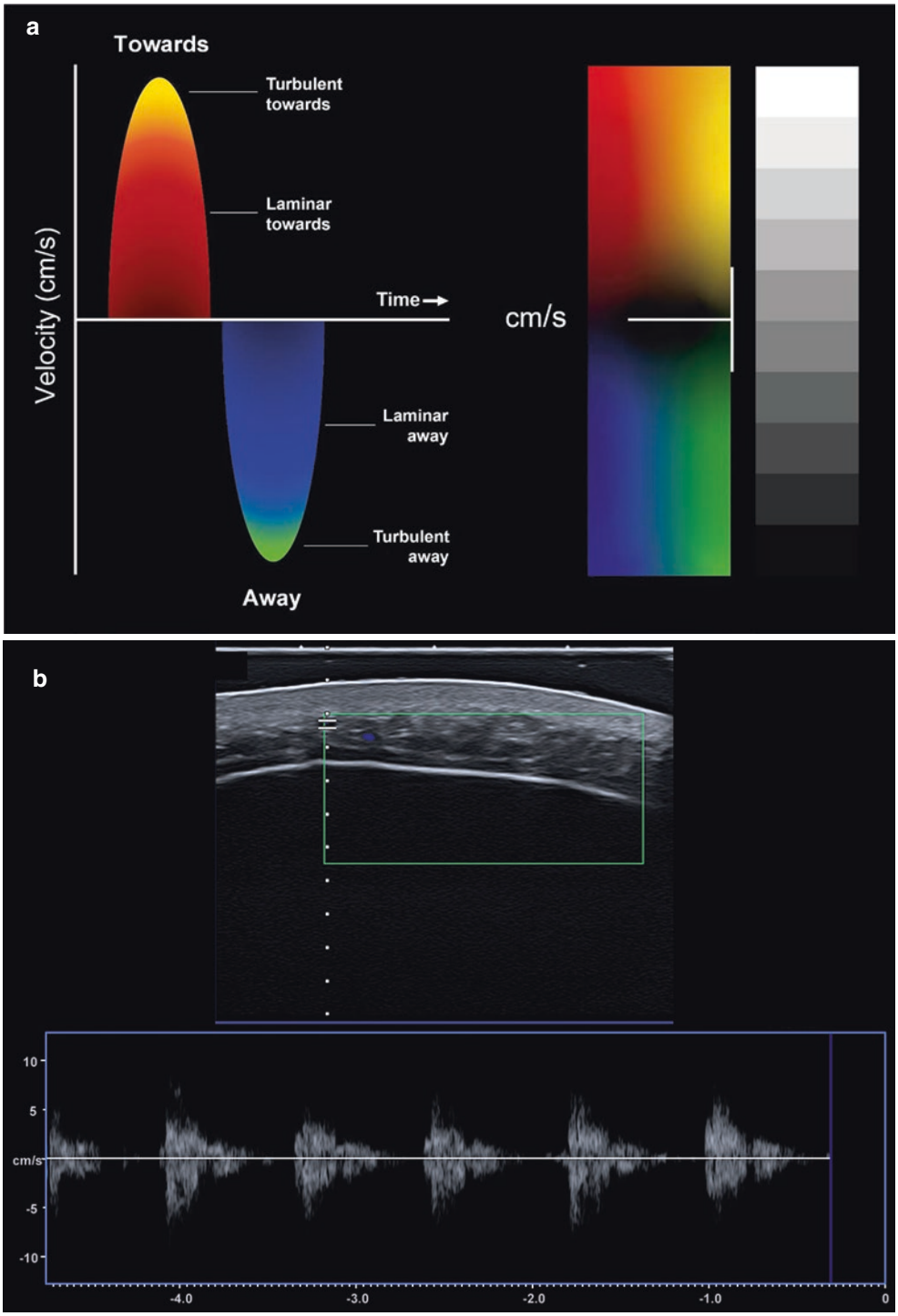

Fig. 1.16 Color and spectral Doppler. (**a**) Illustration of color Doppler and (**b**) artery in normal triphasic flow spectrum. (Published with kind permission of © Hee-Jin Kim and Kwan-Hyun Youn 2020. All Rights Reserved)

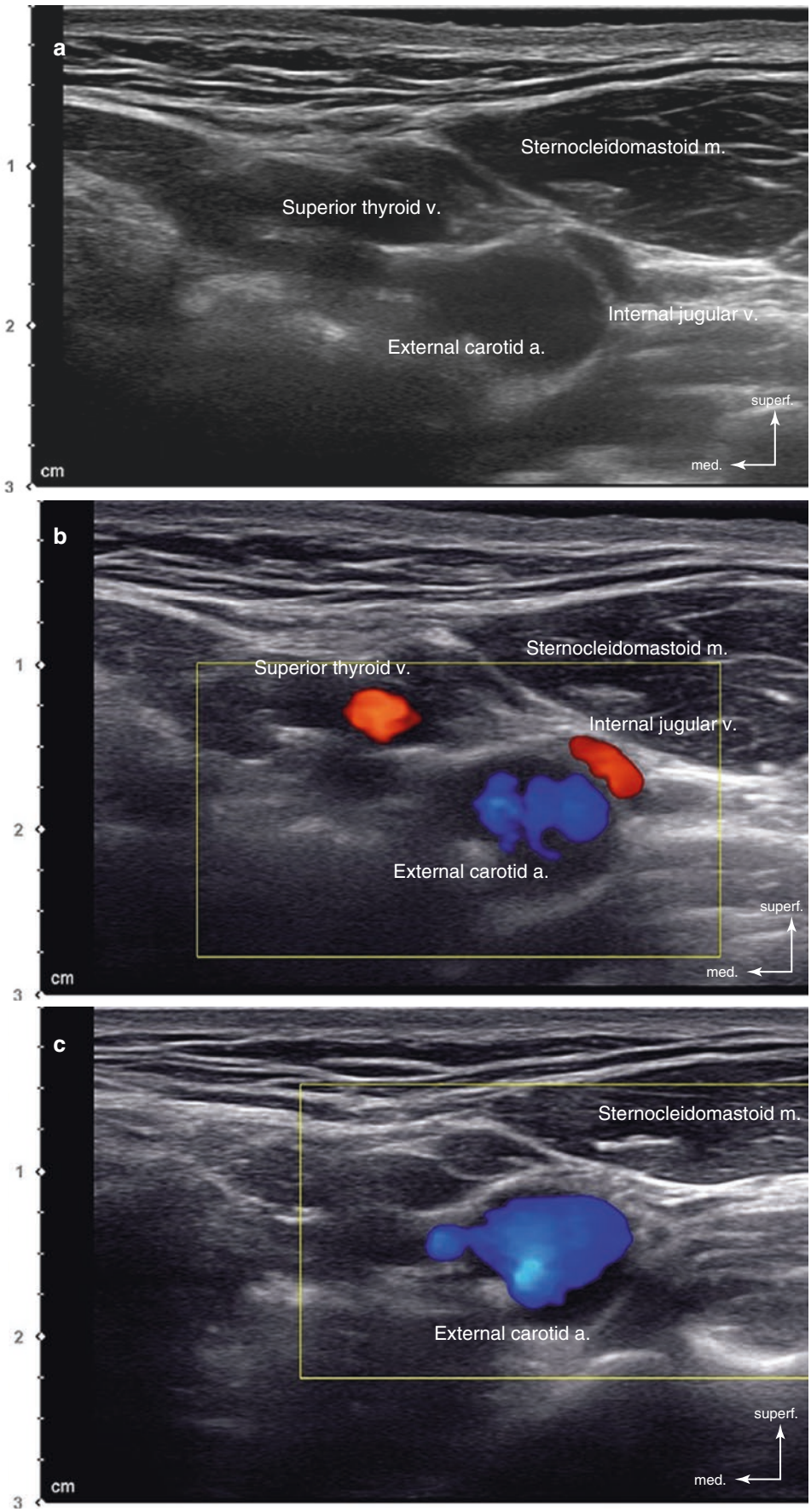

Fig. 1.17 Color Doppler used to locate vessels. (**a**) Ultrasonographic image of neck vessels without color Doppler, (**b**) easy to find facial vessels on a color Doppler image, and (**c**) vein is not seen on the subsequent image of the same region after transducer compression. (Published with kind permission of © Hee-Jin Kim 2020. All Rights Reserved)

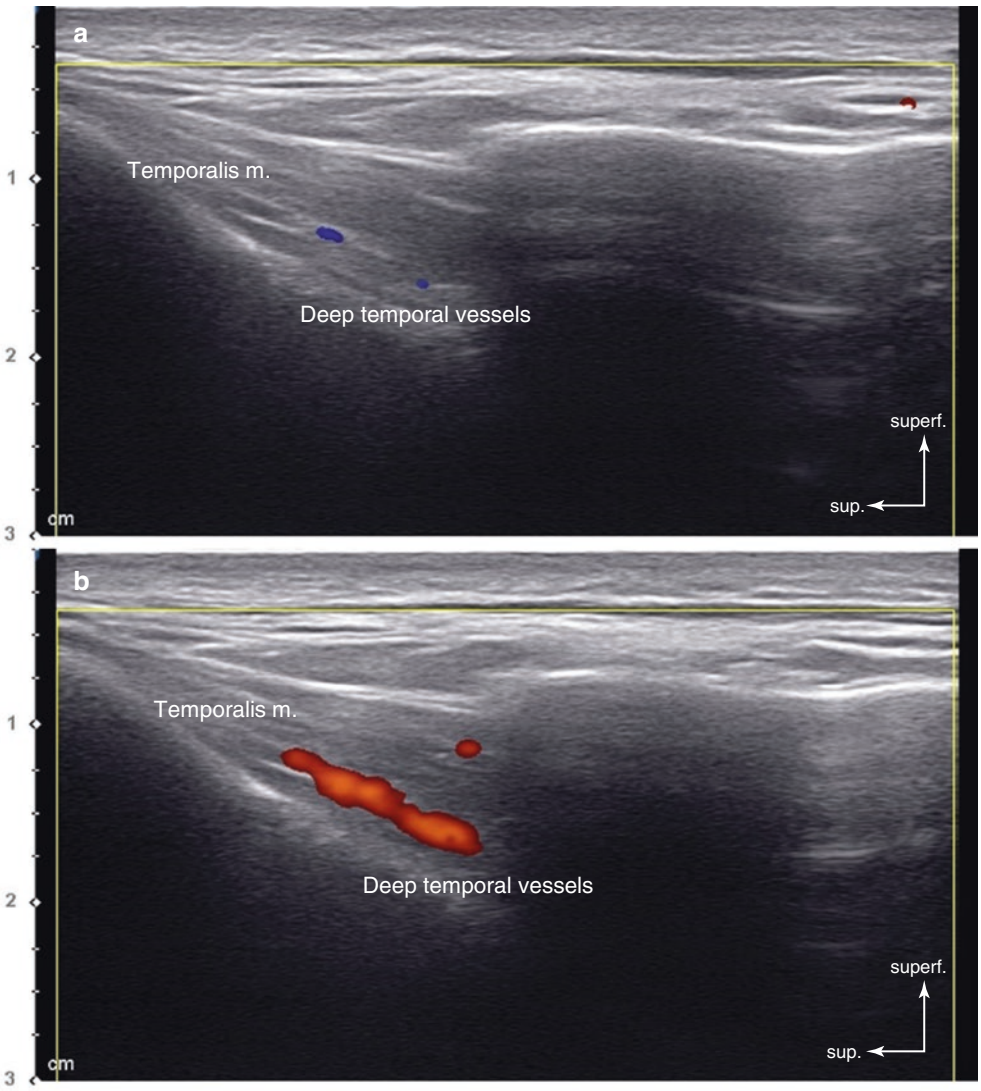

Fig. 1.18 Power Doppler image of deep temporal artery at the temple. (**a**) Color Doppler image and (**b**) power Doppler image. (Published with kind permission of © Hee-Jin Kim 2020. All Rights Reserved)

1.4 How to Start Minimally Invasive Aesthetic Procedures Using US

US in the face and neck area is effective in not only detecting the anatomical structures but also guiding minimally invasive aesthetic procedures such as botulinum toxin injection, filler injection, and thread lifting. Real-time US allows the practitioner to trace the needle tip and guide it to precisely inject in ideal locations.

1.4.1 US View

The needle should be placed in the middle half of the screen during the procedure. The needle will appear hyperechoic under US. The needle should be observed from both short- and long-axis views for accurate positioning. If the needle is placed parallel to the long-axis plane, an image of the needle can be observed. This plane of the image is easy to manipulate; however, the exact location of the needle tip is difficult to detect.

The short-axis view or the out-of-plane view rotates the transducer 90° from the long axis to find the needle tip. The needle tip shines like a bright star among the pitch dark sky. Tracing the needle from the proximal direction is beneficial in finding its precise location (Fig. 1.19).

1.4.2 Improving Needle Visualization

In most cases, the hyperechoic needle tip is obscure in the long-axis view. As previously mentioned, structures are clearly shown when the transducer is placed at 90°. Since the needle is generally inserted obliquely, the insonating angle gets out of

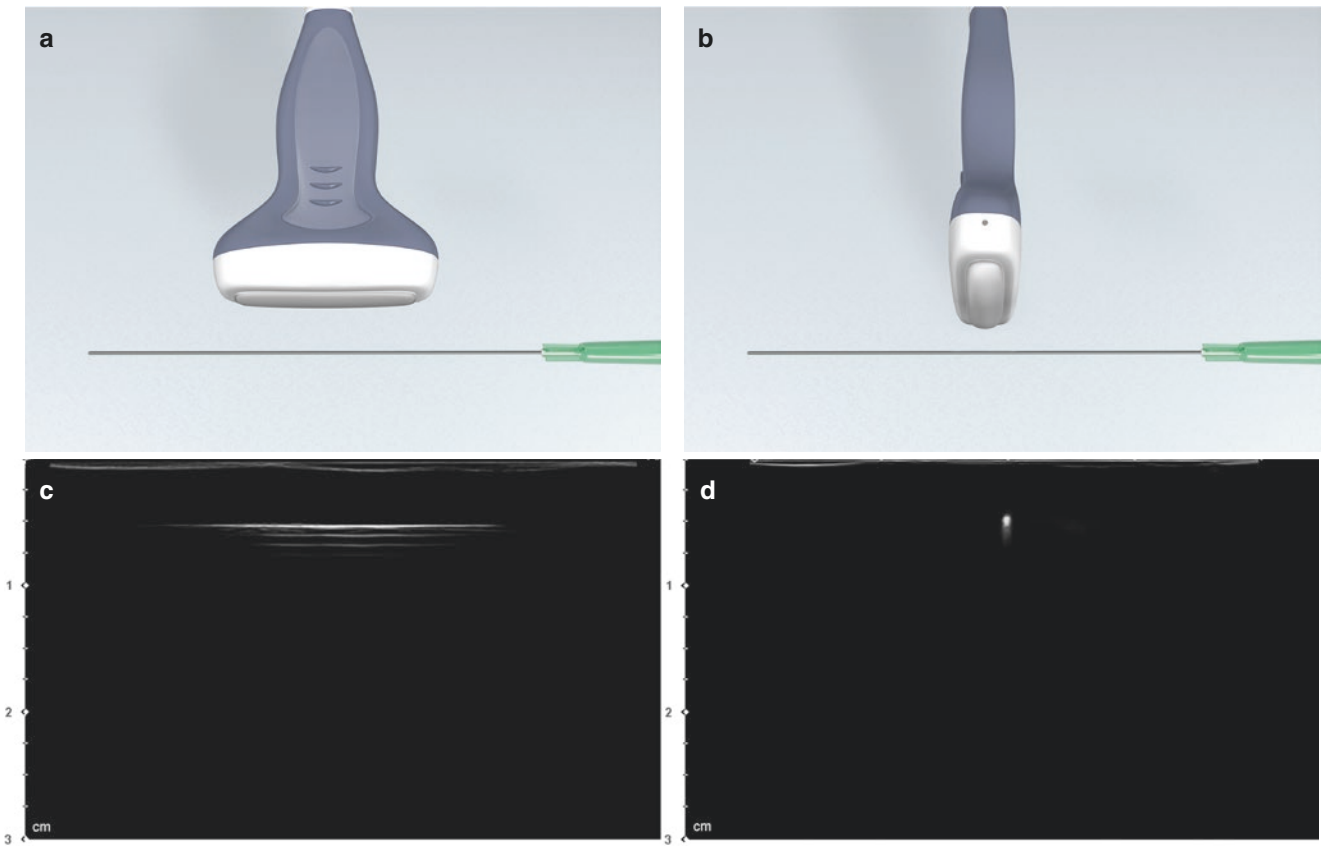

Fig. 1.19 Two views of ultrasound-guided injection. (**a**, **c**) Long-axis or in-plane view and (**b**, **d**) short-axis or out-of-plane view. (Published with kind permission of © Hee-Jin Kim and Kwan-Hyun Youn 2020. All Rights Reserved)

range as it progresses toward the distal needle and is presented as an ambiguous image. To reduce this phenomenon, the needle should be addressed in a parallel direction (Fig. 1.20).

There are several techniques to adjust the needle in the parallel direction. One technique is to apply a longer needle with an injection point further away from the targeted structure. It becomes difficult to locate a 90° insonating angle when the needle is inserted close to the transducer. Using a long needle would be helpful in facial aesthetic practices (Fig. 1.21).

In an out-of-plane view, while advancing the needle, dynamic tilting and sliding of the transducer is advantageous in forming a 90° insonating angle, thus easily tracking the needle tip (Fig. 1.22).

1.4.3 Practices of US-Guided Procedures

The practice of US-guided botulinum toxin injection will be discussed in depth in Chap. 8. For example, the temporalis m. can be palpated from the skin, but the definite borders are not evident. Distinguishing the muscle is difficult without bone touch through a deep vertical injection. Additionally, perforation of the periosteum can lead to postprocedural pain. US-guided injection can meticulously find the temporalis m. improving efficacy and reducing tissue damage (Fig. 1.23).

US-guided filler injection procedures are also applicable and efficient in clinical settings because it is difficult to precisely inject into the subcutaneous fat layer blindly. If the filler is injected too superficially, the skin will be lumpy, and if the injection is too deep, filler resorption is expedited. Injection into the exact layer will extend the longevity of the filler. The shape, distribution, and location of fillers are easily observed using US since fillers appear hypoechoic (Fig. 1.24). To resolve inadequately injected filler materials, US-guided injection of hyaluronidase is effective.

US can also be beneficial in thread lifting procedures. The ideal layer is just superior to the superficial musculoaponeurotic system (SMAS) layer. Even though the pinch technique is advantageous when inserting threading cannulas, it is challenging to exactly locate and maintain the threads in the desired layer. The threading cannula can be observed when using US, and we can minimize complications and maximize lifting efficacy by finding the preferred layer (Fig. 1.25).

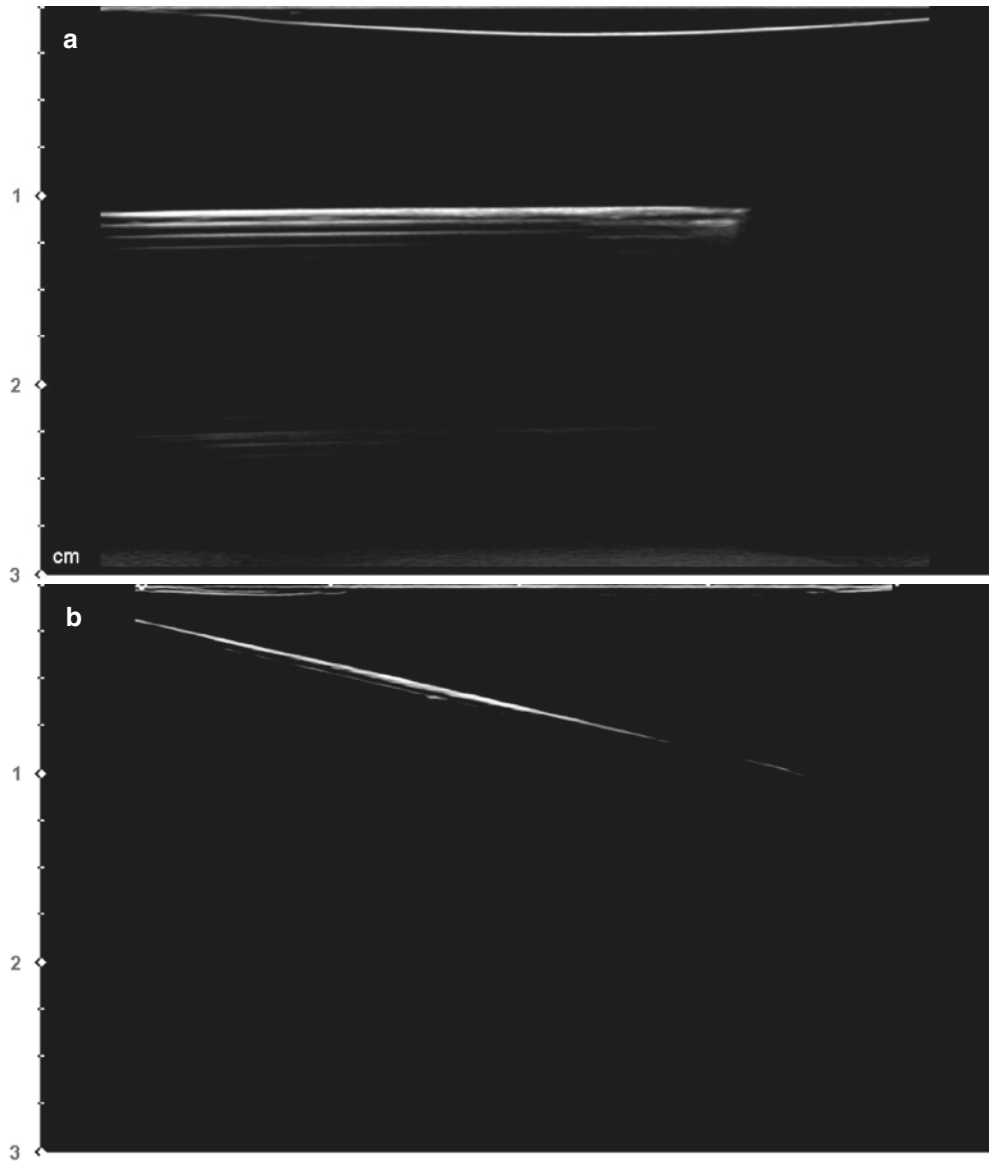

Fig. 1.20 Adequate ultrasonographic image of needle advancement. (**a**) Needle tip is clearly observed as the needle advances parallel to the surface of the transducer and (**b**) blurred needle tip as the needle advances in an oblique direction. (Published with kind permission of © Hee-Jin Kim 2020. All Rights Reserved)

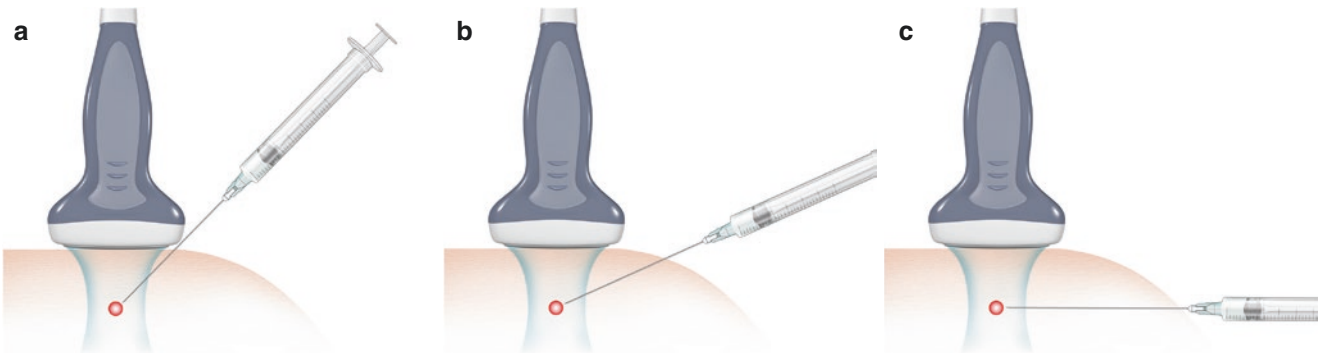

Fig. 1.21 Adequate needle advancement in the long-axis view. (**a**) Excessively low insonating angle, (**b**) low insonating angle, and (**c**) adequate insonating angle (nearly 90°). (Published with kind permission of © Kwan-Hyun Youn 2020. All Rights Reserved)

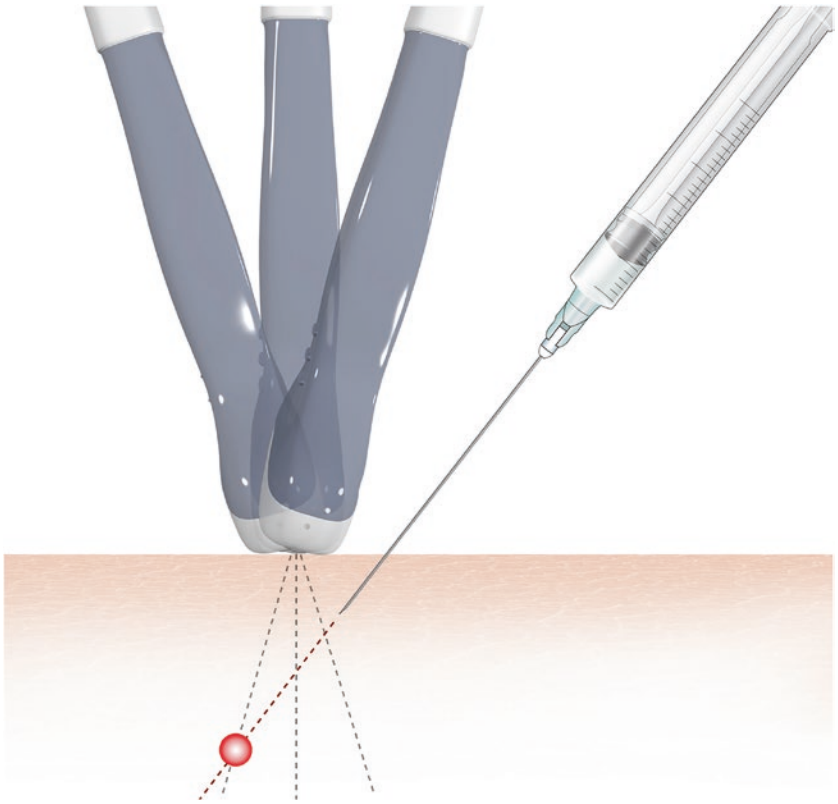

Fig. 1.22 Manipulation of the transducer in short-axis view for clear images. (Published with kind permission of © Kwan-Hyun Youn 2020. All Rights Reserved)

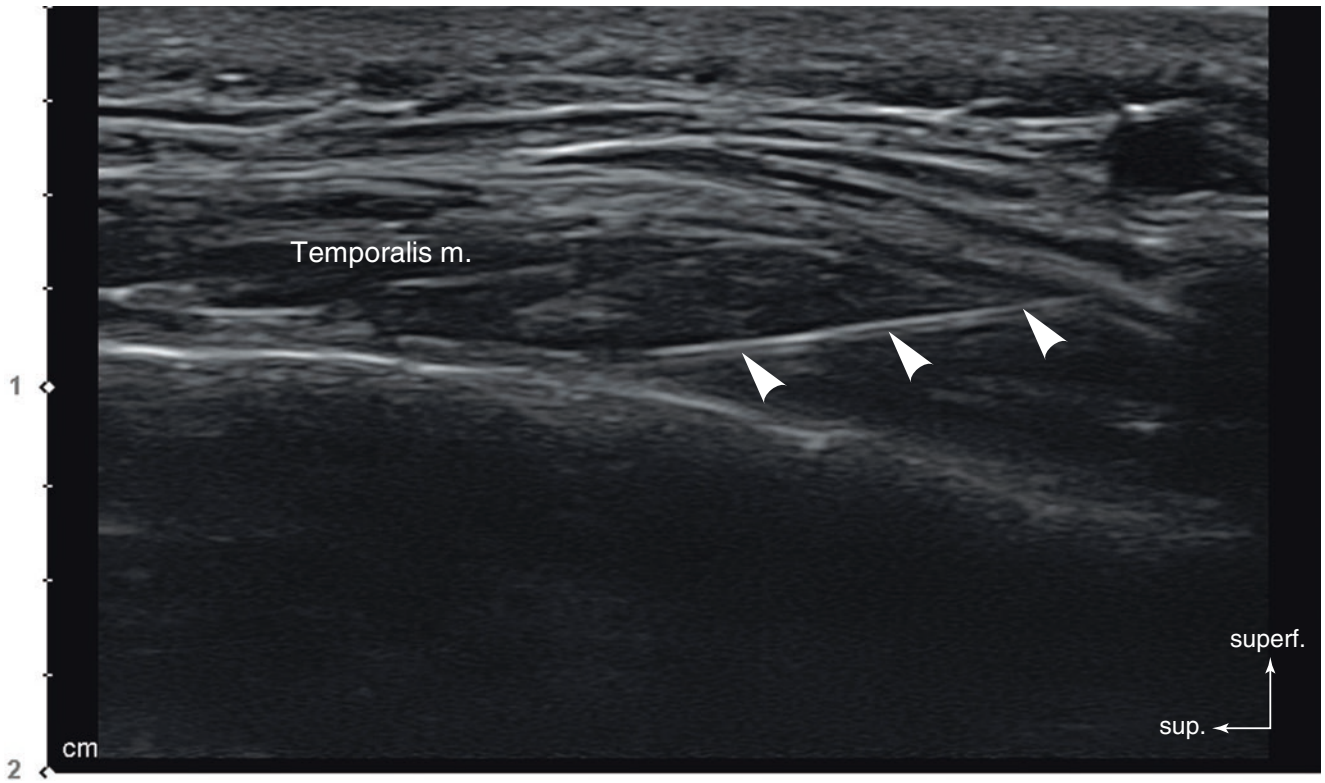

Fig. 1.23 Ultrasonography-guided botulinum toxin injection of the temporalis muscle (arrowheads: injection needle). (Published with kind permission of © Ji-Soo Kim 2020. All Rights Reserved)

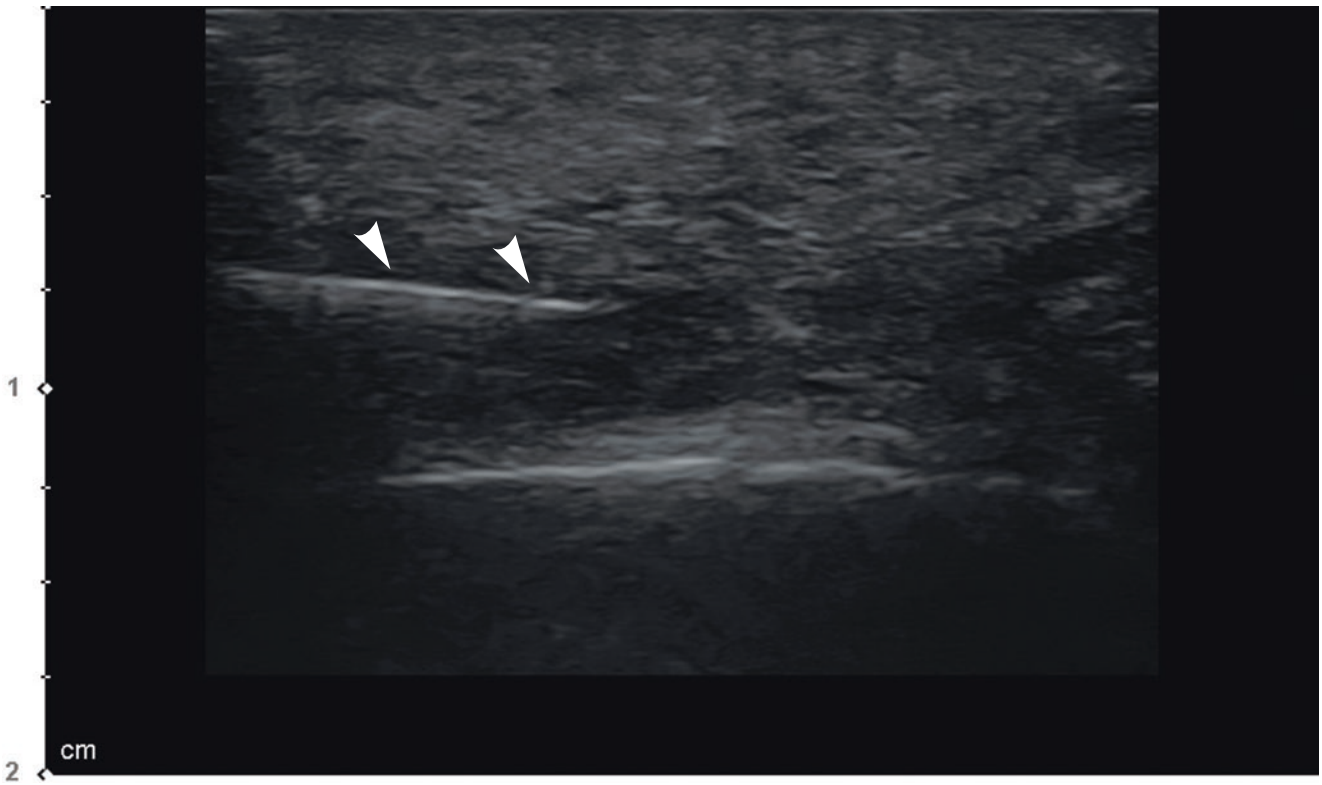

Fig. 1.24 Ultrasonography-guided filler injection of subcutaneous tissue in the chin (arrowheads: injection needle). (Published with kind permission of © Ji-Soo Kim 2020. All Rights Reserved)

Fig. 1.25 Ultrasonography-guided thread injection at the upper superficial cervical region (arrowheads: injection needle, arrows: thread). (Published with kind permission of © Ji-Soo Kim 2020. All Rights Reserved)

Bibliography

1. Antonakakis JG, Sites BL. The 5 most common ultrasound artifacts encountered during ultrasound-guided regional anesthesia. Int Anesthesiol Clin. 2011;49:52–66.
2. Boesen MI, Boesen M, Langberg H, et al. Musculoskeletal colour/power Doppler in sports medicine: image parameters, arifacts, image interpretation and therapy. Clin Exp Rheumatol. 2010;28:103–13.
3. Brull R, Macfarlane AJR, Cyrus CH. Practical knobology for ultrasound-guided regional anesthesia. Reg Anesth Pain Med. 2010;35:S68–73.
4. Feldman MK, Katyal S, Blackwood MS. US artifacts. Radiographics. 2009;29:1179–89.
5. Ihnatsenka B, Boezaart AP. Ultrasound basic understanding and learning the language. Int J Shoulder Surg. 2010;4:55–62.
6. Jacobson J. Fundamentals of musculoskeletal ultrasound. Philadelphia, PA: Elsevier Saunders; 2017.
7. O'Neill J. Musculoskeletal ultrasound anatomy and technique. New York, NY: Springer; 2008.
8. Scanlan KA. Sonographic artifacts and their origins. AJR Am J Roentgenol. 1991;156:1267–72.
9. Sites BD, Brull R, Chan VWS, Spence BC, et al. Artifacts and pitfall errors associated with ultrasound-guided regional anesthesia: Part I: Understanding the basic principles of ultrasound physics and machine operations. Reg Anesth Pain Med. 2007;32:412–8.
10. Sites BD, Brull R, Chan VWS, et al. Artifacts and pitfall errors associated with ultrasound-guided regional anesthesia: Part II: A pictorial approach to understanding and avoidance. Reg Anesth Pain Med. 2007;32:419–33.
11. Smith CF, Dilley A, Mitchell B, Drake R. Gray's surface anatomy and ultrasound: a foundation for clinical practice. Amsterdam: Elsevier; 2017.
12. Smith J, Finnoff JT. Diagnostic and interventional musculoskeletal ultrasound: Part 1. Fundamentals. J Inj Funct Rehabil. 2009;1:64–75.
13. Teh J. Applications of Doppler imaging in the musculoskeletal system. Curr Porbl Diagn Radiol. 2006;35:22–34.

General US Anatomy of the Face and Neck

2

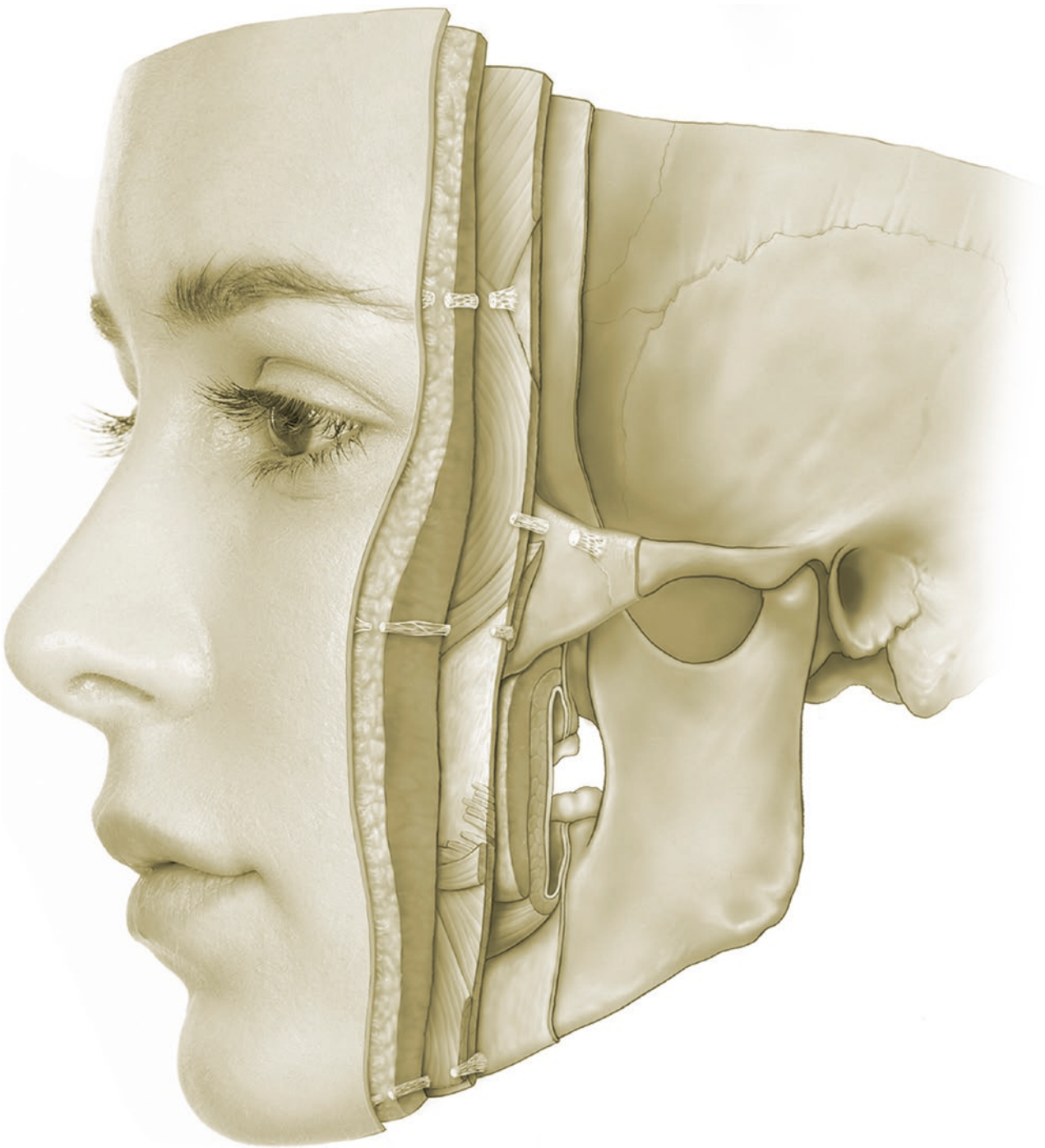

H.-J. Kim et al., *Ultrasonographic Anatomy of the Face and Neck for Minimally Invasive Procedures*,
https://doi.org/10.1007/978-981-15-6560-1_2

2.1 General Anatomy of the Face and Neck

2.1.1 Fascial Layer of the Face

The facial soft tissues can be divided into five layers: (1) skin, (2) subcutaneous layer, (3) superficial musculoaponeurotic system (SMAS), (4) retaining ligaments and spaces, and (5) periosteum and deep fascia (Fig. 2.1). The skin is the most superficial layer that moves freely over the loose areolar connective tissue layer. An exception is the skin in the auricle and nose ala area which is less elastic due to the connecting cartilage.

The subcutaneous layer lies deep to the skin, and the SMAS lies deep to the subcutaneous layer. The SMAS is composed of muscle fibers and superficial facial fascia connected to the facial m. The SMAS extends from the platysma m. in continuation with the superficial temporal fascia (i.e., temporoparietal fascia) extending to the galea aponeurotica. The SMAS consists of three distinct layers: (1) a fascial layer superficial to the muscles, (2) a layer intimately associated with the facial m., and (3) a deep layer extensively attached to the periosteum of facial bones (Fig. 2.2).

2.1.2 Muscles of the Face and Neck

The facial mm. lie beneath the skin or subcutaneous tissue attached to the facial skeleton and membranous superficial fascia. The topography of the facial m. varies by gender and even in individuals within the same sex. Facial mm. are extensively distributed in different regions of the face. The facial mm. are engaged in facial expressions such as sadness, anger, joy, fear, disgust, and surprise. Facial m. nomenclature is generally categorized according to its origin such as the forehead, the orbit, the nose, and other perioral regions. The platysma m. is mainly located in the neck region; however, it can also be considered a facial m. due to its involvement in perioral movement (Fig. 2.3).

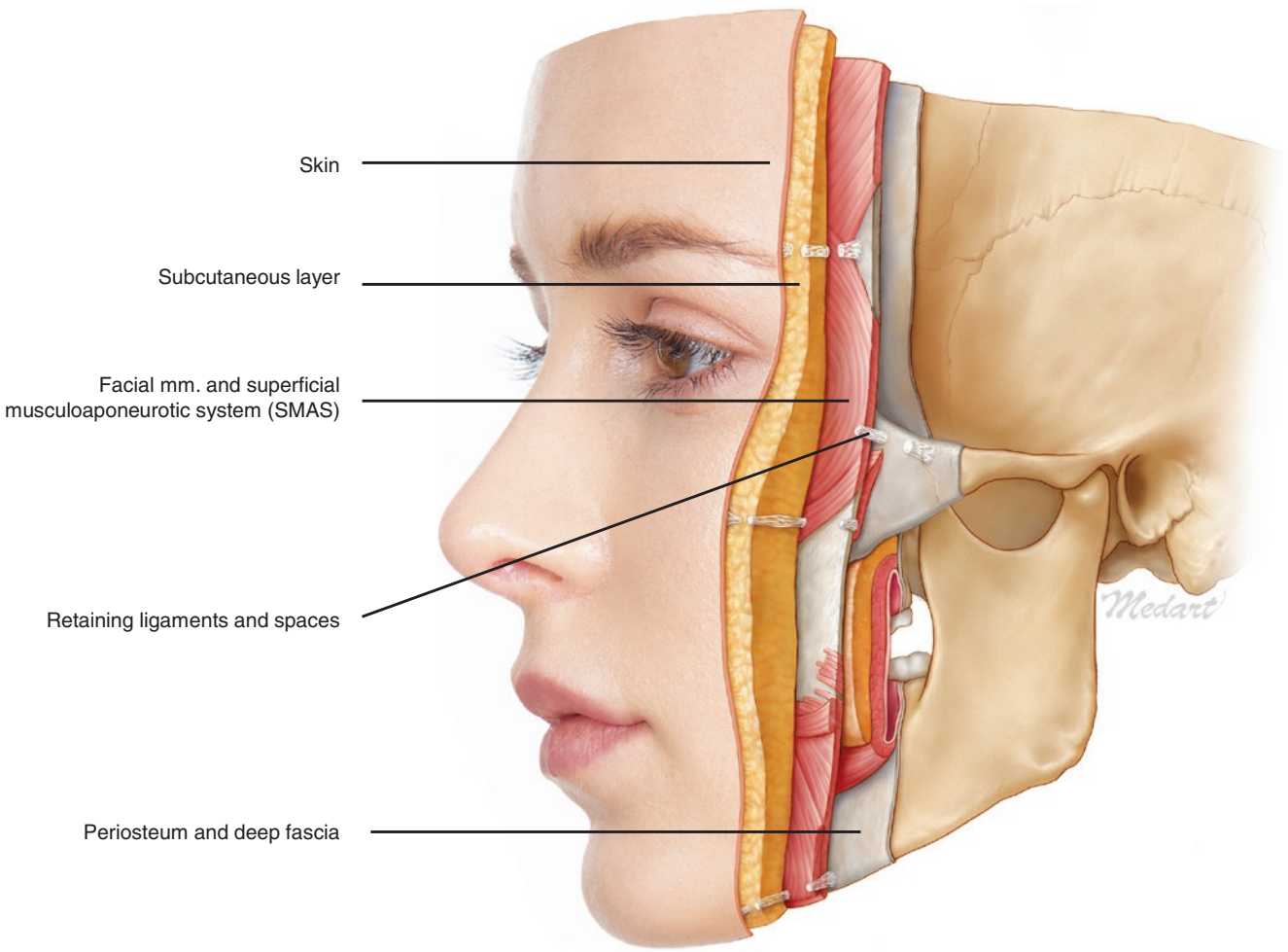

Fig. 2.1 Anatomical layers of the face. (Published with kind permission of © Kwan-Hyun Youn 2020. All Rights Reserved)

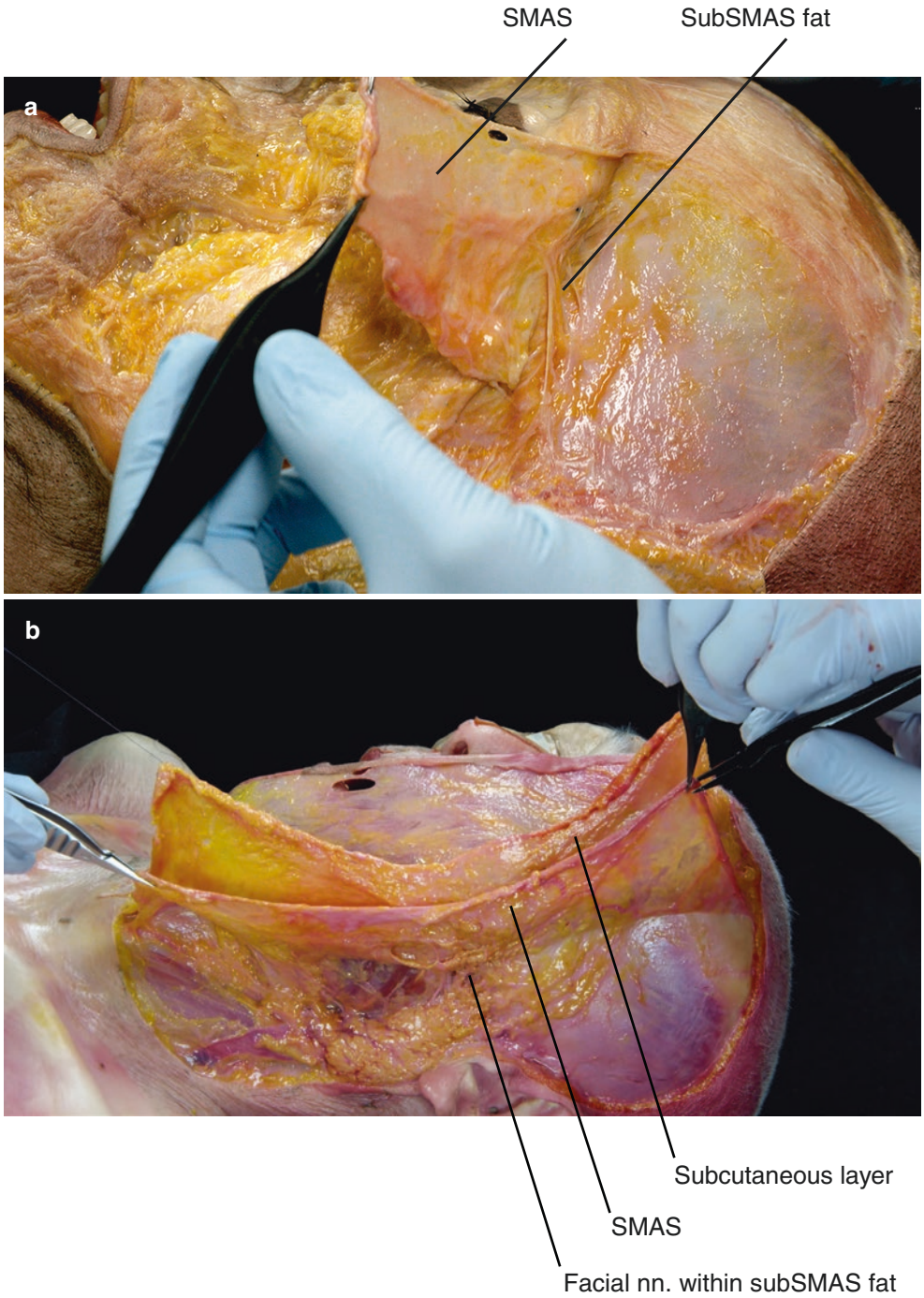

Fig. 2.2 Photographs showing the dissection of SMAS and subSMAS fat. (**a**) SMAS and subSMAS fat at the lateral aspect of the face and (**b**) subSMAS fat with facial nerve branches underneath SMAS. (Published with kind permission of © Hee-Jin Kim 2020. All Rights Reserved)

Masticatory mm. are comprised of the masseter, temporalis, and medial and lateral pterygoid mm. They are involved in jaw movement and aid in closing the mouth (temporalis, masseter, and medial pterygoid mm.), protruding the chin (temporalis and lateral pterygoid mm.), retracting the mandible (temporalis m.), and laterally excursing the mandible (Fig. 2.4).

The lateral pterygoid m. is the only masticatory muscle that assists in opening the mouth. The gravitational pull and some of the supra- (digastric, mylohyoid, geniohyoid mm.) and infrahyoid mm. facilitate this action (Fig. 2.5). Masseter m. is located at the external side of the mandibular ramus, and the temporalis m. lies within the temporal fossa, which inserts onto the coronoid process of the mandible. The

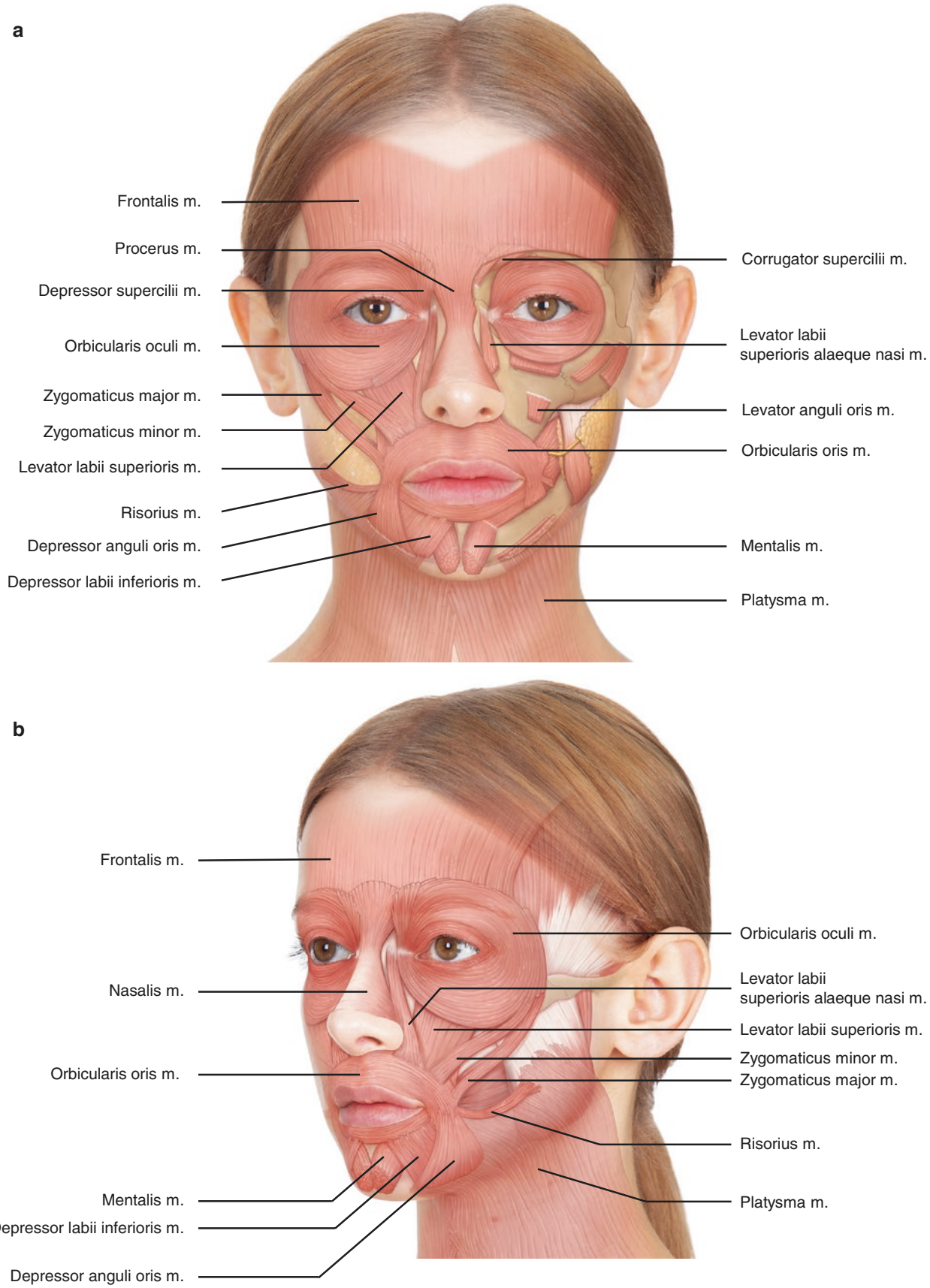

Fig. 2.3 Facial muscles. (**a**) Frontal view, (**b**) oblique view, and (**c**) lateral view. (Published with kind permission of © Kwan-Hyun Youn 2020. All Rights Reserved)

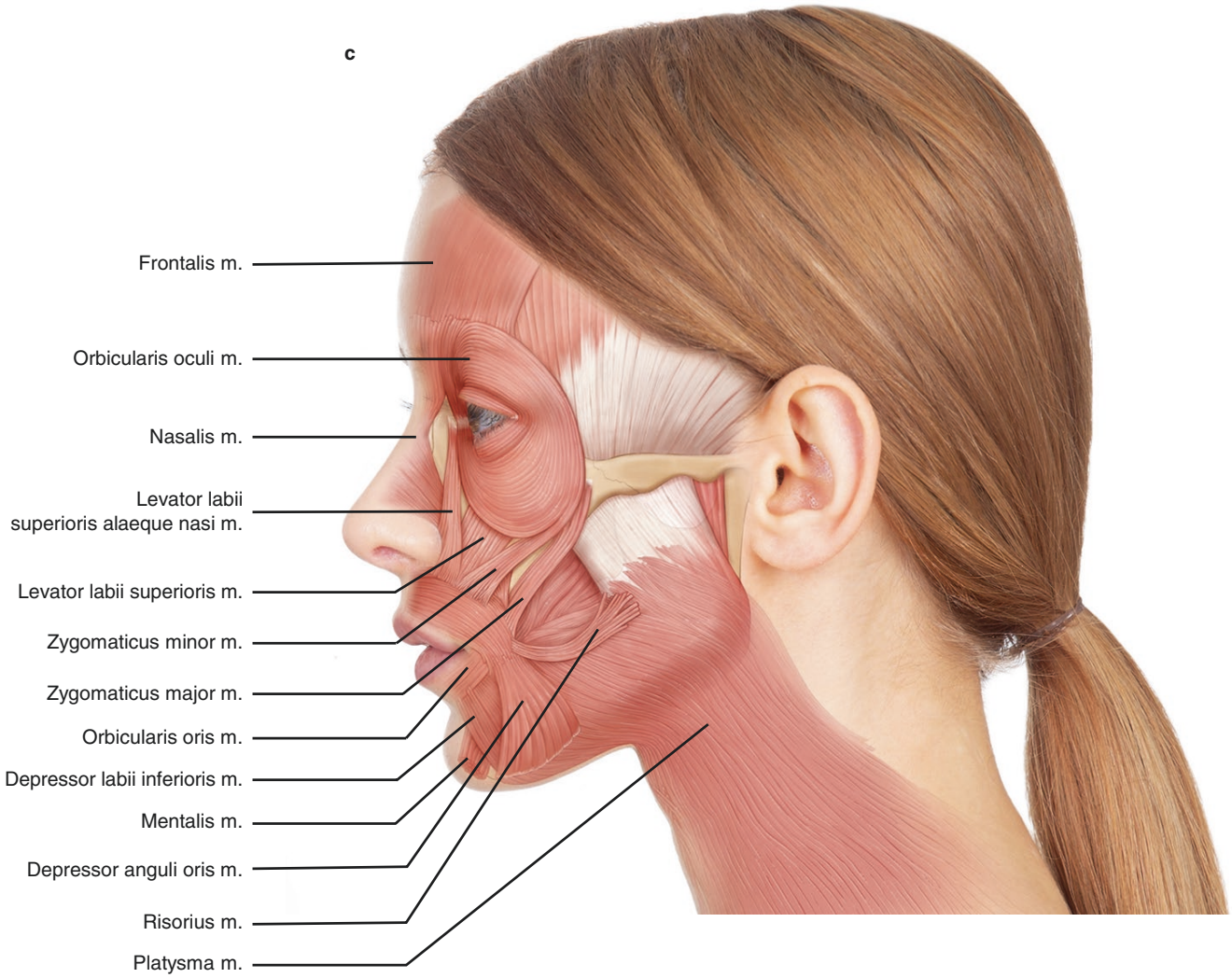

Fig. 2.3 (continued)

medial and lateral pterygoid mm. are in the medial side of the mandible and fill the space of the infratemporal fossa.

The platysma m. is a superficial muscle located within the subcutaneous layer of the neck. The platysma m. attaches to the inferior border of the mandible and mandibular septum, which merges with the lower perioral facial m. It consists of two types of fibers: (1) a flattened bundle passes superomedially to the lateral border of the depressor anguli oris m. and (2) the other remains deep into the depressor anguli oris m. and reappears at its medial border (Fig. 2.6).

The sternocleidomastoid m. is a large muscle that divides the neck into the anterior and posterior cervical triangles. The sternocleidomastoid m. has two heads; (1) a sternal head originating from the upper part of the manubrium of the sternum as a thick tendon and (2) a clavicular head originating from the medial 1/3 of the clavicle (Fig. 2.5). The two heads of the sternocleidomastoid m. gradually blend into a thick rounded strong tendon in the middle of the neck and inserts into the mastoid process and the lateral half of the superior nuchal line. In some cases, one or two accessory bellies may arise on the side of the clavicular head.

The suprahyoid mm. act in elevating the hyoid bone and the larynx. Four pairs of suprahyoid mm. are found above the hyoid bone level: digastric m. (anterior and posterior belly), stylohyoid m., mylohyoid m., and geniohyoid m. (Fig. 2.5). All suprahyoid mm. except the stylohyoid m. play a role in depressing the mandible when the hyoid bone is fixed and act during swallowing.

2.1.3 Vessels of the Face and Neck

Facial and neck blood vessels do not follow one specific pattern and have many variations. The common carotid a. is the main blood supply in the head and neck area. The common carotid a. divides into the internal and external carotid aa. at

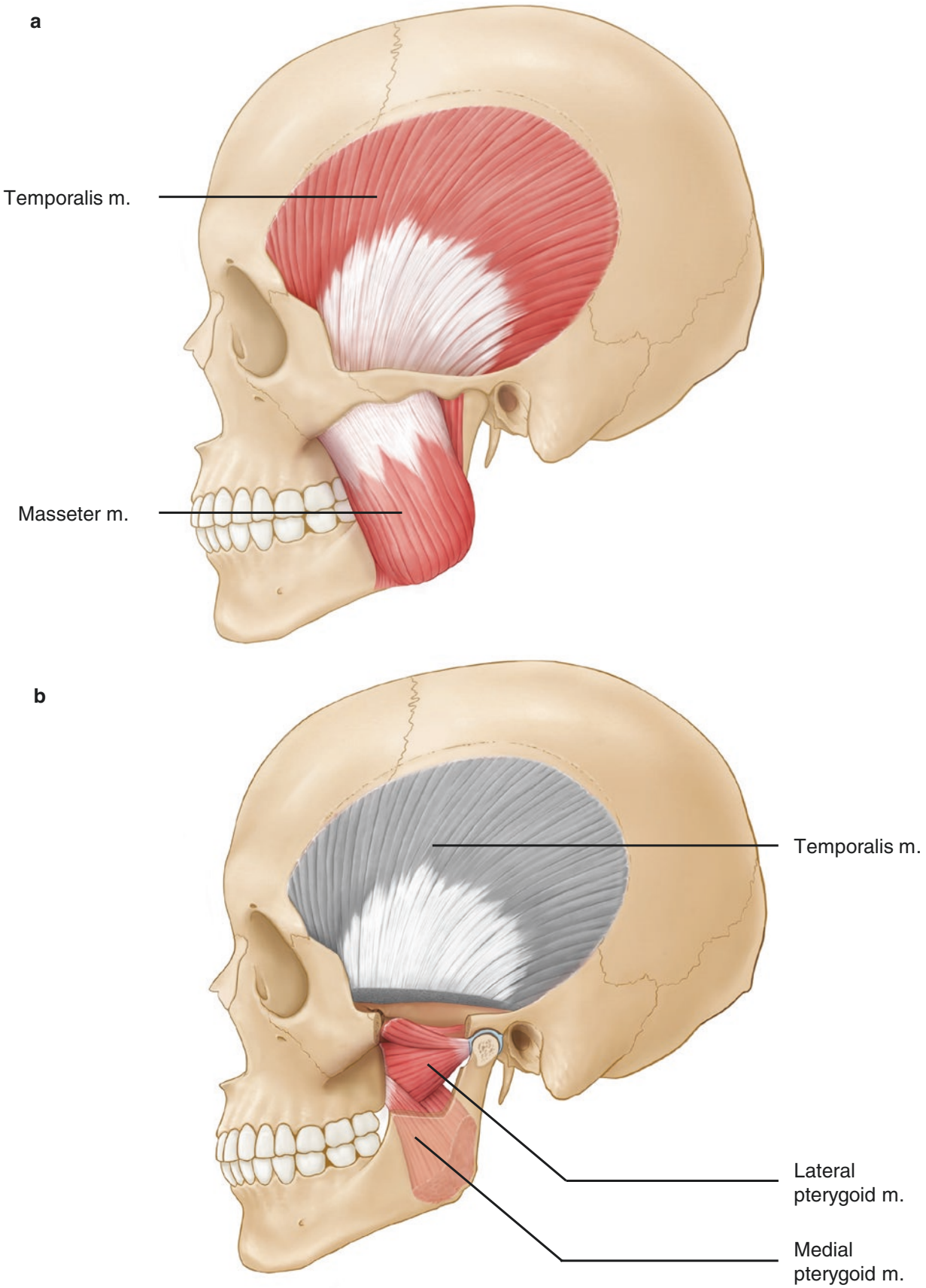

Fig. 2.4 Masticatory muscles. (**a**) Temporalis and masseter muscles and (**b**) medial and lateral pterygoid muscles. (Published with kind permission of © Kwan-Hyun Youn 2020. All Rights Reserved)

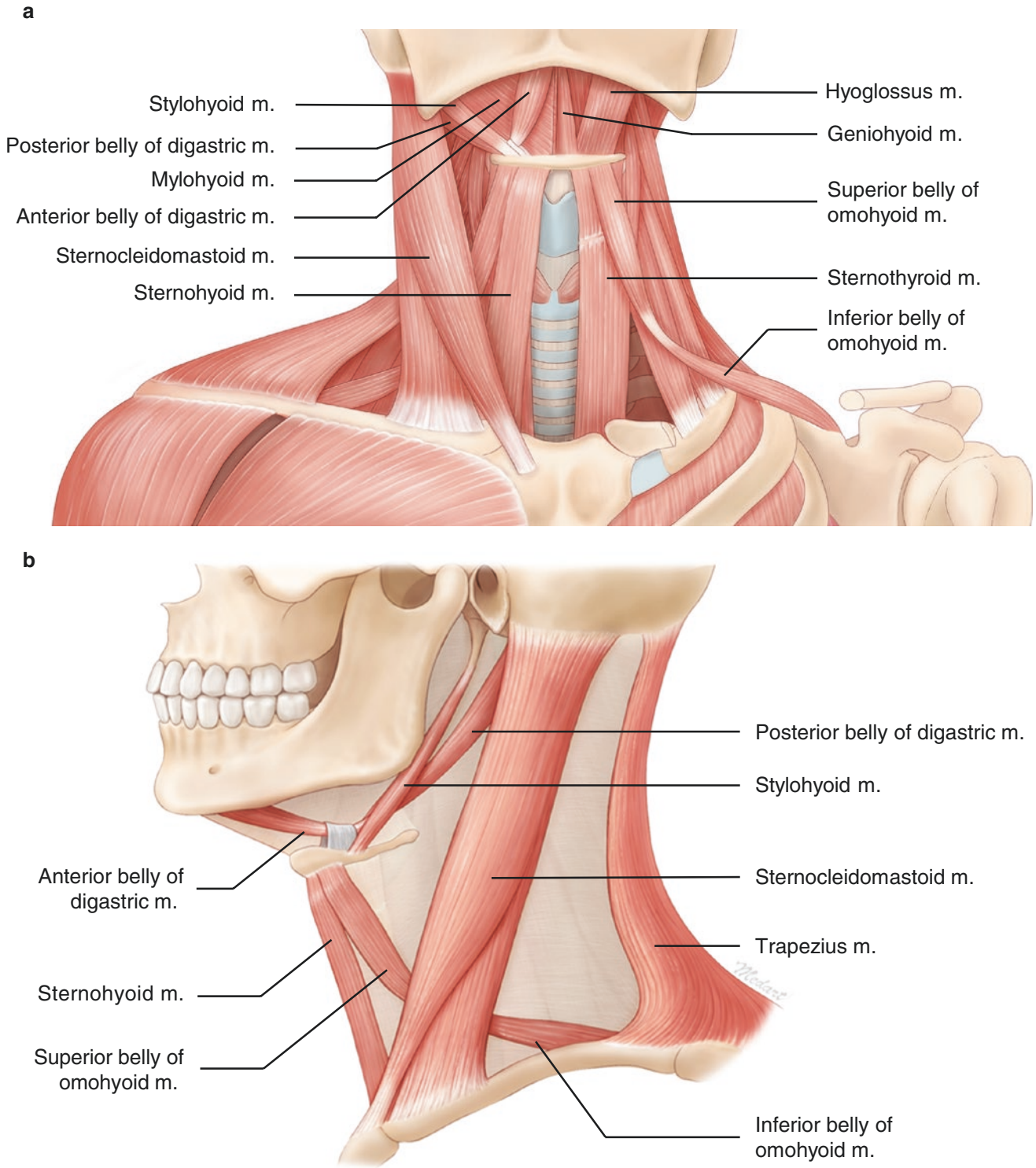

Fig. 2.5 Muscles of the neck. (**a**) Frontal view and (**b**) lateral view. (Published with kind permission of © Kwan-Hyun Youn 2020. All Rights Reserved)

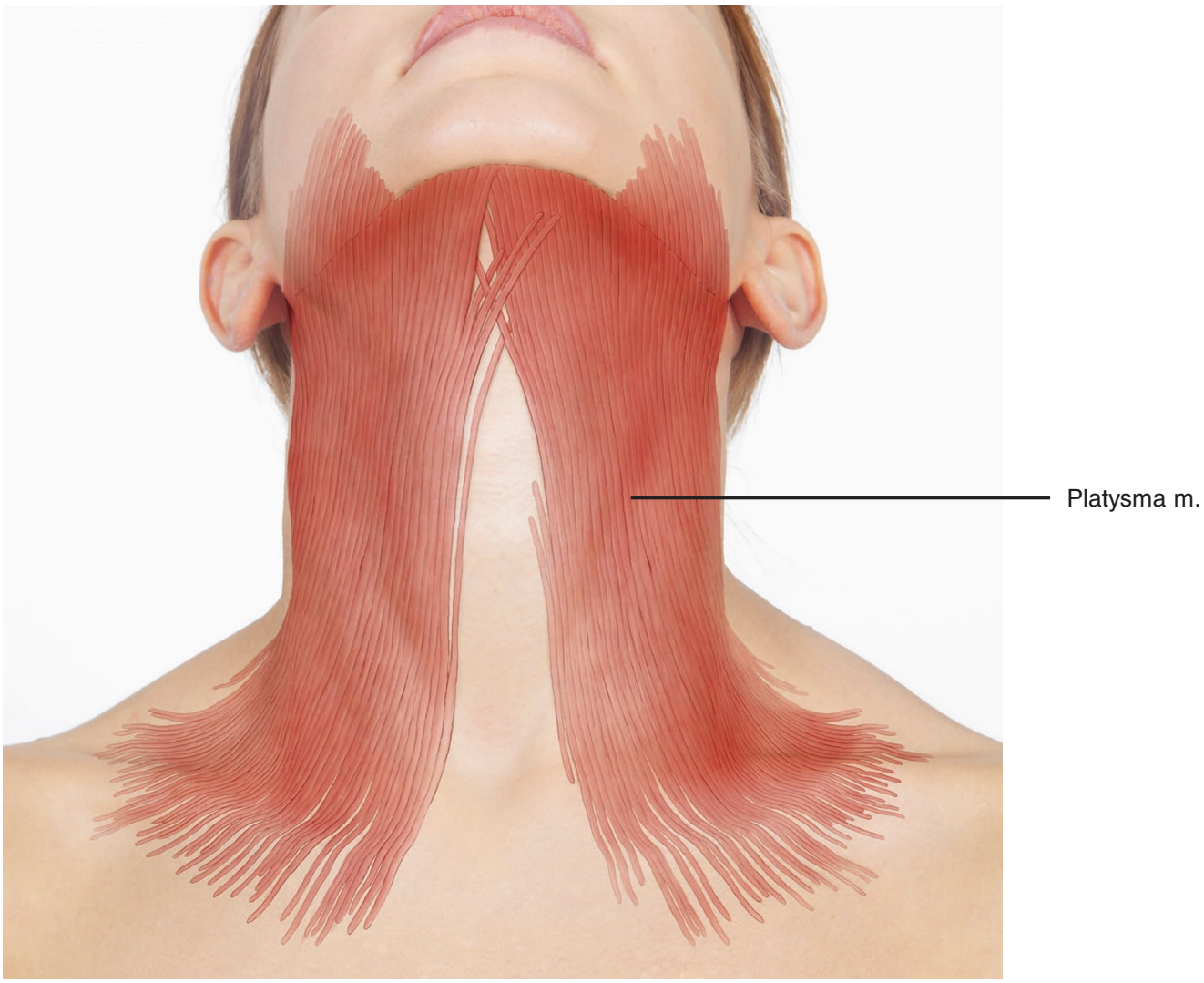

Fig. 2.6 Platysma muscle. (Published with kind permission of © Kwan-Hyun Youn 2020. All Rights Reserved)

the level of the superior border of the thyroid cartilage. At this level, the pulse of the common carotid a. can be felt when touching the anterior border of the sternocleidomastoid m. (Fig. 2.7).

The internal carotid a. and the external carotid a. contribute to facial blood supply. The internal carotid a. runs anteromedially through the carotid canal and enters the middle cranial fossa. The internal carotid a. supplies blood to the brain cerebrum, eye, orbit, and lacrimal gland from the superomedial side of the orbit. The external carotid a. lies anteriorly and medially to the internal carotid a. and divides into eight branches as it ascends.

The branches of the external carotid a. (facial a., superficial temporal a., and facial branches of the maxillary a.) and the internal carotid a. (supraorbital a. branching from the ophthalmic a., supratrochlear a., and infratrochlear a.) supply blood to the superficial layer of the skin (Figs. 2.8 and 2.9).

The facial v. follows the same distribution pattern as the facial a. However, the facial v. has more variation in its distribution pattern and runs deeper than the facial a. Veins of the forehead, the scalp, and the upper eyelid run to the superior ophthalmic v. of the orbit. The veins of the upper lip, the lateral side of the nose, and the lower eyelid run

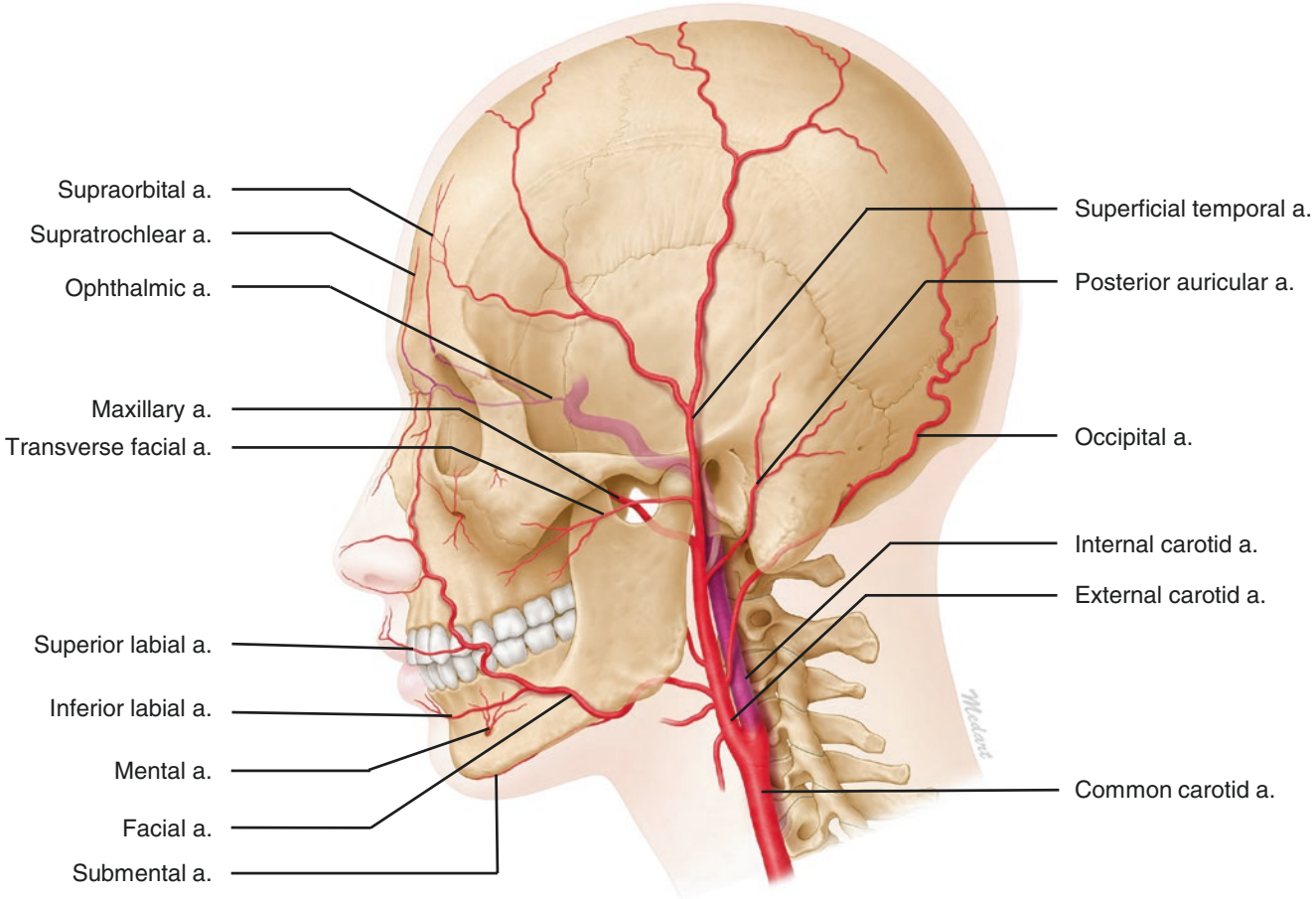

Fig. 2.7 External and internal carotid arterial system and their branches. (Published with kind permission of © Kwan-Hyun Youn 2020. All Rights Reserved)

through the infraorbital v. to the infratemporal region and the pterygoid plexus (Figs. 2.8 and 2.9).

2.1.4 Nerves of the Face and Their Distribution

The facial n. and the trigeminal n. are major cranial nerves distributed in the face. The trigeminal n. consists of three parts: the ophthalmic n., the maxillary n., and the mandibular n. The trigeminal n. runs out from the skull foramina and branches facial sensory nn. (Fig. 2.10).

The facial n. has one nerve trunk that comes out from the stylomastoid foramen and branches into two divisions (temporofacial and cervicofacial divisions) within the parotid gland. They branch into five separate nerve bundles transmitting motor impulses to specific facial mm. (Fig. 2.11).

2.1.4.1 Distribution of the Sensory Nerve

- Supraorbital n., supratrochlear n. (ophthalmic n.): forehead, glabellar region
- Infratrochlear n. (ophthalmic n.): glabella, radix
- Infraorbital n. (maxillary n.): external nose, nasal septum, lower eyelid, upper lip
- Buccal n. (mandibular n.): cheek, cheilion
- Mental n. (mandibular n.): lower lip, mentum, cheilion

2.1.4.2 Distribution of the Motor Nerve

The facial n., which transmits the motor impulse to facial and neck muscles, consists of five branches: temporal, zygo-

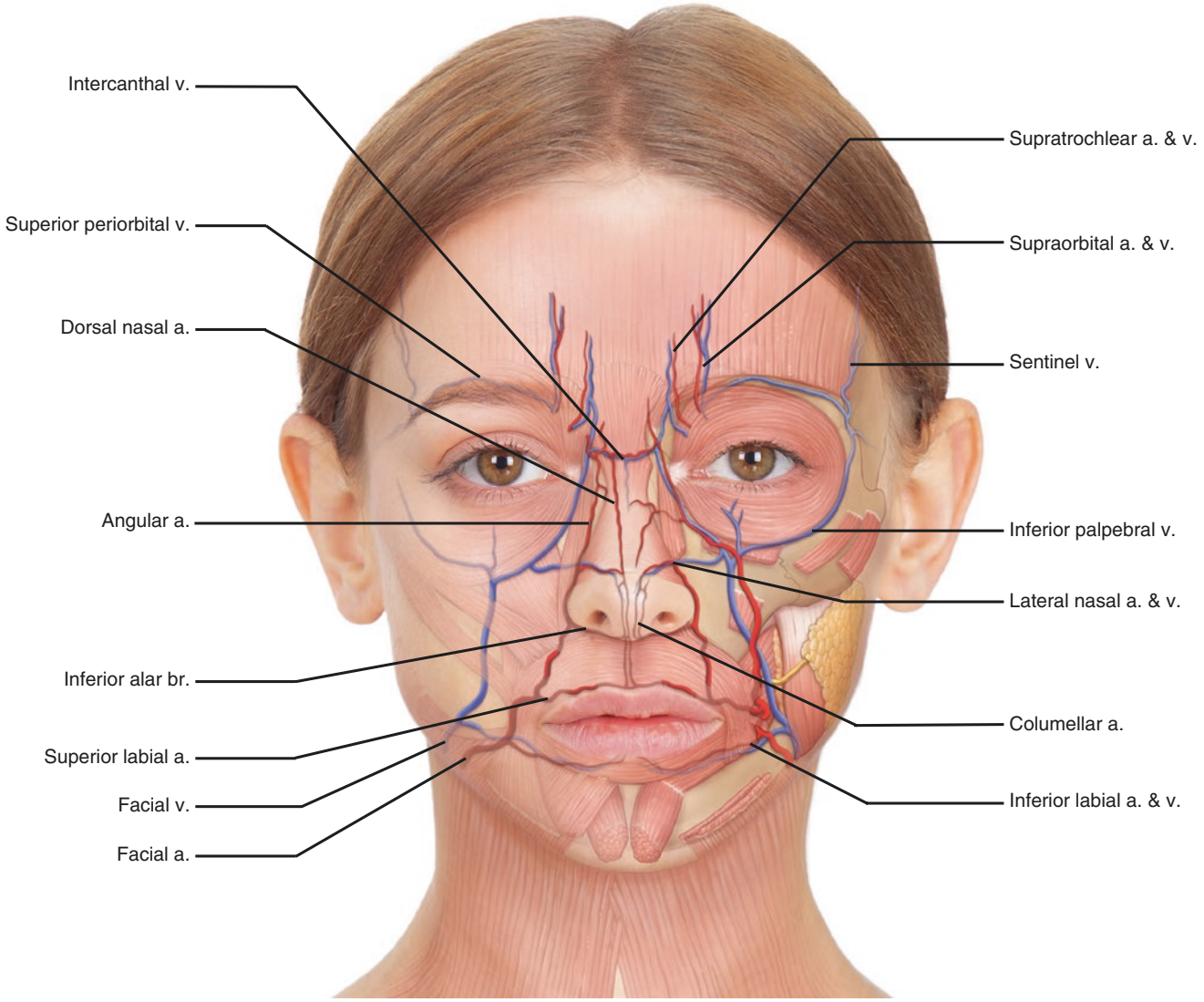

Fig. 2.8 General courses and locations of the arteries and veins on the face. (Published with kind permission of © Kwan-Hyun Youn 2020. All Rights Reserved)

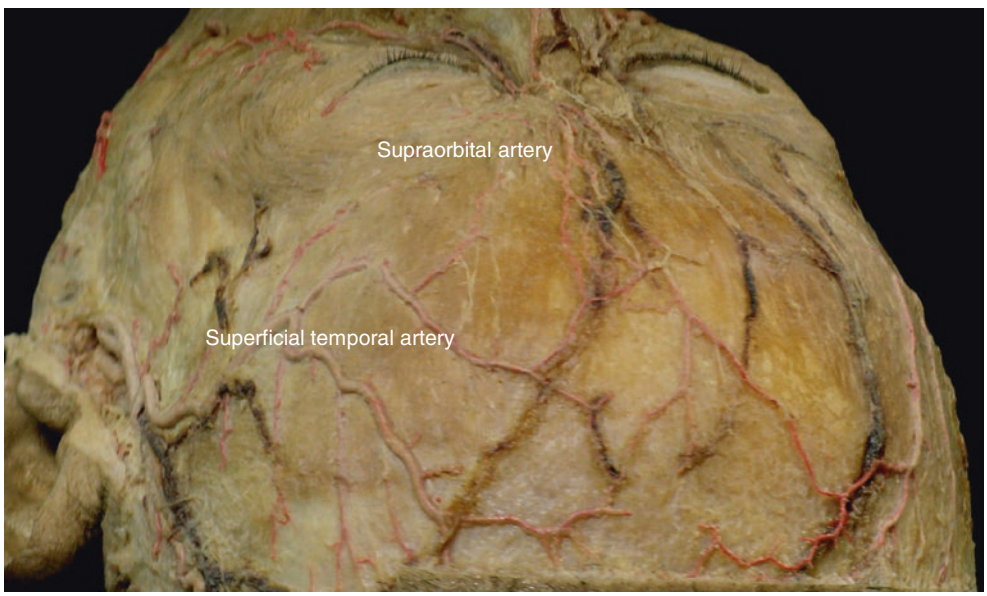

Fig. 2.9 Vascular distribution of the ophthalmic and superficial temporal artery on the forehead and temple. (Published with kind permission of © Hee-Jin Kim 2020. All Rights Reserved)

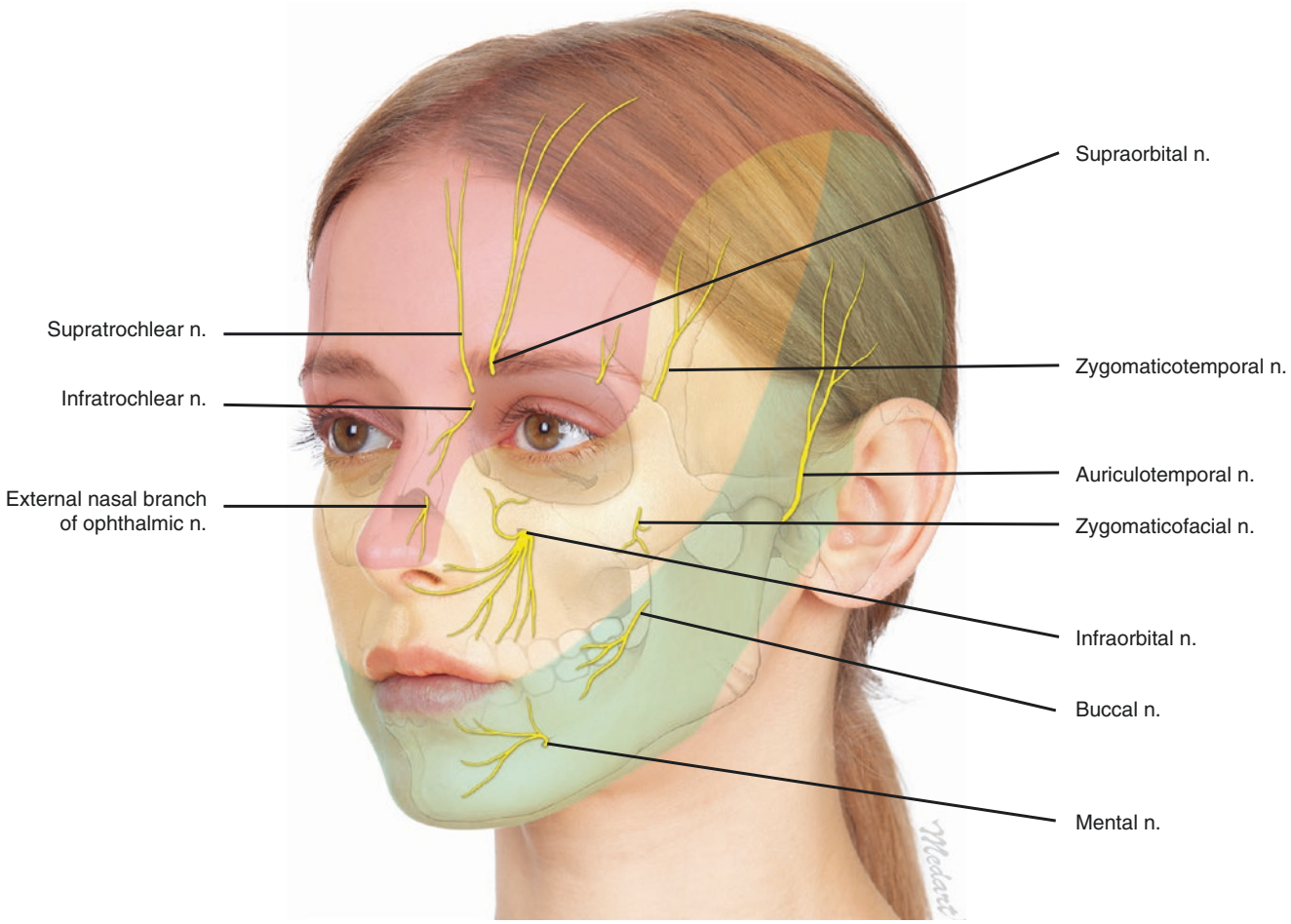

Fig. 2.10 The cutaneous sensory distribution of the face (red zone area of the ophthalmic nerve (V1) branches, yellow zone area of the maxillary nerve (V2) branches, green zone area of the mandibular nerve (V3) branches). (Published with kind permission of © Kwan-Hyun Youn 2020. All Rights Reserved)

matic, buccal, marginal mandibular, and cervical nerve branches. These minute nerve branches are randomly dispersed into muscles making it difficult to determine the nerve innervation of specific muscle (Fig. 2.11b).

2.2 US Images of the Normal Facial Skin, Subcutaneous Tissues, and Gland

It is well known that the thinnest part of the facial skin is located at the upper eyelid (0.38–0.80 mm) and the thickest at the nose ala, nose tip, and chin (1.22–2.01 mm). Recent studies demonstrated that the skin layer at the anterior cheek and mental region is relatively thicker. The facial skin was more than 2.0 mm thick at landmarks on the pogonion, zygion, and cheek. This concludes that the facial skin is thicker in the chin, lower face, and zygomatic arch area than the other areas (Table 2.1; Figs. 2.12 and 2.13).

On the US images, the epidermis and dermis can be observed from the facial and cervical skin. The epidermis is the outer layer of the skin, and dermis is right beneath the epidermis. The skin has echogenic properties due to the keratinized layer; however, the dermis is relatively less hyperechoic compared to the epidermis for its high collagen content. The echogenicity of the dermis varies due to the regional differences in the thickness of the dermis (Figs. 2.14 and 2.15).

The spatial relationship of the soft tissues of the face can be classified by layers. Deep to the skin is the subcutaneous fat tissue with superficial and deep layers. The superficial layer of subcutaneous fat tissue covers the whole face. The deep layer of subcutaneous fat is located deep to the facial muscles and is demarcated by dense connective tissues such as the capsules or retaining ligaments. The characteristics of the deep layer of subcutaneous fat are different from the superficial layer. The suborbicularis oculi fat (SOOF), retro-

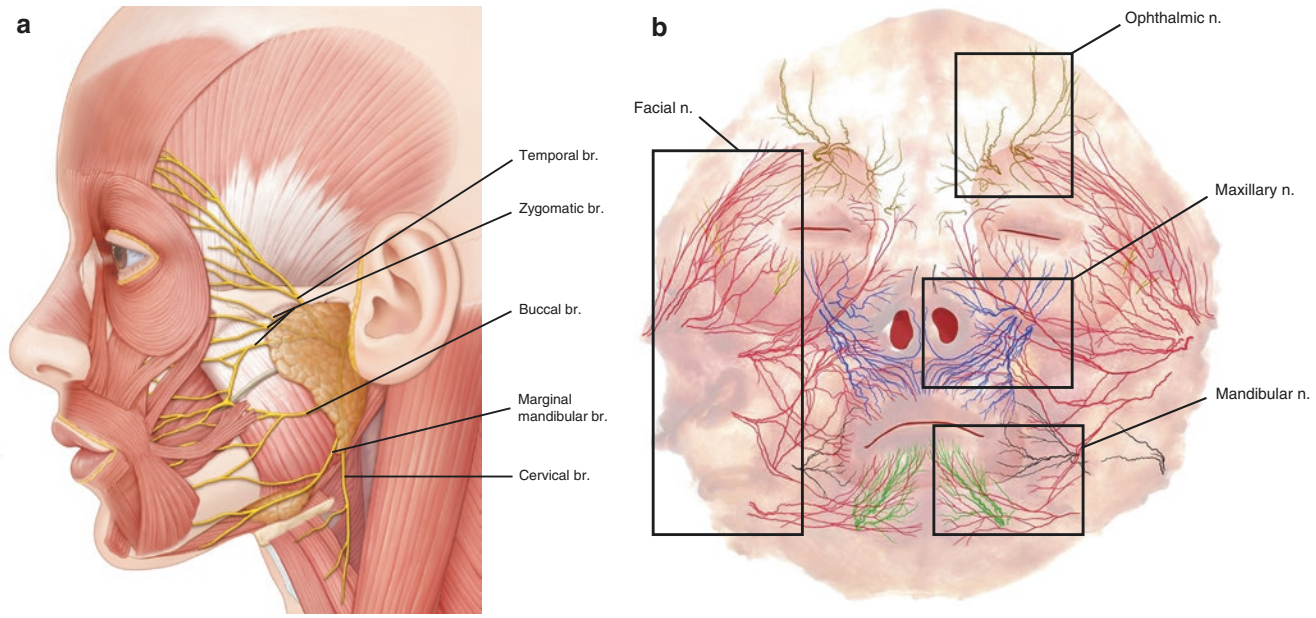

Fig. 2.11 Topography of the facial nerve. (**a**) Facial nerve and its temporofacial and cervicofacial divisions and (**b**) sensory and motor nerve distribution on the face. (Published with kind permission of © Hee-Jin Kim and Kwan-Hyun Youn 2020. All Rights Reserved)

Table 2.1 Overall thicknesses of the facial skin and superficial fat based on the anatomical regions

	Skin		Superficial fat	
Regions	Mean	SD	Mean	SD
Forehead	1.70	0.71	1.99	1.21
Radix and dorsum	1.51	0.55	1.61	1.07
Supraorbital	1.67	0.83	1.82	1.22
Infraorbital	1.97	0.84	4.93	2.98
Perioral	1.82	0.83	5.14	3.31
Temple	1.65	0.91	2.58	1.68
Cheek	1.85	1.03	4.54	2.71

Unit: mm
SD standard deviation

orbicularis oculi fat (ROOF), buccal fat, and deep cheek fat are considered deep fat layers of the face. Fibrous connective tissues pass through facial fat tissues and contribute to connecting the fat tissue, facial muscles, dermis, and bone (Fig. 2.16).

The superficial fascia, or subcutaneous connective tissue, contains unequal amounts of fat tissue, which are broadly distributed between facial musculature and the skin. The buccal fat is an encapsulated pad that forms bulged cheeks that are connected to the scalp and temple region. The facial v., the trigeminal n., the facial n., and the superficial facial m. lie within the subcutaneous tissue (Fig. 2.17).

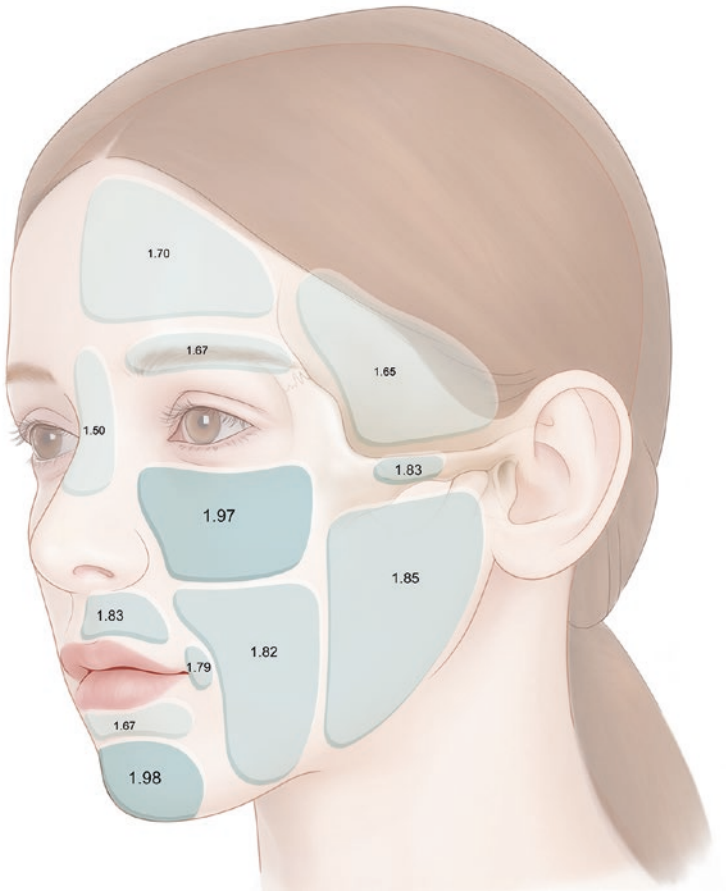

Fig. 2.12 Mean skin thickness of the face based on anatomical regions. (Published with kind permission of © Kwan-Hyun Youn 2020. All Rights Reserved)

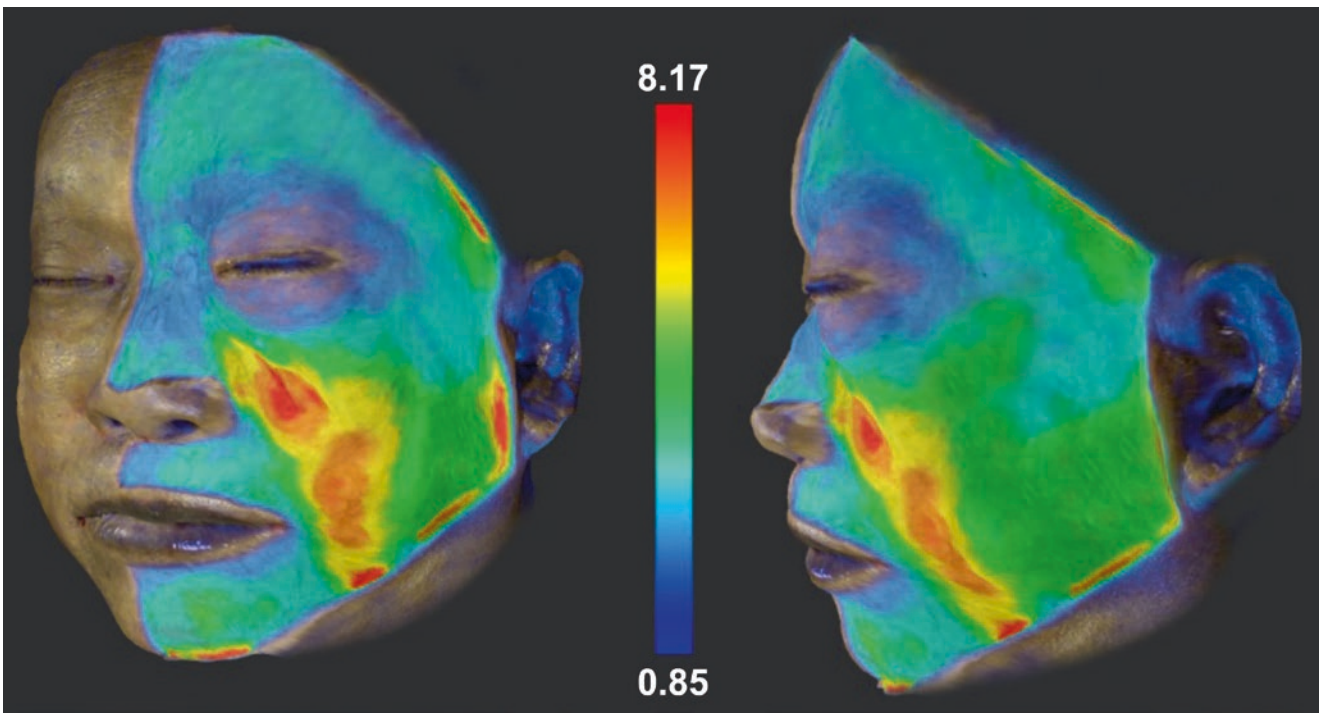

Fig. 2.13 3D images representing the mean thickness of the subcutaneous layer of the face (unit: mm). (Published with kind permission of © Hee-Jin Kim 2020. All Rights Reserved)

The subcutaneous tissue (called subcutis or hypodermis) is shown as a hypoechoic layer because of its fatty lobules. Between the fatty lobules, hyperechoic linear fibrous septa can be seen. The level of hypoechogenicity varies depending on the fat component (dense or loose) (Fig. 2.18).

There are three major salivary glands in the facial area: parotid, submandibular, and sublingual glands. There are also several minor salivary glands located in the submucosal region of the lips and so on. The parotid gland is the largest major salivary gland and situated on the posterior border of the mandible and above and below the mandibular angle. It is divided into superficial and deep layers. The superficial layer is located on the masseteric fascia, and the deep layer overlays the masseter m. and the mandible and covers the medial side of the mandibular ramus (Fig. 2.19).

There are frequent anatomical variants in the prominence of the parotid gland in the superficial upper 1/3 of the masseter m. Another anatomical variant is the accessory parotid gland, which is located superficial to the masseter m. but separated from the main parotid gland (Fig. 2.20).

The submandibular gland is located within the submandibular triangle of the neck. It lies inferior to the mandible and superficial to the mylohyoid m. It is the second largest major salivary gland, and its size is similar to that of a walnut. The submandibular gland is divided into the superficial and deep portions relative to the posterior free margin of the mylohyoid m. (Figs. 2.19 and 2.21).

Minor salivary glands are located beneath the oral mucosa and are distributed all over the face, lips, tongue, tonsil, buccal cheek, and palate (Fig. 2.22). The parotid and submandibular glands are hyperechoic in comparison with the adjacent muscles (Figs. 2.19 and 2.21), while the minor salivary glands are hypoechoic. The submucosal minor salivary glands located in the oral mucosa appear as well-defined, round, hypoechoic structures (Fig. 2.23).

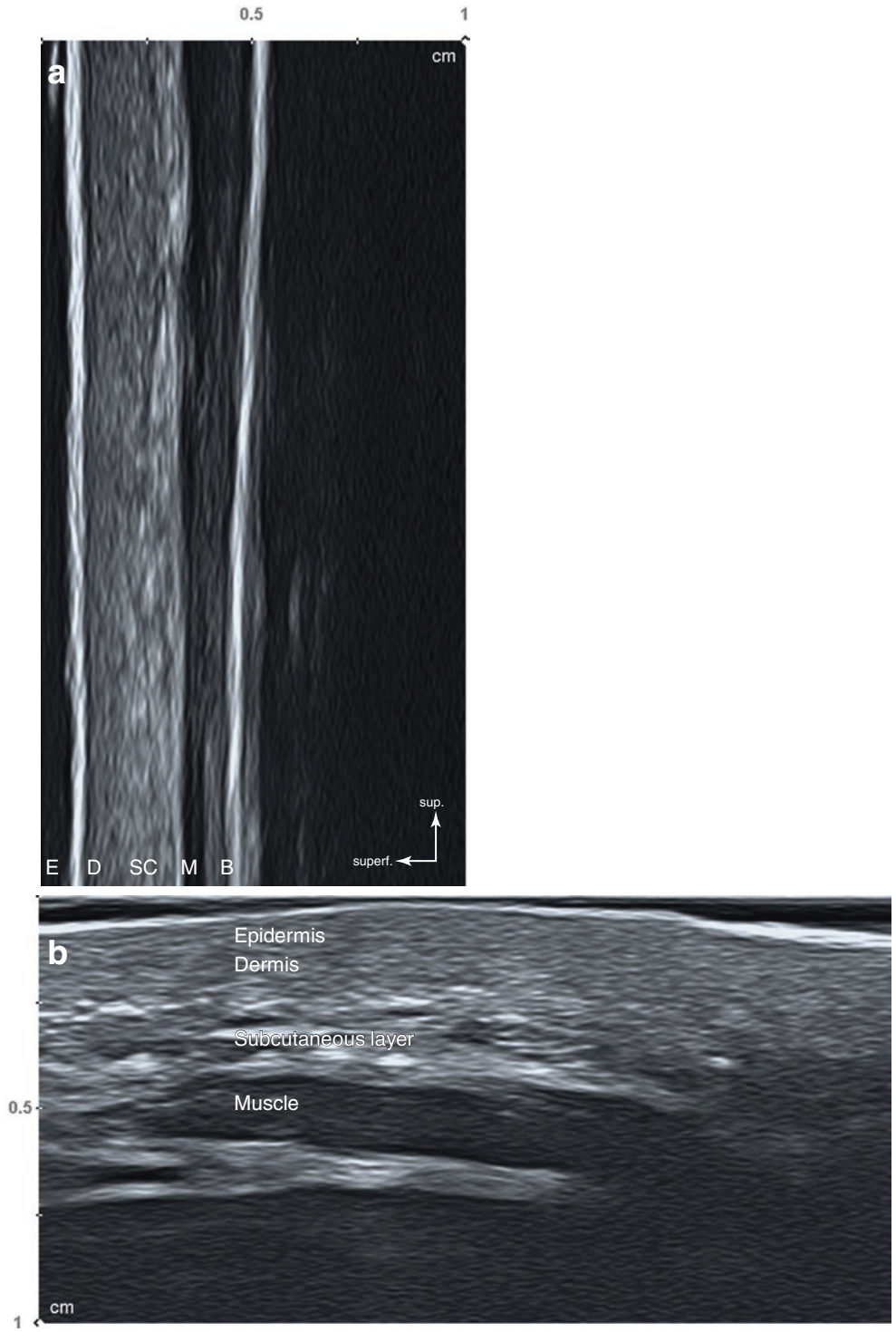

Fig. 2.14 Ultrasonography representing the regional difference of the epidermis (E), dermis (D), subcutaneous tissue (SC), muscle (M), and bone (B). (**a**) Radix (sagittal view, 24 MHz by linear transducer) and (**b**) subzygomatic area (transverse view, 24 MHz by linear transducer). (Published with kind permission of © Hee-Jin Kim 2020. All Rights Reserved)

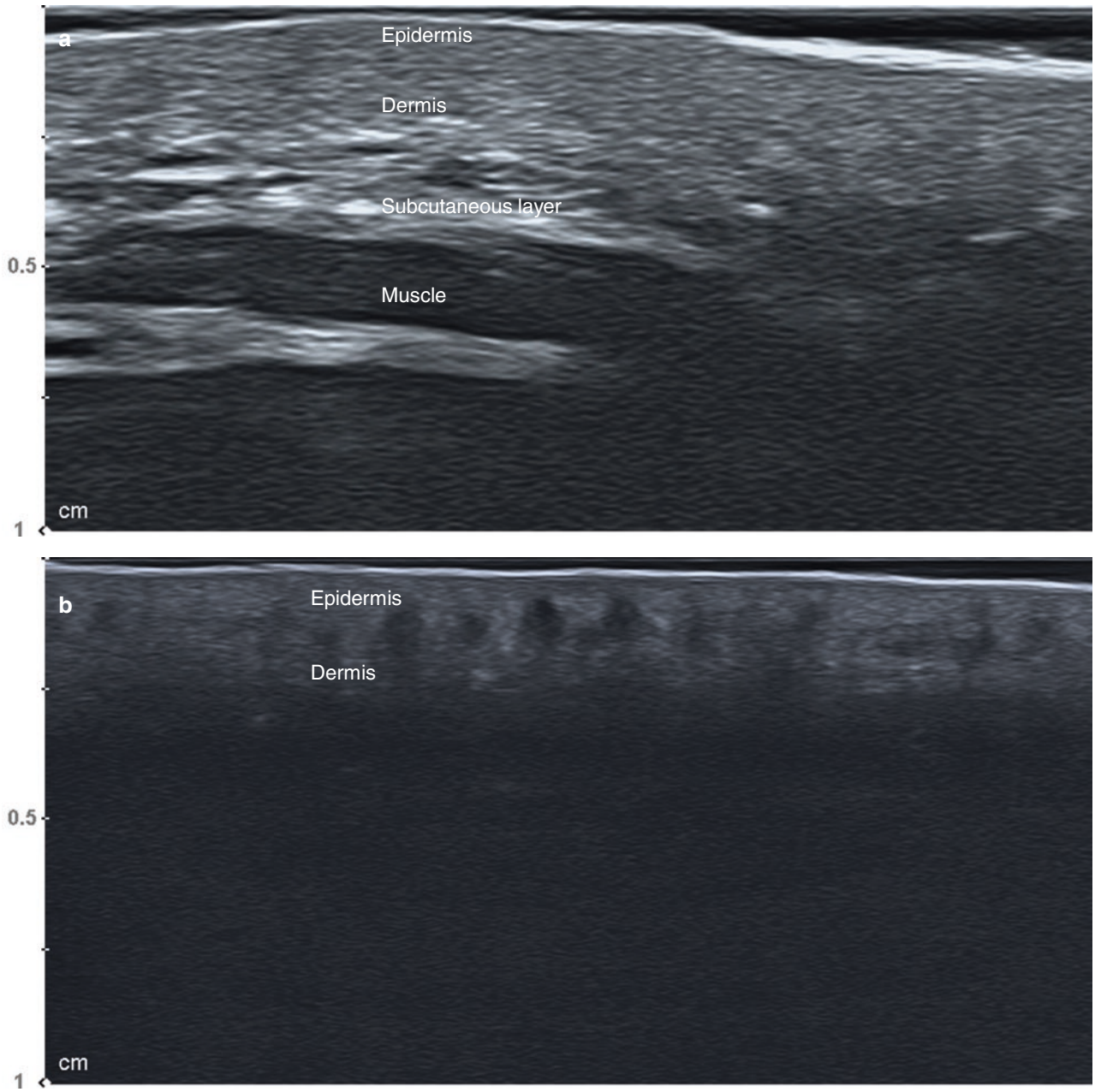

Fig. 2.15 Differences in image resolution of the ultrasonography depending on the frequency. (**a**) 24 MHz by linear transducer (subzygomatic area, transverse view) and (**b**) 32 MHz by linear transducer (subzygomatic area, transverse view). (Published with kind permission of © Hee-Jin Kim 2020. All Rights Reserved)

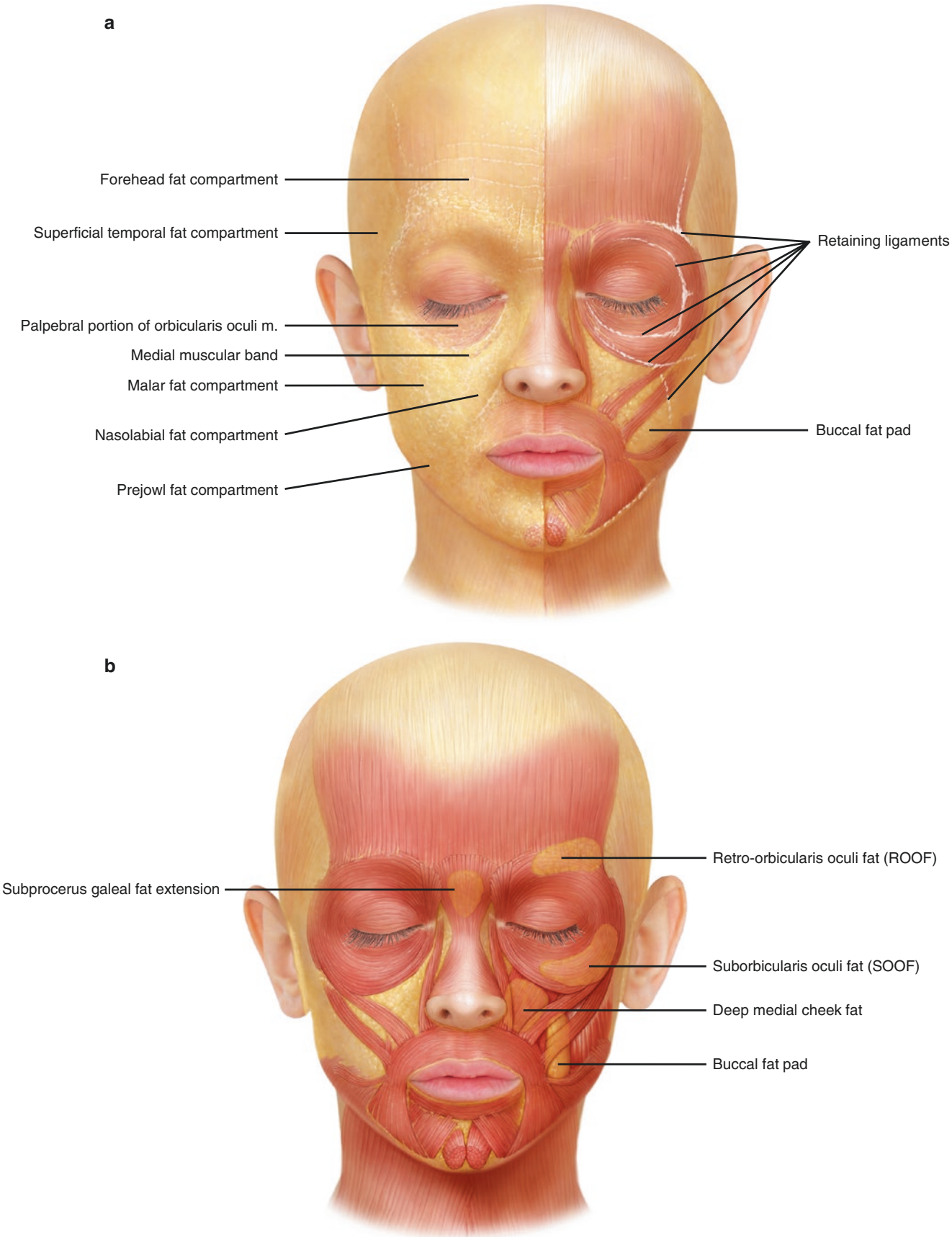

Fig. 2.16 Facial fat compartments. (**a**) Subcutaneous fat and superficial muscles of the face and (**b**) deep fat compartments of the face. (Published with kind permission of © Kwan-Hyun Youn 2020. All Rights Reserved)

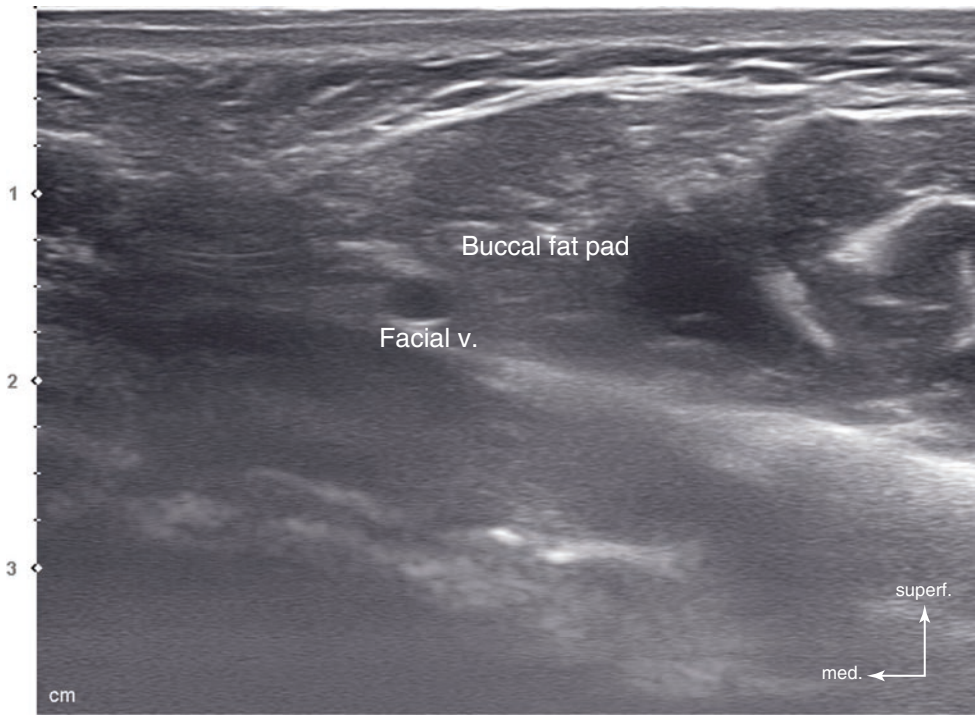

Fig. 2.17 Ultrasonography representing buccal fat pad (transverse view, 15 MHz by linear transducer). (Published with kind permission of © Hee-Jin Kim 2020. All Rights Reserved)

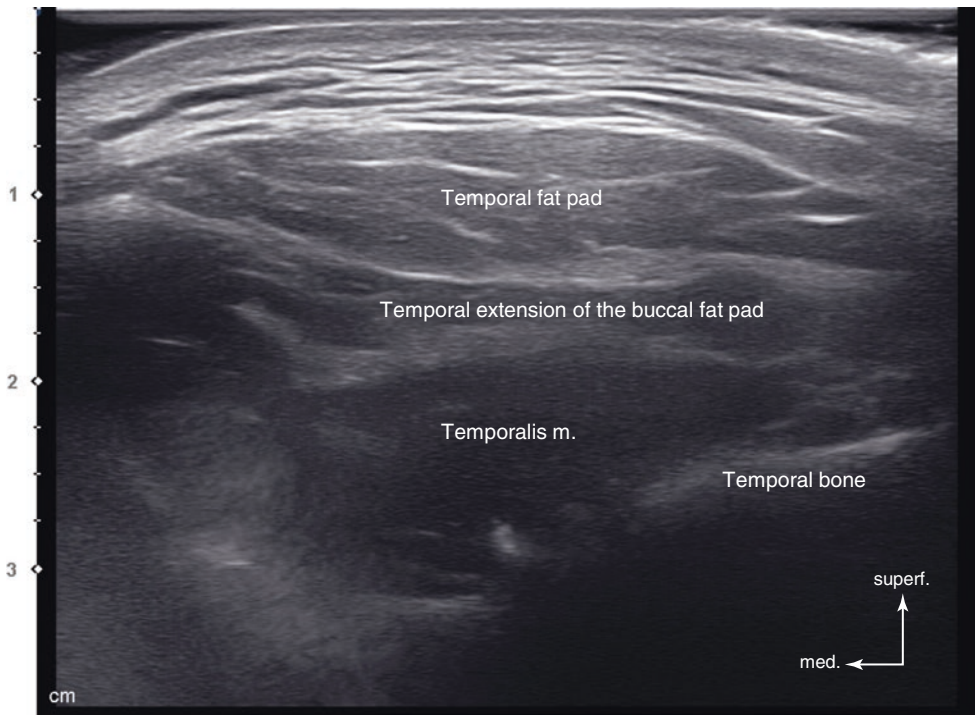

Fig. 2.18 Variable hypoechogenecity depending on the fat compartments of the temple. (Published with kind permission of © Hee-Jin Kim 2020. All Rights Reserved)

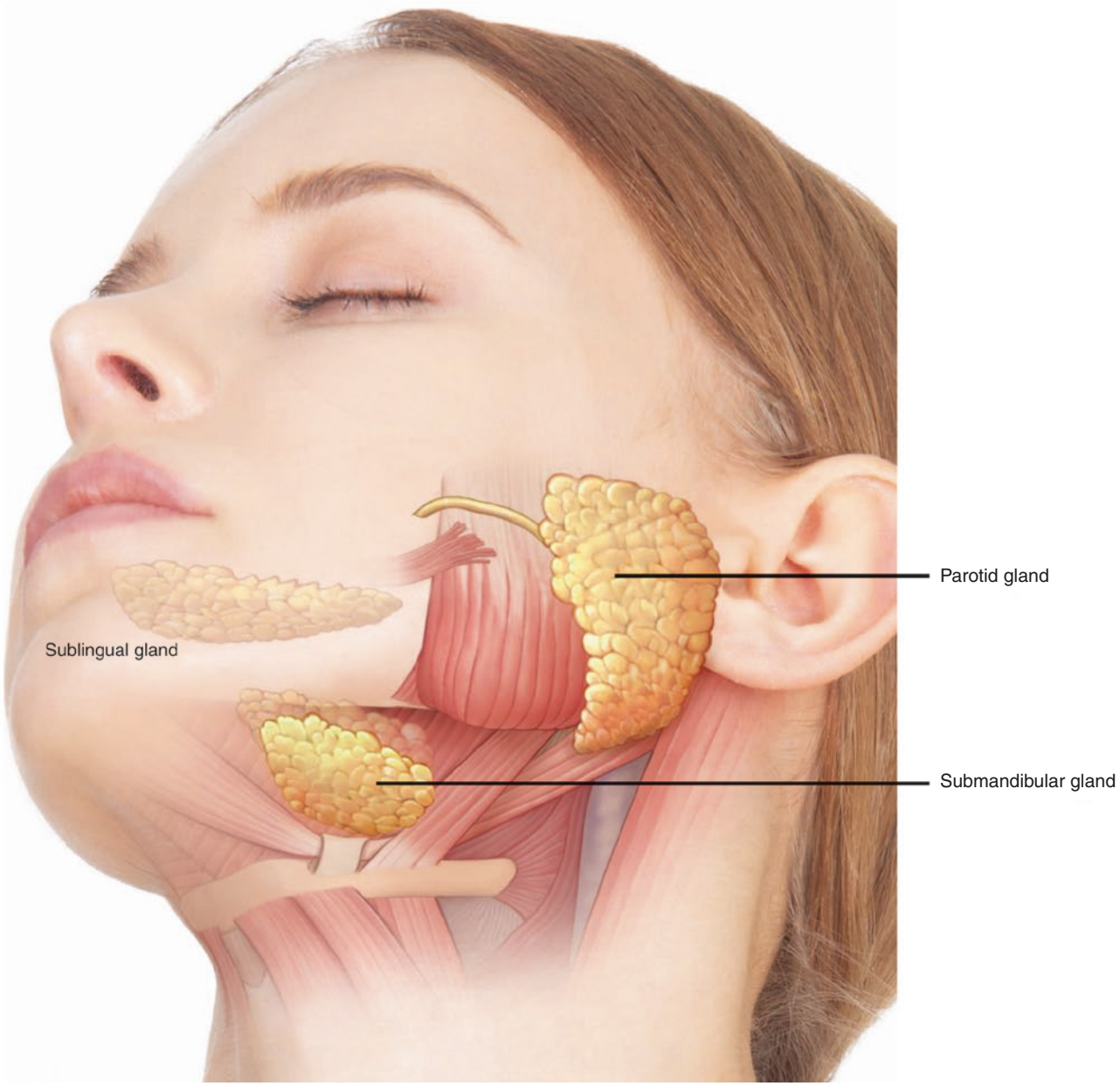

Fig. 2.19 Illustration of three major salivary glands. (Published with kind permission of © Kwan-Hyun Youn 2020. All Rights Reserved)

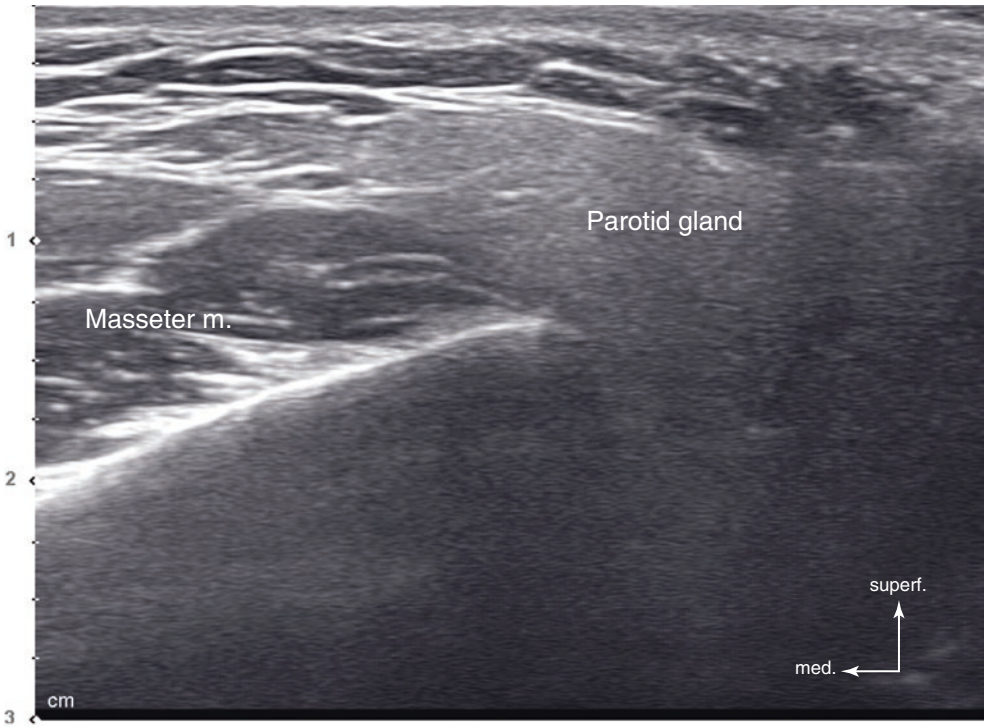

Fig. 2.20 Ultrasonography of the parotid gland (transverse view, 15 MHz by linear transducer). (Published with kind permission of © Hee-Jin Kim 2020. All Rights Reserved)

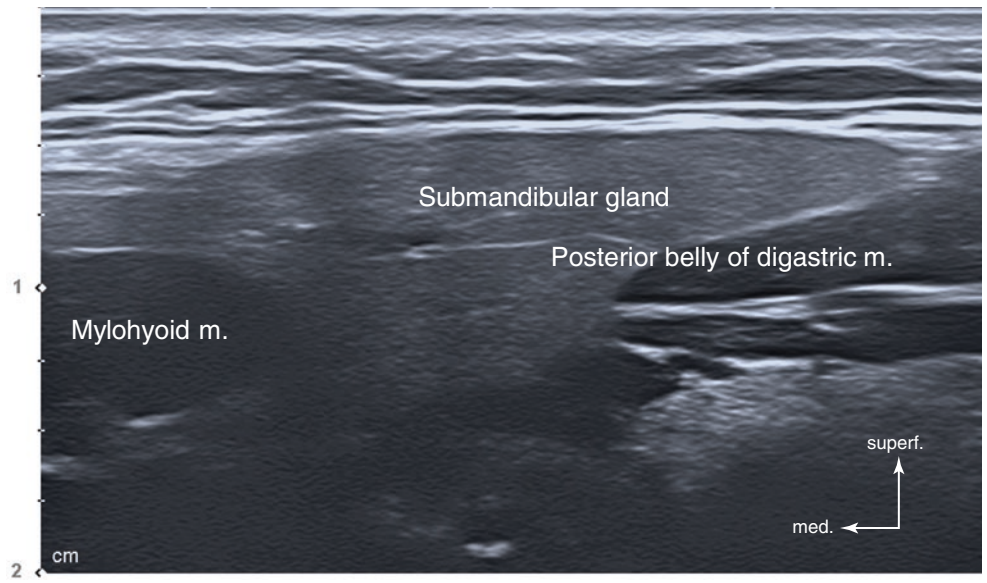

Fig. 2.21 Ultrasonography of the submandibular gland (transverse view, 15 MHz by linear transducer). (Published with kind permission of © Hee-Jin Kim 2020. All Rights Reserved)

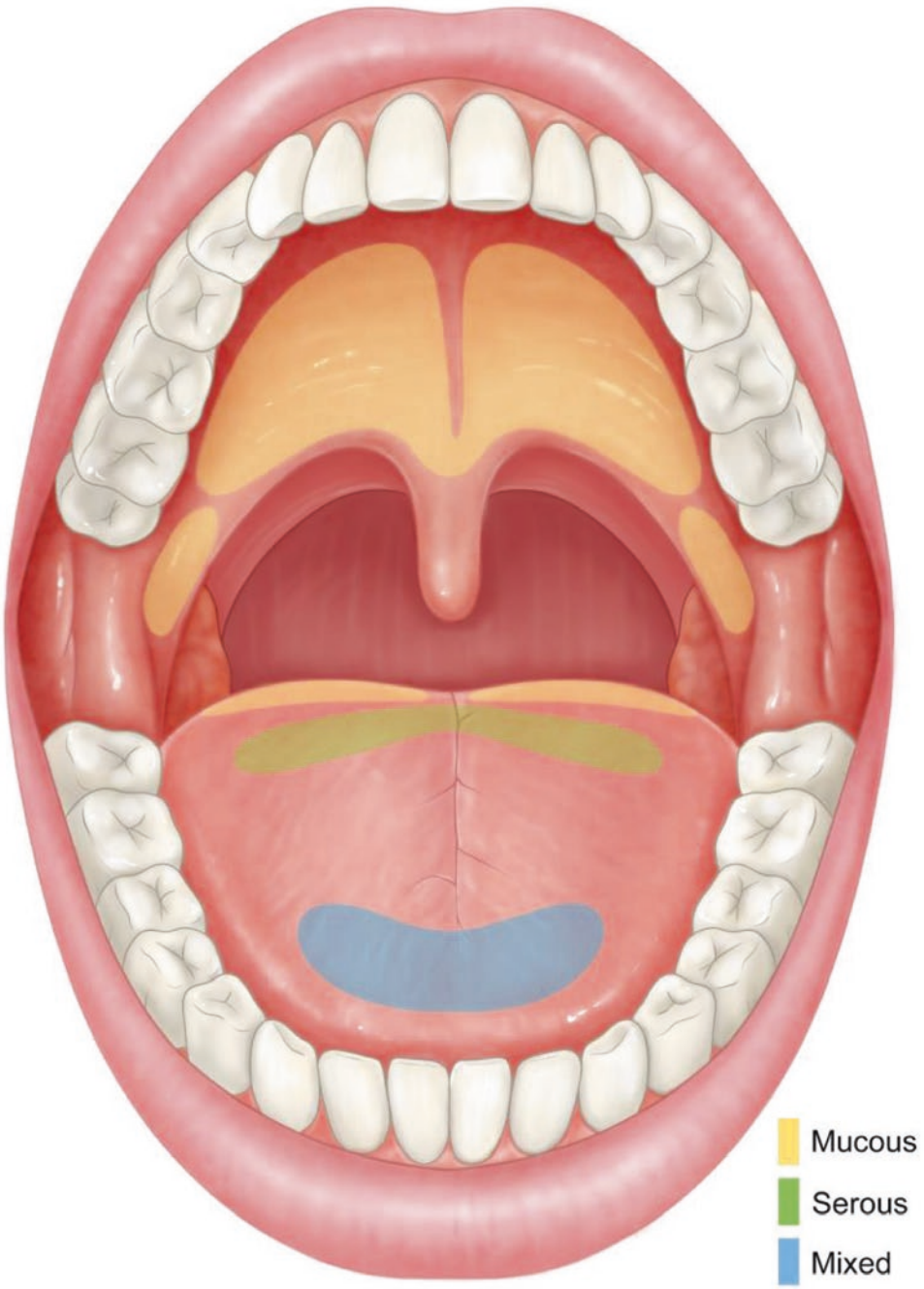

Fig. 2.22 Illustration of the locations and components of the minor salivary glands. (Published with kind permission of © Kwan-Hyun Youn 2020. All Rights Reserved)

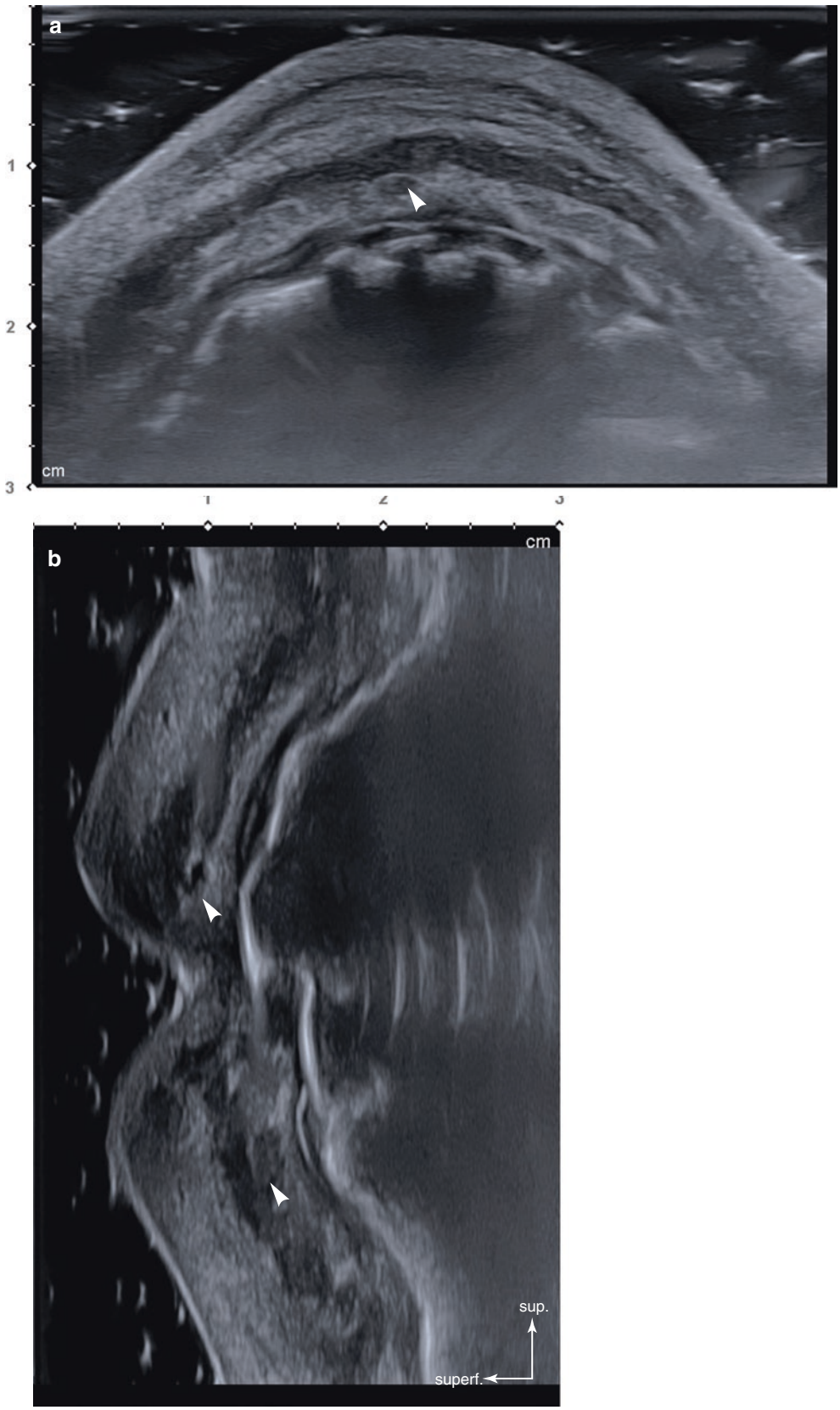

Fig. 2.23 Ultrasonography representing the minor salivary glands (arrowheads) of the lip. (**a**) Transverse view, 15 MHz by linear transducer and (**b**) sagittal view, 15 MHz by linear transducer. (Published with kind permission of © Hee-Jin Kim 2020. All Rights Reserved)

2.3 US Images of the Musculoskeletal Structures and Fasciae of the Face and Neck

The cortex of the bone appears as a hyperechoic line with posterior acoustic shadowing artifacts (Fig. 2.24).

The cartilage appears in US as hypoechoic bands, usually without detectable vascularity. These anatomical characteristics are seen in the nasal cartilages (upper and lower alar) and the ear cartilage (Fig. 2.25).

The muscles appear hypoechoic with muscle fibers and intramuscular tendinous structures showing dynamic changes under contraction and rest (Fig. 2.26). The tendons appear as hyperechoic structures with a fibrillary network, which are formed by parallel bundles of collagen (Fig. 2.27).

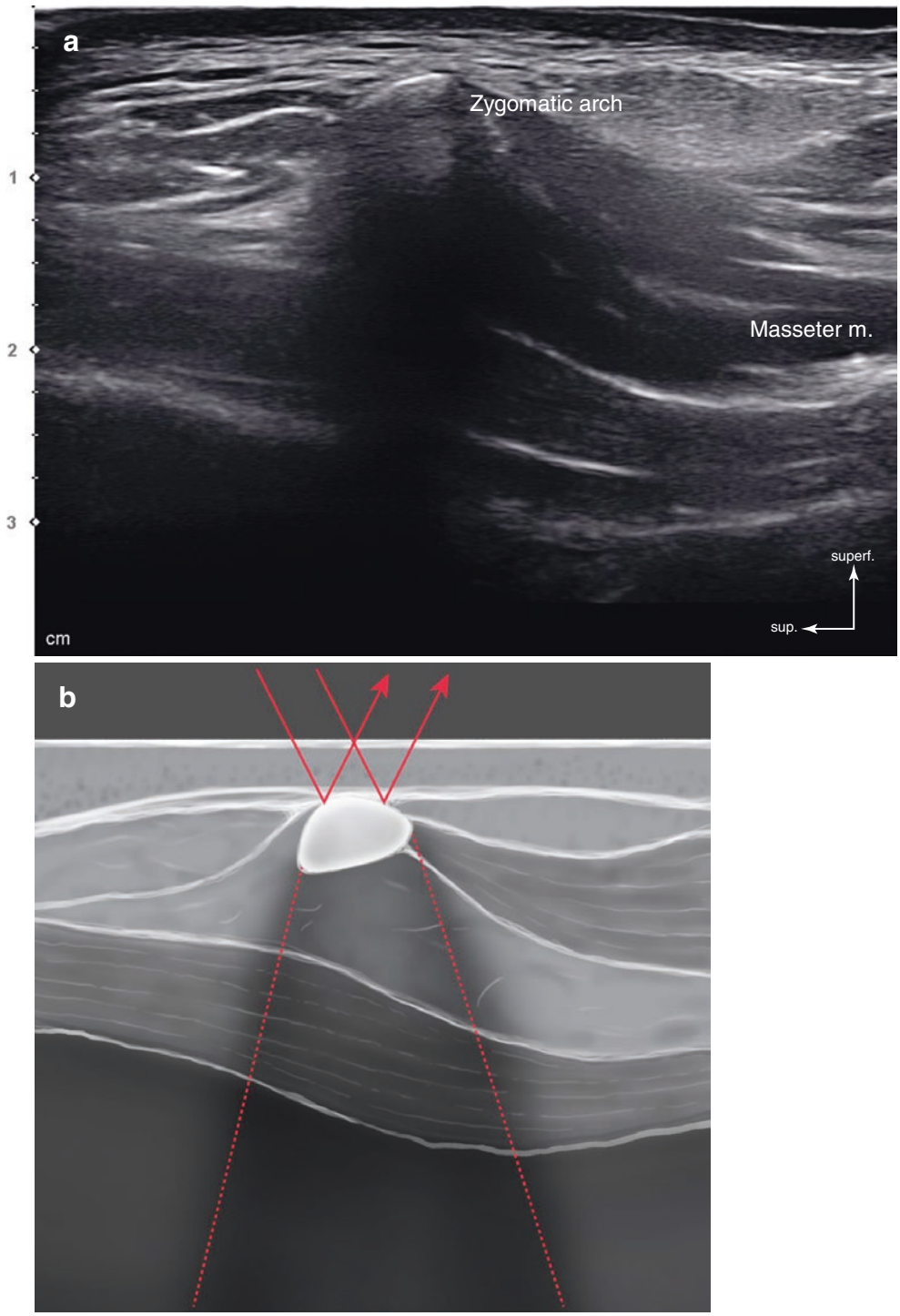

Fig. 2.24 Ultrasonography of bone and muscle. (**a**) Zygomatic arch (coronal view, 15 MHz by linear transducer) and (**b**) illustration representing phenomenon of the posterior acoustic shadowing. (Published with kind permission of © Hee-Jin Kim and Kwan-Hyun Youn 2020. All Rights Reserved)

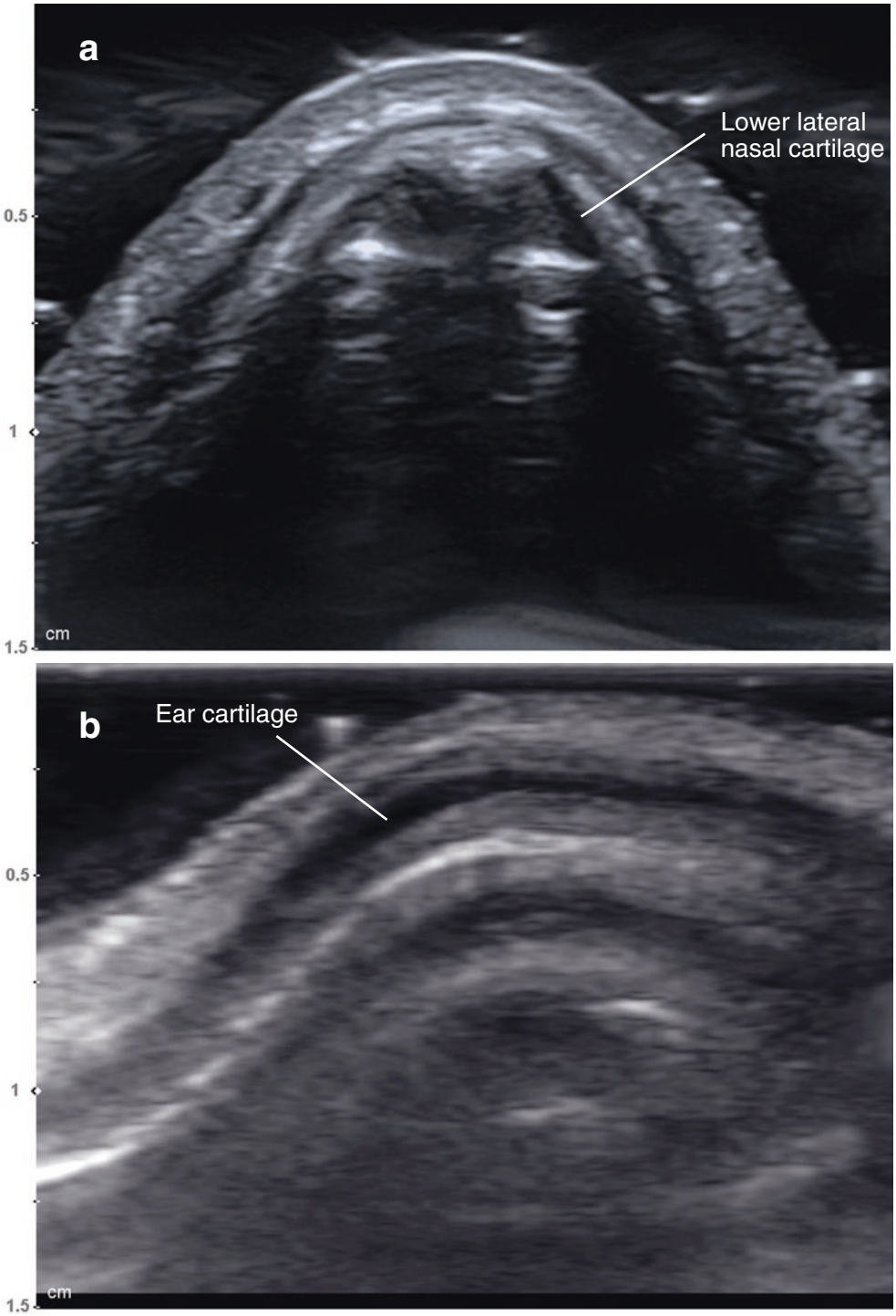

Fig. 2.25 Ultrasonography of cartilage. (**a**) Lower lateral nasal cartilage (transverse view, 15 MHz by linear transducer) and (**b**) ear cartilage (sagittal view, 15 MHz by linear transducer). (Published with kind permission of © Hee-Jin Kim 2020. All Rights Reserved)

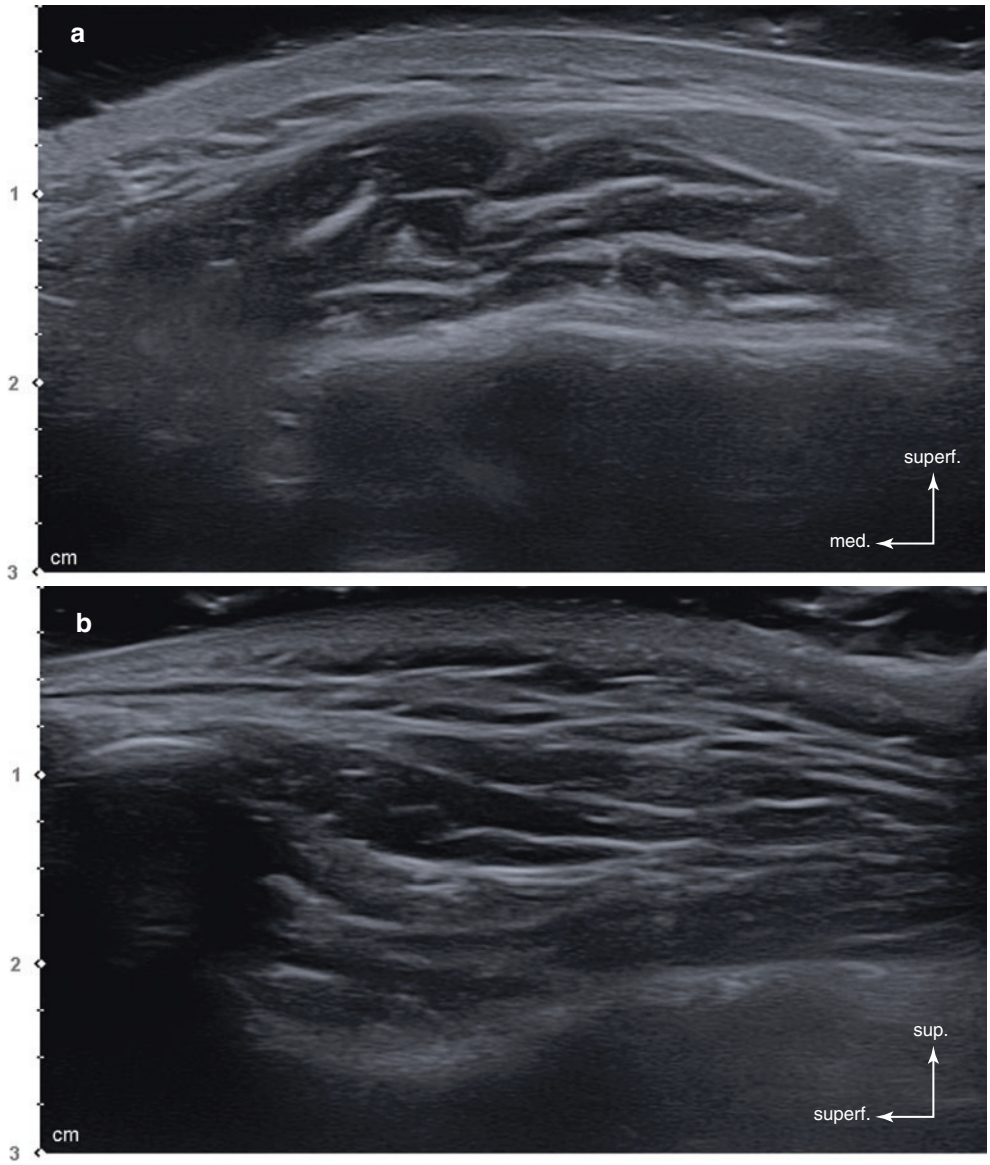

Fig. 2.26 Ultrasonography of intramuscular tendinous structures. (**a**) Masseter muscle (transverse view, 15 MHz by linear transducer) and (**b**) temporalis muscle (coronal view, 15 MHz by linear transducer). (Published with kind permission of © Hee-Jin Kim 2020. All Rights Reserved)

2.4 Facial Landmarks and Reference Lines

2.4.1 Surface Anatomy Based on the Anthropologic Bony and Soft Tissue Landmarks

The frontal notch and the supraorbital foramen: The frontal notch is located medially in the orbit, which is palpable near the glabella along the supraorbital margin. The supraorbital foramen is palpable slightly lateral to the frontal notch. The supratrochlear a. and supratrochlear n. pass through the frontal notch, and the supraorbital a. and supraorbital n. pass through the supraorbital foramen.

The infraorbital foramen is located on the upper third of the line connecting the infraorbital margin to the nose ala. The infraorbital foramen locates medial to the vertical line connecting the pupil and mental foramen. The infraorbital a. and infraorbital n. exit through the infraorbital foramen. The mental foramen is located along the same line used to locate the infraorbital foramen 2 cm inferior to the oral commissure. The mental n. exits through the mental foramen (Fig. 2.28).

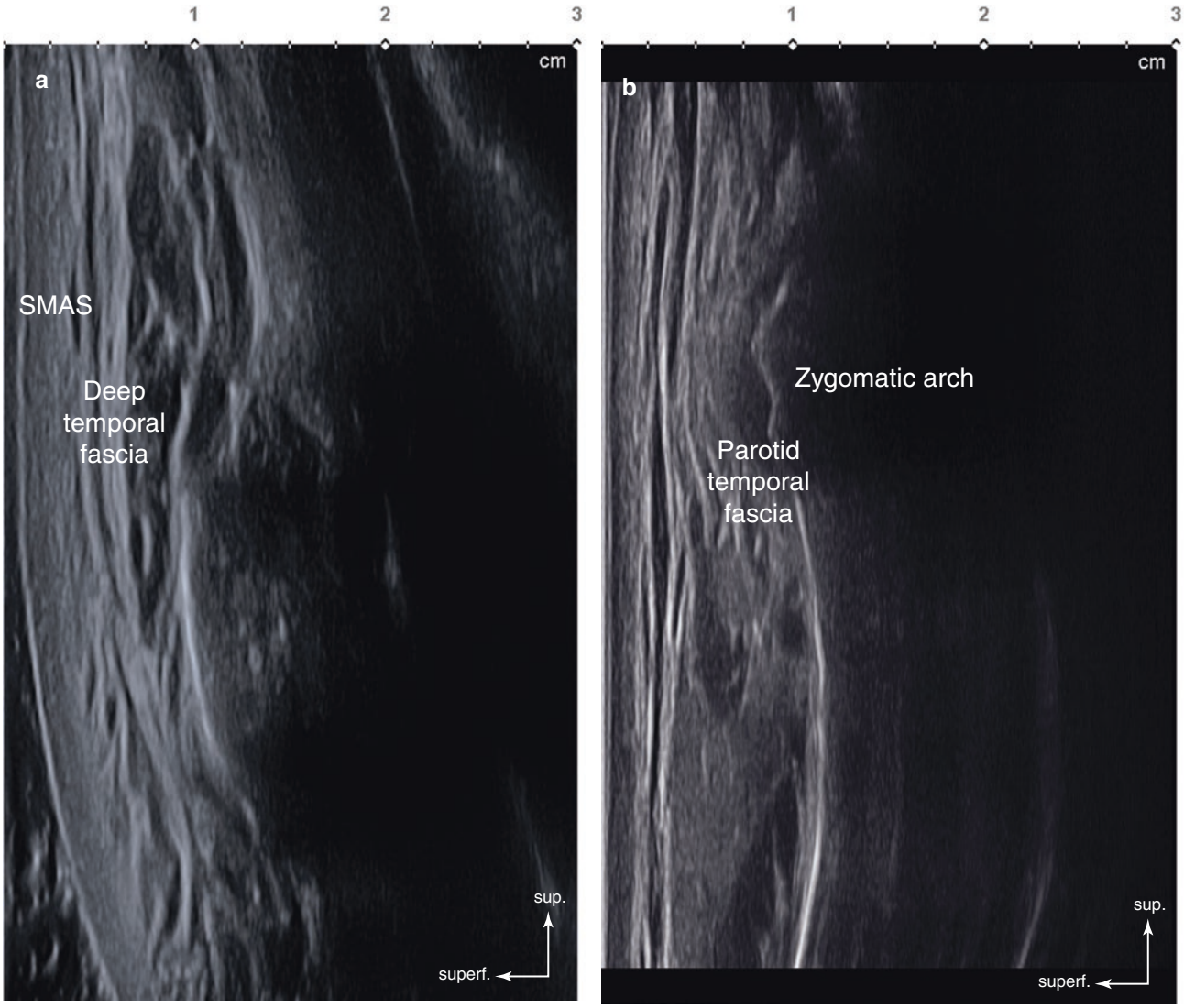

Fig. 2.27 Ultrasonography of fascia of the face. (**a**) Temple (coronal view, 15 MHz by linear transducer) and (**b**) subzygomatic area including parotid gland (coronal view, 15 MHz by linear transducer). (Published with kind permission of © Hee-Jin Kim 2020. All Rights Reserved)

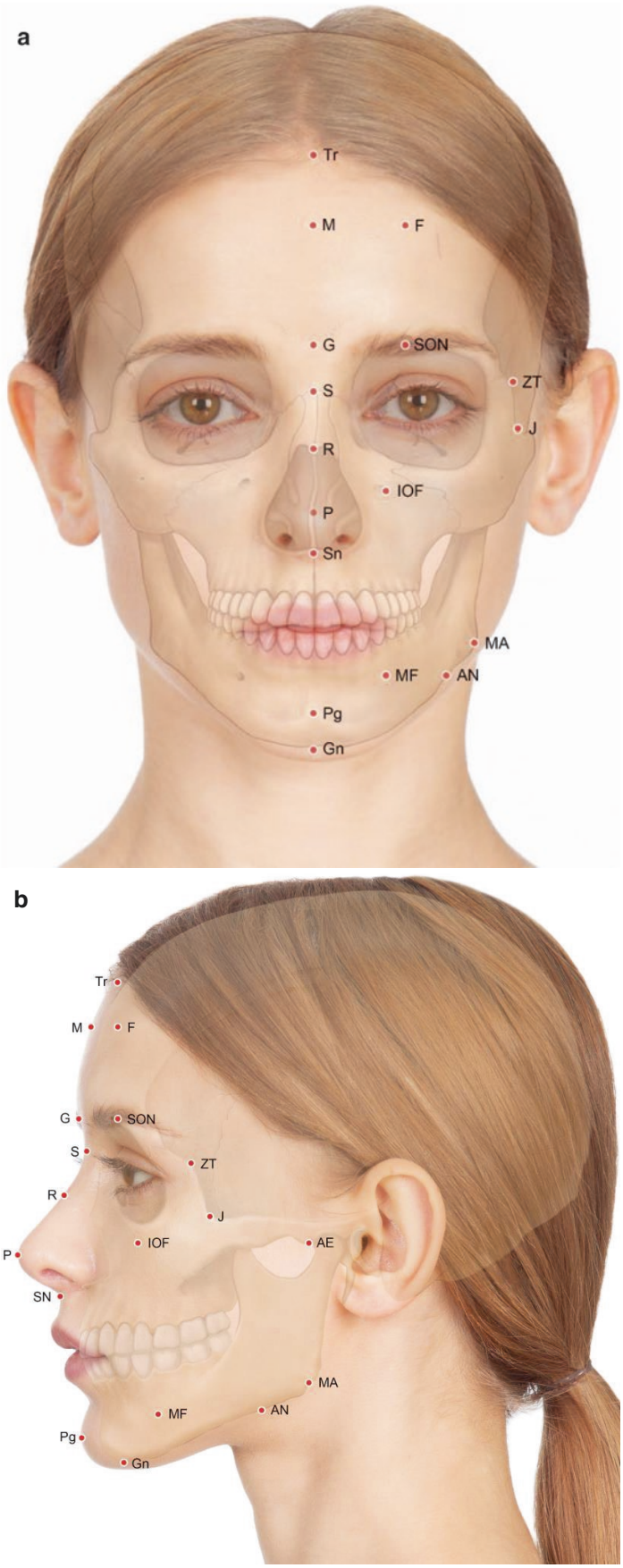

Fig. 2.28 Major anatomical landmarks of the face. (**a**) Frontal view and (**b**) lateral view. Tr: Trichion (hairline); M: Metopion (midpoint between bilateral frontal eminence); G: Glabella (most anterior projection of the forehead); S: Sellion (the deepest point of the nasofrontal concavity; R: Rhinion (midline junction between the nasal bone and cartilage); P: Pronasale (apex nasi, nasal tip); SN: Subnasale (the point at which the nasal septum merges); Pg: Pogonion (the most prominent point of the soft tissue of chin); Gn: Gnathion (the lowest part of the soft tissue of chin); F: Frontal eminence; SON: Supraorbital notch; IOF: Infraorbital foramen; MF: Mental foramen; Zt: Zygomatic tubercle (the most posteriorly projecting point of the frontal process of the zygomatic bone); J: Jugale (angle between the frontal process and the temporal process of the zygomatic bone); AE: Articular eminence (protrusion of the temporal bone anterior to the mandibular fossa); MA: Mandible angle; AN: Antegonial notch. (Published with kind permission of © Kwan-Hyun Youn 2020. All Rights Reserved)

2.4.2 Facial Landmarks and Reference Lines for the US Examination (Fig. 2.29)

Forehead and temple region	
F1: Metopion (midpoint of bilateral eminence)	**T1**: transverse line passing the eyebrow
F2: midpoint between F1 and F3	**T2**: transverse line passing the zygomatic tubercle
F3: Glabella	**T3**: perpendicular line passing the jugale
F4: frontal eminence	**T4**: perpendicular line passing the midpoint between T3 and T5
F5: intersection point of TL1 and PL1	**T5**: perpendicular line passing the articular eminence
F6: intersection point of TL1 and PL2	
F7: intersection point of TL1 and PL3	
F8: intersection point of TL1 and PL4	

Periorbital region	
P1: intersection point of TL2 and PL1	**P6**: intersection point of TL3 and PL1
P2: intersection point of TL2 and PL2	**P7**: intersection point of TL3 and PL2
P3: intersection point of TL2 and PL3	**P8**: intersection point of TL3 and PL3
P4: intersection point of TL2 and PL4	**P9**: intersection point of TL3 and PL4
P5: lateral orbital rim at the level of lateral canthus	

Midface and nose	
M1: intersection point of TL4 and PL1	**N1**: sellion (the deepest point on the radix)
M2: intersection point of TL4 and PL2	**N2**: rhinion (midline junction between the nasal bone and cartilage)
M3: intersection point of TL4 and PL3	**N3**: pronasale (tip of the nose)
M4: intersection point of TL4 and PL4	
M5: intersection point of TL5 and PL1	
M6: intersection point of TL5 and PL2	
M7: intersection point of TL5 and PL3	
M8: intersection point of TL5 and PL4	

Perioral region and lip	
O1: midpoint between Subnasale and lowest point of Cupid's bow (Ls1)	**Ls1**: intersection point of vermilion border of upper lip and ML
O2: midpoint between Li1 and gnathion	**Ls2–Ls3**: oblique line between Ls2 and Ls3
O3: Pogonion	**Ls1–Li1**: perpendicular line between Ls1 and Li1
O4: intersection point of TL6 and PL2	**Ls2**: point on the upper vermilion border passing the medial 1/3 between the ML and cheilion
O5: intersection point of TL6 and PL3	**Ls3**: point on the upper vermilion border passing the lateral 1/3 between the ML and cheilion
O6: point of 1.5 cm lateral to the cheilion	**Li1**: intersection point of vermilion border of lower lip and ML
O7: intersection point of TL7 and PL3	**Li2–Li3**: oblique line between Li2 and Li3
O8: intersection point of TL8 and PL1 (DLI point)	**Li2**: point on the lower vermilion border passing the medial 1/3 between the ML and cheilion
O9: intersection point of TL8 and PL2 (DAO point)	**Li3**: point on the lower vermilion border passing the medial 1/3 between the ML and cheilion
O10: intersection point of TL8 and PL3	
O11: antegonial notch	

Masseter region	
Ma1: anterior margin of the masseter muscle	**Ma4**: upper 1/3 line of the masseter muscle perpendicular to Ma2
Ma2: mid-half line parallel to Ma1 and Ma3	**Ma5**: lower 1/3 line of the masseter muscle perpendicular to Ma2
Ma3: posterior margin of the masseter muscle	**Ma6**: inferior margin of the masseter muscle perpendicular to Ma2

Upper superficial cervical region	
C1: gnathion	**C3**: submandibular triangle
C2: point 2 cm posterior to the point C1	**C4**: mandibular angle

Reference lines and points	
ML: midsagittal line	**PL1**: perpendicular line passing the medial canthus
TL1: transverse line passing F2	**PL2**: perpendicular line passing the midpupil
TL2: transverse line passing F3	**PL3**: perpendicular line passing the lateral canthus
TL3: transverse line passing inferior orbital rim	**PL4**: perpendicular line passing the lateral orbital rim
TL4: mid-half line between the TL3 and TL5	
TL5: transverse line passing bilateral alare	**A:** zygomatic tubercle
TL6: transverse line passing O1	**B:** jugale
TL7: transverse line passing bilateral cheilion	**C:** articular eminence
TL8: oblique line passing between O2 and otobasion inferius	**D:** otobasion inferius

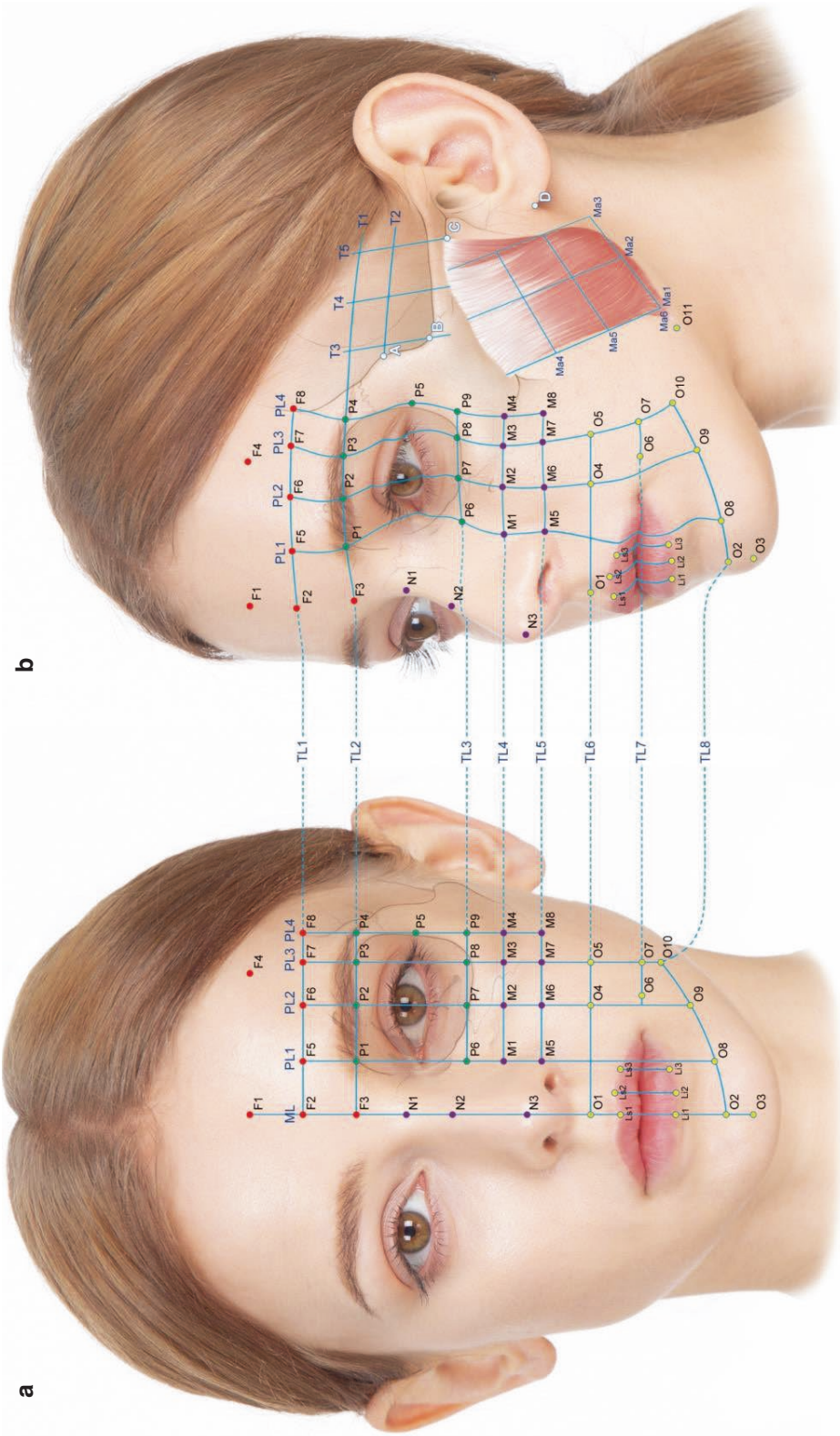

Fig. 2.29 Surface landmarks and reference lines of the face. (**a**) Frontal view and (**b**) oblique view (see details in the text). (Published with kind permission of © Kwan-Hyun Youn 2020. All Rights Reserved)

2.4.3 Facial Landmarks and Reference Lines for the US Examination (Figs. 2.30 and 2.31)

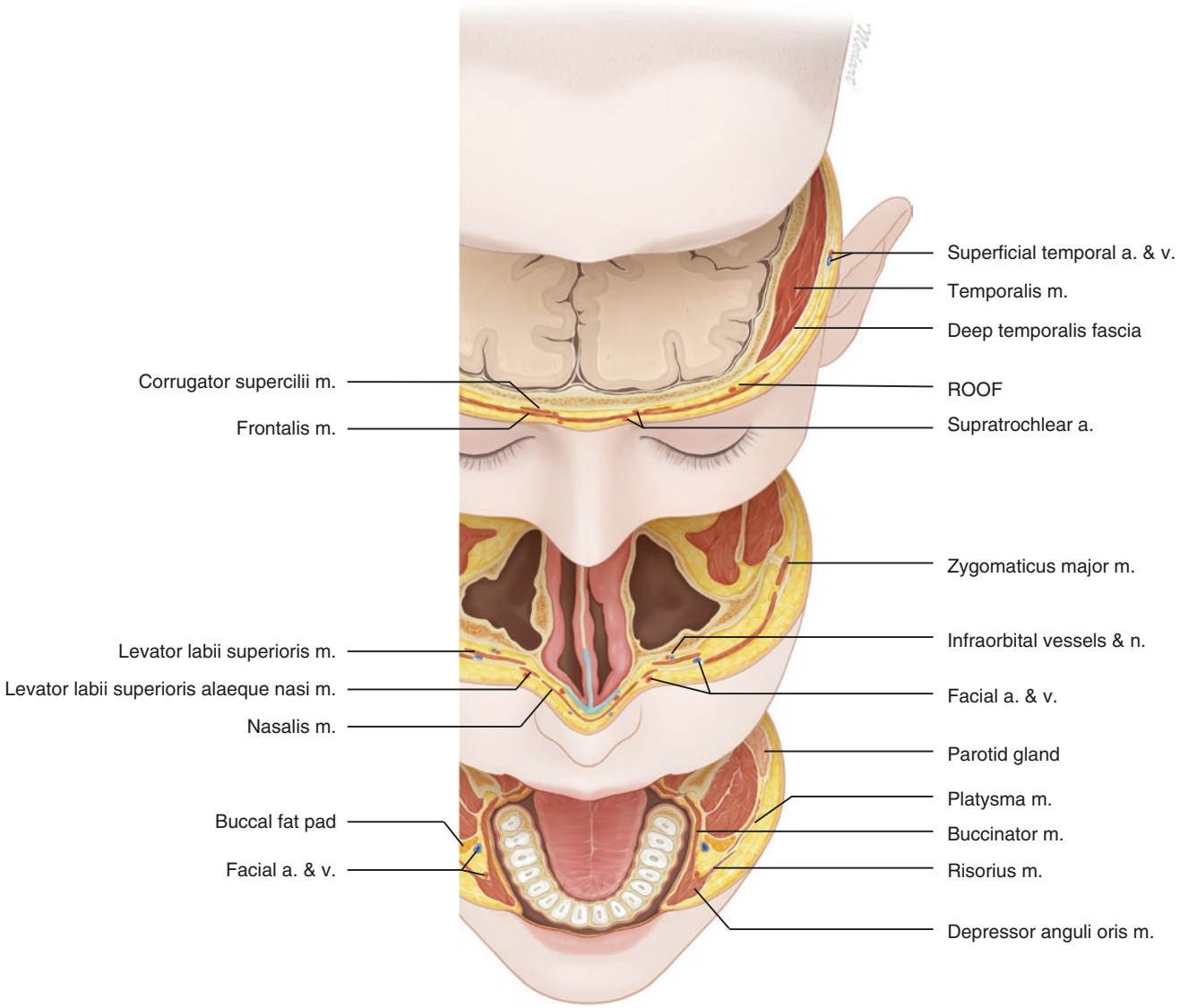

Fig. 2.30 Illustration representing three transverse sections of the head (plane a: transverse section passing the eyebrow; plane b: transverse section passing the rhinion; plane c: transverse section passing the bilateral cheilion). (Published with kind permission of © Kwan-Hyun Youn 2020. All Rights Reserved)

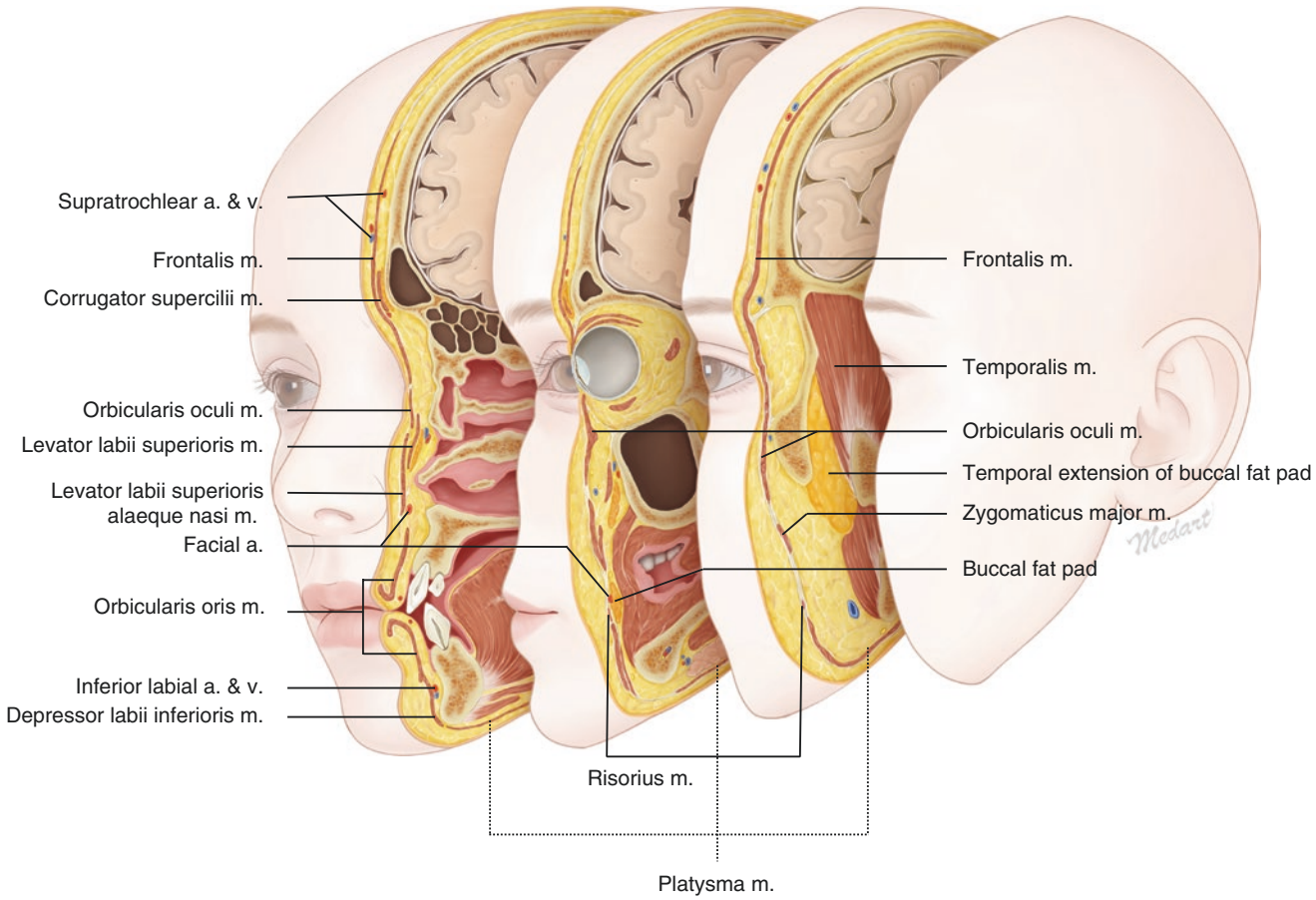

Fig. 2.31 Illustration representing three sagittal sections of the head (plane a: sagittal section passing the medial canthus; plane b: sagittal section passing the midpupil; plane c: sagittal section passing the lateral canthus). (Published with kind permission of © Kwan-Hyun Youn 2020. All Rights Reserved)

2.5 US Images of the Nerves and Blood Vessels of the Face

Arteries and veins appear as anechoic tubular structures with a variable thickness according to the anatomical location. The arteries sustain their shape while veins are compressible with the transducer and may easily collapse (Figs. 2.32, 2.33, 2.34, and 2.35). The spectral curve analysis shows the systolic and diastolic phases in the arteries, and the monophasic type flow in the veins (Fig. 2.36a, b).

Nerves present as fascicular structures with a mixed hyperechoic and hypoechoic pattern. In the transverse view, they appear as oval-shaped, hyperechoic structures with multiple hypoechoic dots that resemble the ultrasound appearance of an ovary (honeycomb appearance) (Figs. 2.37, 2.38, 2.39, and 2.40).

2.5.1 Facial Vessels at the Antegonial Notch (Fig. 2.32)

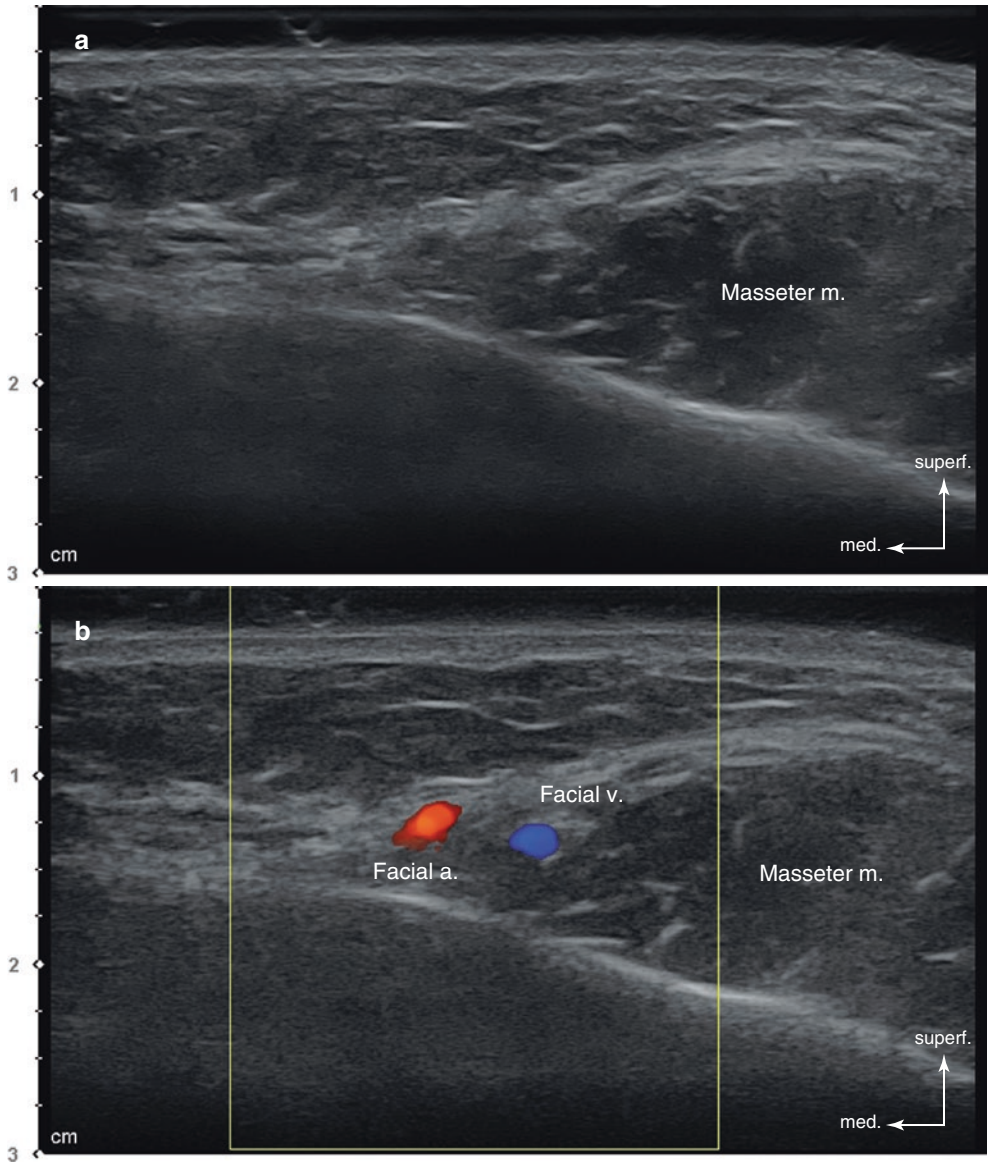

Fig. 2.32 Ultrasonography representing the facial artery and vein at the antegonial notch. (**a**) B mode (transverse view, 15 MHz by linear transducer) and (**b**) Doppler mode (transverse view, 15 MHz by linear transducer). (Published with kind permission of © Hee-Jin Kim 2020. All Rights Reserved)

2.5.2 Emerging Point (EMP) of the Ophthalmic Artery (Fig. 2.33)

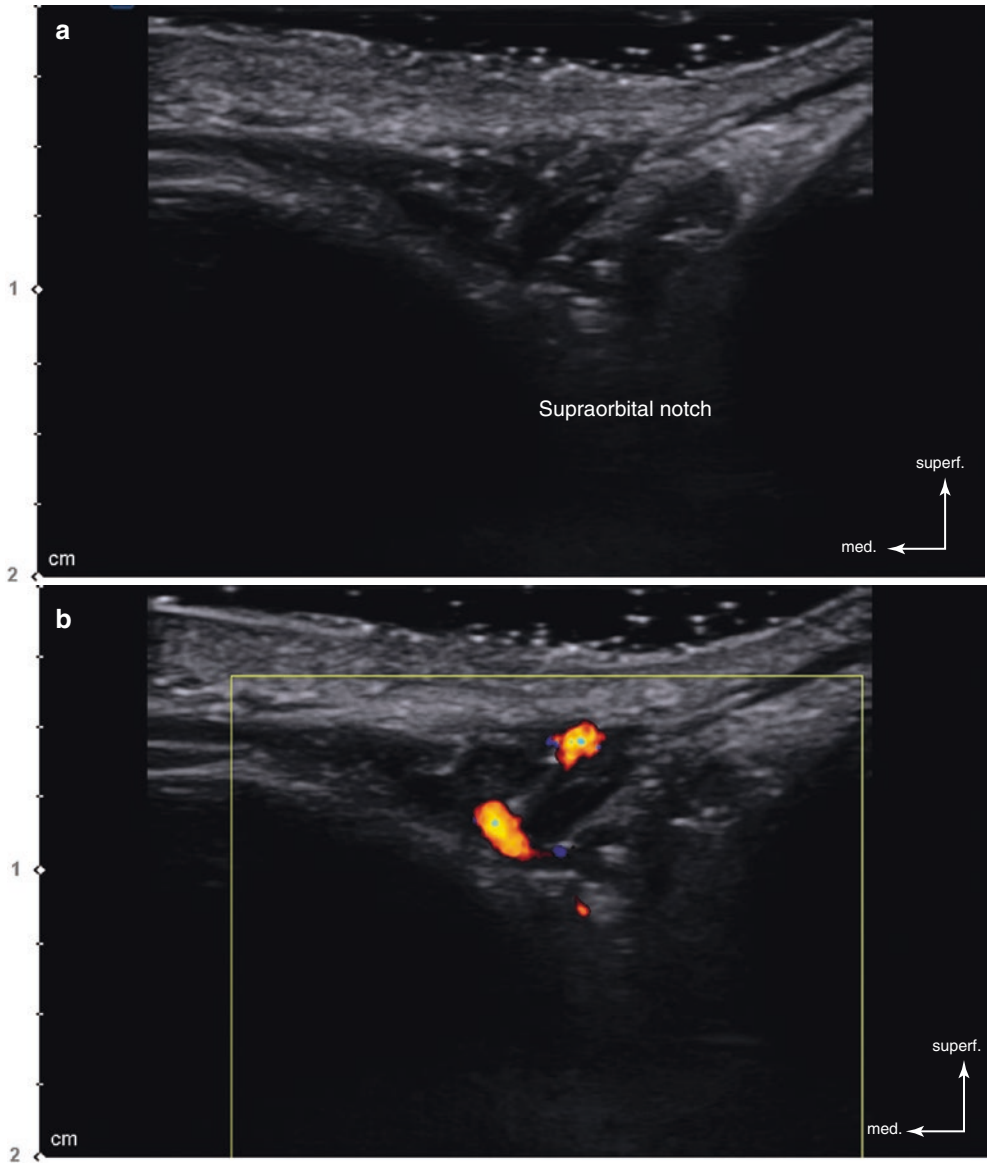

Fig. 2.33 Ultrasonography representing the emerging point of the ophthalmic artery at the supraorbital notch. (**a**) B mode (transverse view, 15 MHz by linear transducer) and (**b**) Doppler mode (transverse view, 15 MHz by linear transducer). (Published with kind permission of © Hee-Jin Kim 2020. All Rights Reserved)

2.5.3 Carotid Artery Branches (Fig. 2.34)

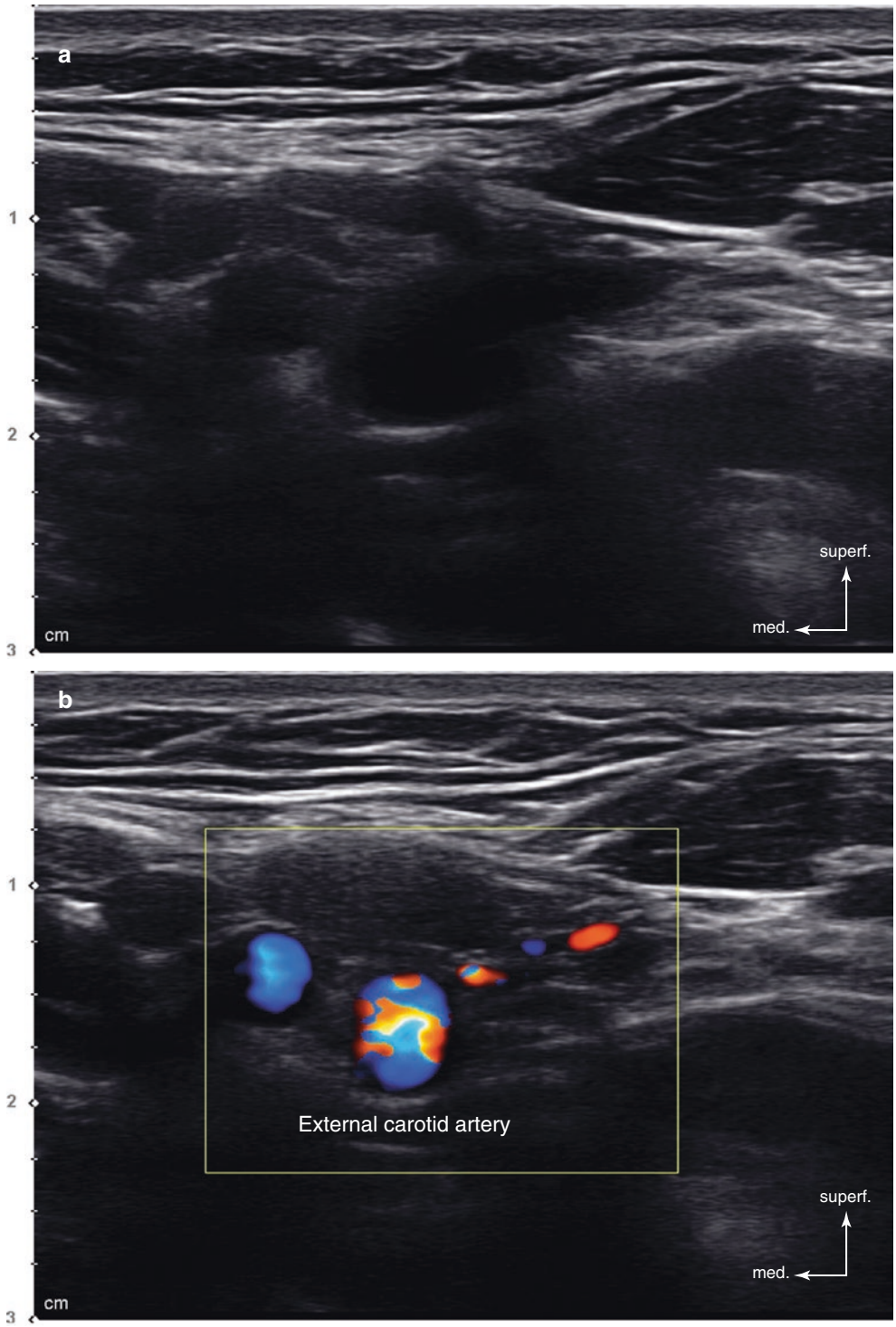

Fig. 2.34 Ultrasonography representing the carotid artery branches at the carotid triangle. (**a**) B mode (transverse view, 15 MHz by linear transducer) and (**b**) Doppler mode (transverse view, 15 MHz by linear transducer). (Published with kind permission of © Hee-Jin Kim 2020. All Rights Reserved)

2.5.4 Sentinel Vein on the Temple (Fig. 2.35)

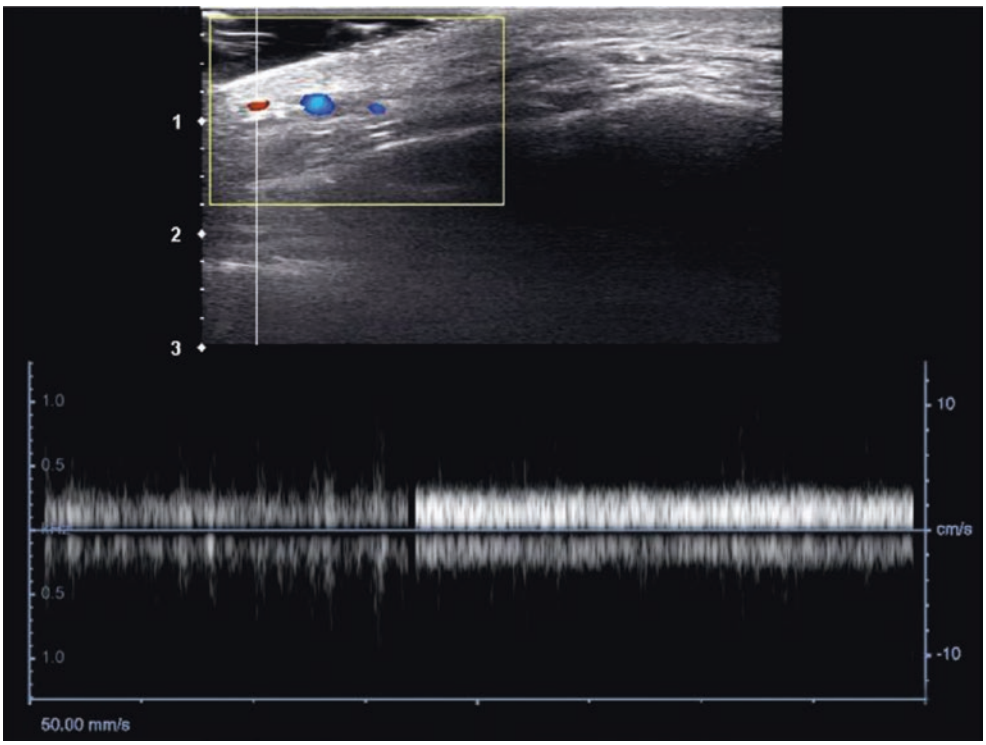

Fig. 2.35 Ultrasonography representing the sentinel vein at the temple area; spectral Doppler mode (transverse view, 15 MHz by linear transducer). (Published with kind permission of © Hee-Jin Kim 2020. All Rights Reserved)

2.5.5 Vessels and Nerves at the Supraorbital Notch (Fig. 2.36)

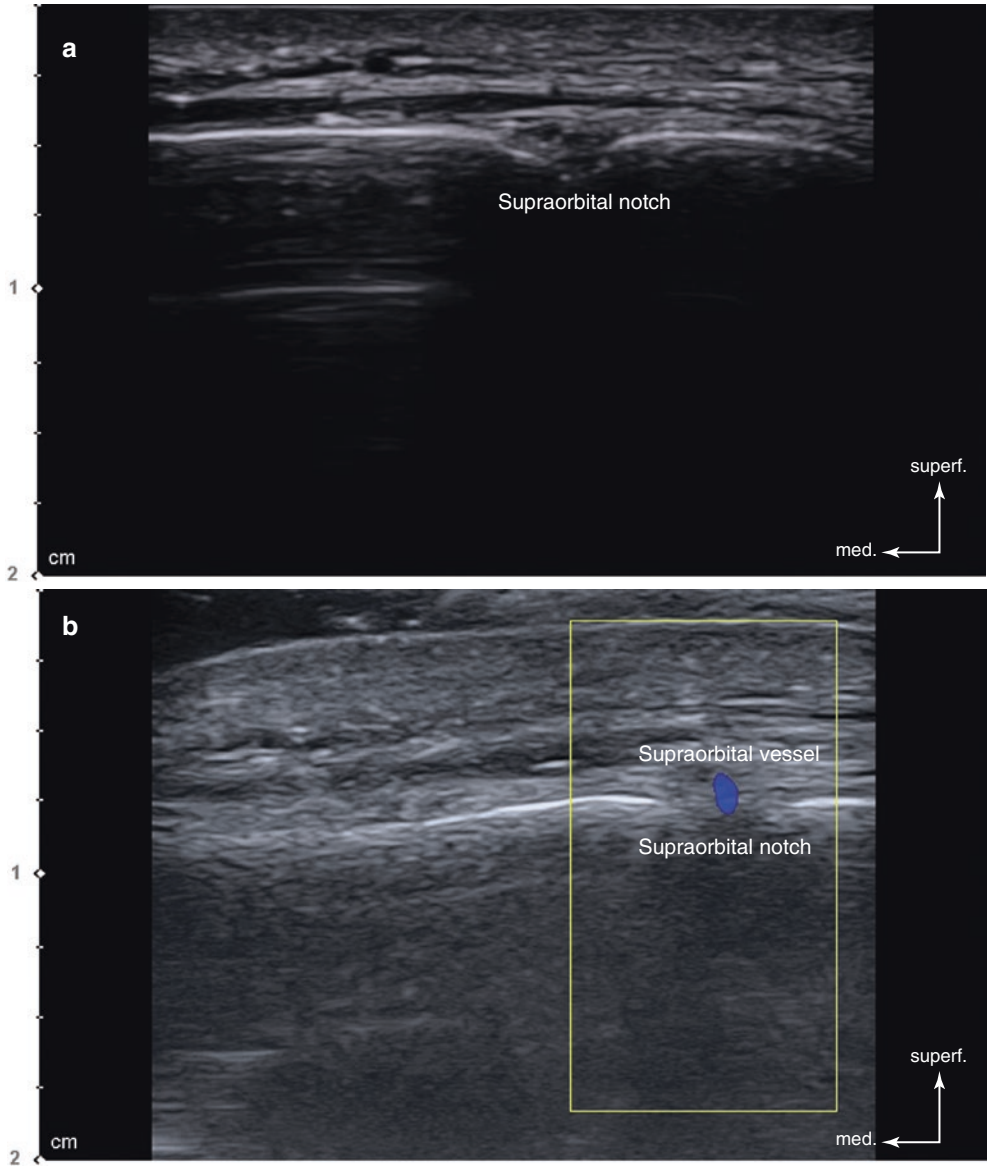

Fig. 2.36 Ultrasonography representing the supraorbital vessels and nerve at the supraorbital notch. (**a**) B mode (transverse view, 15 MHz by linear transducer) and (**b**) Doppler mode (transverse view, 15 MHz by linear transducer). (Published with kind permission of © Hee-Jin Kim 2020. All Rights Reserved)

2.5.6 Vessels and Nerves at the Infraorbital Foramen (Fig. 2.37)

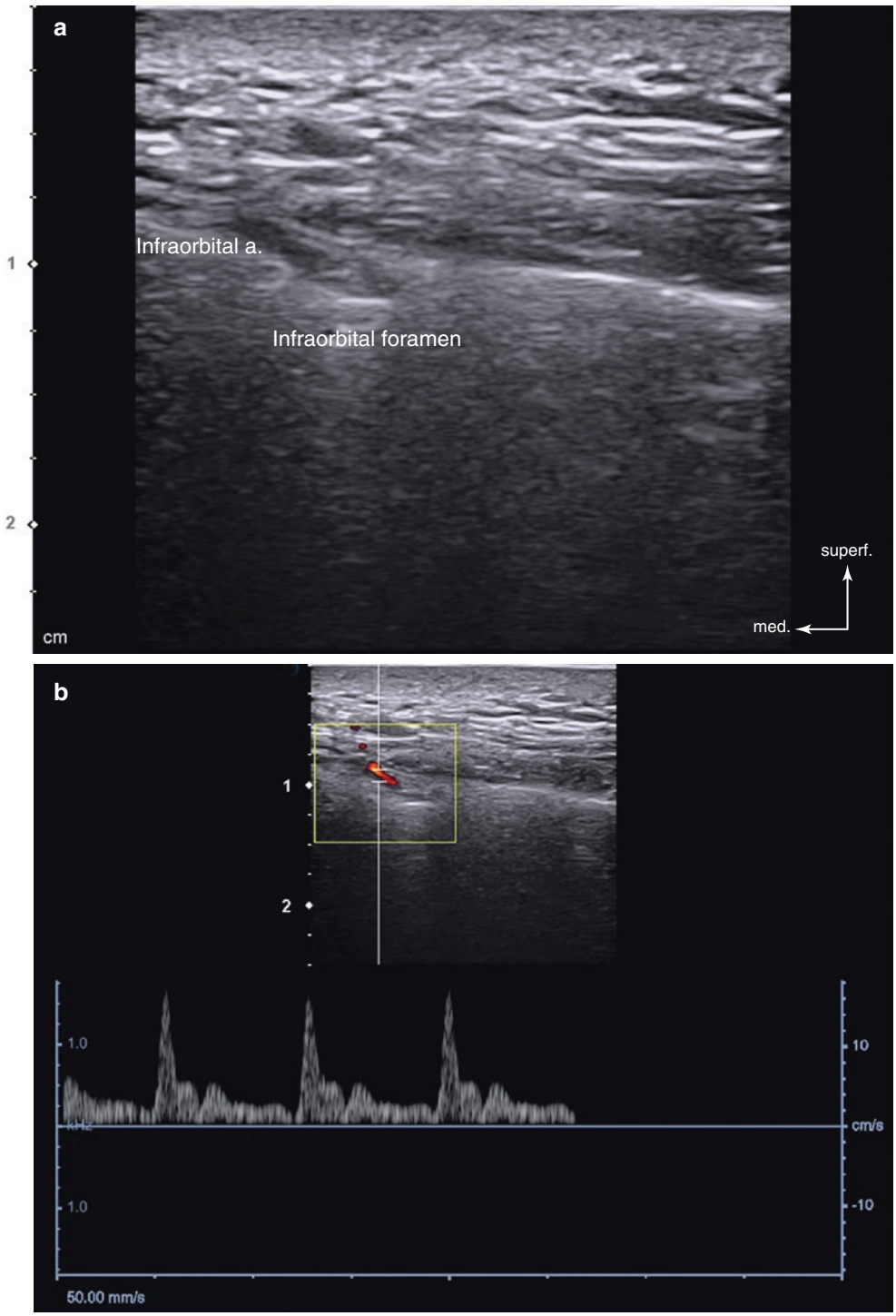

Fig. 2.37 Ultrasonography representing the infraorbital vessels and nerve at the infraorbital foramen. (**a**) B mode (transverse view, 15 MHz by linear transducer) and (**b**) spectral Doppler mode (transverse view, 15 MHz by linear transducer). (Published with kind permission of © Hee-Jin Kim 2020. All Rights Reserved)

2.5.7 Mental Foramen and Nerves (Fig. 2.38)

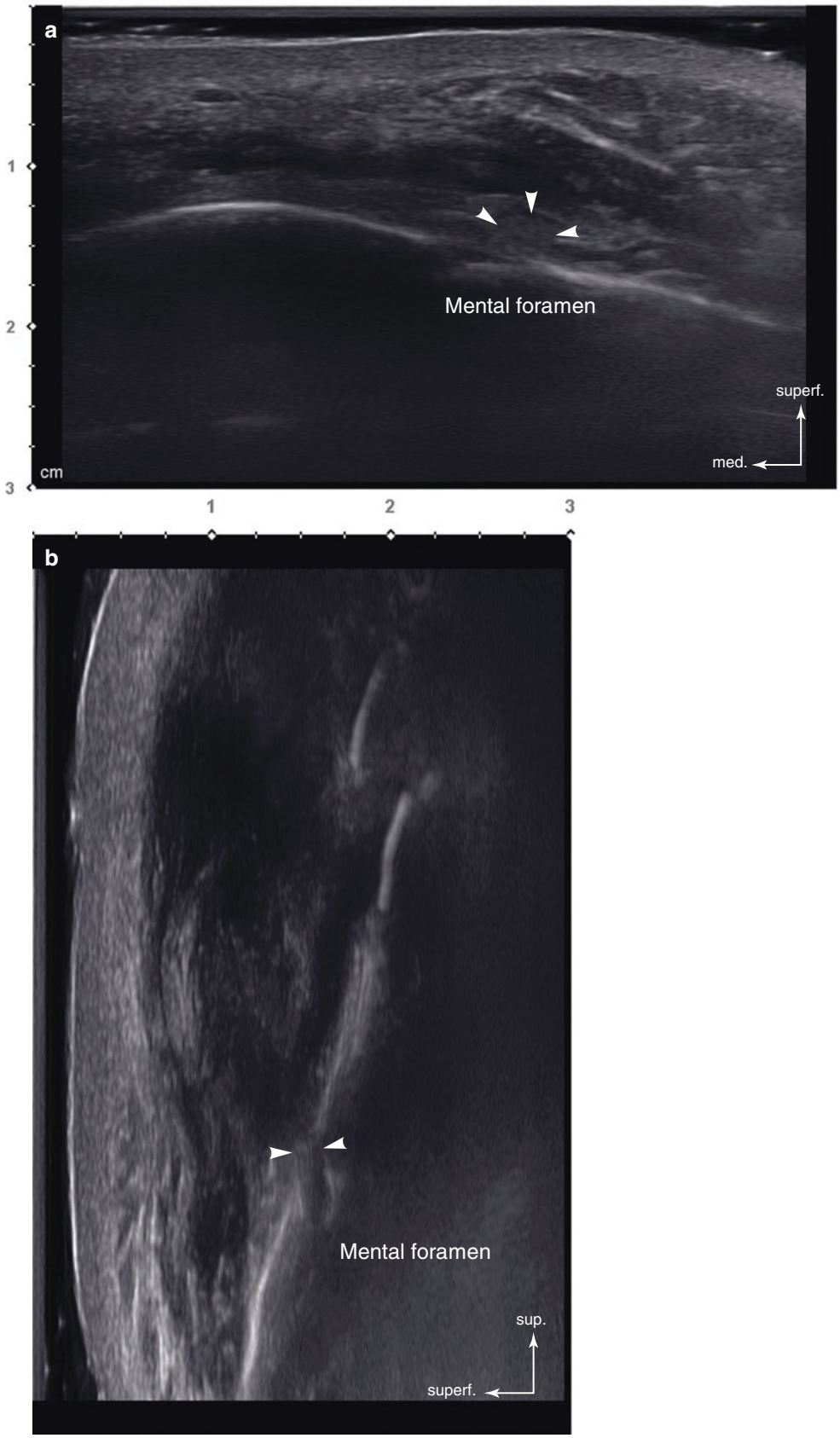

Fig. 2.38 Ultrasonography representing the mental nerve (arrowheads) at the mental foramen. (**a**) B mode (transverse view, 15 MHz by linear transducer) and (**b**) B mode (sagittal view, 15 MHz by linear transducer). (Published with kind permission of © Hee-Jin Kim 2020. All Rights Reserved)

2.5.8 Facial Nerve Within Parotid Gland (Serial Images, Fig. 2.39)

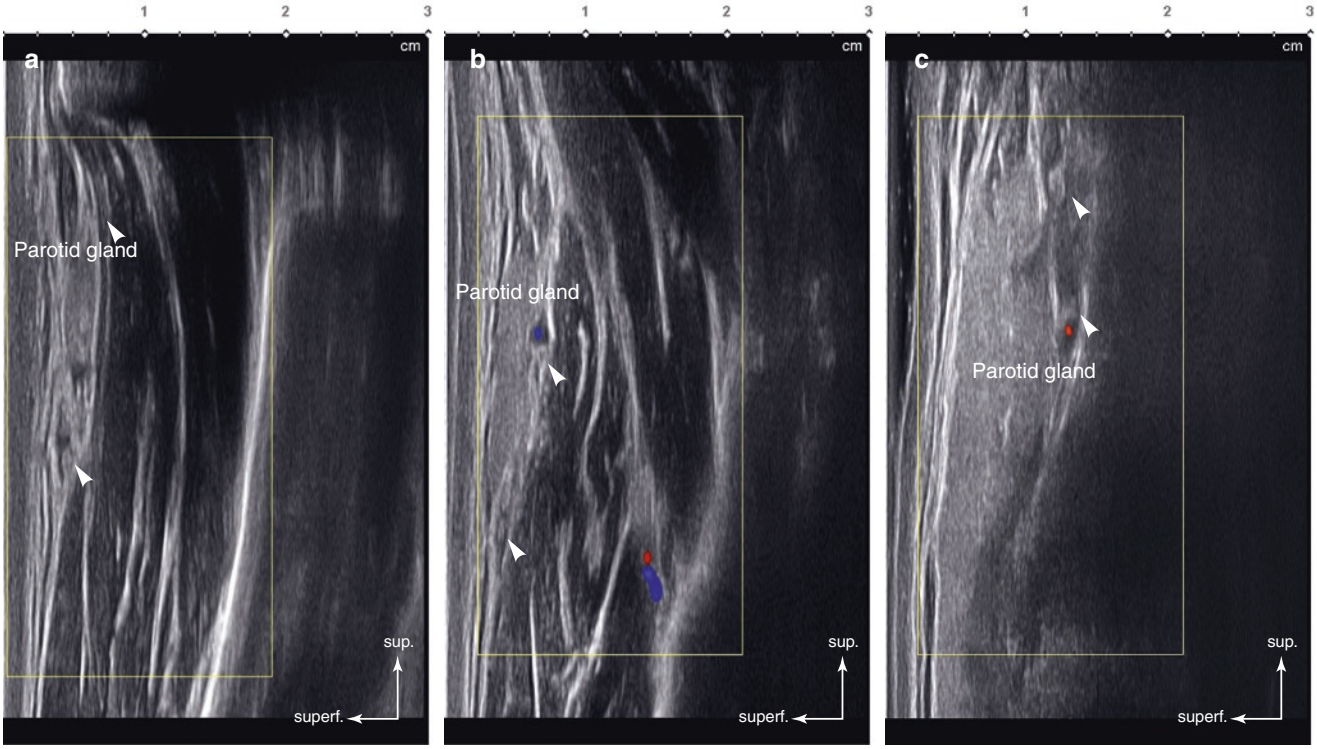

Fig. 2.39 Ultrasonography representing the facial nerve branches (arrowheads) at the parotid gland. (**a**) Doppler mode at the anterior border of the parotid gland (coronal view, 15 MHz by linear transducer), (**b**) Doppler mode at the middle of the parotid gland (coronal view, 15 MHz by linear transducer), and (**c**) Doppler mode at the posterior region of the parotid gland (coronal view, 15 MHz by linear transducer). (Published with kind permission of © Hee-Jin Kim 2020. All Rights Reserved)

2.6 Dynamic Changes of the Facial Structures in US (During Animation and Skin Pinching)

2.6.1 Zygomaticus Major Muscle During Smiling (Fig. 2.40)

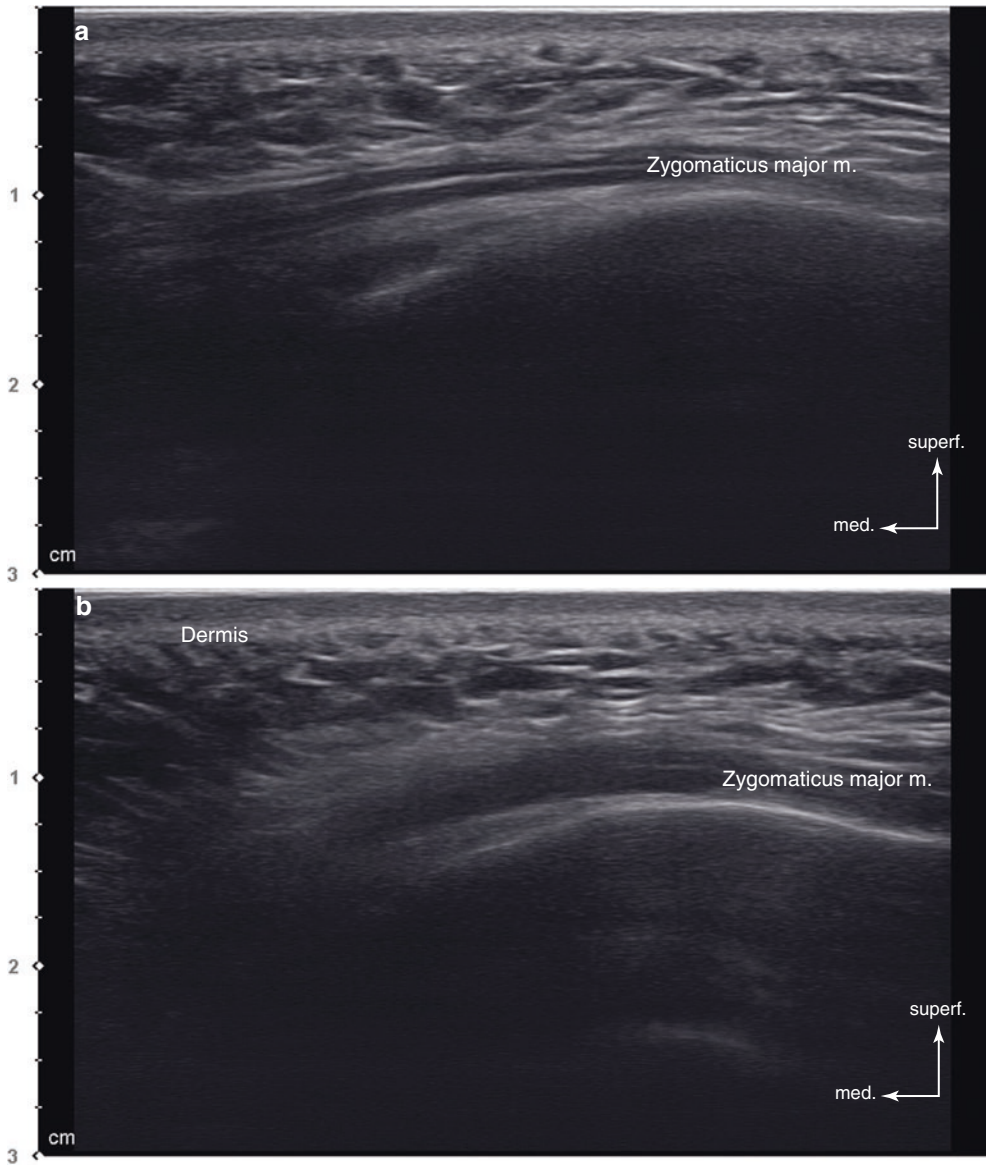

Fig. 2.40 Ultrasonography representing the dynamic movement by the zygomaticus major muscle. (**a**) Resting status (oblique view, 15 MHz by linear transducer) and (**b**) smiling status (oblique view, 15 MHz by linear transducer). (Published with kind permission of © Hee-Jin Kim 2020. All Rights Reserved)

2.6.2 Dimple Formation (Fig. 2.41)

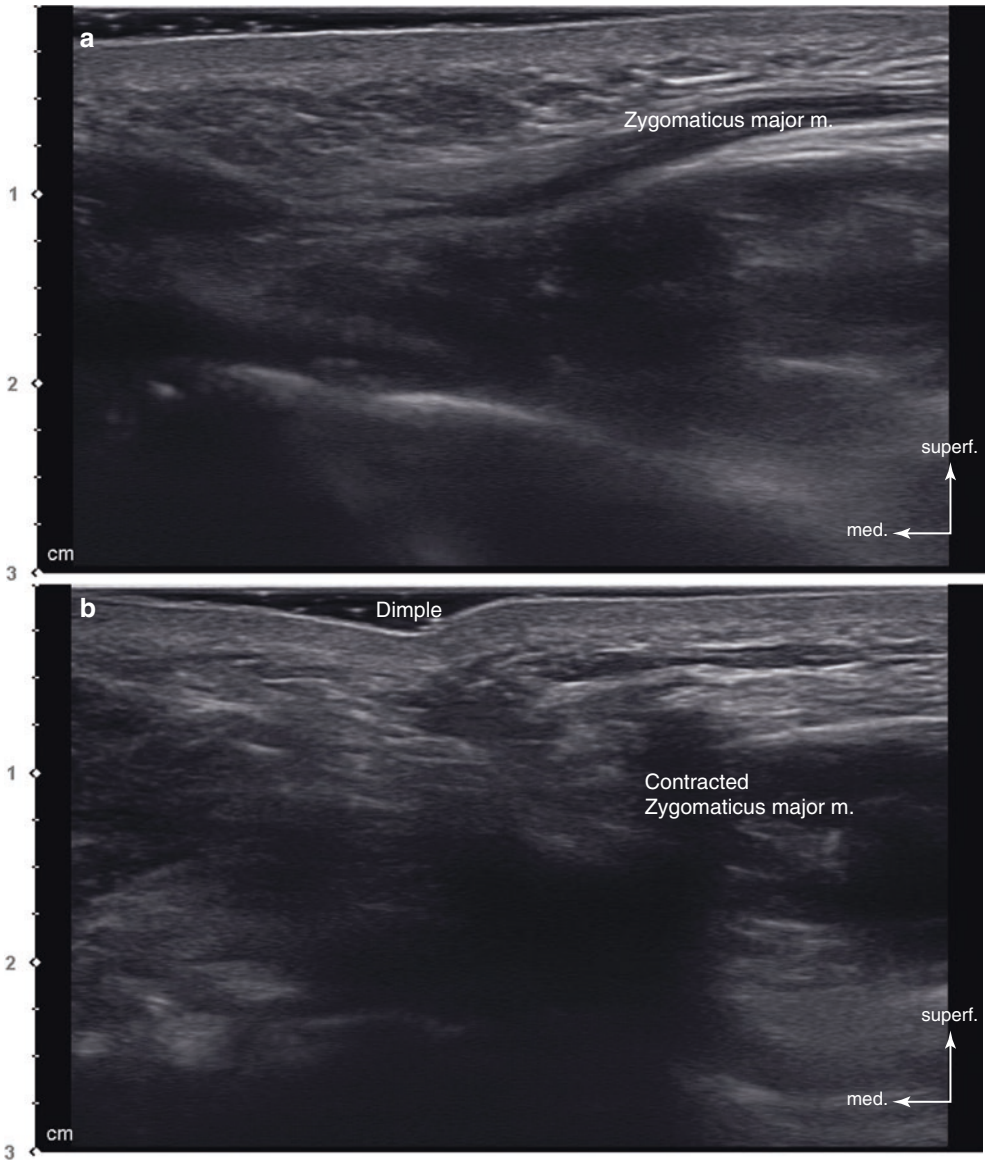

Fig. 2.41 Ultrasonography representing the dimple formation by the zygomaticus major muscle. (**a**) Resting status (oblique view, 15 MHz by linear transducer) and (**b**) smiling status (oblique view, 15 MHz by linear transducer). (Published with kind permission of © Hee-Jin Kim 2020. All Rights Reserved)

2.6.3 Risorius Muscle During Smiling
(Fig. 2.42)

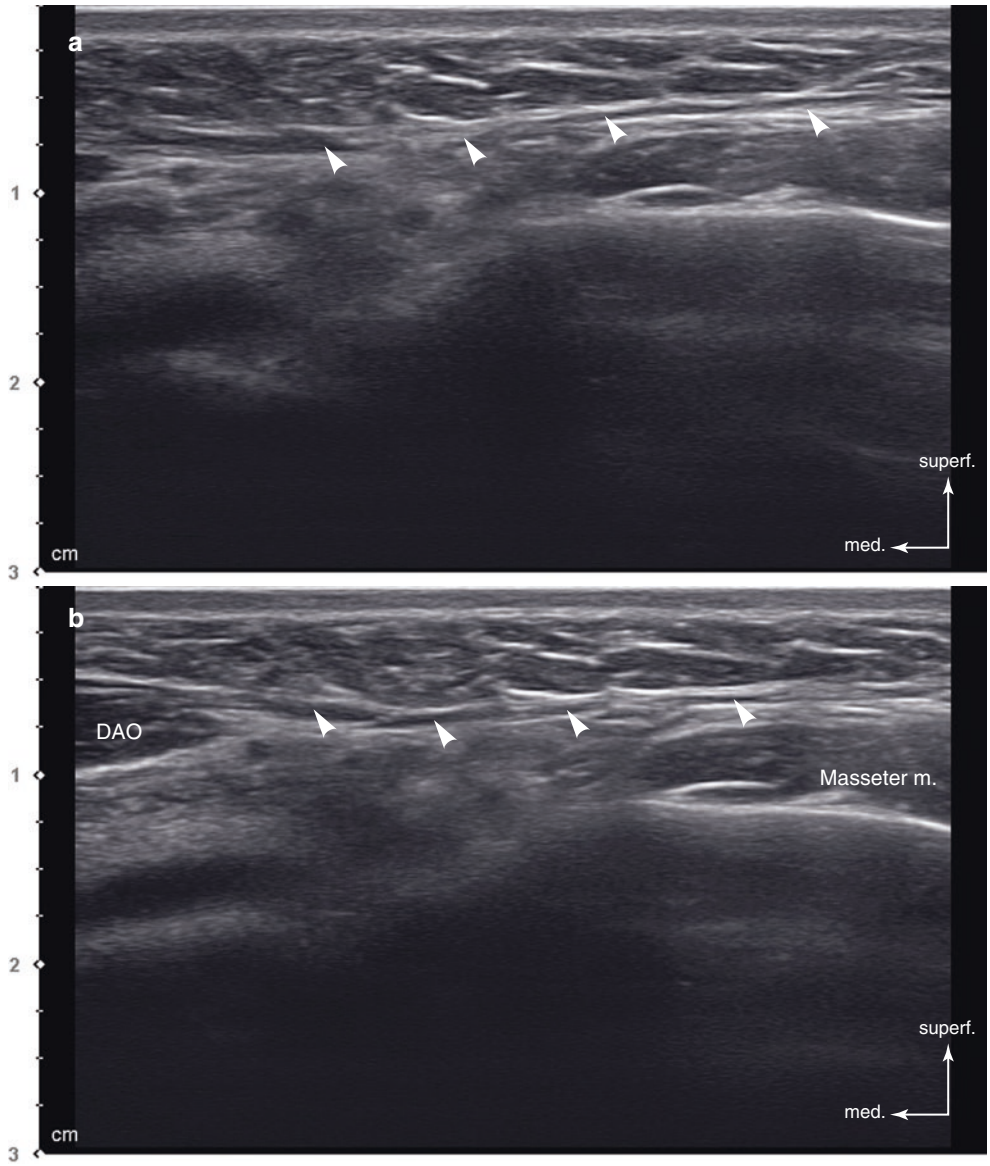

Fig. 2.42 Ultrasonography representing the dynamic movement by the risorius muscle (arrowheads) (DAO: depressor anguli oris m.). (**a**) Resting status (oblique view, 15 MHz by linear transducer) and (**b**) smiling status (oblique view, 15 MHz by linear transducer). (Published with kind permission of © Hee-Jin Kim 2020. All Rights Reserved)

2.6.4 **Clenching** (Fig. 2.43)

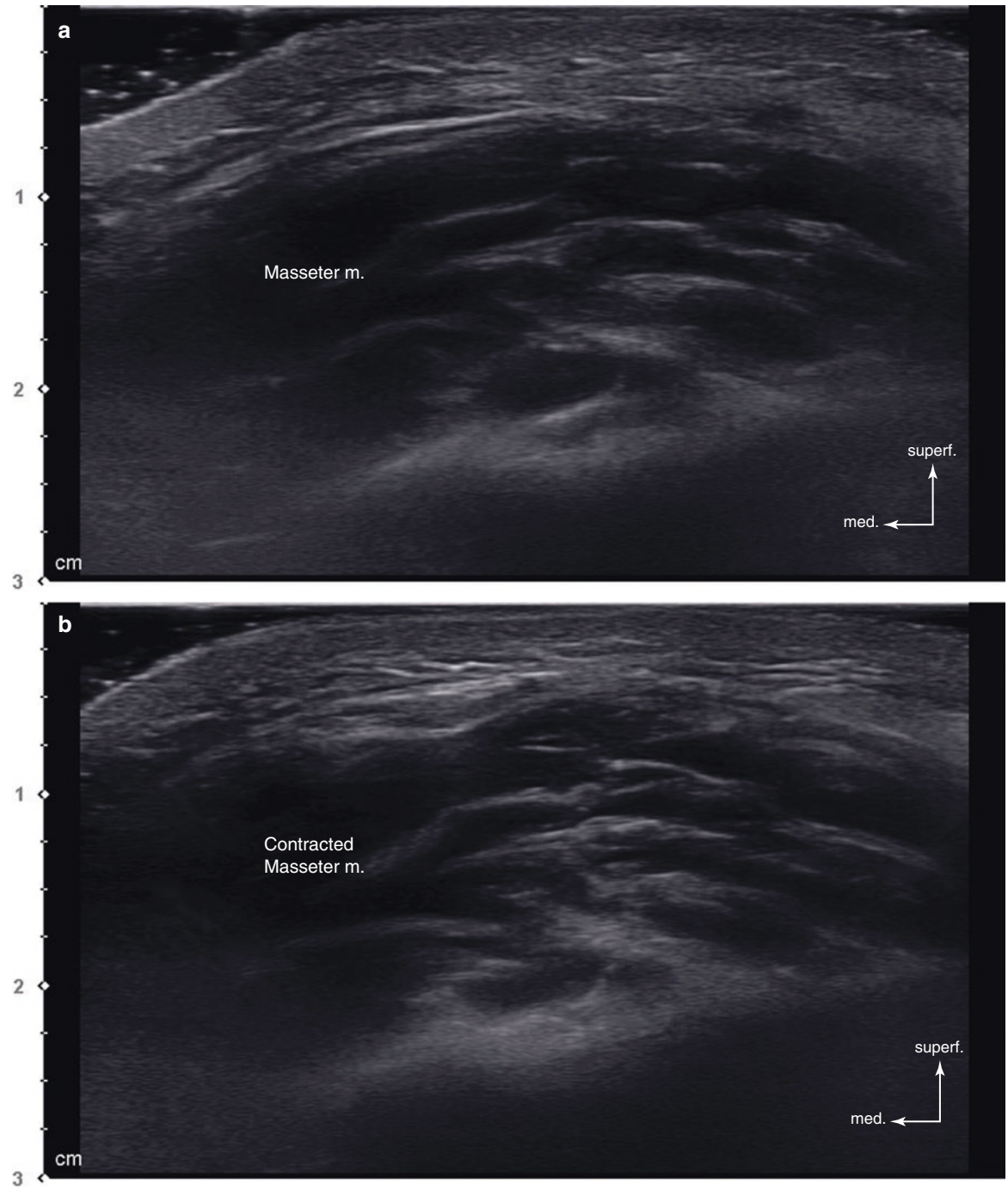

Fig. 2.43 Ultrasonography representing the dynamic movement by the masseter muscle. (**a**) Resting status (transverse view, 15 MHz by linear transducer), (**b**) clenching status (transverse view, 15 MHz by linear transducer), (**c**) resting status (coronal view, 15 MHz by linear transducer), and (**d**) clenching status (coronal view, 15 MHz by linear transducer). (Published with kind permission of © Hee-Jin Kim 2020. All Rights Reserved)

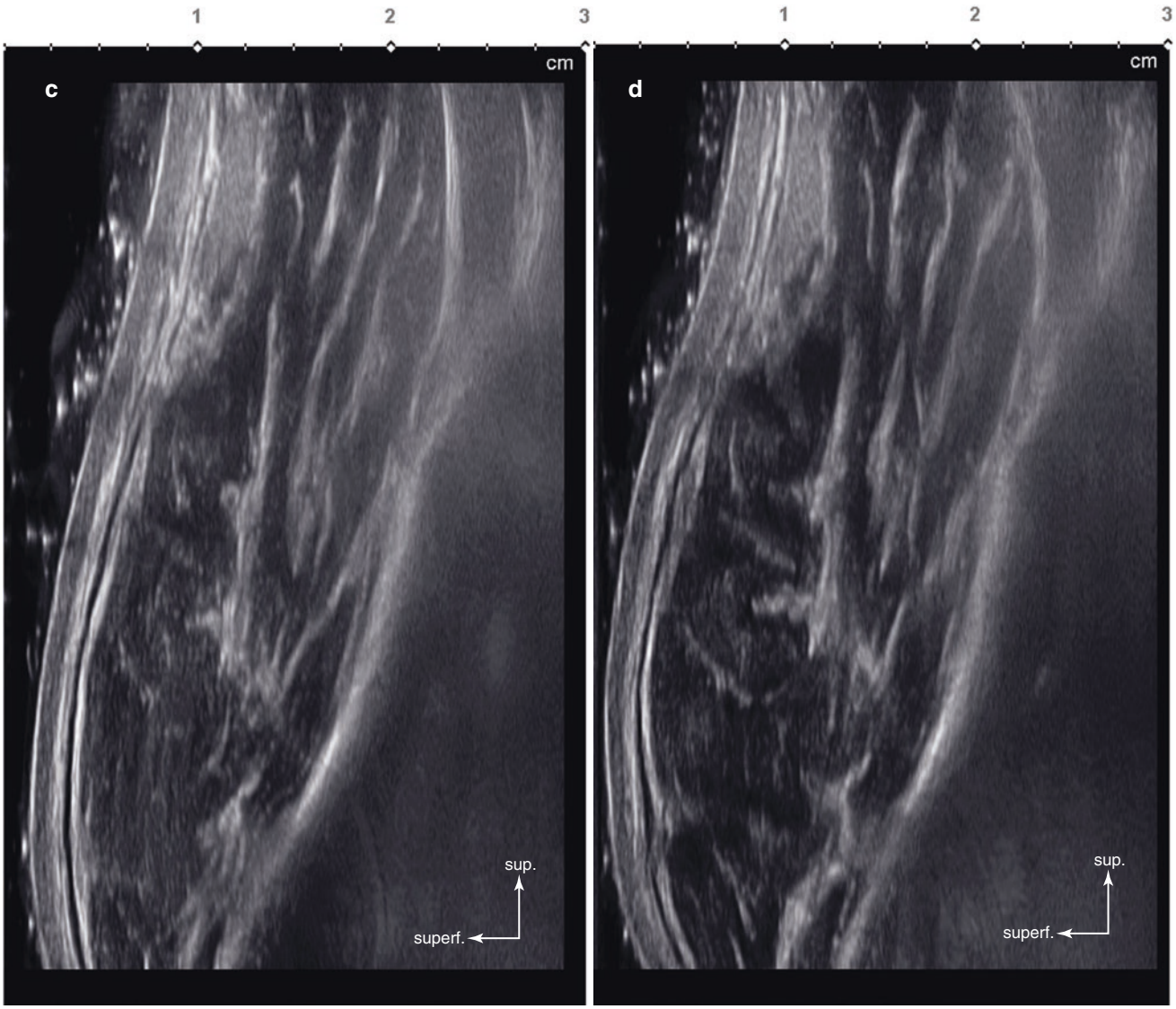

Fig. 2.43 (continued)

2.6.5 **Wrinkle Formation** (Fig. 2.44)

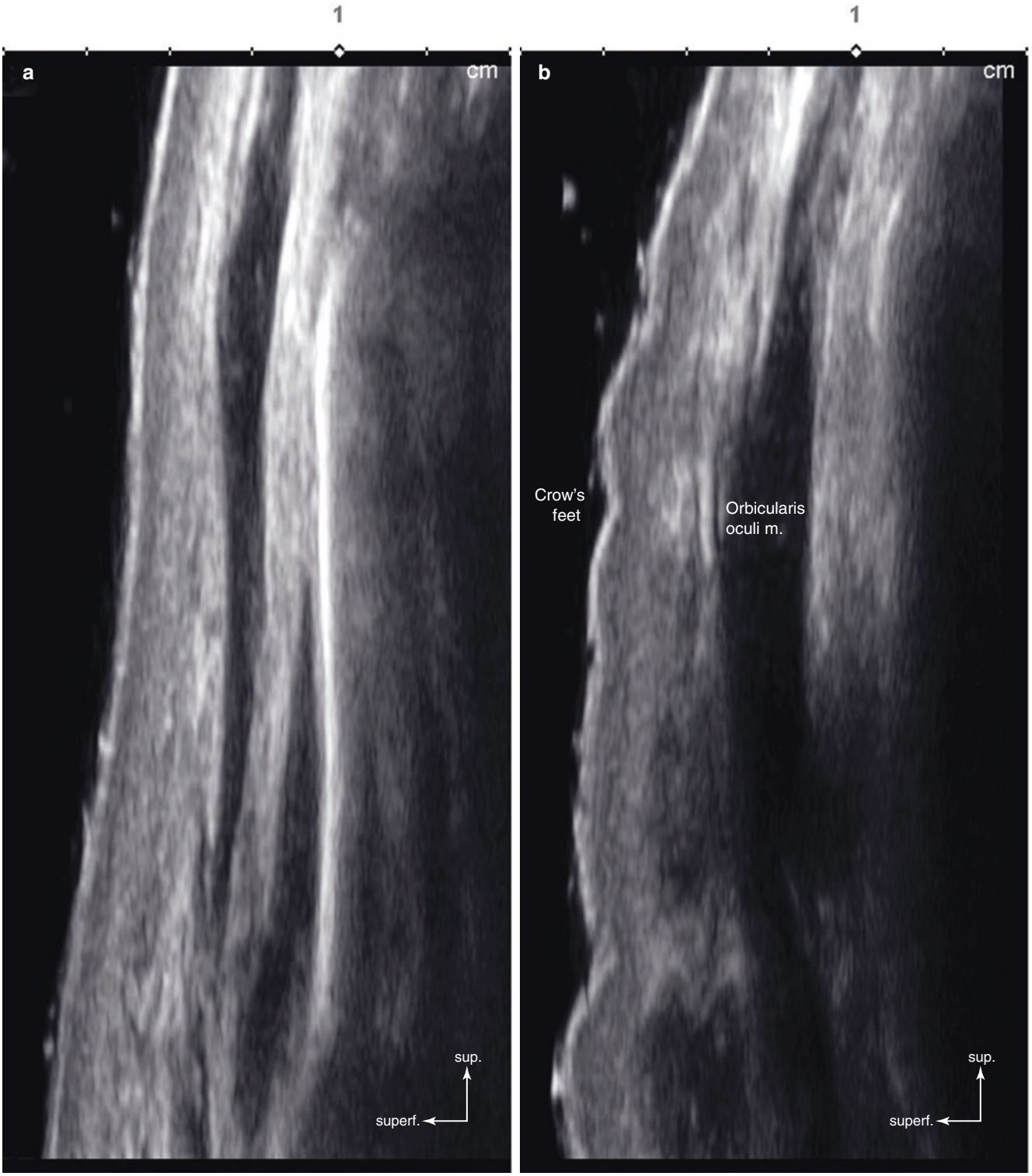

Fig. 2.44 Ultrasonography representing the wrinkle (crow's feet) formation by the orbicularis oculi muscle. (**a**) Resting status (coronal view, 15 MHz by linear transducer) and (**b**) contracted status (coronal view, 15 MHz by linear transducer). (Published with kind permission of © Hee-Jin Kim 2020. All Rights Reserved)

2.6.6 **Pinching** (Fig. 2.45)

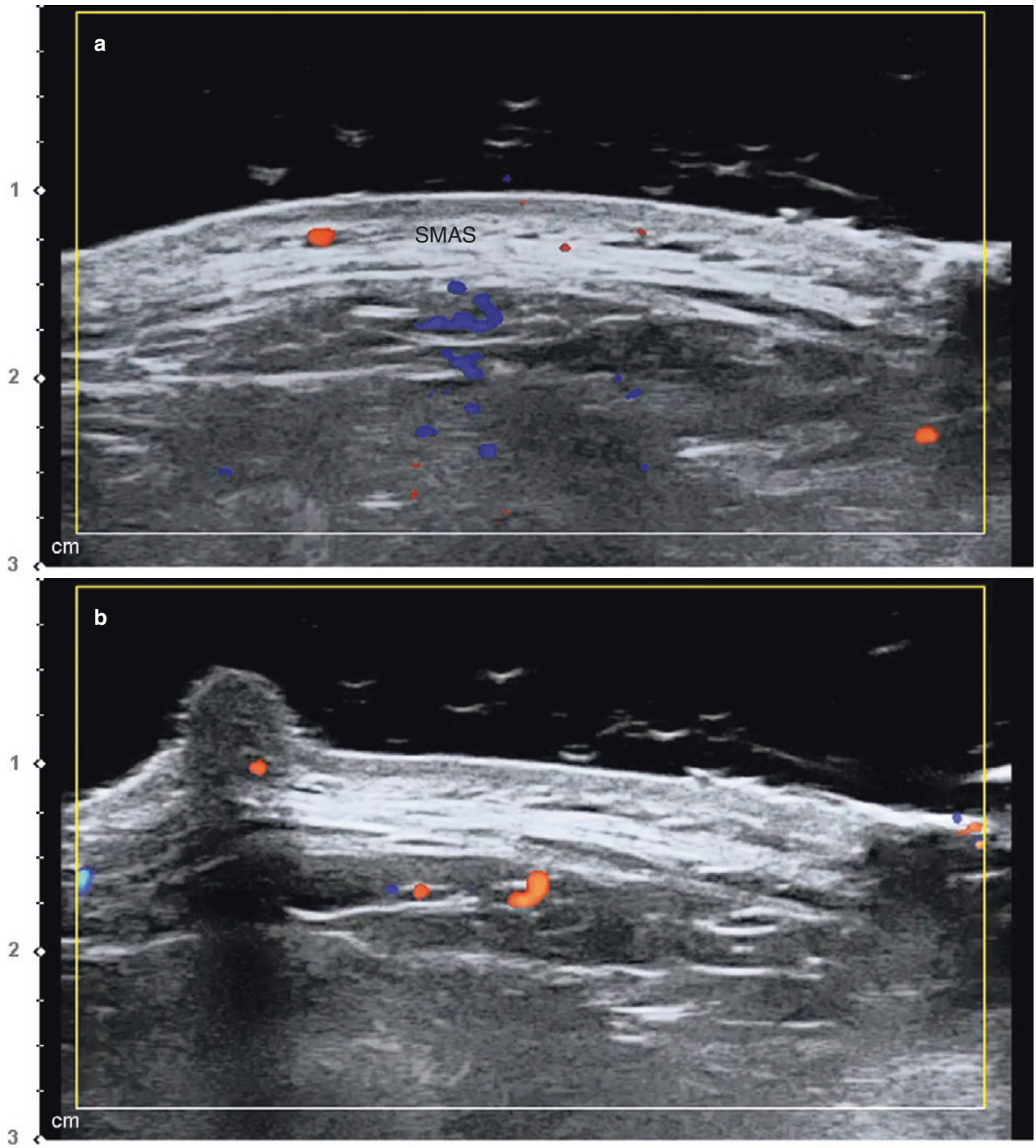

Fig. 2.45 Ultrasonography representing the skin pinching at the temple. (**a**) Normal status (transverse view, 15 MHz by linear transducer) and (**b**) pinched status (transvers view, 15 MHz by linear transducer). (Published with kind permission of © Hee-Jin Kim 2020. All Rights Reserved)

Bibliography

1. Bae JH, Choi DY, Lee JG, Tansatit T, Kim HJ. The risorius muscle: anatomic considerations with reference to botulinum neurotoxin injection for masseteric hypertrophy. Dermatol Surg. 2014;40(12):1334–9.
2. Bae JH, Lee JH, Youn KH, Hur MS, Hu KS, Tansatit T, Kim HJ. Surgical consideration of the anatomic origin of the risorius in relation to facial planes. Aesthet Surg J. 2014;34:NP43–9.
3. Bae JH, Youn KH, Hu KS, Lee JH, Tansatit T, Kim HJ. Clinical implications of the extension of platysmal fibers on the middle and lower faces. Plast Reconstr Surg. 2016;138(2):365–71.
4. Choi DY, Bae JH, Youn KH, Kim W, Suwanchinda A, Tansatit T, Kim HJ. Topography of the dorsal nasal artery and its clinical implications for augmentation of the dorsum of the nose. J Cosmet Dermatol. 2018;17:637–42.
5. Choi DY, Kim JS, Youn KH, Hur MS, Kim JS, Hu KS, Kim HJ. Clinical anatomic considerations of the zygomaticus minor muscle based on the morphology and insertion pattern. Dermatol Surg. 2014;40(8):858–63.
6. Choi YJ, Kim JS, Gil YC, Phetudom T, Kim HJ, Tansatit T, Hu KS. Anatomic considerations regarding the location and boundary of the depressor anguli oris muscle with reference to botulinum toxin injection. Plast Reconstr Surg. 2014;134(5):917–21.
7. Choi YJ, We YJ, Lee HJ, Lee KW, Gil YC, Hu KS, Tansatit T, Kim HJ. Three-dimensional evaluation of the depressor anguli oris and depressor labii inferioris for botulinum toxin injections. Aesthet Surg J. 2020;
8. Choi YJ, Won SY, Lee JG, Hu KS, Kim ST, Tansatit T, Kim HJ. Characterizing the Lateral Border of the Frontalis for Safe and Effective Injection of Botulinum Toxin. Aesthet Surg J. 2016;36(3):344–8.
9. Chung MS, Kim HJ, Kang HS, Chung IH. Locational relationship of the supraorbital notch or foramen and infraorbital and mental foramina in Koreans. Acta Anat. 1995;154:162–6.
10. Con LY, Phothong W, Lee SH, Wanitphakdeedecha R, Koh I, Tansatit T, Kim HJ. Topographic Analysis of the Supratrochlear Artery and the Supraorbital Artery: Implication for Improving the Safety of Forehead Augmentation. Plast Reconstr Surg. 2017;139:620e.
11. Cong LY, Choi YJ, Hu KS, Tansatit T, Kim HJ. Three-dimensional topography of the emerging point of the ophthalmic artery. Plast Reconstr Surg. 2019;143:32e–8e.
12. Cong LY, Lee SH, Hu KS, Tansatit T, Kim HJ. Topographic anatomy of the inferior medial palpebral artery and its relevance to the pretarsal roll augmentation. Plast Reconstr Surg. 2016;138:430–6.
13. Hu KS, Jin GC, Youn KH, Kwak HH, Koh KS, Fontaine C, Kim HJ. An anatomic study of the bifid zygomaticus major muscle. J Craniofac Surg. 2008;19(2):534–5.
14. Hu KS, Kim ST, Hur MS, Park JH, Song WC, Koh KS, Kim HJ. Topography of the masseter muscle in relation to treatment with botulinum toxin type A. Oral Surg Oral Med Oral Pathol Oral Radiol Endod. 2010;110(2):167–71.
15. Hu KS, Kwak HH, Song WC, Kang HJ, Kim HC, Fontaine C, Kim HJ. Branching patterns of the infraorbital nerve and topography within the infraorbital space. J Craniofac Surg. 2006;17(6):1111–5.
16. Hu KS, Kwak J, Koh KS, Abe S, Fontaine C, Kim HJ. Topographic distribution area of the infraorbital nerve. Surg Radiol Anat. 2007;29(5):383–8.
17. Hu KS, Yang SJ, Kwak HH, Park HD, Youn KH, Jung HS, Kim HJ. Location of the modiolous and the morphologic variations of the risorius and zygomaticus major muscle related to the facial expression in Koreans. Korean J Phys Anthropol. 2005;18:1–11.
18. Hu KS, Yun HS, Hur MS, Kwon HJ, Abe S, Kim HJ. Branching patterns and intraosseous course of the mental nerve. J Oral Maxillofac Surg. 2007;65(11):2288–94.
19. Hur MS, Hu KS, Cho JY, Kwak HH, Song WC, Koh KS, Lorente M, Kim HJ. Topography and location of the depressor anguli oris muscle with a reference to the mental foramen. Surg Radiol Anat. 2008;30(5):403–7.
20. Hur MS, Hu KS, Kwak HH, Lee KS, Kim HJ. Inferior bundle (fourth band) of the buccinators and the incisivus labii inferioris muscle. J Craniofac Surg. 2011;22(1):289–92.
21. Hur MS, Hu KS, Park JT, Youn KH, Kim HJ. New anatomical insight of the levator labii superioris alaeque nasi and the transverse part of the nasalis. Surg Radiol Anat. 2010;32(8):753–6.
22. Hur MS, Hu KS, Youn KH, Song WC, Abe S, Kim HJ. New Anatomical profile of the nasal musculature: dilator naris vestibularis, dilator naris anterior, and alar part of the nasalis. Clin Anat. 2011;24(2):162–7.
23. Hur MS, Kim HJ, Choi BY, Hu KS, Kim HJ, Lee KS. Morphology of the mentalis muscle and its relationship with the orbicularis oris and incisivus labii inferioris muscles. J Craniofac Surg. 2013;24(2):602–4.
24. Hur MS, Youn KH, Hu KS, Song WC, Koh KS, Fontaine C, Kim HJ. New anatomic considerations on the levator labii superioris related with the nasal ala. J Craniofac Surg. 2010;21(1):258–60.
25. Hwang WS, Hur MS, Hu KS, Song WC, Koh KS, Baik HS, Kim ST, Kim HJ, Lee KJ. Surface anatomy of the lip elevator muscles for the treatment of gummy smile using botulinum toxin. Angle Orthod. 2009;79(1):70–7.
26. Jung DH, Kim HJ, Koh KS, Oh CS, Kim KS, Yoon JH, Chung IH. Arterial supply of the nasal tip in Asians. Laryngoscope. 2000;110(2):308–11.
27. Jung W, Youn KH, Won SY, Park JT, Hu KS, Kim HJ. Clinical implications of the middle temporal vein with regard to temporal fossa augmentation. Dermatol Surg. 2014;40(6):618–23.
28. Kim DH, Hong HS, Won SY, Kim HJ, Hu KS, Choi JH, Kim HJ. Intramuscular nerve distribution of the masseter muscle for botulinum toxin injection. J Craniofac Surg. 2010;21(2):588–91.
29. Kim HJ, Hu KS, Kang MK, Hwang K, Chung IH. Decussation patterns of the platysma in Koreans. Br J Plast Surg. 2001;54(5):400–2.
30. Kim HJ, Koh KS, Oh CS, Hu KS, Kang JW, Chung IH. Emerging patterns of the cervical cutaneous nerves in Asians. Int J Oral Maxillofac Surg. 2002;31(1):53–6.
31. Kim HS, Lee KL, Gil YC, Hu KS, Tansatit T, Kim HJ. Topographic Anatomy of the Infraorbital Artery and its Clinical Implications for Nasolabial Fold Augmentation. Plast Reconstr Surg. 2018;142(3):273e–80e.
32. Kim HS, Pae C, Bae JH, Hu KS, Chang BM, Tansatit T, Kim HJ. An anatomical study of the risorius in Asians and its insertion at the modiolus. Surg Radiol Anat. 2014;37(2):147–51.
33. Kim YS, Choi DY, Gil YC, Hu KS, Tansatit T, Kim HJ. The anatomical origin and course of the angular artery regarding its clinical implications. Dermatol Surg. 2014;40(10):1070–6.
34. Kim YS, Lee KW, Kim JS, Gil YC, Tanvaa T, Shin DH, Kim HJ. Regional thickness of facial skin and superficial fat: application to the minimally invasive procedures. Clin Anat. 2020;32:1008–18.
35. Koh KS, KIM HJ, Oh CS, Chung IH. Branching patterns and symmetry of the course of the facial artery in Koreans. Int J Oral Maxillofac Surg. 2003;32(4):414–8.
36. Kwak HH, Hu KS, Youn KH, Jin KH, Shim KS, Fontaine C, Kim HJ. Topographic relationship between the muscle bands of the zygomaticus major muscle and the facial artery. Surg Radiol Anat. 2006;28(5):477–80.
37. Kwak HH, Jo JB, Hu KS, Oh CS, Koh KS, Chung IH, Kim HJ. Topography of the third portion of the maxillary artery via the transantral approach in Asians. J Craniofac Surg. 2010;21(4):1284–9.
38. Kwak HH, Ko SJ, Jung HS, Park HD, Chung IH, Kim HJ. Topographic anatomy of the deep temporal nerves, with refer-

ences to the superior head of lateral pterygoid. Surg Radiol Anat. 2003;25(5-6):393–9.
39. Kwak HH, Park HD, Youn KH, Hu KS, Koh KS, Han SH, Kim HJ. Branching patterns of the facial nerve and its communication with the auriculotemporal nerve. Surg Radiol Anat. 2004;26(6):494–500.
40. Kwak HH, Park HD, Youn KH, Hu KS, Koh KS, Han SH, Kim HJ. Branching patterns of the facial nerve in Korean. Korean J Phys Anthrop. 2003;16:66–74.
41. Lee HJ, Choi KS, Won SY, Prawit A, Hu KS, Kim ST, Tanvaa T, Kim HJ. Topographic relationship between the supratrochlear nerve and corrugator supercilii muscle for the botulinum toxin injections in chronic migraine. Toxins. 2015;7:2629–38.
42. Lee HJ, Choi YJ, Lee KW, Kim HJ. Positional patterns among the auriculotemporal nerve, superficial temporal artery, and superficial temporal vein for use in decompression treatments for migraine. Sci Rep. 2018;8:16539.
43. Lee HJ, Kang IW, Won SY, Lee JG, Hu KS, Tansatit T, Kim HJ. Description of a novel anatomical venous structure in the nasoglabellar area. J Craniofac Surg. 2014;25(2):633–5.
44. Lee HJ, Won SY, O J, Hu KS, Mun SY, Yang HM, Kim HJ. The facial artery: a comprehensive anatomical review. Clin Anat. 2018;31:99–108.
45. Lee JG, Yang HM, Choi YJ, Favero V, Kim YS, Hu KS, Kim HJ. Facial arterial depth and layered relationship with facial musculatures. Plast Reconstr Surg. 2015;135:437–44.
46. Lee JG, Yang HM, Hu KS, Lee YI, Lee HJ, Choi YJ, Kim HJ. Frontal branch of the superficial temporal artery: anatomical study and clinical implications regarding injectable treatments. Surg Radiol Anat. 2015;37(1):61–8.
47. Lee JH, Lee K, Jung W, Youn KH, Hu KS, Tansatit T, Kim HJ. A novel anatomical consideration on the exposed segment of the facial artery. Clin Anat. 2020;33:257–64.
48. Lee JY, Kim JN, Kim SH, Choi HG, Hu KS, Kim HJ, Song WC, Koh KS. Anatomical verification and designation of the superficial layer of the temporalis muscle. Clin Anat. 2012;25(2):176–81.
49. Lee JY, Kim JN, Yoo JY, Hu KS, Kim HJ, Song WC, Koh KS. Topographic anatomy of the masseter muscle focusing on the tendinous digitation. Clin Anat. 2012;25(7):889–92.
50. Lee KL, Choi YJ, Gil YC, Hu KS, Tansatit T, Kim HJ. Locational relationship between the lateral border of the frontalis muscle and the superior temporal line. Plast Reconstr Surg. 2019;143:293e–298e.
51. Lee KW, Kim SH, Gil YC, Hu KS, Kim HJ. Validity and reliability of a structured-light 3D scanner and an ultrasound imaging system for measurements of facial skin thickness. Clin Anat. 2017;30:878–86.
52. Lee SH, Gil YC, Choi YJ, Tansatit T, Kim HJ, Hu KS. Topographic anatomy of superior labial artery for dermal filler injection. Plast Reconstr Surg. 2015;135:445–50.
53. Lee SH, Lee HJ, Kim YS, Kim HJ, Hu KS. What's difference between the inferior labial artery and horizontal labiomental artery? Surg Radiol Anat. 2015;37(8):947–53.
54. Lee SH, Lee HJ, Kim YS, Tansatit T, Kim HJ. Novel anatomic description of the course of the inferior palpebral vein from minimally invasive aesthetic treatments. Dermatol Surg. 2016;42:618–23.
55. Lee SH, Lee M, Kim HJ. Anatomy-based image-processing analysis for the running pattern of the perioral artery for minimally invasive surgery. Br J Oral Maxillofac Surg. 2014;52(8):688–92.
56. Lee YI, Yang HM, Pyeon HJ, Lee HK, Kim HJ. Anatomical and histological study of the arterial distribution in the columellar area, and the clinical implications. Surg Radiol Anat. 2014;36(7):669–74.
57. Park JT, Youn KH, Hu KS, Kim HJ. Medial muscular band of the orbicularis oculi muscle. J Craniofac Surg. 2012;23(1):195–7.
58. Park JT, Youn KH, Hur MS, Hu KS, Kim HJ, Kim HJ. Malaris muscle, the lateral muscular band of orbicularis oculi muscle. J Craniofac Surg. 2011;22(2):659–62.
59. Park KH, Kim YK, Woo SJ, Kang SW, Lee WK, Choi KS, Kwak HW, Yoon IH, Huh K, Kim JW. Iatrogenic occlusion of the ophthalmic artery after cosmetic facial filler injections: a national survey by the Korean Retina Society. JAMA Ophthalmol. 2014;132(6):714–23.
60. Rho NK, Chang YY, Chao YY, Furuyama N, Huang P, Kerscher M, Kim HJ, Park JY, Peng P, Rummaneethorn P, Rzany B, Sundaram H, Wong CH, Yang Y, Prasetyo AD. Consensus recommendations for optimal augmentation of the asian face with hyaluronic acid and calcium hydroxylapatite fillers. Plast Reconstr Surg. 2015;136(5):940–56.
61. Shim KS, Hu KS, Kwak HH, Youn KH, Koh KS, Fontaine C, Kim HJ. An anatomy of the insertion of the zygomaticus major muscle in human focused on the muscle arrangement at the mouth corner. Plast Reconstr Surg. 2008;121(2):466–73.
62. Song WC, Kim SH, Paik DJ, Han SH, Hu KS, Kim HJ, Koh KS. Location of the infra-orbital and mental foramen with reference to the soft tissue landmarks. Plast Reconstr Surg. 2007;120:1343–7.
63. Won SY, Kim DH, Yang HM, Park JT, Kwak HH, Hu KS, Kim HJ. Clinical and anatomical approach using Sihler's staining technique (whole mount nerve stain). Anat Cell Biol. 2011;44(1):1–7.
64. Won SY, Yang HM, Woo HS, Chang KY, Youn KH, Kim HJ, Hu KS. Neuroanastomosis and the innervation territory of the mental nerve. Clin Anat. 2014;27(4):598–602.
65. Yang HM, Hu KS, Kim HJ. Nervous communication and facial expresssion muscles. Korean J Phys Anthropol. 2013;26:1–12.
66. Yang HM, Jung W, Won SY, Youn KH, Hu KS, Kim HJ. Anatomical study of medial zygomaticotemporal vein and its clinical implication regarding the injectable treatments. Surg Radiol Anat. 2014;37(2):175–80.
67. Yang HM, Kim HJ, Park HW, Sohn HJ, Ok HT, Moon JH, Woo SH. Revisiting the topographic anatomy of the marginal mandibular branch of facial nerve relating to the surgical approach. Aesthet Surg J. 2016;36(9):977–82.
68. Yang HM, Kim HJ. Anatomical study of the corrugator supercilii muscle and its clinical implication with botulinum toxin A injection. Surg Radiol Anat. 2013;35(9):817–21.
69. Yang HM, Lee JG, Hu KS, Gil YC, Choi YJ, Lee HK, Kim HJ. New anatomical insights of the course and branching patterns of the facial artery: clinical implications regarding injectable treatments to the nasolabial fold and nasojugal groove. Plast Reconstr Surg. 2014;133(5):1077–82.
70. Yang HM, Lee YI, Lee JG, Choi YJ, Lee HJ, Lee SH, Hu KS, Kim HJ. Topography of superficial arteries on the face. J Physiol Anthropol. 2013;26:131–40.
71. Yang HM, Won SY, Kim HJ, Hu KS. Sihler staining study of anastomosis between the facial and trigeminal nerves in the ocular area and its clinical implications. Muscle Nerve. 2013;48(4):545–50.
72. Yang HM, Won SY, Kim HJ, Hu KS. Sihler's staining study of the infraorbital nerve and its clinical complication. J Craniofac Surg. 2014;25(6):2209–13.
73. Yang HM, Won SY, Lee JG, Han SH, Kim HJ, Hu KS. Sihler-stain study of buccal nerve distribution and its clinical implications. Oral Surg Oral Med Oral Pathol Oral Radiol Endod. 2012;113(3):334–9.
74. Youn KH, Park JT, Park DS, Koh KS, Kim HJ, Paik DJ. Morphology of the zygomaticus minor and its relationship with the orbicularis oculi muscle. J Craniofac Surg. 2012;23(2):546–8.
75. Yu SK, Lee MH, Kim HS, Park JT, Kim HJ, Kim HJ. Histomorphologic approach for the modiolus with reference to reconstructive and aesthetic surgery. J Craniofac Surg. 2013;24(4):1414–7.

US Anatomy of the Forehead and Temple

3

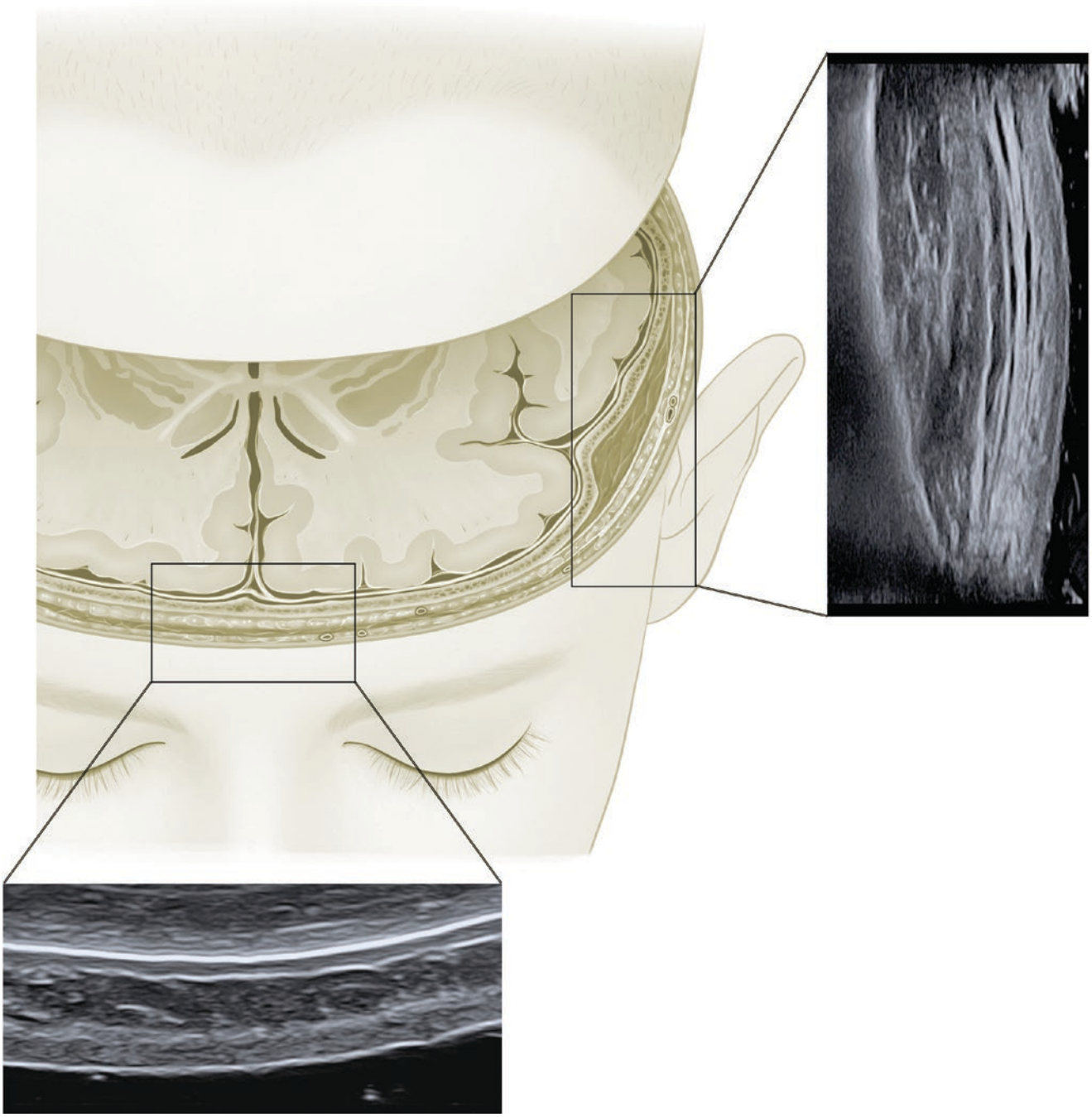

H.-J. Kim et al., *Ultrasonographic Anatomy of the Face and Neck for Minimally Invasive Procedures*,
https://doi.org/10.1007/978-981-15-6560-1_3

3.1 Clinical Anatomy of the Forehead and Temple

The forehead is a region with boundaries of the hairline as the upper border and the eyebrow as the lower border. In this region, the frontalis m. is broadly placed. The function of this muscle is related to facial expressions, and as people age, they develop facial wrinkles.

The figure of the frontalis m. is rectangular and symmetrical. The muscle originates from the galea aponeurotica, and its medial fibers run into the procerus m., central fibers to the corrugator supercilii m., and lateral fibers to the orbicularis oculi m. (Fig. 3.1).

The lateral margin of the frontalis m. has not been defined yet in the textbook. At present, it is incorrectly known that the lateral border of the frontalis m. is on the temporal line. The actual anatomy and US data represent that, in the majority of the cases (about 84%, Fig. 3.2), the lateral border of the frontalis m. is found beyond the temporal line. Figure 3.2 describes the 1 cm distant gap apart from the lateral border of the frontalis m. and the temporal line. These findings can also be noticed using the US examination.

The forehead region is predominantly innervated by the supratrochlear and supraorbital nn. The supratrochlear n. distributes in the area above the supraorbital margin. Also, the nerve innervates the region between the bilateral medial canthus, including the medial part of the upper eyelid. As the supraorbital n. runs out from the orbit, it penetrates the lower part of the corrugator supercilii m. and runs superficial to it. At a distance of 1–1.5 cm above the supraorbital margin, the supratrochlear n. finally pierces the frontalis m. and runs into the subcutaneous layer. The supraorbital n. innervates the lateral side from the vertical line passing the medial canthus. In most cases, as the supraorbital n. runs out from the supraorbital foramen (or notch), the nerve divides into three or more smaller branches and runs under the corrugator plane. Based on the supraorbital margin, the nerve pierces the frontalis m. 2–3 cm above and runs into the subcutaneous layer (Fig. 3.3).

Likewise, the supratrochlear a. and supraorbital a. run beside the nerves providing blood supply to the glabella, upper eyelid, and forehead region. Additionally, the central a. (originating from the dorsal nasal a.) and the paracentral a. (originating from the angular a.) supply the region around the mid-sagittal line. On the lateral perspective, the frontal branch originated from the superficial temporal a. runs across the forehead at 2 cm above the eyebrow in the lateral canthus's perpendicular line (PL3). Lastly, the frontal branch of superficial temporal a. anastomoses with the supraorbital a. (Fig. 3.4).

The thicknesses of scalp layers (skin, subcutaneous tissue, muscle, and loose connective tissue) are presented in Table 3.1. Without a doubt, the muscular layer (the third layer of the scalp) is the thicker of all, especially at the lower forehead. Particularly, the thickness of the muscle exceeded 2 mm at points F3 and F5. The overall soft-tissue thickness of the forehead region ranged from 4.3 to 5.3 mm, with an average of 4.7 ± 0.3 mm (mean ± SD). With the average difference of 0.4 mm (4.9 ± 0.1 mm and 4.5 ± 0.1 mm, respectively), the soft tissue was significantly thicker in males than in females at all points (Fig. 3.5).

The temporal fossa is the hollow region of the lateral side of the skull. A comprehensive understanding of the anatomy of the temporal fossa is necessary in clinical settings. Anatomically, the fossa has the superior temporal line as the superior and posterior boundary, frontal bone and zygomatic bone as the anterior boundary, the infratemporal crest of the sphenoid bone as the inferior boundary, and the zygomatic arch as the lateral boundary. The temporal fossa is a multilayered structure being supplied with many blood vessels. Superficially, skin and subcutaneous tissue are placed in the outermost surface. Under the subcutaneous layer, there is the superficial temporal fascia (STF), which continues to the

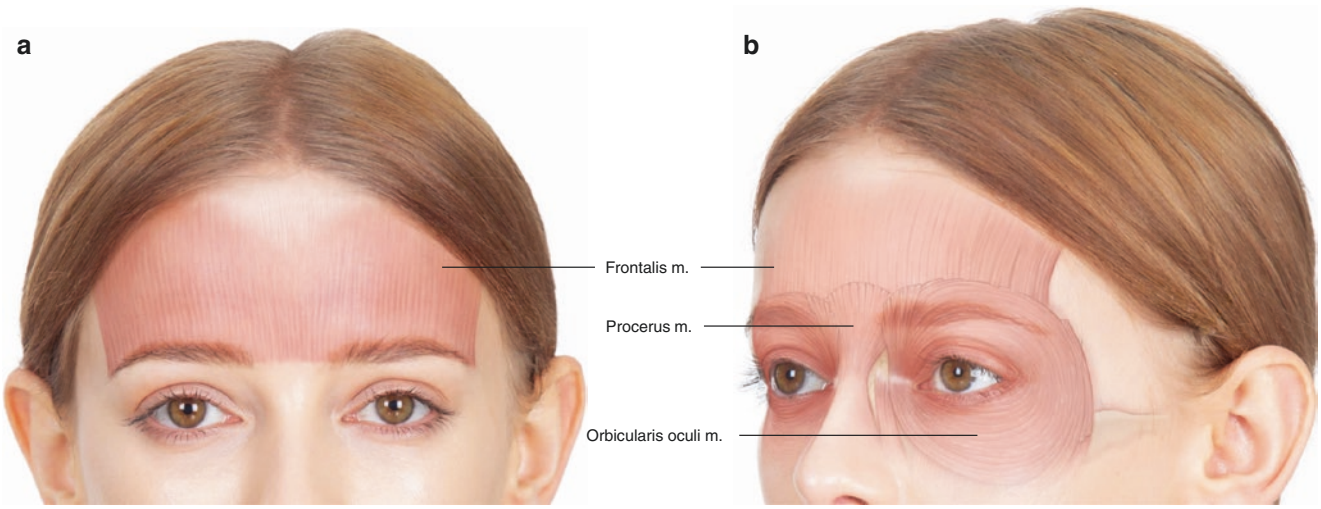

Fig. 3.1 Illustration of the frontalis muscle on the forehead. (**a**) Frontal view and (**b**) oblique view. (Published with kind permission of © Kwan-Hyun Youn 2020. All Rights Reserved)

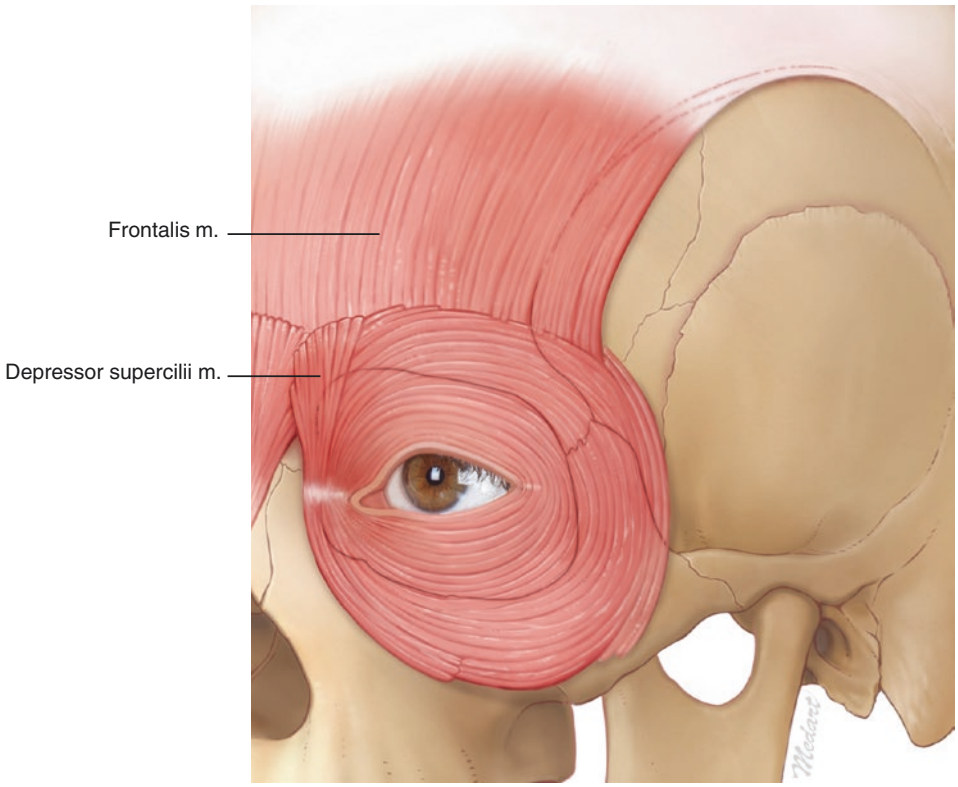

Fig. 3.2 Illustration representing the lateral border of the frontalis muscle. In most of the cases, lateral border of the frontalis muscle is located about 1 cm lateral from the superior temporal line. Dotted line, temporal line. (Published with kind permission of © Kwan-Hyun Youn 2020. All Rights Reserved)

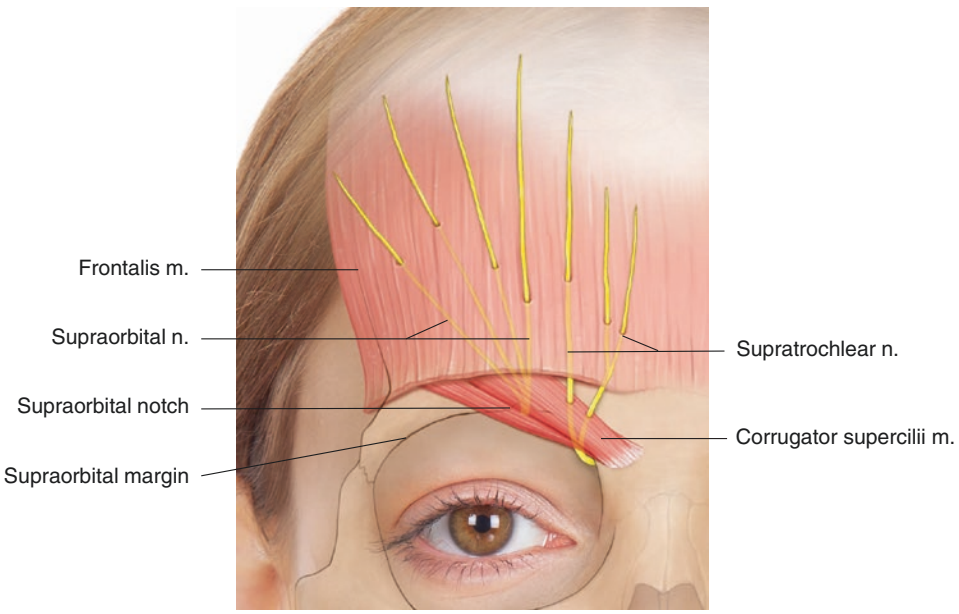

Fig. 3.3 Illustration representing the topographic courses of the supratrochlear and supraorbital nerve branches. (Published with kind permission of © Kwan-Hyun Youn 2020. All Rights Reserved)

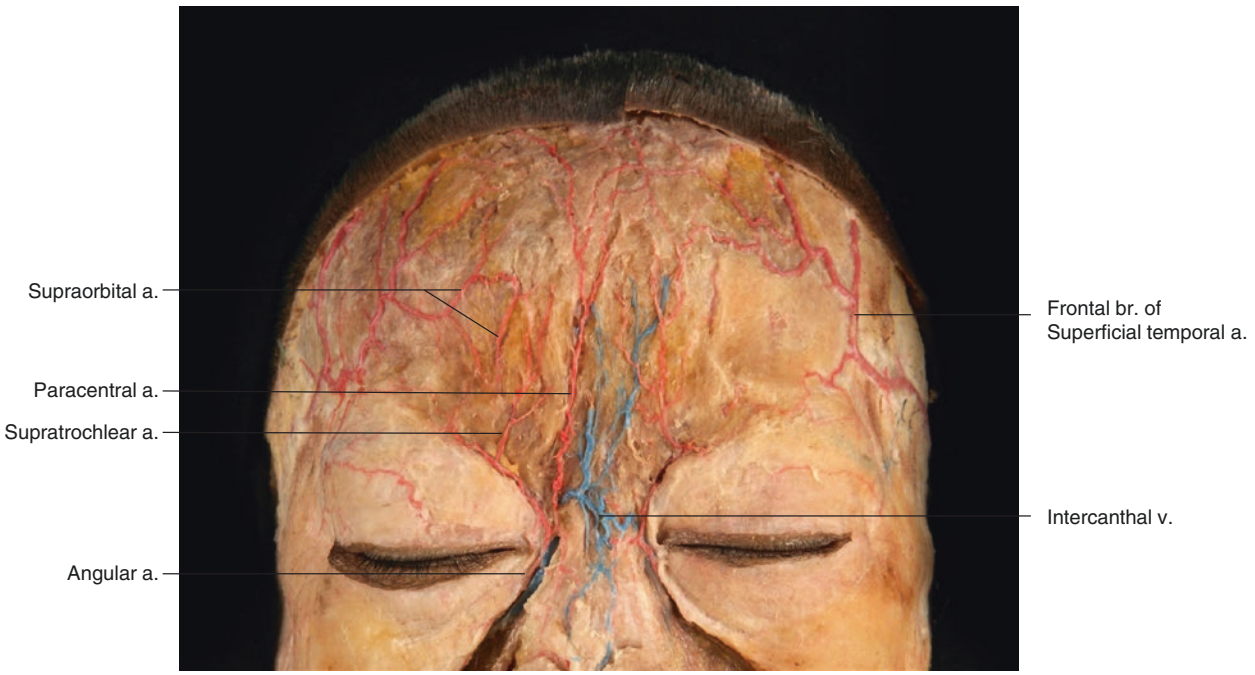

Fig. 3.4 Distribution pattern of the supratrochlear and supraorbital artery on the forehead and glabella. (Published with kind permission of © Hee-Jin Kim 2020. All Rights Reserved)

Table 3.1 Soft-tissue thickness based on the reference points of the forehead

		Point F1	Point F2	Point F4	Point F5	Point F6	Point F7
Skin	Male	1.1 ± 0.2	1.3 ± 0.2	1.1 ± 0.2	1.1 ± 0.2	1.1 ± 0.1	1.1 ± 0.1
	Female	1.0 ± 0.1	1.2 ± 0.2	1.0 ± 0.2	1.0 ± 0.2	0.9 ± 0.1	1.0 ± 0.2
Subcutaneous tissue	Male	0.8 ± 0.3	0.9 ± 0.3	0.8 ± 0.3	1.0 ± 0.3	0.9 ± 0.2	0.8 ± 0.2
	Female	0.7 ± 0.2	0.7 ± 0.2	0.8 ± 0.2	0.8 ± 0.2	0.8 ± 0.3	0.6 ± 0.2
Aponeurotic layer (frontalis)	Male	1.8 ± 0.4	2.2 ± 0.5	1.5 ± 0.4	2.2 ± 0.4	1.8 ± 0.4	1.7 ± 0.3
	Female	1.7 ± 0.4	2.1 ± 0.5	1.8 ± 0.5	2.2 ± 0.5	1.8 ± 0.5	1.4 ± 0.3
Loose connective tissue	Male	0.8 ± 0.2	0.8 ± 0.2	1.0 ± 0.2	1.2 ± 0.2	1.3 ± 0.2	1.5 ± 0.3
	Female	0.7 ± 0.1	0.7 ± 0.1	0.7 ± 0.1	1.0 ± 0.1	1.2 ± 0.4	1.4 ± 0.3
Total	Male	4.5 ± 0.7	5.2 ± 0.7	4.5 ± 0.6	5.4 ± 0.6	5.0 ± 0.6	5.0 ± 0.6
	Female	4.1 ± 0.6	4.6 ± 0.6	4.3 ± 0.7	5.1 ± 0.7	4.7 ± 0.9	4.4 ± 0.7

Results expressed as the mean ± standard deviation in millimeters

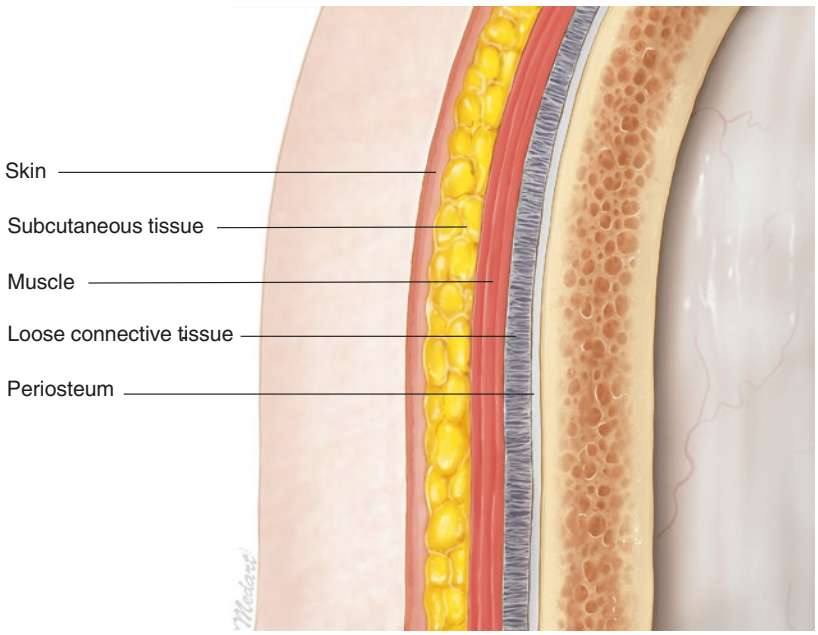

Fig. 3.5 Illustration representing the layers of the forehead. (Published with kind permission of © Kwan-Hyun Youn 2020. All Rights Reserved)

same layer as the frontalis and the superficial musculoaponeurotic system (SMAS). The subSMAS fat layer (innominate fascia) is located deep to the STF, and the deep temporal fascia (DTF, called temporalis m. fascia) is deep to the subSMAS fat layer. This DTF layer is divided into two layers which run into the zygomatic arch. In the existing space between the two layers of DTF, middle temporal v. runs within the fat tissue. This will be mentioned again in the US anatomy section in detail. The temporalis m. is placed in the space between the deep layer of the DTF and the bony surface of the temporal fossa (Fig. 3.6).

The temporalis m. is a major muscle deeply placed in the temporal region. The action of the muscle is to move the mandible, close the mouth, and keep the mouth closed with its constant tension. The temporalis m. originates from the deep layer of the DTF and inserts in the medial side of the mandibular coronoid process and the frontal margin of the ramus of the mandible. The structure of the muscle is fan-shaped for its broad origin and narrow insertion. The anterior portion of temporalis m. fiber runs vertically, but the posterior portion of muscle fibers runs horizontally. For the arterial supplies of the temporalis m., there are deep temporal arteries (DTAs) branching out from the maxillary a. The artery originates from the second part of the maxillary a. dividing into the anterior and posterior deep temporal a. They are known to give branches into the anterior and middle part of the temporalis m. (Fig. 3.7).

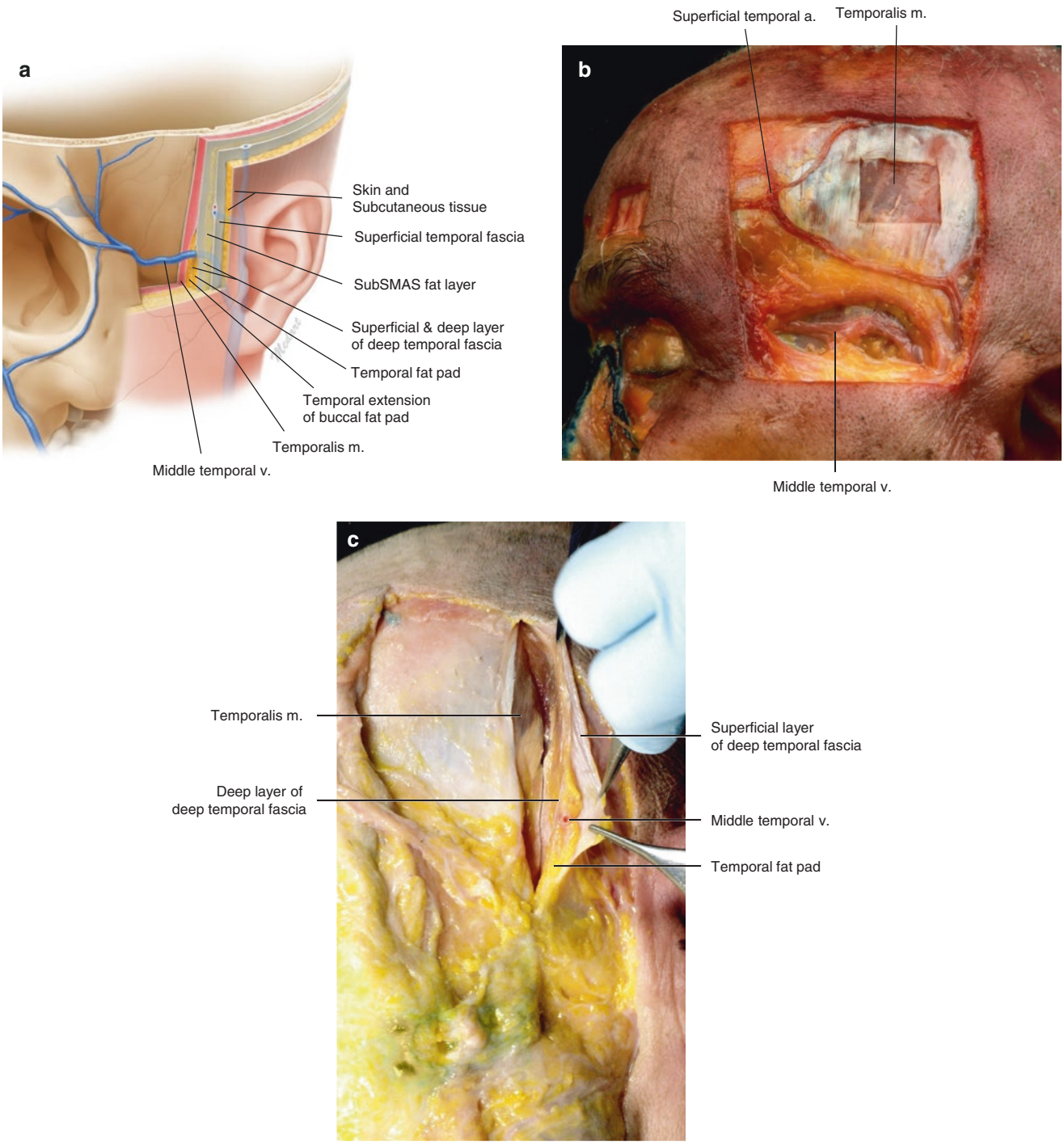

Fig. 3.6 Anatomical layers of the temple. (**a**) Illustration representing the topographic temple layers including the vessels and fat compartment, (**b**) photograph of the dissected cadaveric specimen, and (**c**) photograph of the dissected temporal fat pad with retracted superficial layer of the deep temporal fascia. (Published with kind permission of © Hee-Jin Kim and Kwan-Hyun Youn 2020. All Rights Reserved)

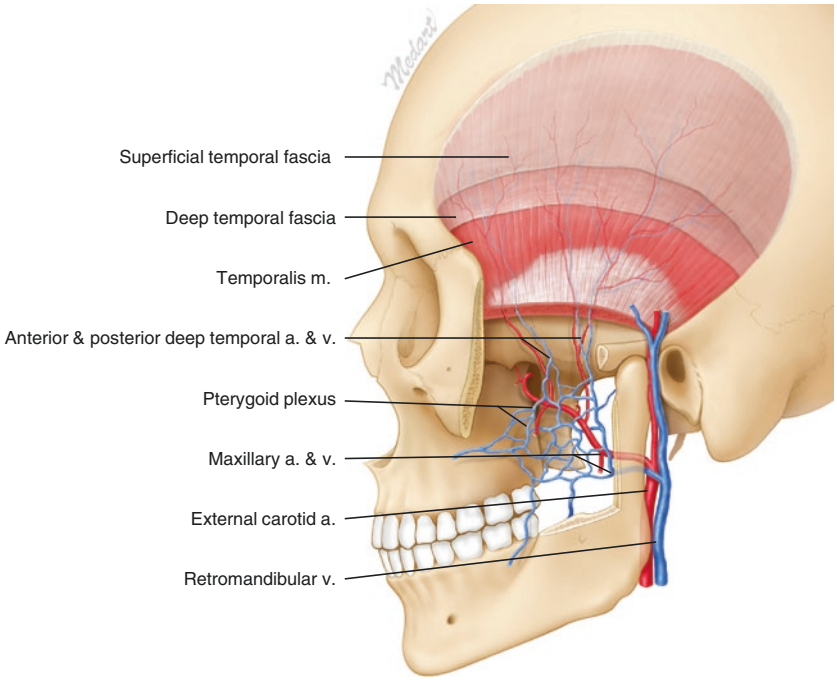

Fig. 3.7 Distribution of the deep temporal artery and vein within the temporalis muscle. (Published with kind permission of © Kwan-Hyun Youn 2020. All Rights Reserved)

3.1.1 Facial Landmarks and Reference Lines for the US Examination of the Forehead and Temple (Fig. 3.8)

Forehead and temple region	
F1: metopion (midpoint of bilateral eminence)	**T1**: transverse line passing the eyebrow
F2: midpoint between F1 and F3	**T2**: transverse line passing the zygomatic tubercle
F3: glabella	**T3**: perpendicular line passing the jugale
F4: frontal eminence	**T4**: perpendicular line passing the midpoint between T3 and T5
F5: intersection point of TL1 and PL1	**T5**: perpendicular line passing the articular eminence
F6: intersection point of TL1 and PL2	
F7: intersection point of TL1 and PL3	
F8: intersection point of TL1 and PL4	

3.1.2 Checklists in Forehead Region

Objective structures	Facial landmarks where the structures can be observed
Superior temporal line	F8
Zygomatic arch	T3, T4, T5
Frontalis m.	F1, F2, F3, F4, F5, F6, F7, F8
Procerus m.	F3
Superficial temporal fascia (SMAS)	F8, T1, T2, T3, T4, T5
subSMAS fat	F8, T1, T2, T3
Deep temporal fascia	T1, T2, T3, T4, T5

Objective structures	Facial landmarks where the structures can be observed
ROOF	F6, F7, F8
Temporal fat pad	T2, T3, T4, T5
Supraorbital a. and n.	F4, F5, F6, F7, F8
Supratrochlear a. and n.	F1, F2, F3, F5
Central or paracentral a.	F1, F2, F3
Superficial temporal a. (frontal branch)	F7, F8
Deep temporal vessels	T1, T2

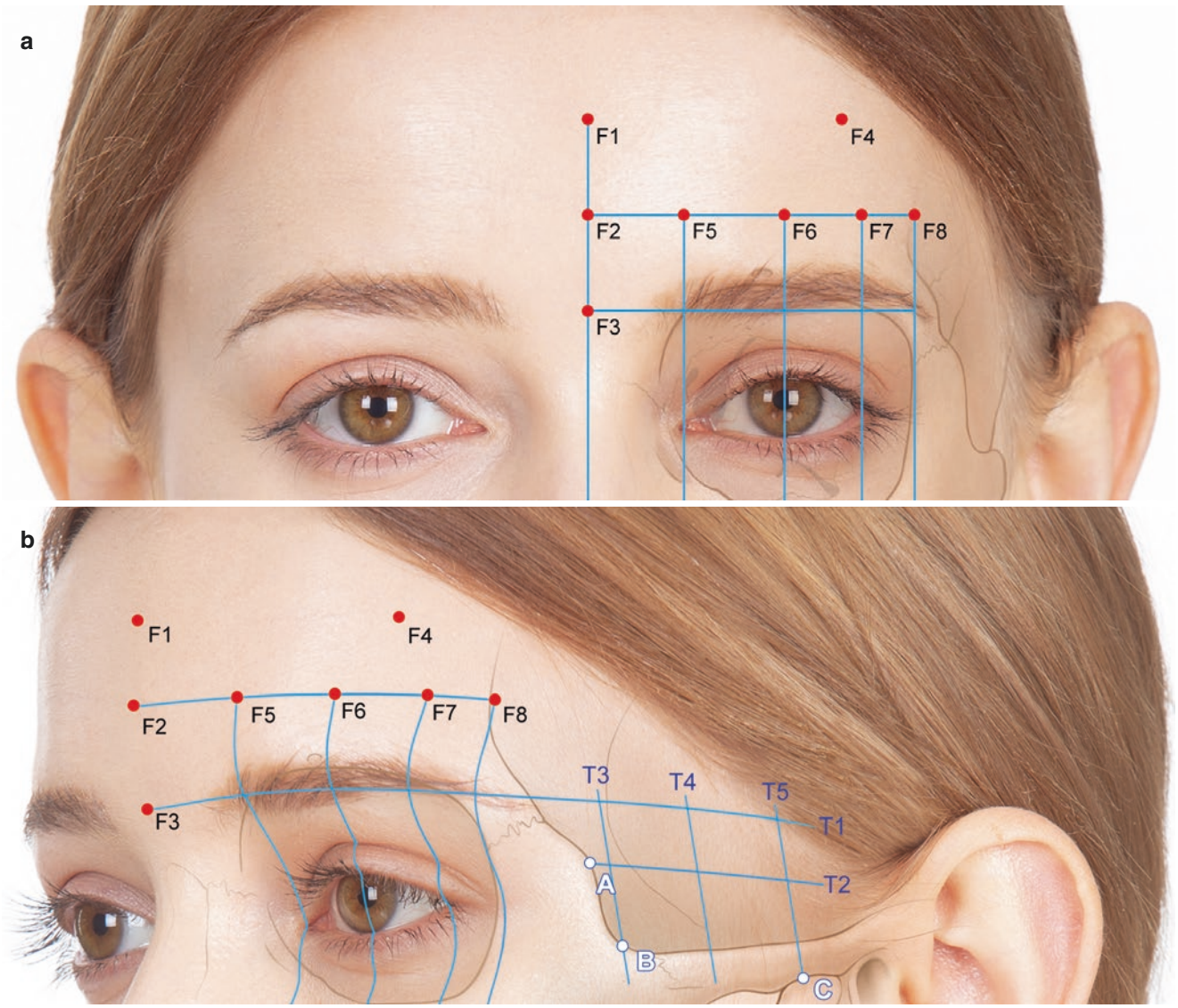

Fig. 3.8 Facial landmarks and reference lines for the ultrasonographic examination of the forehead and temple. (**a**) Frontal view and (**b**) oblique view. (Published with kind permission of © Kwan-Hyun Youn 2020. All Rights Reserved)

3.2 US Images of the Forehead and Temple

3.2.1 US Anatomical Images

The epidermis of the forehead is hyperechoic in the US image due to its keratin contents. The dermis, in comparison, is slightly hyperechoic than the epidermis. The subcutaneous layer appears as an irregular hypoechoic due to its fatty lobules. The linear fibrous septa can be displayed as quite hyperechoic lines. The frontalis m. is located below the subcutaneous layer with hypoechogenicity. The US image of the loose connective tissue appears differently depending on its locations. For example, an area of the inferolateral forehead occupied by the retro-orbicularis oculi fat (ROOF) displays slightly hyperechoic, while the other areas are shown as hypoechoic images (Figs. 3.9, 3.10, 3.11, and 3.12).

As discussed above, the temporal region has multiple layers that are distinctively different from layer to layer. To describe the superficial layer, the epidermis shows as a hyperechoic band. Deep to the epidermis, the dermis and subcutaneous layer show slight or irregularly hypoechoic images. The superficial temporal fascia located deep to the subcutaneous layer is observed as a hyperechoic image. Underneath the superficial temporal fascia is the tiny hypoechoic subSMAS fat layer (innominate fascia). The most distinct hyperechoic DTF is shown as a single layer at the upper temple, and 3–3.5 cm above the zygomatic arch where the DTF is divided into the superficial and deep layer. As the DTF diverges into two fasciae, it forms a space with a fatty component (temporal fat pad). The middle temporal v. (anechoic) runs within this space. The superficial layer of the DTF, in most cases, does not attach into the superior margin of the zygomatic arch, but these fasciae run downward

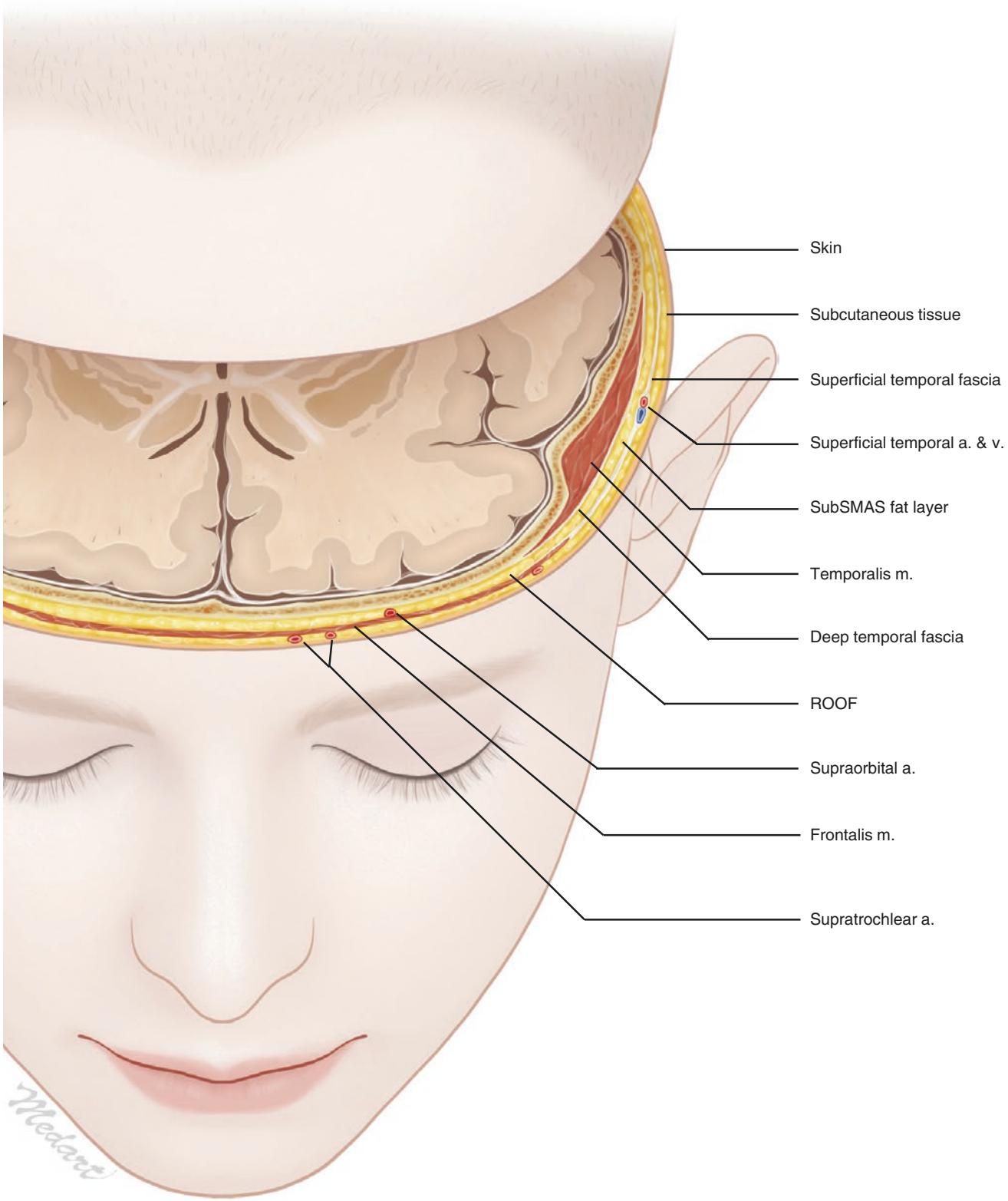

Fig. 3.9 Illustration representing the transverse section of the forehead and temple passing the TL1. (Published with kind permission of © Kwan-Hyun Youn 2020. All Rights Reserved)

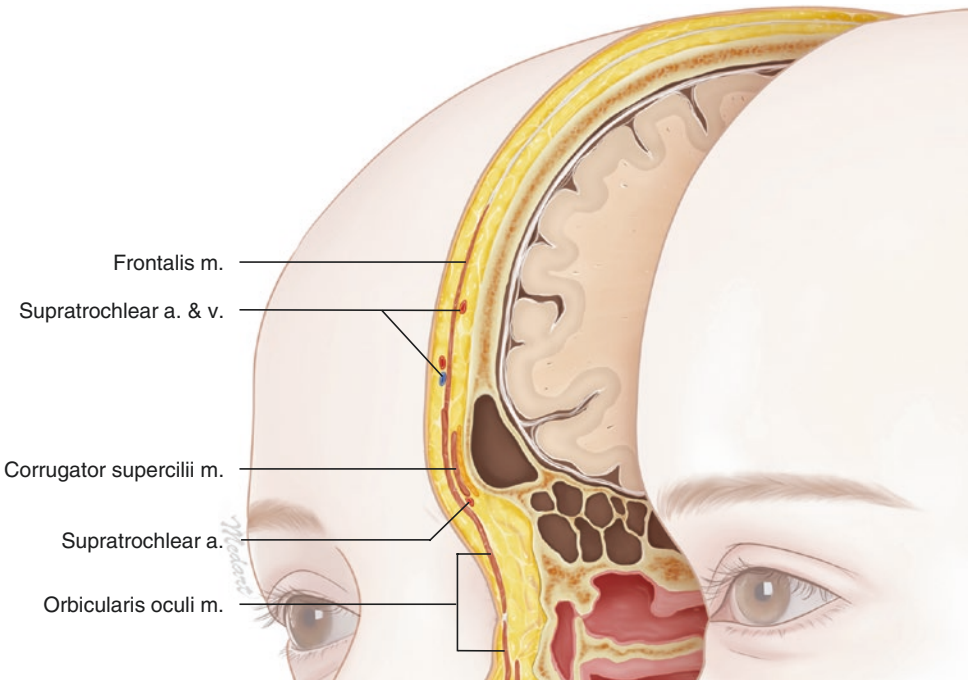

Fig. 3.10 Illustration representing the sagittal section of the forehead passing the PL1 (medial canthus). (Published with kind permission of © Kwan-Hyun Youn 2020. All Rights Reserved)

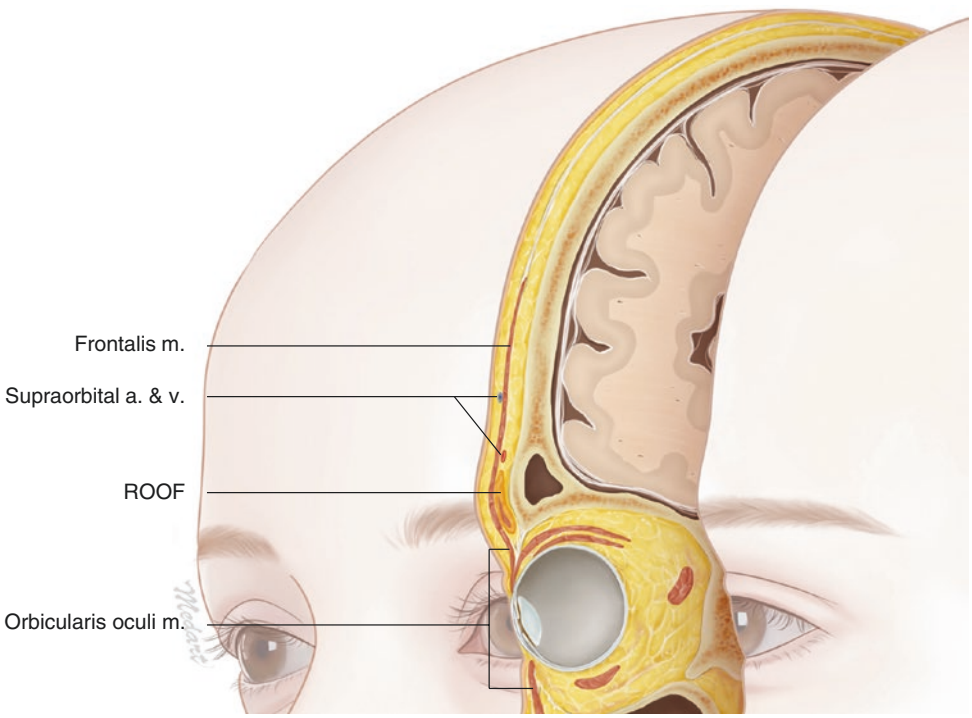

Fig. 3.11 Illustration representing the sagittal section of the forehead passing the PL2 (mid-pupil). (Published with kind permission of © Kwan-Hyun Youn 2020. All Rights Reserved)

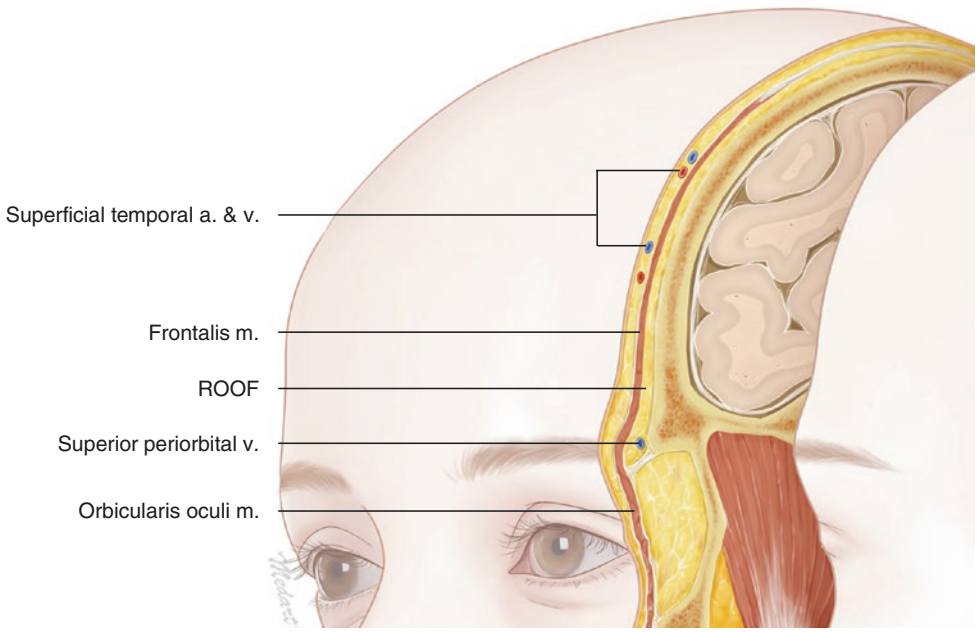

Fig. 3.12 Illustration representing the sagittal section of the forehead passing the PL3 (lateral canthus). (Published with kind permission of © Kwan-Hyun Youn 2020. All Rights Reserved)

becoming the parotid temporal fascia. Underneath the deep layer of DTF, there is the temporalis m. with the tendinous portion superficially and muscle belly deeply (Fig. 3.13).

3.2.2 B Mode and Doppler Images

F1: Metopion (Midpoint of Bilateral Eminence)
The point F1 is the midpoint of the bilateral frontal eminences. This point is similar to the diverging point where the medial border of the frontalis m. divides into the left and right sides. Therefore, it is not possible to exactly define whether the third layer is the frontalis m. or the galea aponeurotica under the ultrasonographic examination. Yet, other structures such as the skin, subcutaneous layer, and loose connective tissue layer are clearly definable (Fig. 3.14a, c). Images of the Doppler mode display the midline vessels such as the central a. and paracentral a. (Fig. 3.14b, d).

F2: Midpoint Between F1 and F3
The point F2 is the midpoint of point F1 and the glabella (F3). This is the area where the frontalis m. can be observed. The boundary between the subcutaneous layer and frontalis m. is not exactly distinguished since muscle fibers of the frontalis m. attach to the skin (cutaneous insertion). There were no significant differences in the other layers compared to other points (Fig. 3.15a). In the images of the Doppler mode, midline vessels such as the supratrochlear a., central a., and paracentral a. could be found (Fig. 3.15b).

F3: Glabella
The point F3 is where the glabella is located. At this point, the hyperechoic band of the epidermis is observed and deep to that is a relatively thicker subcutaneous fat layer. Deep to the subcutaneous fat, the procerus m. is placed at depths of 3.8 ± 0.7 mm in US images (Fig. 3.16). In most of the cases (79.7%), the procerus m. was easily distinguishable from other adjacent facial expression muscles shown from the transverse US images. In other cases, the procerus m. is not noticeable at the midline, being divided into two lateral portions. In these cases, a thin isoechoic bandlike structure was observed at the midline (Fig. 3.17a, c). According to the image, bilateral insertion of corrugator supercilii m. could be identified deep to the procerus m.

F4: Frontal Eminence
The point F4 represents the frontal eminence. This is the point where only the frontalis m. could be observed. At this point, the Doppler mode image demonstrates the superficial branch of the supraorbital a. and the frontal branch of superficial temporal a. These arteries may run superficial to or within the frontalis m. (Fig. 3.18).

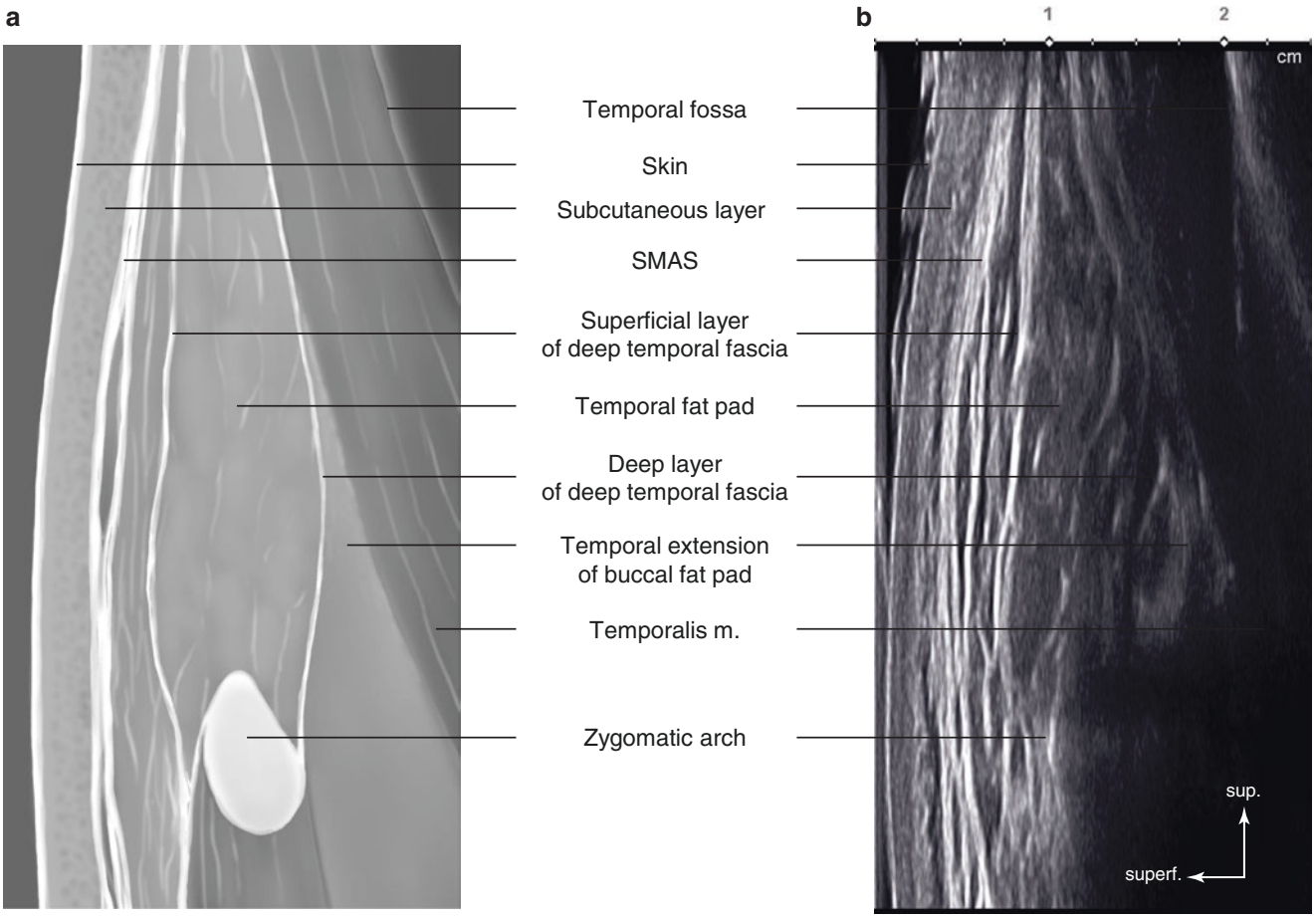

Fig. 3.13 Fascial structure layer of the temple. (**a**) Anatomical illustration and (**b**) ultrasonographic image. (Published with kind permission of © Hee-Jin Kim and Kwan-Hyun Youn 2020. All Rights Reserved)

F5: Intersection Point of TL1 and PL1

The point F5 is the intersection point of TL1 and PL1, and its layered structure is clearly distinguishable in US images. The muscle layer of the frontalis m. is thick and hyperechoic at F5 (Fig. 3.19a). The Doppler mode image demonstrates the supratrochlear a. running superficial to the frontalis m. (superficial branch of the supratrochlear a. and v., 45%), deep to the frontalis m. (deep branch of the supratrochlear a. and v., 20%), or both superficial and deep to the m. (superficial and deep branch of the supratrochlear a. and v., 35%) (Fig. 3.19b, c).

F6: Intersection Point of TL1 and PL2

The point F6 is the intersection point of TL1 and PL2. In comparison to F5, the muscle is thinner, while the loose connective tissue is thicker (Fig. 3.20a). The Doppler mode image at the point F6 exhibits the supraorbital a. running deep to the frontalis m. (deep branch of the supraorbital a. and v.) (Fig. 3.20b). The supraorbital a. runs superolaterally and 3 cm above the point F6, and it pierces the frontalis m., becoming the superficial branch of the supraorbital a. (Fig. 3.20c).

F7: Intersection Point of TL1 and PL3

The point F7 is the intersection point of TL1 and PL3. The structure observed at this point is similar to the point F6. The temporal line is the anatomical structure that separates the forehead and the temporal fossa, observed laterally to F7. The ROOF can be observed in this area. The loose connective

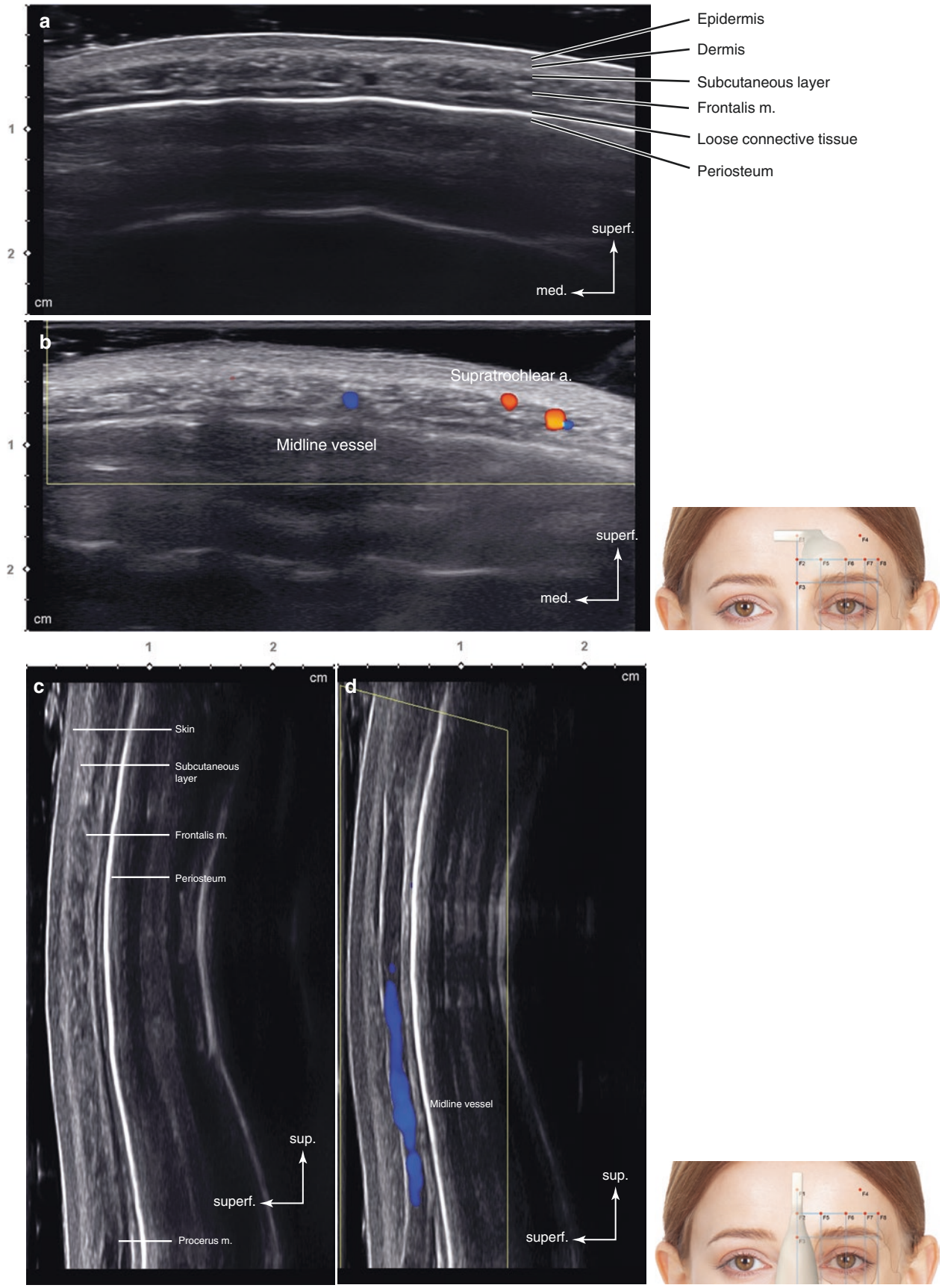

Fig. 3.14 Ultrasonography on the metopion (F1). (**a**) B mode (transverse view, 15 MHz by linear transducer), (**b**) Doppler mode (transverse view, 15 MHz by linear transducer), (**c**) B mode (sagittal view, 15 MHz by linear transducer), and (**d**) Doppler mode (sagittal view, 15 MHz by linear transducer). (Published with kind permission of © Hee-Jin Kim 2020. All Rights Reserved)

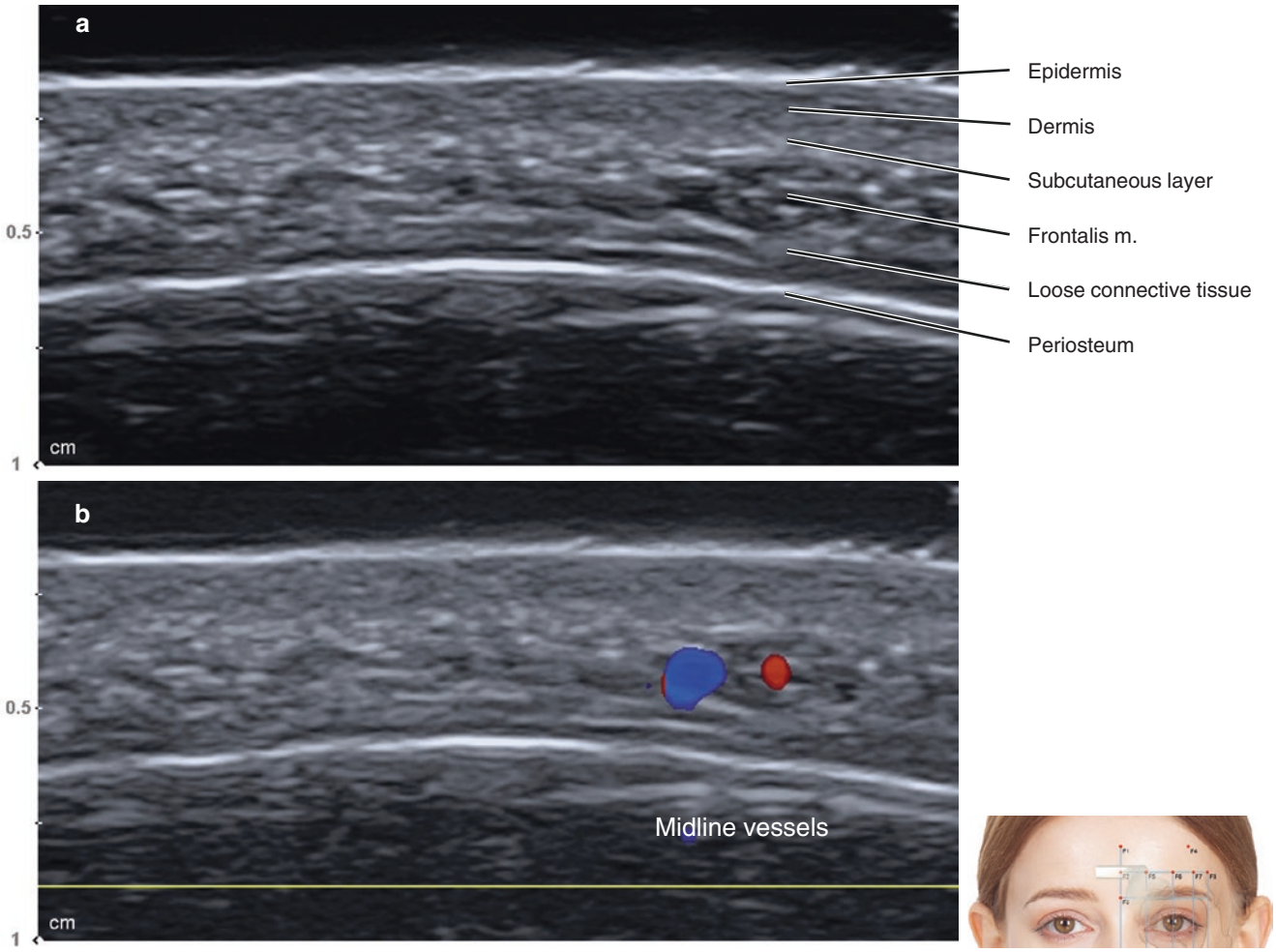

Fig. 3.15 Ultrasonography on the midpoint between F1 and F3. (**a**) B mode (transverse view, 15 MHz by linear transducer) and (**b**) Doppler mode (transverse view, 15 MHz by linear transducer). (Published with kind permission of © Hee-Jin Kim 2020. All Rights Reserved)

tissue displayed in this area is slightly different from the US images of the points F2, F5, and F6 (Fig. 3.21a). In the Doppler mode images, the frontal branch of the superficial temporal a. runs superficial to the frontalis m. (Fig. 3.21b).

F8: Intersection Point of TL1 and PL4

The point F8 is the intersection point of TL1 and PL4, passing the superior temporal line (temporal crest). As other forehead images display, five layers of the soft tissue can be precisely identified. Particularly, the thickened ROOF dimension can be observed in F8. The lateral border of the frontalis m. can be observed, which lies within 1 cm to the temporal line (or crest). The ROOF is connected laterally to the subSMAS fat (Fig. 3.22a). The lateral border of the frontalis m. is in the same layer with the superficial temporal fascia (a part of SMAS) (Fig. 3.22a, c). Unlike other layers of the face, the layers of the upper temple consist of skin, subcutaneous fat, superficial temporal fascia, subSMAS fat, DTF, and temporalis m. In the Doppler mode images, the frontal branch of the superficial temporal a. runs in the same plane of the frontalis m. and the superficial temporal fascia. The US images at this point can identify 88% of the superficial temporal vessels (Fig. 3.22b).

T1: Transverse Line Passing the Eyebrow

The horizontal line passing the eyebrow is defined as T1. The layered structures of the temporal fossa are not parallel to the skin surface. For this reason, clinicians are recommended to adjust the angle of the transducer perpendicularly for optimal view.

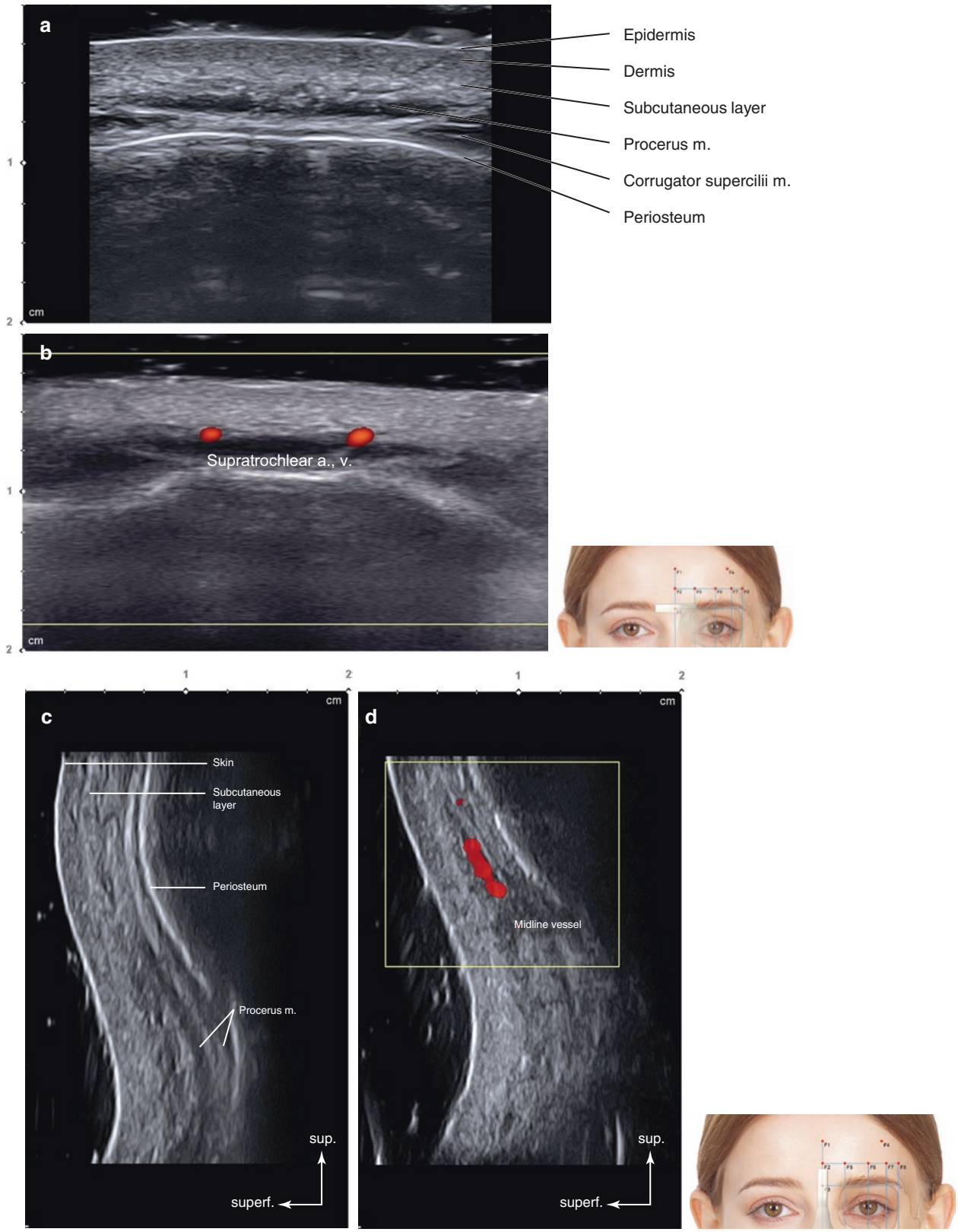

Fig. 3.16 Ultrasonography on the glabella (F3). (**a**) B mode (transverse view, 15 MHz by linear transducer), (**b**) Doppler mode (transverse view, 15 MHz by linear transducer), (**c**) B mode (sagittal view, 15 MHz by linear transducer), and (**d**) Doppler mode (sagittal view, 15 MHz by linear transducer). (Published with kind permission of © Hee-Jin Kim 2020. All Rights Reserved)

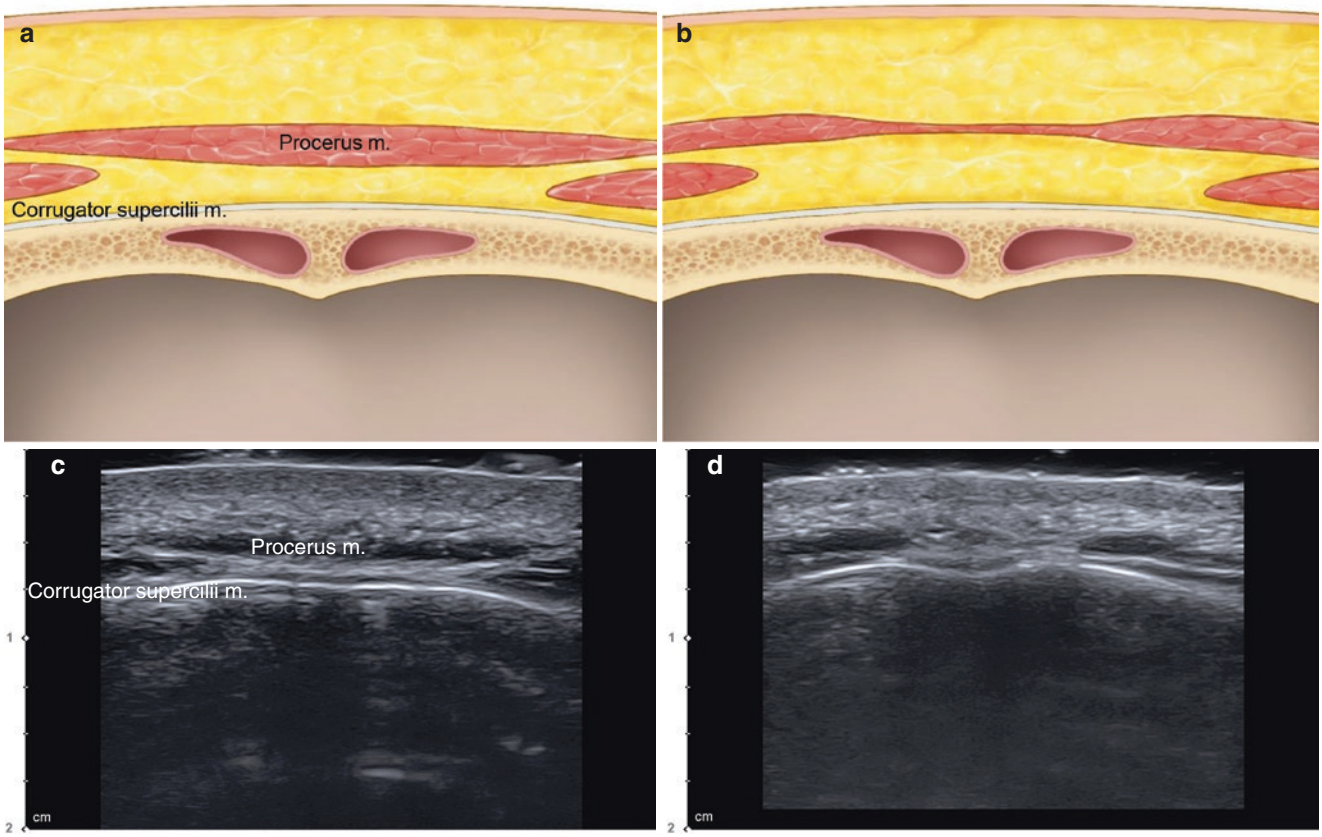

Fig. 3.17 Two types of the procerus muscle according to the shape in the transverse view of the ultrasonography. (**a**, **c**) Illustration and ultrasonography of type I procerus muscle and (**b**, **d**) illustration and ultrasonography of type II procerus muscle. (Published with kind permission of © Hee-Jin Kim and Kwan-Hyun Youn 2020. All Rights Reserved)

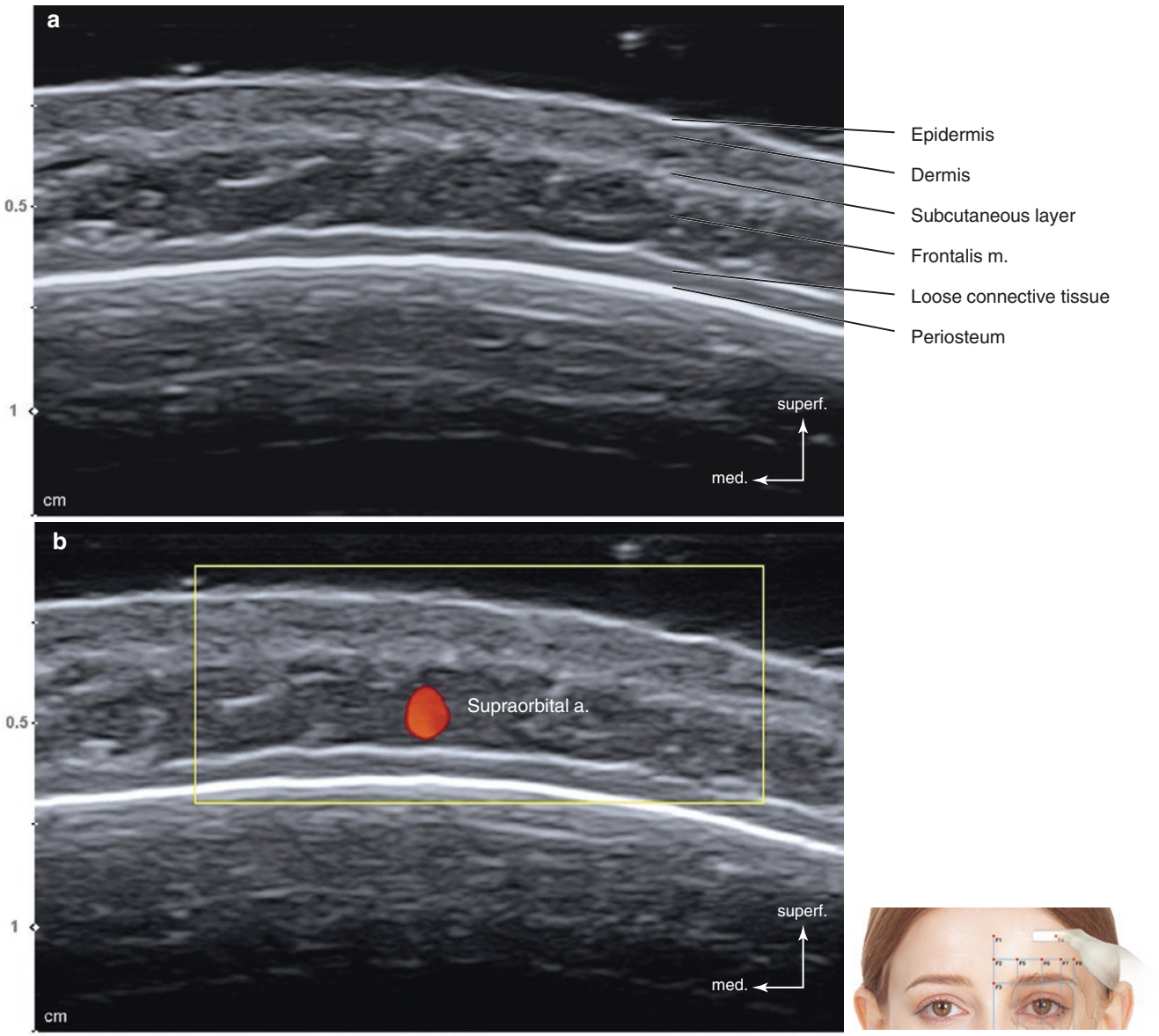

Fig. 3.18 Ultrasonography on the frontal eminence (F4). (**a**) B mode (transverse view, 15 MHz by linear transducer) and (**b**) Doppler mode (transverse view, 15 MHz by linear transducer). (Published with kind permission of © Hee-Jin Kim 2020. All Rights Reserved)

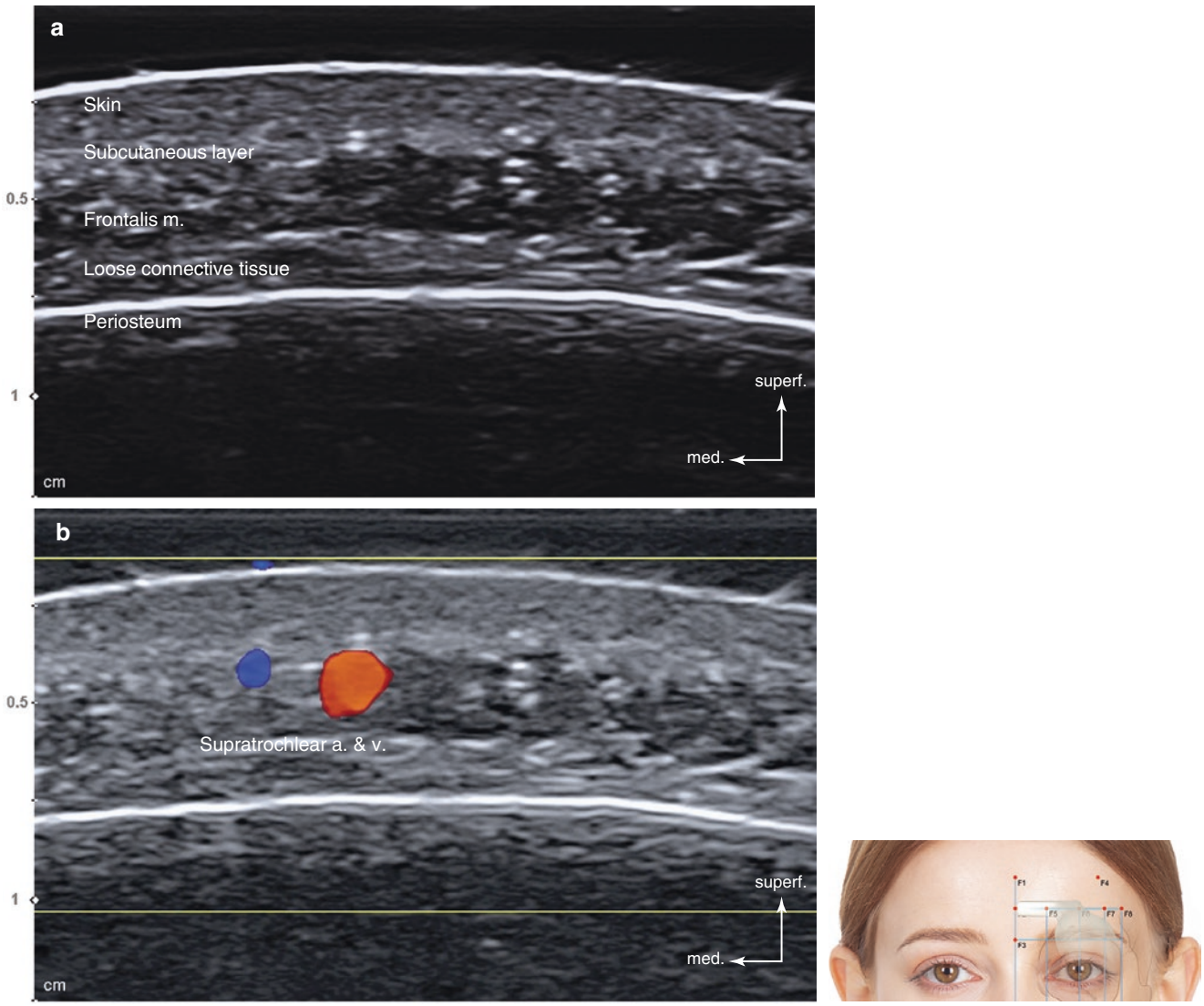

Fig. 3.19 Ultrasonography of the intersection point of TL1 and PL1 (F5). (**a**) B mode (transverse view, 15 MHz by linear transducer), (**b**) Doppler mode (transverse view, 15 MHz by linear transducer), and (**c**) arterial distribution on the forehead and glabella. (Published with kind permission of © Hee-Jin Kim and Kwan-Hyun Youn 2020. All Rights Reserved)

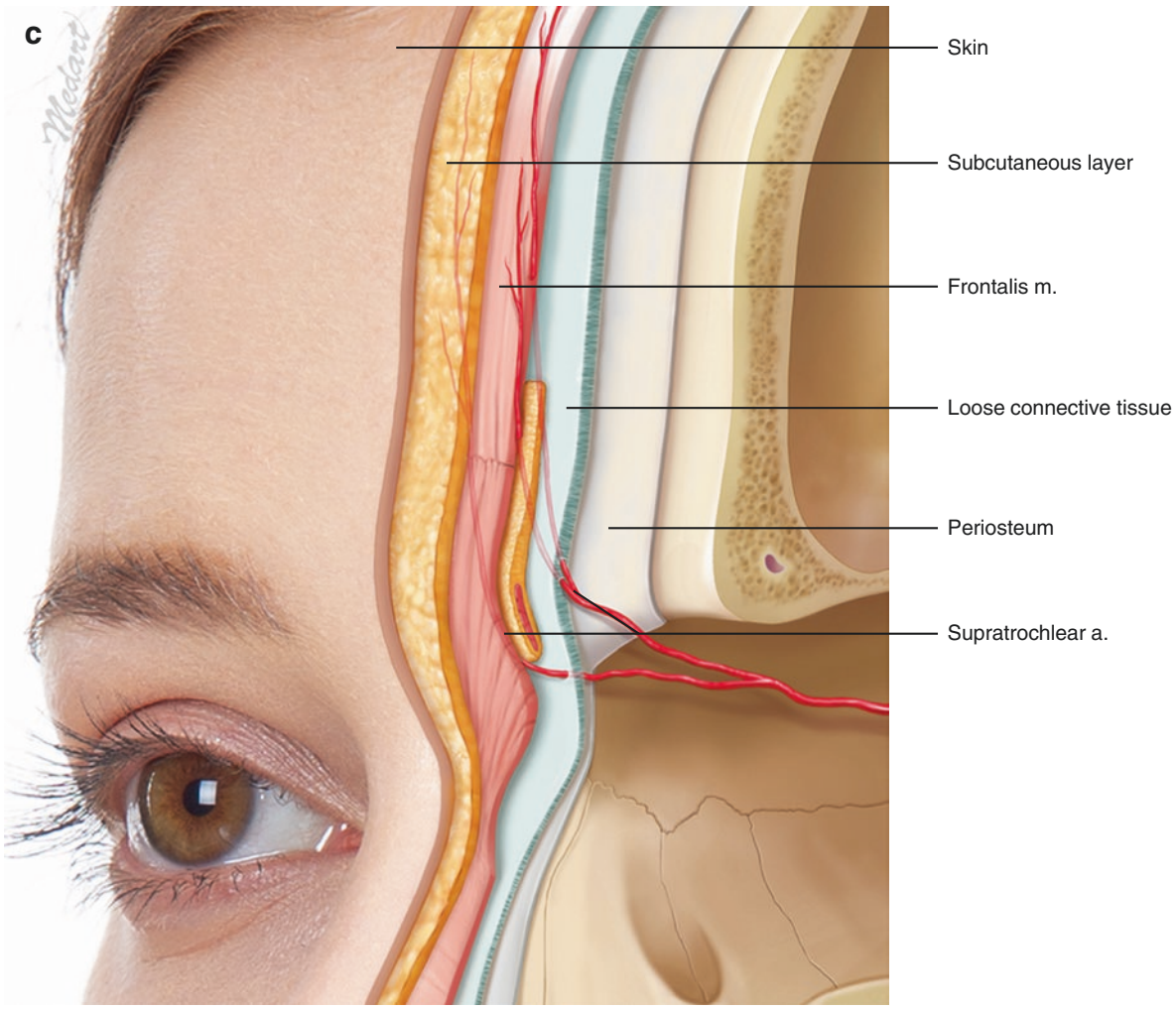

Fig. 3.19 (continued)

The temporal crest is observed as a protruded structure in comparison to the sunken temporal fossa. The frontalis m., which laterally extends beyond the superior temporal line, appears hypoechoic. On the other hand, the superficial temporal fascia which is placed in the same layer as the frontalis m. appears hyperechoic. Underneath the superficial temporal fascia, the DTF begins from the superior temporal line as hyperechoic. The hypoechoic subSMAS fat layer beneath the superficial temporal fascia is observed. In the Doppler mode images, the anterior deep temporal a. runs within the temporalis m. (Fig. 3.23a, b).

T2: Transverse Line Passing the Zygomatic Tubercle

The horizontal line passing the zygomatic tubercle is defined as T2. The zygomatic tubercle is the slightly elevated portion of the orbital surface in the zygomatic bone. The bony landmark is easily palpated by clinicians.

The deepest part is the temporalis m. presented as hypoechoic, the tendon of the temporalis m. as hyperechoic, and the deep temporal fat pad (temporal extension of the buccal fat pad) as a hypoechoic image. Differing from the images of T1, the DTF is shown in two layers, superficial and deep. In the space between the two layers, the temporal fat pad is occupied (Fig. 3.24a).

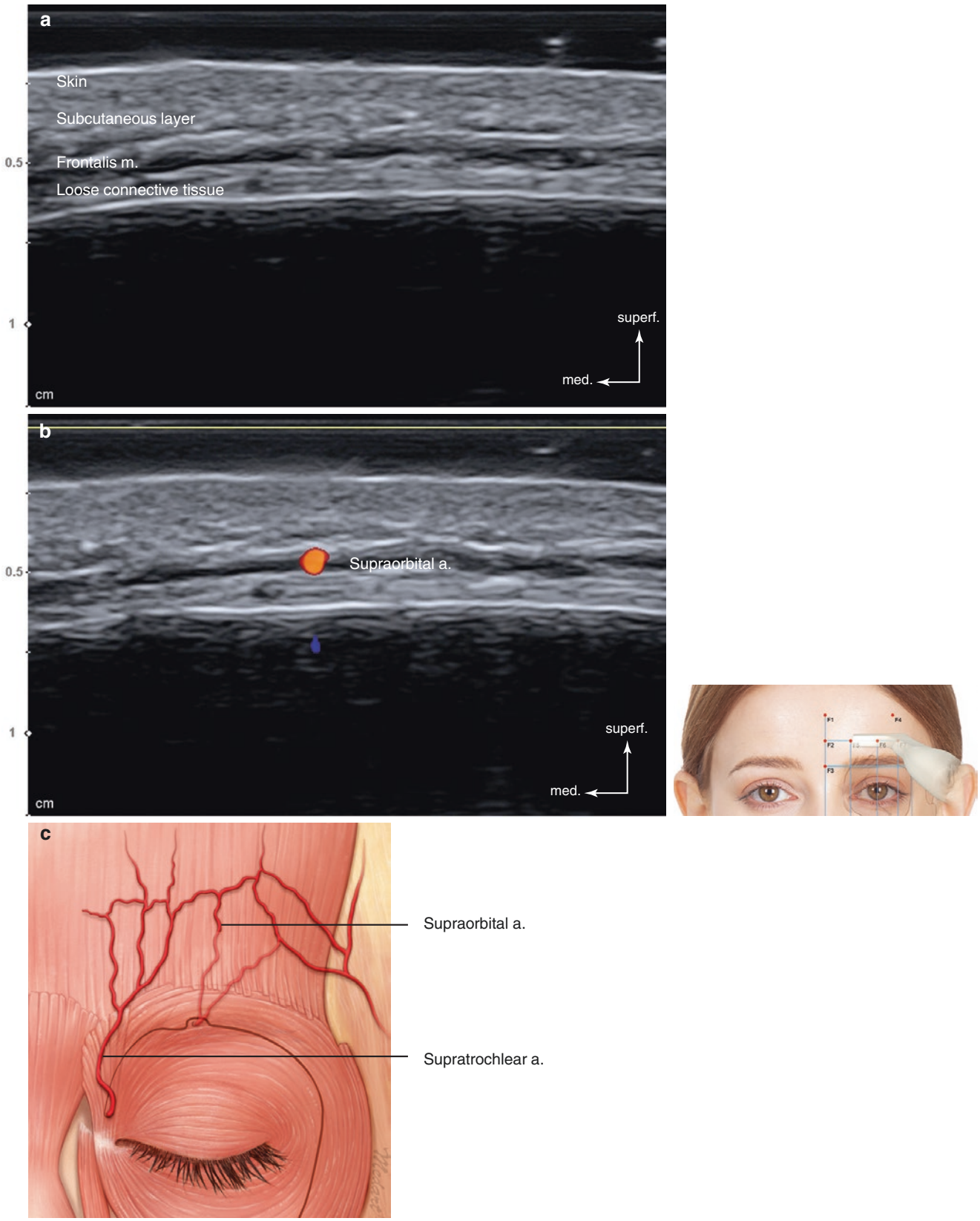

Fig. 3.20 Ultrasonography of the intersection point of TL1 and PL2 (F6). (**a**) B mode (transverse view, 15 MHz by linear transducer), (**b**) Doppler mode (transverse view, 15 MHz by linear transducer), and (**c**) arterial distribution on the forehead. (Published with kind permission of © Hee-Jin Kim and Kwan-Hyun Youn 2020. All Rights Reserved)

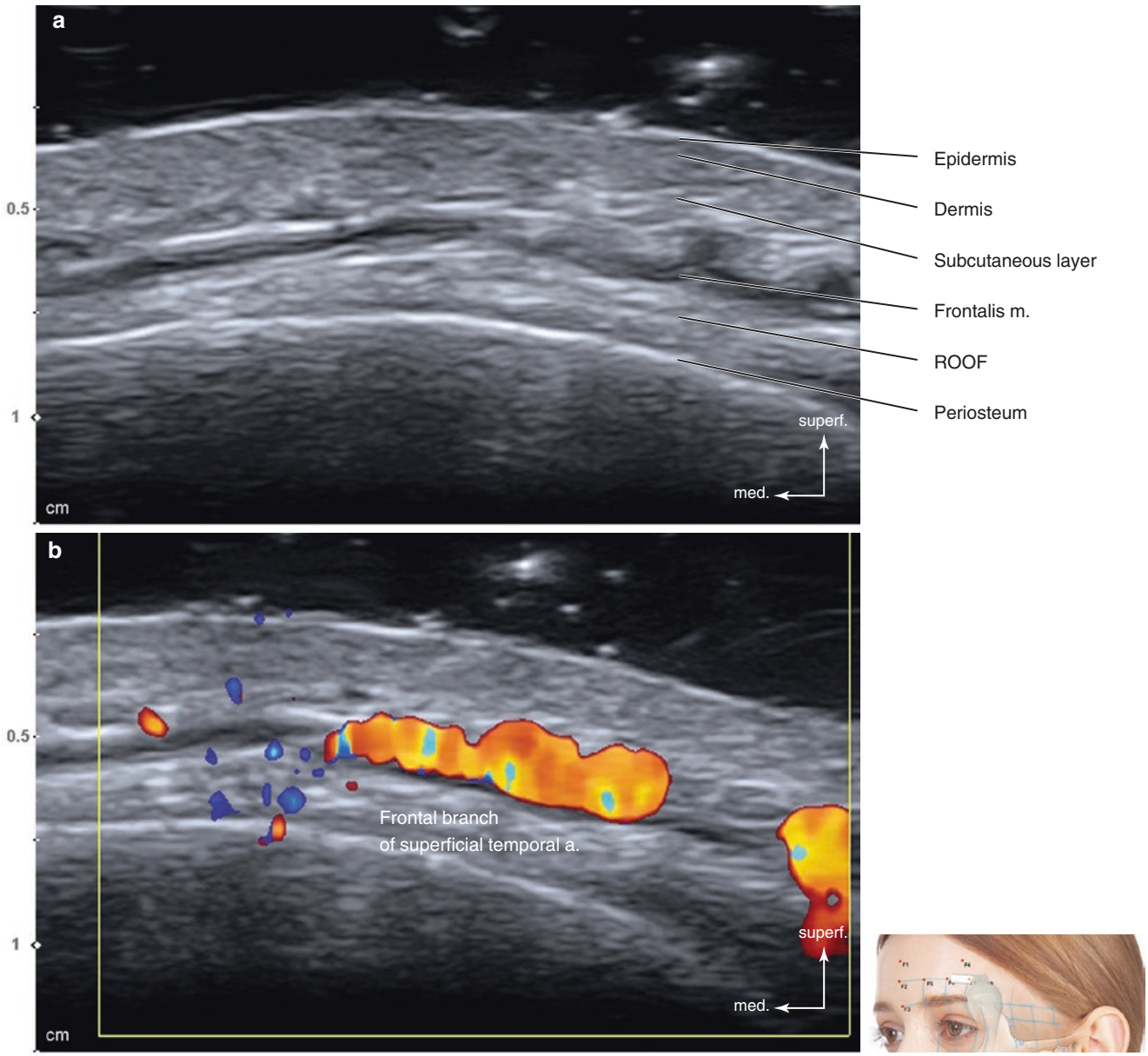

Fig. 3.21 Ultrasonography of the intersection point of TL1 and PL3 (F7). (**a**) B mode (transverse view, 15 MHz by linear transducer) and (**b**) Doppler mode (transverse view, 15 MHz by linear transducer). (Published with kind permission of © Hee-Jin Kim 2020. All Rights Reserved)

In the Doppler mode images, both the anterior and posterior DTAs could be noticed. Infrequently, the middle temporal v. may appear in this US image. On average, the middle temporal v. runs about 20 mm above the zygomatic arch, and clinicians may use their index finger placing it on the upper margin of the zygomatic arch to estimate the location of the middle temporal v. The facial venous systems, including the sentinel v., the inferior palpebral v., and the periorbital v., drain into this middle temporal v., which continues to the superficial temporal v. (Fig. 3.24b).

T3: Perpendicular Line Passing the Jugale

The perpendicular line passing the jugale was defined as T3. In this view, the zygomatic arch is covering the lower 2/3 of the image, making it unable to observe within the temporal fossa. Superficial to the zygomatic arch, it is possible to observe the hyperechoic SMAS and superficial layer of the DTF. It is difficult to distinguish these two fascial structures through US. Under the deep layer of the DTF, the buccal fat exists as a hyperechoic structure. And deep to the fat pad, the temporalis m. is observed as a hypoechoic structure and the temporal bone is observed in the hindmost region (Fig. 3.25).

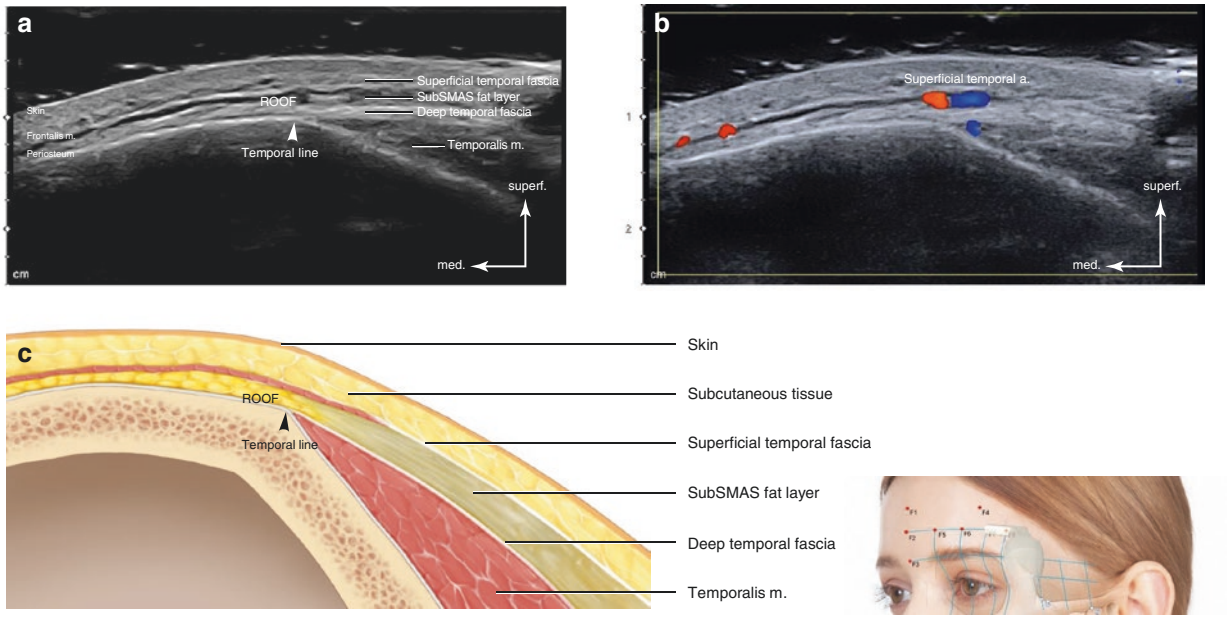

Fig. 3.22 Ultrasonography of the intersection point of TL1 and PL4 (F8). (**a**) B mode (transverse view, 15 MHz by linear transducer), (**b**) corresponding illustration, and (**c**) Doppler mode (transverse view, 15 MHz by linear transducer). (Published with kind permission of © Hee-Jin Kim and Kwan-Hyun Youn 2020. All Rights Reserved)

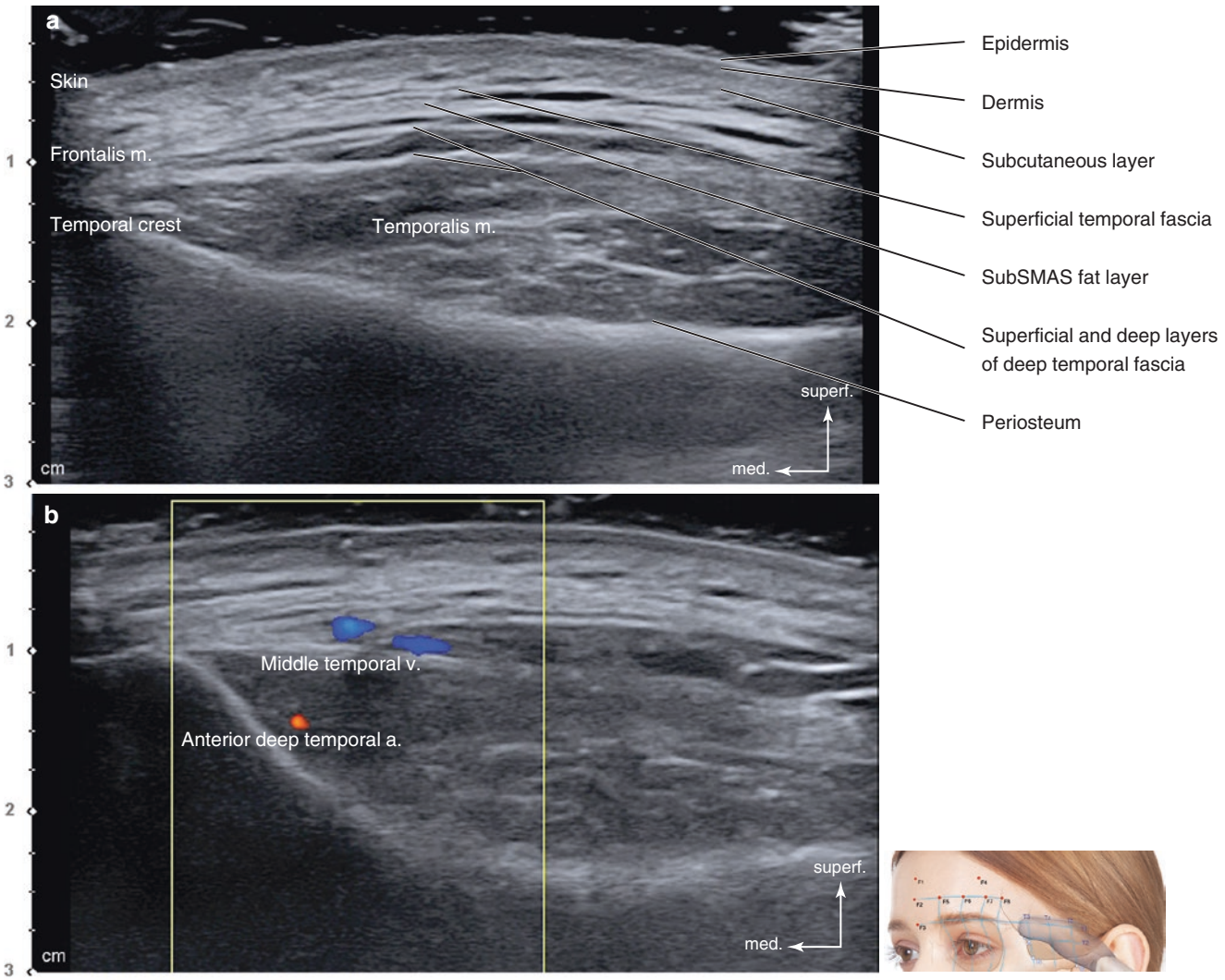

Fig. 3.23 Ultrasonography of the transverse line passing the eyebrow (T1). (**a**) B mode (transverse view, 15 MHz by linear transducer) and (**b**) Doppler mode (transverse view, 15 MHz by linear transducer). (Published with kind permission of © Hee-Jin Kim 2020. All Rights Reserved)

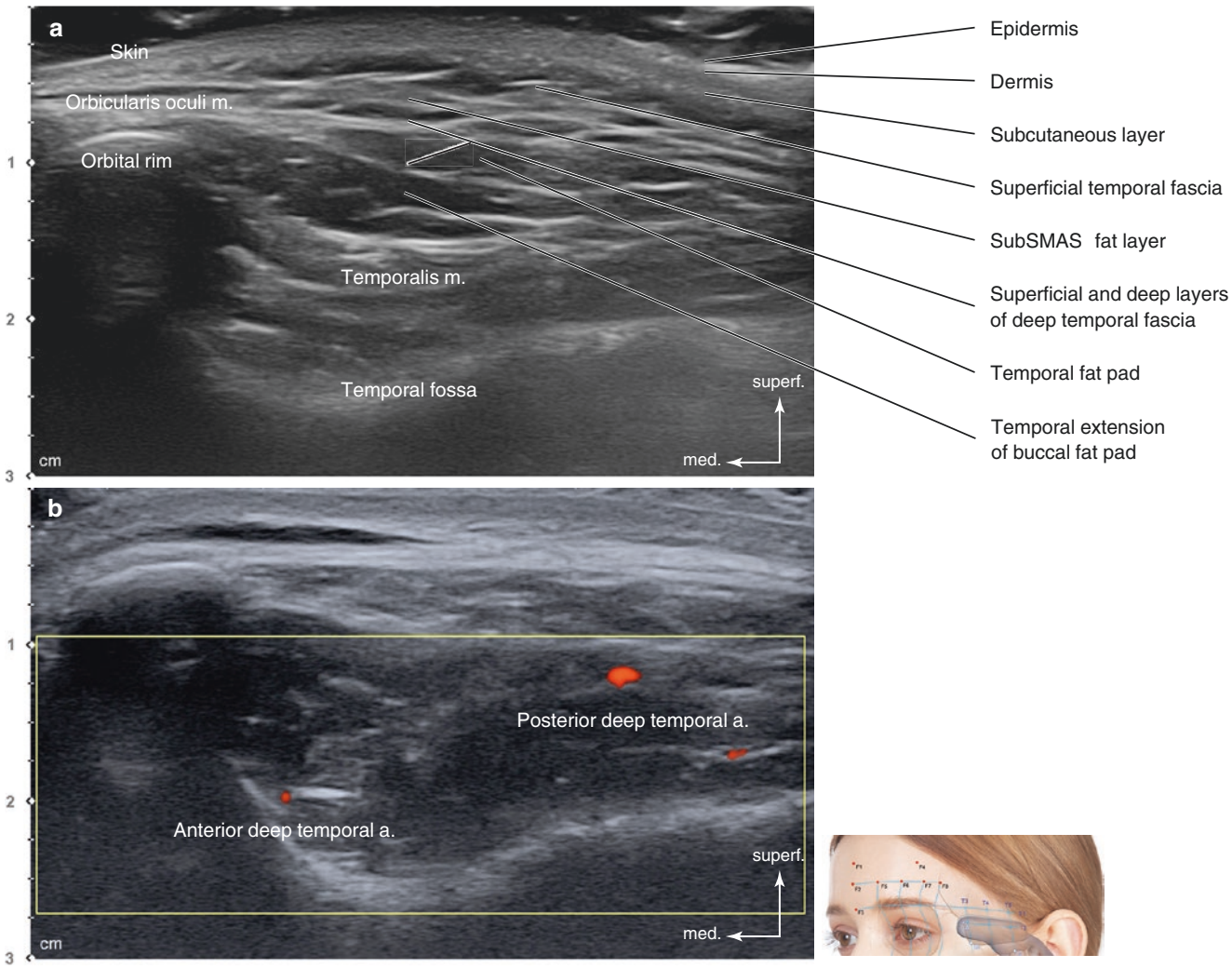

Fig. 3.24 Ultrasonography of the transverse line passing the zygomatic tubercle (T2). (**a**) B mode (transverse view, 15 MHz by linear transducer) and (**b**) Doppler mode (transverse view, 15 MHz by linear transducer). (Published with kind permission of © Hee-Jin Kim 2020. All Rights Reserved)

T4: Perpendicular Line Passing the Midpoint Between T3 and T5

The perpendicular line passing the midpoint between T3 and T5 is defined as T4. Similar to the images of the T3 point, the posterior acoustic shadowing of the zygomatic arch was observed. In this view, typical anatomical structures, including SMAS, subSMAS fat, superficial and deep layer of the DTF, the temporal extension of the buccal fat pad, and temporalis m., are identified. The hypoechoic subSMAS fat is observed between the SMAS and the superficial layer of the DTF. The superficial layer of the DTF partially crossing the zygomatic arch and running down towards the parotid gland is clearly depicted (Fig. 3.26).

T5: Perpendicular Line Passing the Articular Eminence

The perpendicular line passing the articular eminence is defined as T5. The fascial structure, including the SMAS and the superficial and deep layer of the DTF, converges in this view making it difficult to distinguish each fascial layer (Fig. 3.27).

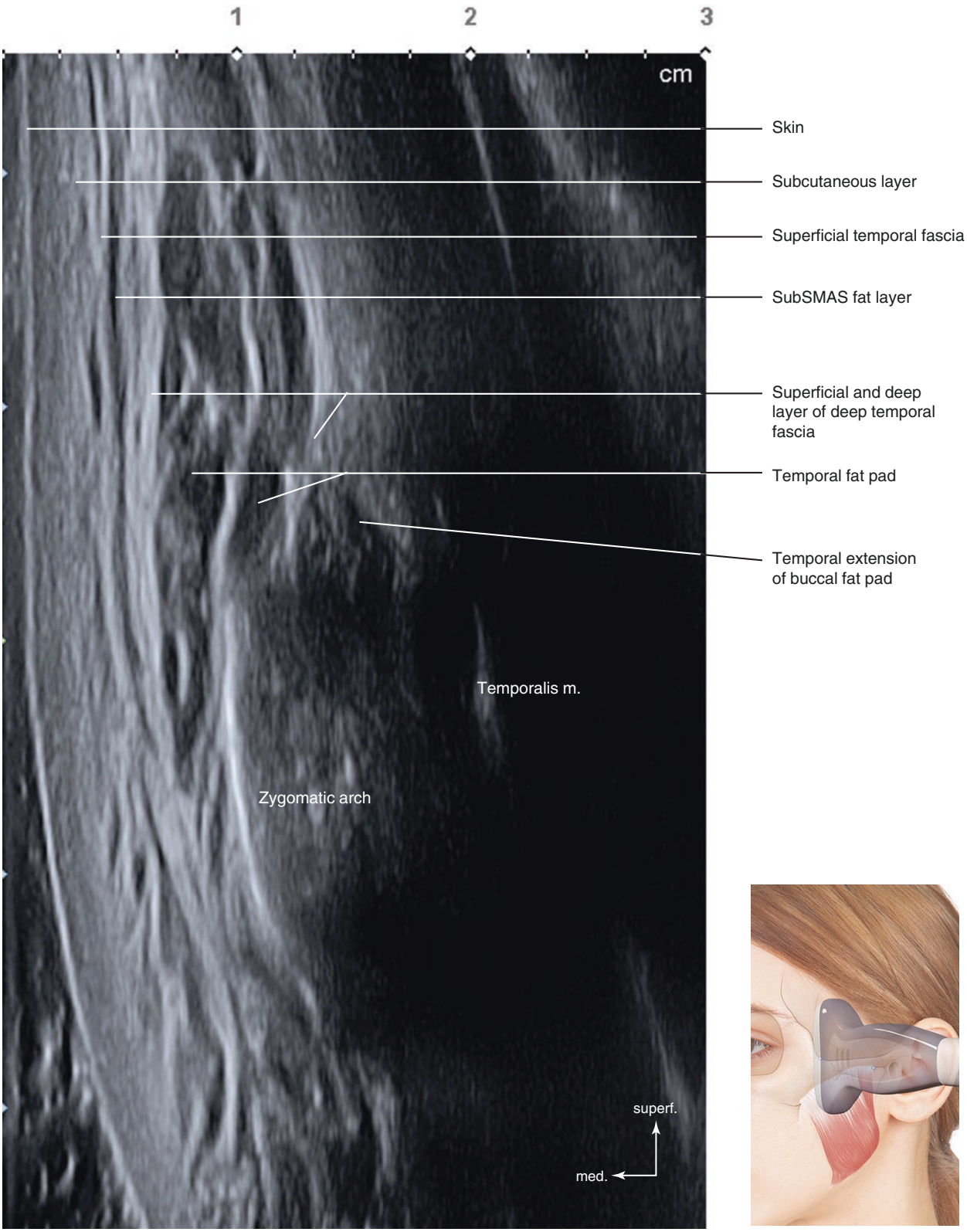

Fig. 3.25 Ultrasonography of the perpendicular line passing the jugale (T3). B mode (coronal view, 15 MHz by linear transducer). (Published with kind permission of © Hee-Jin Kim 2020. All Rights Reserved)

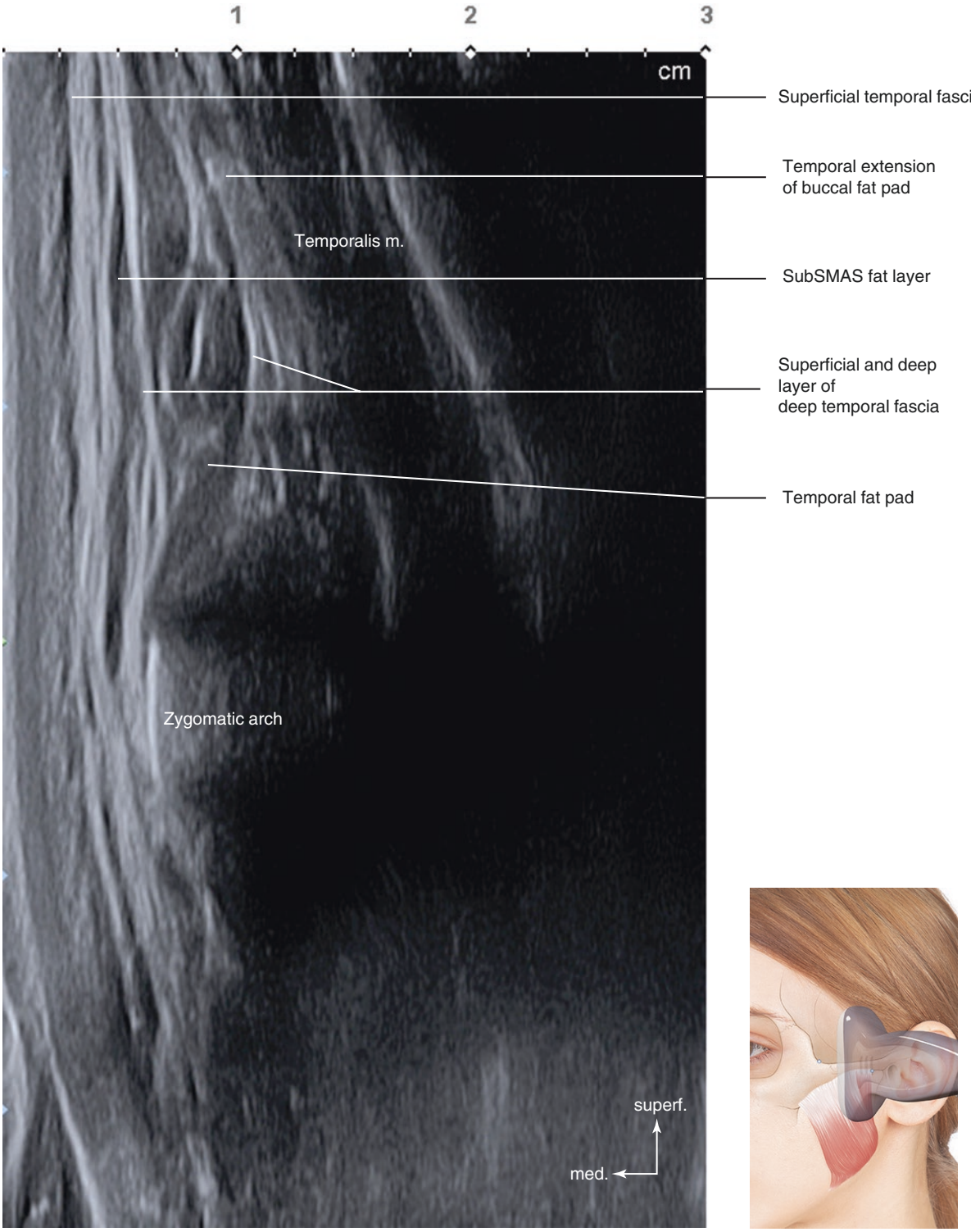

Fig. 3.26 Ultrasonography of the perpendicular line passing the midpoint between T3 and T5 (T4). B mode (coronal view, 15 MHz by linear transducer). (Published with kind permission of © Hee-Jin Kim 2020. All Rights Reserved)

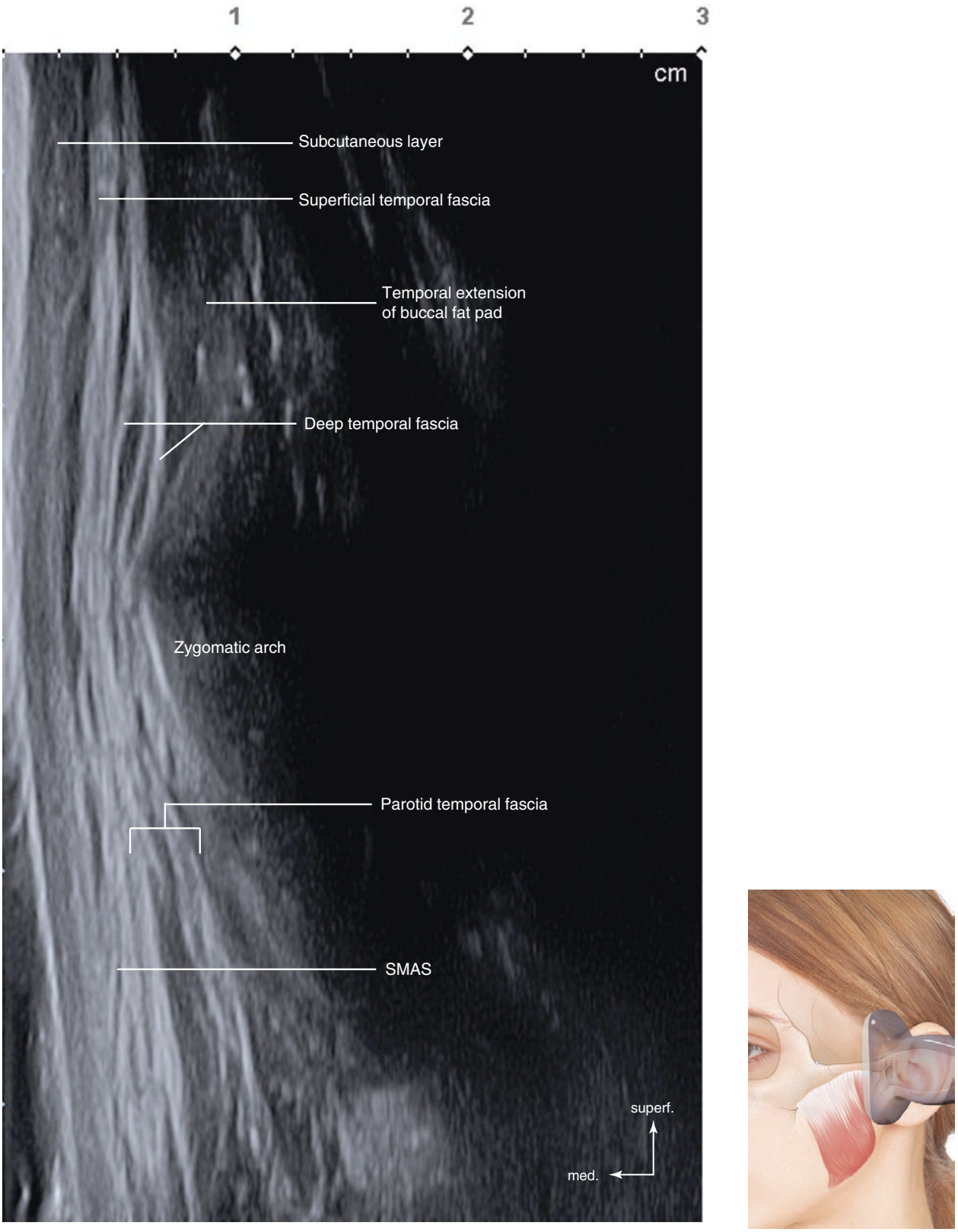

Fig. 3.27 Ultrasonography of the perpendicular line passing the articular eminence (T5). B mode (coronal view, 15 MHz by linear transducer). (Published with kind permission of © Hee-Jin Kim 2020. All Rights Reserved)

Bibliography

1. Choi YJ, Lee KW, Gil YC, Hu KS, Kim HJ. Ultrasonographic analyses of the forehead region for injectable treatments. Ultrasound Med Biol. 2019;45:2641–8.
2. Choi YJ, Won SY, Lee JG, Hu KS, Kim ST, Tansatit T, Kim HJ. Characterizing the lateral border of the frontalis for safe and effective injection of botulinum toxin. Aesthet Surg J. 2016;36:344–8.
3. Cong LY, Lee SH, Tansatit T, Hu KS, Kim HJ. Topographic anatomy of the inferior medial palpebral artery and Its relevance to the pretarsal roll augmentation. Plast Reconstr Surg. 2016;138:430e–6e.
4. Cong LY, Phothong W, Lee SH, Wanitphakdeedecha R, Koh I, Tansatit T, Kim HJ. Topographic analysis of the supratrochlear artery and the supraorbital artery: implication for improving the safety of forehead augmentation. Plast Reconstr Surg. 2017;139:620e.
5. Frankel AS, Kamer FM. Chemical browlift. Arch Otolaryngol Head Neck Surg. 1998;124:321–3.
6. Gil YC, Lee SH, Shin KJ, Song WC, Koh KS, Shin HJ. Three-dimensional topography of the supratrochlear nerve with reference to the lacrimal caruncle, and its danger zone in Asians. Dermatol Surg. 2017;43:1458–65.
7. Gil YC, Shin KJ, Lee SH, Song WC, Koh KS, Shin HJ. Topography of the supraorbital nerve with reference to the lacrimal caruncle: danger zone for direct browplasty. Br J Ophthalmol. 2017;101:940–5.
8. Huilgol SC, Carruthers A, Carruthers JD. Raising eyebrows with botulinum toxin. Dermatol Surg. 1999;25:373–5.
9. Hur MS. Anatomical relationships of the procerus with the nasal ala and the nasal muscles: transverse part of the nasalis and levator labii superioris alaeque nasi. Surg Radiol Anat. 2017;39:865–9.
10. Jung W, Youn KH, Won SY, Park JT, Hu KS, Kim HJ. Clinical implications of the middle temporal vein with regard to temporal fossa augmentation. Dermatol Surg. 2014;40:618–23.
11. Kwak HH, Ko SJ, Jung HS, Park HD, Chung IH, Kim HJ. Topographic anatomy of the deep temporal nerves, with references to the superior head of lateral pterygoid. Surg Radiol Anat. 2003;25:393–6.
12. Lee HJ, Choi KS, Won SY, Apinuntrum P, Hu KS, Kim ST, Tansatit T, Kim HJ. Topographic relationship between the supratrochlear nerve and corrugator supercilii muscle--can this anatomical knowledge improve the response to botulinum toxin injections in chronic migraine. Toxins. 2015;17(7):2629–38.
13. Lee HJ, Choi YJ, Lee KW, Kim HJ. Positional patterns among the auriculotemporal nerve, superficial temporal artery, and superficial temporal vein for use in decompression treatments for migraine. Sci Rep. 2018;8(8):16539.
14. Lee HJ, Kang IW, Won SY, Lee JG, Hu KS, Tansatit T, Kim HJ. Description of a novel anatomic venous structure in the nasoglabellar area. J Craniofac Surg. 2014;25:633–5.
15. Lee HJ, Lee KW, Tansatit T, Kim HJ. Three-dimensional territory and depth of the corrugator supercilii: application to botulinum neurotoxin injection. Clin Anat. 2020;
16. Lee JG, Yang HM, Hu KS, Lee YI, Lee HJ, Choi YJ, Kim HJ. Frontal branch of the superficial temporal artery: anatomical study and clinical implications regarding injectable treatments. Surg Radiol Anat. 2015;37:61–8.
17. Lee JY, Kim JN, Kim SH, Choi HG, Hu KS, Kim HJ, Song WC, Koh KS. Anatomical verification and designation of the superficial layer of the temporalis muscle. Clin Anat. 2012;25:176–81.
18. Lee KL, Choi YJ, Gil YC, Hu KS, Tansatit T, Kim HJ. Locational relationship between the lateral border of the frontalis muscle and the superior temporal line. Plast Reconstr Surg. 2019;143:293e–8e.
19. Park JT, Youn KH, Hur MS, Hu KS, Kim HJ, Kim HJ. Malaris muscle, the lateral muscular band of orbicularis oculi muscle. J Craniofac Surg. 2011;22:659–62.
20. Song WC, Choi HG, Kim SH, Kim SH, Hu KS, Kim HJ, Koh KS. Topographic anatomy of the zygomatic arch and temporal fossa: a cadaveric study. J Plast Reconstr Aesthet Surg. 2009;62:1375–8.
21. Song WC, Kim SJ, Kim SH, Hu KS, Kim HJ, Koh KS. Asymmetry of the palpebral fissure and upper eyelid crease in Koreans. J Plast Reconstr Aesthet Surg. 2007;60:251–5.
22. Yang HM, Jung W, Won SY, Youn KH, Hu KS, Kim HJ. Anatomical study of medial zygomaticotemporal vein and its clinical implication regarding the injectable treatments. Surg Radiol Anat. 2015;37:175–80.
23. Yang HM, Kim HJ. Anatomical study of the corrugator supercilii muscle and its clinical implication with botulinum toxin A injection. Surg Radiol Anat. 2013;35:817–21.

US Anatomy of the Periorbital Region

4

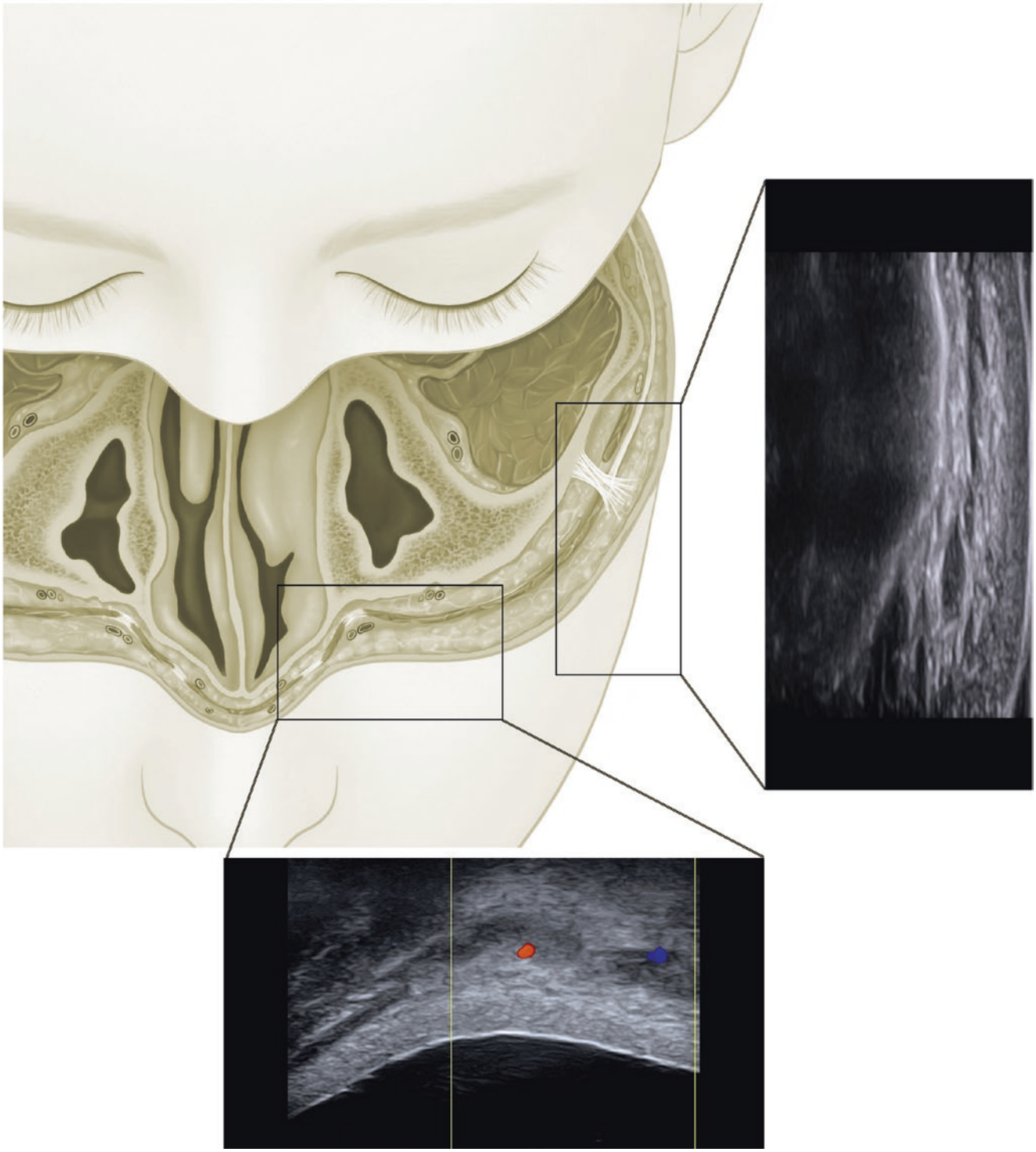

H.-J. Kim et al., *Ultrasonographic Anatomy of the Face and Neck for Minimally Invasive Procedures*,
https://doi.org/10.1007/978-981-15-6560-1_4

4.1 Clinical Anatomy of the Periorbital Region

The area covered by the orbicularis oculi (OOc) m. is considered the "periorbital region." This territory extends from the upper and lower eyelids to the eyebrows. The OOc m. is the muscle that determines the shape of the eyes and facial expressions. The OOc m. is an elliptically broad and flat muscle that acts in closing the eyelid, which also protects the eyeballs. The component of the OOc m. can be subdivided as the orbital and the palpebral part by its location. Furthermore the palpebral portion can be classified by preseptal and pretarsal portions (Fig. 4.1). These portions are positioned in the superficial layer of both the tarsal plate and the orbital septum. The palpebral part of the muscle involuntarily closes the eyelids by making vertical wrinkles in the area of the medial canthus.

The orbital part of the OOc m. begins from both the infraorbital and supraorbital margins and runs to the tendinous portion of the lateral and medial canthus lower margin of the frontalis m., the procerus m., the corrugator supercilii m., and the skin. In cases of Asians, the average distance from the lateral canthus to lateral edge of the OOc m. is about 3.1 cm. The lateral and medial muscular bands of the OOc m. are identifiable by the rate of 54% and 64% of the cases, respectively (Fig. 4.2).

The OOc m. is one of the most complex facial muscles because it overlaps with neighboring muscles (e.g., corrugator supercilii m., procerus m., frontalis m., zygomaticus major m., and zygomaticus minor m.). These muscles are directly and indirectly connected to each other. These muscular connections take part in alternative facial expressions. In 89% of the Asians, the zygomaticus minor and the OOc mm. are directly connected to each other.

The corrugator supercilii (CS) m. lies underneath the layer of the OOc m. The CS m. begins from the periosteum of the medial side of the superciliary arch of the frontal bone. Then, it runs superiorly and laterally merging to the frontalis m. The muscle can subdivide into two distinct bellies, which are the transverse and oblique belly. The transverse belly of the CS m. originates superiorly and laterally to the origin of the oblique belly. Most of the muscle fibers of the transverse belly insert to the frontalis m. (Fig. 4.3) and superolateral orbital part of the OOc m. The transverse belly is located deep to the oblique belly and runs horizontally compared to the oblique belly. The CS m. and part of the frontalis m. are responsible for vertical lines on the glabellar region. On average, the origin of the CS m. starts from 16 mm above the horizontal intercanthal line and 4–14 mm bilaterally from the midline. Then, the muscle interlaces into the frontalis m. and to the dermis, which lays about 30 mm above the intercanthal

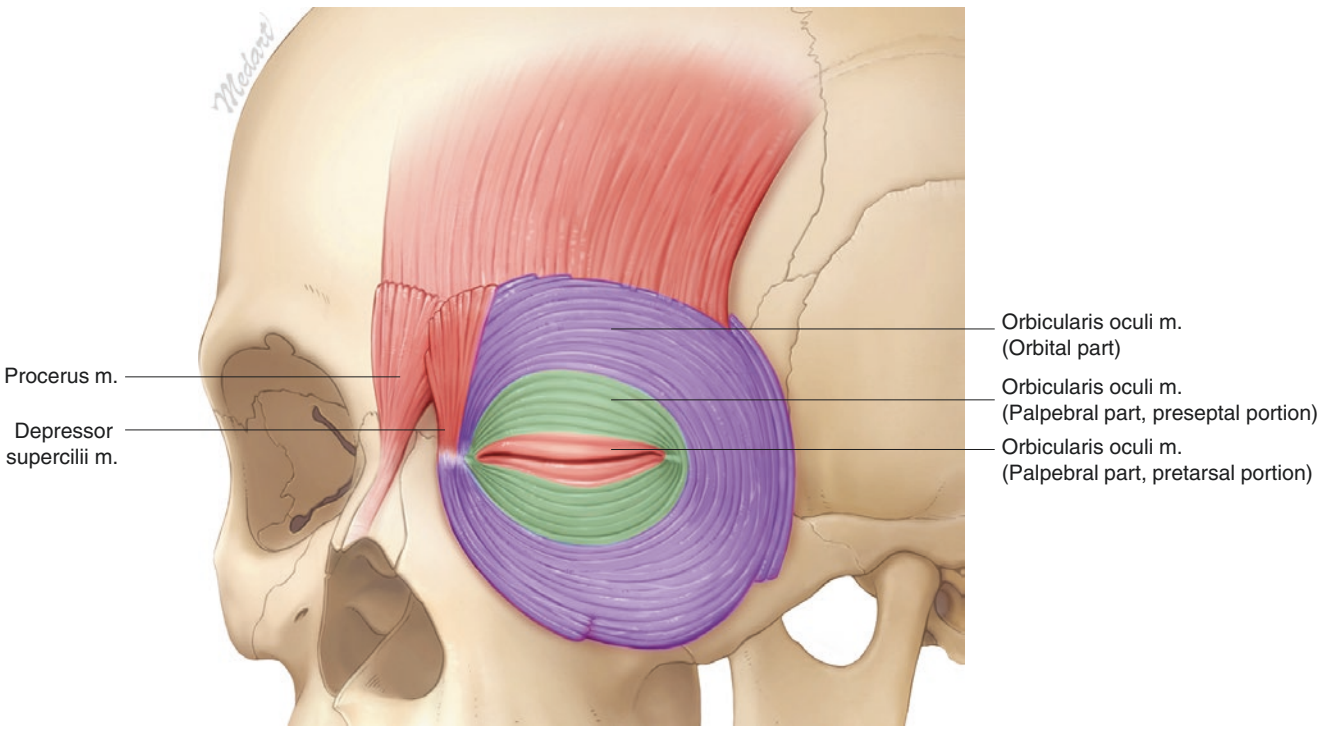

Fig. 4.1 Illustration of the periorbital musculature. (Published with kind permission of © Kwan-Hyun Youn 2020. All Rights Reserved)

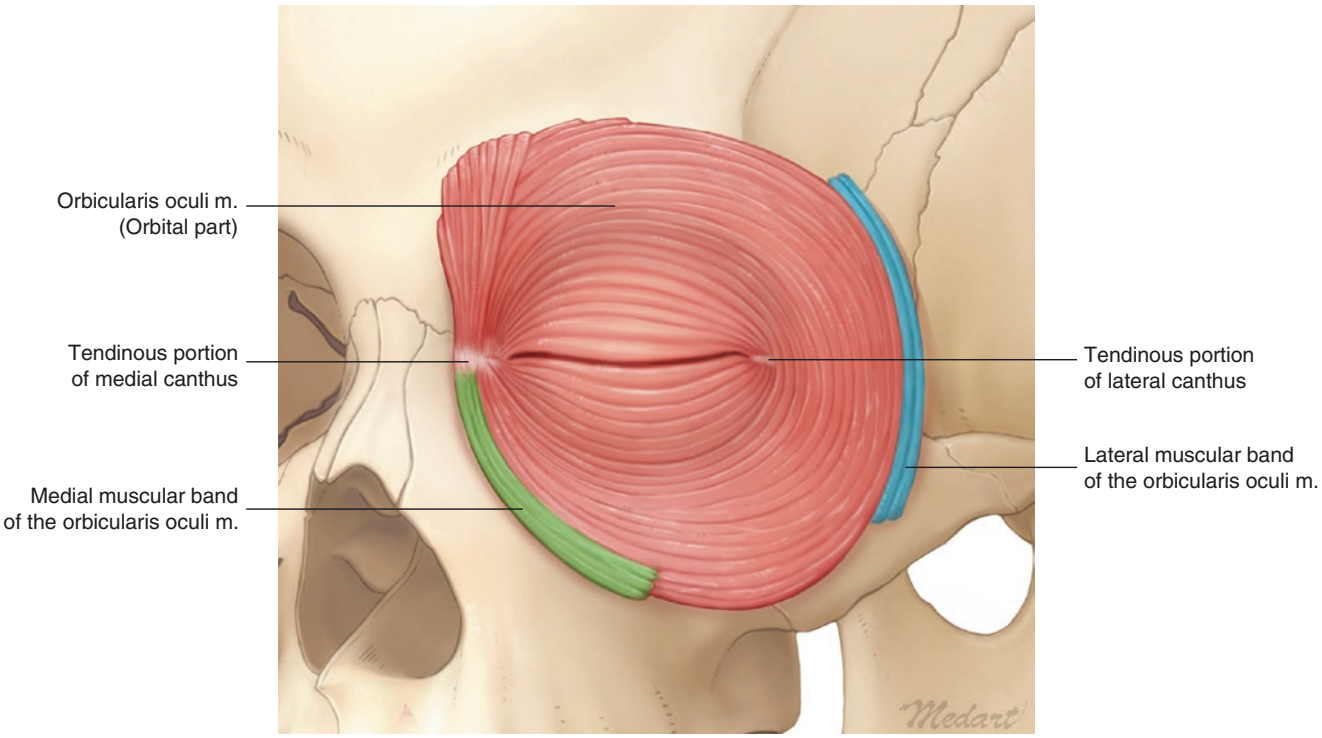

Fig. 4.2 Illustration of the orbicularis oculi muscle and medial and lateral muscular band. (Published with kind permission of © Kwan-Hyun Youn 2020. All Rights Reserved)

Fig. 4.3 Glabellar frown lines and its corresponding corrugator supercilii muscle. (Published with kind permission of © Kwan-Hyun Youn 2020. All Rights Reserved)

horizontal line and 16–35 mm bilaterally from the midline. The average vertical length of the CS m. is 15 mm in Asians and 21 mm in Caucasians, respectively.

The depressor supercilii (DS) m. is a fan-shaped muscle that originates from the frontal process of the maxilla and nasal portion of the frontal bone. The DS m. runs over the glabellar region, where it intermingles with the CS and medial fibers of the OOc m. (Fig. 4.1).

The frontal notch is a distinct bony landmark located medially in the supraorbital margin. On the other hand, the

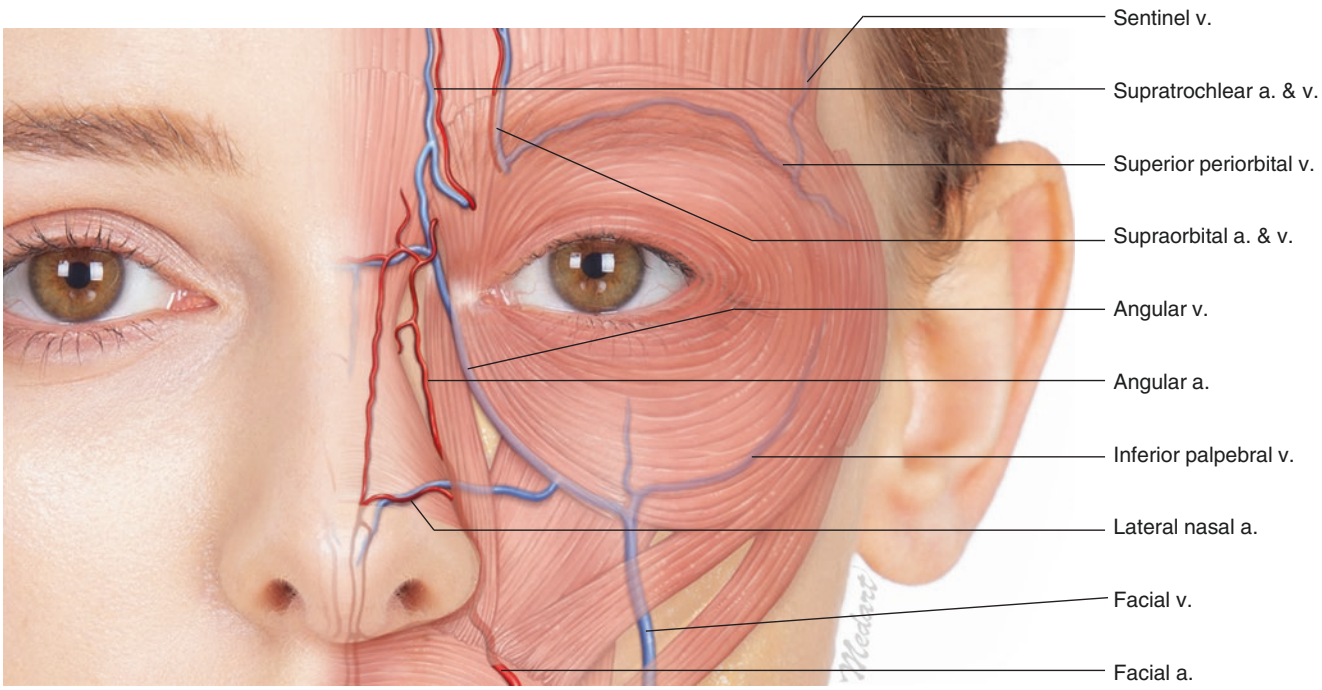

Fig. 4.4 Illustration representing the periorbital vasculature. (Published with kind permission of © Kwan-Hyun Youn 2020. All Rights Reserved)

supraorbital notch (or foramen) is located laterally to the frontal notch. The supratrochlear vessels and nerves emerge at the frontal notch. In cases of supraorbital vessels and nerves, these structures emerge from the supraorbital notch (or foramen).

The angular vessels run medially to the medial canthal area. The facial a. branches off the lateral nasal artery, and then, it becomes the angular a. as it runs superiorly to the forehead. The angular a. ends near to the medial canthal area with minor branches to the medial side of the nose and the eyelid. In 25% of the population, the angular a. originates from the ophthalmic a. rather than the facial a. On the other hand the angular v. is formed by merging of the supraorbital and the supratrochlear vv. These veins merge at the medial canthal region and become the angular v. The angular v. then diverges to two branches, with one becoming the superior ophthalmic and the facial vv. The facial v. perforates deeply and runs inferiorly (Fig. 4.4). Compared to the angular a., the angular v. runs more deeply at the medial canthal region. The inferior palpebral v. (IPV) is usually be found within the suborbicularis oculi fat (SOOF) at the midface. The SOOF is the prezygomatic space bordered by the orbital retaining ligament superiorly, zygomatic cutaneous ligament inferiorly, OOc m. superficially, and zygomatic bone deeply. In 58% of the cases, the IPV is located deep to the lateral part of the OOc m.

4.1.1 Facial Landmarks and Reference Lines for the US Examination of the Periorbital Region (Fig. 4.5)

Periorbital region	
P1: intersection point of TL2 and PL1	**P6**: intersection point of TL3 and PL1
P2: intersection point of TL2 and PL2	**P7**: intersection point of TL3 and PL2
P3: intersection point of TL2 and PL3	**P8**: intersection point of TL3 and PL3
P4: intersection point of TL2 and PL4	**P9**: intersection point of TL3 and PL4
P5: lateral orbital rim at the level of lateral canthus	

4.1.2 Checklists in Periorbital Region

Objective structures	Facial landmarks where the structures can be observed
Orbicularis oculi m.	P1, P2, P3, P4, P5, P6, P7, P8, P9
Corrugator supercilii m.	P1, P2
Temporalis m.	P4
Levator labii superioris m.	P7
Levator labii superioris alaeque nasi m.	P6
Zygomaticus minor m.	P9
Frontalis m.	P4
Superficial temporal fascia (SMAS)	P4
Deep temporal fascia	P4
ROOF	P2, P3, P4
SOOF	P8, P9
Angular a. and v.	P6
Anterior deep temporal a.	P4
Supratrochlear a. and n.	P1
Supraorbital a. and n.	P2
Periorbital v.	P4

4.2 US Images of the Periorbital Region

4.2.1 US Anatomy Images

In the US image of the periorbital region, the epidermis is shown as a thin hyperechoic line and the dermis as a slightly hyperechoic line. Compared to the eyelid region, eyebrow regions show thicker subcutaneous layer with an irregular hypoechoic image. The OOc m. lying underneath the sub-

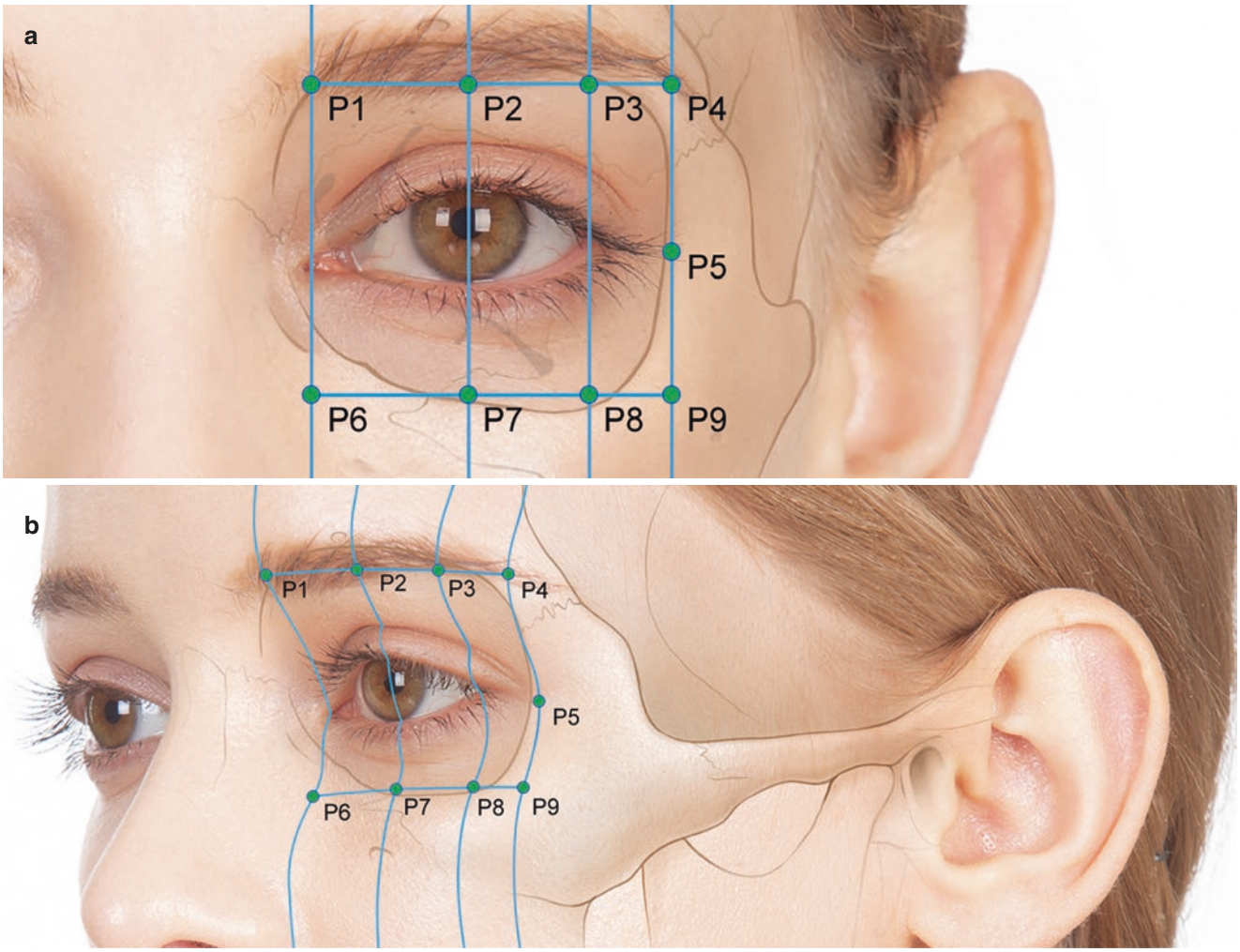

Fig. 4.5 Facial landmarks and reference lines for the ultrasonographic examination of the periorbital region. (**a**) Frontal view and (**b**) oblique view. (Published with kind permission of © Kwan-Hyun Youn 2020. All Rights Reserved)

cutaneous layer is shown as a hypoechoic image. The SOOF is shown as a slightly hyperechoic image while the supraorbital vessels are shown as anechoic from the lateral aspect of the eyebrow. The supraorbital n. is shown as honeycomb at the supraorbital notch (or foramen) (Figs. 4.6, 4.7, 4.8, 4.9, 4.10, and 4.11).

4.2.2 B Mode and Doppler Images

P1: Intersection Point of TL2 and PL1

The hair in the eyebrows makes it hard to observe through US. However, US shows that the skin of the eyelids becomes thinner as it goes downward. The subcutaneous layer of the

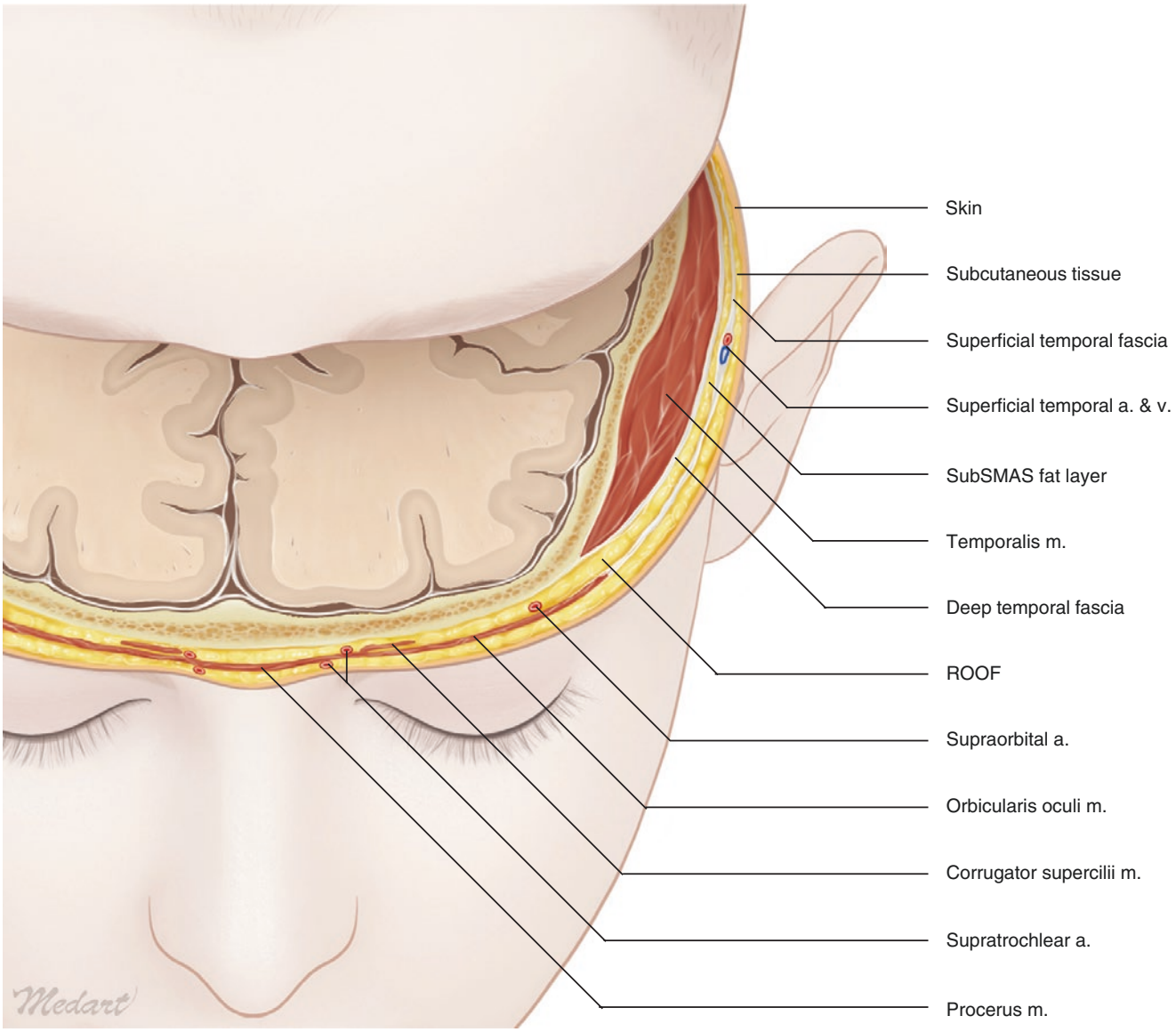

Fig. 4.6 Illustration representing the transverse section of the periorbital region passing the TL2. (Published with kind permission of © Kwan-Hyun Youn 2020. All Rights Reserved)

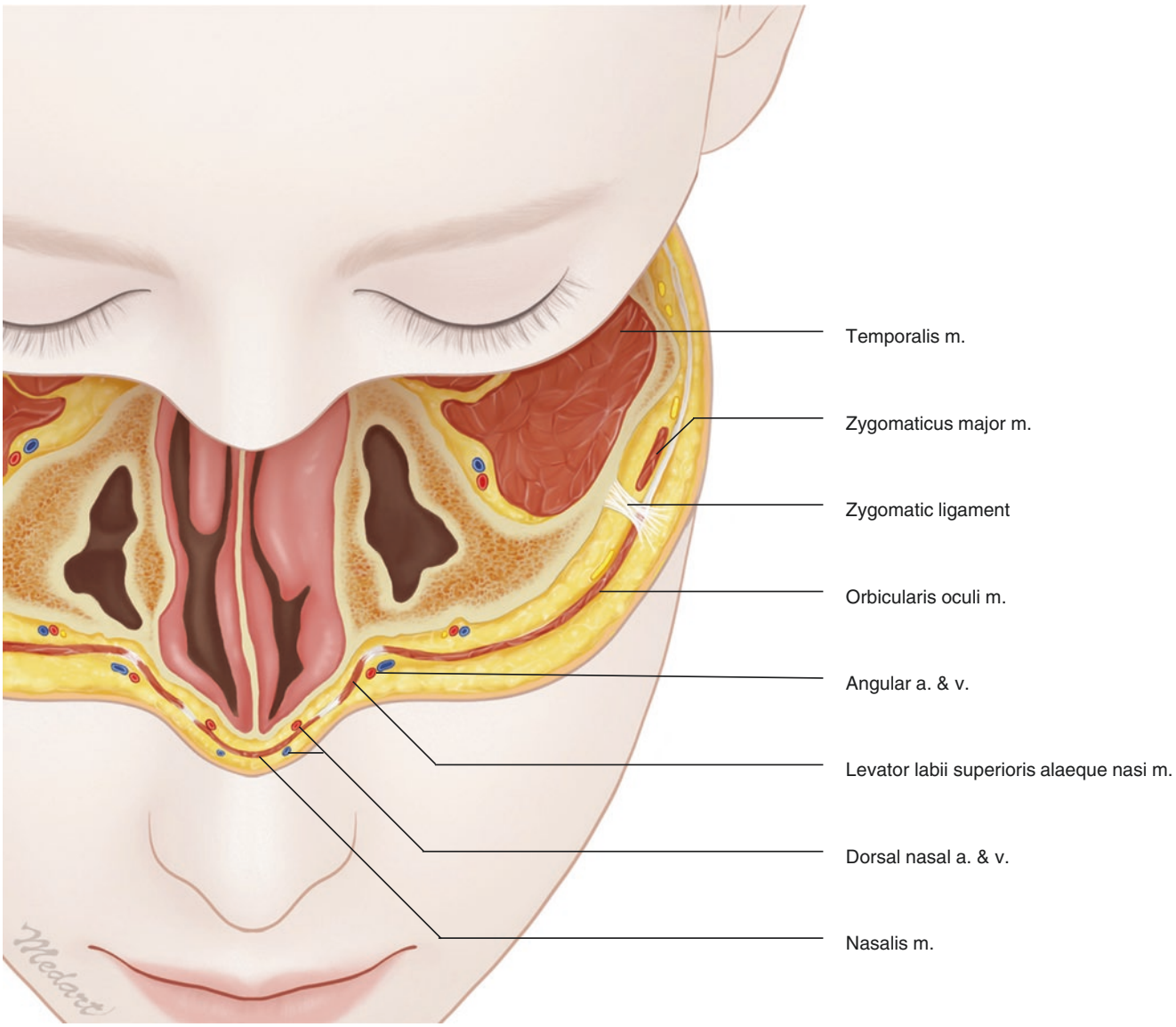

Fig. 4.7 Illustration representing the transverse section of the periorbital region passing the TL3. (Published with kind permission of © Kwan-Hyun Youn 2020. All Rights Reserved)

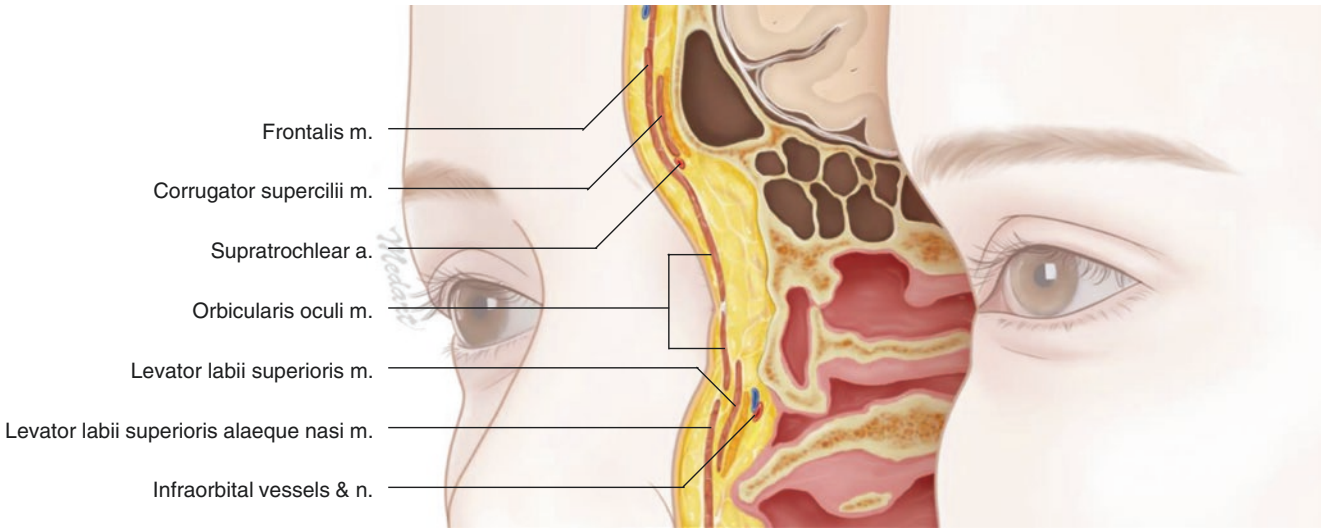

Fig. 4.8 Illustration representing the sagittal section of the periorbital region passing the PL1 (medial canthus). (Published with kind permission of © Kwan-Hyun Youn 2020. All Rights Reserved)

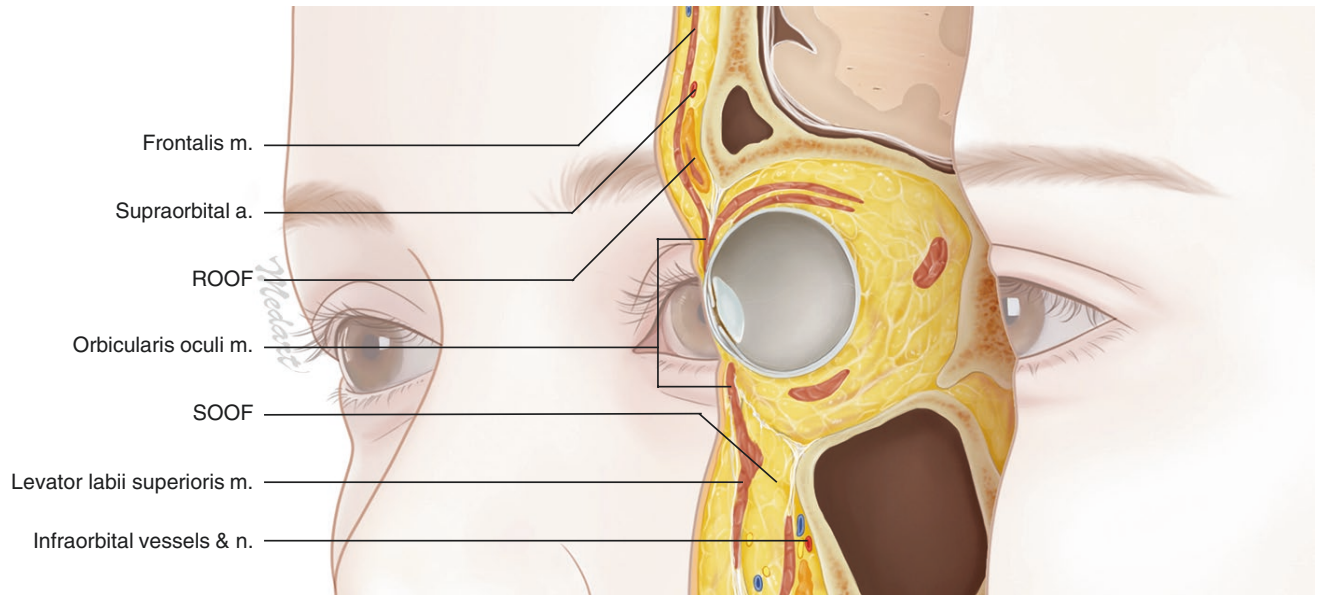

Fig. 4.9 Illustration representing the sagittal section of the periorbital region passing the PL2 (midpupil). (Published with kind permission of © Kwan-Hyun Youn 2020. All Rights Reserved)

medial eyebrow region is relatively thicker than the surrounding areas. The eyeball may be deeply observed depending on the angle of the transducer placement. The hypoechoic OOc m. is observed right below the skin layer. Deep to the OOc m., the origin of the CS m. can be observed. The fan-shaped DS m. is shown in the medial side of the OOc m. The DS m. runs through the glabellar region where it intermingles with the medial fibers of the OOc m. The supratrochlear a. is observed superficial to the periosteal layer and deep to the CS m. on the Doppler mode images. The ophthalmic a. emerges at this point 4.5 ± 1.1 mm deep to the skin surface (Fig. 4.11).

P2: Intersection Point of TL2 and PL2

At this point, unlike the P1 point, the OOc and the CS mm. are distinctively observed. The retro-orbicularis oculi fat (ROOF) is located between the muscles and the periosteum of the frontal bone. The supraorbital vessels are located near the supraorbital notch or foramen via

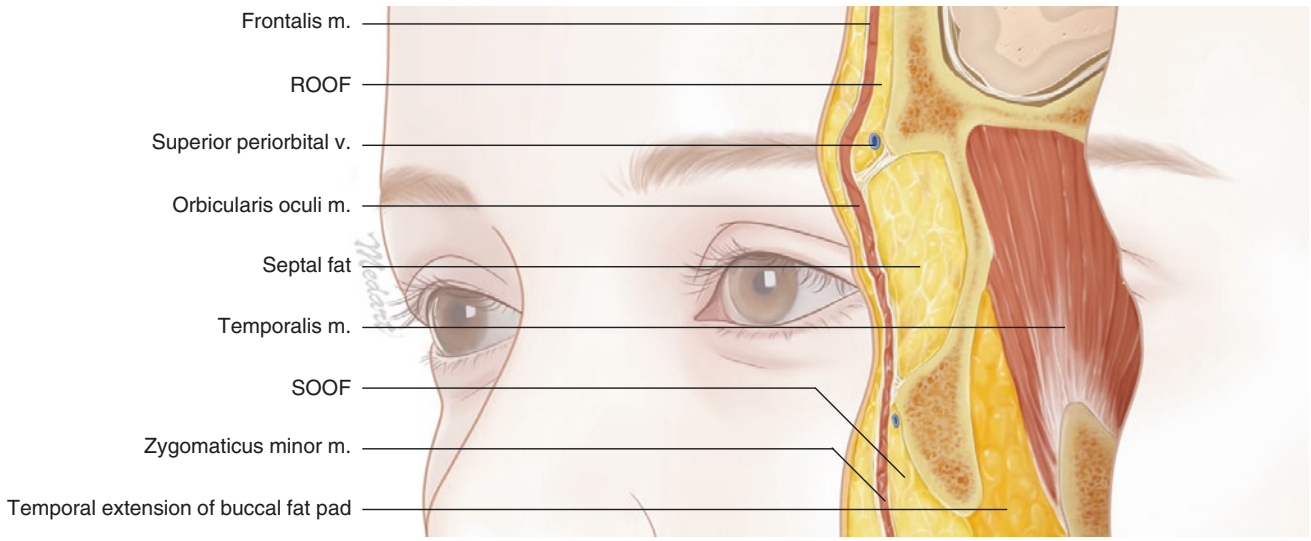

Fig. 4.10 Illustration representing the sagittal section of the periorbital region passing the PL3 (lateral canthus). (Published with kind permission of © Kwan-Hyun Youn 2020. All Rights Reserved)

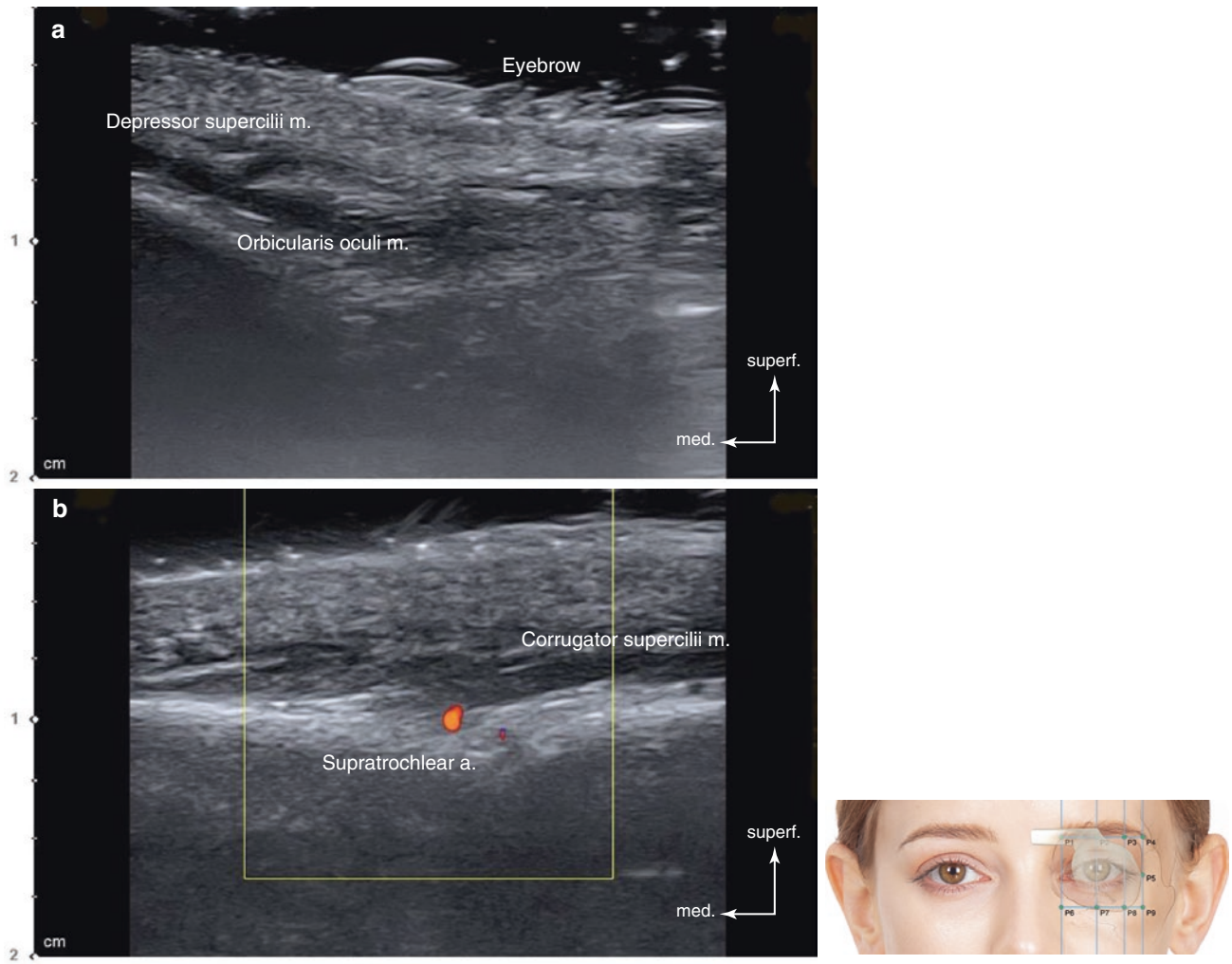

Fig. 4.11 Ultrasonography of the intersection point of TL2 and PL1 (P1). (**a**) B mode (transverse view, 15 MHz by linear transducer), (**b**) Doppler mode (transverse view, 15 MHz by linear transducer), (**c**) B mode (sagittal view, 15 MHz by linear transducer), and (**d**) Doppler mode (sagittal view, 15 MHz by linear transducer). (Published with kind permission of © Hee-Jin Kim 2020. All Rights Reserved)

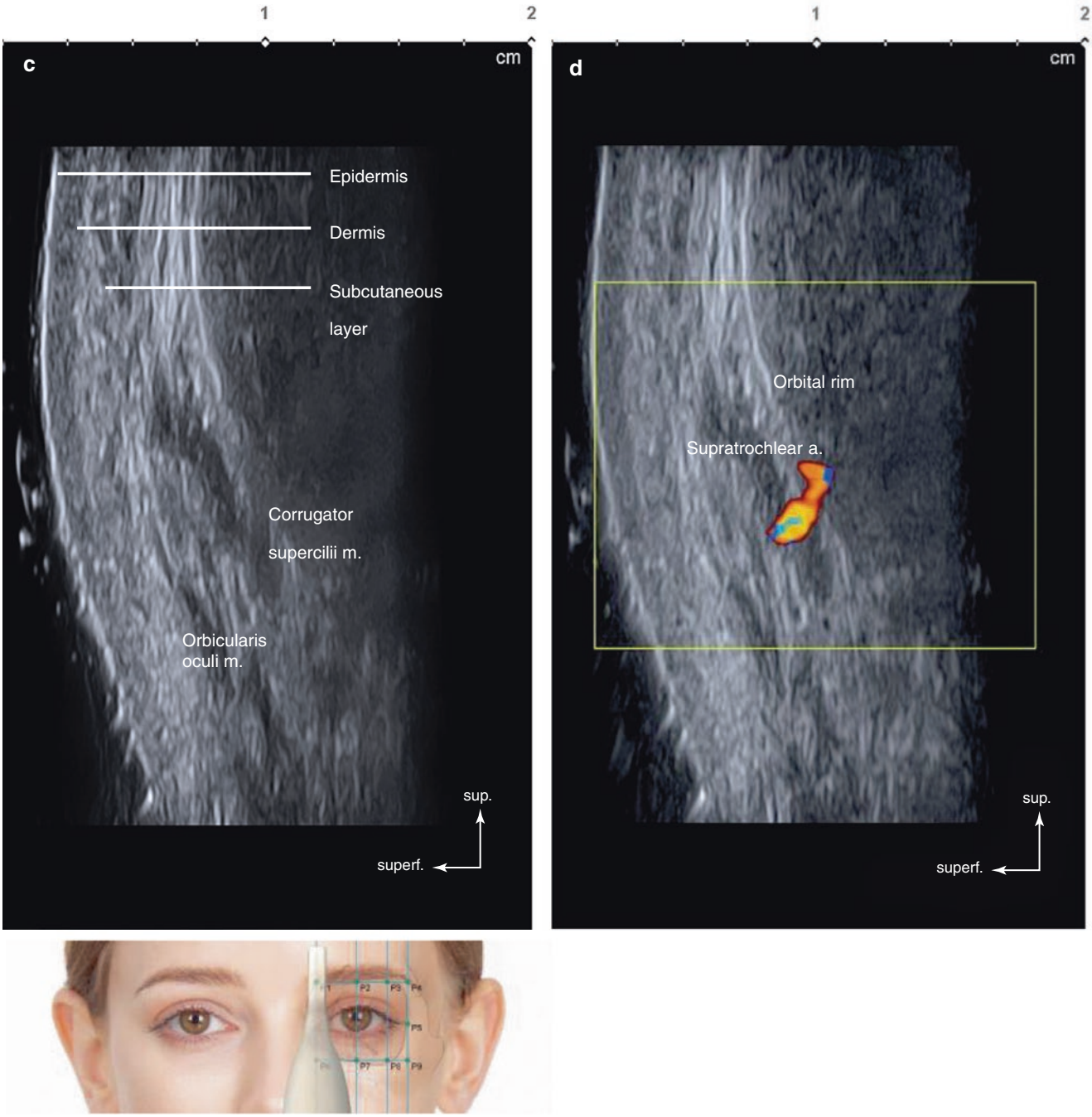

Fig. 4.11 (continued)

Doppler mode. The supraorbital n. is observed within the neurovascular bundle showing a honeycomb appearance (Fig. 4.12).

P3: Intersection Point of TL2 and PL3

At this point, the thicker and clearer OOc m. can be seen. The ROOF is located underneath the OOc m., shown as hyperechoic along the superciliary arch. The orbital septum can be occasionally observed beneath the palpebral portion of the OOc m. The amount of the subcutaneous fat is thinner at the upper eyelid area compared to the supraorbital margin (Fig. 4.13).

P4: Intersection Point of TL2 and PL4

At this point, the tissue beneath the subcutaneous layer of the lateral border of the OOc m. appear as hyperechoic images. The ROOF and subSMAS fat are shown as an irregular hyperechoic image located underneath the layer of OOc m.

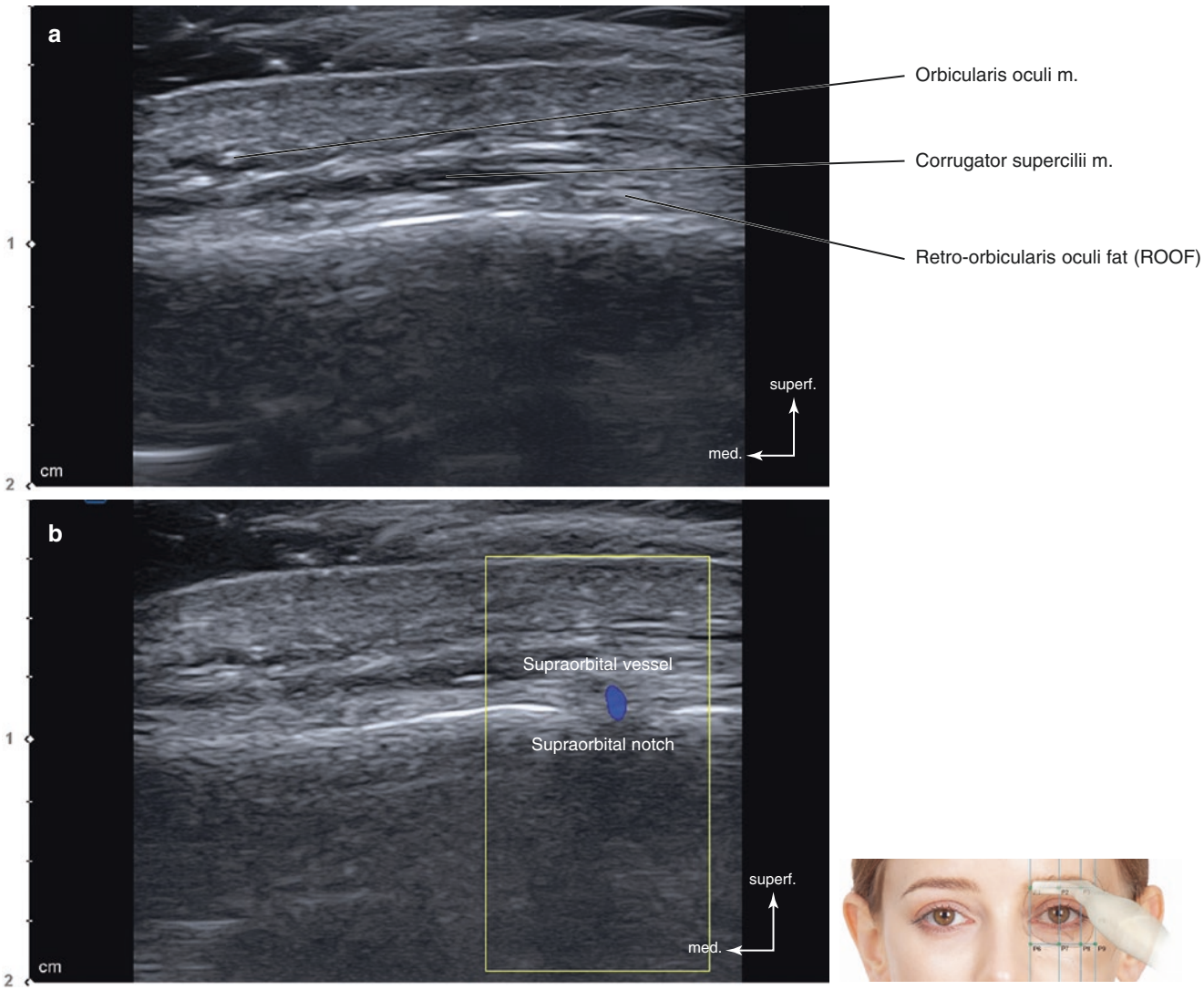

Fig. 4.12 Ultrasonography on the intersection point of TL2 and PL2 (P2). (**a**) B mode (transverse view, 15 MHz by linear transducer), (**b**) Doppler mode (transverse view, 15 MHz by linear transducer), (**c**) B mode (sagittal view, 15 MHz by linear transducer), and (**d**) Doppler mode (sagittal view, 15 MHz by linear transducer). (Published with kind permission of © Hee-Jin Kim 2020. All Rights Reserved)

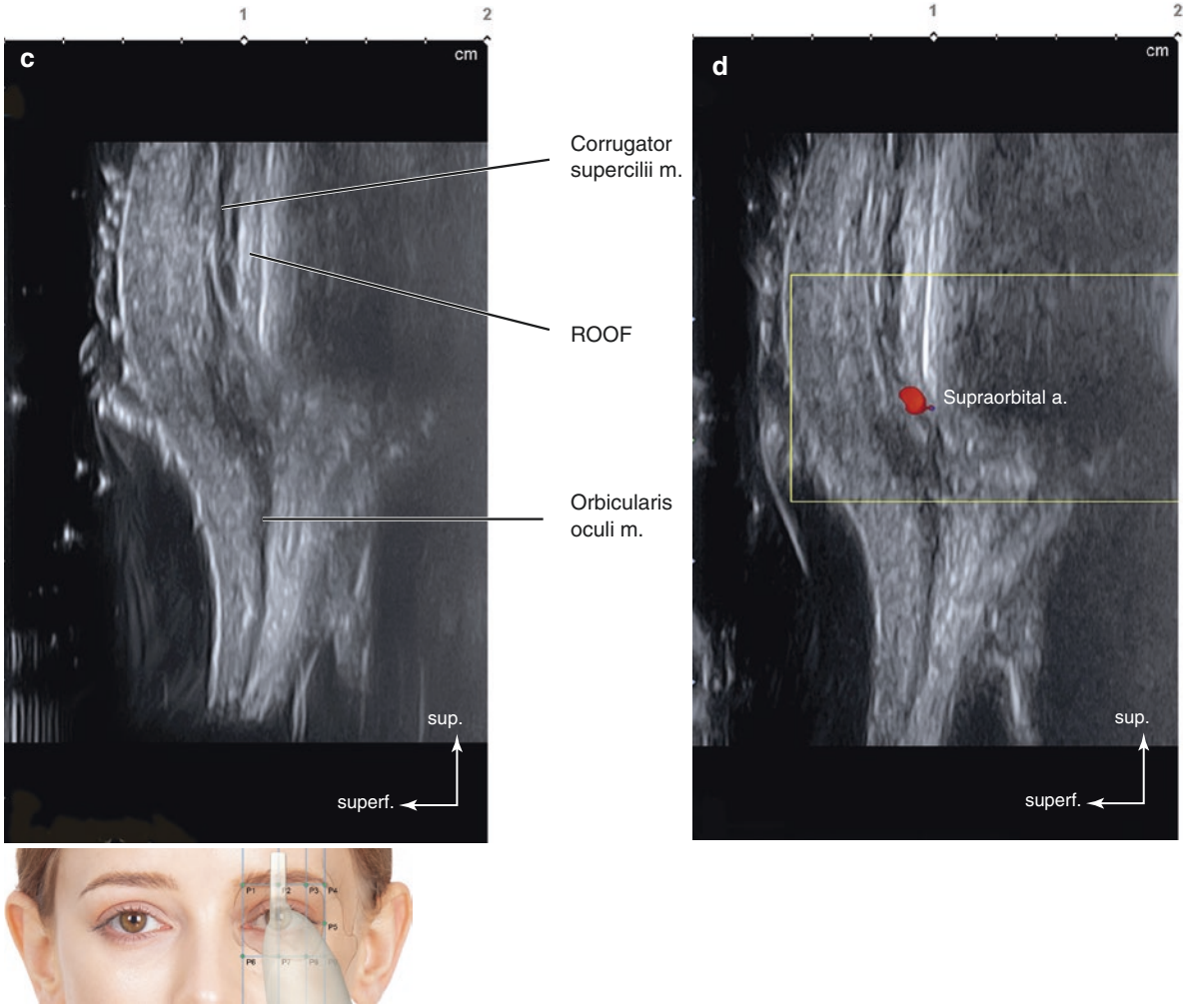

Fig. 4.12 (continued)

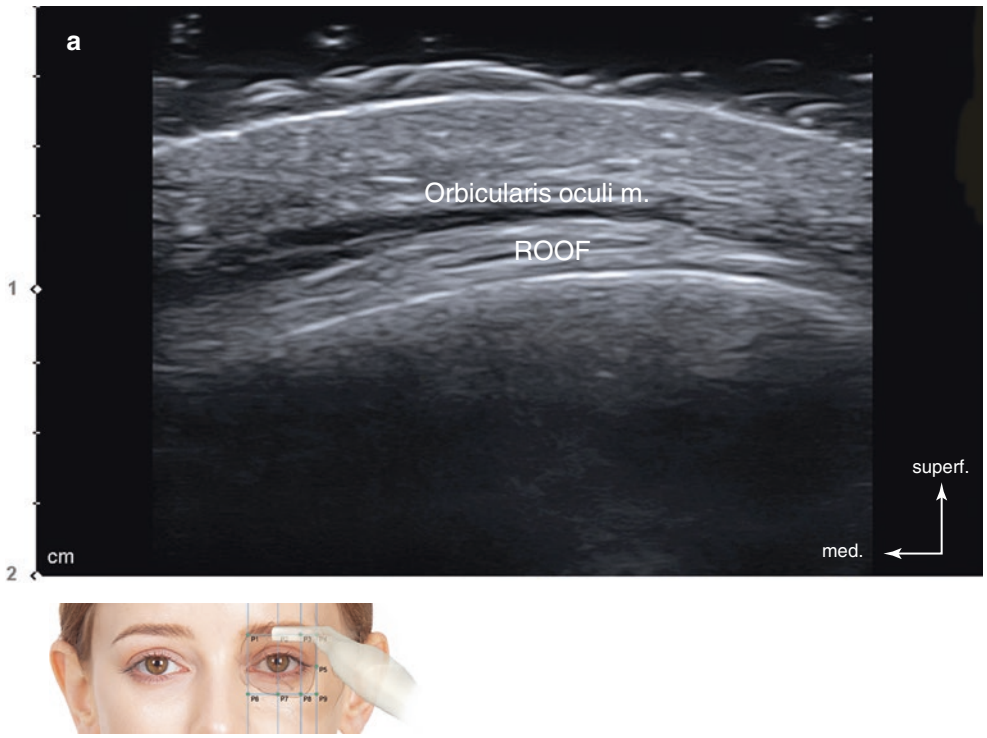

Fig. 4.13 Ultrasonography on the intersection point of TL2 and PL3 (P3). (**a**) B mode (transverse view, 15 MHz by linear transducer) and (**b**) B mode (sagittal view, 15 MHz by linear transducer). (Published with kind permission of © Hee-Jin Kim 2020. All Rights Reserved)

Fig. 4.13 (continued)

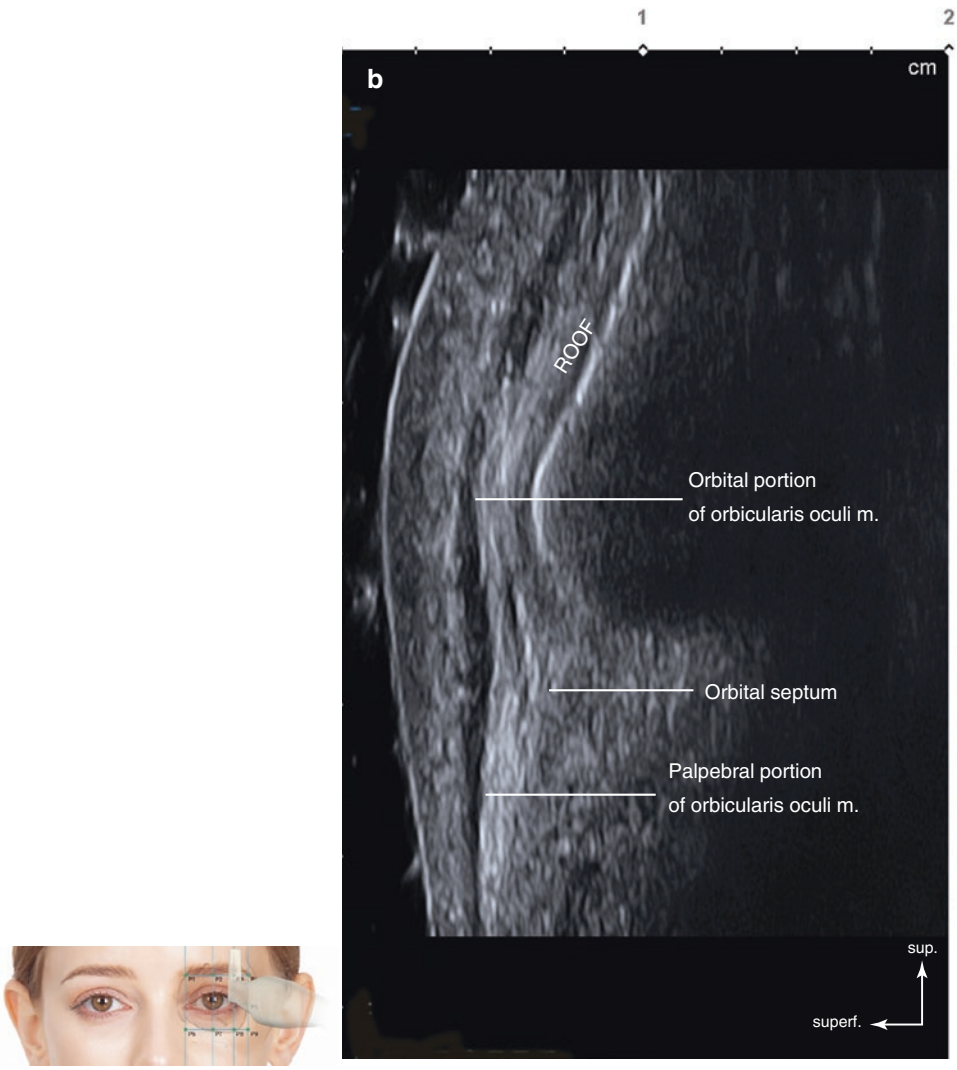

and SMAS. The temporalis m. is covered by a single-layered deep temporal fascia, which can be observed at the area of the anterior temple. The deep temporal a. is observed by Doppler mode image however, the artery can be observed during masticatory movement. The sentinel v. is observed in the longitudinal image, which may be located superficial to or deep to the OOc m. (Fig. 4.14).

P5: Lateral Orbital Rim at the Level of Lateral Canthus
The OOc m. is shown as a hypoechoic image beneath the layer of the skin. Moving the transducer laterally, it gets thicker and finally reaches the lateral margin of the OOc m., which can be found at the anterior temple. The lateral orbital fat compartment is located bordering the lateral orbital rim. At this point, the superficial malar fat compartment becomes thicker inferiorly, which is shown as an irregular hyperechoic image. At this point, the Doppler mode detects the branches of the lacrimal a. and periorbital v. underneath the OOc m. (Fig. 4.15). Also, the inferior palpebral v. may be observed running deeply along the lateral orbital rim.

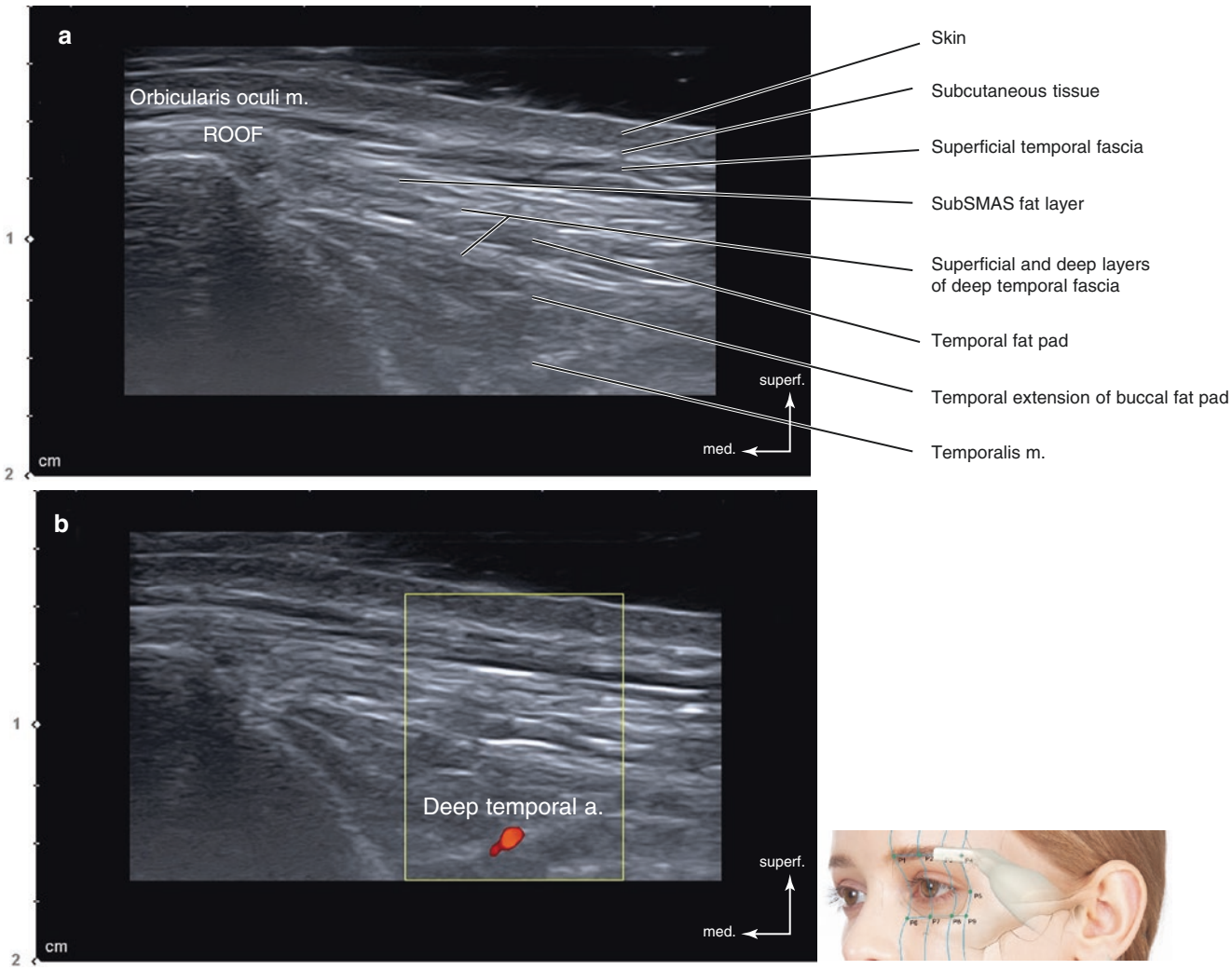

Fig. 4.14 Ultrasonography on the intersection point of TL2 and PL4 (P4). (**a**) B mode (transverse view, 15 MHz by linear transducer), (**b**) Doppler mode (transverse view, 15 MHz by linear transducer), (**c**) B mode (sagittal view, 15 MHz by linear transducer), and (**d**) Doppler mode (sagittal view, 15 MHz by linear transducer). (Published with kind permission of © Hee-Jin Kim 2020. All Rights Reserved)

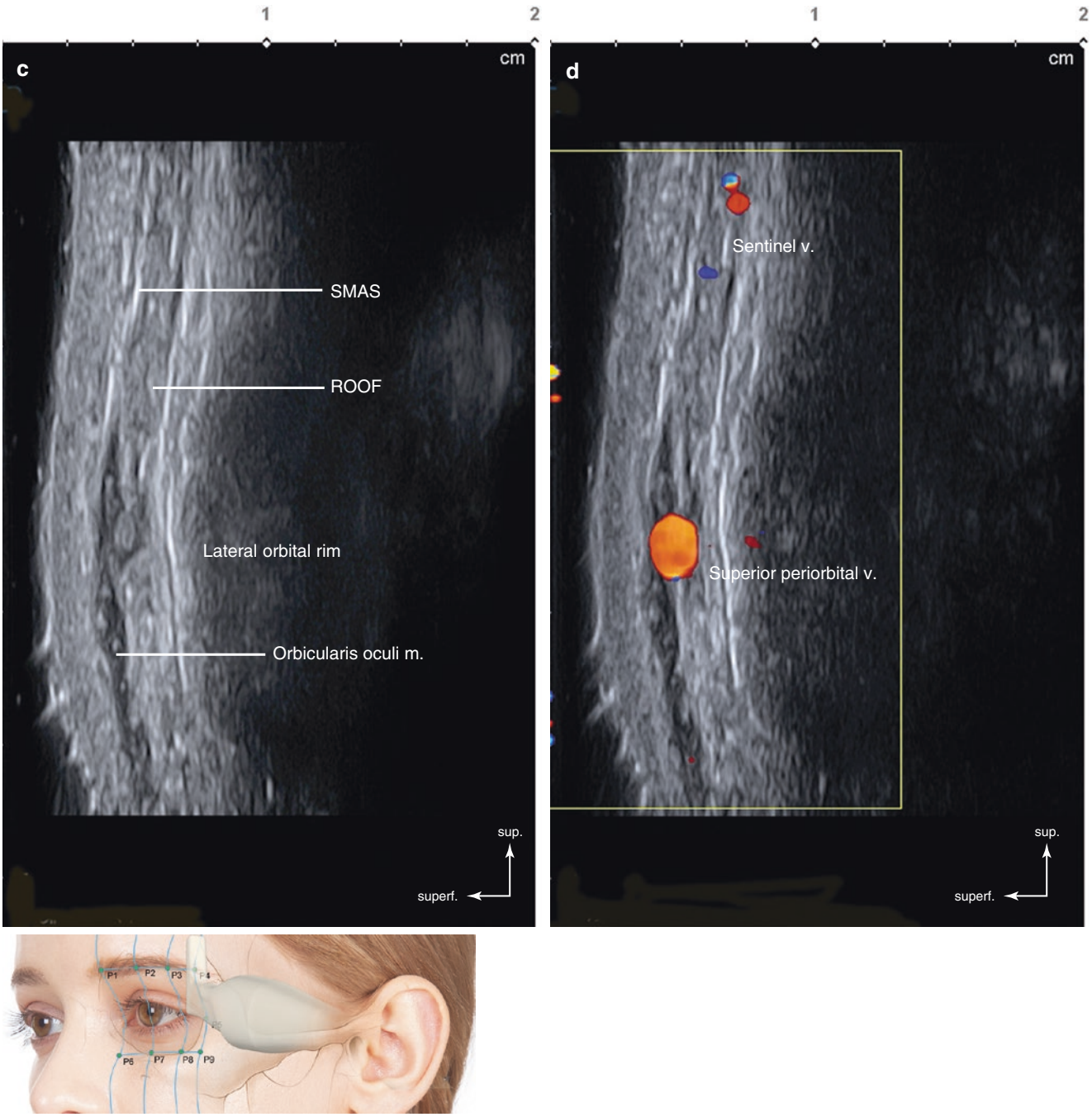

Fig. 4.14 (continued)

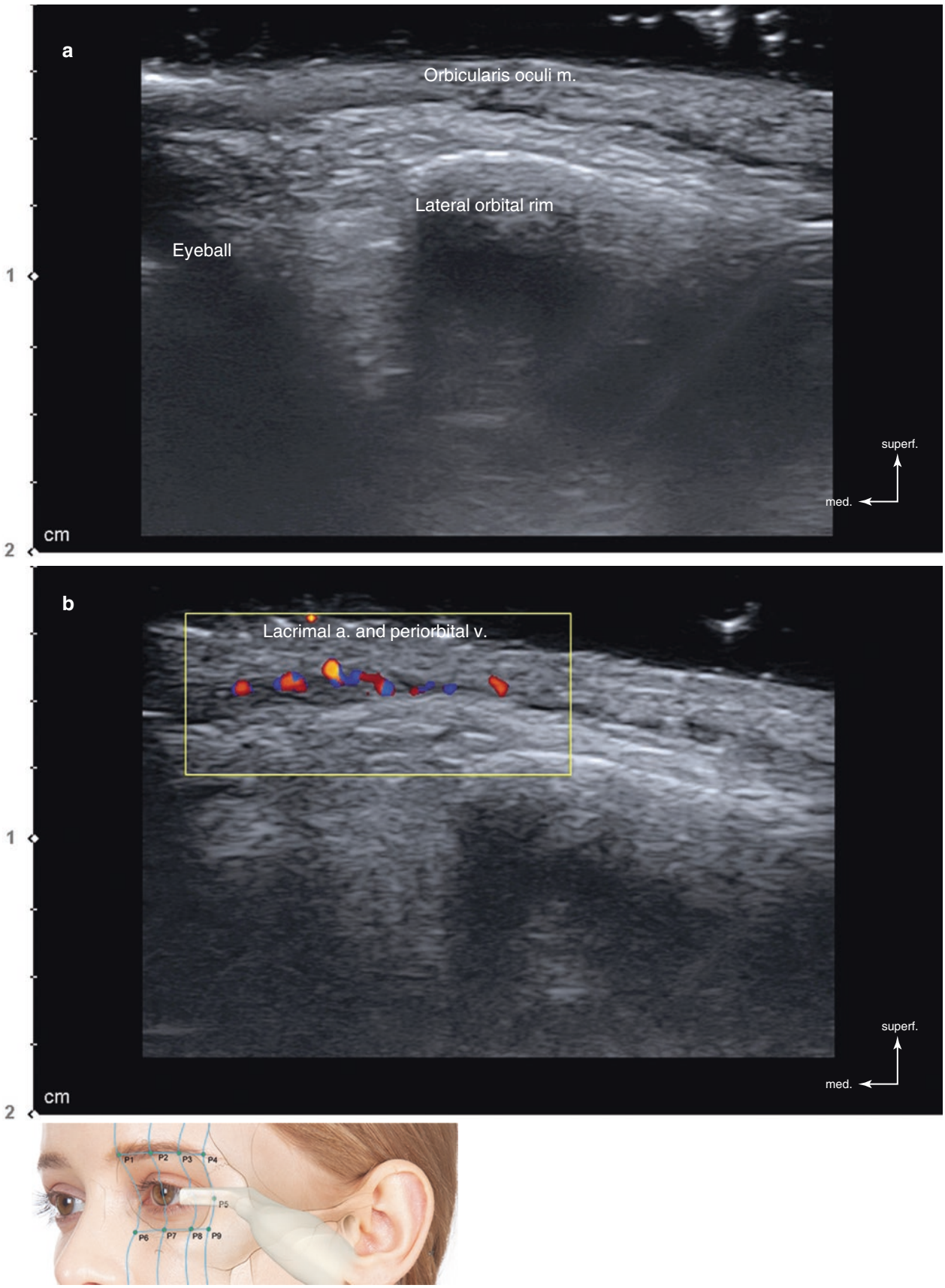

Fig. 4.15 Ultrasonography on the lateral orbital rim at the level of the lateral canthus (P5). (**a**) B mode (transverse view, 15 MHz by linear transducer), (**b**) Doppler mode (transverse view, 15 MHz by linear transducer), and (**c**) B mode (sagittal view, 15 MHz by linear transducer). (Published with kind permission of © Hee-Jin Kim 2020. All Rights Reserved)

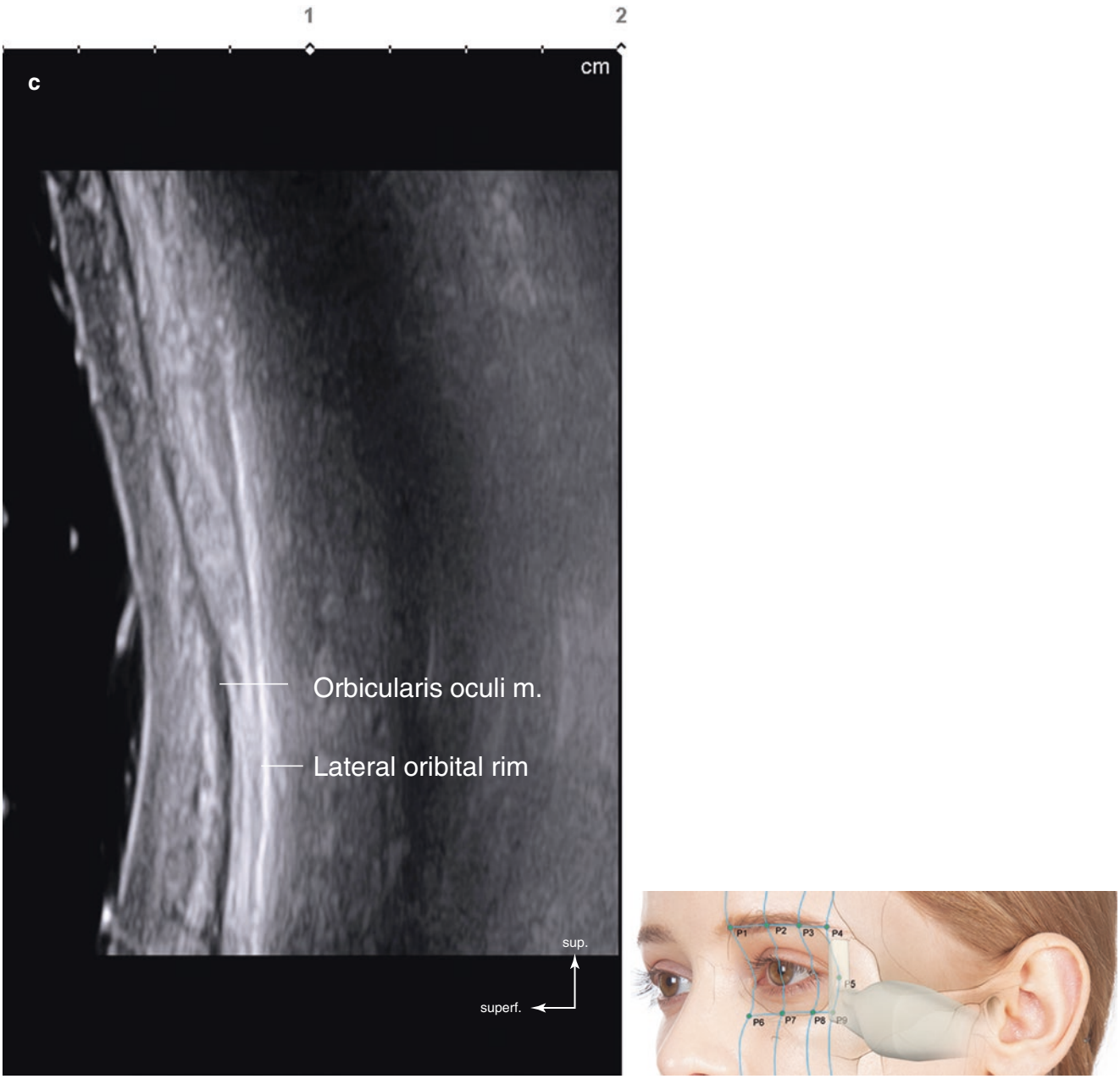

Fig. 4.15 (continued)

P6: Intersection Point of TL3 and PL1

The P6 is the intersection point of TL3 and PL1. At this point, the OOc m. (orbital part and medial muscular band) and the levator labii suprioris alaeque nasi (LLSAN) m. can be distinguished 0.5–1 cm underneath the skin. These structures are clearly identifiable from the medial to lateral aspect. The angular vessels run medially from the muscular band of the OOc m. The artery runs superficially, and the vein runs deeply (Fig. 4.16).

P7: Intersection Point of TL3 and PL2

The P7 is the intersection point of TL3 and PL2. At this point, the junction of palpebral and orbital portion of OOc m. and the origin of the levator labii superioris (LLS) m. can be observed. The skin layer of the palpebral portion of OOc m. is thinner than other facial parts. Underneath the skin layer, the subcutaneous layer is observed as an irregular hyperechoic image. Beneath the palpebral portion of the OOc m., the inferior orbital fat is observed. In aged people, this fat is usually in a protruded

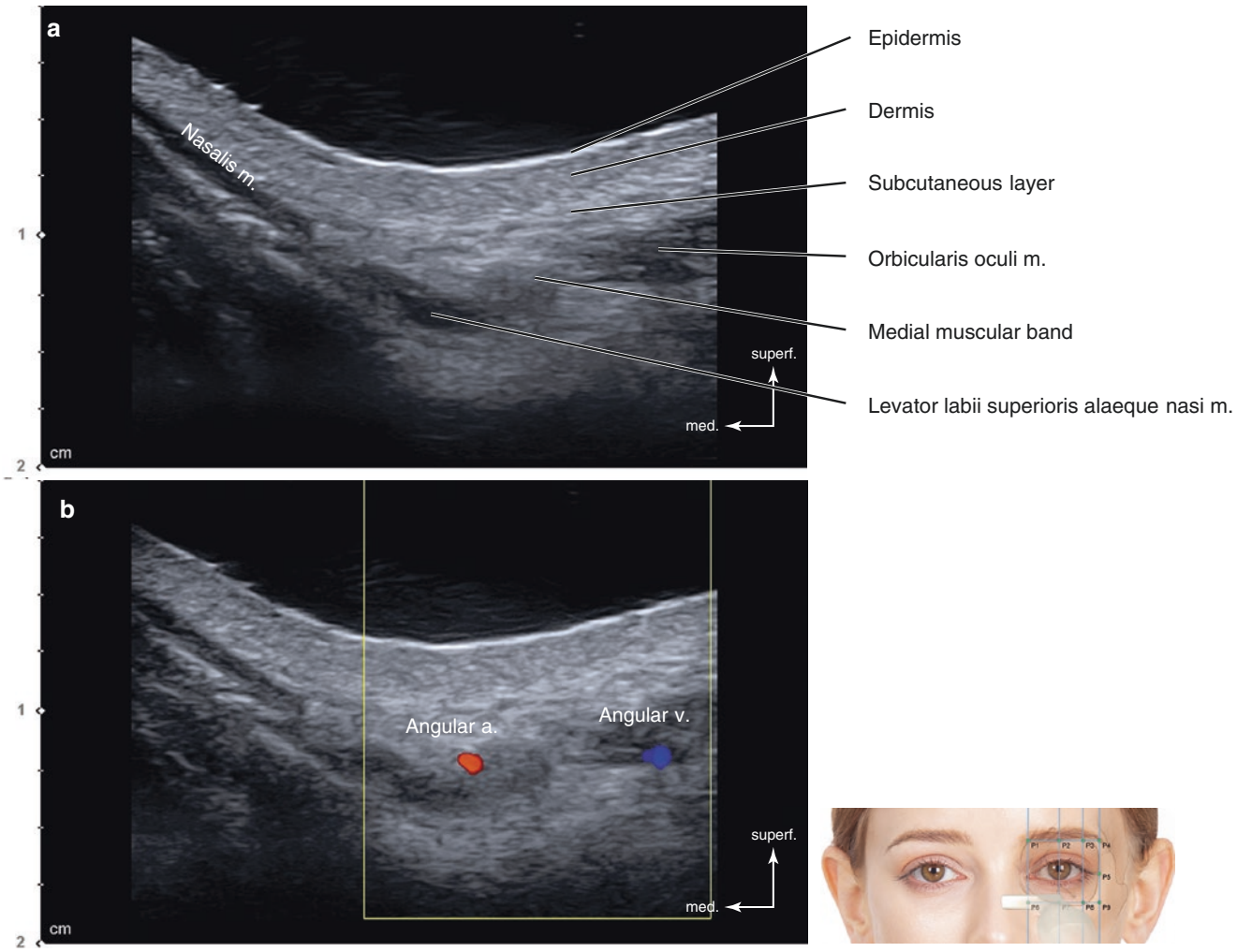

Fig. 4.16 Ultrasonography on the intersection point of TL3 and PL1 (P6). (**a**) B mode (transverse view, 15 MHz by linear transducer), (**b**) Doppler mode (transverse view, 15 MHz by linear transducer), (**c**) B mode (sagittal view, 15 MHz by linear transducer), and (**d**) Doppler mode (sagittal view, 15 MHz by linear transducer). (Published with kind permission of © Hee-Jin Kim 2020. All Rights Reserved)

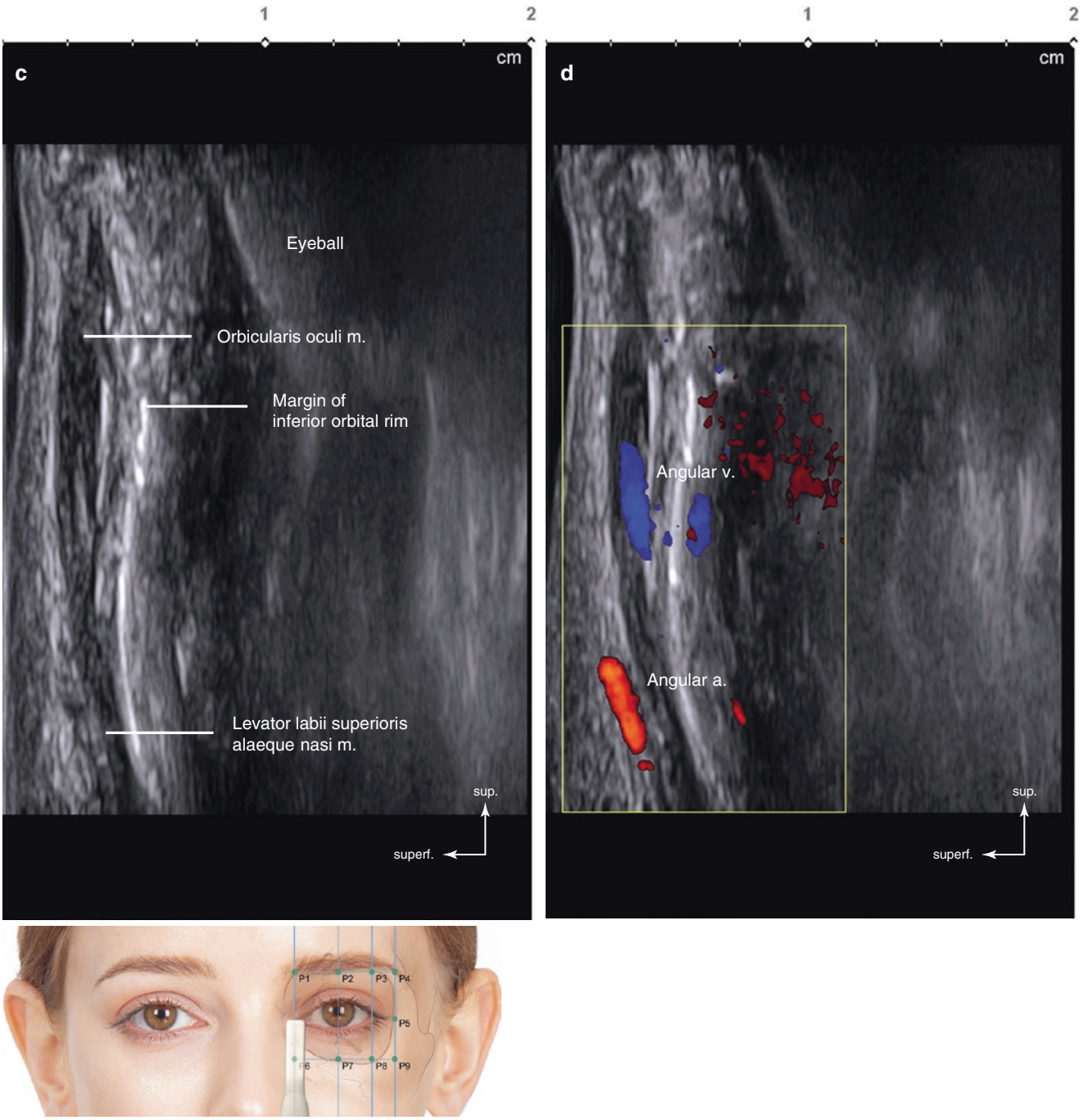

Fig. 4.16 (continued)

status. The orbital septum is hardly observable, which lies underneath the OOc m. The medial part of the LLS m. is located 5 mm (medial) to 10 mm (lateral) below the inferior orbital rim as hypoechoic images. In the Doppler mode images, the facial v. is observed superficial to the LLS m. (Fig. 4.17).

P8: Intersection Point of TL3 and PL3

The P8 is the intersection point of TL3 and PL3. The P8 has thicker orbital portion of the OOc m. compared to P6 and P7. Also, P8 has relatively thicker skin and subcutaneous fat layer. The OOc m. is identified as a hypoechoic image and SOOF locates beneath the muscle, which is shown as a hyperechoic line (Fig. 4.18).

P9: Intersection Point of TL3 and PL4

The P9 is the intersection point of TL3 and PL4. The inferior and lateral border of the orbital portion of the OOc m. is well identified as a hypoechoic image. At this point, the subcutaneous fat is thicker than other facial parts. The OOc m. fibers inserting into the dermis are observed as hyperechoic lines. The lateral portion of the SOOF and the origin of the zygomaticus minor m. are shown deep to the OOc m. (Fig. 4.19).

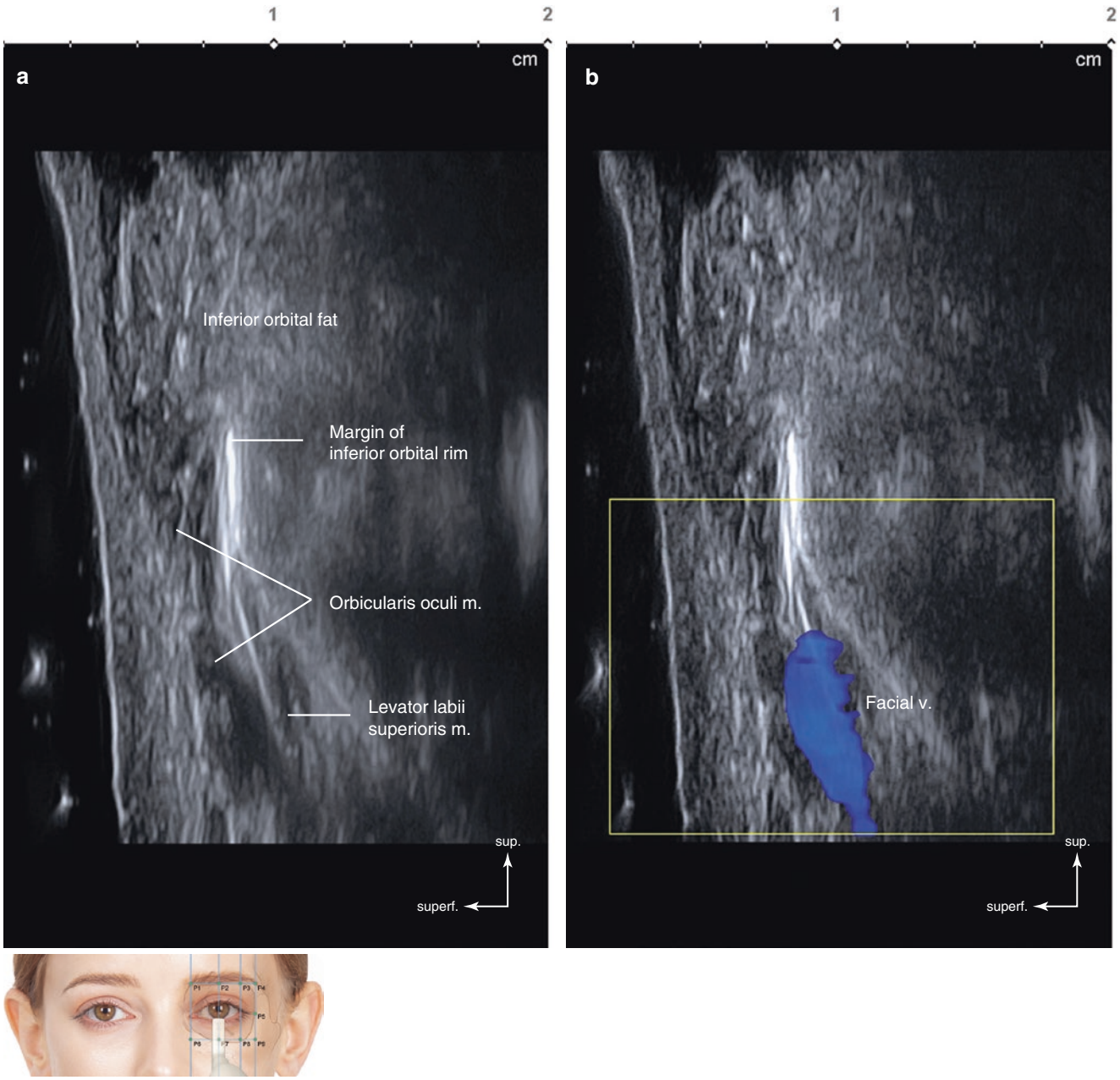

Fig. 4.17 Ultrasonography on the intersection point of TL3 and PL2 (P7). (**a**) B mode (sagittal view, 15 MHz by linear transducer) and (**b**) Doppler mode (sagittal view, 15 MHz by linear transducer). (Published with kind permission of © Hee-Jin Kim 2020. All Rights Reserved)

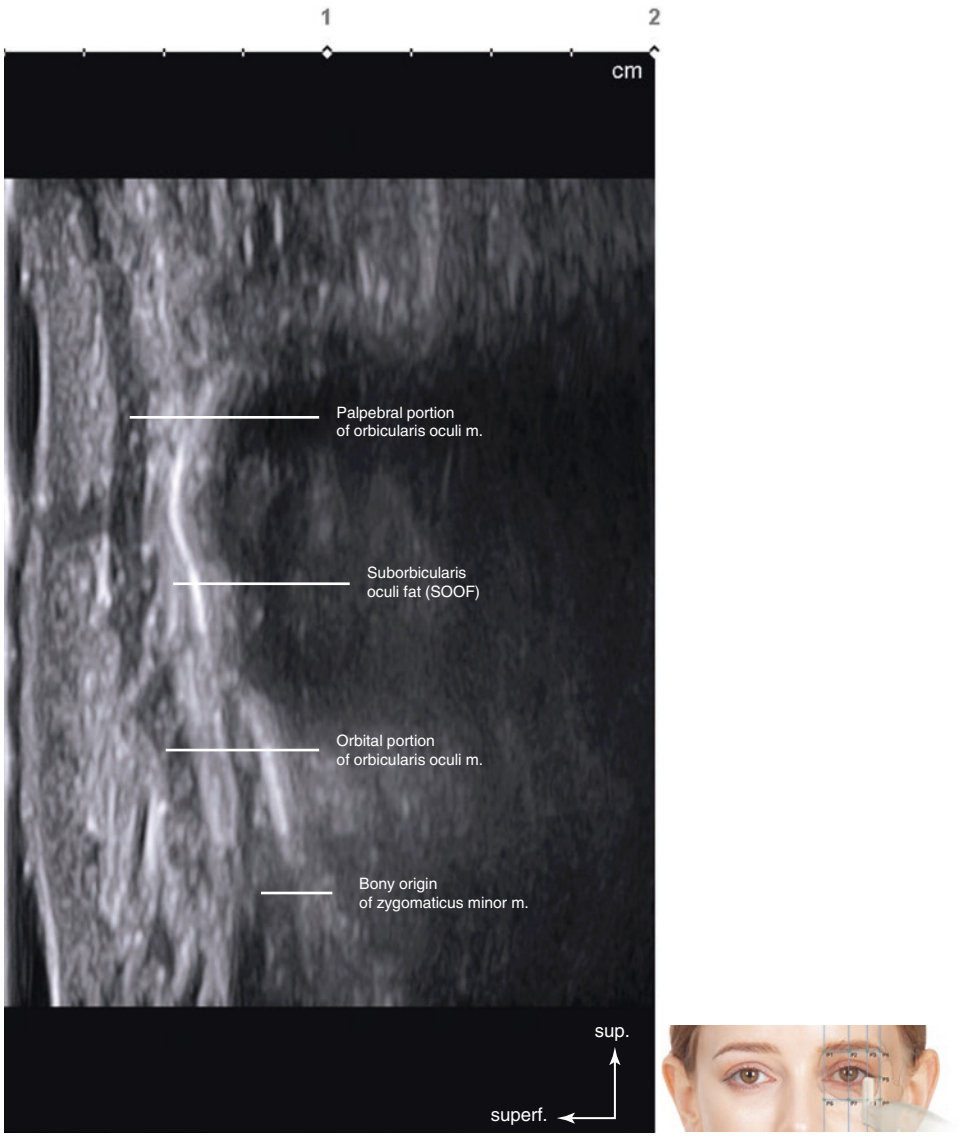

Fig. 4.18 Ultrasonography on the intersection point of TL3 and PL3 (P8). B mode (sagittal view, 15 MHz by linear transducer). (Published with kind permission of © Hee-Jin Kim 2020. All Rights Reserved)

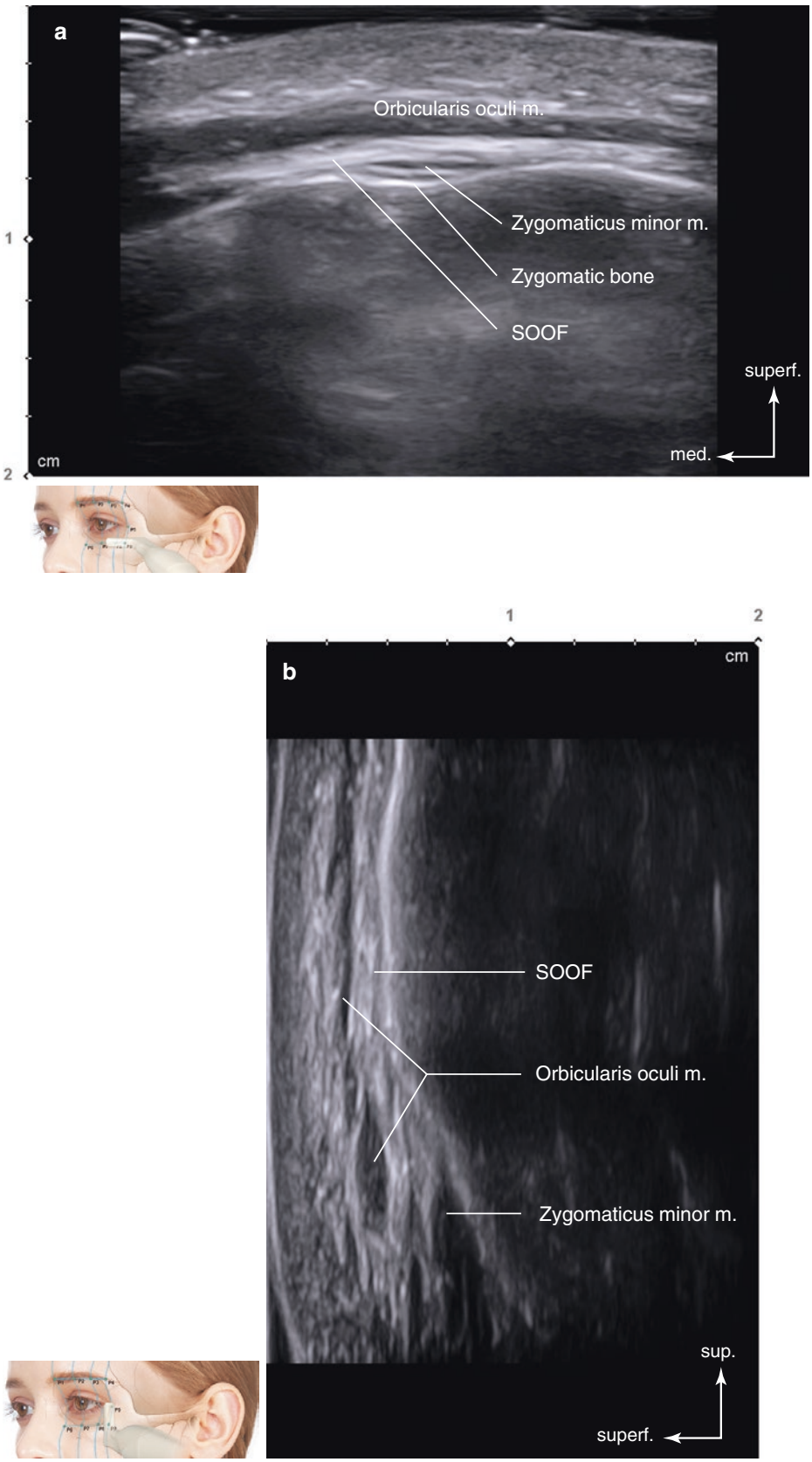

Fig. 4.19 Ultrasonography on the intersection point of TL3 and PL4 (P9). (**a**) B mode (transverse view, 15 MHz by linear transducer) and (**b**) B mode (sagittal view, 15 MHz by linear transducer). (Published with kind permission of © Hee-Jin Kim 2020. All Rights Reserved)

Bibliography

1. Chung MS, Kim HJ, Kang HS, Chung IH. Locational relationship of the supraorbital notch or foramen and infraorbital and mental foramina in Koreans. Acta Anat. 1995;154:162–6.
2. Choi DY, Kim JS, Youn KH, Hur MS, Kim JS, Hu KS, Kim HJ. Clinical anatomic considerations of the zygomaticus minor muscle based on the morphology and insertion pattern. Dermatol Surg. 2014;40(8):858–63.
3. Choi YJ, Won SY, Lee JG, Hu KS, Kim ST, Tansatit T, Kim HJ. Characterizing the lateral border of the frontalis for safe and effective injection of botulinum toxin. Aesthet Surg J. 2016;36(3):344–8.
4. Hur MS, Hu KS, Park JT, Youn KH, Kim HJ. New anatomical insight of the levator labii superioris alaeque nasi and the transverse part of the nasalis. Surg Radiol Anat. 2010;32(8):753–6.
5. Hur MS, Youn KH, Hu KS, Song WC, Koh KS, Fontaine C, Kim HJ. New anatomic considerations on the levator labii superioris related with the nasal Ala. J Craniofac Surg. 2010;21(1):258–60.
6. Kang HJ, Yoon KH, Hur MS, Kim YH, Kwak HH, Park JT, Hu KS, Kim HJ. Morphological patterns of the zygomaticus minor and its relationship with the orbicularis oculi muscle. In: 27th Annual Meeting of the American Association of Clinical Anatomists & International Society for Plastination. 19–24 July, 2010, Hawaii, USA; 2010. p. 125.
7. Kim HJ, Yoon KH, Hur MS, Kim YH, Kwak HH, Park JT, Hu KS, Kim HJ. Positional relationship between the orbital rim and orbicularis oculi muscle. In: 27th Annual Meeting of the American Association of Clinical Anatomists & International Society for Plastination. 19–24 July, 2010, Hawaii, USA; 2010. p. 127.
8. Lee HJ, Choi KS, Won SY, Apinuntrum P, Hu KS, Kim ST, Tansatit T, Kim HJ. Topographic relationship between the supratrochlear nerve and corrugator supercilii muscle for the botulinum toxin injections in chronic migraine. Toxins. 2015;7:2629–38.
9. Lee JY, Kim JN, Kim SH, Choi HG, Hu KS, Kim HJ, Song WC, Koh KS. Anatomical verification and designation of the superficial layer of the temporalis muscle. Clin Anat. 2012;25(2):176–81.
10. Lee KL, Choi YJ, Gil YC, Hu KS, Tansatit T, Kim HJ. Locational relationship between the lateral border of the frontalis muscle and the superior temporal line. Plast Reconstr Surg. 2019;143:293e–8e.
11. Park JT, Yoon KH, Kim YH, Kwak HH, Hu KS, Kim HJ. An anatomic study of lateral muscular band of orbicularis oculi muscle. In: 27th Annual Meeting of the American Association of Clinical Anatomists & International Society for Plastination. 19–24 July, 2010, Hawaii, USA; 2010. p. 148.
12. Park JT, Youn KH, Hu KS, Kim HJ. Medial muscular band of the orbicularis oculi muscle. J Craniofac Surg. 2012;23(1):195–7.
13. Park JT, Youn KH, Hur MS, Hu KS, Kim HJ. Malaris muscle, the lateral muscular band of orbicularis oculi muscle. J Craniofac Surg. 2011;22(2):659–62.
14. Park JT, Youn KH, Lee JG, Hu KS, Kim HJ. An anatomical study of the medial muscular band of the orbicularis oculi muscle. In: 11th Congress of European Association of Clinical Anatomy. 29 June to 1 July, 2011, Padova, Italia; 2011. p. 82.
15. Yang HM, Kim HJ. Anatomical study of the corrugator supercilii muscle and its clinical implication with Botulinum toxin A injection. Surg Radiol Anat. 2013;35:817–21.
16. Youn KH, Park JT, Park DS, Koh KS, Kim HJ, Paik DJ. Morphology of the zygomaticus minor and its relationship with the orbicularis oculi muscle. J Craniofac Surg. 2012;23(2):546–8.
17. Cong LY, Phothong W, Lee SH, Wanitphakdeedecha R, Koh IS, Tansatit T, Kim HJ. Topographic analysis of the supratrochlear artery and the supraorbital artery: implication for improving the safety of forehead augmentation. Plast Reconstr Surg. 2017;139:620e.
18. Cong LY, Choi YJ, Hu KS, Tansatit T, Kim HJ. Three-dimensional topography of the emerging point of the ophthalmic artery. Plast Reconstr Surg. 2019;143:32e–8e.
19. Kim YS, Choi DY, Gil YC, Hu KS, Tansatit T, Kim HJ. The anatomical origin and course of the angular artery regarding its clinical implications. Dermatol Surg. 2014;40(10):1070–6.

US Anatomy of the Midface and Nose

5

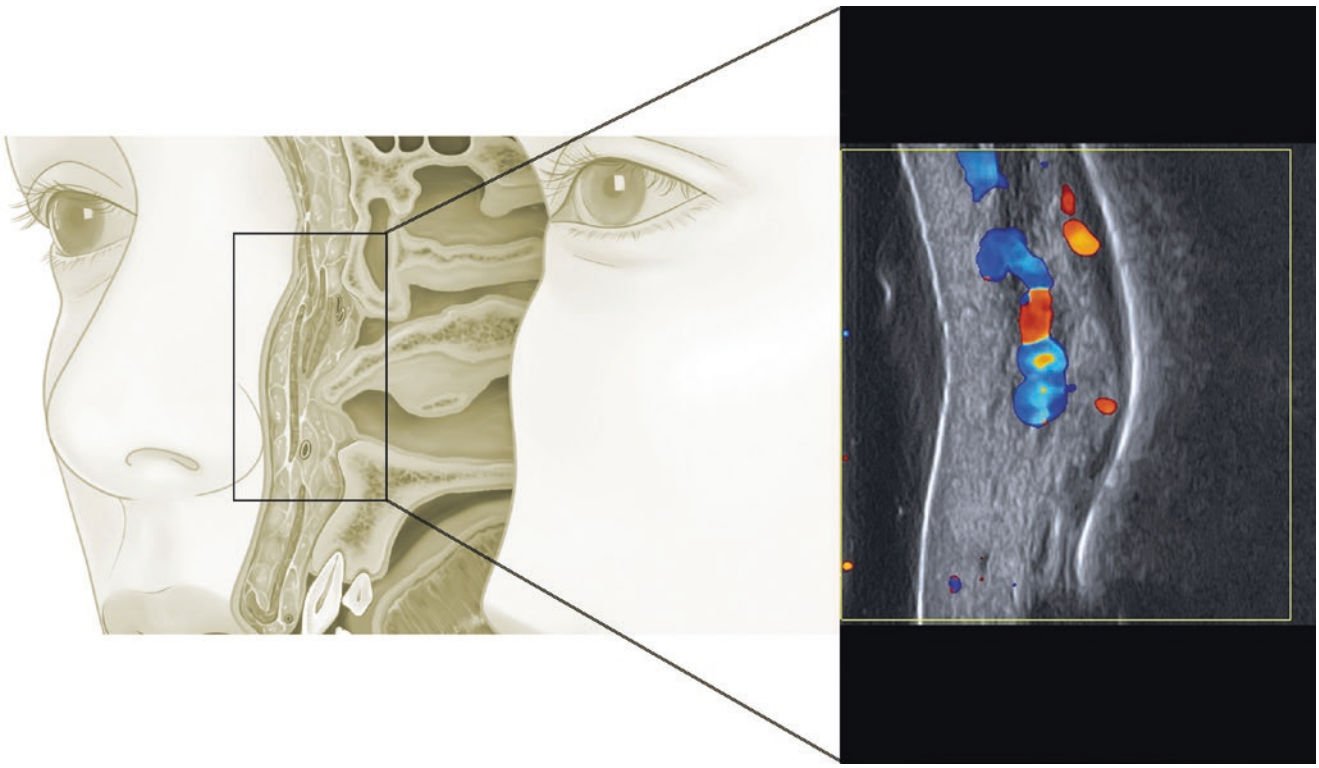

H.-J. Kim et al., *Ultrasonographic Anatomy of the Face and Neck for Minimally Invasive Procedures*,
https://doi.org/10.1007/978-981-15-6560-1_5

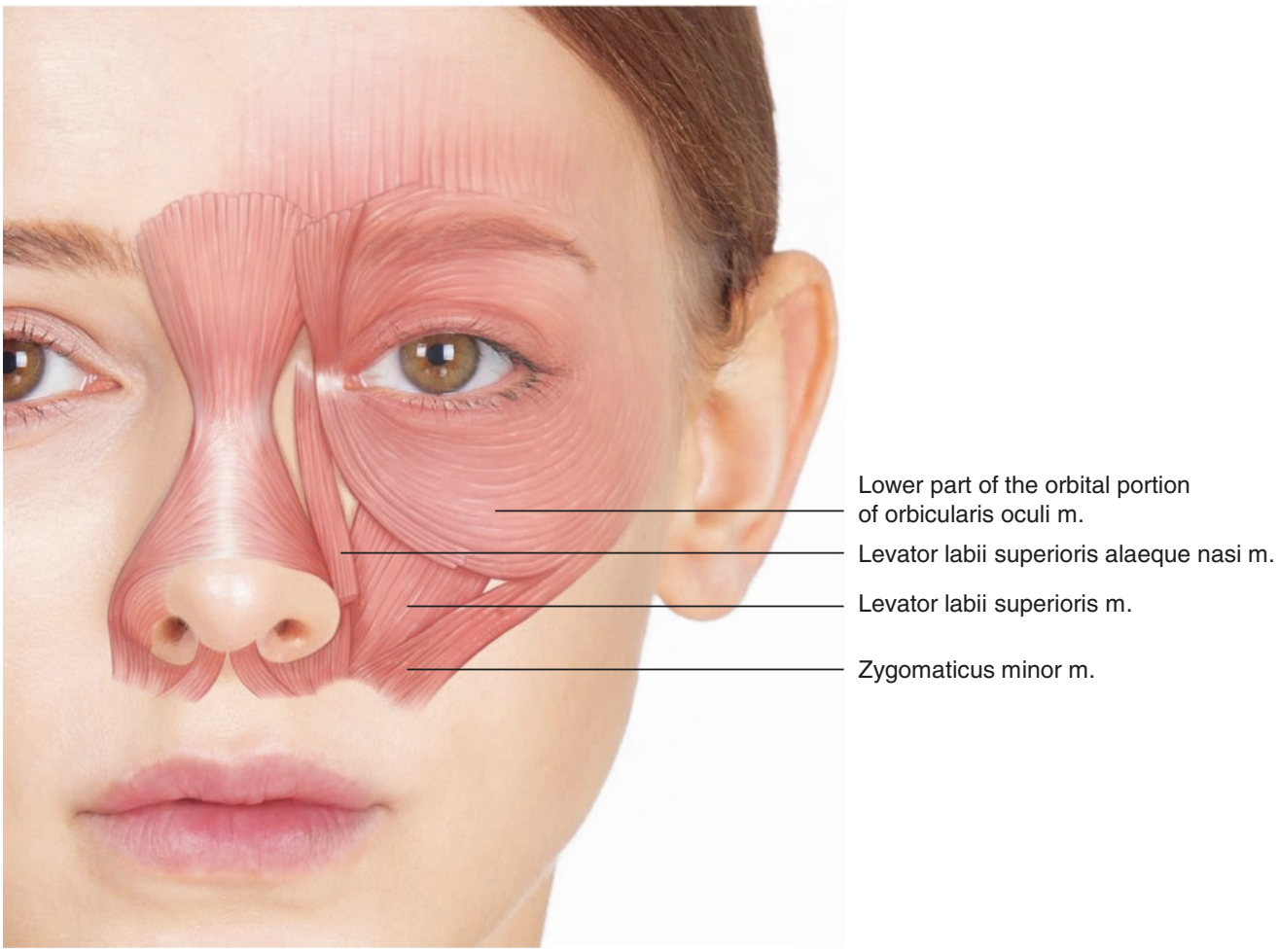

Fig. 5.1 Illustration of the midfacial musculature. (Published with kind permission of © Kwan-Hyun Youn 2020. All Rights Reserved)

5.1 Clinical Anatomy of the Midface and Nose Region

The midface includes the area of nose and cheek covering the middle third of the face. The upper border of the midface extends from the inferior orbital rim to the upper zygomatic arch. The midface is occupied by the maxilla, zygomatic bone, and a large amount of superficial malar fat. These convex structures contribute to making one look younger. However, the aging of the midface is noticeable by decreased fat volume and sagged soft tissue.

There are five major facial muscles located in the midface: zygomaticus minor (Zmi), zygomaticus major (ZMj), levator labii superioris (LLS), levator labii superioris alaeque nasi (LLSAN), and the lower part of the orbital portion of orbicularis oculi (OOc) mm. (Fig. 5.1). These muscles are involved in major facial expressions. The wrinkles and furrows appear as aging process and are aggravated by repeated movements of the muscles.

The LLSAN, LLS, and zygomaticus minor mm. are the upper lip elevators. These muscles act in elevating upper lips, which plays a role in making facial expressions of joy and sadness. The muscles can be subdivided into two layers: superficial and deep. The Zmi and LLSAN mm. are located in the superficial layer while LLS m. is located in the deep layer. These muscles are located on the lateral side of the nose ala and insert into the orbicularis oris (OOr) m. These muscles contribute to form the nasolabial fold (Fig. 5.2).

The region around the tear trough and extended nasojugal groove comprises well-developed blood vessels such as the inferior palpebral and angular vv. These veins are located superficial to the periosteum, deep to the OOc m. These veins run near the orbit and deep to the muscular structure. The angular a. detours the anterior zygomatic region and follows the inferomedial border of the OOc m. In other words, the angular a. generally runs along the nasojugal groove and runs medially to the infraorbital area. Finally, the artery emerges superficially as it reaches the tear trough (Fig. 5.3).

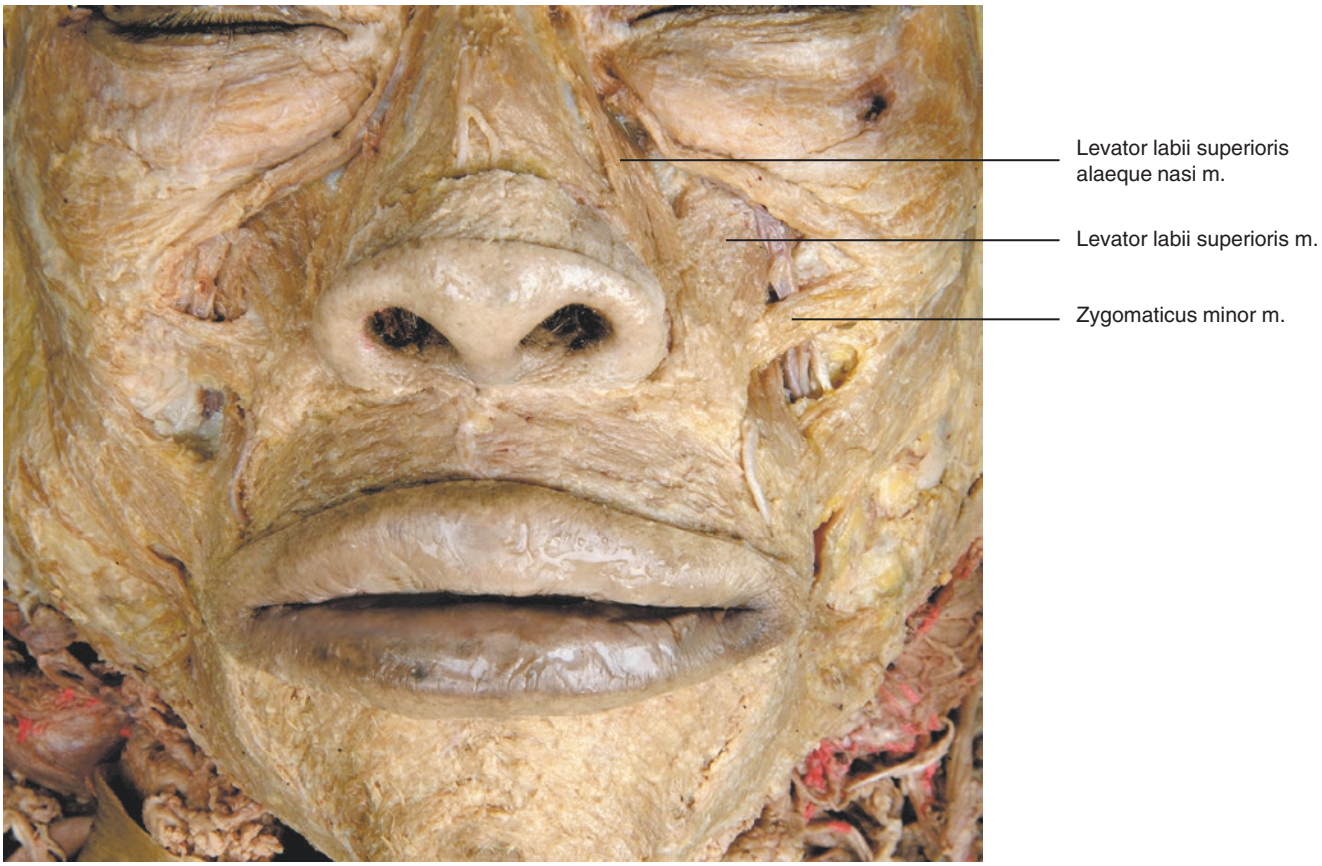

Fig. 5.2 Major upper lip elevators. This muscle group includes the levator labii superioris alaeque nasi, levator labii superioris, and zygomaticus minor muscles. (Published with kind permission of © Hee-Jin Kim 2020. All Rights Reserved)

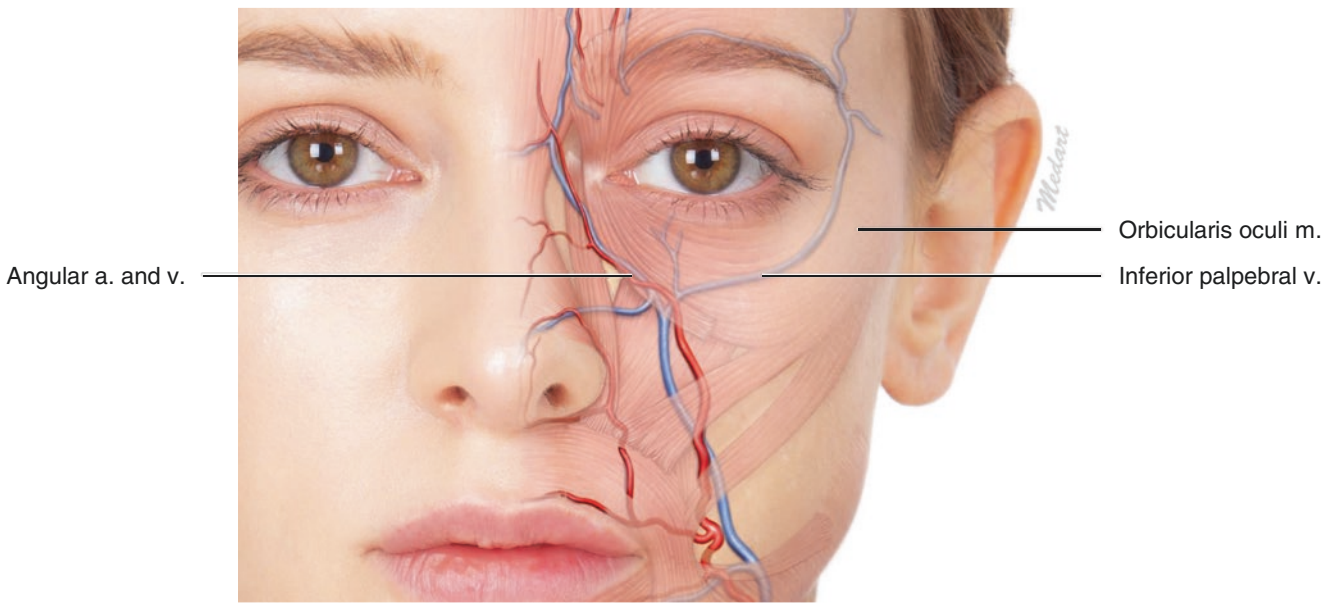

Fig. 5.3 Illustration representing the midfacial vasculature. (Published with kind permission of © Kwan-Hyun Youn 2020. All Rights Reserved)

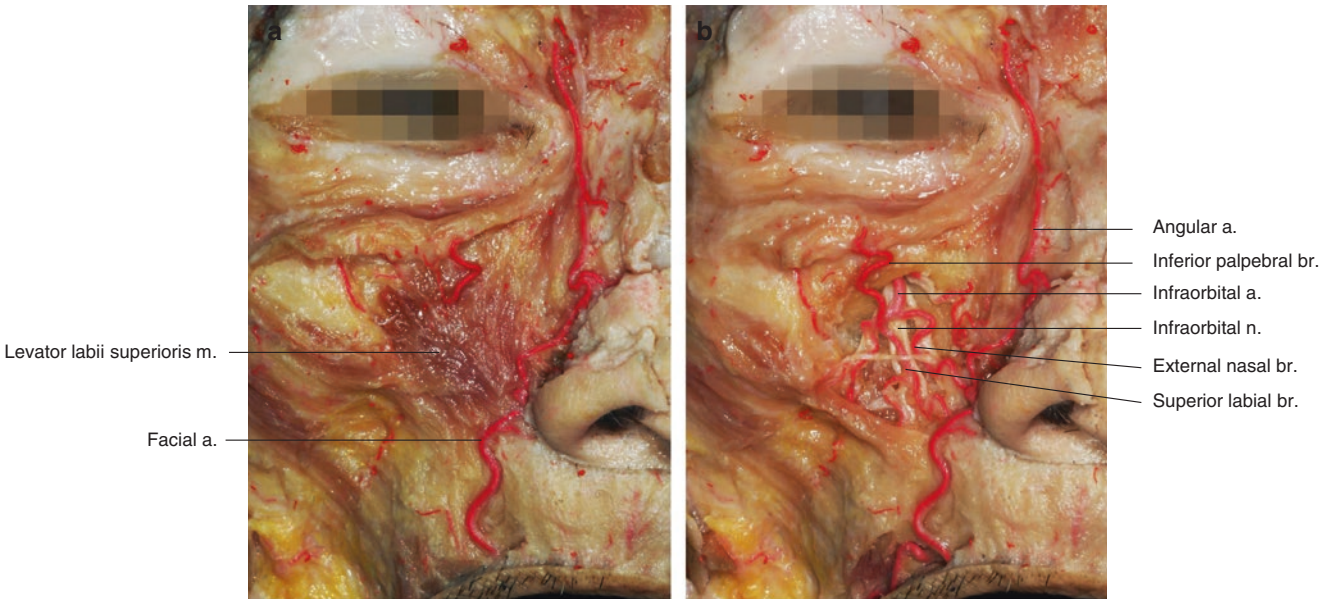

Fig. 5.4 Distribution pattern of the infraorbital arterial branch. (**a**) The palpebral branches of the infraorbital artery penetrate the levator labii superioris and enter the lower eyelid area, and (**b**) the labial and nasal branches of the infraorbital artery enter the superior labial and lateral alar regions, respectively. (Published with kind permission of © Hee-Jin Kim 2020. All Rights Reserved)

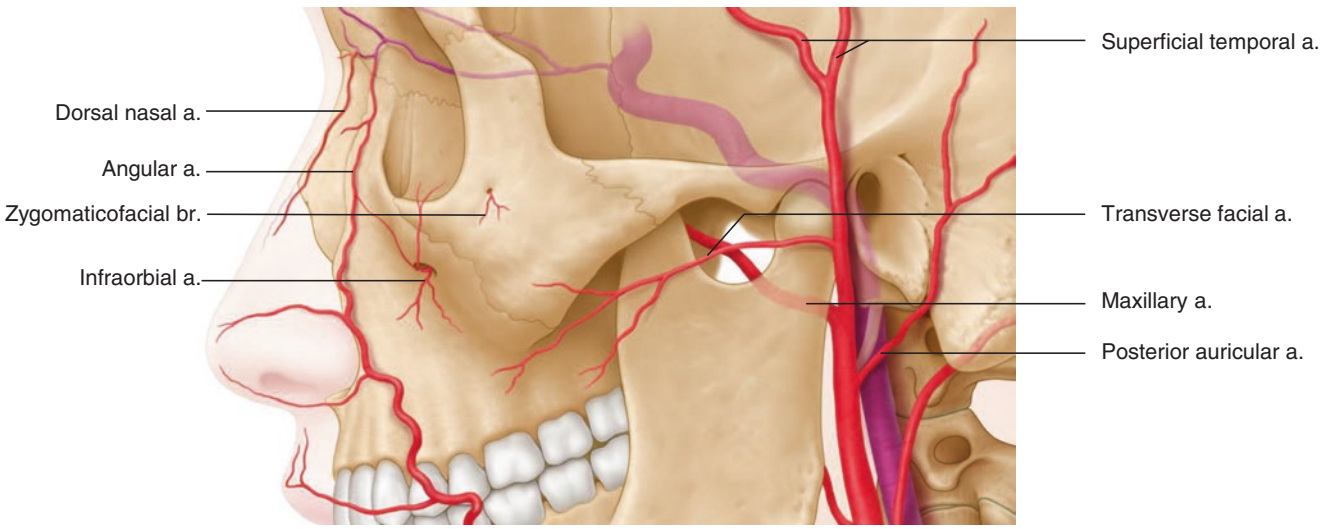

Fig. 5.5 Illustration of the vasculature of the zygomatic and temporal region. (Published with kind permission of © Kwan-Hyun Youn 2020. All Rights Reserved)

The infraorbital space is located beneath the LLS m. The infraorbital space is bounded by the origin of the LLS m., inferior border at the OOr m., medial border at the LLSAN m., and lateral border at the levator angular oris (LAO) m. The infraorbital vessels and nerves run through the infraorbital space surrounded by the deep medial cheek fat. The infraorbital artery (IOA) leaves the infraorbital foramen and divides into the inferior palpebral the lateral nasal and the superior labial branches. The IOA locates superficially to the infraorbital n. (in 73.8%), and these IOA branches run superficially and some anastomoses with the facial a. (Fig. 5.4).

The zygomatic a. divides into two branches: zygomaticofacial and zygomaticotemporal branches. These arteries emerge from the zygomaticofacial and zygomaticotemporal foramina located on the lateral and medial aspects of the zygomatic bone, respectively. The zygomaticofacial branch supplies the zygomatic region and the cutaneous layer of the cheek while the zygomaticotemporal branch supplies the cutaneous layer of the anterior and superficial temporal region (Fig. 5.5).

The infraorbital n. (ION) is a major cutaneous nerve providing a general sensation of the midface, infraorbital region, and part of the nose and upper lip. The ION is subdivided into five different nerves: inferior palpebral n. which

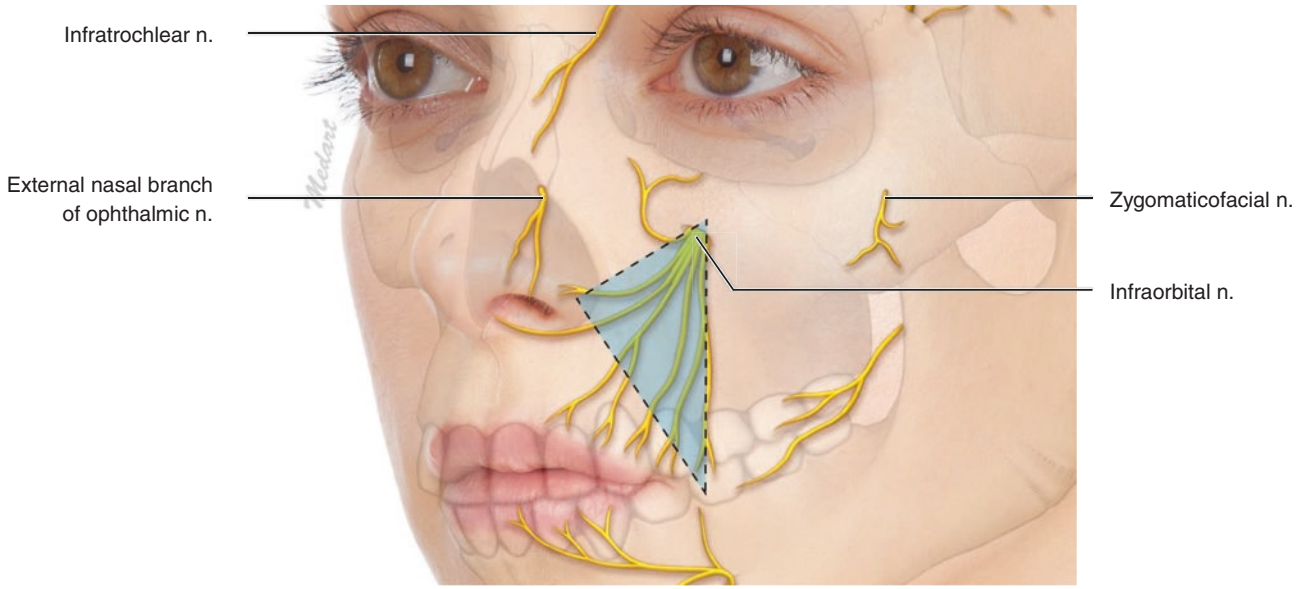

Fig. 5.6 Illustration of the sensory distribution of the midface and nose. (Blue dotted area: infraorbital triangle) (Published with kind permission of © Kwan-Hyun Youn 2020. All Rights Reserved)

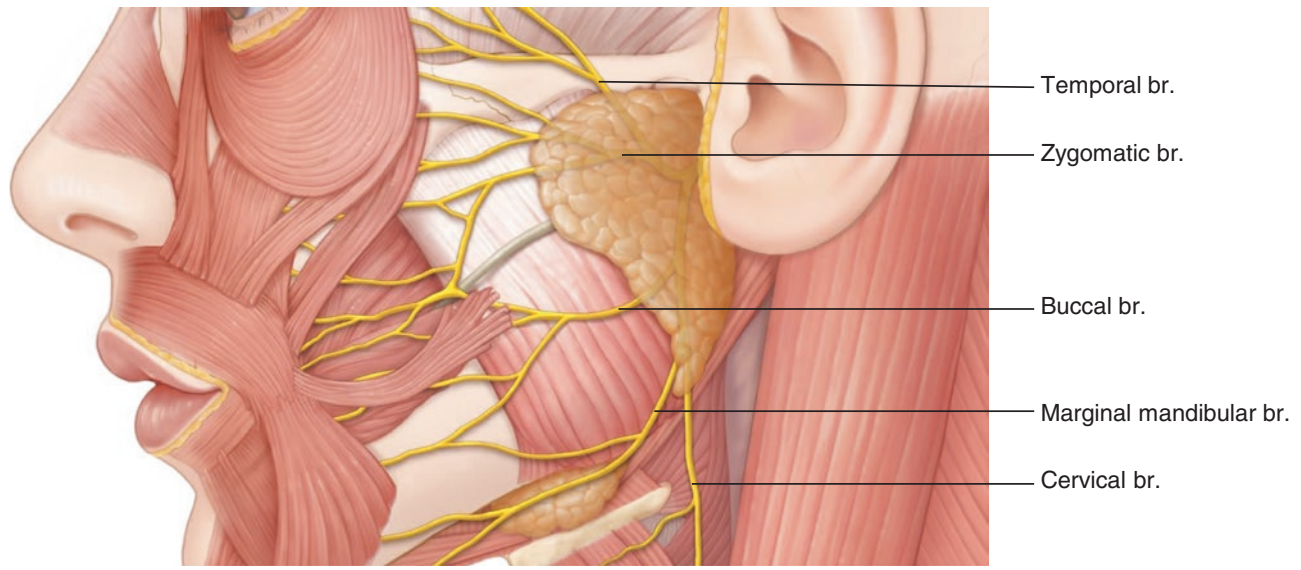

Fig. 5.7 Illustration of the motor distribution of the midface and nose. (Published with kind permission of © Kwan-Hyun Youn 2020. All Rights Reserved)

innervates the lower eyelid in a fan-shaped area; external nasal n. which innervates the nose ala; internal nasal n. which innervates the philtrum including the septal area; and medial and lateral superior labial nn. which supply the superior labial area ranging from the midline to the mouth corner.

The infraorbital triangle is bordered by the infraorbital foramen, the most lateral point of the nose ala, and the mouth corner. Mostly, the superior labial n. innervates the area of infraorbital triangle (Fig. 5.6). The external nose is innervated by the infraorbital n. with the exception of some areas that are innervated by the external nasal branch of the nasociliary n. (branch from the ophthalmic n.).

The buccal branch of the facial n. runs medially, and some branches spread to the cheek. These branches overlay with the superior labial branch of the ION. The buccal branch of the facial n. innervates the upper 3/4 of the infraorbital region. The buccal branch is the main nerve that innervates LLSAN, LLS, and Zmi mm.; however, some branches run to the ZMj, risorius, and the superior portion of the OOr mm. (Fig. 5.7).

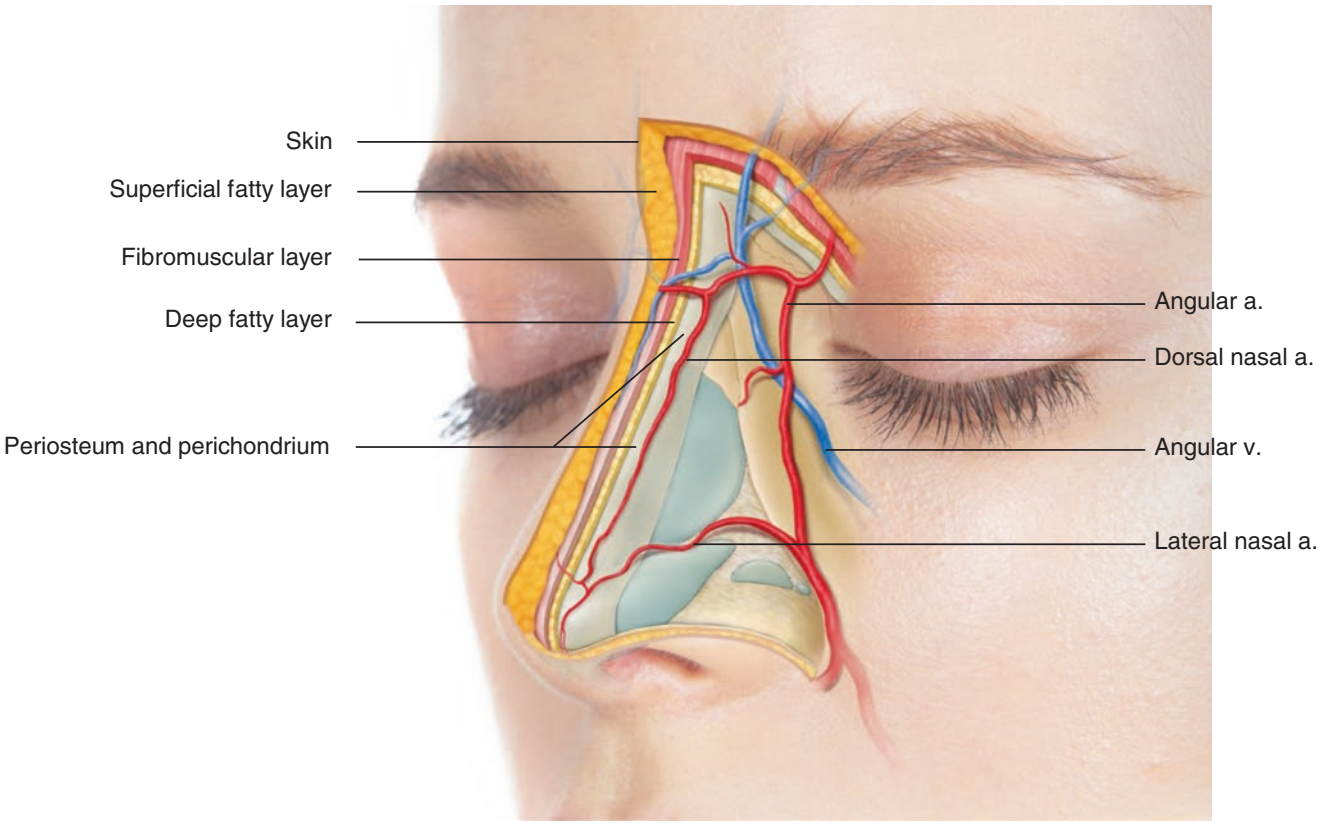

Fig. 5.8 Anatomical layers of the nose. (Published with kind permission of © Kwan-Hyun Youn 2020. All Rights Reserved)

The nose is a complex structure with different features by its locations. They have different thicknesses of the skin and subcutaneous tissue, and the components of anatomical structures vary within their location. Generally, the nose consists of five layers: the skin, superficial fatty layer, fibromuscular layer, deep fatty layer, and periosteum (or perichondrium). The fibromuscular layer lies between the superficial and deep fatty layers. This fibromuscular layer is in the same layer as the SMAS located in the lateral face (Fig. 5.8). The muscles surrounding the nose are the nasalis, depressor septi nasi, procerus mm., and other muscles that attach to the nostrils.

The procerus m. is a pyramidal-shaped muscle. The muscle originates from the nasal bone and the lateral nasal cartilage and inserts to the skin of the radix and glabella. The procerus m. is intertwined with the frontalis m. fiber area around its insertion. The nasalis m. can be divided into two parts: the transverse (compressor) and the alar (dilator). The transverse part is a triangular-shaped muscle that originates from the canine fossa of the maxilla and inserts into the lateral nasal cartilage. The alar part is a small square-shaped muscle that originates from the maxilla at the lateral incisor region and inserts into the lower part of the alar cartilage (Fig. 5.9).

The depressor septi nasi m. is located in the deep part of the midline of the lips. The muscle originates from the incisive fossa of the maxilla and insert to the movable part of the nasal septum. The muscle acts to pull down the tip of the nose and flare nostrils. Furthermore, the nose ala is known for its insertion site for the LLSAN (100%) m., the LLS (90%) m., and the partial muscle fibers of the Zmi (28%) m. (Figs. 5.1 and 5.9).

The lateral nasal and dorsal nasal aa. are the two arteries that supply the external nose. The lateral nasal a. is an artery branched from the facial a. while the dorsal nasal a. is a branch of the ophthalmic a. The columella branch, originated from the superior labial a., supplies to the columella and the tip of the nose. The inferior alar a. running below the nose is derived from the lateral nasal a. The dorsal nasal a. is a fine arterial branch that runs superficial to the fibromuscular layer of the bony nose. The artery runs inferolaterally along the dorsum of the nose. As the artery reaches the cartilaginous nose region, it runs underneath the fibromuscular layer (Fig. 5.10).

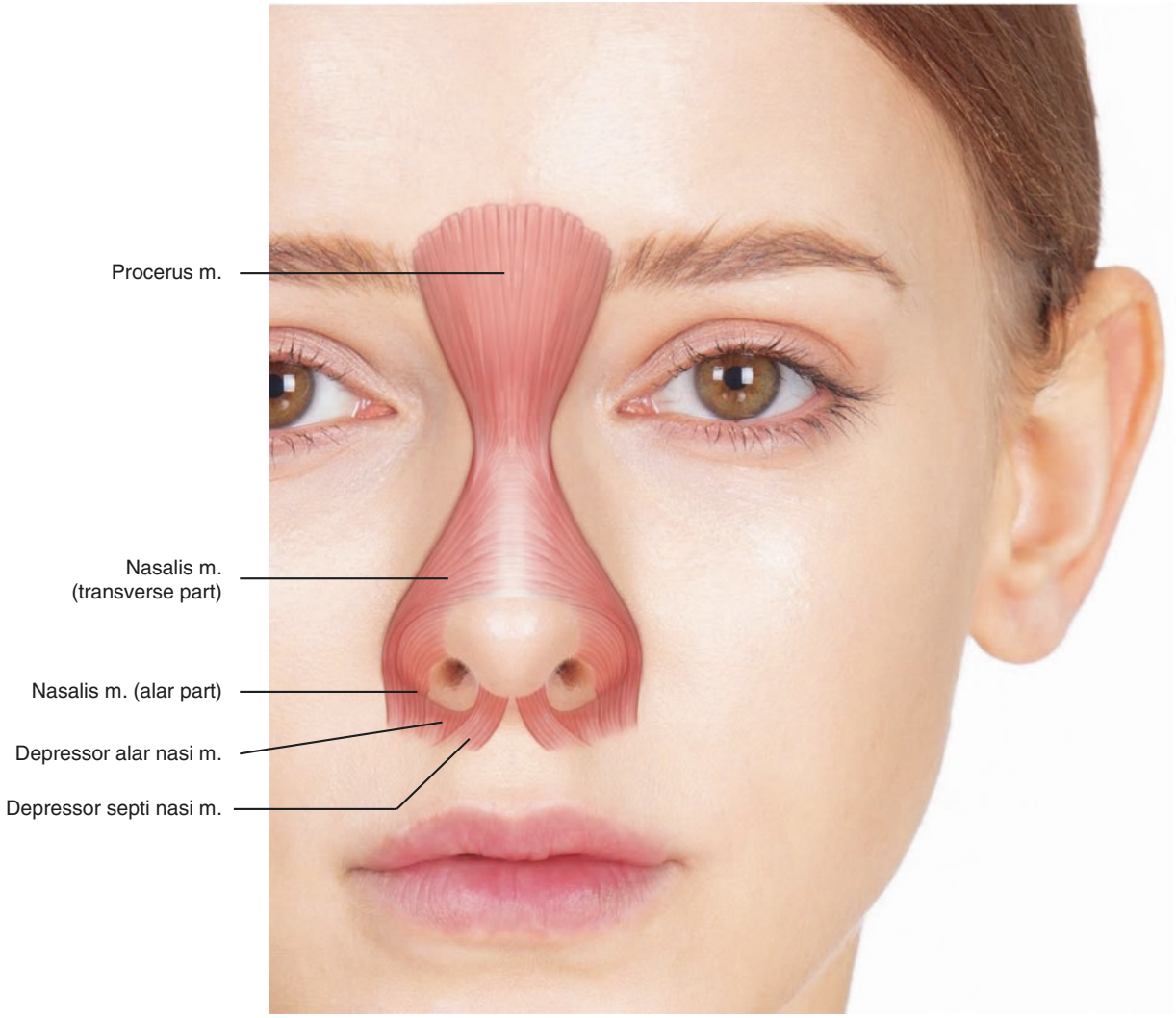

Fig. 5.9 Illustration of the nasal and perinasal musculature. (Published with kind permission of © Kwan-Hyun Youn 2020. All Rights Reserved)

5.1.1 Facial Landmarks and Reference Lines for the US Examination of the Midface and Nose Region (Fig. 5.11)

Midface and nose	
M1: intersection point of TL4 and PL1	**N1**: sellion (the deepest point on the radix)
M2: intersection point of TL4 and PL2	**N2**: rhinion (midline junction between the nasal bone and cartilage)
M3: intersection point of TL4 and PL3	**N3**: pronasale (tip of the nose)
M4: intersection point of TL4 and PL4	
M5: intersection point of TL5 and PL1	
M6: intersection point of TL5 and PL2	
M7: intersection point of TL5 and PL3	
M8: intersection point of TL5 and PL4	

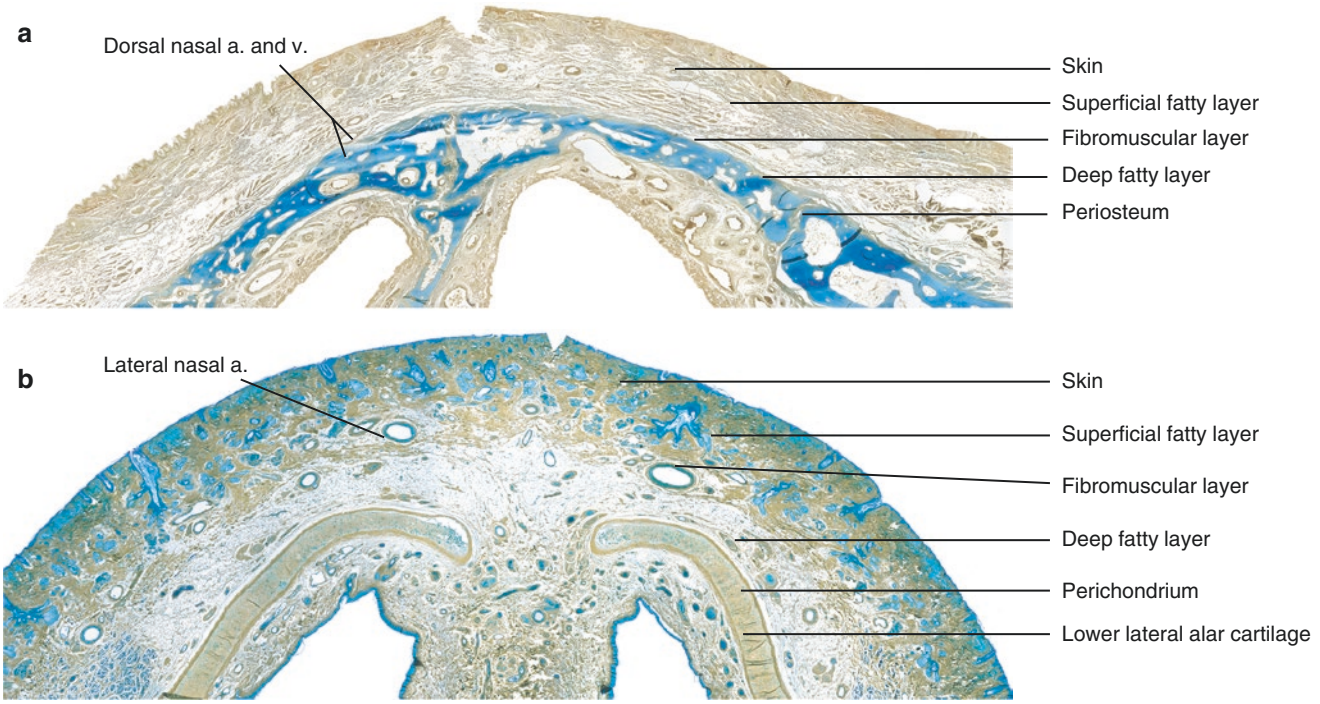

Fig. 5.10 Histological demonstrations representing the layers of the external nose. (**a**) Upper bony nose and (**b**) lower cartillagenous nose. (Published with kind permission of © Hee-Jin Kim 2020. All Rights Reserved)

5.1.2 Checklists in Midface and Nose Region

Objective structures	Facial landmarks where the structures can be observed
Orbicularis oculi m.	M2, M3, M4
Medial muscular band of orbicularis oculi m.	M1
Zygomaticus major m.	M4, M7, M8
Levator labii superioris alaeque nasi m.	M1, M5
Levator labii superioris m.	M2, M5, M6
Zygomaticus minor m.	M3, M6, M7
Procerus m.	N1
Nasalis m.	N2, M1, M5
Angular a. and v.	M1, M5
Perforators from facial a.	M4, M8
Infraorbital a. and v.	M2, M6
Lateral nasal a.	N3
Dorsal nasal a.	N1, N2
Facial v.	M2, M6
Intercanthal v.	N1
SOOF	M3, M4
Deep medial cheek fat	M5, M6
Zygomatic ligament	M4
Superficial malar fat	M3

5.2 US Images of the Midface and Nose Region

5.2.1 US Anatomy Images

The midface has a thicker epidermis and dermis than the forehead and periorbital regions. The US image shows a uniformly hyperechoic line of the epidermis and slightly hyperechoic dermis. The thickness of the skin in the midface differs by its location. The thickest skin depth is at the infraorbital region (1.97 mm) and thinnest at the radix and dorsum (1.51 mm). The skin thickness of the infraorbital region is relatively uniform, ranging from 1.82 to 1.97 mm. However, the thickness of subcutaneous fat varies markedly by differing points in this region.

The subcutaneous layer of the midface appears as an irregular hypoechoic image. Additionally, the midface subcutaneous layer was thicker than the upper region of the face. The thickness of the subcutaneous fat tends to increase from the upper to the lower area of the midface. Also, the thickness of subcutaneous fat gets thicker from the medial (2.39–6.51 mm) to the lateral area (3.47–7.84 mm). The skin thicknesses of points at the sellion and the rhinion are

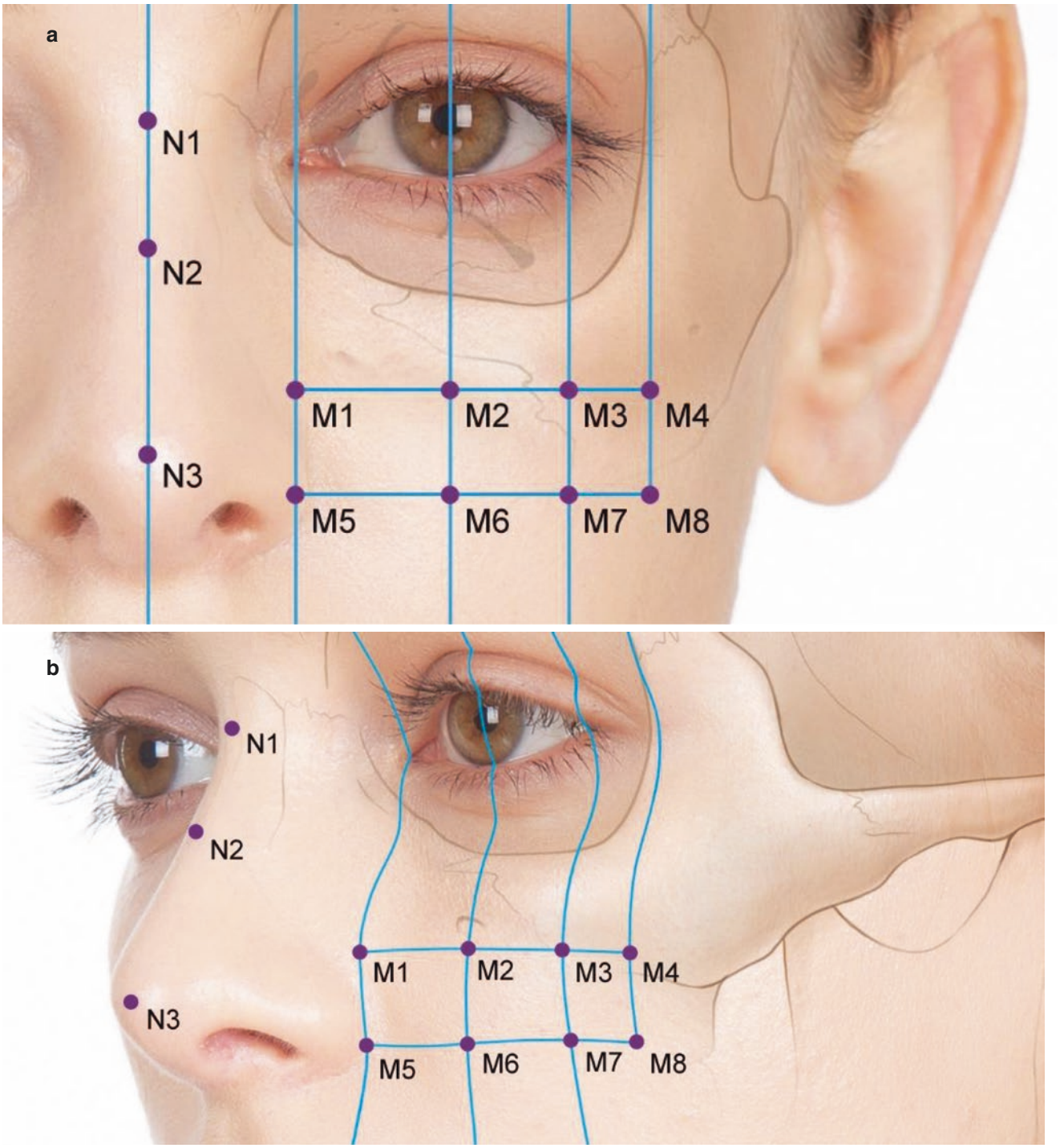

Fig. 5.11 Facial landmarks and reference lines for the ultrasonographic examination of the midface and nose. (**a**) Frontal view and (**b**) oblique view. (Published with kind permission of © Kwan-Hyun Youn 2020. All Rights Reserved)

1.36 mm and 1.42 mm, respectively. The thicknesses of subcutaneous fat at points of sellion and the rhinion are 1.61 mm and 0.85 mm, respectively.

The muscular components underneath the subcutaneous layer are shown as hypoechoic images. Few hypoechoic lines may be observed at the dermis where the cutaneous insertion locates. The hyperechoic lines presenting the true retaining ligament can be not frequently observed.

At zygomatic bone area, the inferior part of the OOc m. and the SOOF appear as slightly hyperechoic images. The SOOF is a deep fat structure located inferolateral to the inferior orbital rim, and some anechoic vascular components can be observed.

A well-defined infraorbital space can be observed in the area deep to the LLS m. and superficial to the periosteum of the anterior maxilla. Inside the infraorbital space, the deep medial cheek fat, the infraorbital vessels, and the infraorbital n. branches are observed. The deep medial cheek fat is shown as anechoic, and vessels and nerves have a honeycomb appearance (Figs. 5.12, 5.13, 5.14, 5.15, and 5.16).

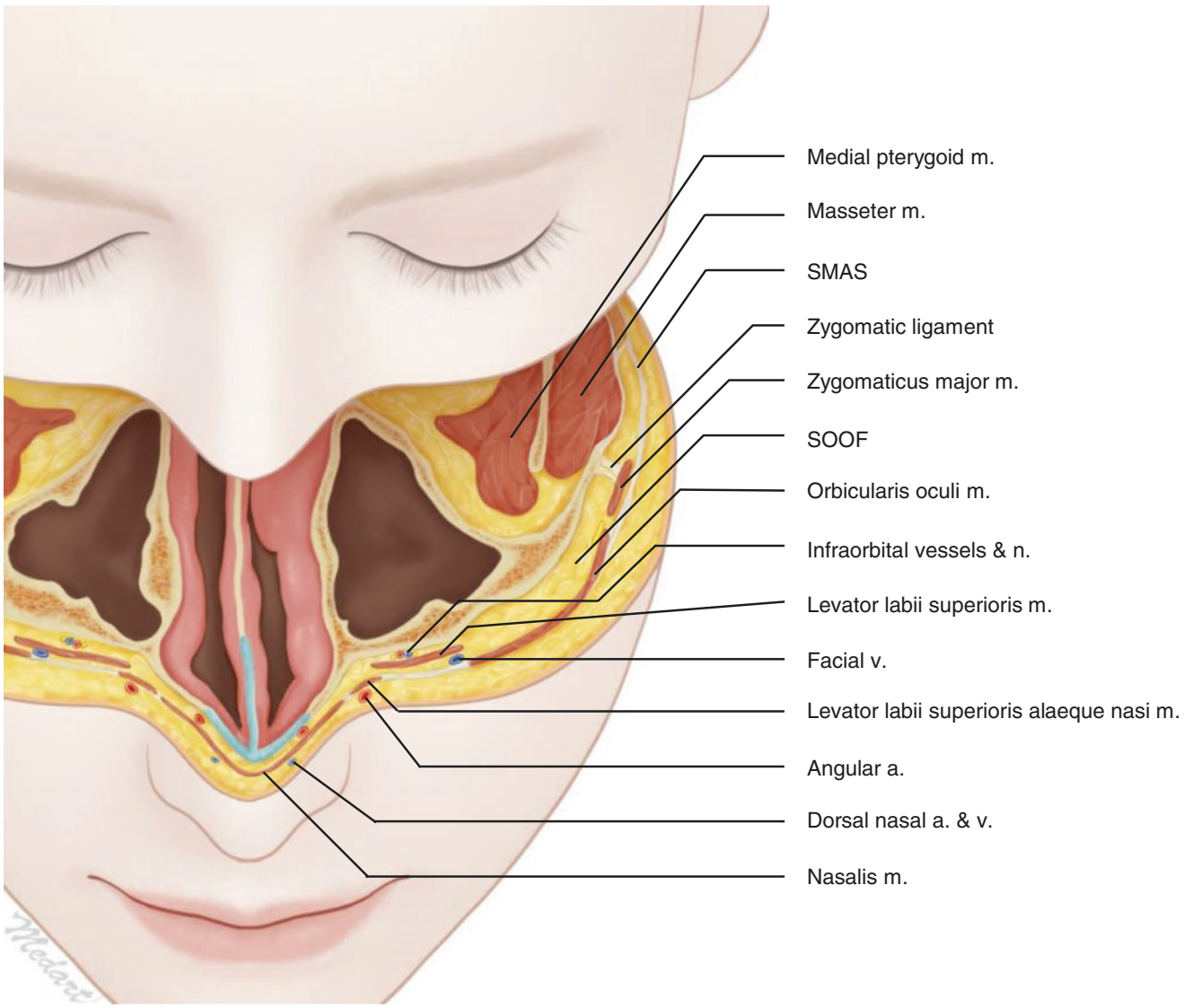

Fig. 5.12 Illustration representing the transverse section of the midface passing the TL4. (Published with kind permission of © Kwan-Hyun Youn 2020. All Rights Reserved)

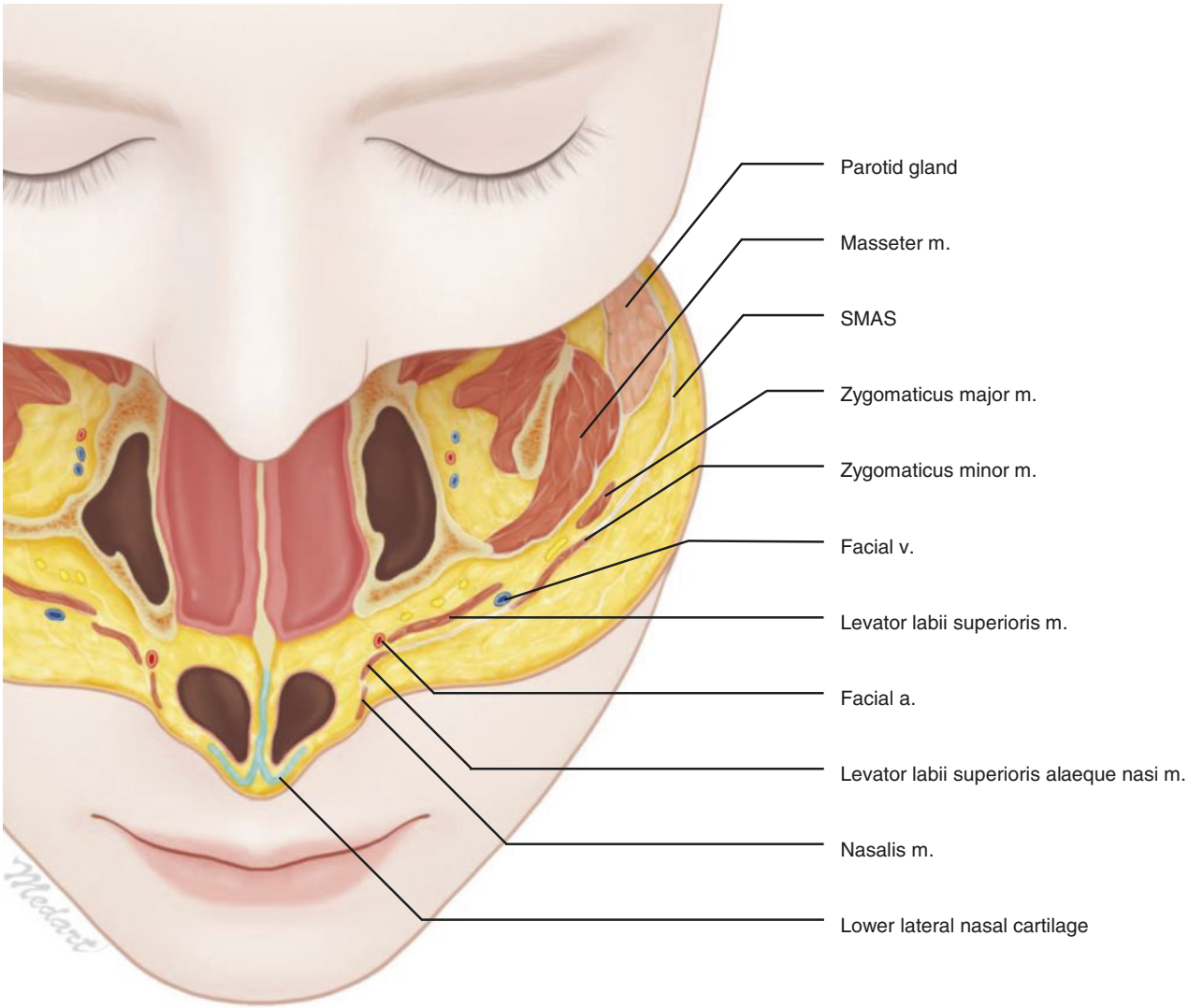

Fig. 5.13 Illustration representing the transverse section of the midface passing the TL5. (Published with kind permission of © Kwan-Hyun Youn 2020. All Rights Reserved)

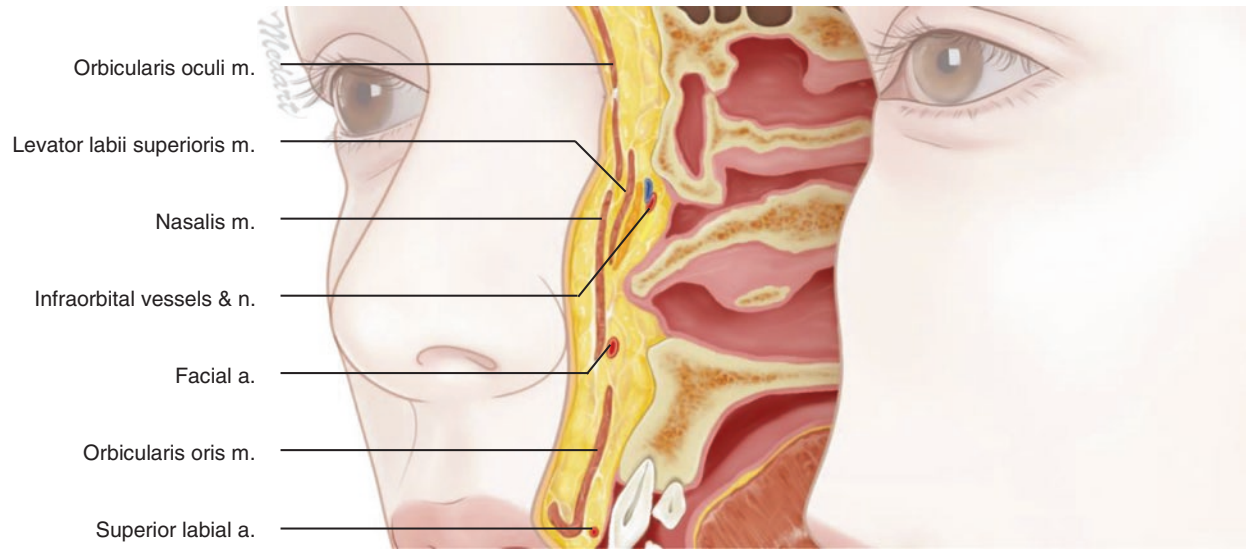

Fig. 5.14 Illustration representing the sagittal section of the midface passing the PL1 (medial canthus). (Published with kind permission of © Kwan-Hyun Youn 2020. All Rights Reserved)

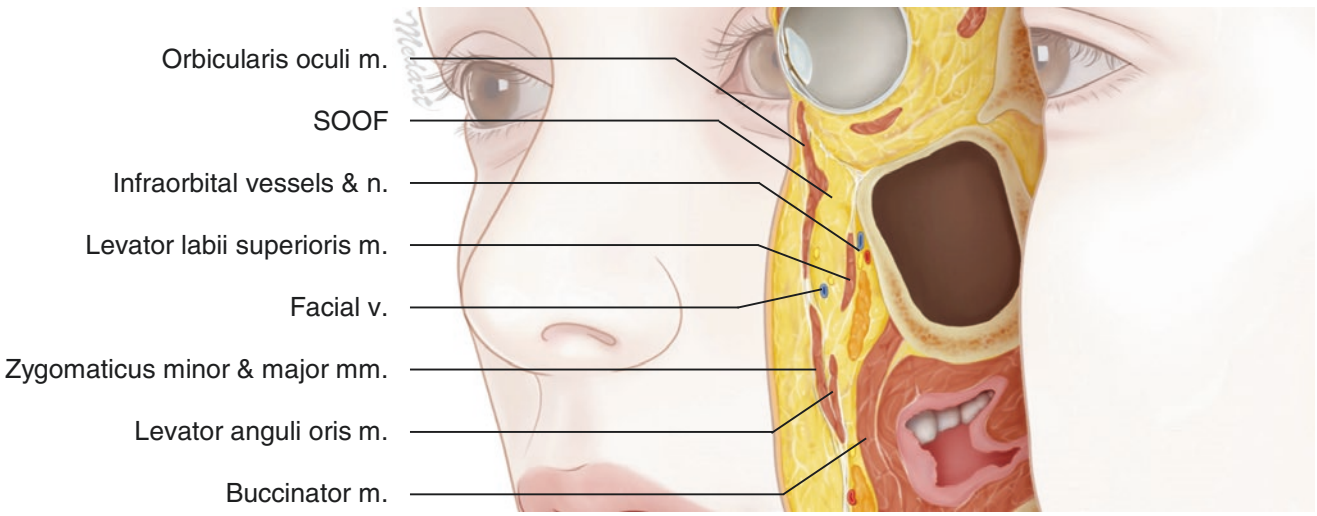

Fig. 5.15 Illustration representing the sagittal section of the midface passing the PL2 (midpupil). (Published with kind permission of © Kwan-Hyun Youn 2020. All Rights Reserved)

Fig. 5.16 Illustration representing the sagittal section of the midface passing the PL3 (lateral canthus). (Published with kind permission of © Kwan-Hyun Youn 2020. All Rights Reserved)

5.2.2 B Mode and Doppler Images

M1: Intersection Point of TL4 and PL1

At this point, the lateral side of the nose and the medial midface region is shown together when the transducer is horizontally positioned. The concave boundary between the nose and midface is shown in the middle of the image. The image shows dense connective tissue where thickened hyperechoic structure is seen beneath the hyperechoic band of the epidermis. Observing from the medial to lateral aspect, a hypoechoic upper lateral cartilage, nasalis m., the LLSAN m., the medial muscular band of OOc m., and the medial part of the OOc m. are detected, respectively. A gap of irregular hyperechoic subcutaneous tissue is observed between the nose and midfacial muscular components. The hypoechoic LLS m. is located under the OOc m.

By placing the transducer longitudinally, the hypoechoic medial muscular band of OOc m. is observed located under the thick hyperechoic subcutaneous tissue. Additionally, the medial part of the LLS m. is seen as a hypoechoic image deep to the OOc m. component. In the Doppler mode image, the angular a. a is observed above the LLSAN m. (Fig. 5.17).

M2: Intersection Point of TL4 and PL2

At this point, the hyperechoic epidermis, less hyperechoic dermis layer, and irregular hyperechoic subcutaneous layer can be observed.

In both transverse and sagittal views, the LLS m. is observed superficial to the maxilla. The M2 is the point where the subcutaneous layer becomes thicker than other points in the midface. Also, at this point, muscle components appear relatively unclear and hard to distinguish from the fat compartments. When the transducer is placed longitudinally, the facial v. is observed superficial to the LLS m. in the Doppler mode image. The infraorbital space is observed beneath the LLS m. The infraorbital space is occupied by a deep fat compartment (i.e., DMCF (deep medial cheek fat)), which is observed as an irregularly hyperechoic image. The neurovascular bundle is located inside the DMCF; however, the vascular component is located more superficially than the neural component. The infraorbital n. branches and infraorbital vessels are also located within the DMCF component. On the longitudinal view, many other structures can be observed. The hypoechoic LLS m. is observed superiorly, while the hypoechoic origin of the LAO m. is shown inferiorly (Fig. 5.18).

M3: Intersection Point of TL4 and PL3

The thick subcutaneous layer is observed as an irregularly hyperechoic image. Underneath the subcutaneous layer, there is the hypoechoic lower part of the OOc m. Beneath the OOc m., the bony origin of the Zmi m. is detected (Fig. 5.19).

M4: Intersection Point of TL4 and PL4

At this point, from superficial to deep, relatively thinner hyperechoic subcutaneous layer, thick hypoechoic inferolateral part of the orbital portion of OOc m., irregular hyperechoic image of SOOF, hypoechoic bony origin of the ZMj m., and hyperechoic band of the periosteum of zygomatic bone are observed.

The hyperechoic oblique fibers passing through the OOc m. can be observed when the transducer is placed longitudinally. These oblique fibers are called "zygomatic ligament," which runs from the periosteum to the dermis as the true ligaments. These hyperechoic oblique patterns are hard to distinguish in many cases. Underneath the OOc m. and superficial to the periosteum, the origin of the ZMj m. is clearly identified. Numerous perforator vessels are irregularly located beneath the hyperechoic dermis layer (Fig. 5.20).

M5: Intersection Point of TL5 and PL1

The M5 is the point at the alar facial crease region. Under the strong hyperechoic band of the epidermis and dermis, the dense uniformly hyperechoic subcutaneous layer is observed. The hypoechoic perinasal musculature located lateral to the alare point can be divided into four layers: from the superficial to deep, (1) the LLSAN m.; (2) the LLS m.; (3) the alar part of the nasalis m., the infraorbital plexus, and adipose tissue; and (4) the transverse part of the nasalis m. At the

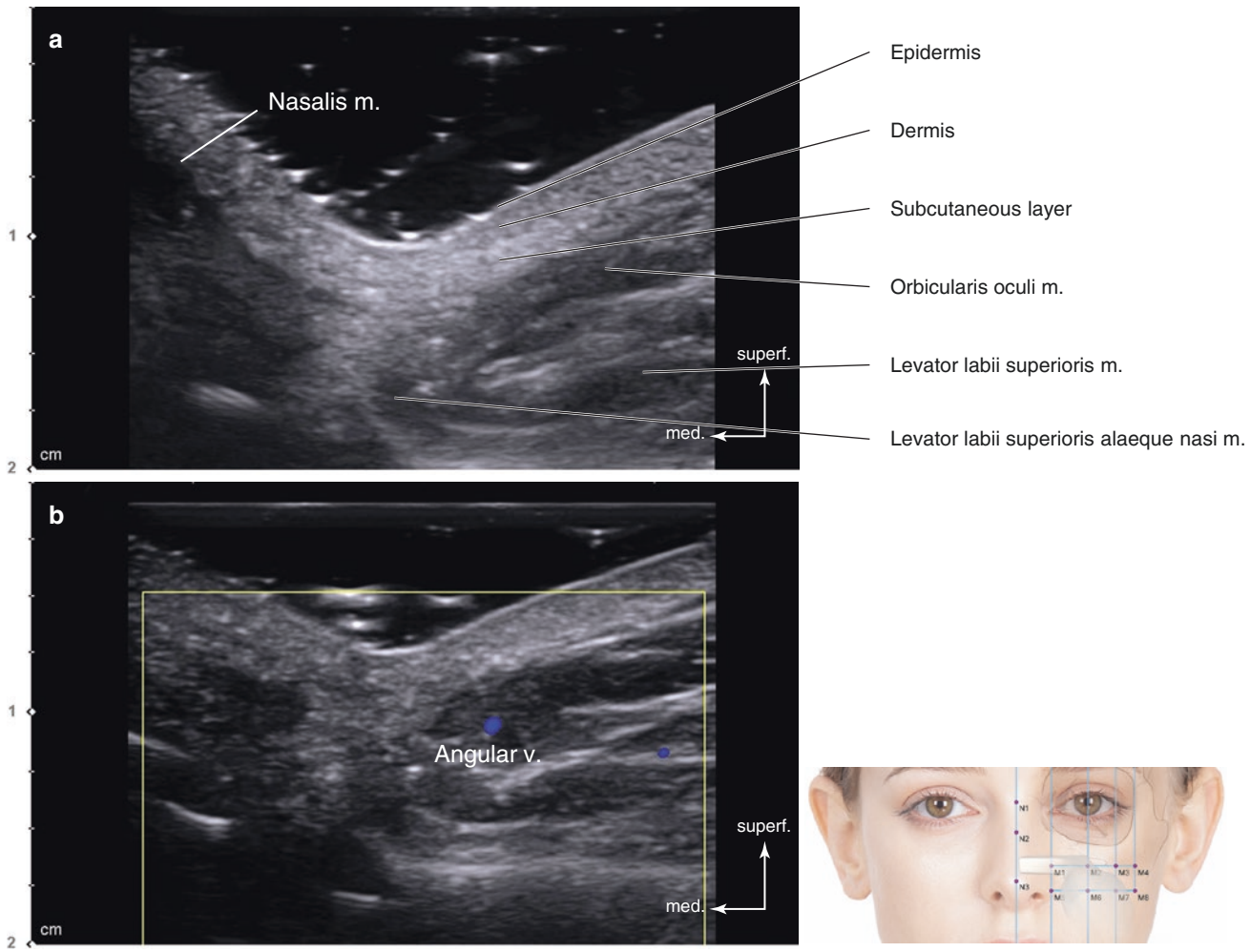

Fig. 5.17 Ultrasonography on the intersection point of TL4 and PL1 (M1). (**a**) B mode (transverse view, 15 MHz by linear transducer), (**b**) Doppler mode (transverse view, 15 MHz by linear transducer), (**c**) B mode (sagittal view, 15 MHz by linear transducer), and (**d**) Doppler mode (sagittal view, 15 MHz by linear transducer). (Published with kind permission of © Hee-Jin Kim 2020. All Rights Reserved)

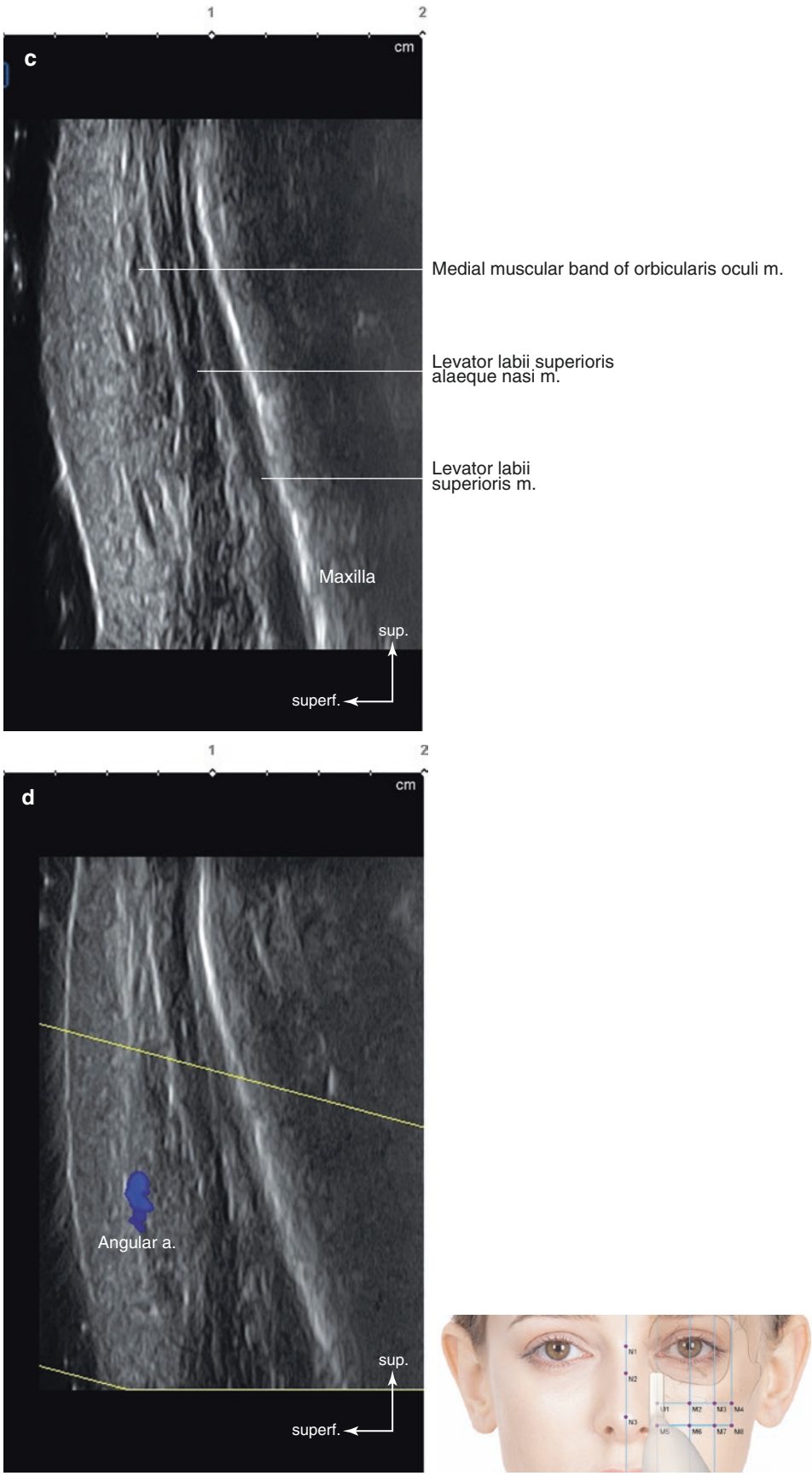

Fig. 5.17 (continued)

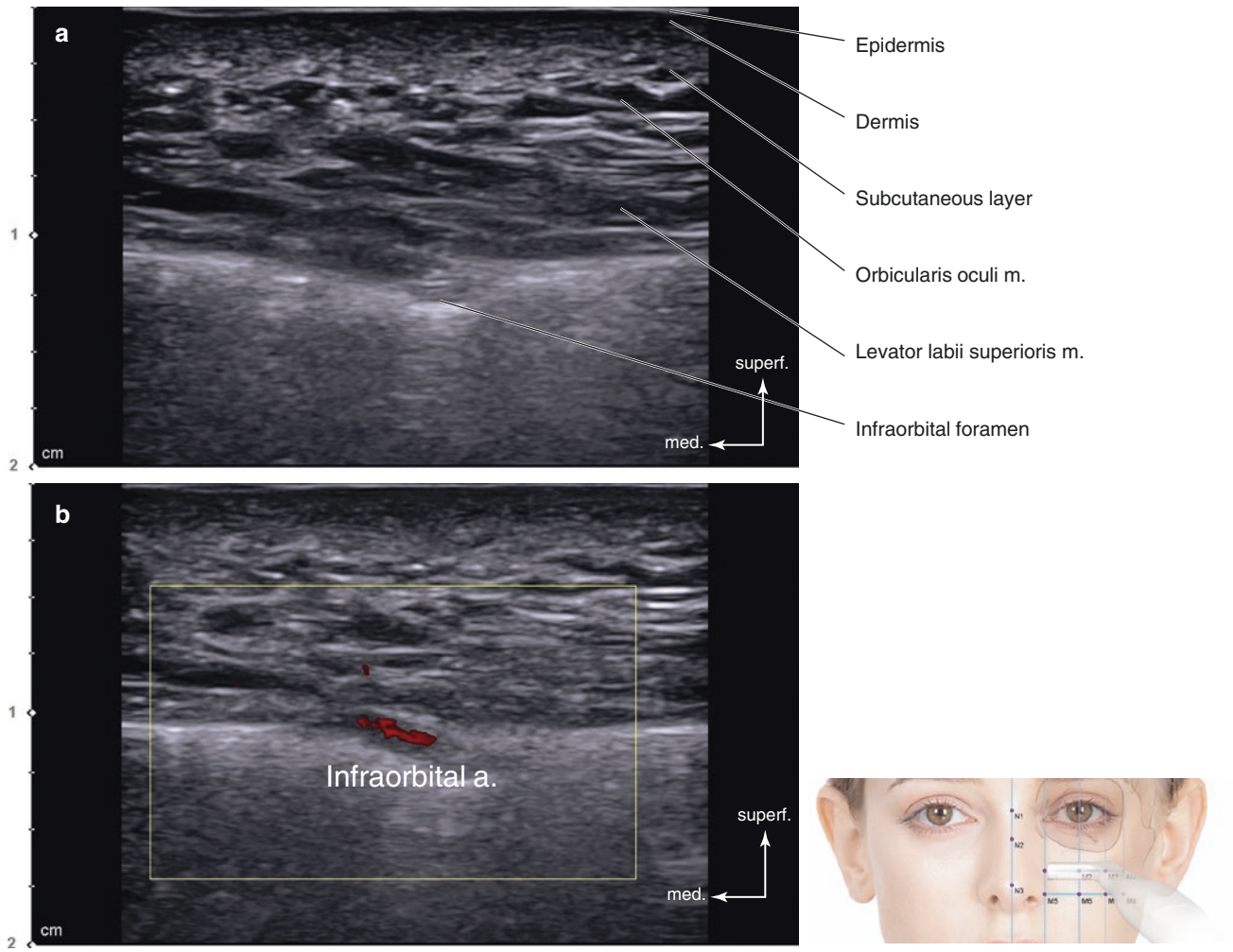

Fig. 5.18 Ultrasonography on the intersection point of TL4 and PL2 (M2). (**a**) B mode (transverse view, 15 MHz by linear transducer), (**b**) Doppler mode (transverse view, 15 MHz by linear transducer), (**c**) B mode (sagittal view, 15 MHz by linear transducer), and (**d**) Doppler mode (sagittal view, 15 MHz by linear transducer). (Published with kind permission of © Hee-Jin Kim 2020. All Rights Reserved)

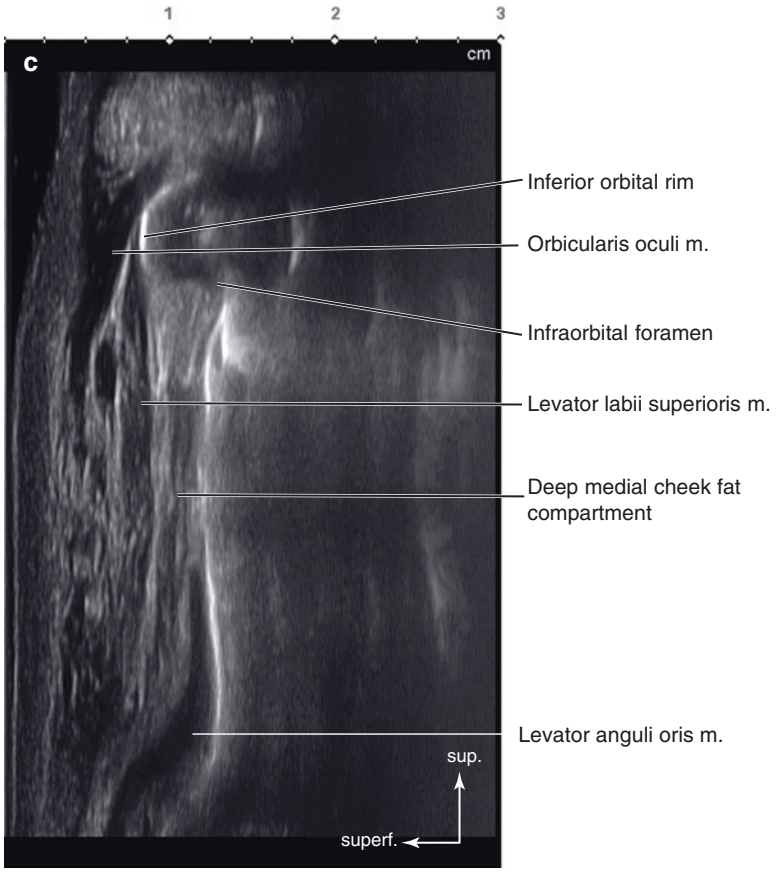

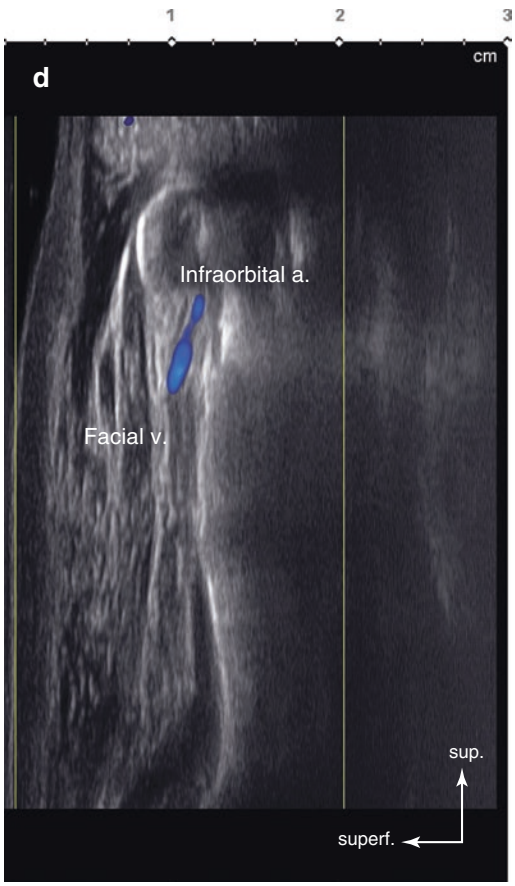

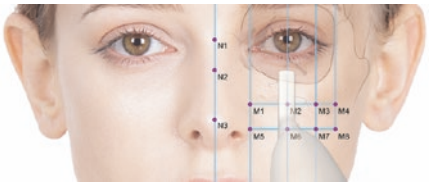

Fig. 5.18 (continued)

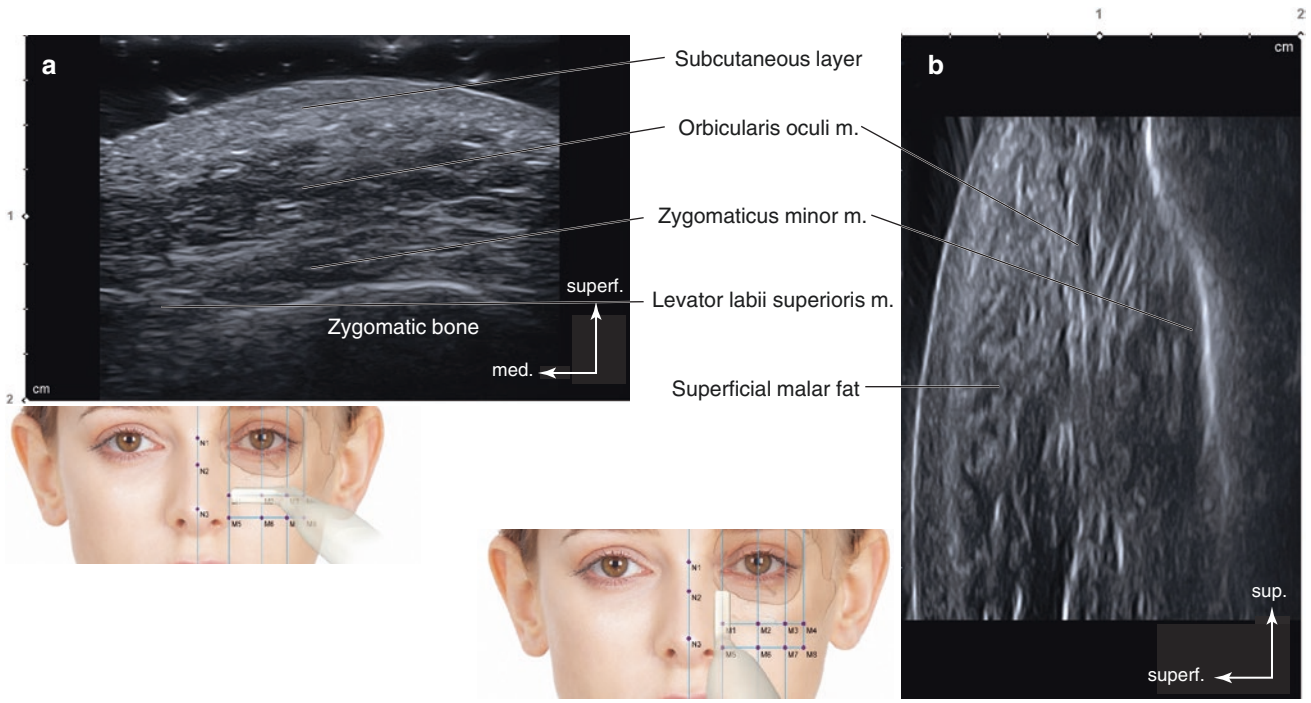

Fig. 5.19 Ultrasonography on the intersection point of TL4 and PL3 (M3). (**a**) B mode (transverse view, 15 MHz by linear transducer) and (**b**) B mode (sagittal view, 15 MHz by linear transducer). (Published with kind permission of © Hee-Jin Kim 2020. All Rights Reserved)

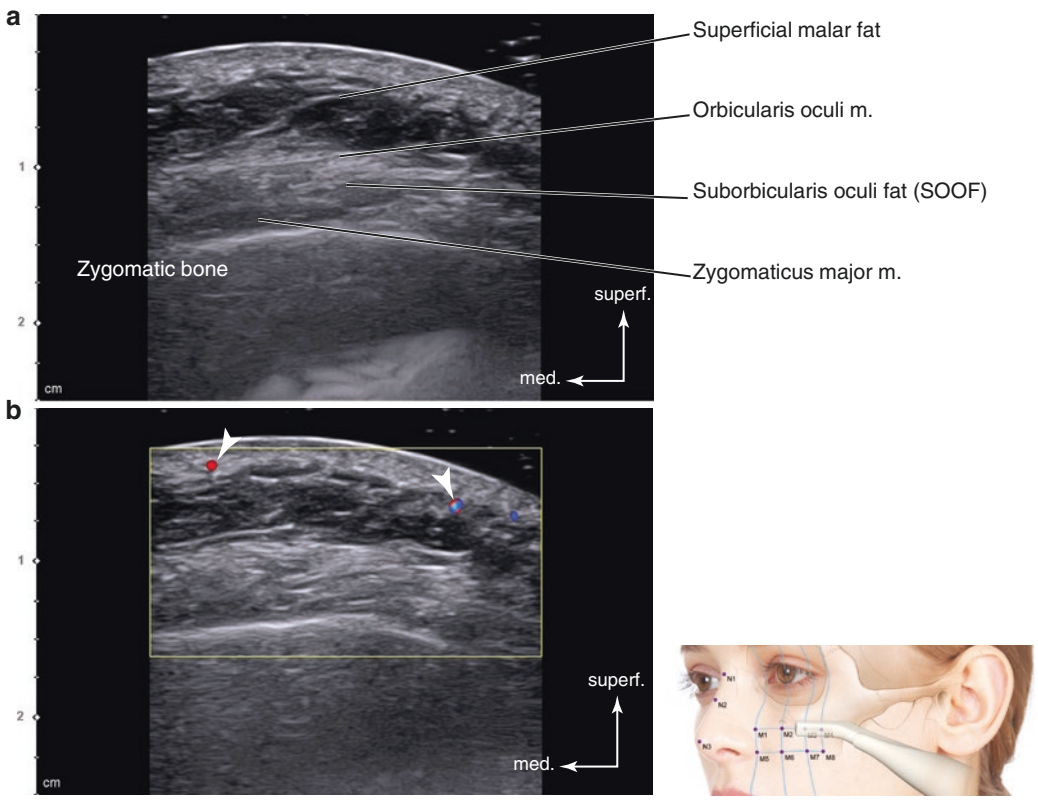

Fig. 5.20 Ultrasonography on the intersection point of TL4 and PL4 (M4). (**a**) B mode (transverse view, 15 MHz by linear transducer), (**b**) Doppler mode (transverse view, 15 MHz by linear transducer), (**c**) B mode (sagittal view, 15 MHz by linear transducer), and (**d**) Doppler mode (sagittal view, 15 MHz by linear transducer) (arrowheads: perforators). (Published with kind permission of © Hee-Jin Kim 2020. All Rights Reserved)

Fig. 5.20 (continued)

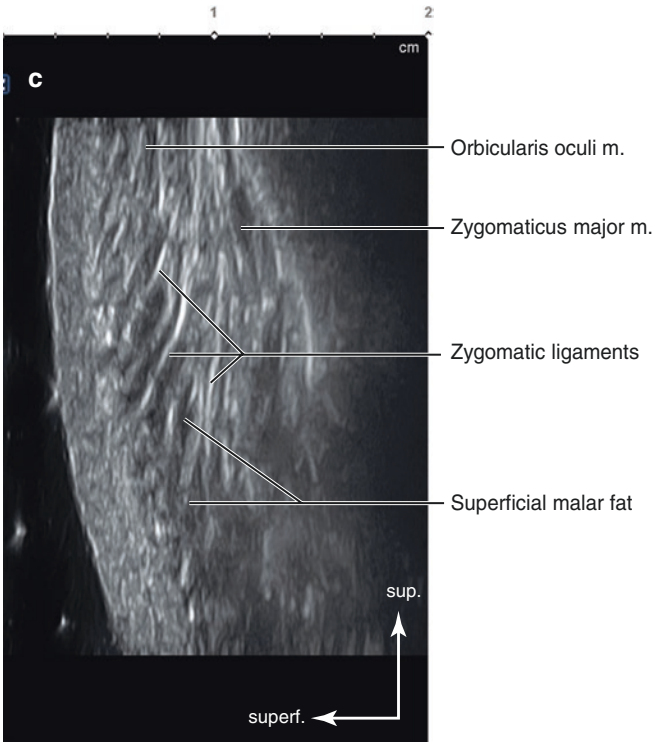

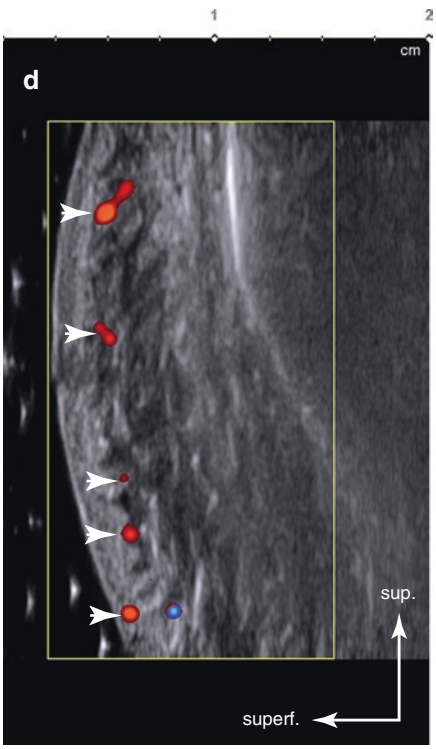

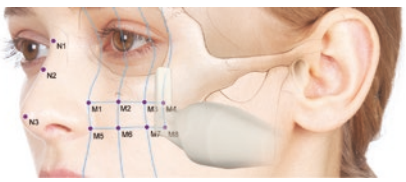

nose ala, the lateral nasal cartilage is hardly distinguishable; however, vestibular skin is observed as a hyperechoic band. Between the external and vestibular skin the hypoechoic dilator naris vestibularis m. is observed with adipose tissue. The Doppler mode image shows that the facial a. runs close to the nose ala. The facial a. is observed from the longitudinal view. The arterial diameter and depth are unpredictable at this point (Fig. 5.21).

M6: Intersection Point of TL5 and PL2

The M6 is the point where TL5 and PL2 cross. The transverse view shows a relatively simpler structure than in the sagittal US view. A thick hyperechoic dermis and subcutaneous layer can be observed under the epidermis. Beneath the subcutaneous layer is the thick hypoechoic LLS m. In the lateral aspect, the muscle fiber of the Zmi m. runs obliquely. In the Doppler mode image, the facial v. runs deeply above the LLS m. (Fig. 5.22).

M7: Intersection Point of TL5 and PL3

The images at this point show thick hyperechoic skin and subcutaneous layers. The hypoechoic Zmi and a part of ZMj mm. are observable at this point. It is hard to distinguish the anatomical structures at this point due to abundant superficial fat. The perforator a. is distributed underneath the skin layer just like the point M4 in the Doppler mode image (Fig. 5.23).

M8: Intersection Point of TL5 and PL4

The M8 is the intersection point of TL5 and PL4, showing similar feature as the point M7. From superficial to deep, the

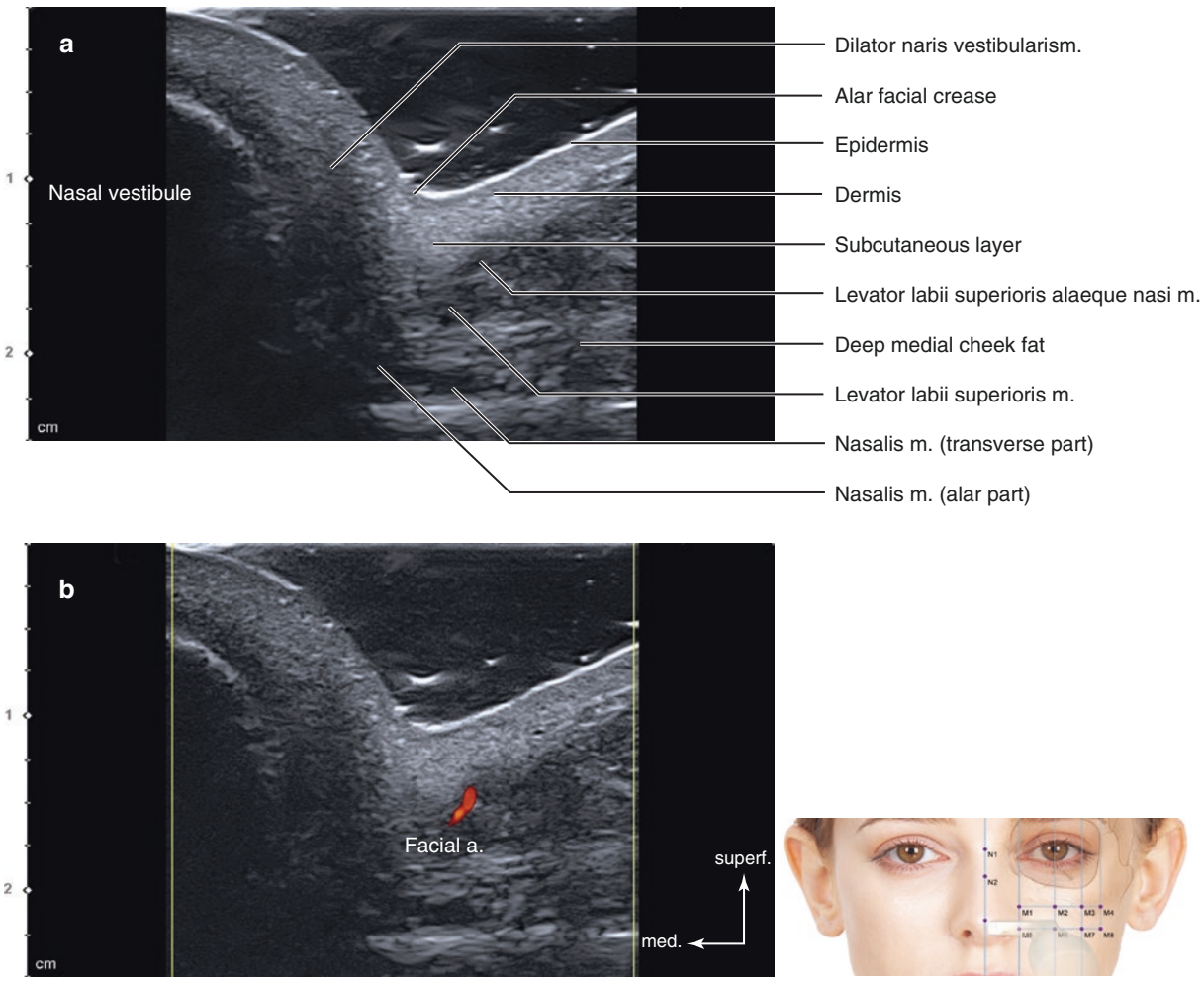

Fig. 5.21 Ultrasonography on the intersection point of TL5 and PL1 (M5). (**a**) B mode (transverse view, 15 MHz by linear transducer), (**b**) Doppler mode (transverse view, 15 MHz by linear transducer), (**c**) B mode (sagittal view, 15 MHz by linear transducer), and (**d**) Doppler mode (sagittal view, 15 MHz by linear transducer). (Published with kind permission of © Hee-Jin Kim 2020. All Rights Reserved)

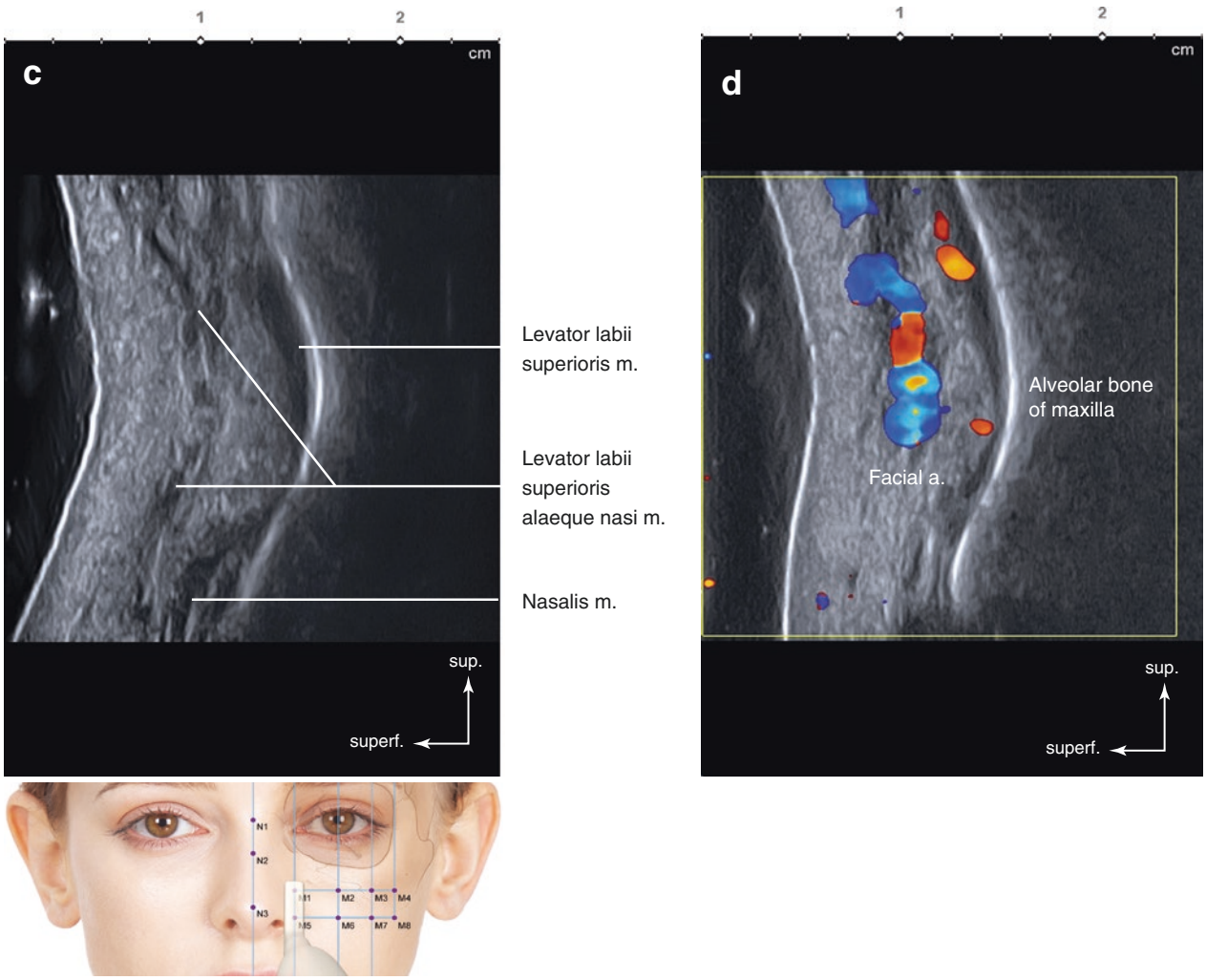

Fig. 5.21 (continued)

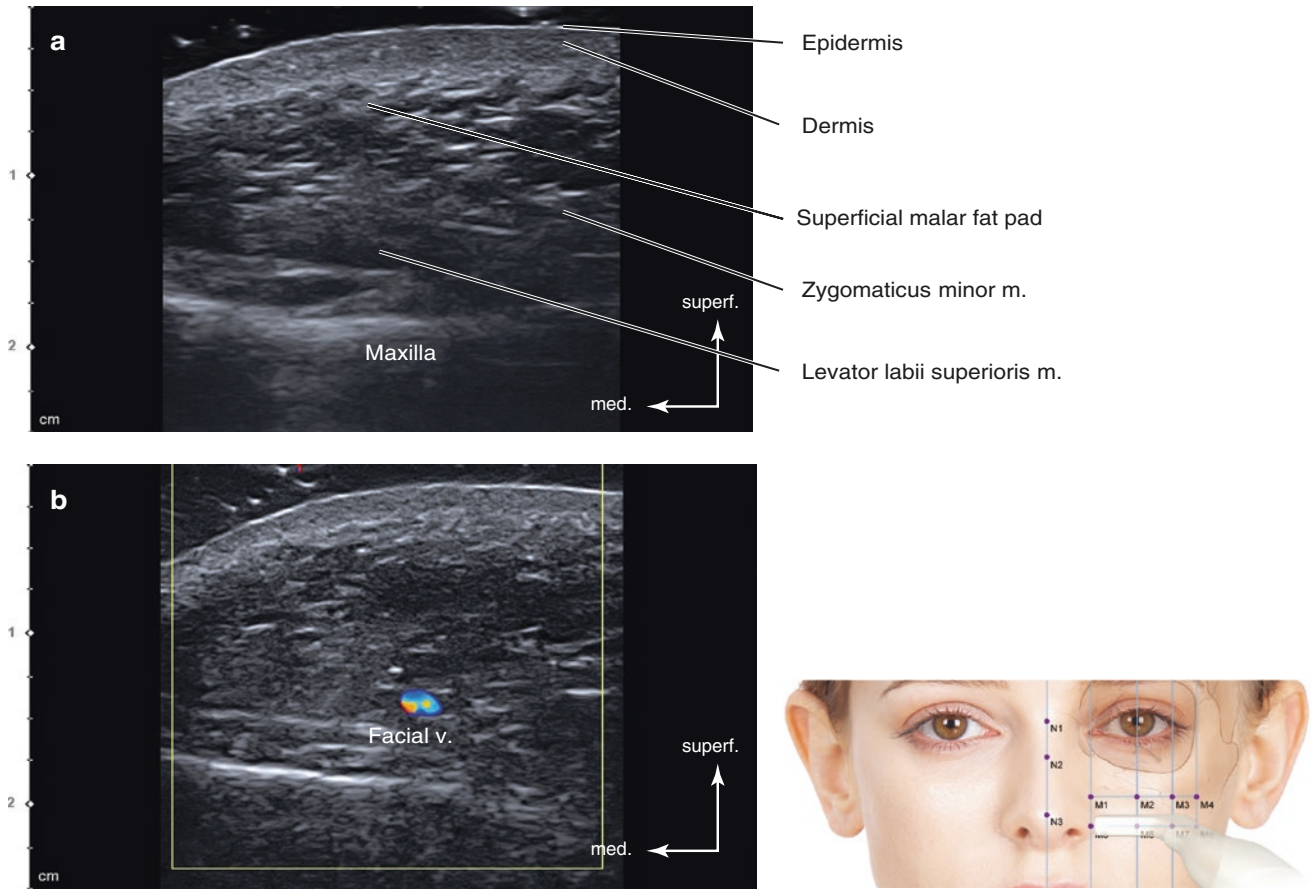

Fig. 5.22 Ultrasonography on the intersection point of TL5 and PL2 (M6). (**a**) B mode (transverse view, 15 MHz by linear transducer), (**b**) Doppler mode (transverse view, 15 MHz by linear transducer), (**c**) B mode (sagittal view, 15 MHz by linear transducer), and (**d**) Doppler mode (sagittal view, 15 MHz by linear transducer). (Published with kind permission of © Hee-Jin Kim 2020. All Rights Reserved)

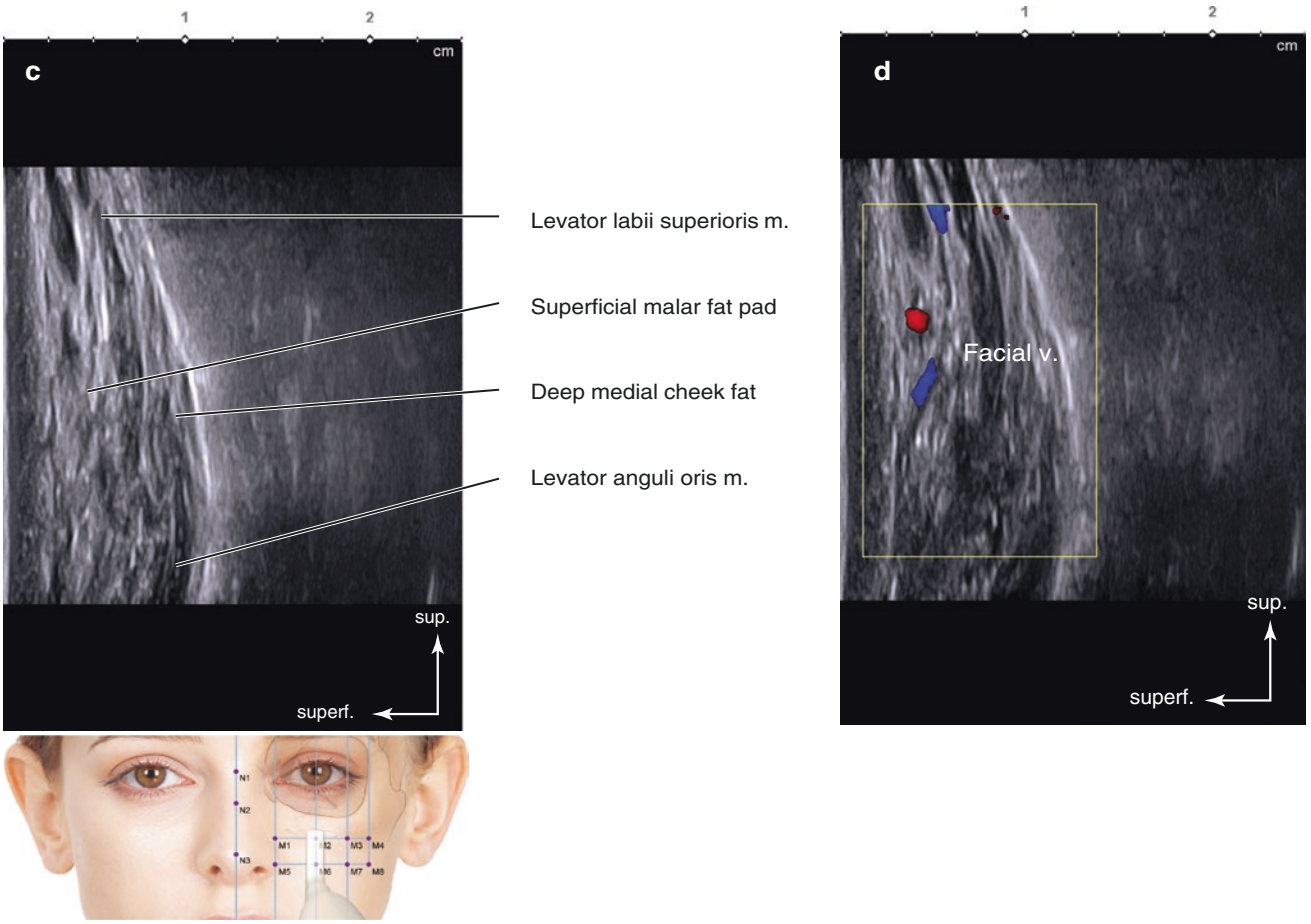

Fig. 5.22 (continued)

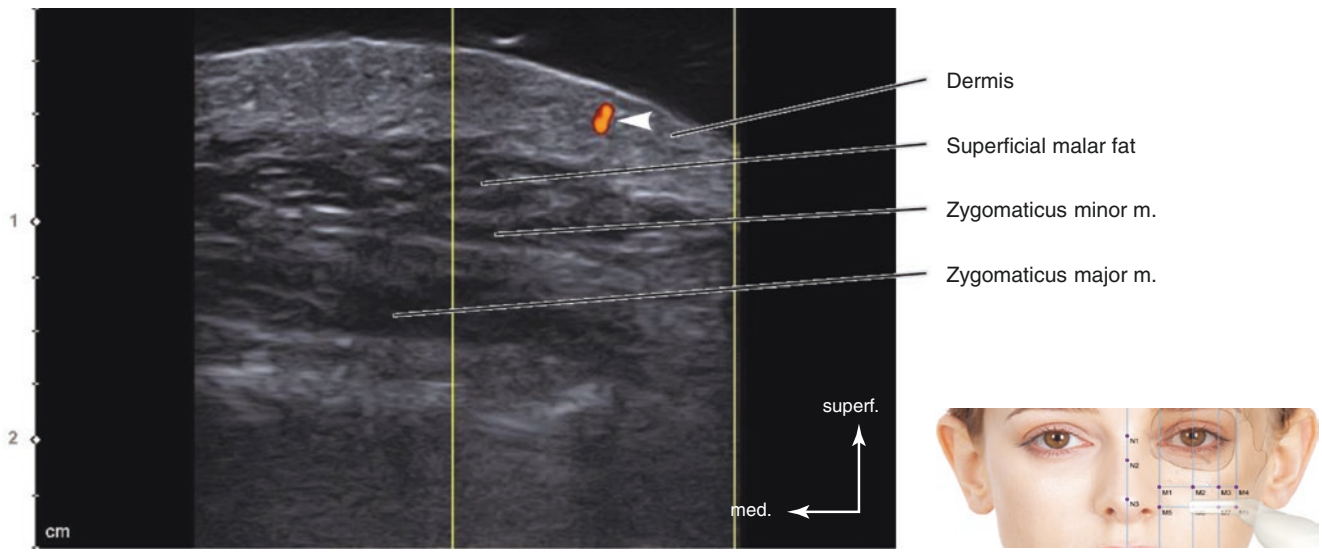

Fig. 5.23 Ultrasonography on the intersection point of TL5 and PL3 (M7). Doppler mode, (transverse view, 15 MHz by linear transducer) (arrowhead: perforator). (Published with kind permission of © Hee-Jin Kim 2020. All Rights Reserved)

thick hyperechoic skin and subcutaneous layer and hypoechoic ZMj m. are clearly shown. However, other surrounding anatomical structures are not distinguishable. At this point, the transverse facial a. (or a perforator) runs right beneath the layer of skin (Fig. 5.24).

N1: Sellion (the Deepest Point on the Radix)

The point N1 is called "sellion," and it is the deepest point of the frontonasal angle. From superficial to deep, the skin, the superficial fatty layer (subcutaneous layer), the fibromuscular layer (procerus m.), and the periosteum of the nasal bone are observed. The superficial fatty layer is thicker than other points of the dorsum, while the deep fatty layer is thinner. The periosteum of the nasal bone is hyperechoic; however, due to the curved surface of the bone, it may seem indefinite in the US image. The procerus m. and blood vessels are observed as hypoechoic and anechoic images. The Doppler mode image can distinguish these arteries, veins, and muscle structures. The dorsal nasal vessels located near the midline and the angular a. are laterally located. The vascular structures are located superficial to or within the fibromuscular layer. In the midsagittal view of the Doppler mode image, the intercanthal v. locates within the subcutaneous layer on the glabella and radix (Fig. 5.25).

N2: Rhinion (Midline Junction Between the Nasal Bone and Cartilage)

The rhinion is the meeting point of the lower margin of the nasal bone and the upper lateral nasal cartilage. Superficially, the hyperechoic epidermis, dermis, and thin superficial fatty layer can be observed. Underneath the superficial fatty layer, the thin hypoechoic nasalis m. can be observed. In the transverse view, the lateral portion of nasalis m. is thicker than the medial portion of the muscle. Beneath the fibromuscular

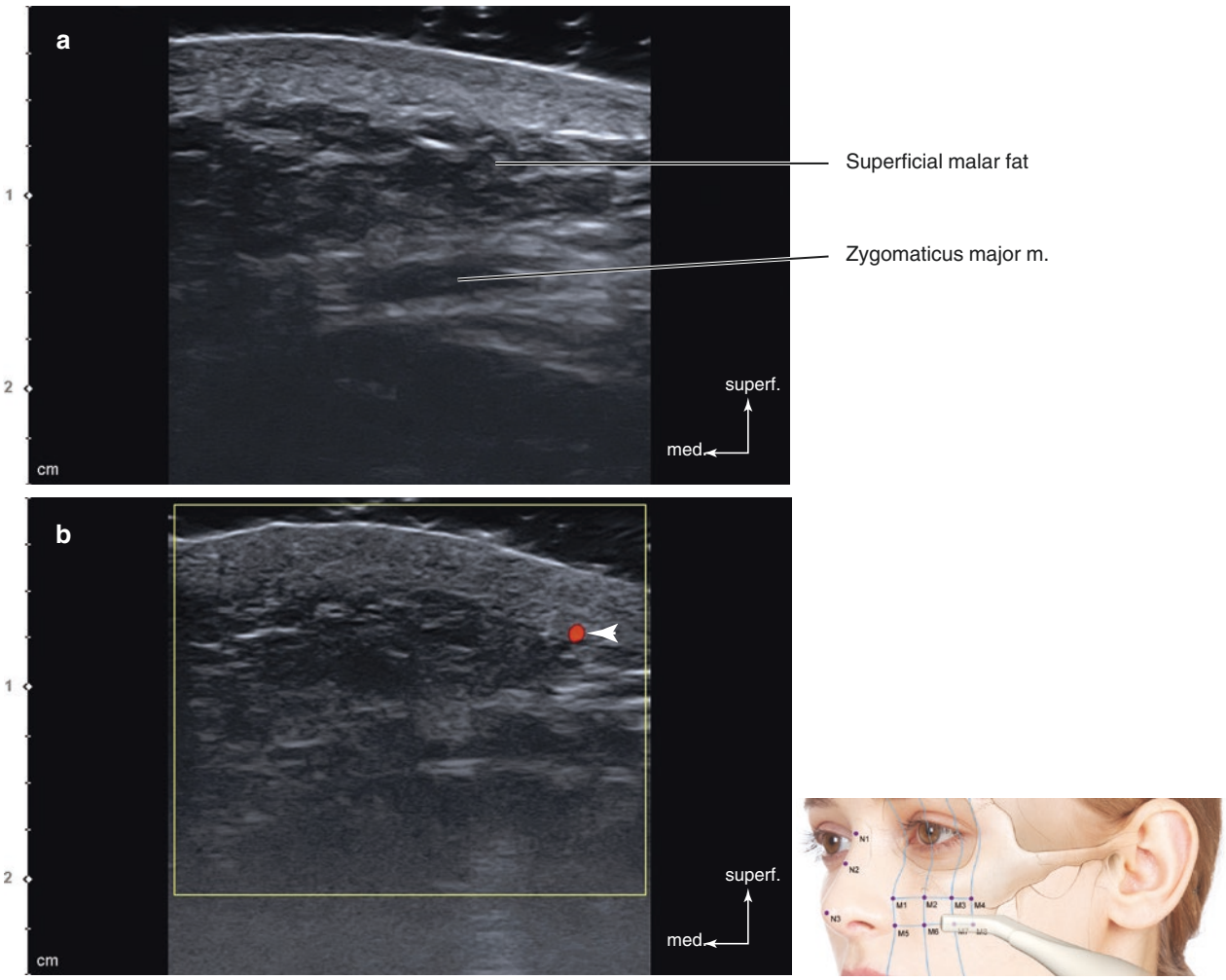

Fig. 5.24 Ultrasonography on the intersection point of TL5 and PL4 (M8). (**a**) B mode (transverse view, 15 MHz by linear transducer) and (**b**) Doppler mode (transverse view, 15 MHz by linear transducer) (arrowhead: perforator). (Published with kind permission of © Hee-Jin Kim 2020. All Rights Reserved)

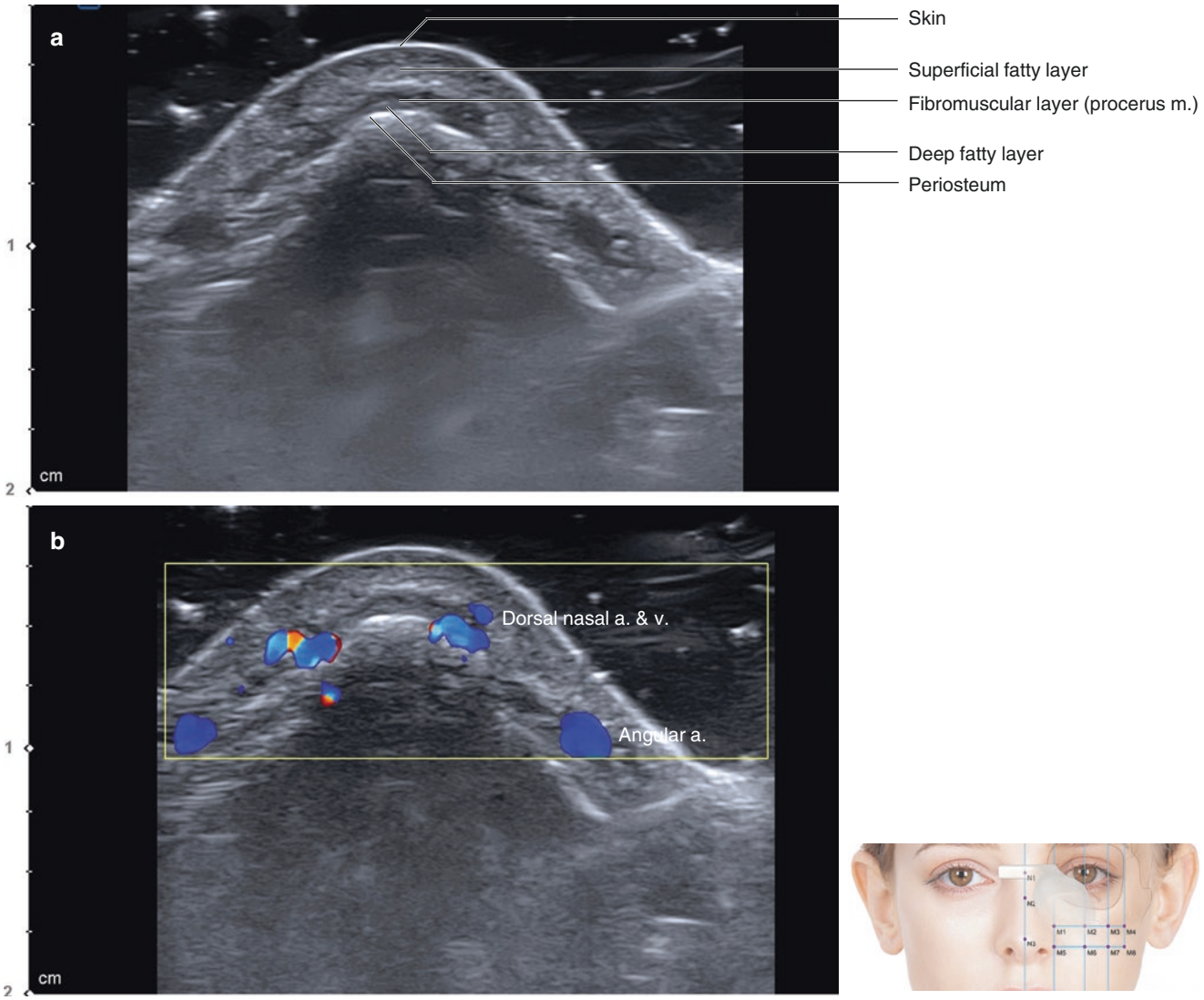

Fig. 5.25 Ultrasonography of the sellion (N1). (**a**) B mode (transverse view, 15 MHz by linear transducer), (**b**) Doppler mode (transverse view, 15 MHz by linear transducer), and (**c**) Doppler mode (midsagittal view, 15 MHz by linear transducer). (Published with kind permission of © Hee-Jin Kim 2020. All Rights Reserved)

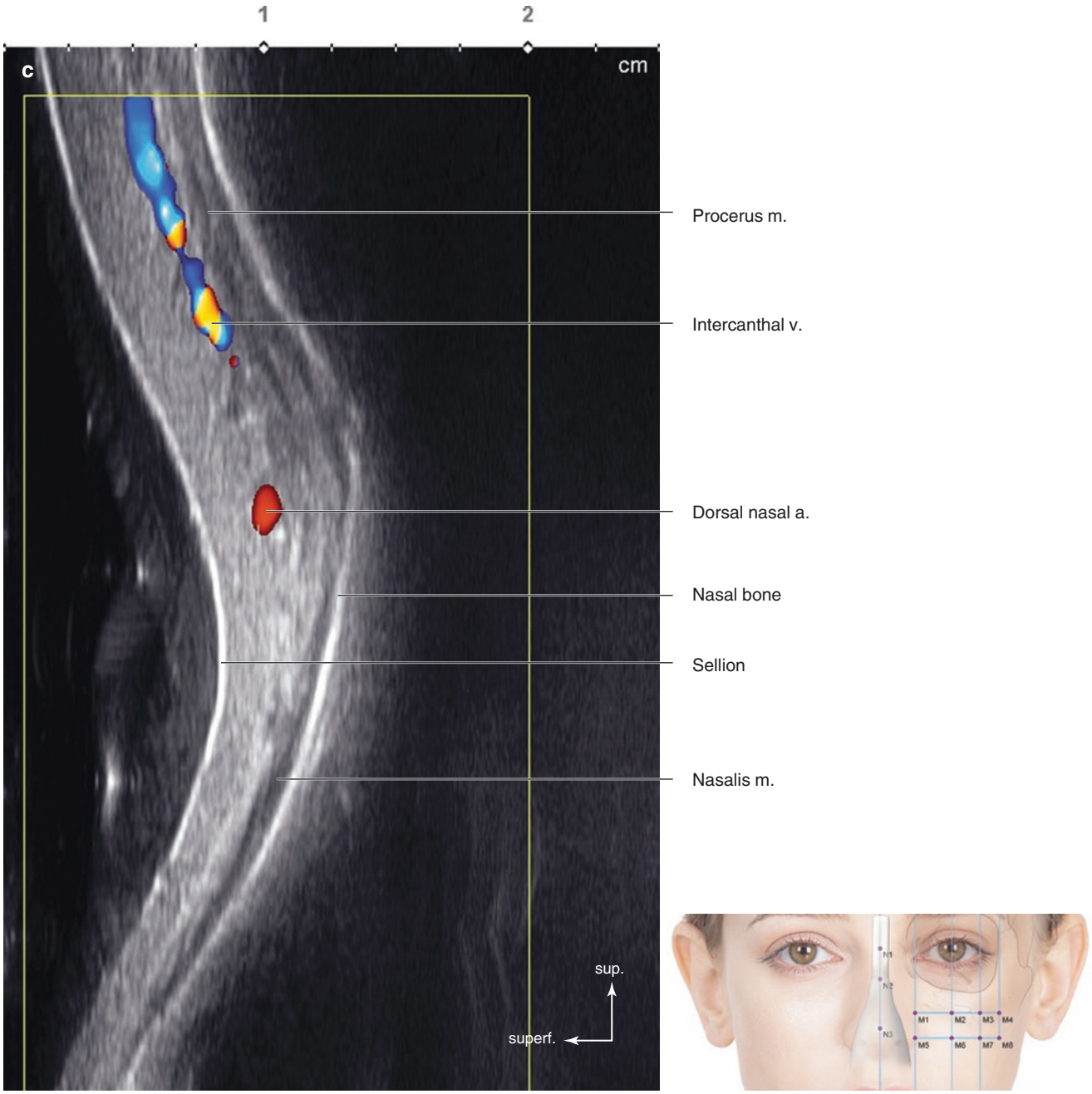

Fig. 5.25 (continued)

layer, the hyperechoic deep fatty layer and hypoechoic upper lateral nasal cartilage are located. At this point, the dorsal nasal a. and v. can be identified. The Doppler mode image is helpful in distinguishing vessels by checking the pulse and blood flow.

In the longitudinal view, multilayered anatomy of the dorsum of the nose is clearly observed. The superficial fatty layer is observed underneath the hyperechoic skin layer. The hypoechoic muscular layer can be observed: the procerus m. superiorly and the nasalis m. inferiorly. In reference to the rhinion, the upper structure is the surface of the hyperechoic band of the nasal bone and the lower is the hypoechoic upper lateral nasal cartilage. The Doppler mode shows the dorsal nasal vessels running 4–5 mm apart from the midline and the lateral nasal a. running transversely below the rhinion. Deep to the lateral nasal cartilage, some branches of the anterior ethmoidal a. are also observed (Fig. 5.26).

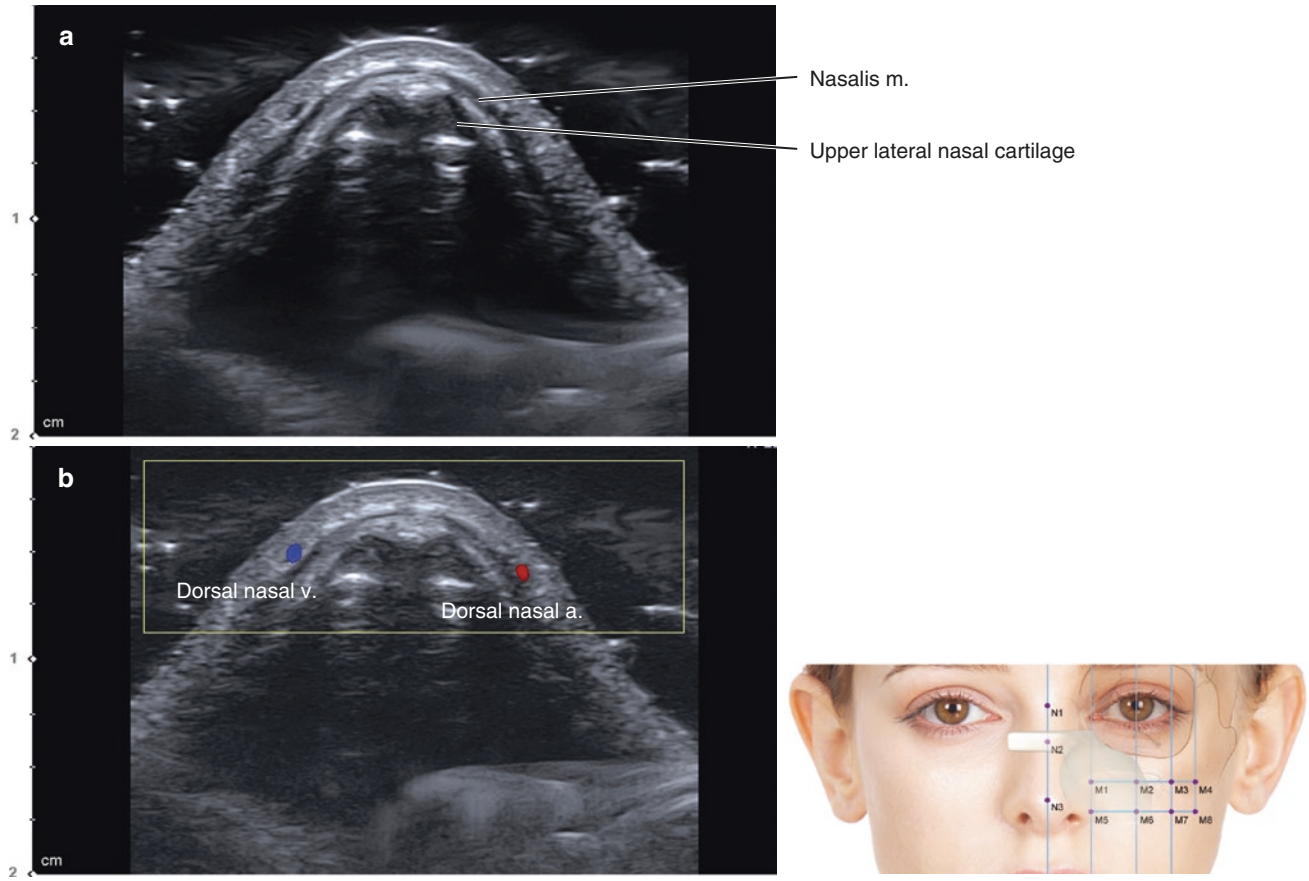

Fig. 5.26 Ultrasonography of the rhinion (N2). (**a**) B mode (transverse view, 15 MHz by linear transducer), (**b**) Doppler mode (transverse view, 15 MHz by linear transducer), (**c**) B mode (sagittal view, 15 MHz by linear transducer), and (**d**) Doppler mode (sagittal view, 15 MHz by linear transducer). (Published with kind permission of © Hee-Jin Kim 2020. All Rights Reserved)

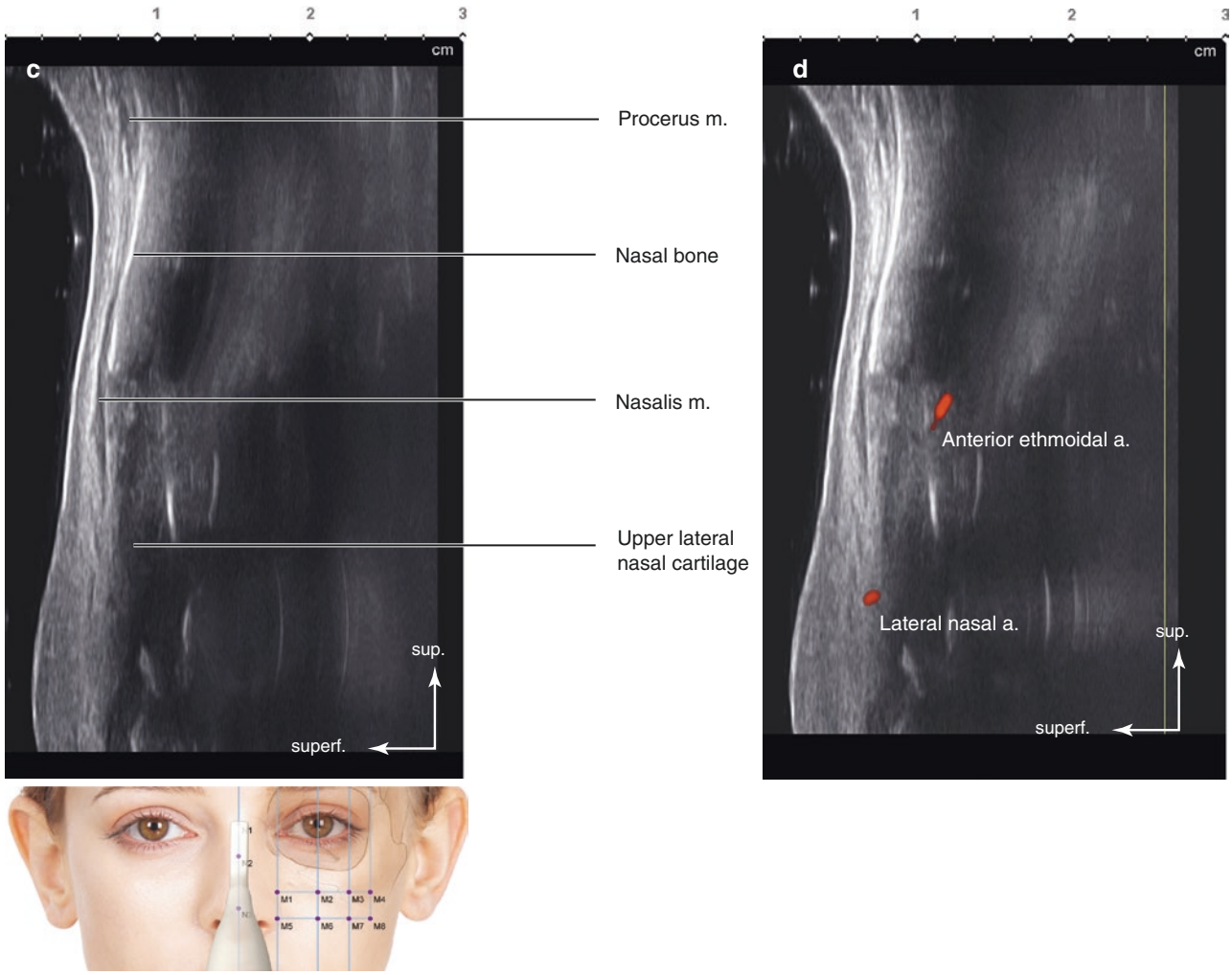

Fig. 5.26 (continued)

N3: Pronasale (Tip of the Nose)

The pronasale is the point at the tip of the nose. At this region, it is hard to observe the fibromuscular layer. The hypoechoic lower lateral nasal cartilage is observed beneath the irregularly hyperechoic subcutaneous tissue layer. The Doppler mode image demonstrates several blood vessels within the subcutaneous layer. Higher vascularity is observed at the tip of the nose (Fig. 5.27).

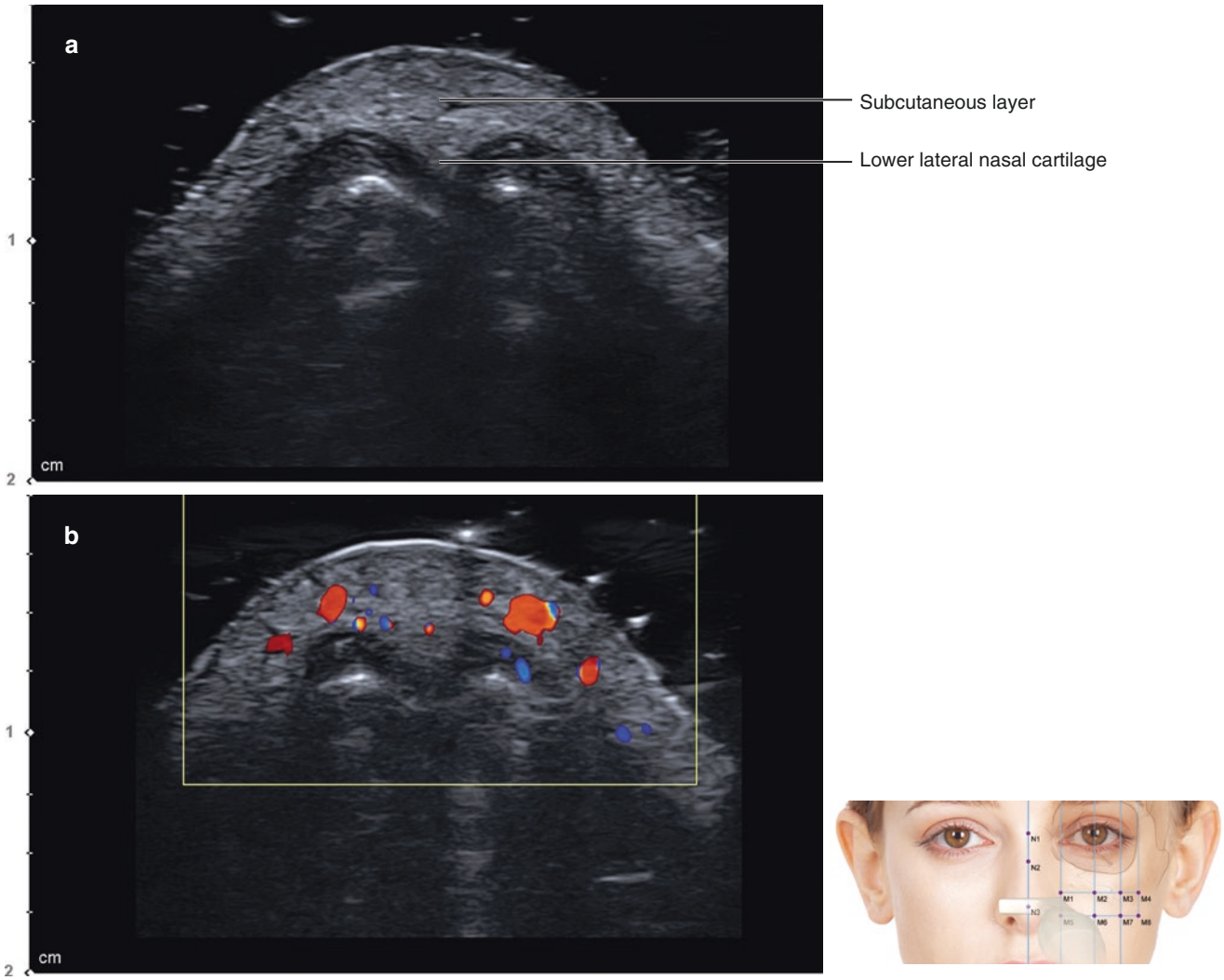

Fig. 5.27 Ultrasonography of the pronasale (N3). (**a**) B mode (transverse view, 15 MHz by linear transducer) and (**b**) Doppler mode (transverse view, 15 MHz by linear transducer). (Published with kind permission of © Hee-Jin Kim 2020. All Rights Reserved)

Bibliography

1. Cho Y, Lee HJ, Lee KW, Lee KL, Kang JS, Kim HJ. Ultrasonographic and three-dimensional analyses at the glabella and radix of the nose for botulinum neurotoxin injection procedures into the procerus muscle. Toxins. 2019;11(10):560.
2. Choi DY, Bae JH, Youn KH, Kim W, Suwanchinda A, Tanvaa T, Kim HJ. Topography of the dorsal nasal artery and its clinical implications for augmentation of the dorsum of the nose. J Cosmet Dermatol. 2018;17:637–42.
3. Choi DY, Kim JS, Youn KH, Hur MS, Kim JS, Hu KS, Kim HJ. Clinical anatomic considerations of the zygomaticus minor muscle based on the morphology and insertion pattern. Dermatol Surg. 2014;40(8):858–63.
4. Hu KS, Kwak HH, Song WC, Kang HJ, Kim HC, Fontaine C, Kim HJ. Branching patterns of the infraorbital nerve and topography within the infraorbital space. J Craniofac Surg. 2006;17(6):1111–5.
5. Hu KS, Kwak J, Koh KS, Abe S, Fontaine C, Kim HJ. Topographic distribution area of the infraorbital nerve. Surg Radiol Anat. 2007;29(5):383–8.
6. Hur MS, Hu KS, Park JT, Youn KH, Kim HJ. New anatomical insight of the levator labii superioris alaeque nasi and the transverse part of the nasalis. Surg Radiol Anat. 2010;32(8):753–6.
7. Hur MS, Hu KS, Youn KH, Song WC, Abe S, Kim HJ. New anatomical of the nasal musculature: dilator naris vestibularis, dilator naris anterior, and alar part of the nasalis. Clin Anat. 2011;24(2):162–7.
8. Hur MS, Youn KH, Hu KS, Song WC, Koh KS, Fontaine C, Kim HJ. New anatomic considerations on the levator labii superioris related with the nasal ala. J Craniofac Surg. 2010;21(1):258–60.
9. Hwang WS, Hur MS, Hu KS, Song WC, Koh KS, Baik HS, Kim ST, Kim HJ, Lee KJ. Surface anatomy of the lip elevator muscles for the treatment of gummy smile using botulinum toxin. Angle Orthod. 2009;79(1):70–7.
10. Jung DH, Kim HJ, Koh KS, Oh CS, Kim KS, Yoon JH, Chung IH. Arterial supply of the nasal tip in Asians. Laryngoscope. 2000;110(2):308–11.
11. Jung W, Yang HM, Lee SH, Kim JS, Lee HK, Kyle SK, Moon HJ, Kim HJ. Accidental intravenous invasion of HA filler in the case of cannula application on the nose. JPRAS. 2018;
12. Kim HS, Lee KL, Gil YC, Hu KS, Tansatit T, Kim HJ. Topographic anatomy of the infraorbital artery and its clinical implications for nasolabial fold augmentation. Plast Reconstr Surg. 2018;142(3):273e–80e.
13. Kim SH, Whang E, Choi HG, Shin DH, Uhm KI, Chung H, Song WC, Koh KS. Analysis of the midface, focusing on the nose: an anthropometric study in young Koreans. J Craniofac Surg. 2010;21:1941–4.
14. Kim YS, Choi DY, Gil YC, Hu KS, Tansatit T, Kim HJ. The anatomical origin and course of the angular artery regarding its clinical implications. Dermatol Surg. 2014;40(10):1070–6.
15. Kim YS, Lee KW, Kim JS, Gil UC, Tanvaa T, Shin DH, KIM HJ. Regional thickness of facial skin and superficial fat: application to the minimally invasive procedures. Clin Anat. 2020;32:1008–18.
16. Koh KS, KIM HJ, Oh CS, Chung IH. Branching patterns and symmetry of the course of the facial artery in Koreans. Int J Oral Maxillofac Surg. 2003;32(4):414–8.
17. Kwak HH, Hu KS, Youn KH, Jin KH, Shim KS, Fontaine C, Kim HJ. Topographic relationship between the muscle bands of the zygomaticus major muscle and the facial artery. Surg Radiol Anat. 2006;28(5):477–80.
18. Lee HJ, Won SY, O J, Hu KS, Mun SY, Yang HM, Kim HJ. The facial artery: a comprehensive anatomical review. Clin Anat. 2018;31:99–108.
19. Lee JH, Lee K, Jung W, Youn KH, Hu KS, Tansatit T, KIM HJ. A novel anatomical consideration on the exposed segment of the facial artery. Clin Anat. 2020;33:257–64.
20. Lee YI, Yang HM, Pyeon HJ, Lee HK, Kim HJ. Anatomical and histological study of the arterial distribution in the columellar area, and the clinical implications. Surg Radiol Anat. 2014;36(7):669–74.
21. Park JT, Youn KH, Hu KS, Kim HJ. Medial muscular band of the orbicularis oculi muscle. J Craniofac Surg. 2012;23(1):195–7.
22. Park JT, Youn KH, Hur MS, Hu KS, Kim HJ, Kim HJ. Malaris muscle, the lateral muscular band of orbicularis oculi muscle. J Craniofac Surg. 2011;22(2):659–62.
23. Shim KS, Hu KS, Kwak HH, Youn KH, Koh KS, Fontaine C, Kim HJ. An anatomy of the insertion of the zygomaticus major muscle in human focused on the muscle arrangement at the mouth corner. Plast Reconstr Surg. 2008;121(2):466–73.
24. Yang HM, Lee JG, Hu KS, Gil YC, Choi YJ, Lee HK, Kim HJ. New anatomical insights of the course and branching patterns of the facial artery: clinical implications regarding injectable treatments to the nasolabial fold and nasojugal groove. Plast Reconstr Surg. 2014;133(5):1077–82.
25. Yang HM, Lee YI, Lee JG, Choi YJ, Lee HJ, Lee SH, Hu KS, Kim HJ. Topography of superficial arteries on the face. J Physiol Anthropol. 2013;26:131–40.
26. Yang HM, Won SY, Kim HJ, Hu KS. Sihler staining study of anastomosis between the facial and trigeminal nerves in the ocular area and its clinical implications. Muscle Nerve. 2013;48(4):545–50.
27. Yang HM, Won SY, Kim HJ, Hu KS. Sihler's staining study of the infraorbital nerve and its clinical complication. J Craniofac Surg. 2014;25(6):2209–13.
28. Youn KH, Park JT, Park DS, Koh KS, Kim HJ, Paik DJ. Morphology of the zygomaticus minor and its relationship with the orbicularis oculi muscle. J Craniofac Surg. 2012;23(2):546–8.

US Anatomy of the Perioral and Masseter Region

6

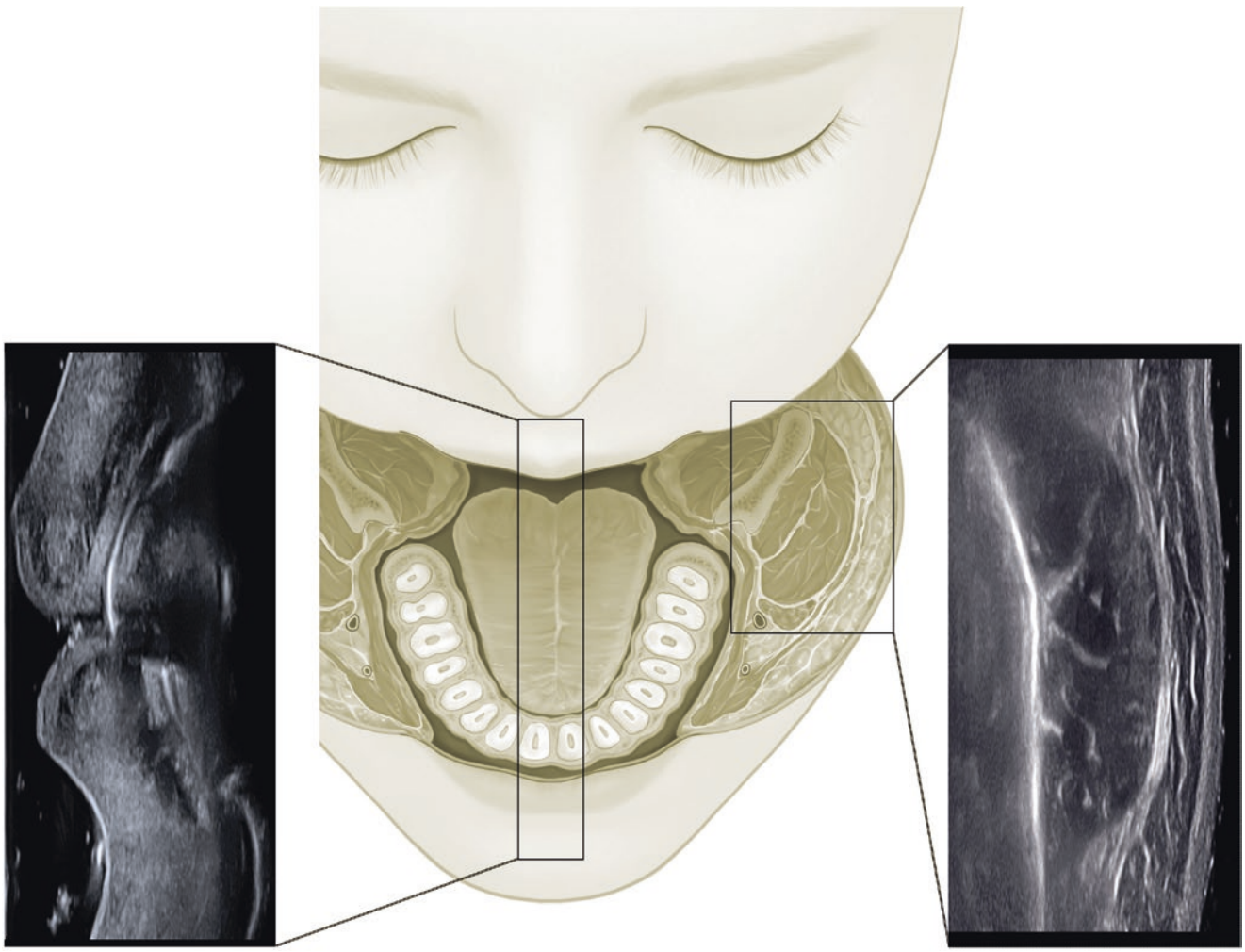

H.-J. Kim et al., *Ultrasonographic Anatomy of the Face and Neck for Minimally Invasive Procedures*,
https://doi.org/10.1007/978-981-15-6560-1_6

6.1 Clinical Anatomy of the Perioral and Masseter Region

6.1.1 General Topographic Anatomy of the Perioral Region

The perioral area includes several anatomical regions: the upper lip including the philtrum area, lower lip, nasolabial fold region, mouth corner, cheek, and chin. The appearance of the perioral region changes with the aging process, repeated movements, loss of bony support, and sagging of the fat tissue. Other environmental factors, such as smoking, sunlight hazard, and poor oral hygiene can accelerate the aging process. Rejuvenation of the perioral region can be challenging. The perioral region is a high risky area in minimally invasive procedures; therefore, anatomical understanding is critical to prevent serious complications.

There are 12 facial muscles that affect the shape and function of the perioral area. Muscles in the perioral region can be classified based on their origin and insertion, as well as by their location, with respect to the major structures (Fig. 6.1). The orbicularis oris (OOr) m. is the only mouth

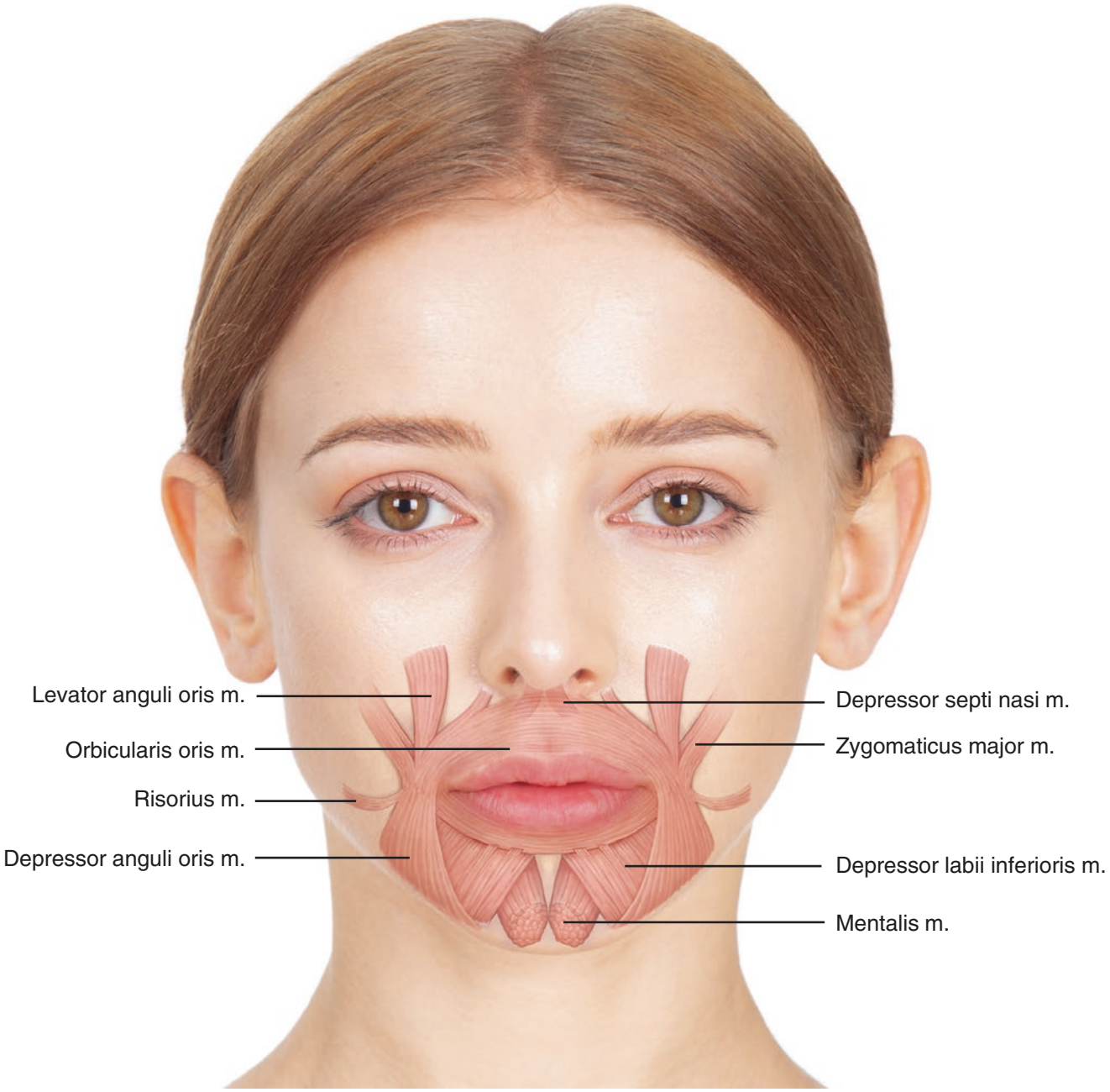

Fig. 6.1 Illustration of the perioral musculature. (Published with kind permission of © Kwan-Hyun Youn 2020. All Rights Reserved)

constrictor that surrounds the mouth region. Most muscle fibers are continuations from various muscles in the mouth region. Intrinsic OOr m. fibers originate from the alveolar bone of the maxillary and mandibular incisors (i.e., incisivus labii superioris and incisivus labii inferioris mm.). The buccinator m. originates from the external side of the alveolar portion of the maxillary, and mandibular molars and the anterior border of the pterygomandibular raphe. The buccinator m. consists of four bands: the first band (the superior band) originating from the maxilla, the second band originating from pterygomandibular raphe, the third band originating from the mandible, and the fourth band (the inferior band) originating inferiorly to the third band. These muscle fibers extend inferiorly, and medially to the OOr m. fibers. Unlike other bands of the buccinator m., the fourth band continues bilaterally to the median plane of the mandible (Fig. 6.2).

The other perioral muscles can be classified into groups based on their insertion into the modiolus. The modiolus is a fibromuscular structure that decussates between the OOr m. and the dilators of the lips ending at the lateral border of the cheilion. The location of the modiolus may be superior to or inferior to the level of the intercheilion line. It is strongly associated with facial expression, beauty, aging, and formation of the nasolabial fold. Muscles that terminate into the modiolus are engaged in facial expressions. The modiolus is a dense, compact, and mobile muscular node formed by the convergence of muscle fibers from the zygomaticus major (ZMj), levator anguli oris (LAO), depressor anguli oris (DAO), and risorius mm. The OOr and buccinator mm. also insert into the modiolus and interlace with the other muscles after passing through the modiolus (Fig. 6.3).

The ZMj m. originates from the facial surface of the zygomatic bone, proceeds inferiorly and medially, joining the OOr m., and inserts into the modiolus. Thus, the well-known function of ZMj m. is elevating the mouth corner. However, the insertion of ZMj m. varies, and the fiber running deep to the LAO m. is always observed. These deep fibers insert into the anterior region of the buccinator m. The LAO m. originates from the canine fossa inferior to the infraorbital foramen, which joins with the OOr m., and attaches into the modiolus. It serves to elevate the mouth corner. The DAO m.

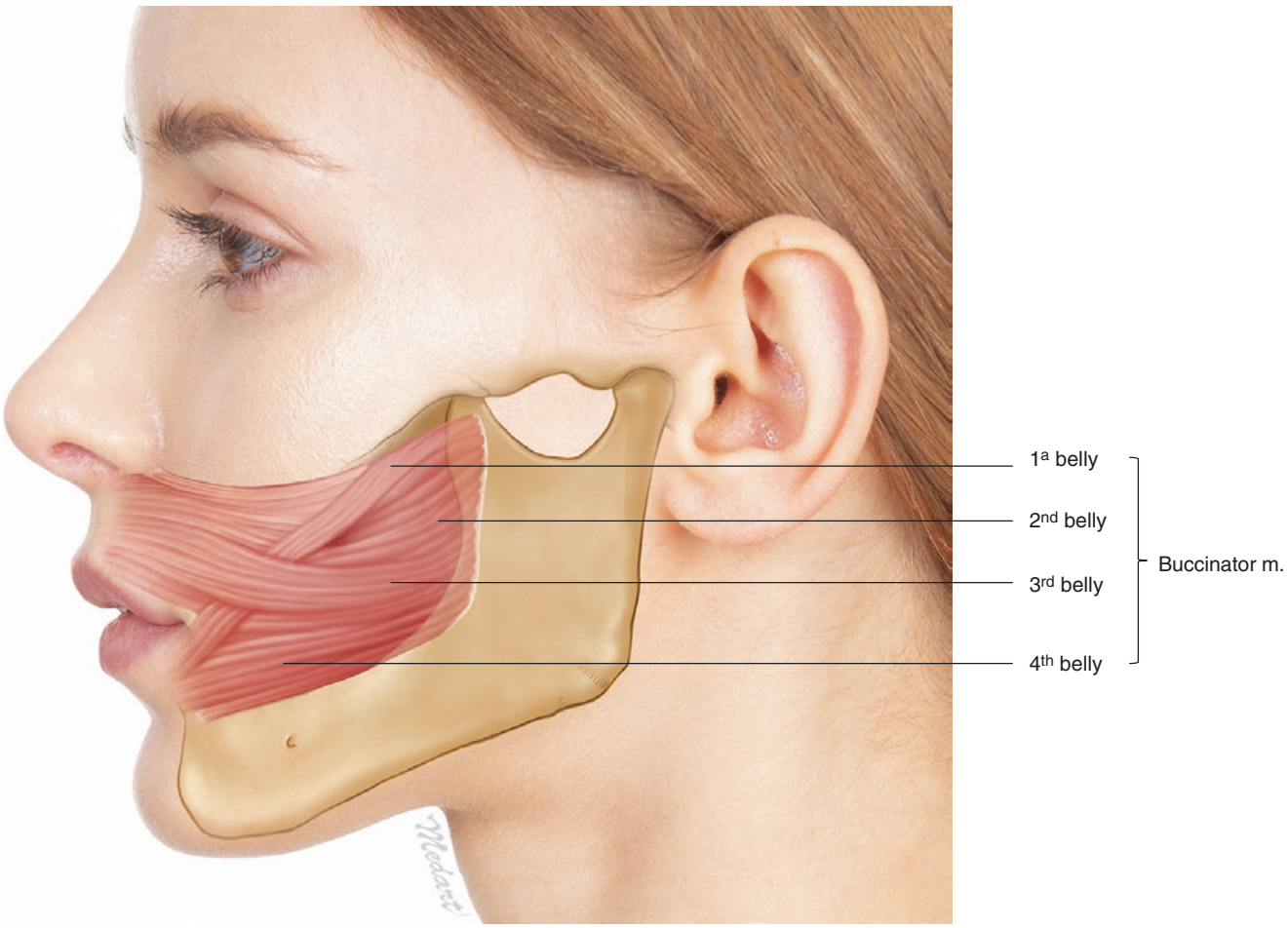

Fig. 6.2 Illustration of the orbicularis oris and buccinator muscles. (Published with kind permission of © Kwan-Hyun Youn 2020. All Rights Reserved)

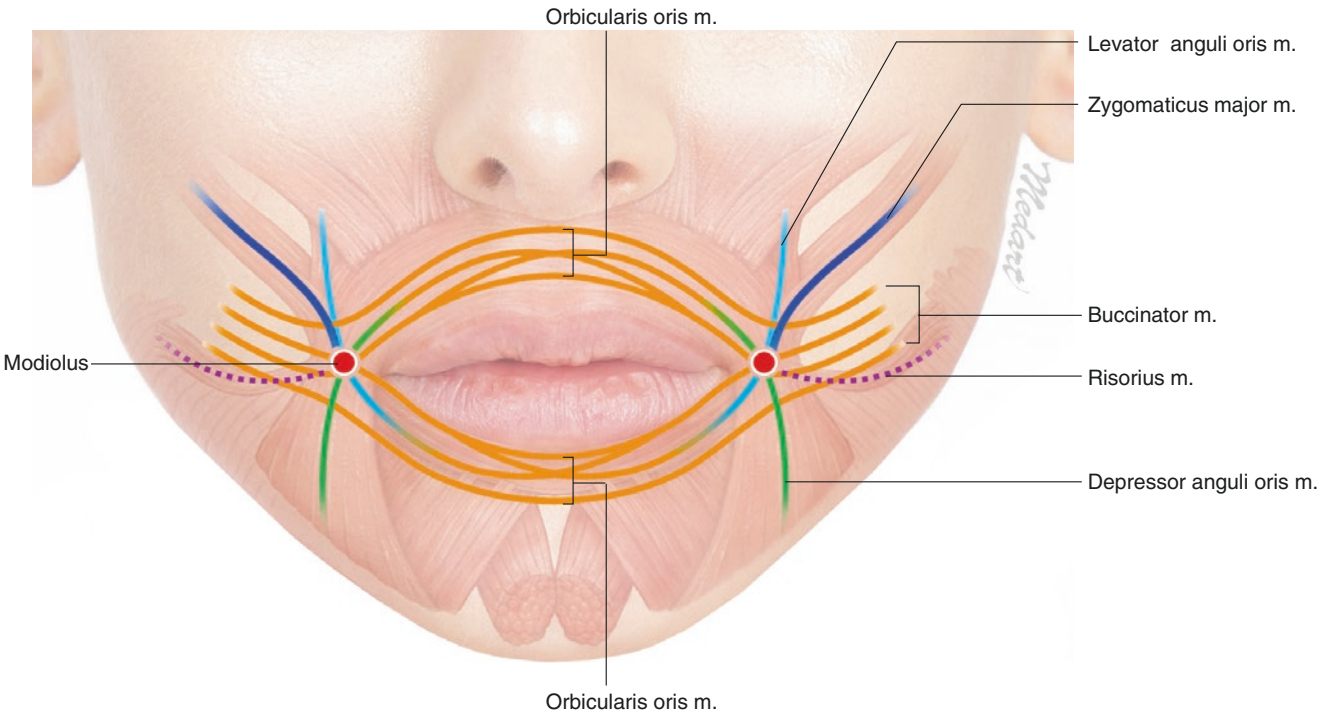

Fig. 6.3 Schematic illustration of the muscles interlacing at the modiolus. (Published with kind permission of © Kwan-Hyun Youn 2020. All Rights Reserved)

is a triangular muscle located on the most superficial layer of the perioral region with the same layer of the risorius m. The DAO m. arises from the oblique line of the mandible and overlaps with the depressor labii inferioris (DLI) m. at the origin. The DAO m. becomes narrower, proceeds to the mouth corner (modiolus), and merges with the risorius m. The risorius m. is a thin and slender muscle, and it is predominantly located 20–50 mm lateral to the mouth corner and 0–15 mm below the intercheilion horizontal line. Most fibers originate from the SMAS, the parotid fascia, and the masseteric fascia. The risorius m. sometimes originates from the platysma m. The risorius m. fibers insert into the modiolus and pull the mouth corner laterally when smiling (Figs. 6.3 and 6.4).

The muscles inserting into the upper and lower lip include the levator labii superioris alaque nasi (LLSAN), levator labii superioris (LLS), zygomaticus minor (Zmi), and DLI mm. (Fig. 6.5). Perioral muscles that insert into the upper lip originate from the maxilla below the infraorbital foramen and insert into the OOr m. of the upper lip to elevate the upper lip. The LLS m. originates from 5 (medial) to 10 (lateral) mm inferior to the infraorbital margin of the maxilla and inserts into the lateral side of the upper lip. The LLS m. is rectangular-shaped rather than triangular-shaped, and its medial fibers are attached into the nose ala deep to the alar facial crease. Also, 90% of the LLS m. fibers are mixed with the alar part of the nasalis m. The LLSAN m. originates from the frontal process of the maxilla and inserts into the upper lip and the nose ala. The LLSAN m. is divided into superficial and deep layers. The superficial layer proceeds inferiorly to the surface layer of the LLS m., and the deep layer proceeds deep to the LLS m. (Fig. 6.5).

Perioral muscles that insert into the lower lip originate from the lower border of the mandible and insert into the surrounding muscles and skin to depress the lower lip. The DLI m. originates from the lower part of the oblique line of the mandible (medial to the mental foramen) and passes upwards and medially into the skin and mucosa of the lower lip (Figs. 6.4 and 6.5).

The mentalis m. is the only chin tensor muscle. This muscle is a cone-shaped muscle originating from the incisive fossa of the mandible. Its medial muscle fibers descend anteromedially and decussate each other, forming a dome-shaped chin prominence. Due to the decussation of the medial fiber of the mentalis m., there is a vacant space interspersed with fat and ligamentous structure between the muscle fibers (Figs. 6.3, 6.4, and 6.5). The mentalis m. elevates the chin and provides major vertical support for the lower lip.

The platysma m. is the subcutaneous muscle of the neck. This muscle attaches to the inferior border of the mandible through the mandibular septum and interlaces with the lower facial muscles around the lower lip. At the perioral region, platysma muscle

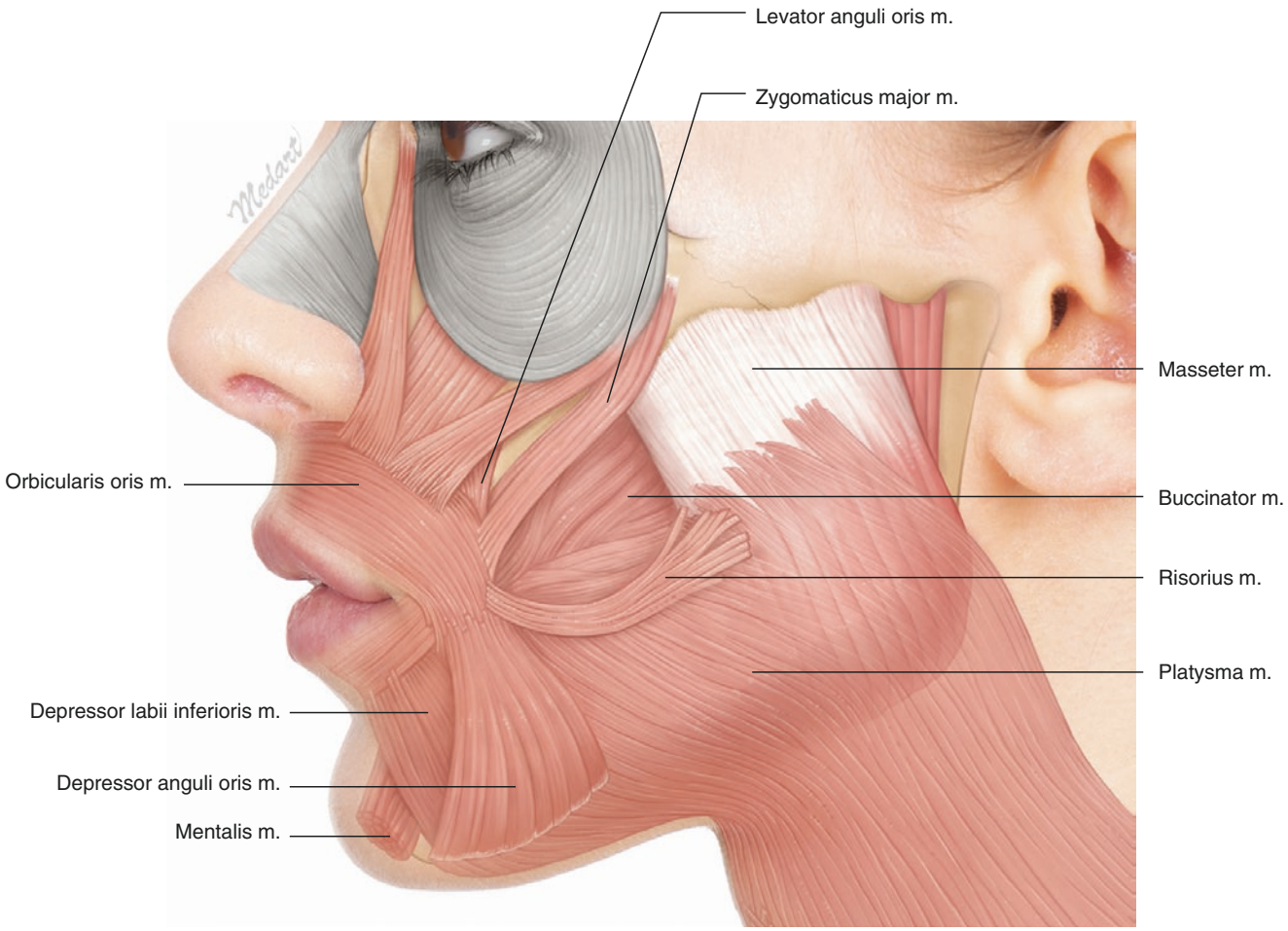

Fig. 6.4 Illustration of the lower facial musculature. (Published with kind permission of © Kwan-Hyun Youn 2020. All Rights Reserved)

fibers proceed superomedially to the lateral border of the DAO m. and cover the cheek and masseter region (Fig. 6.6).

The masseter m. originates from the inferior border of the zygomatic bone and zygomatic arch, runs obliquely and inferoposteriorly, and inserts to the mandibular angle and the mandibular ramus. It consists of three layers according to depth. The superficial portion originates from the zygomatic bone and the anterior 2/3 of the lower border of the zygomatic arch. The superficial portion of masseter m. runs posteriorly and inferiorly and inserts into the masseteric tuberosity on the outer surface of the mandibular ramus around the mandibular angle. The middle portion originates from the deep surface of the anterior 2/3 of the zygomatic arch and the lower border of the posterior 1/3 of the arch. The middle portion of the masseter m. runs vertically and inserts on the upper and lateral surface of the ramus (Fig. 6.7).

The deepest portion, also known as the zygomaticomandibularis m., arises from the deep surface of the zygomatic bone and zygomatic arch and attaches to the middle part of the ramus. The masseteric n., a branch of the mandibular n., passes between the middle and deep layer of the masseter m. and separates the middle layer from the deep layer of the masseter m. (Fig. 6.8).

In the perioral region, facial expression muscles are arranged in four layers based on their origin. The individual muscles are arranged in the superficial (first, second, and third) layer and the deepest (fourth) layer (Fig. 6.9).

6.1.2 Nerve and Vascular Distribution of the Perioral Region

For the sensory innervation of the perioral region, the mandibular n. distributes to the mouth corner, the lower lip, and to the mentum. The buccal n. proceeds medially along the occlusal plane of the dentition to the cheilion. The mental n. runs through the mental foramen and is distributed to the lower lip, which includes the cheilion and the mandible. The

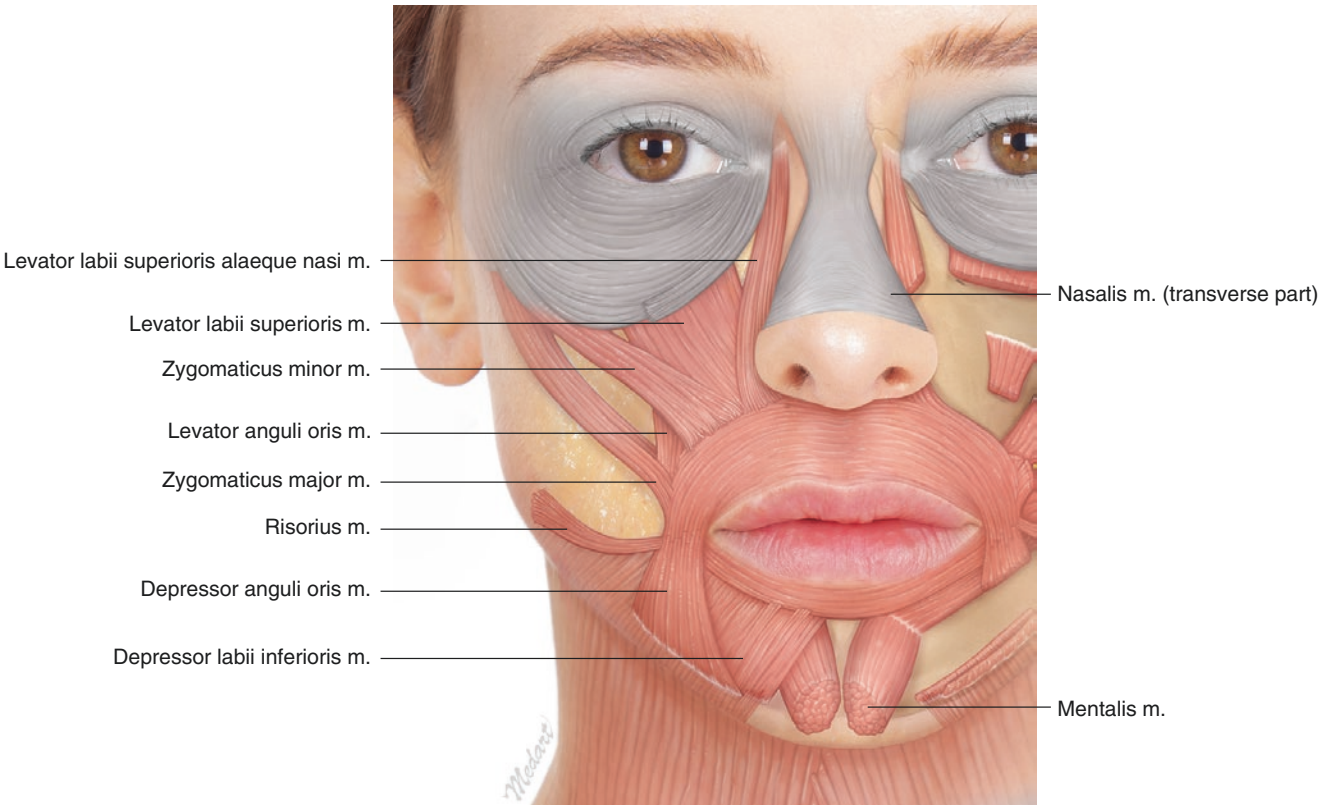

Fig. 6.5 Illustration of the muscles inserting into the upper and lower lip. (Published with kind permission of © Kwan-Hyun Youn 2020. All Rights Reserved)

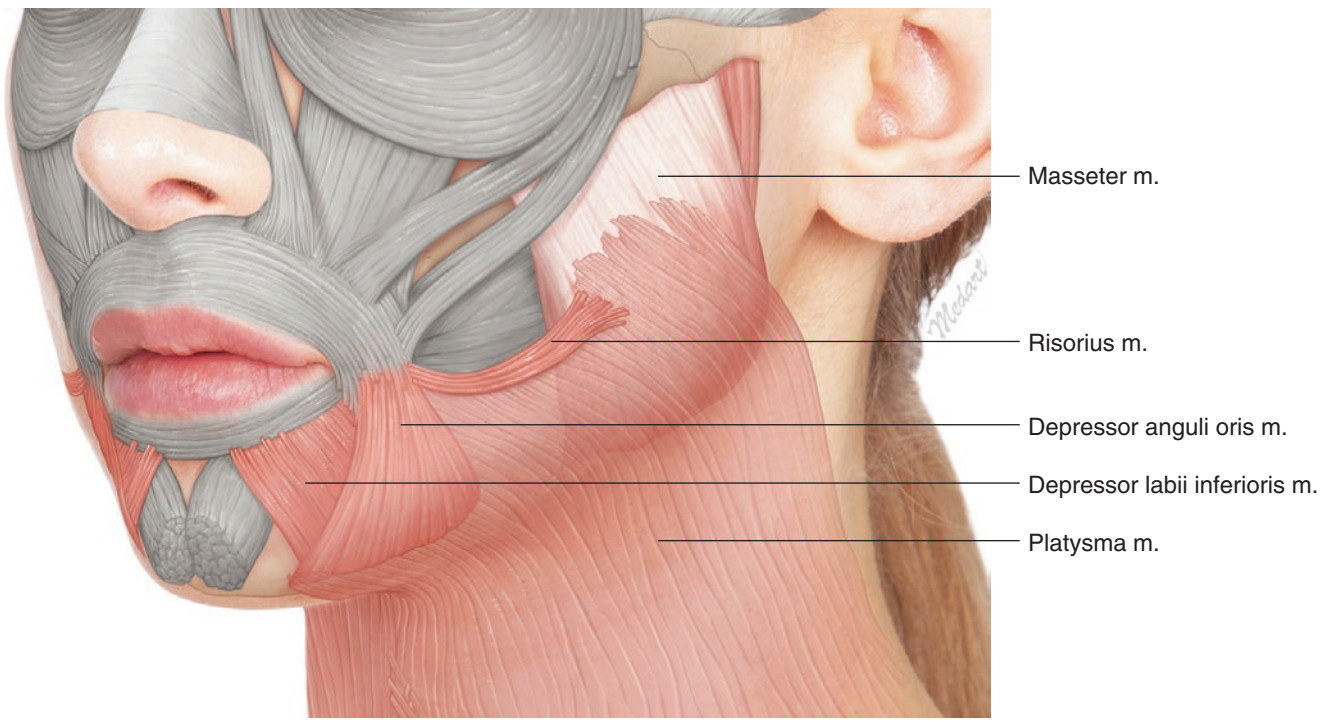

Fig. 6.6 Illustration of the platysma muscle and surrounding perioral musculature. (Published with kind permission of © Kwan-Hyun Youn 2020. All Rights Reserved)

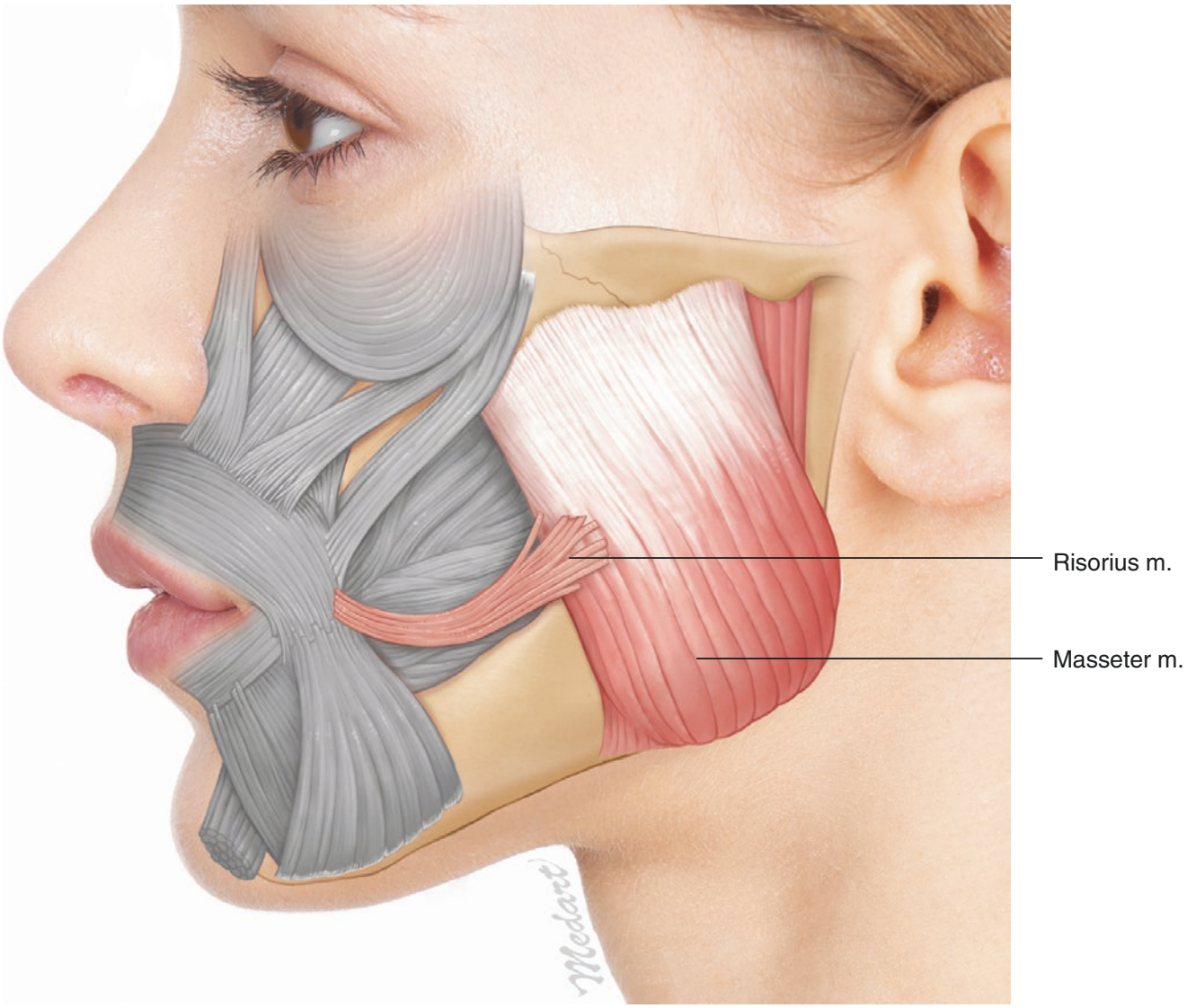

Fig. 6.7 Illustration of the masseter muscle. (Published with kind permission of © Kwan-Hyun Youn 2020. All Rights Reserved)

superior labial branch of the infraorbital n., the buccal n., and the angular branch of the mental n. distributes to the mouth corner. Furthermore, various nerve communications are formed between the infraorbital n. and the buccal n. and also between the buccal n. and the mental n. above and below the mouth corner, respectively (Fig. 6.10).

The motor impulse is conveyed by the marginal mandibular branch of the facial n. These nerves innervate the mentalis, the DAO, the DLI, and the inferior portion of the OOr mm. (Fig. 6.11).

Due to the high risk of complications during the minimally invasive procedures, understanding the vascular anatomy is necessary. The facial a. should be cautiously considered since embolization followed by the various procedures of the cheek, nasolabial folds, and lips may occur. The facial a. is a branch of the external carotid a. and has many branches to the perioral region after emerging at the antegonial notch in front of the masseter m. (Fig. 6.12). The facial a. passes forward and upward across the cheek to the mouth corner, where it gives rise to the inferior labial and the superior labial aa. At the level of the middle 1/3 of the DAO m., the inferior labial a. originates and runs deep to the DAO m. to supply the lower lip along the mental crease. The furcation area where the superior labial a. is branched off can be seen at approximately 1.5 cm superolateral to the corner of the mouth, at a depth of approximately 3–5 mm. The superior and inferior labial aa. form a circular vascular network around the mouth, with several small blood vessels branching out radially.

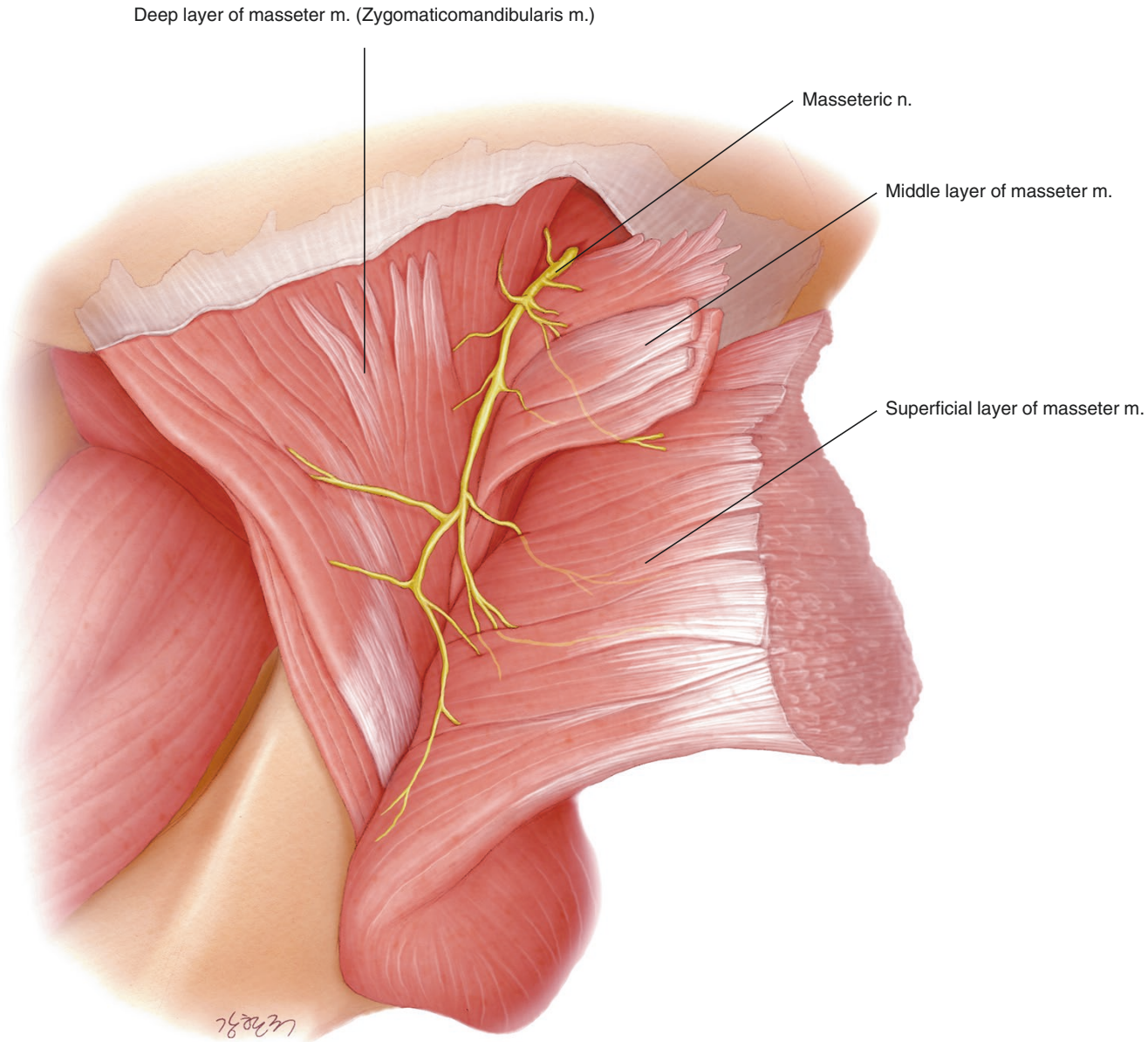

Fig. 6.8 Illustration of the three layers of the masseter muscle innervated by the masseteric nerve. (Published with kind permission of © Kwan-Hyun Youn 2020. All Rights Reserved)

The facial a. then continues along the mouth corner and the nasolabial fold. Generally, the facial a. is located deep to the SMAS, platysma, risorius, and ZMj and Zmi mm. However, there are many variations in the arterial depths. As the facial a. approaches the nose ala, it gives off the lateral nasal a. that supplies the ala and dorsum of the nose; at this point, the facial a. continues and becomes the angular a. (Fig. 6.13).

6.1.3 Lips

The "vermilion border" is the boundary that forms the lip's outer contour, between the skin and the intermediate zone (red portion). The "Cupid's bow" is the heart-shaped area in the middle of the upper lip, and the "philtrum" refers to the two vertical lines that connect the nose and lips. The "oral

Fig. 6.9 The layers of the perioral musculature (yellow first layer, green second layer, pink third layer, purple fourth layer). (Published with kind permission of © Kwan-Hyun Youn 2020. All Rights Reserved)

commissure" is the corner where the upper and lower lips meet (Fig. 6.14).

Lips consist of the outer skin and the inner mucosa portions with the middle red portion. The mucosa portion of the lip can be divided into the outer dry and inner wet mucosa, with the dry–wet mucosal junction between them. Underneath the mucosal layer, there are the OOr m., the superior and inferior labial aa., mental n., and labial glands (Fig. 6.15). Considering the vascular anatomy of lips, it is important to keep in mind the running patterns of the superior and inferior labial aa. and v. Most commonly, the superior and inferior labial aa. are located deep to the dry–wet mucosal junction and deep to the OOr m.

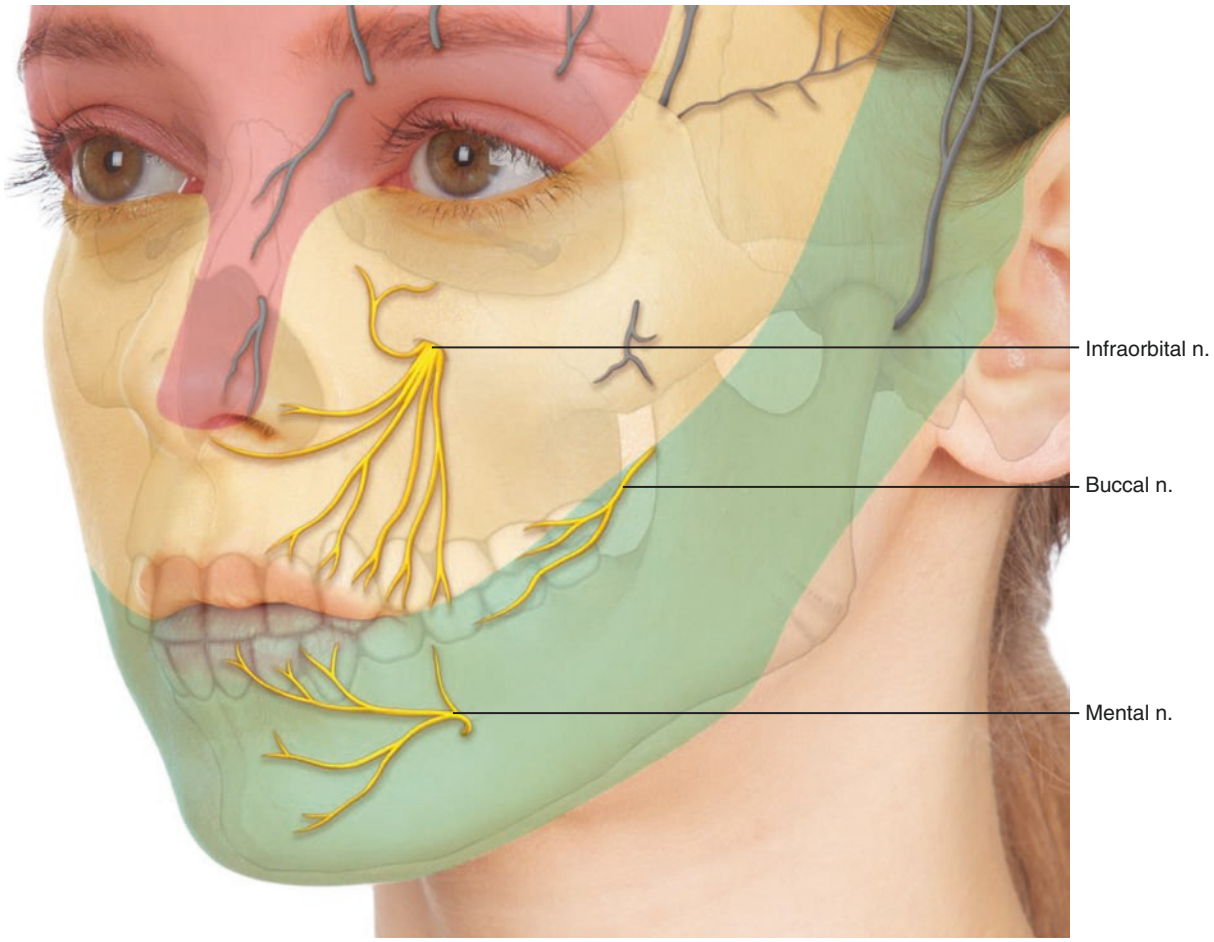

Fig. 6.10 Illustration of the sensory distribution of the perioral and masseter region. (Published with kind permission of © Kwan-Hyun Youn 2020. All Rights Reserved)

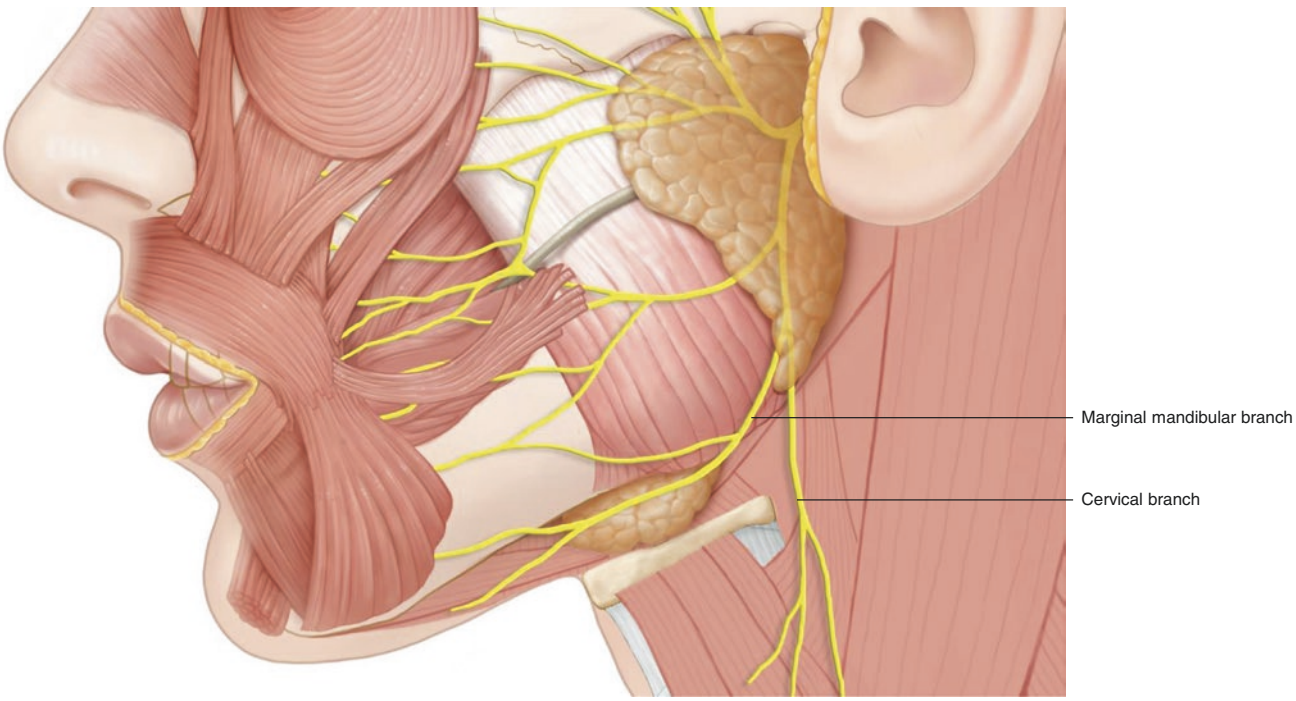

Fig. 6.11 Illustration of the motor distribution of the perioral and masseter region. (Published with kind permission of © Kwan-Hyun Youn 2020. All Rights Reserved)

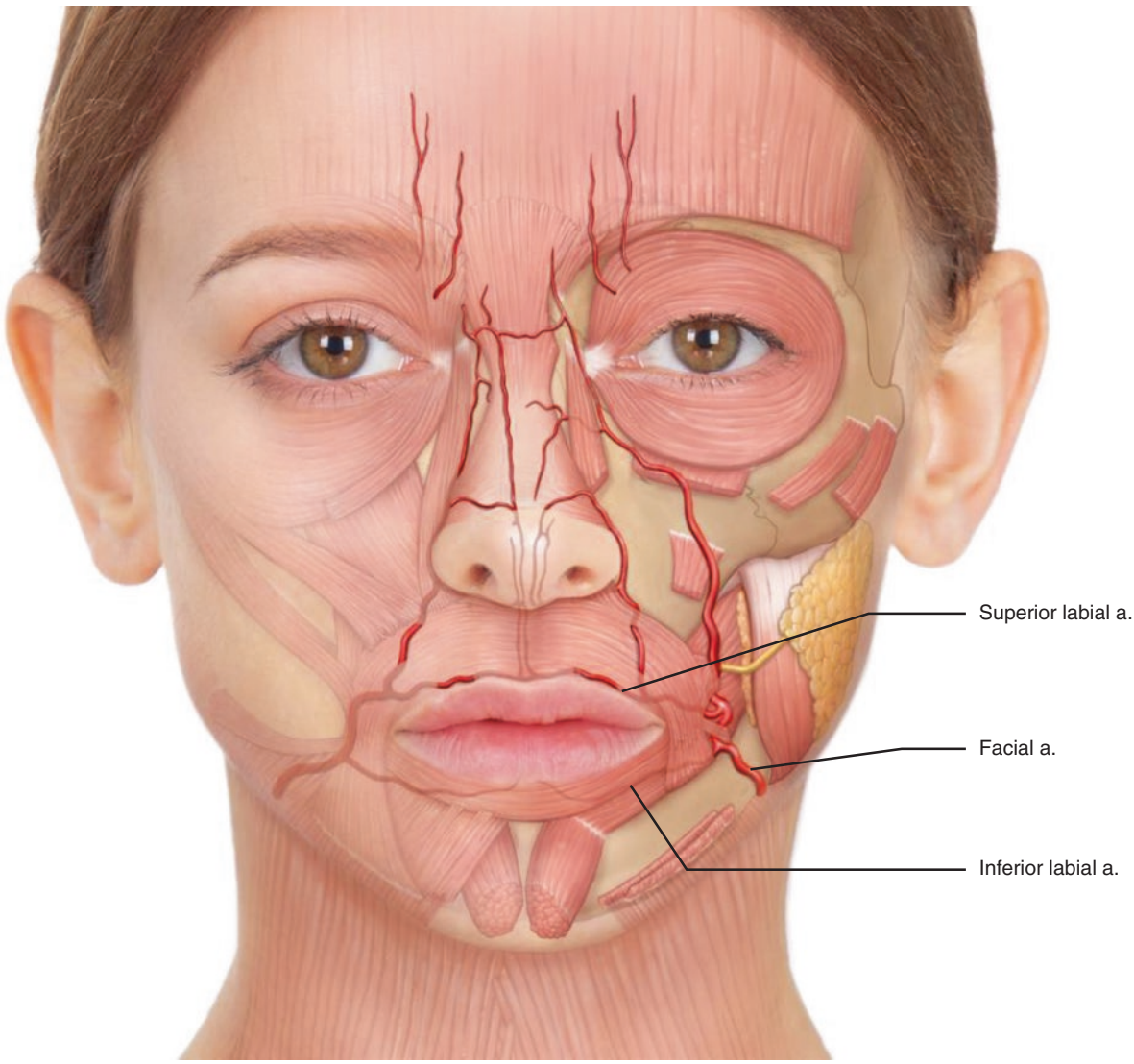

Fig. 6.12 Illustration of the perioral arterial distribution. (Published with kind permission of © Kwan-Hyun Youn 2020. All Rights Reserved)

Fig. 6.13 Topographic distribution of the superior and inferior labial arteries. (Published with kind permission of © Hee-Jin Kim 2020. All Rights Reserved)

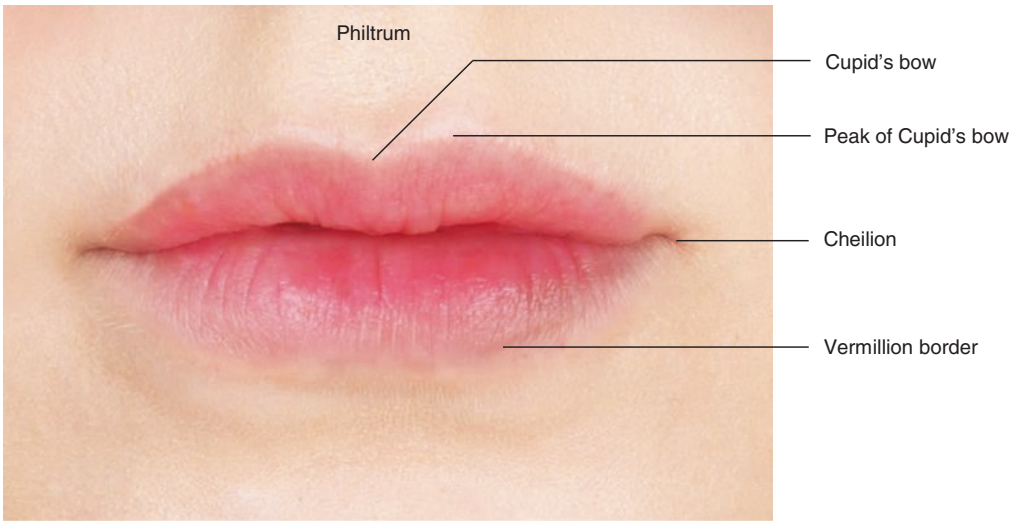

Fig. 6.14 Surface anatomy of the lip. (Published with kind permission of © Kwan-Hyun Youn 2020. All Rights Reserved)

6.1.4 Facial Landmarks and Reference Lines for the US Examination of the Perioral and Masseter Region (Fig. 6.16)

Perioral region and lip	
O1: midpoint between subnasale and lowest point of Cupid's bow (Ls1)	**Ls1**: intersection point of vermilion border of upper lip and ML
O2: midpoint between Li1 and gnathion	**Ls2–Ls3**: oblique line between Ls2 and Ls3
O3: Pogonion	**Ls1–Li1**: perpendicular line between Ls1 and Li1
O4: intersection point of TL6 and PL2	**Ls2**: point on the upper vermilion border passing the medial 1/3 between the ML and cheilion
O5: intersection point of TL6 and PL3	**Ls3**: point on the upper vermilion border passing the lateral 1/3 between the ML and cheilion
O6: point of 1.5 cm lateral to the cheilion	**Li1**: intersection point of vermilion border of lower lip and ML
O7: intersection point of TL7 and PL3	**Li2 - Li3**: oblique line between Li2 and Li3
O8: intersection point of TL8 and PL1 (DLI point)	**Li2**: point on the lower vermilion border passing the medial 1/3 between the ML and cheilion
O9: intersection point of TL8 and PL2 (DAO point)	**Li3**: point on the lower vermilion border passing the medial 1/3 between the ML and cheilion
O10: intersection point of TL8 and PL3	
O11: antegonial notch	

Masseter region	
Ma1: anterior margin of the masseter muscle	**Ma4**: upper 1/3 line of the masseter muscle perpendicular to Ma2
Ma2: mid-half line parallel to Ma1 and Ma3	**Ma5**: lower 1/3 line of the masseter muscle perpendicular to Ma2
Ma3: posterior margin of the masseter muscle	**Ma6**: Inferiormarginofthemasseter muscle perpendicular to Ma2

6.1.5 Checklists in Perioral and Masseter Region

Objective structures	Facial landmarks where the structures can be observed
Orbicularis oris m.	O1, O4, O6, O8, O9, Ls1, Ls2, Ls3, Li1, Li2, Li3
Zygomaticus major m.	O4
Depressor anguli oris m.	O6, O7, O8, O9
Depressor labii inferioris m.	O8, O9
Depressor septi nasi m.	O1
Risorius m.	O10
Buccinator m.	O6, O7
Mentalis m.	O2, O3

Objective structures	Facial landmarks where the structures can be observed
Platysma m.	O9, O10
Masseter m.	Ma1, Ma2, Ma3, Ma4, Ma5, Ma6
Facial a.	O4, O6, O7, O10, O11
Facial v.	Ma5, Ma6
Superior labial a.	Ls1, Ls2, Ls3
Inferior labial a.	Li1, Li2, Li3, O8, O9
Submental a.	O2, O3
Buccal fat pad	O6, O7, Ma4, Ma5

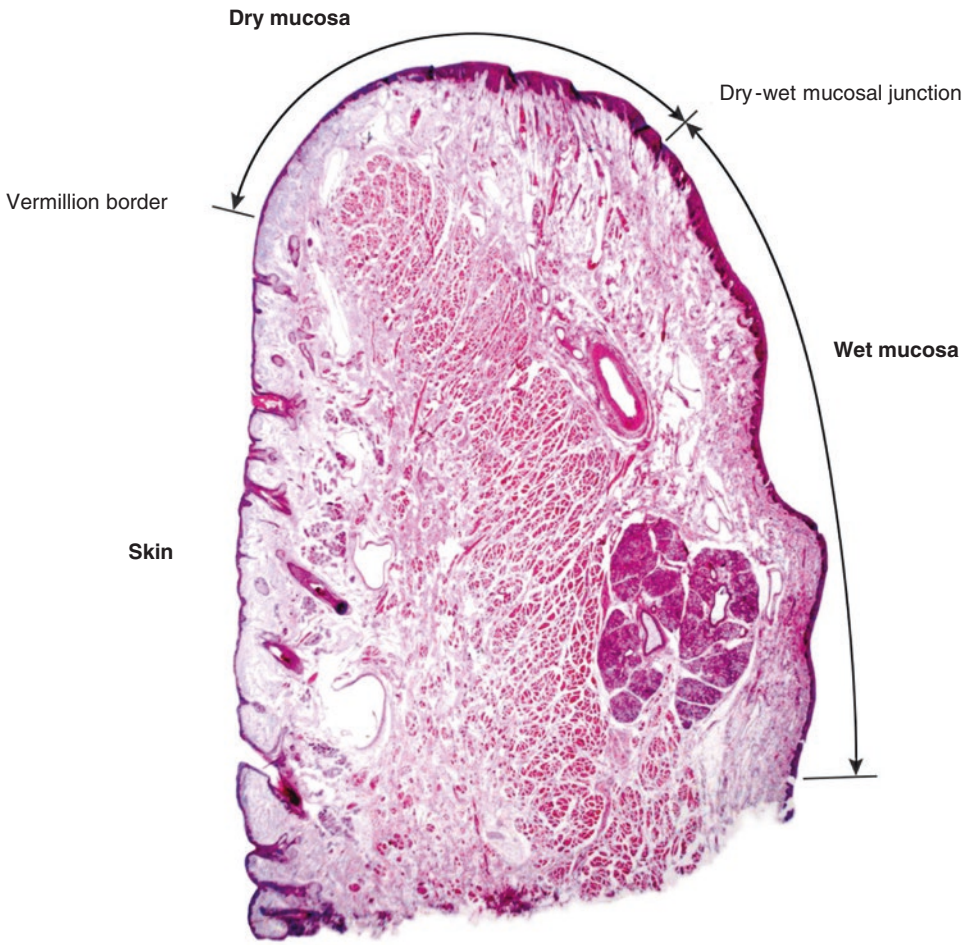

Fig. 6.15 Sagittal section of the lip. (Published with kind permission of © Hee-Jin Kim 2020. All Rights Reserved)

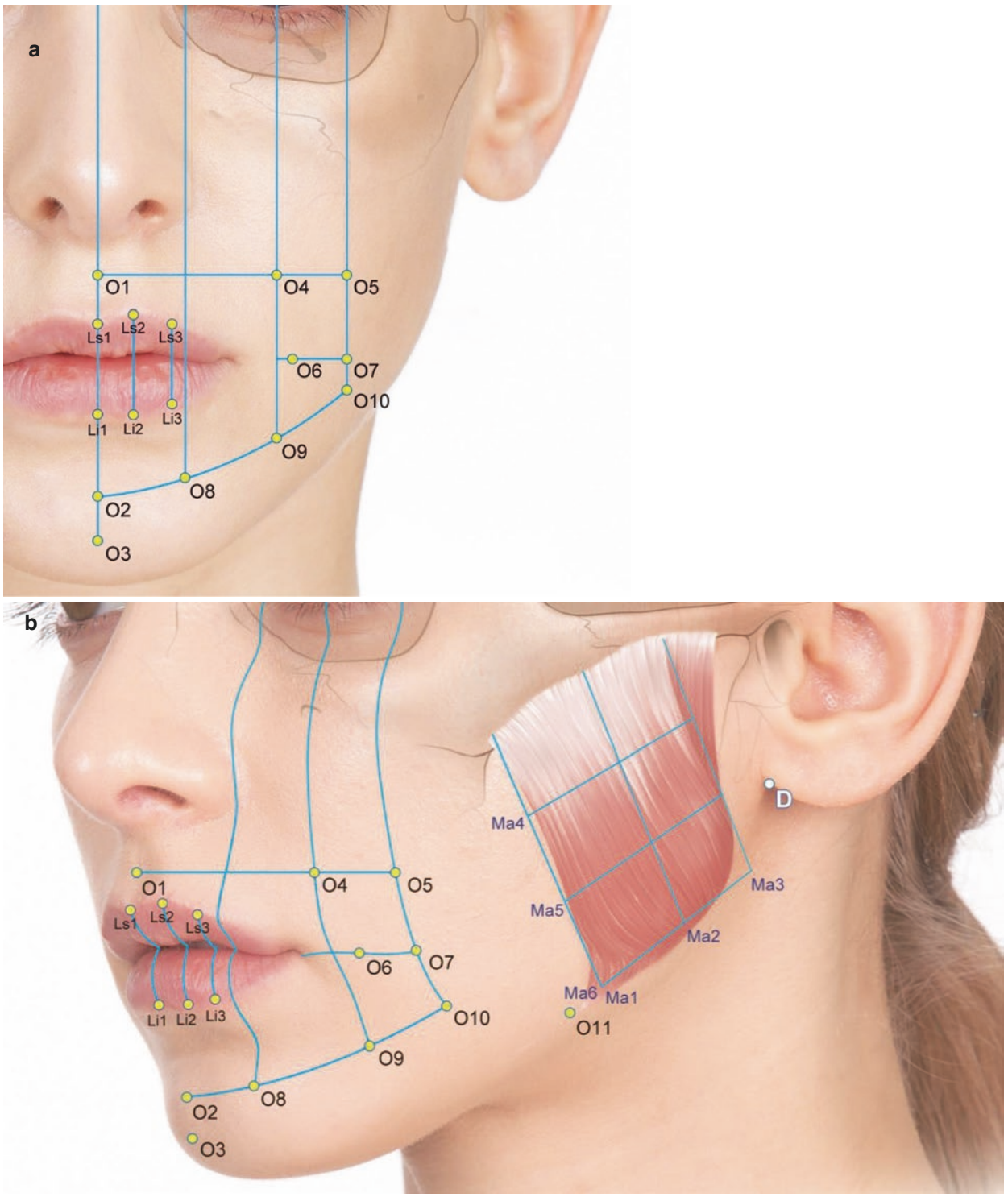

Fig. 6.16 Facial landmarks and reference lines for the ultrasonographic examination of the perioral and masseter region. (**a**) Frontal view and (**b**) oblique view. (Published with kind permission of © Kwan-Hyun Youn 2020. All Rights Reserved)

6.2 US Images of the Perioral and Masseter Region

6.2.1 US Anatomy Images

Compared with the other regions of the face, the perioral regions show a unique anatomical layered structure due to the presence of the oral cavity and cheek including (1) perioral facial muscles, (2) upper and lower lips with oral mucosa, (3) teeth and alveolar portion of the jaw, (4) maxilla and mandible, (5) chin, (6) masseter m., and (7) parotid gland.

The general mean thickness of the perioral skin and the superficial fat tends to be the thicker among the perioral regions (1.82 ± 0.83 mm and 5.14 ± 3.31 mm, respectively). In perioral regions excluding the lips, the skin thickness was relatively uniform, ranging from 1.40 to 2.10 mm, whereas the superficial fat thickness varied markedly relative to the regions. The superficial fat tends to be the thinnest at the point lateral to the cheilion (1.71 mm) and thickest at the point lateral to the nasolabial fold (8.17 mm). Based on the location of the nasolabial fold, the superficial fat becomes clearly thicker in the lateral perioral region (6.62–8.17 mm) than in the medial perioral region (1.71–3.98 mm).

In the cheek region, the mean superficial fat thickness of the anterior cheek is about 4.98 mm (range 3.74–6.30 mm) while the posterior cheek covering the masseter muscle tends to become thinner averaging 4.17 mm (range 3.58–4.91 mm). The detailed US anatomy for each region will be described (Figs. 6.17, 6.18, 6.19, 6.20, 6.21, and 6.22).

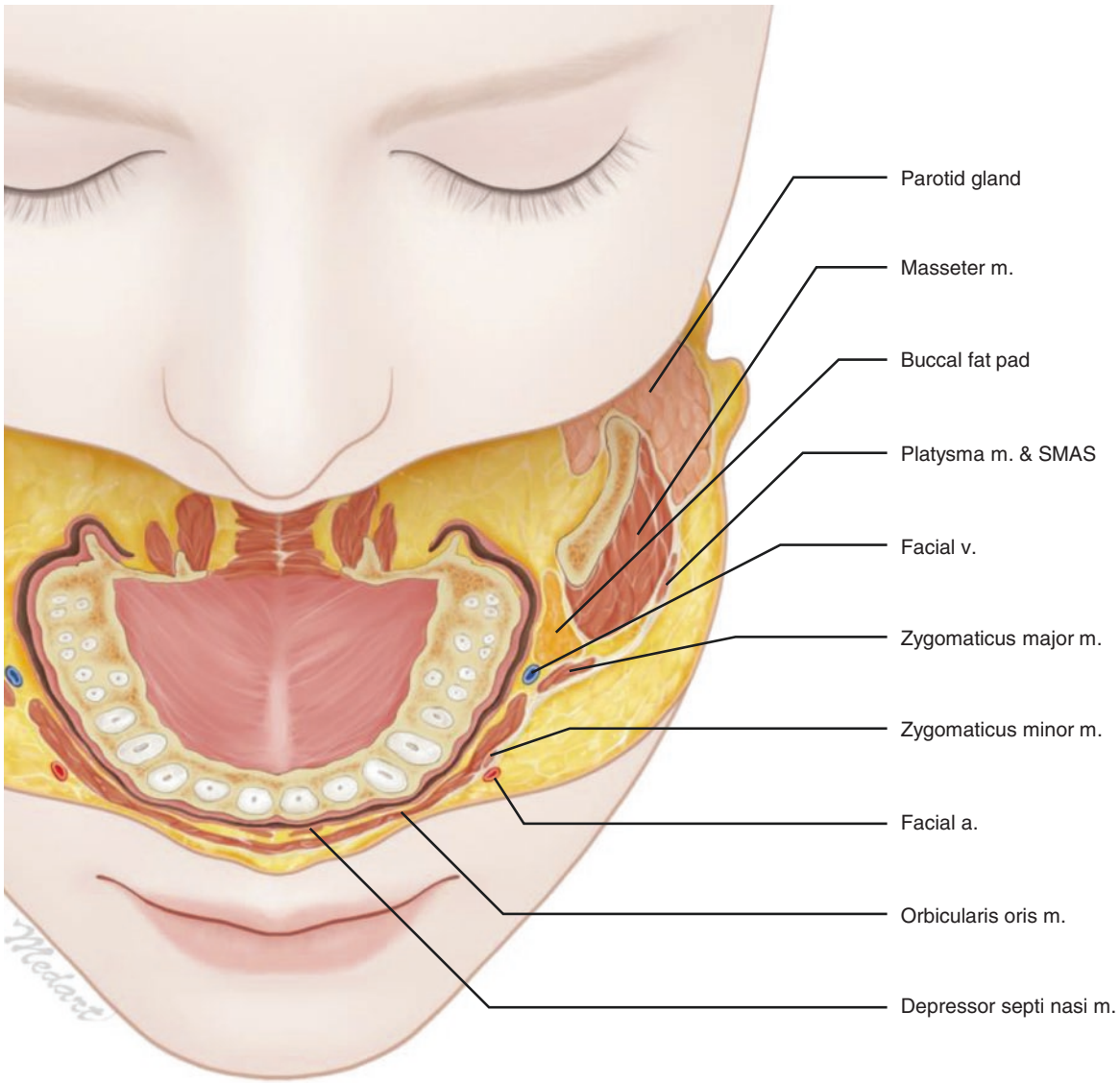

Fig. 6.17 Illustration representing the transverse section of the lower face passing the TL6. (Published with kind permission of © Kwan-Hyun Youn 2020. All Rights Reserved)

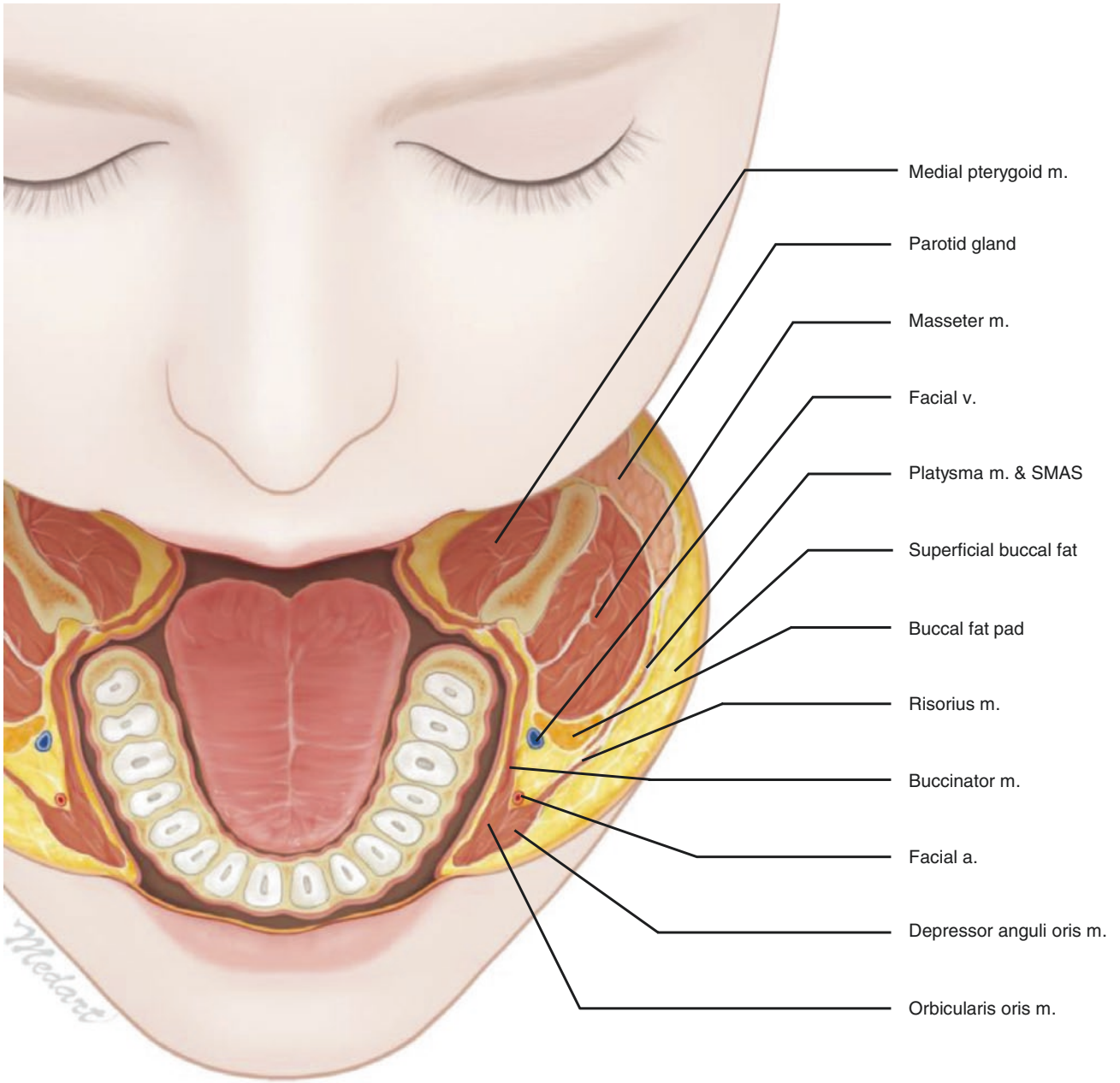

Fig. 6.18 Illustration representing the transverse section of the lower face passing the TL7. (Published with kind permission of © Kwan-Hyun Youn 2020. All Rights Reserved)

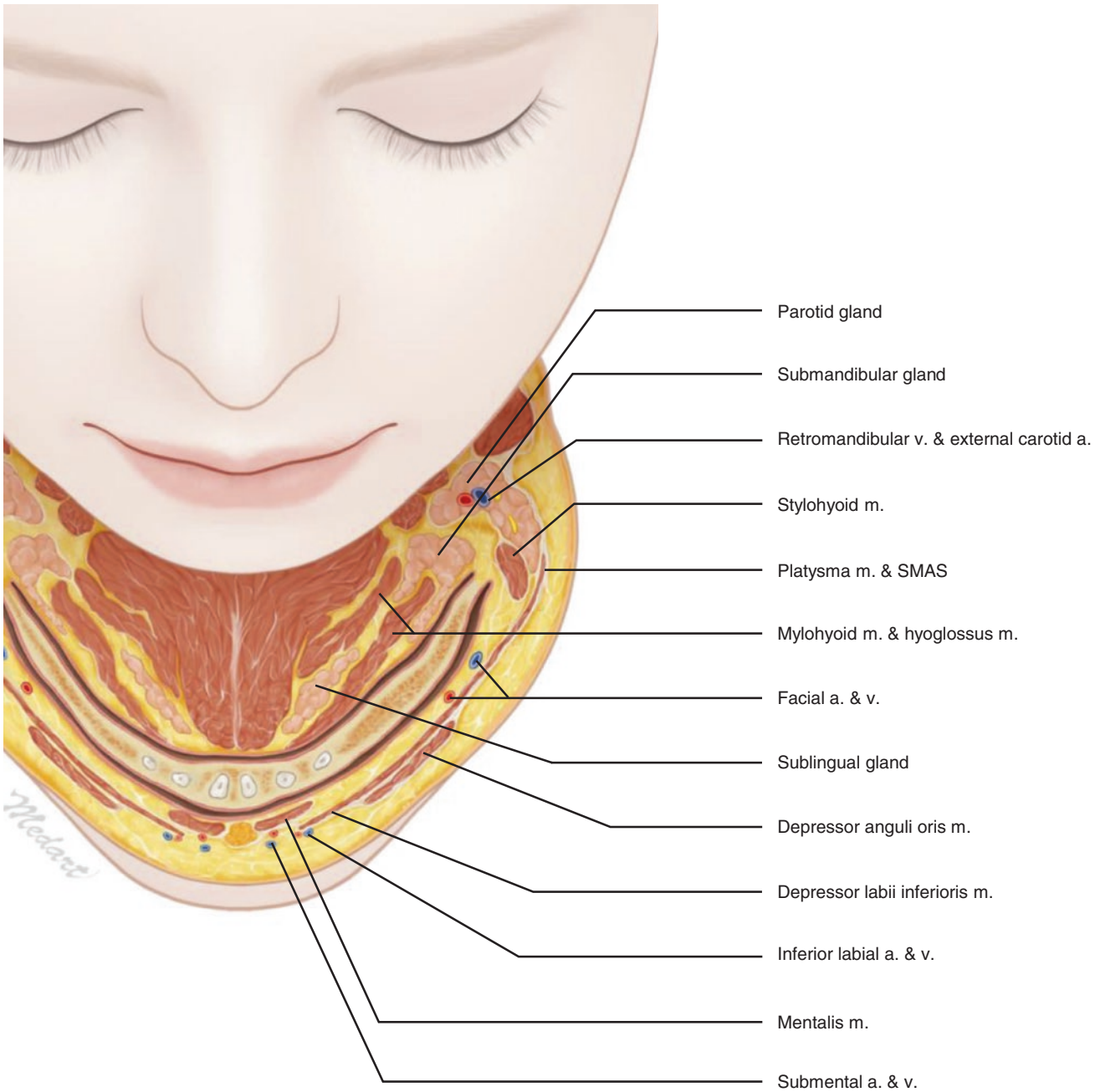

Fig. 6.19 Illustration representing the transverse section of the lower face passing the TL8. (Published with kind permission of © Kwan-Hyun Youn 2020. All Rights Reserved)

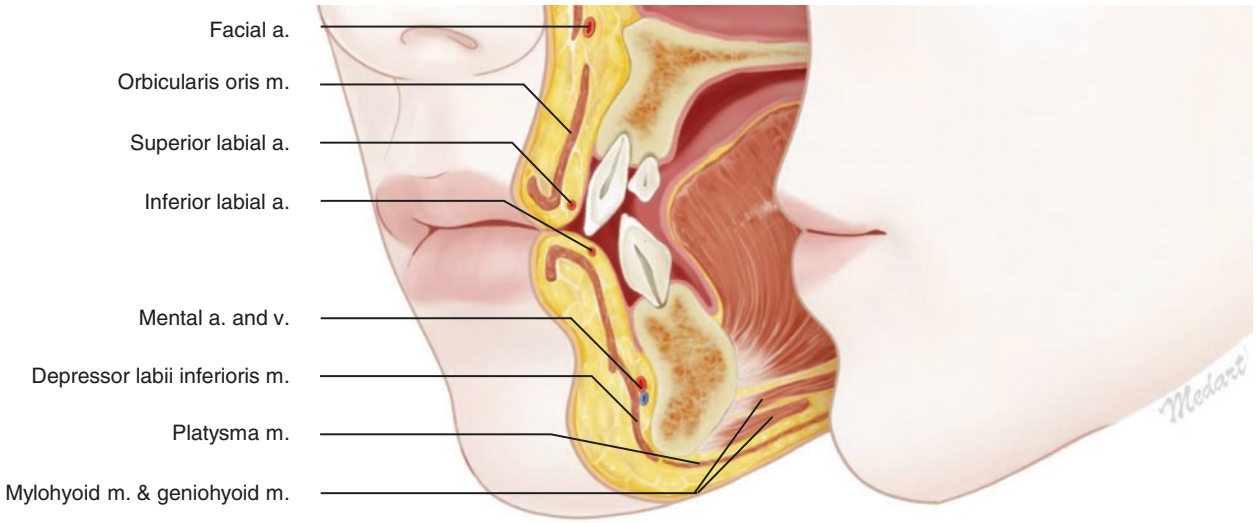

Fig. 6.20 Illustration representing the sagittal section of the lower face passing the PL1 (medial canthus). (Published with kind permission of © Kwan-Hyun Youn 2020. All Rights Reserved)

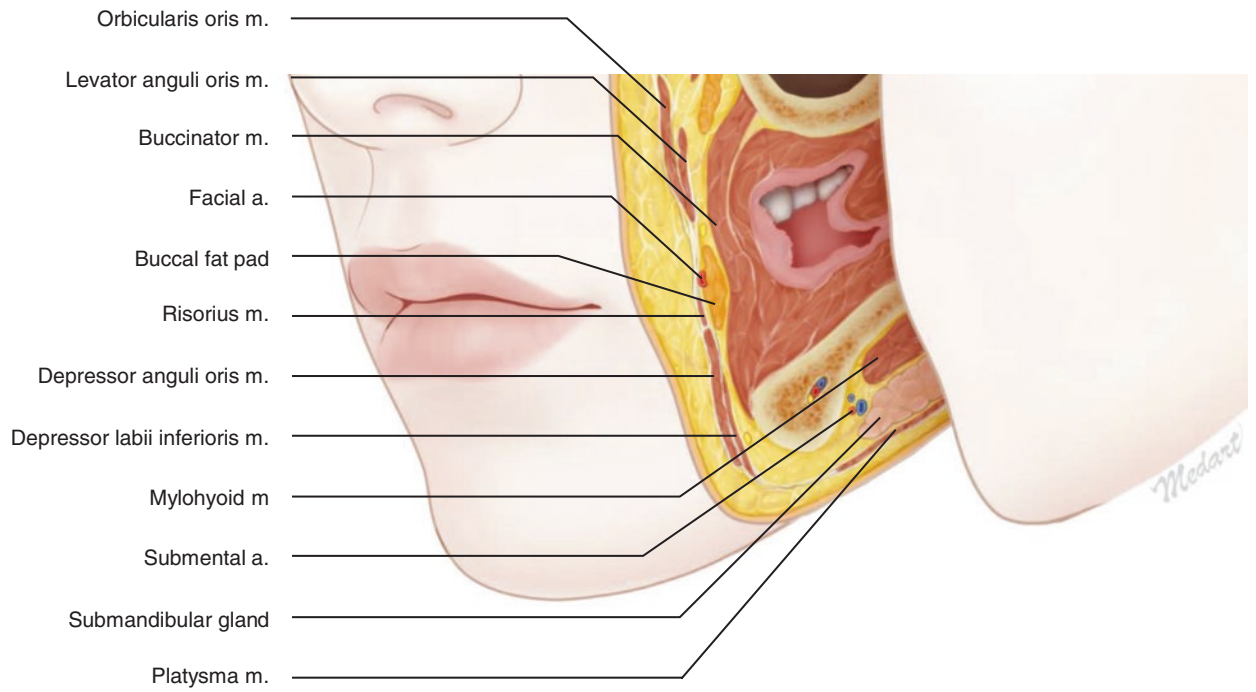

Fig. 6.21 Illustration representing the sagittal section of the lower face passing the PL2 (midpupil). (Published with kind permission of © Kwan-Hyun Youn 2020. All Rights Reserved)

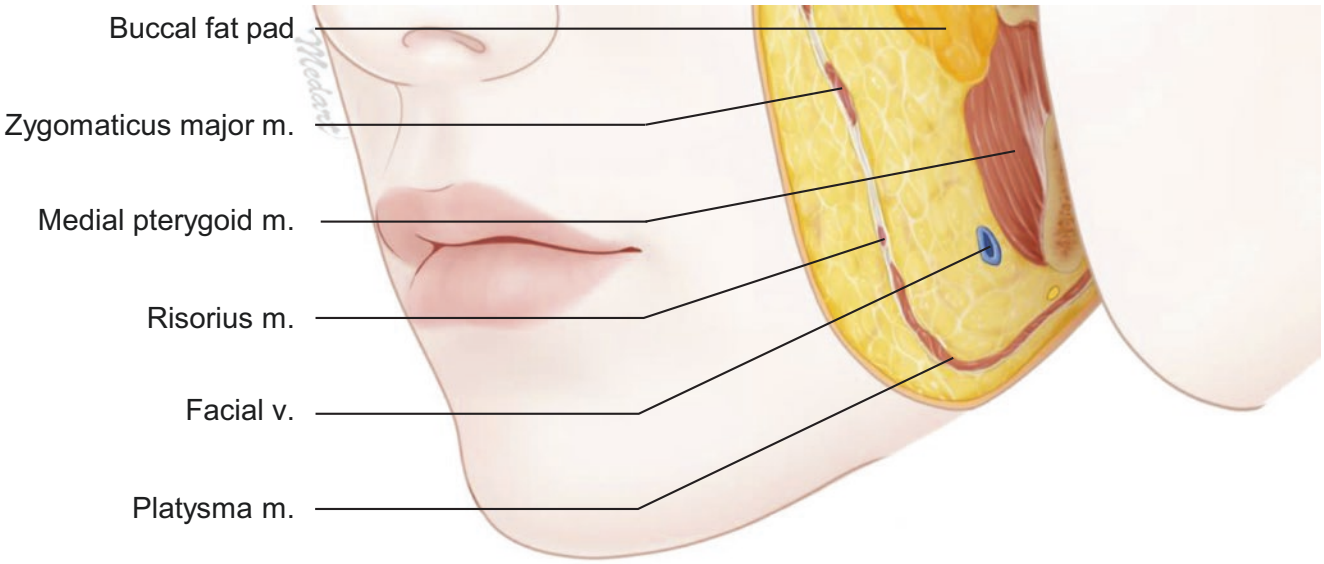

Fig. 6.22 Illustration representing the sagittal section of the lower face passing the PL3 (lateral canthus). (Published with kind permission of © Kwan-Hyun Youn 2020. All Rights Reserved)

6.2.2 B Mode and Doppler Images

6.2.2.1 Perioral Region Including the Cheek and Premasseteric Area

O1: Midpoint Between Subnasale and Lowest Point of Cupid's Bow (Ls1)

At the point of the middle of the philtrum, the groove is clearly observed on the epidermis (hyperechoic line). The broad hypoechoic image represents the OOr m. underneath the irregular hyperechoic subcutaneous fat layer. Sometimes, the depressor septi nasi m. exists deep to the OOr m. layer of this area; however, it is very difficult to distinguish these two muscles by the US image because the depressor septi nasi m. fibers join and blend with the OOr m. fibers. Deep to the OOr m., thin hyperechoic oral mucosa and submucosa are seen and the maxillary central and lateral incisor are shown as a discontinuous hyperechoic line. The Doppler mode image demonstrates the bilateral columellar branches from the superior labial a. traveling to the surface of the OOr m. The small vessel in the midline can also be identified as one of the columellar branches (Fig. 6.23).

O2: Midpoint Between Li1 and Gnathion

Point O2 is the midpoint between the lower lip and the mandibular border on the midsagittal line. This point has a relatively thicker hyperechoic skin and subcutaneous layer compared to other perioral regions. The mentalis m. is observed as an irregular hypoechoic image. The DLI m. is partially observed at both lateral sides of the mentalis m. The Doppler mode image demonstrates the cutaneous branches originating from the inferior labial or submental a. within the hyperechoic subcutaneous layer (Fig. 6.24). A detection of a branch of the submental a. can be traced by moving the transducer from the mandibular border to the mentum.

O3: Pogonion

At the most projecting point of the chin on the midsagittal plane, the tissue layers are defined as the hyperechoic band of the skin, an irregular subcutaneous tissue, the hypoechoic mentalis m., and hyperechoic mandibular surface (pogonion point). Since the layers that compose the chin are not strictly aligned, a three-dimensional approach to its anatomical composition is highly recommended. The mentalis m. is seen

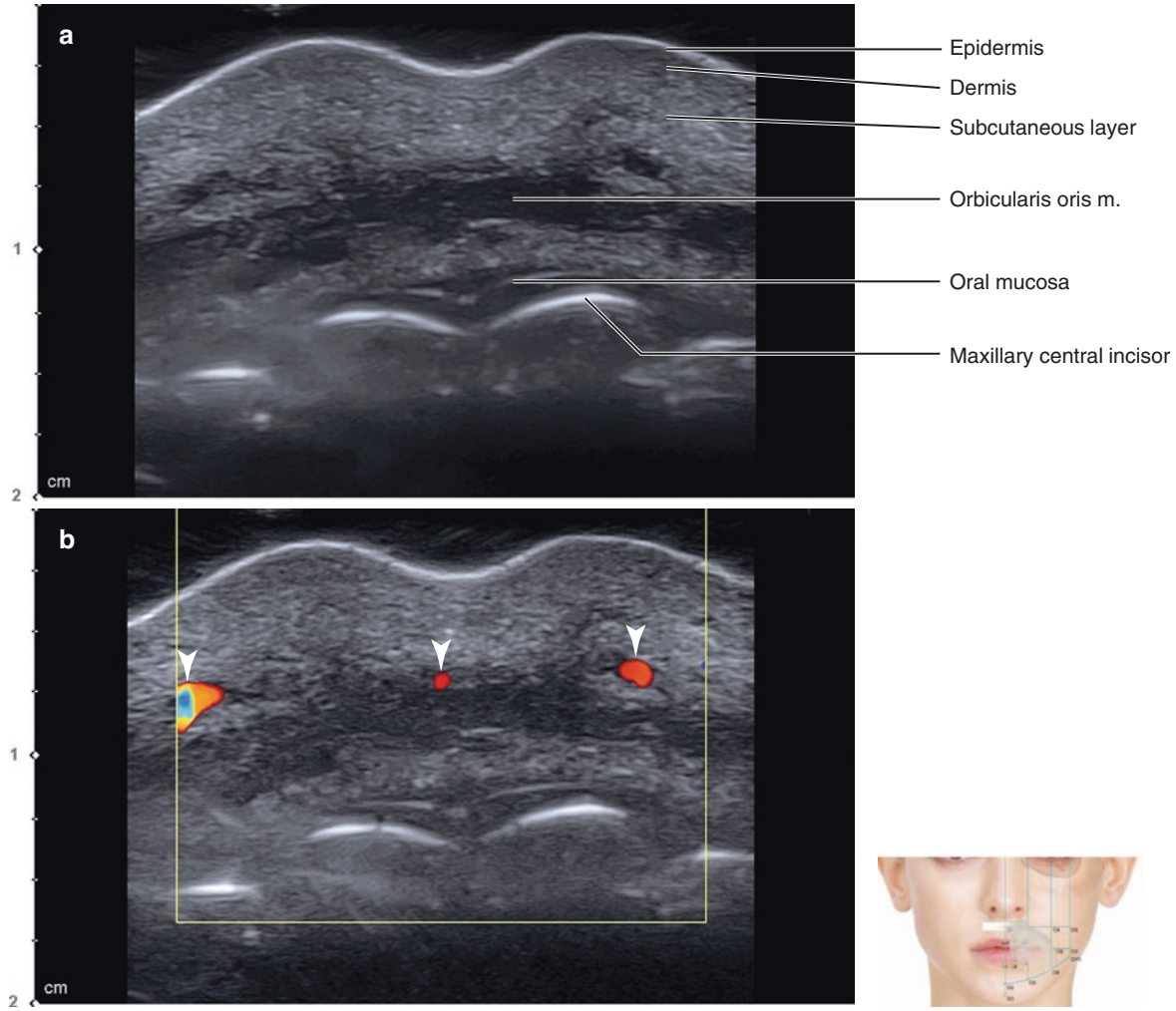

Fig. 6.23 Ultrasonography on the midpoint between subnasale and lowest point of Cupid's bow (O1). (**a**) B mode (transverse view, 15 MHz by linear transducer) and (**b**) Doppler mode (transverse view, 15 MHz by linear transducer) (arrowheads: columellar branches). (Published with kind permission of © Hee-Jin Kim 2020. All Rights Reserved)

more broadly at this point than the point O2. Due to the cutaneous insertion by the mentalis m. in this area, the boundary between the subcutaneous layer and mentalis m. is not clearly observed, and an irregular hypoechoic image from the mentalis m. is observed within the subcutaneous layer. Above the hyperechoic mandibular surface, the irregular hyperechoic deep areolar tissues are shown within the dome-shaped space created by the mentalis m. The Doppler mode image demonstrates the vascular components from the submental a., which can be observed within the subcutaneous layer (Fig. 6.25).

O4: Intersection Point of TL6 and PL2

This point corresponds to the midpoint of the nasolabial fold, which shows a relatively thicker skin and abundant hyperechoic subcutaneous fat tissues. The nasolabial fold is apparently observed in the middle of the image. In reference to the nasolabial fold, the amount of subcutaneous tissues at the medial and lateral aspects is different. Significantly, abundant hypoechoic fat tissues are observed on the lateral aspect of the nasolabial fold. Medial to the nasolabial fold, the hypoechoic OOr m. is observed deep to the subcutaneous layer. The hyperechoic band of the

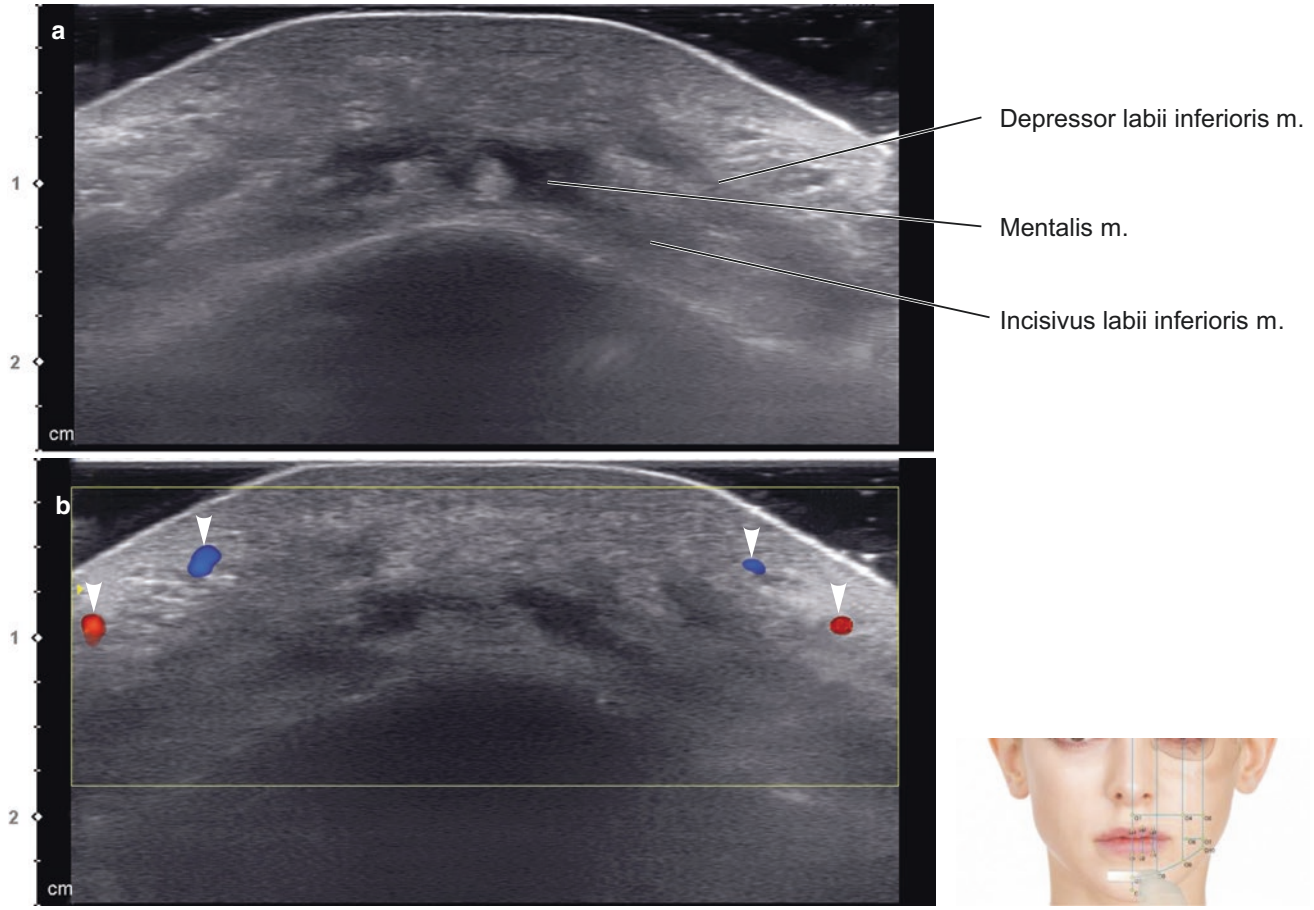

Fig. 6.24 Ultrasonography on the midpoint between Li1 and gnathion (O2). (**a**) B mode (transverse view, 15 MHz by linear transducer) and (**b**) Doppler mode (transverse view, 15 MHz by linear transducer) (arrowheads: cutaneous branches). (Published with kind permission of © Hee-Jin Kim 2020. All Rights Reserved)

oral mucosa and the surface of the maxillary alveolar bone are shown. Lateral to the nasolabial fold, the thick hypoechoic upper lip elevators including the LLS and Zmi mm. are observed.

Medial to the nasolabial fold, anechoic blood vessels are seen, and the artery on the nasolabial fold within the subcutaneous layer is identified from the Doppler mode image. The facial a. is located near the nasolabial fold (within 5 mm range in 43% of Asian cases). In addition, the facial a. on the nasolabial fold is shown within the subcutaneous layer in about 68.5% of the cases. Therefore, the use of the Doppler mode image is very useful in identifying the facial a. prior to performing the nasolabial fold augmentation procedures (Fig. 6.26).

O5: Intersection Point of TL6 and PL3

At the point of the upper anterior cheek, a thick hyperechoic epidermis and dermis layers are clearly distinguished. Deep to the irregular hyperechoic subcutaneous fat layer, the hypoechoic ZMj m. and the irregular hyperechoic buccal fat pad are observed. Deep to the buccal fat pad, the buccinator m. is located above the hyperechoic maxillary alveolar bone. The upper anterior part of the masseter m. can be seen at the lateral aspect of this image (Fig. 6.27).

O6: Point of 1.5 cm Lateral to the Cheilion

At the point lateral to the cheilion, a relatively thinner skin and subcutaneous layer are observed. From the transverse view, the OOr m. and modiolus with insertion of the ZMj m. and buccinator m. are clearly shown. Deep to the buccinator m., anechoic space of the oral vestibule with hyperechoic oral mucosa components are seen. Intermittent hyperechoic bands of the maxillary teeth are shown in the oral cavity. The buccal fat pad is a relatively dense and hyperechoic tissue

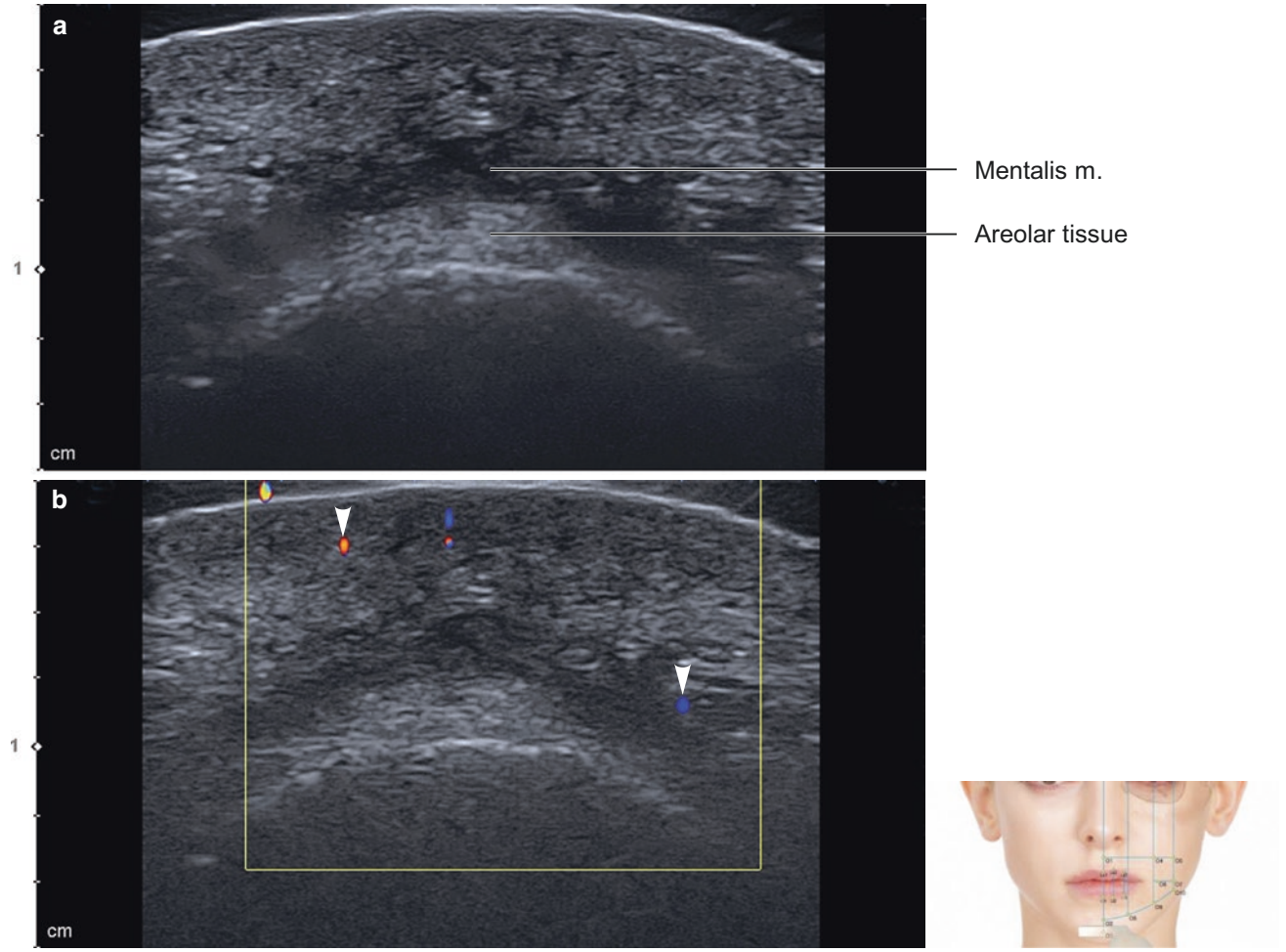

Fig. 6.25 Ultrasonography of the pogonion (O3). (**a**) B mode (transverse view, 15 MHz by linear transducer) and (**b**) Doppler mode (transverse view, 15 MHz by linear transducer) (arrowheads: cutaneous branches). (Published with kind permission of © Hee-Jin Kim 2020. All Rights Reserved)

that is observed deep to the ZMj m. and above the buccinator m. at the lateral aspect of this image.

The Doppler mode image at this point demonstrates the exposed segment (ES) of the facial a. just lateral to the modiolus that is clearly identified within the subcutaneous layer. The ES of the facial a. can be observed in 82% of cases and locates 7.6 mm deep to the facial skin and 20–25 mm lateral to the cheilion. Understanding the location of the ES is necessary for selecting safe areas in various treatments such as botulinum toxin and filler injections, face lifting, skin flaps, and thread lifting. A blunt cannula should be used when injecting into this region, and it should be inserted slowly while considering the location and depth of the ES of the facial a. (Fig. 6.28).

O7: Intersection Point of TL7 and PL3

This point is located lateral to the ES of the facial a. on the plane between the cheilion and the otobasion inferius. Under the thick hyperechoic epidermis and dermis, abundant irregular subcutaneous fat tissues are clearly observed. Similar to the image at point O6, the hypoechoic ZMj and buccinator mm. are seen at the medial aspect, and the anterior margin of the masseter m. can be observed at the lateral aspect. Between the perioral and masseter mm., a well-encapsulated hyperechoic buccal fat pad is observed underneath the subcutaneous layer. The Doppler mode image demonstrates the ES of the facial a. distinctively with color. The mandibular teeth and alveolar bone can be seen deep to the soft tissues (Fig. 6.29).

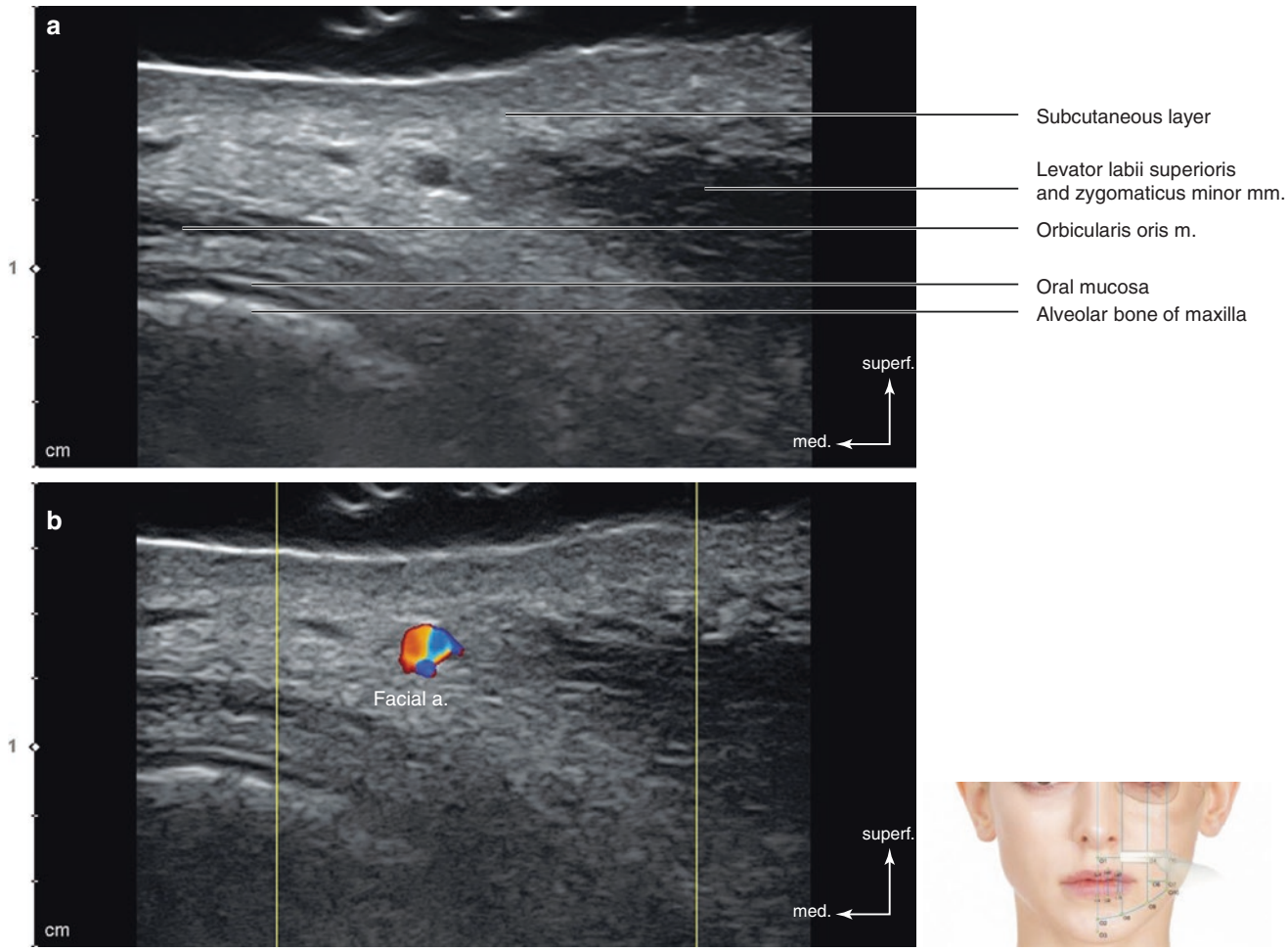

Fig. 6.26 Ultrasonography of the intersection point of TL6 and PL2 (O4). (**a**) B mode (transverse view, 15 MHz by linear transducer) and (**b**) Doppler mode (transverse view, 15 MHz by linear transducer). (Published with kind permission of © Hee-Jin Kim 2020. All Rights Reserved)

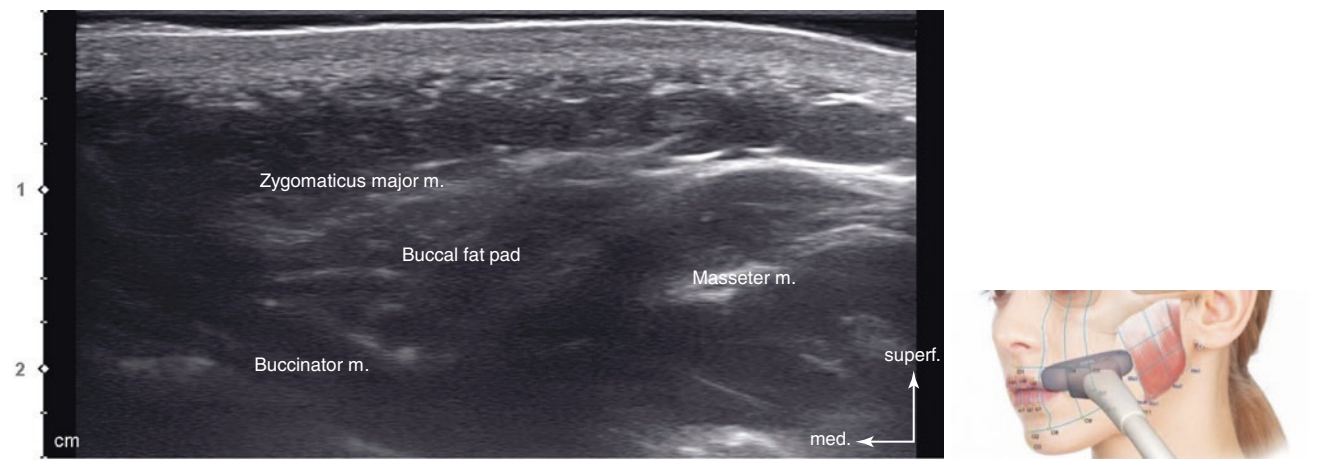

Fig. 6.27 Ultrasonography of the intersection point of TL6 and PL3 (O5). B mode (transverse view, 15 MHz by linear transducer). (Published with kind permission of © Hee-Jin Kim 2020. All Rights Reserved)

O8: Intersection Point of TL8 and PL1 (DLI Point)

The layers of the perioral m. are clearly distinguishable at this point underneath the thick hyperechoic skin and subcutaneous layer. At the medial aspect of the transverse US image, the mentalis m. originating from the mandible and inserting into the dermis is observed. The linear hypoechoic image of the mandible is observed just lateral to the origin of the mentalis m. Superficial to the mandible, the incisivus labii inferioris m. lies and joins with the mentalis m. This muscle originates from the posterior mandibular region and is covered by the fibers of DLI m. The DLI m. shows irregular hypoechoic images superficial to the incisivus labii inferioris m. Because some fat tissue exists between the DLI and the incisivus labii inferioris mm., these muscles can be observed as a more hyperechoic image compared to the muscular layer. The DAO m. exists lateral and superficial to the DLI m. The anterior margin of the DAO m. can be seen as the hypoechoic image overlapped with the DLI m. The Doppler mode image demonstrates the inferior labial a. horizontally running, deep to the DAO m. (Fig. 6.30).

O9: Intersection Point of TL8 and PL2 (DAO Point)

The O9 is the point located 1.5 cm lateral to the point O8. The transverse view of the point shows similar layered patterns as the point O8. Major hypoechoic image of the DAO and the DLI mm. can be observed. Similar to the point O8, the mentalis m. (most medial hypoechoic shadow) and the incisivus labii inferioris m. (linear hypoechoic image just lateral to the mentalis m. and superficial to the mandible) are seen at the medial aspect of the image. Deep to the DAO m., some fat tissue is observed as a hyperechoic image, and the inferior labial a. is traveling toward the lower lip (Fig. 6.31).

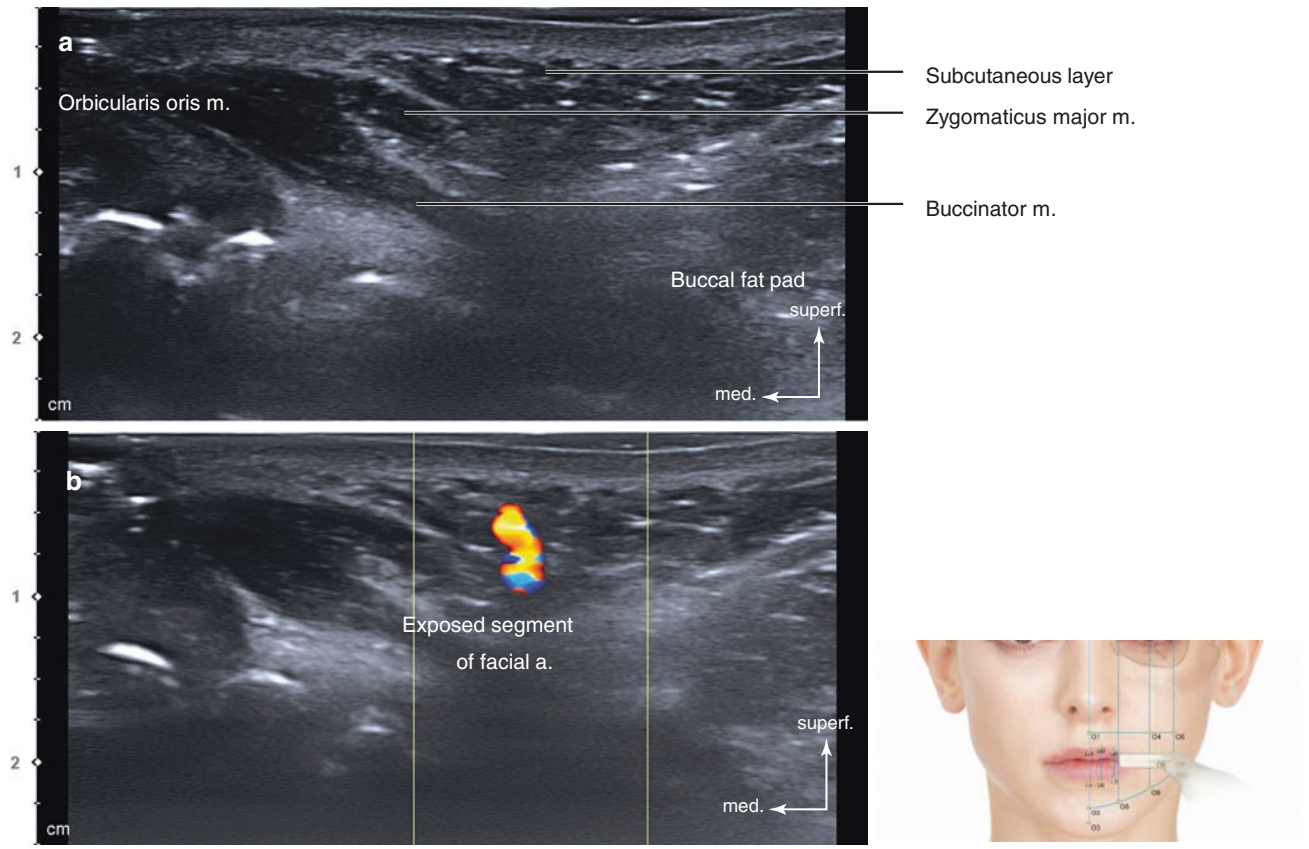

Fig. 6.28 Ultrasonography of the point at 1.5 cm lateral to the cheilion (O6). (**a**) B mode (transverse view, 15 MHz by linear transducer), (**b**) Doppler mode (transverse view, 15 MHz by linear transducer), (**c**) B mode (sagittal view, 15 MHz by linear transducer), and (**d**) Doppler mode (sagittal view, 15 MHz by linear transducer). (Published with kind permission of © Hee-Jin Kim 2020. All Rights Reserved)

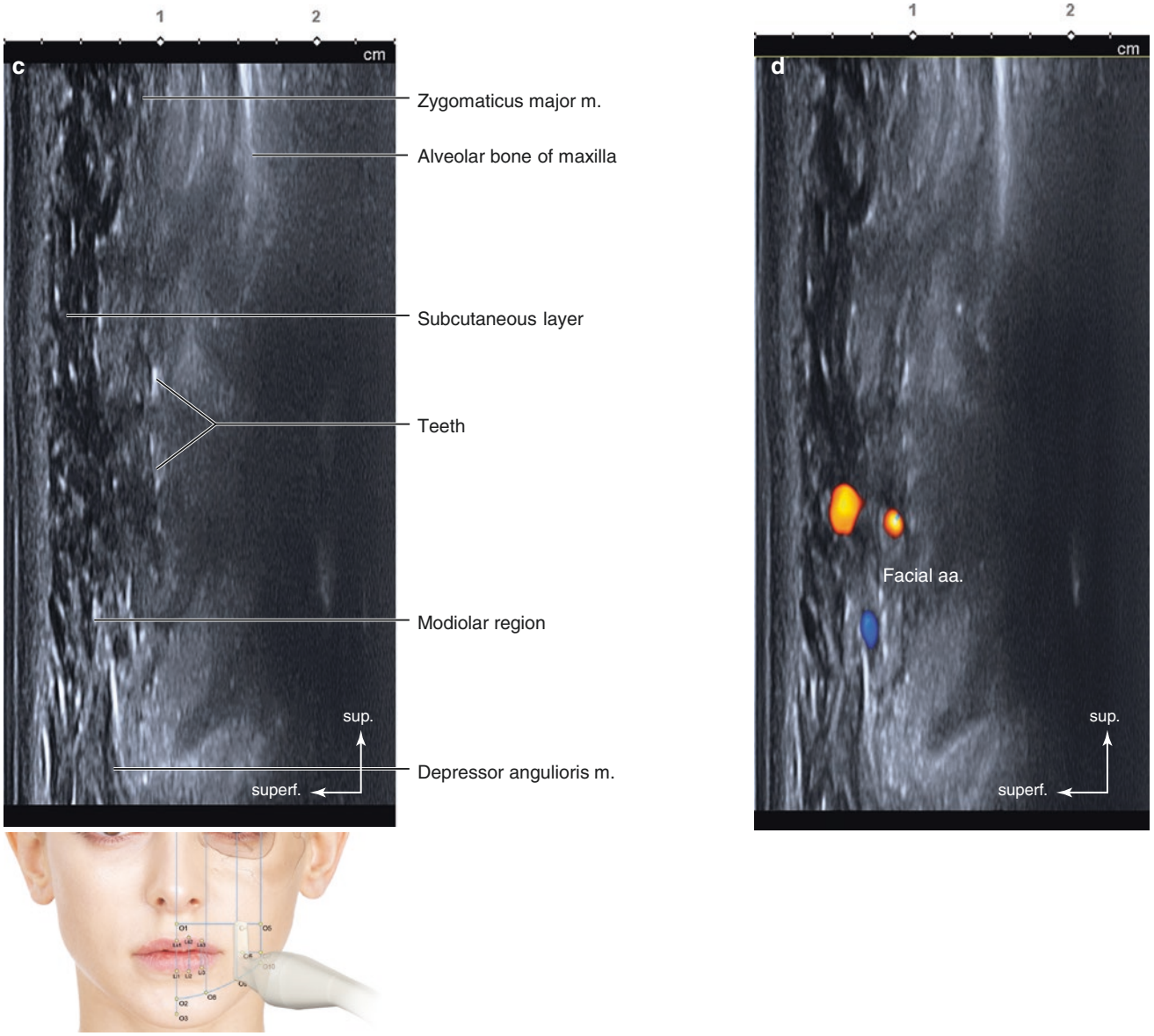

Fig. 6.28 (continued)

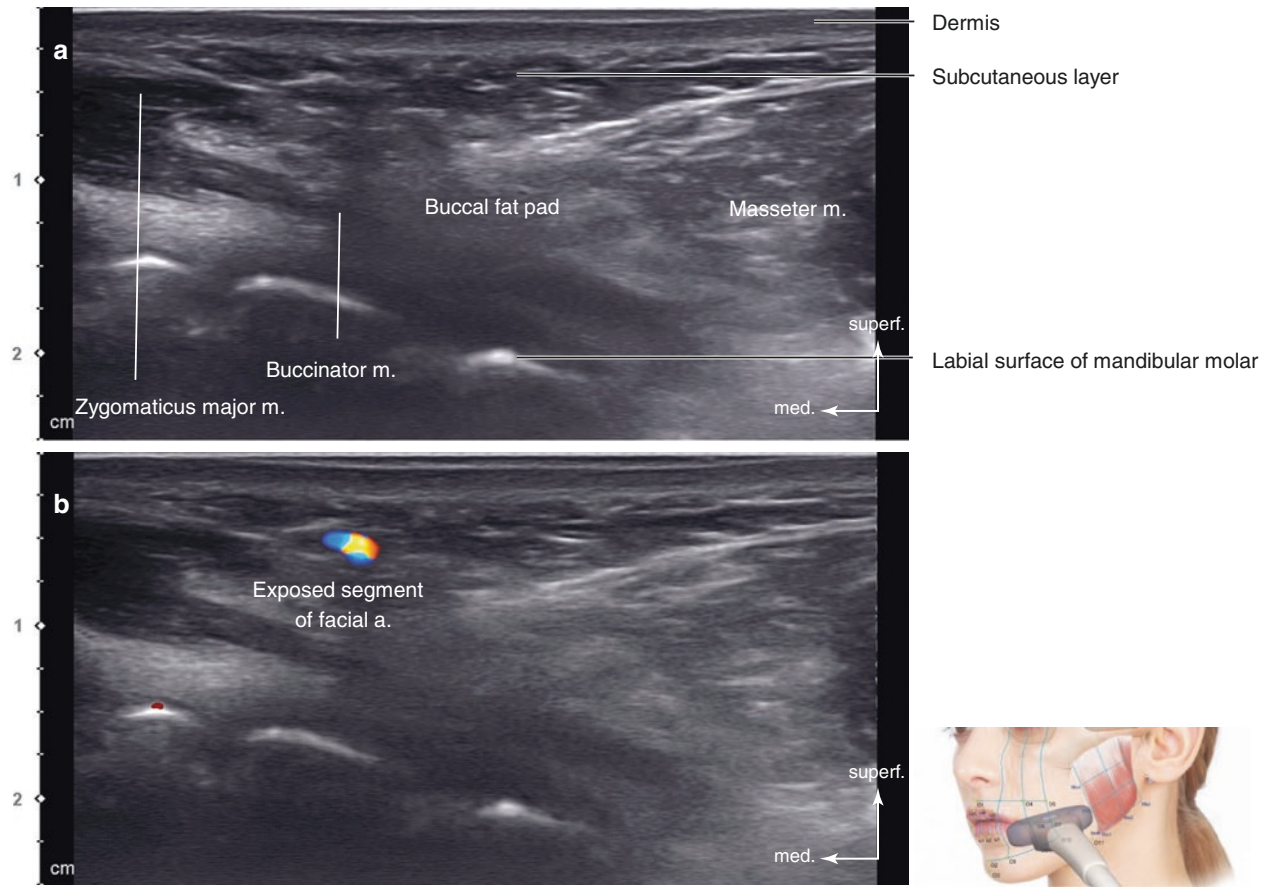

Fig. 6.29 Ultrasonography of the intersection point of TL7 and PL3 (O7). (**a**) B mode (transverse view, 15 MHz by linear transducer) and (**b**) Doppler mode (transverse view, 15 MHz by linear transducer). (Published with kind permission of © Hee-Jin Kim 2020. All Rights Reserved)

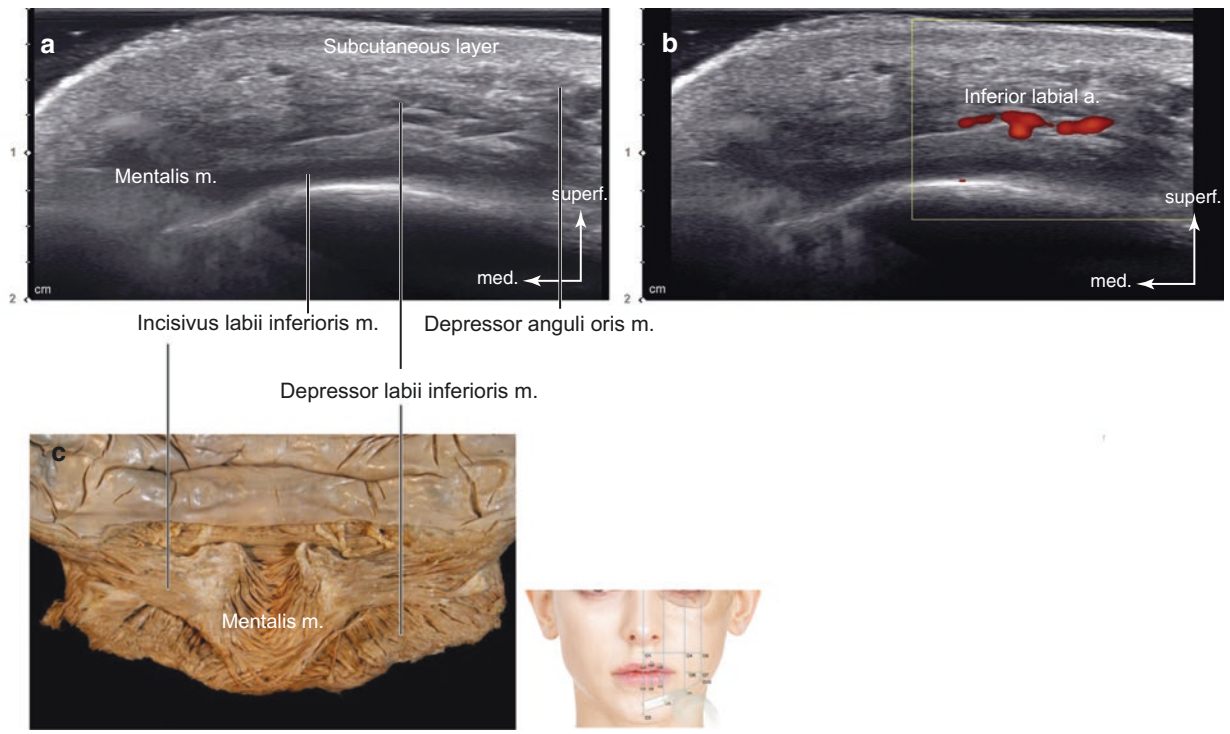

Fig. 6.30 Ultrasonography of the intersection point of TL8 and PL1 (O8). (**a**) B mode (transverse view, 15 MHz by linear transducer), (**b**) Doppler mode (transverse view, 15 MHz by linear transducer), and (**c**) posterior aspect of the dissected mentalis muscle. Medial fibers of the mentalis muscle forming a dome-shape chin prominence. (Published with kind permission of © Hee-Jin Kim 2020. All Rights Reserved)

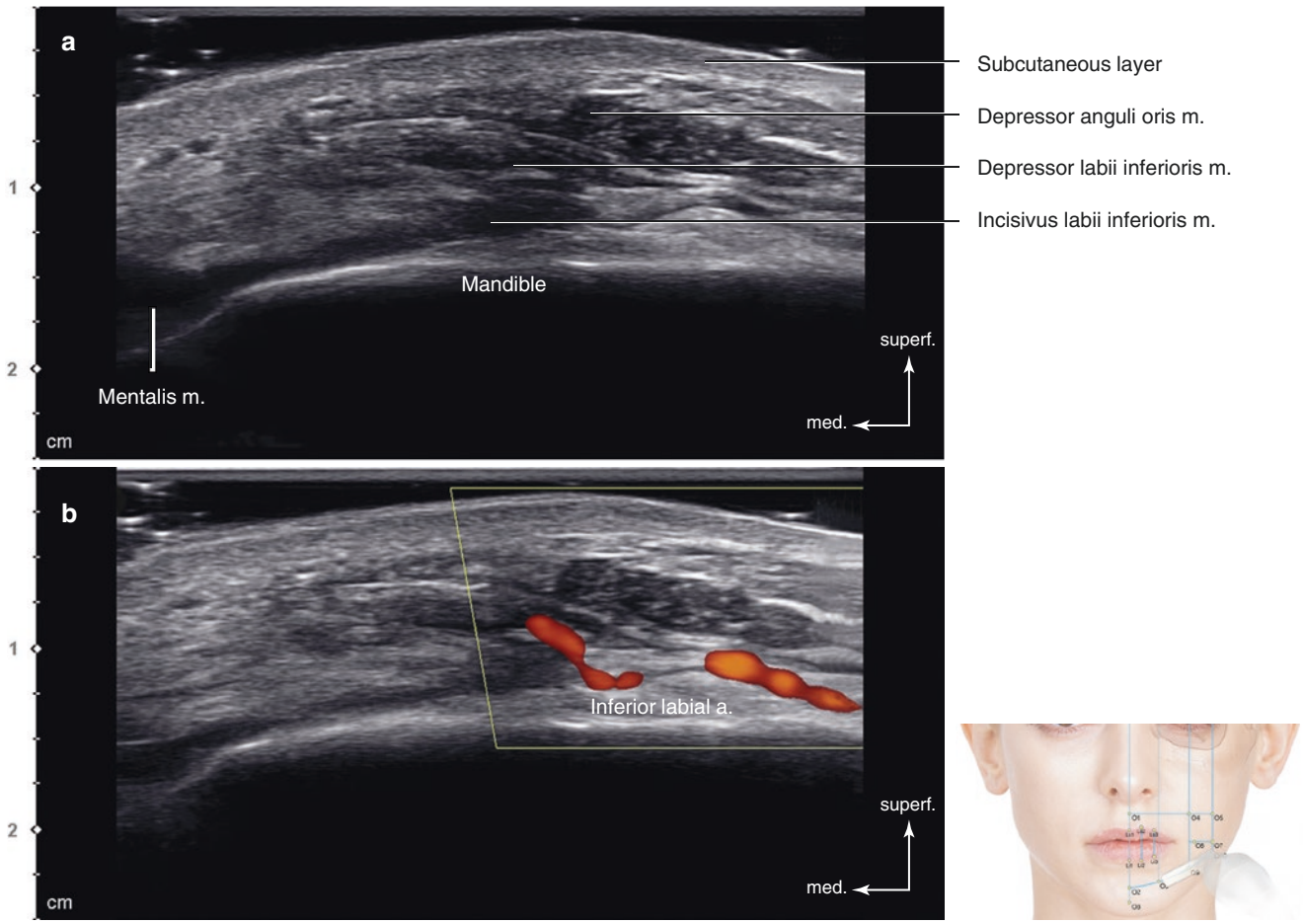

Fig. 6.31 Ultrasonography of the intersection point of TL8 and PL2 (O9). (**a**) B mode (transverse view, 15 MHz by linear transducer) and (**b**) Doppler mode (transverse view, 15 MHz by linear transducer). (Published with kind permission of © Hee-Jin Kim 2020. All Rights Reserved)

O10: Intersection Point of TL8 and PL3

In this point O10, anatomical structures between the DAO and the masseter mm. are clearly demonstrated. The DAO and masseter mm. are observed as a hypoechoic image at the medial and lateral aspects, respectively. The risorius m. shows as a thin hypoechoic line between the DAO and masseter mm. superficial to the irregular hyperechoic buccal fat pad. Because the risorius m. originates from the superficial SMAS plane as muscle fibers or from the masseteric fascia as tendinous structures, it can be observed as a hyperechoic line from the origin site on the masseter m. surface. However, due to the variable muscle patterns of the risorius m., the angulation of the transducer should be adequately adjusted to get the definite linear image of the risorius m. at this point. The Doppler mode image shows the facial a. deep to the DAO m. and the furcation of the inferior labial a. within the buccal fat pad (Fig. 6.32).

O11: Antegonial Notch

At the antegonial notch just anterior to the masseter m., a thin hyperechoic band of epidermis and an irregular hyperechoic dermis layer are seen. Underneath the skin structure, a thick hypoechoic lobulated jowl fat (subcutaneous layer) is observed, and its thickness varies. Between the fatty lobules of the jowl fat, the linear fibrous septa is shown as hyperechoic lines. The masseter m. is shown as the main thick hypoechoic image with a short discontinuous hyperechoic line (deep inferior band). The masseteric fascia covering the masseter m. is observed as a strong hyperechoic line. Between the jowl fat compartments and

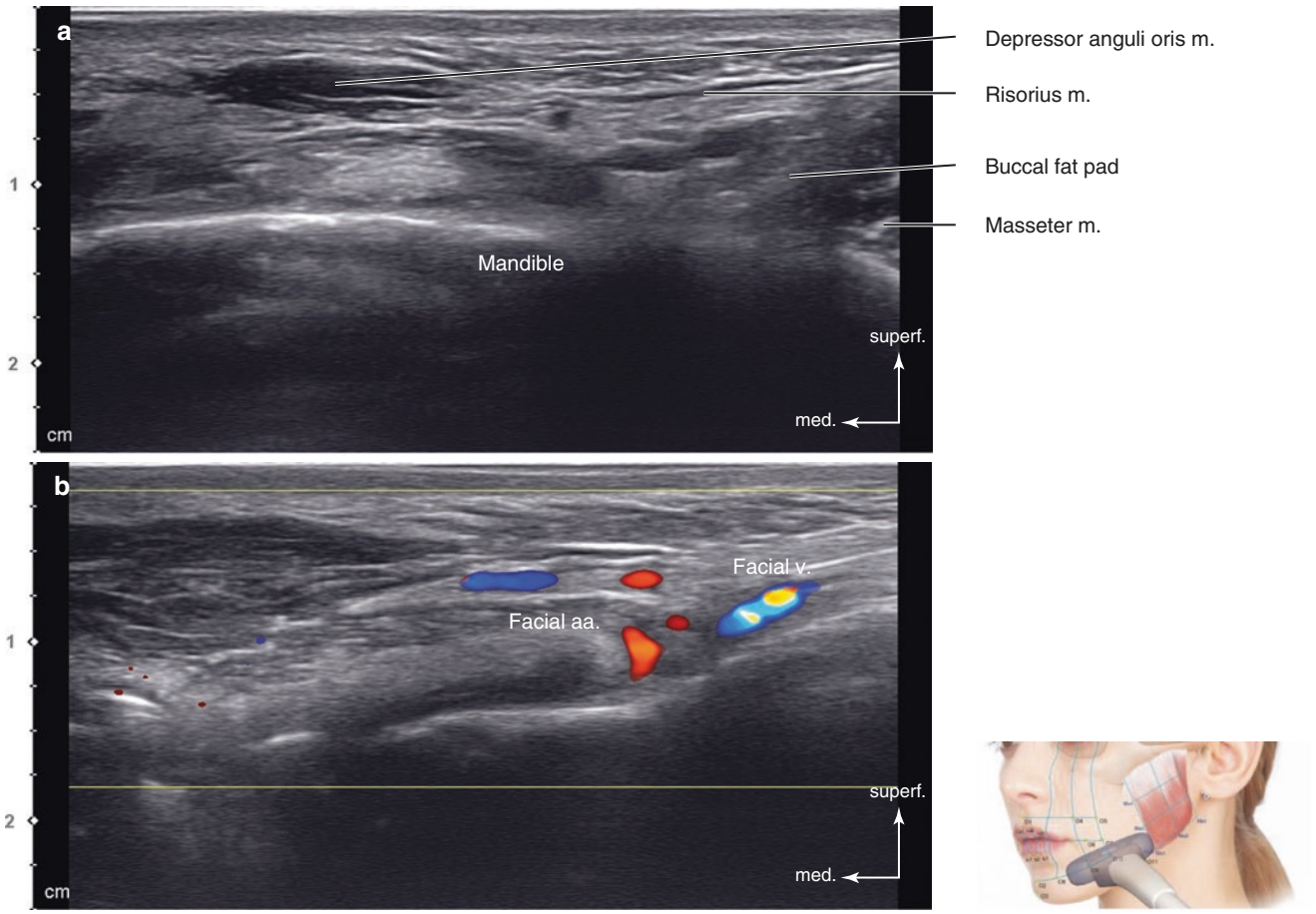

Fig. 6.32 Ultrasonography of the intersection point of TL8 and PL3 (O10). (**a**) B mode (transverse view, 15 MHz by linear transducer) and (**b**) Doppler mode (transverse view, 15 MHz by linear transducer). (Published with kind permission of © Hee-Jin Kim 2020. All Rights Reserved)

masseteric fascia, the intermittent hypoechoic lines are the facial portion of the platysma m. The Doppler mode image demonstrates the emerging portion of the facial a. and v. distinctly. In every case, the facial a. is located anterior to the facial v. In some cases, the facial v. runs superficially at the anterior portion of the masseter m. Around the vascular components, small fat compartments are observed as a slightly hyperechoic image occupying the premasseteric space (Fig. 6.33).

6.2.2.2 Upper and Lower Lips

The lip is composed of the cutaneous portion, intermediate zone (red portion), and mucous portion. The vermillion border is defined as the line between the cutaneous portion (i.e., labial skin) and the intermediate zone. The mucous portion can be further divided into the dry mucosa and the wet mucosa with the junction between the two being defined as the dry–wet mucosal junction. Structures located deep to the mucous portion are the superior labial and the inferior labial aa., the mental n., and the labial gland. They are generally located at a deeper plane than the OOr m.

Ls1–Li1: Perpendicular Line Between Ls1 and Li1

The sagittal view at the midline of the lips includes the whole upper and lower lip contour. The US image demonstrates the shape of the OOr m., and the Doppler mode image visualizes the location of the blood vessels within the lips. Due to the thick keratinized layer of the labial skin and dry mucosa (red portion), it is shown as a thick hyperechoic band of the epidermis. Underneath the epidermis, a relatively thin hyperechoic dermis layer is located superficial to the muscle component. The labial OOr m. can be subdivided into two muscle groups: the pars peripheralis and pars marginalis. Though the patterns of the development

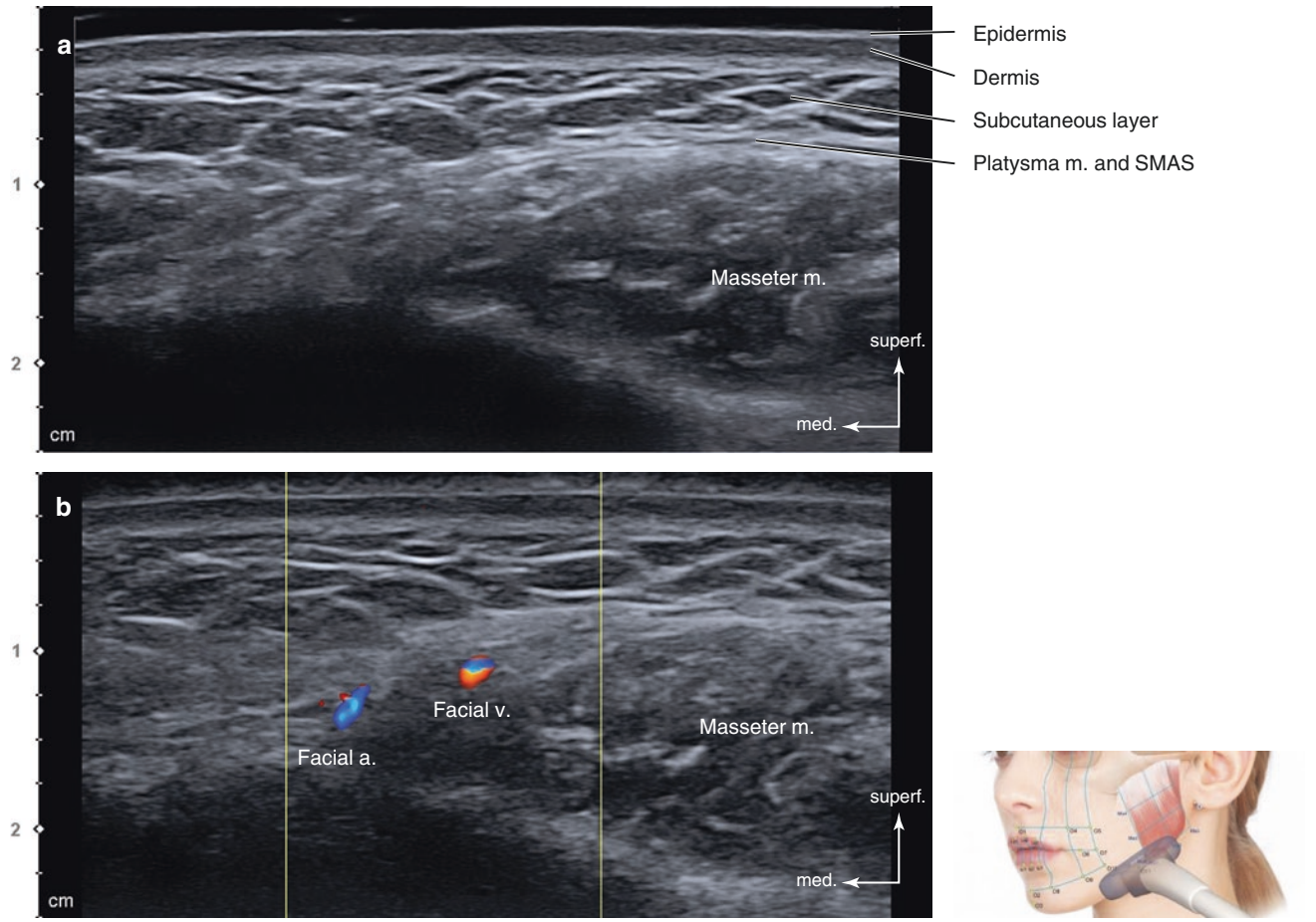

Fig. 6.33 Ultrasonography of the antegonial notch (O11). (**a**) B mode (transverse view, 15 MHz by linear transducer) and (**b**) Doppler mode (transverse view, 15 MHz by linear transducer). (Published with kind permission of © Hee-Jin Kim 2020. All Rights Reserved)

of the pars marginalis are variable, the pars marginalis of the labial OOr m. is observed as a rolled-out pattern like "hockey stick" (Fig. 6.34a). This pattern is more clearly observed in the lower lip. Deep to the OOr m. layer, the oral mucosa and submucosa are identified. In this longitudinal view, the labial surface of the upper and lower incisors is shown. The Doppler mode image demonstrates the labial aa. generally identified within the submucosal or intramuscular layer. These arteries are mainly originated from the superior and inferior labial aa.; however, some inferior labial aa. can be branched from the submental a. In Ls1–Li1, generally, the labial a. is observed within the intramuscular layer or the submucosa of the wet mucosa (Fig. 6.34b, c).

Ls2–Li2: Perpendicular Line Between Ls2 and Li2

The sagittal views on the points passing the Cupid's bow are almost similar to those of points Ls1–Li1. Compared to the Ls1–Ls2 of the upper lip, the pattern of the pars marginalis of the OOr m. is slightly different. The pars marginalis of the upper lip appears in a discontinuous pattern (Fig. 6.35a). The Doppler mode image demonstrates the superior labial aa. running within the intramuscular layer (48%) or submucosa of the wet mucosa (20%). In the lower lip, the inferior labial a. is located within the submucosa of the wet mucosa (45%) or dry mucosa (27%) (Fig. 6.35b, c).

Ls3–Li3: Perpendicular Line Between Ls3 and Li3

The US images at this view are similar to the previous longitudinal views. The general lower lip contour is slightly retruded because the degree of the rolled-out pattern of the pars marginalis of the lower lip is weaker than that of other areas (Fig. 6.36a). The Doppler mode image demonstrates the superior labial a. running within the intramuscular layer (42%) or submucosa of the wet mucosa (40%). In the lower

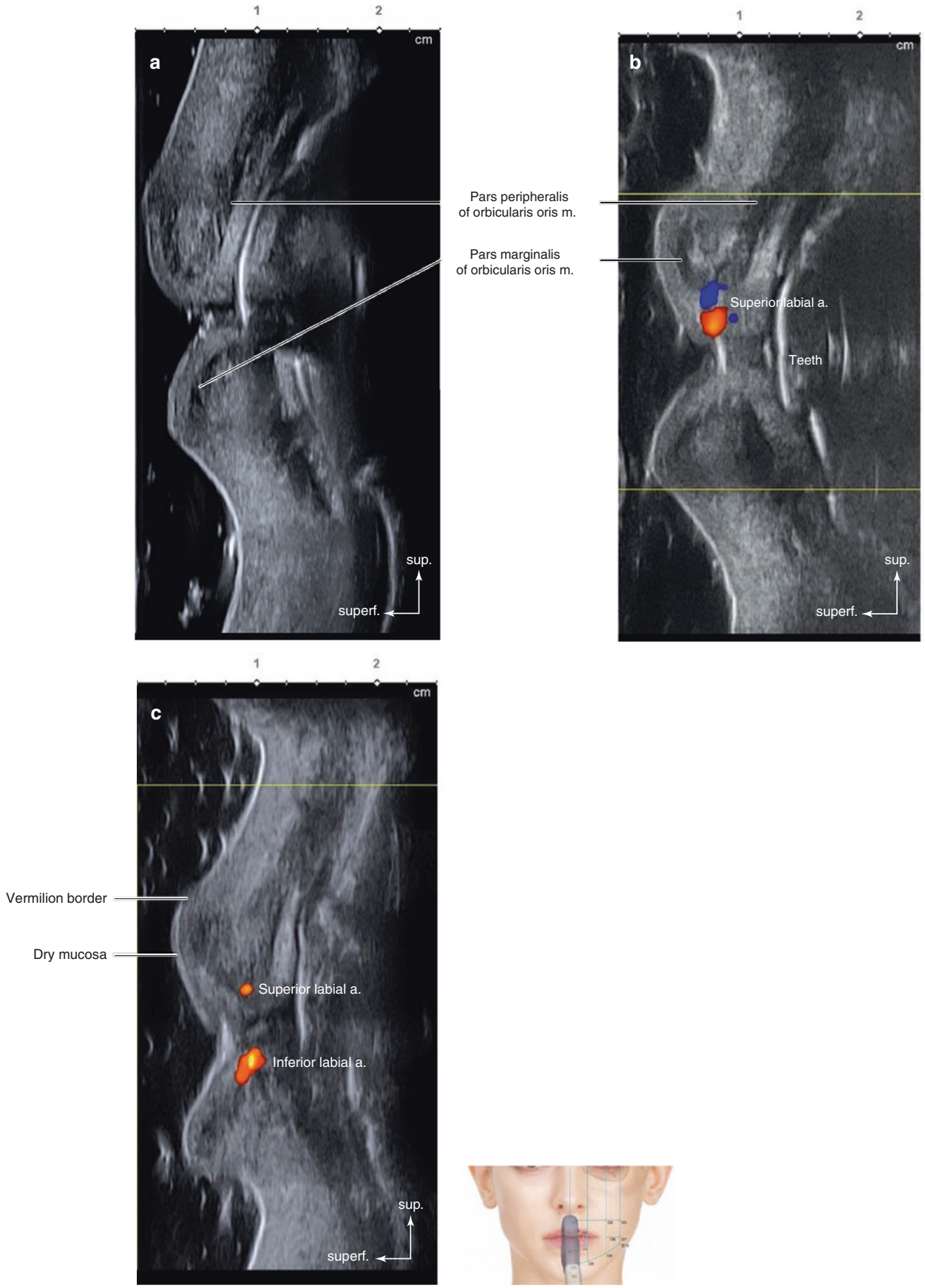

Fig. 6.34 Ultrasonography on the perpendicular line between Ls1 and Li1 (Ls1–Li1). (**a**) B mode (sagittal view, 15 MHz by linear transducer), (**b**) Doppler mode (sagittal view, 15 MHz by linear transducer), and (**c**) Doppler mode (sagittal view, 15 MHz by linear transducer). (Published with kind permission of © Hee-Jin Kim 2020. All Rights Reserved)

Fig. 6.35 Ultrasonography on the perpendicular line between Ls2 and Li2 (Ls2–Li2). (**a**) B mode (sagittal view, 15 MHz by linear transducer), (**b**) Doppler mode (sagittal view, 15 MHz by linear transducer), and (**c**) Doppler mode (sagittal view, 15 MHz by linear transducer). (Published with kind permission of © Hee-Jin Kim 2020. All Rights Reserved)

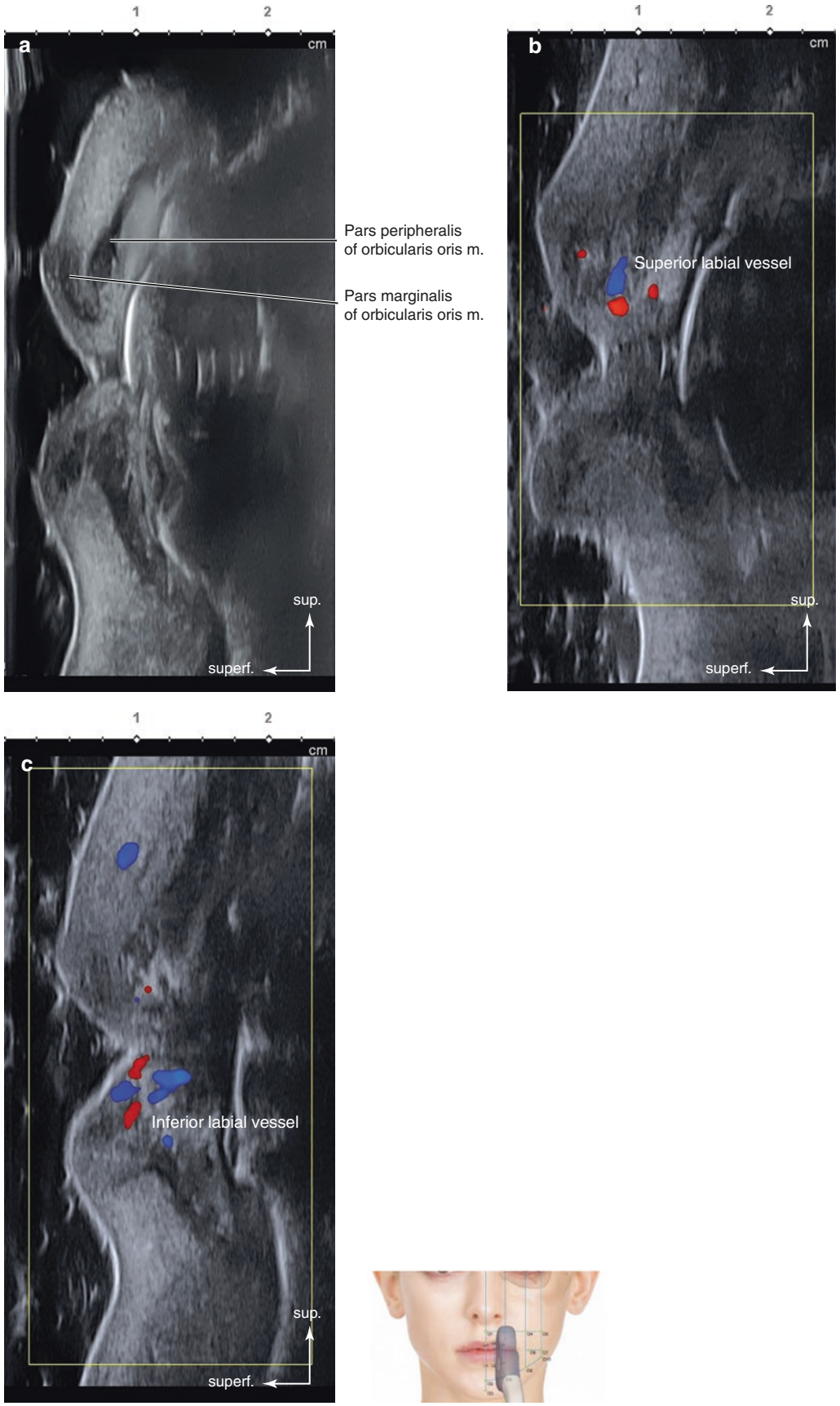

Fig. 6.36 Ultrasonography on the perpendicular line between Ls3 and Li3 (Ls3–Li3). (**a**) B mode (sagittal view, 15 MHz by linear transducer), (**b**) Doppler mode (sagittal view, 15 MHz by linear transducer), and (**c**) Doppler mode (sagittal view, 15 MHz by linear transducer). (Published with kind permission of © Hee-Jin Kim 2020. All Rights Reserved)

lip, the inferior labial a. is located within the submucosa of the wet mucosa (55%) or dry mucosa (18%) (Fig. 6.36b, c).

Ls1: Intersection Point of Vermilion Border of Upper Lip and Midline

In the transverse view at the midline point of the upper vermilion border, the OOr m. is definitely observed and identified as two layers. The superficial and deep hypoechoic images are the pars peripheralis and pars marginalis of the labial OOr m., respectively. Between two muscle layers, an irregularly hyperechoic subcutaneous layer is identified (Fig. 6.37).

Ls2–Ls3: Oblique Line Between Ls2 and Ls3

In the US image taken along the vermilion border between the Cupid's bow peak and the cheilion, the two layers of the OOr m. are identified. However, the lateral aspect of the OOr m. shows two layers of the OOr m. blended with other perioral muscles as a thick hypoechoic image. The hyperechoic subcutaneous layer becomes thicker as it goes to the mouth corner. Likewise, a hyperechoic band of the epidermis tends to be thicker laterally (Fig. 6.38).

Li1: Intersection Point of Vermilion Border of Lower Lip and Midline

The lower lip is usually thicker than the upper lip, and each structure is more clearly observed. Similar to the point Ls1, the pars peripheralis and pars marginalis of the OOr m. are clearly identified, respectively. However, a thinner hyperechoic epidermis and dermis layer are shown, and the hyperechoic subcutaneous or fat layer becomes thicker than the upper lip (Fig. 6.39).

Li2–Li3: Oblique Line Between Li2 and Li3

The transverse image demonstrates a groove shown between the lower lip and the lower cheek. The hyperechoic subcutaneous layer becomes thicker when it goes to the cheek. Similarly, two layers of the OOr m. are well distinguished until the lateral margin of the lower lip and the oral mucosa and submucosa tend to be thickened than the upper lip region. In the oral cavity, a discontinuous hyperechoic band of the mandibular teeth is observed (Fig. 6.40).

6.2.2.3 Masseter Region

At the masseter region, the superficial components, including the hyperechoic band of the epidermis and the less hyperechoic dermis, are observed. The thin irregular hyperechoic subcutaneous layer is observed and the SMAS is shown as multiple hyperechoic lines superficial to the masseteric fascia. The main hypoechoic muscle component is the masseter m. with the intermittent hyperechoic intramuscular bands (deep inferior tendon). The masseter m. is covered by the masseteric fascia, and this layer is observed as a hyperechoic lining underneath the SMAS. Deep to the muscle component, the mandibular ramus is observed as a strong hyperechoic line. Since the US cannot penetrate the bone, posterior acoustic shadowing can be observed in the region behind the mandible.

Ma1: Anterior Margin of the Masseter Muscle

The general skin component with a subcutaneous layer is observed. Beneath the subcutaneous layer, the risorius m. fibers are located and shown as a discontinuous hypoechoic band at the anterior border of the masseter m. Deep to the

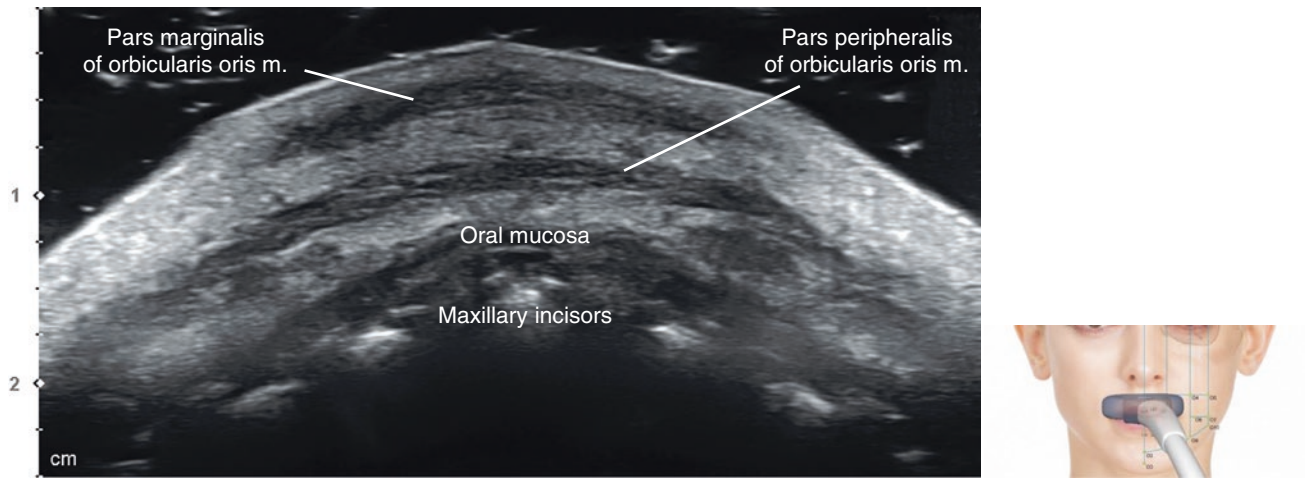

Fig. 6.37 Ultrasonography of the intersection point of vermilion border of upper lip and midline (Ls1). B mode (transverse view, 15 MHz by linear transducer). (Published with kind permission of © Hee-Jin Kim 2020. All Rights Reserved)

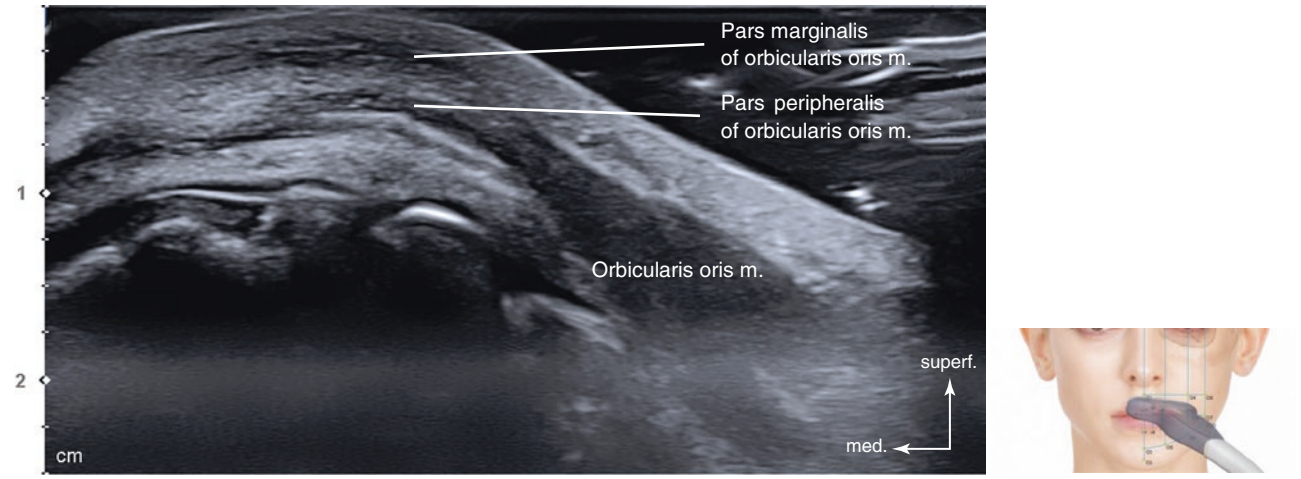

Fig. 6.38 Ultrasonography of the oblique line between Ls2 and Ls3 (Ls2–Ls3). B mode (oblique view, 15 MHz by linear transducer). (Published with kind permission of © Hee-Jin Kim 2020. All Rights Reserved)

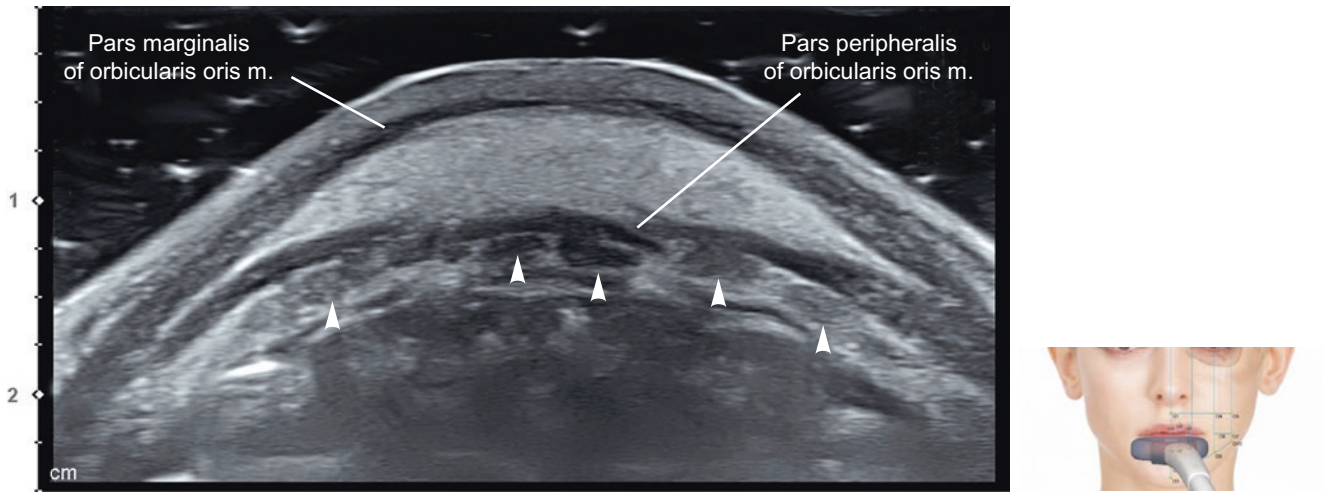

Fig. 6.39 Ultrasonography of intersection point of vermilion border of lower lip and midline (Li1). B mode (transverse view, 15 MHz by linear transducer) (arrowheads: mucous labial glands). (Published with kind permission of © Hee-Jin Kim 2020. All Rights Reserved)

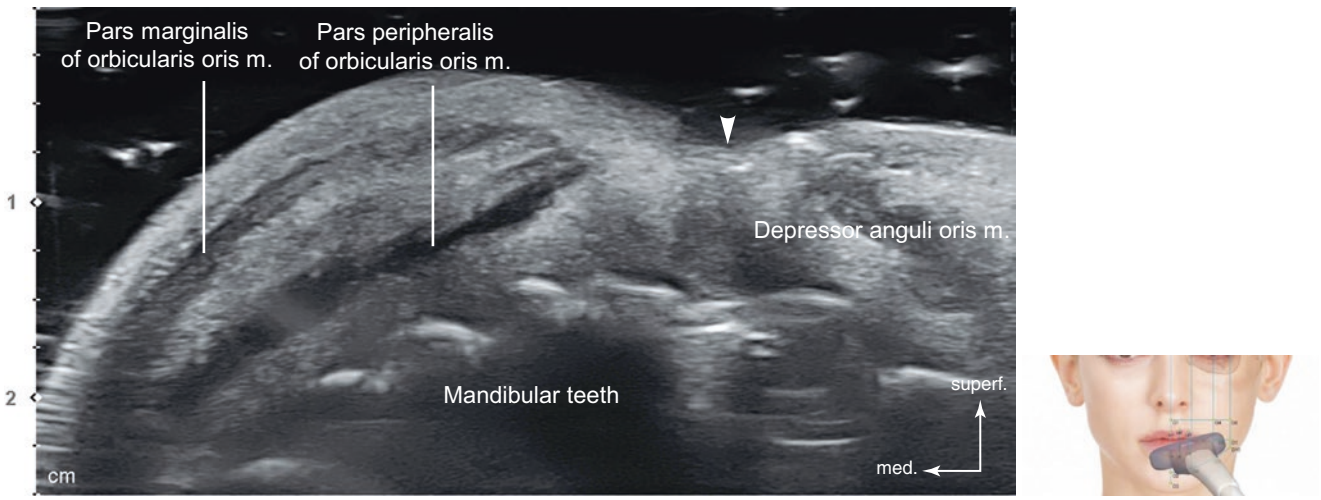

Fig. 6.40 Ultrasonography of the oblique line between Li2 and Li3 (Li2–Li3). B mode (oblique view, 15 MHz by linear transducer) (arrowhead: labiomandibular fold). (Published with kind permission of © Hee-Jin Kim 2020. All Rights Reserved)

risorius m. layer, the thin continuous hypoechoic band of the platysma m. can be observed, and these muscle fibers are continuous from the superficial neck to the hyperechoic SMAS, superficial to the masseteric fascia. Within the hypoechoic masseter m., the intermittent hyperechoic bands of the deep inferior tendon are observed. The strong hyperechoic mandibular surface is apparent due to the thick cortical plate (Fig. 6.41).

Ma2: Mid-Half Line Parallel to Ma1 and Ma3

The longitudinal view passing the middle half of the masseter m. demonstrates the typical feature of the structures. The most remarkable anatomical structure is the deep inferior tendon. This tendinous structure is longitudinally located within the superficial part of the masseter m. as a hyperechoic band. The deep inferior tendon is inserted into the inferior margin of the mandible by dividing the superficial and deep muscle belly of the superficial part of the masseter m.

In addition, flattened facial nerve branches can be seen at the SMAS layer as a small honeycomb appearance. The inferior border of the mandible is observed as a strongly hyperechoic curved line, and the masseter m. seems to extend below the mandibular border. This phenomenon is observed due to the drooping of the relaxed muscle fibers (Fig. 6.42).

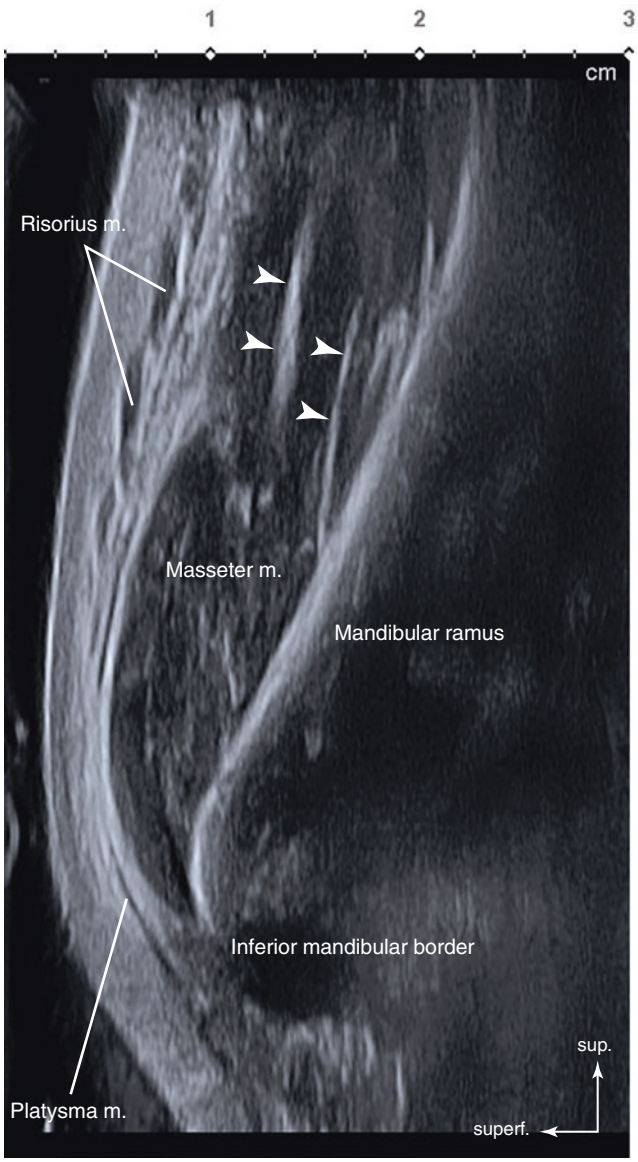

Fig. 6.41 Ultrasonography of the anterior margin of the masseter muscle (Ma1). B mode (coronal view, 15 MHz by linear transducer) (arrowheads: deep inferior tendons). (Published with kind permission of © Hee-Jin Kim 2020. All Rights Reserved)

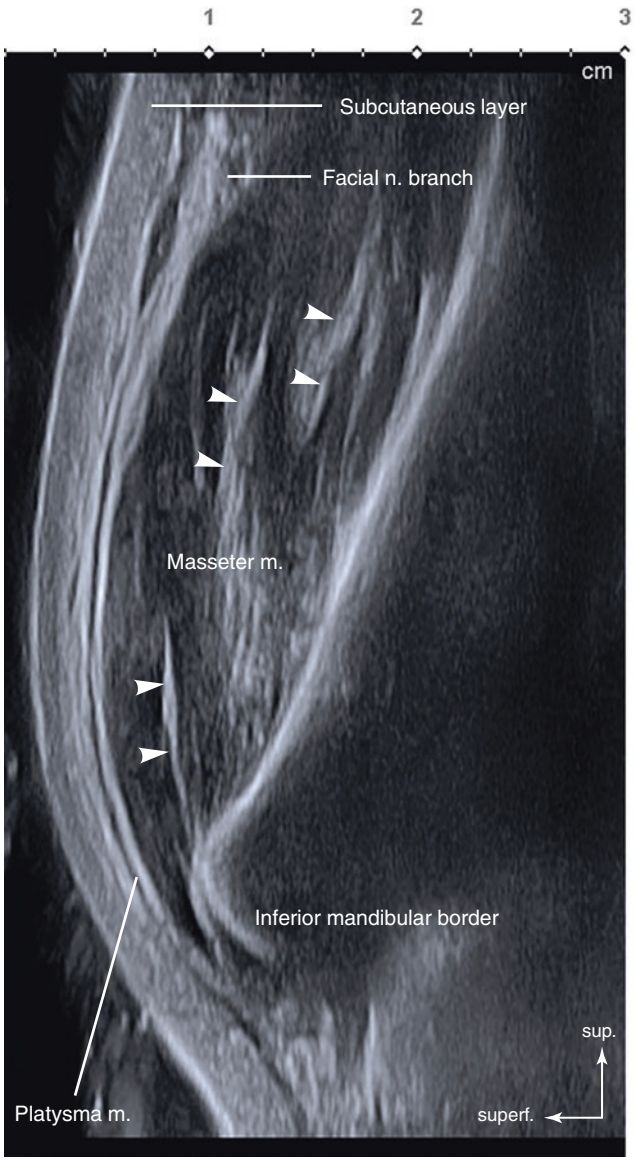

Fig. 6.42 Ultrasonography of the mid-half line parallel to Ma1 and Ma3 (Ma2). B mode (coronal view, 15 MHz by linear transducer) (arrowheads: deep inferior tendons). (Published with kind permission of © Hee-Jin Kim 2020. All Rights Reserved)

Ma3: Posterior Margin of the Masseter Muscle

At the posterior margin of the masseter m., the hyperechoic parotid gland is visible above the masseter m. The parotid gland is also covered by the hyperechoic band of the parotid fascia and hypoechoic line of the platysma m. The deep inferior tendons are also observed as hyperechoic bands (Fig. 6.43).

Ma4: Upper 1/3 Line of the Masseter Muscle Perpendicular to Ma2

The transverse view below the zygomatic bone and arch demonstrates the typical layered structures from the skin to the mandible. Beneath the hyperechoic epidermis and dermis, some muscle fibers of the platysma m. and multiple SMAS layers are observed within the subcutaneous layer superficial to the parotideomasseteric fascia. The hyperechoic lines of the parotideomasseteric fascia cover the masseter m. and also enclose the parotid gland. On this view of the US, an anechoic parotid duct traveling superficial to the masseter m. is observed. Generally, the parotid duct lies at one finger width (about 2 cm) below the zygomatic arch. Most of the superficial regions of the masseter m. consist of muscle belly, but complex tendinous structures are also observed; these tendons subdivide the masseter m. into mul-

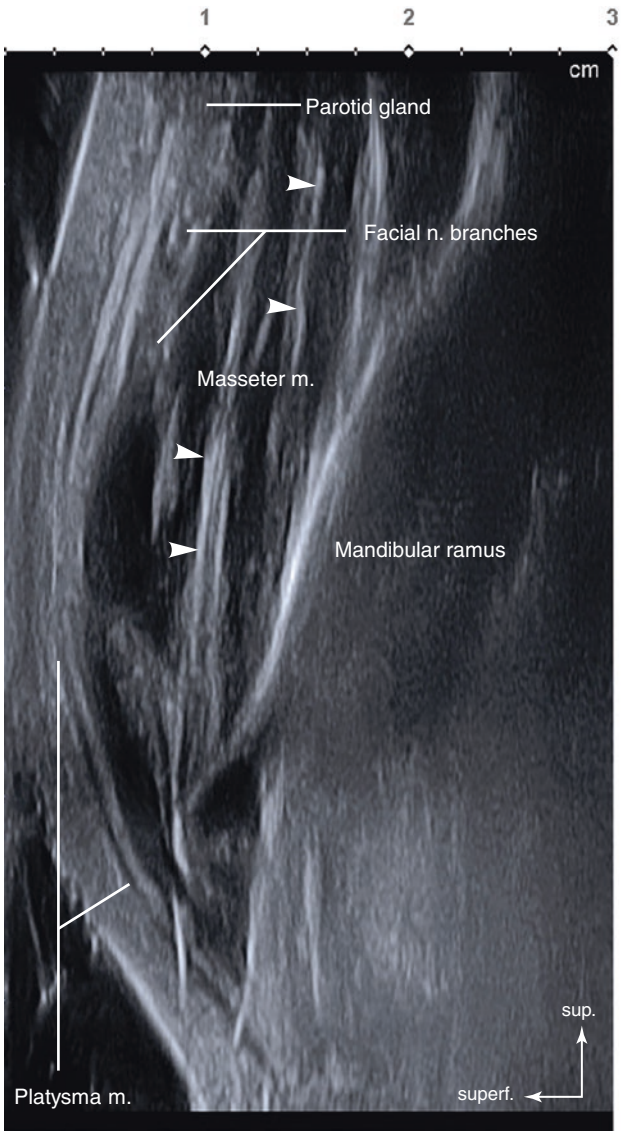

Fig. 6.43 Ultrasonography of the posterior margin of the masseter muscle (Ma3). B mode (coronal view, 15 MHz by linear transducer) (arrowheads: deep inferior tendons). (Published with kind permission of © Hee-Jin Kim 2020. All Rights Reserved)

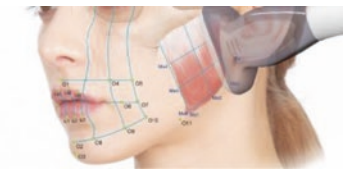

tiple layers. The superficial layer of the masseter m. is covered by numerous tendinous or aponeurotic structures, and these are mainly the superficial and deep aponeurosis. The superficial aponeurosis is located at the upper part of the masseter m., and it can be seen as a thick hyperechoic band at the anterior margin of the muscle. It covers the superior surface of the superficial layer of the masseter m. intertwined with the lower muscle belly. The deep aponeurosis can be distinguished in about 78.8% of the cases, and they are connected with the superficial aponeurosis or surrounding muscle belly. Within the masseter m., two to three layers of the deep inferior tendons are clearly observed as hyperechoic bands. Anterior to the masseter m., an irregular less hyperechoic buccal fat pad is constantly shown. The surface of the mandibular ramus is observed as a strong hyperechoic line (Fig. 6.44).

Ma5: Lower 1/3 Line of the Masseter Muscle Perpendicular to Ma2

Similar structures are observed from the skin to the parotideomasseteric fascia. In this view, the strong intermittent hypoechoic lines of the platysma m. are observed beneath the subcutaneous layer. The hyperechoic parotid gland at this point is well visualized. Within the masseter m., the strong hyperechoic deep inferior tendons are observed, and these divide the superficial layer of the

masseter m. into two or three superficial and deep muscle bellies and attach to the inferior border of the mandible. Based on the transverse US images, the superficial layer of the masseter m. is partially divided transversely and longitudinally into superficial and deep muscle bellies by the deep inferior tendons in 35% and 38.3% of the cases, respectively (Fig. 6.45a, b). The posterior region of the superficial layer of the masseter m. is compartmentalized (partially invested) by the deep inferior tendons in 26.7% of the specimens (Fig. 6.45c). The bony attachment of the deep inferior tendons is observed on the surface of the hyperechoic line of the mandibular ramus. Within the buccal fat pad anterior to the masseter m., anechoic facial v. can be identified (Fig. 6.45d).

Ma6: Inferior Margin of the Masseter Muscle Perpendicular to Ma2

The muscle belly of the masseter m. can be observed, including the deep inferior tendons. The masseter m. is covered by the hypoechoic platysma m. at the inferior border of the mandible. The parotid gland is visible as a smaller hyperechoic structure and is scarcely observed at the posterior part of the masseter m. The most remarkable anatomical structures in this view are the anechoic facial vessels at the anterior border of the masseter m. within the premasseteric space.

In this case, the deep inferior tendon is observed at the center of the muscle belly of the masseter m. and it is compartmentalized in the posterior part of the masseter m. (Fig. 6.46).

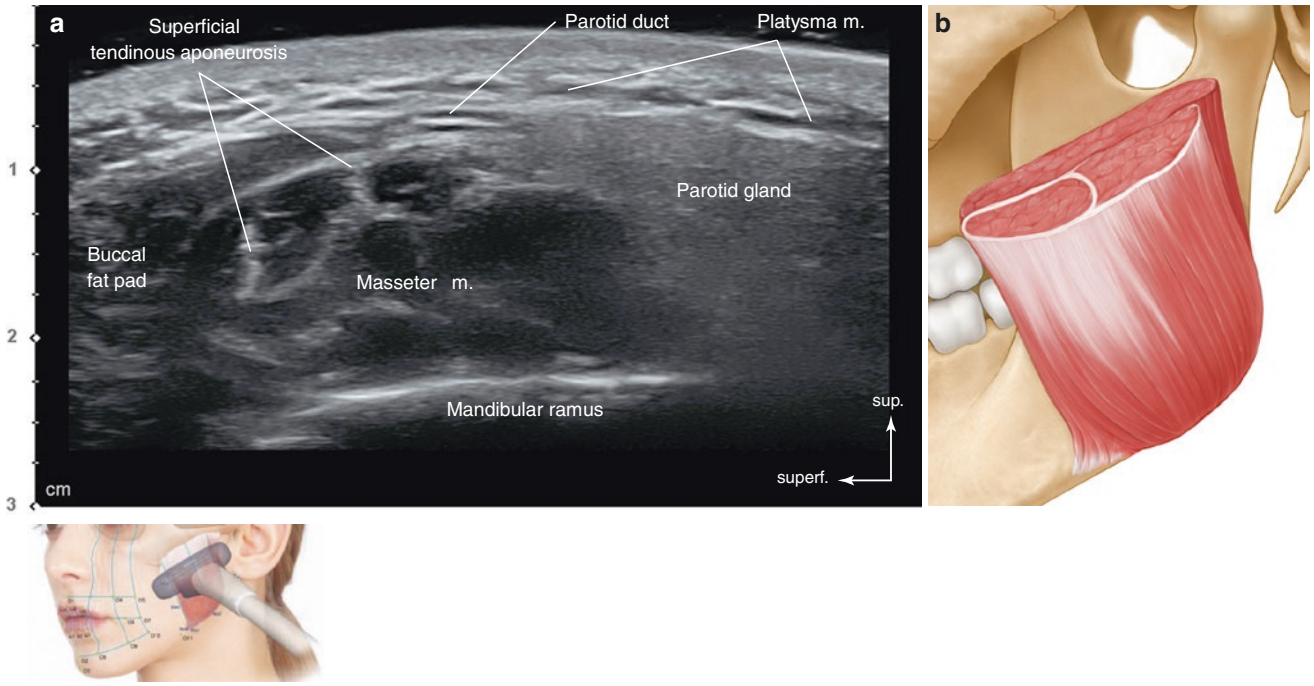

Fig. 6.44 Ultrasonography of the upper 1/3 line of the masseter muscle perpendicular to Ma2 (Ma4). (**a**) B mode (transverse view, 15 MHz by linear transducer), (**b**) corresponding illustration showing the superficial aponeurosis of the upper masseter m. (Published with kind permission of © Hee-Jin Kim 2020. All Rights Reserved)

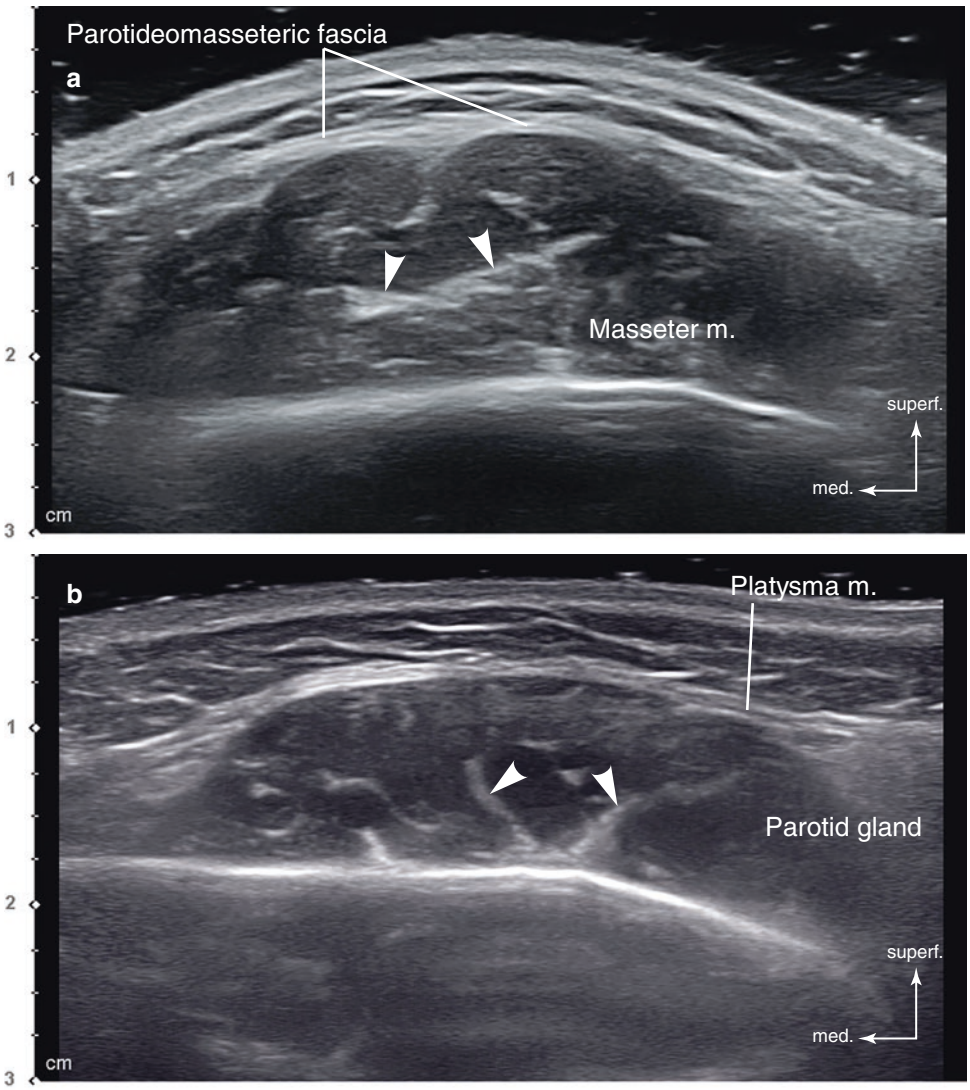

Fig. 6.45 Ultrasonography of the lower 1/3 line of the masseter muscle perpendicular to Ma2 (Ma5). (**a**–**d**) B mode (transverse view, 15 MHz by linear transducer) (arrowheads: deep inferior tendons). (Published with kind permission of © Hee-Jin Kim 2020. All Rights Reserved)

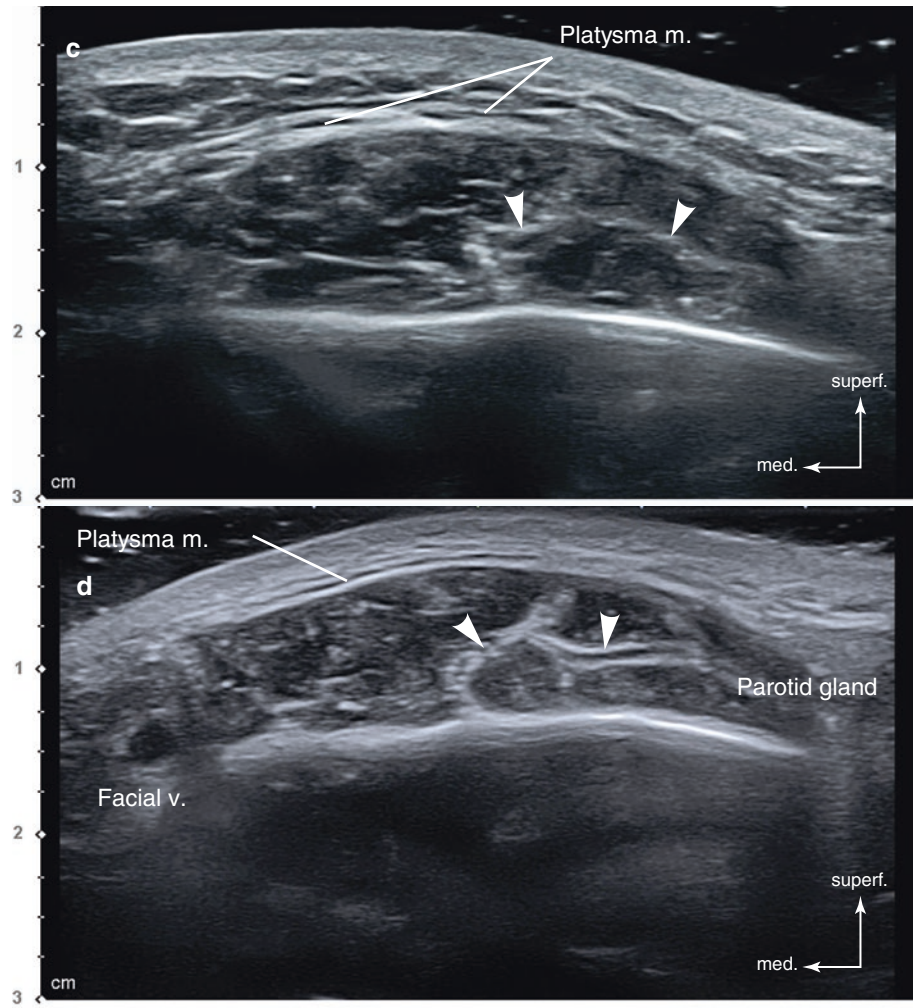

Fig. 6.45 (continued)

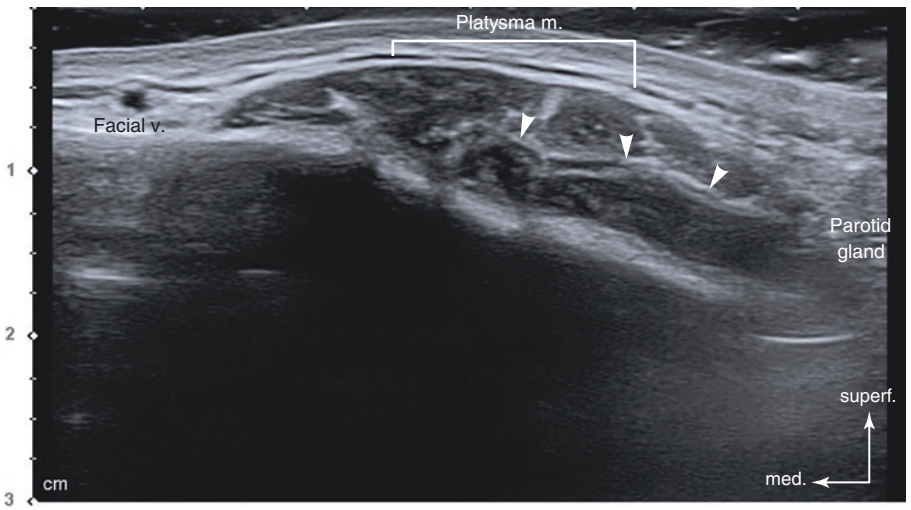

Fig. 6.46 Ultrasonography of the inferior margin of the masseter muscle perpendicular to Ma2 (Ma6). B mode (transverse view, 15 MHz by linear transducer) (arrowheads: deep inferior tendons). (Published with kind permission of © Hee-Jin Kim 2020. All Rights Reserved)

Bibliography

1. Bae JH, Choi DY, Lee JG, Tansatit T, Kim HJ. The risorius muscle: anatomic considerations with reference to botulinum neurotoxin injection for masseteric hypertrophy. Dermatol Surg. 2014;40(12):1334–9.
2. Bae JH, Lee JH, Youn KH, Hur MS, Hu KS, Tansatit T, Kim HJ. Surgical consideration of the anatomic origin of the risorius in relation to facial planes. Aesthet Surg J. 2014;34:NP43–9.
3. Choi DY, Kim JS, Youn KH, Hur MS, Kim JS, Hu KS, Kim HJ. Clinical anatomic considerations of the zygomaticus minor muscle based on the morphology and insertion pattern. Dermatol Surg. 2014;40(8):858–63.
4. Choi YJ, Kim JS, Gil YC, Phetudom T, Kim HJ, Tansatit T, Hu KS. Anatomic considerations regarding the location and boundary of the depressor anguli oris muscle with reference to botulinum toxin injection. Plast Reconstr Surg. 2014;134(5):917–21.
5. Choi YJ, We YJ, Lee HJ, Lee KW, Gil YC, Hu KS, Tansatit T, Kim HJ. Three-dimensional evaluation of the depressor anguli oris and depressor labii inferioris for botulinum toxin injections. Aesthet Surg J. 2020;
6. Hu KS, Kim ST, Hur MS, Park JH, Song WC, Koh KS, Kim HJ. Topography of the masseter muscle in relation to treatment with botulinum toxin type A. Oral Surg Oral Med Oral Pathol Oral Radiol Endod. 2010;110(2):167–71.
7. Hur MS, Bae JH, Kim HJ, Lee HB, Lee KS. Blending of the lateral deep slip of the platysma muscle into the buccinator muscle. Surg Radiol Anat. 2015;37(8):931–4.
8. Hur MS, Hu KS, Cho JY, Kwak HH, Song WC, Koh KS, Lorente M, Kim HJ. Topography and location of the depressor anguli oris muscle with a reference to the mental foramen. Surg Radiol Anat. 2008;30(5):403–7.
9. Hur MS, Hu KS, Kwak H-H, Lee K-S, Kim HJ. Inferior bundle (fourth band) of the buccinator and the incisivus labii inferioris muscle. J Craniofac Surg. 2011;22(1):289–92.
10. Hur MS, Hu KS, Park JT, Youn KH, Kim HJ. New anatomical insight of the levator labii superioris alaeque nasi and the transverse part of the nasalis. Surg Radiol Anat. 2010;32(8):753–6.
11. Hur MS, Hu KS, Youn KH, Song WC, Abe S, Kim HJ. New anatomical profile of the nasal musculature: dilator naris vestibularis, dilator naris anterior, and alar part of the nasalis. Clin Anat. 2011;24(2):162–7.
12. Hur MS, Kim HJ, Choi BY, Hu KS, Kim HJ, Lee KS. Morphology of the mentalis muscle and its relationship with the orbicularis oris and incisivus labii inferioris muscles. J Craniofac Surg. 2013;24:602–4.
13. Hwang WS, Hur MS, Hu KS, Song WC, Koh KS, Baik HS, Kim ST, Kim HJ, Lee KH. Surface anatomy of the lip elevator muscles for the treatment of gummy smile using botulinum toxin. Angle Orthod. 2009;79(1):70–7.
14. Kim DH, Hong HS, Won SY, Kim HJ, Hu KS, Choi JH, Kim HJ. Intramuscular nerve distribution of the masseter muscle for botulinum toxin injection. J Craniofac Surg. 2010;21(2):588–91.
15. Kim HS, Lee KL, Gil YC, Hu KS, Tansatit T, Kim HJ. Topographic anatomy of the infraorbital artery and its clinical implications for nasolabial fold augmentation. Plast Reconstr Surg. 2018;142(3):273e–80e.
16. Kim HS, Pae C, Bae JH, Hu KS, Chang BM, Tansatit T, Kim HJ. An anatomical study of the risorius in Asians and its insertion at the modiolus. Surg Radiol Anat. 2015;37(2):147–51.
17. Kim YS, Lee KW, Kim JS, Gil YC, Tansatit T, Shin DH, Kim HJ. Regional thickness of facial skin and superficial fat: application to the minimally invasive procedures. Clin Anat. 2020;32:1008–18.
18. Kwak HH, Hu KS, Youn KH, Jin GC, Shim KS, Fontaine C, Kim HJ. Topographic relationship between the muscle bands of the zygomaticus major muscle and the facial artery. Surg Radiol Anat. 2006;28(5):477–80.
19. Lee HJ, Choi YJ, Lee KW, Hu KS, Kim ST, Kim HJ. Ultrasonography of the internal architecture of the superficial part of the masseter muscle in vivo. Clin Anat. 2020;32:446–52.
20. Lee HJ, Kang IW, Seo KK, Choi YJ, Kim ST, Hu KS, Kim HJ. The anatomical basis of paradoxical masseteric bulging after botulinum neurotoxin type A injection. Toxins. 2016;9(1):14.
21. Lee HJ, Kim JS, Youn KH, Lee JW, Kim HJ. Ultrasound-guided botulinum neurotoxin type A injection for correcting asymmetrical smiles. Aesthet Surg J. 2018;38(9):NP130–4.
22. Lee HJ, Won SY, O J, Hu KS, Mun SY, Yang HM, Kim HJ. The facial artery: a comprehensive anatomical review. Clin Anat. 2018;31:99–108.
23. Lee JG, Yang HM, Choi YJ, Favero V, Kim YS, Hu KS, Kim HJ. Facial arterial depth and layered relationship with facial musculatures. Plast Reconstr Surg. 2015;135:437–44.
24. Lee JH, Lee K, Jung W, Youn KH, Hu KS, Tansatit T, Kim HJ. A novel anatomical consideration on the exposed segment of the facial artery. Clin Anat. 2020;33:257–64.
25. Lee JY, Kim JN, Yoo JY, Hu KS, Kim HJ, Song WC, Koh KS. Topographic anatomy of the masseter muscle focusing on the tendinous digitation. Clin Anat. 2012;25:889–92.
26. Lee KL, Cho HJ, Bae HK, Park HJ, Park MS, Kim HJ. Anatomical considerations when treating compensatory hypertrophy of the upper part of the masseter after long-term botulinum neurotoxin type a injections. Toxins 22. 2020;12(3):202.
27. Lee KL, Lee HJ, Youn KH, Kim HJ. Positional relationship of superior and inferior labial artery by ultrasonography image analysis for safe lip augmentation procedures. Clin Anat. 2020;33:158–64.
28. Lee SH, Gil YC, Choi YJ, Tansatit T, Kim HJ, HU KS. Topographic anatomy of superior labial artery for dermal filler injection. Plast Reconstr Surg. 2015;135:445–50.
29. Lee SH, Lee HJ, Kim YS, Kim HJ, Hu KS. What's difference between the inferior labial artery and horizontal labiomental artery? Surg Radiol Anat. 2015;37(8):947–53.
30. Lee SH, Lee M, Kim HJ. Anatomy-based image-processing analysis for the running pattern of the perioral artery for minimally invasive surgery. Br J Oral Maxillofac Surg. 2014;52:688–92.
31. Park HJ, Lee KL, Gil YC, Lee JH, Hu KS, Kim HJ. Sonographic analysis of the upper labial orbicularis oris and its clinical implications. Aesthet Surg J. 2020;
32. Shim KS, Hu KS, Kwak HH, Youn KH, Koh KS, Fontaine C, Kim HJ. An anatomy of the insertion of the zygomaticus major muscle in human focused on the muscle arrangement at the mouth corner. Plast Reconstr Surg. 2008;121(2):466–73.
33. Won SY, Choi DY, Kwak HH, Kim ST, Kim HJ, Hu KS. Topography of the arteries supplying the masseter muscle: using dissection and Sihler's method. Clin Anat. 2012;25(3):308–13.
34. Won SY, Yang HM, Woo HS, Chang KY, Youn KH, Kim HJ, Hu KS. Neuroanastomosis and the innervation territory of the mental nerve. Clin Anat. 2014;27:598–602.
35. Yang HM, Hu KS, Song WC, Park JT, Kim HJ, Koh K-S, Kim HJ. Innervation patterns of the canine masticatory muscles with comparison to the human. Anat Rec. 2010;293(1):117–25.
36. Yang HM, Lee JG, Hu KS, Gil YC, Choi YJ, Lee HK, Kim HJ. New anatomical insights on the course and branching patterns of the facial artery: clinical implications of injectable treatments to the nasolabial fold and nasojugal groove. Plast Reconstr Surg. 2014; 133:1077–82.
37. Yu SK, Lee MH, Kim HS, Park JT, Kim HJ, Kim HJ. Histomorphologic approach for the modiolus with reference to reconstructive and aesthetic surgery. J Craniofac Surg. 2013;24(4): 1414–7.

US Anatomy of the Upper Superficial Cervical Region

7

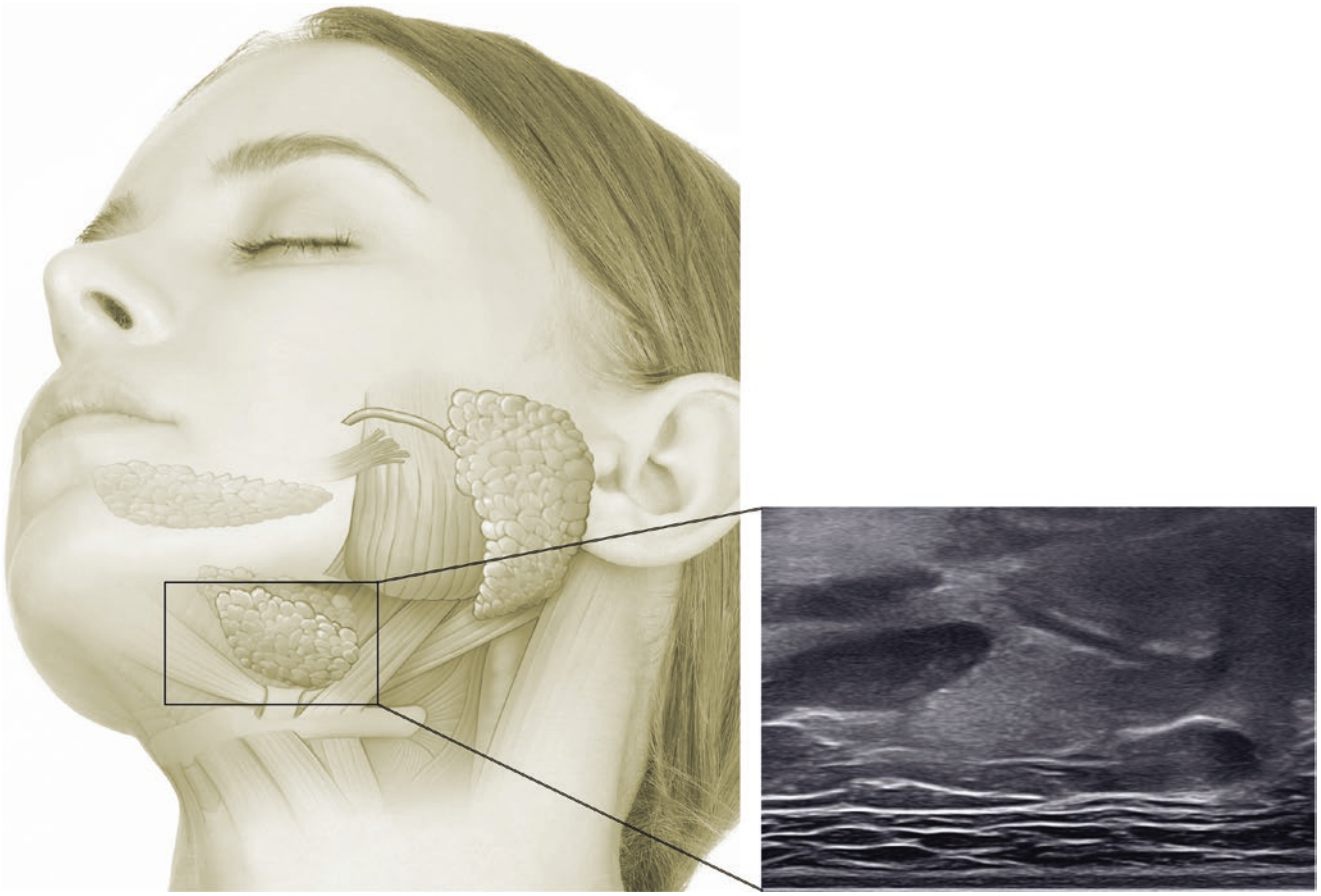

H.-J. Kim et al., *Ultrasonographic Anatomy of the Face and Neck for Minimally Invasive Procedures*,
https://doi.org/10.1007/978-981-15-6560-1_7

7.1 Clinical Anatomy of the Upper Superficial Cervical Region

7.1.1 General Topographic Anatomy of the Upper Superficial Cervical Region

The cervical region has layers that consist of the skin, the subcutaneous or fat layer, and the superficial and deep fascia covering muscles and visceral structures (Fig. 7.1). Understanding the fascial layer and compartments is critical in a clinical setting since infectious and inflammatory spreading can be caused by invasive treatments.

7.1.2 The Superficial Cervical Fascia (Investing Layer) and Platysma Muscle

The superficial cervical fascia refers to the subdermal layer. The subdermal layer includes fatty tissue, superficial lymph nodes, cutaneous nerves and vessels, and the platysma m. The platysma m. is a thin and broad layered musculature covering the frontal and lateral aspects of the neck (Fig. 7.2).

The platysma m. is one of the facial expression muscles. The muscle arises from the pectoral fascia below the clavicle and runs to the mandibular border. The outer muscle fibers merge with the lower facial muscles that extend upward and

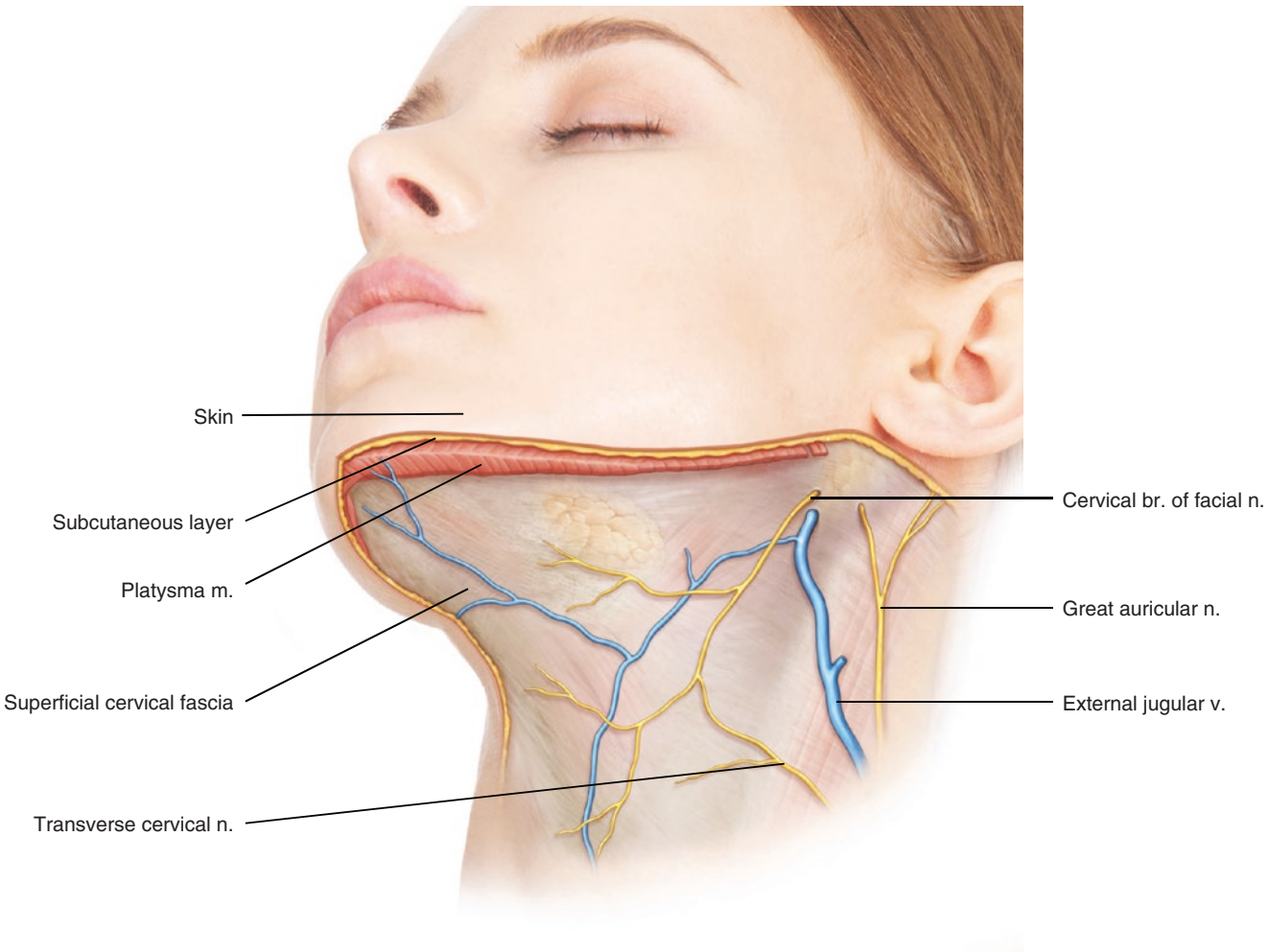

Fig. 7.1 Illustration of the cervical fasciae. (Published with kind permission of © Kwan-Hyun Youn 2020. All Rights Reserved)

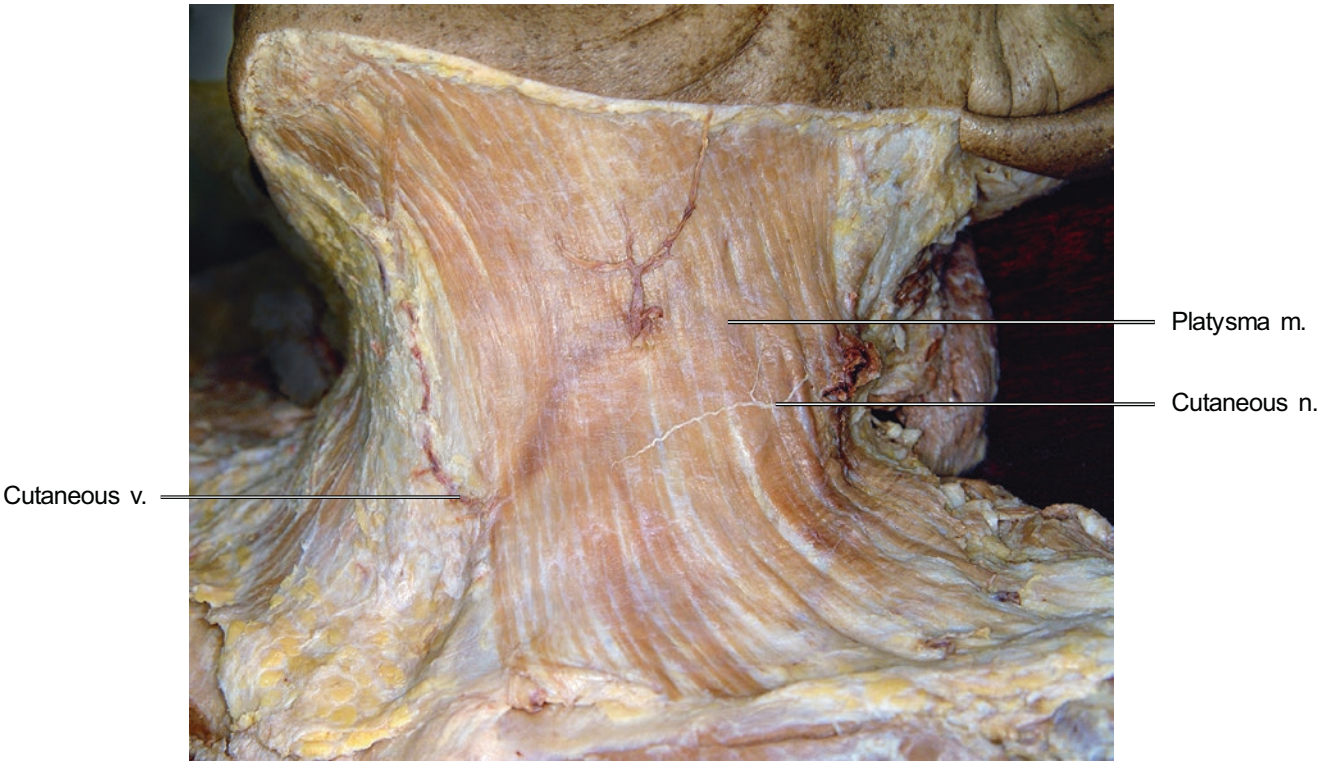

Fig. 7.2 Lateral aspect of the dissection of the platysma muscle. (Published with kind permission of © Hee-Jin Kim 2020. All Rights Reserved)

inward to the lower face. The medial muscle fibers of both sides decussate each other at the submental region and attach to the inferior border of the mandible by the mandibular septum. The lack of decussation of medial muscle fibers results in reduction of skin elasticity causing "gobbler neck deformity" as part of the aging process (Fig. 7.3).

7.1.3 Visceral Fascia

The visceral fascia is the middle layer of the neck surrounding the pharynx, larynx, and thyroid gland. The fascia surrounding the pharynx is called the "buccopharyngeal fascia," and the fascia surrounding the airways and esophagus is called the "pretracheal fascia." The visceral fascia arises from the hyoid bone and attaches to the skull base covering the pharynx. The visceral fascia inferiorly extends to the superior mediastinum and merges with the pericardium.

7.1.4 Triangles of the Neck

The sternocleidomastoid and trapezius mm. divide the neck into anterior and posterior cervical triangles. Other muscles of the neck subdivide the anterior and posterior cervical triangle into smaller triangles.

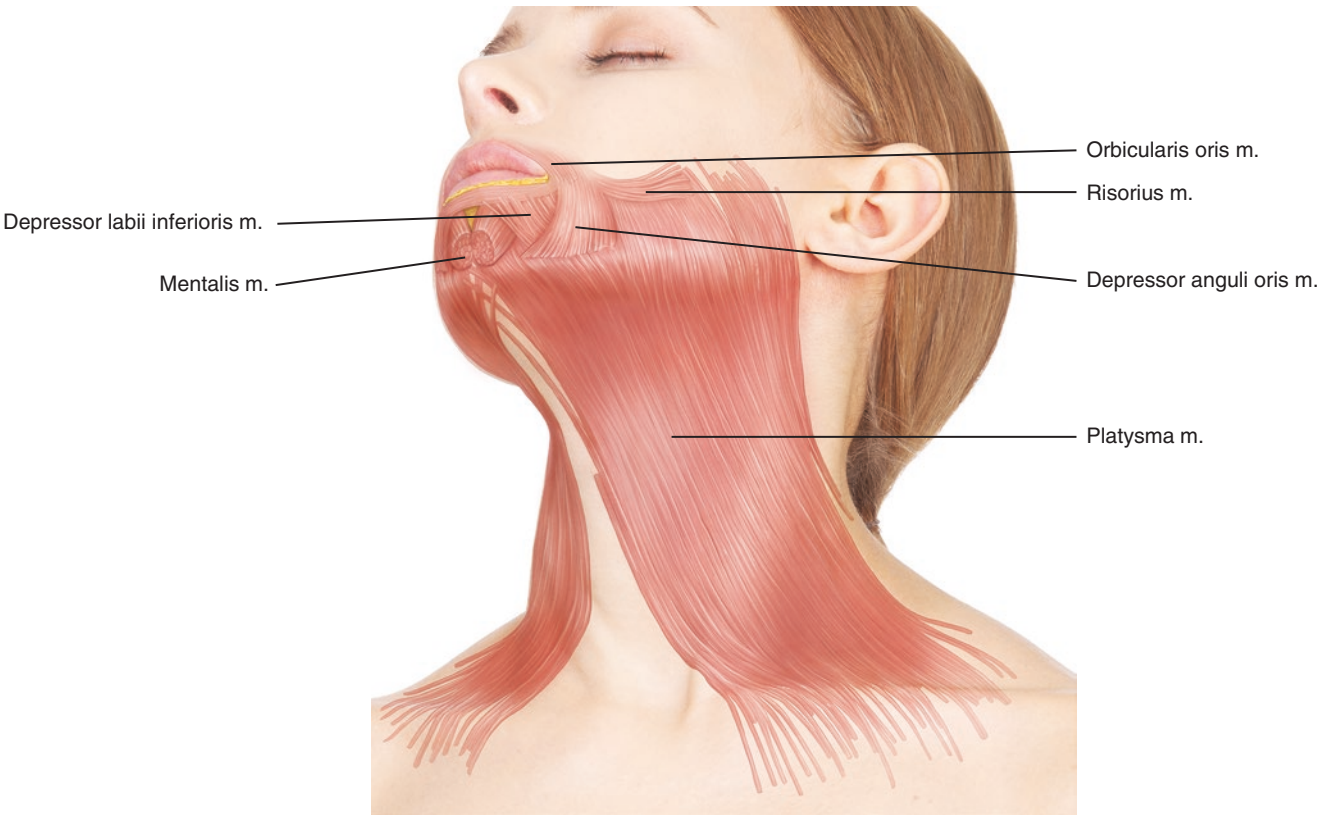

Fig. 7.3 Oblique view of the platysma muscle. (Published with kind permission of © Kwan-Hyun Youn 2020. All Rights Reserved)

The anterior cervical triangle is an inverted triangle bounded by the inferior border of the mandible as the base and the sternal manubrium occupying the anterior region of the neck as the apex. The anterior cervical triangle is subdivided into smaller triangles: muscular, carotid, submental, and submandibular triangles (Fig. 7.4). In this chapter, only the submental and submandibular triangles will be described.

The submental triangle is located below the mentum, which has as boundaries the bilateral anterior digastric mm. and hyoid bone. The submandibular triangle is bounded by the inferior border of the mandible, the anterior and posterior digastric mm. (Fig. 7.5). The submandibular triangle includes the submandibular gland, submandibular lymph nodes, lingual a., facial a., facial n., and mylohyoid m.

7.1.5 Suprahyoid mm.

Four pairs of muscles originate from the upper anatomical structures and insert into the hyoid bone. The posterior belly of the digastric m. originates from the digastric notch (deep aspect of the mastoid process). The posterior belly of the digastric m. becomes narrower as it turns to the intermediate tendon and runs to the hyoid bone. The intermediate tendon is hooked by the canal of the fascia and continues toward the anterior belly of the digastric m. The anterior belly of the digastric m. arises from the intermediate tendon and attaches to the digastric fovea of the mandible.

The mylohyoid m. is flat and broad shaped, which originates from the mylohyoid line of the mandible. The muscle fibers run down and inward, inserting to the median raphe and hyoid body. The median raphe is formed by bilateral mylohyoid m. fibers intertwined at the midline. The geniohyoid m. lies deep to the mylohyoid m. and originates from the genial tubercle and inserts into the hyoid bone. The stylohyoid m. originates from the styloid process of the temporal bone and runs anteroinferiorly and inserts to the hyoid body. The tendon of the stylohyoid m. is divided into two at the hyoid body surrounding the intermediate tendon of the digastric m. (Fig. 7.6).

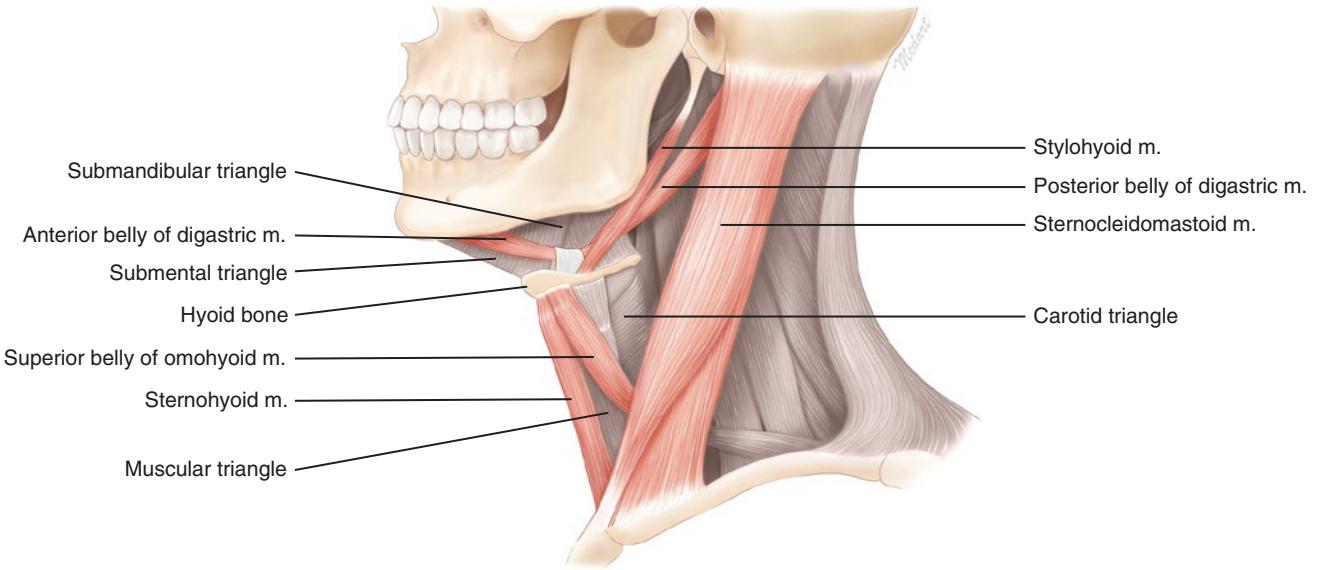

Fig. 7.4 Illustration representing the anterior cervical triangle. (Published with kind permission of © Kwan-Hyun Youn 2020. All Rights Reserved)

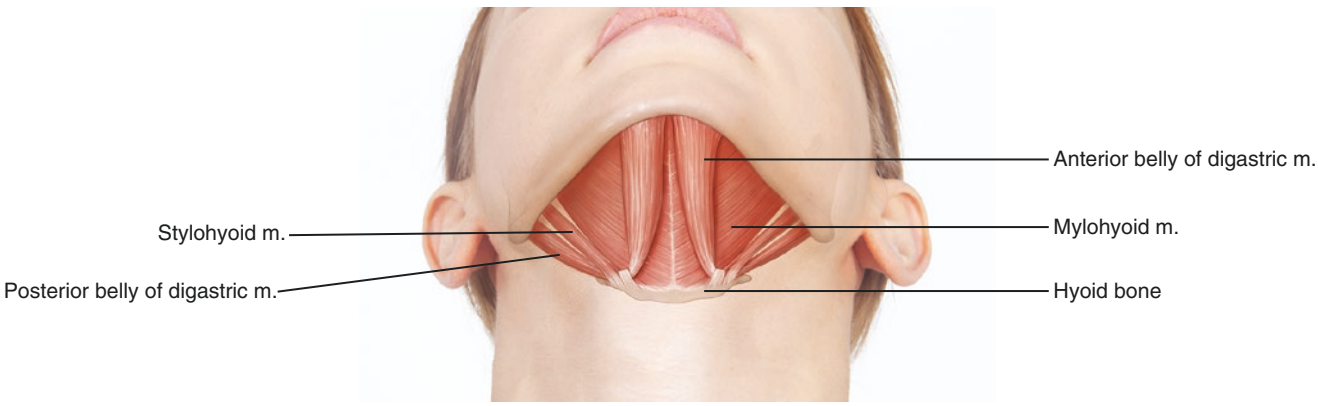

Fig. 7.5 Illustration representing the submental triangle. (Published with kind permission of © Kwan-Hyun Youn 2020. All Rights Reserved)

7.1.6 Vessels of the Upper Superficial Cervical Region

When the facial a. branches off from the external carotid a., the artery runs between the medial side of the mandible and the mylohyoid m. Subsequently, the facial a. turns outward and emerges to the facial surface at the antegonial notch. The pulse of the facial a. is easily palpated at the antegonial notch. The branches of the facial a. around the submandibular region are as follows: the ascending palatal a., the tonsillar branches, and the submental a. The ascending palatal a. and the tonsillar branches supply the submandibular gland while the submental a. runs along the mylohyoid n., which innervates the mentum area.

The lingual a. originates from the external carotid artery and runs deep to the posterior digastric m. Subsequently, the lingual a. comes out superficially at the submandibular area where it again runs deep to the mylohyoid m. supplying the tongue and other structures (Fig. 7.7). The facial and lingual vv. drain into the internal jugular v. which runs along the arteries.

7.1.7 Submandibular and Parotid Gland

The submandibular gland is one of the major salivary glands and is a mixed gland (glands with serous and mucous acini). The submandibular gland lies in the submandibular region both superficial and deep to the mylohyoid m. The superfi-

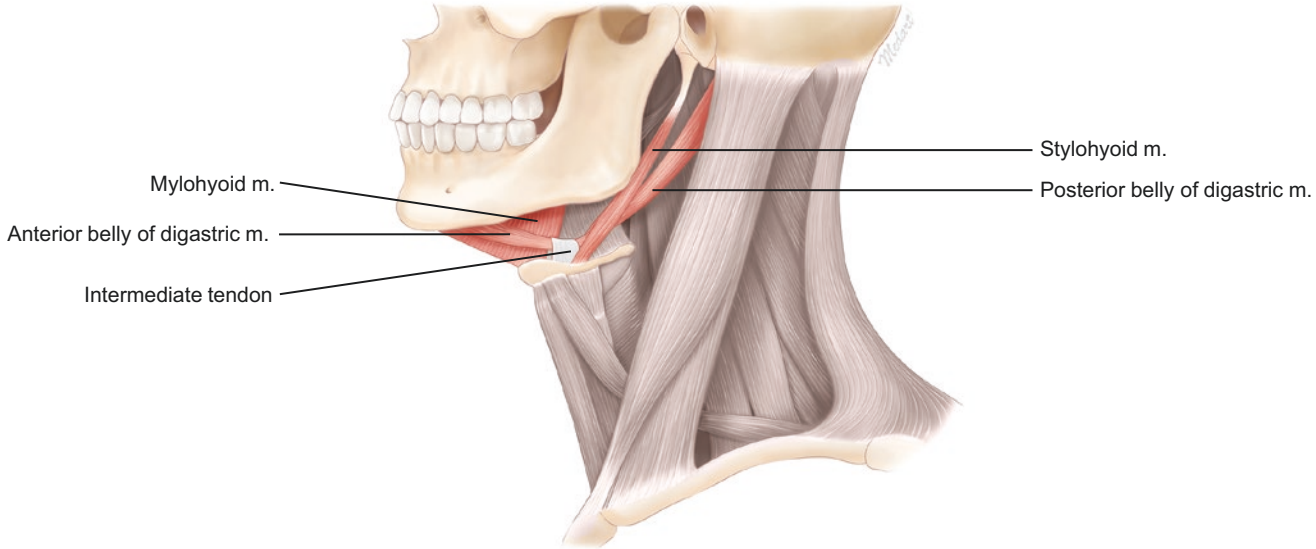

Fig. 7.6 Illustration representing the suprahyoid muscles. (Published with kind permission of © Kwan-Hyun Youn 2020. All Rights Reserved)

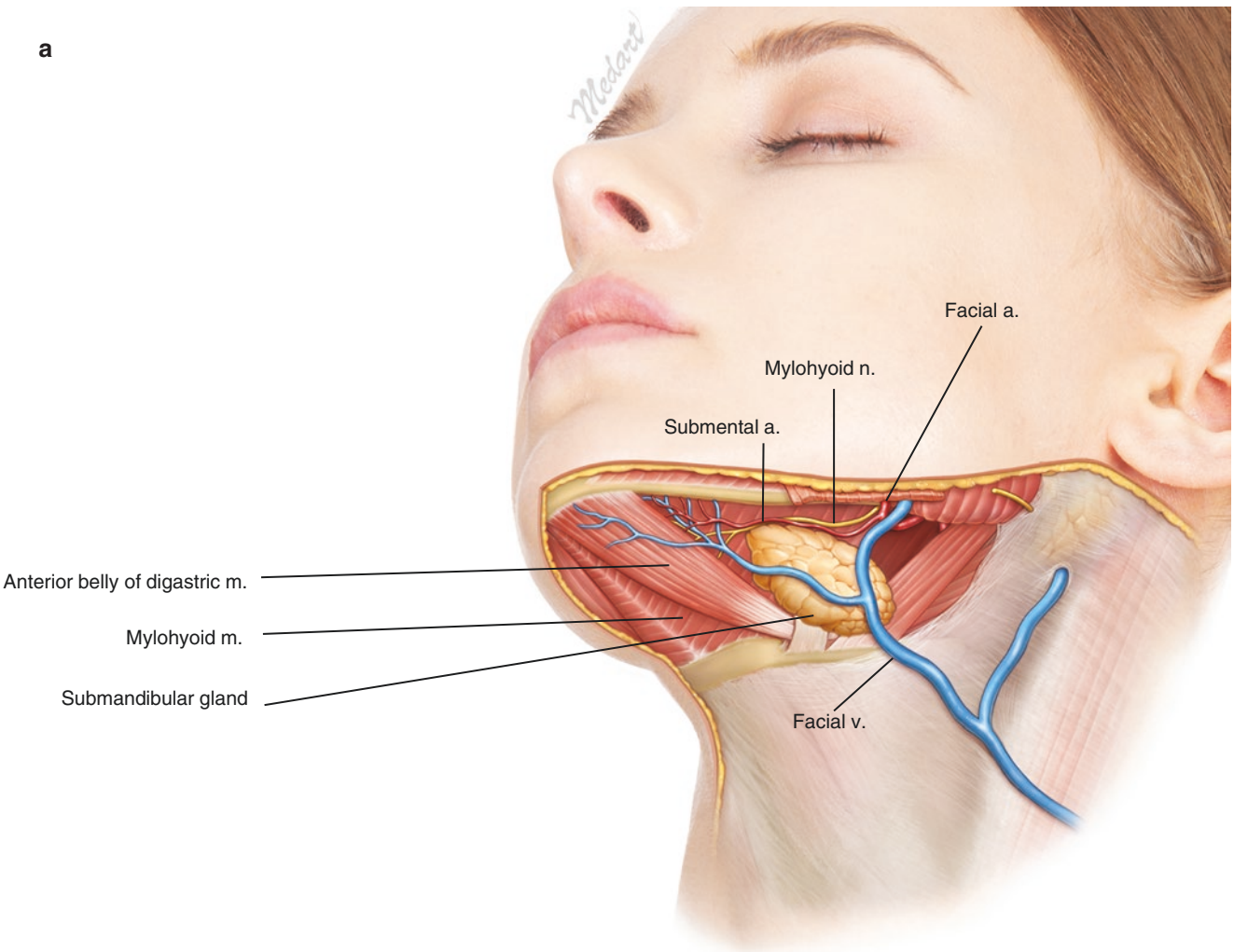

Fig. 7.7 Illustration representing the vasculature of the upper superficial cervical region. (**a**) superficial layer and (**b**) deep layer after exposing digastric and mylohyoid mm. (Published with kind permission of © Kwan-Hyun Youn 2020. All Rights Reserved)

Fig. 7.7 (continued)

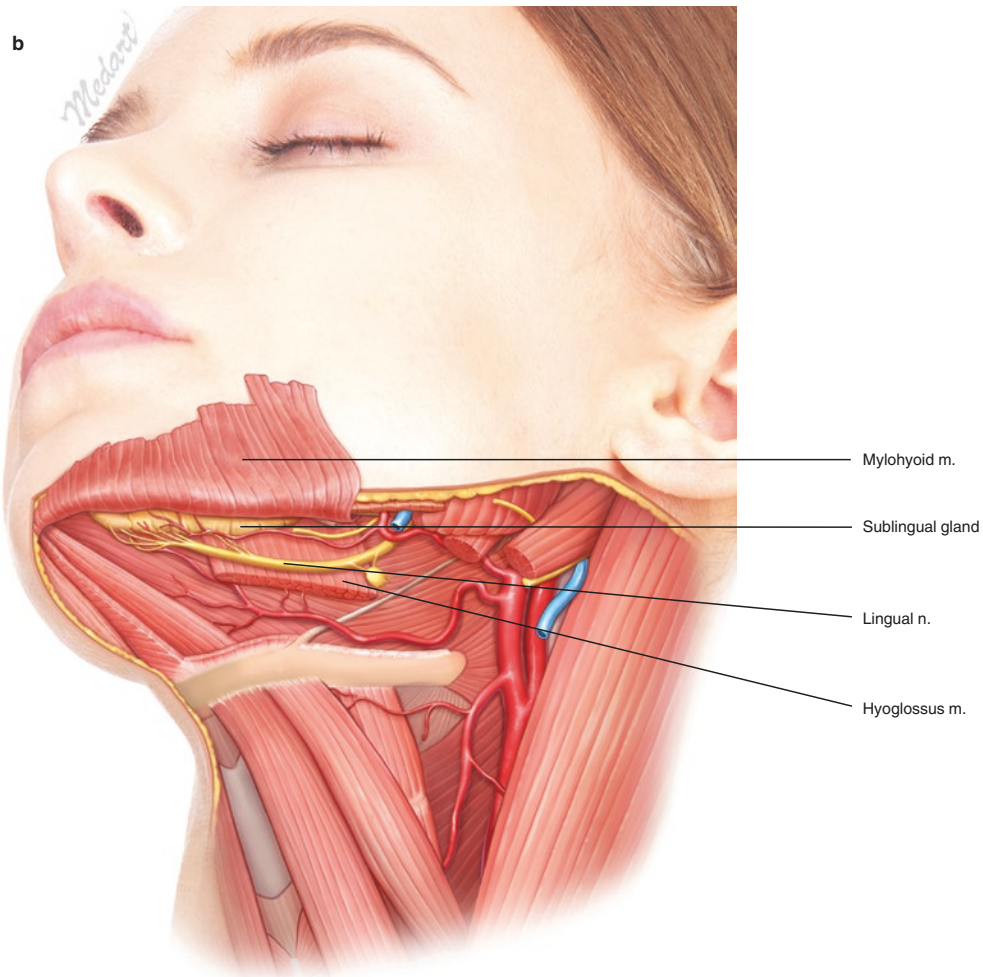

cial portion of the submandibular gland is superficial to the mylohyoid m., and the deep portion extends from the mandibular body to the base of the tongue. The glandular branches of the facial a. supply the submandibular gland (Fig. 7.8).

The parotid gland is the biggest major salivary gland, which secretes pure serous saliva. The parotid gland is enclosed by a fibrous capsule continuous to the fascial layer. The stylomandibular ligament is the structure distinguishing the parotid gland from the infratemporal region and the submandibular gland. The superficial lobe of the parotid gland is the most palpable and dominant portion of the gland (approximately 80% of the total gland). The parotid tail is the most inferior portion of the superficial lobe. It is triangular-shaped, located deep to the platysma m., below the mandibular border, posterolateral to the posterior belly of the digastric m. and anterolateral to the sternocleidomastoid m. The parotid duct is 5 cm in length, with an internal diameter of 3 mm. The wall of the parotid duct is thick and consists of the mucosal and fibrous coat with smooth muscle cells (Fig. 7.9). Structures passing the parotid area include (1) the facial n. and its branches; (2) the retromandibular v. and its tributaries; and (3) the maxillary and superficial temporal aa. and the external carotid a. itself.

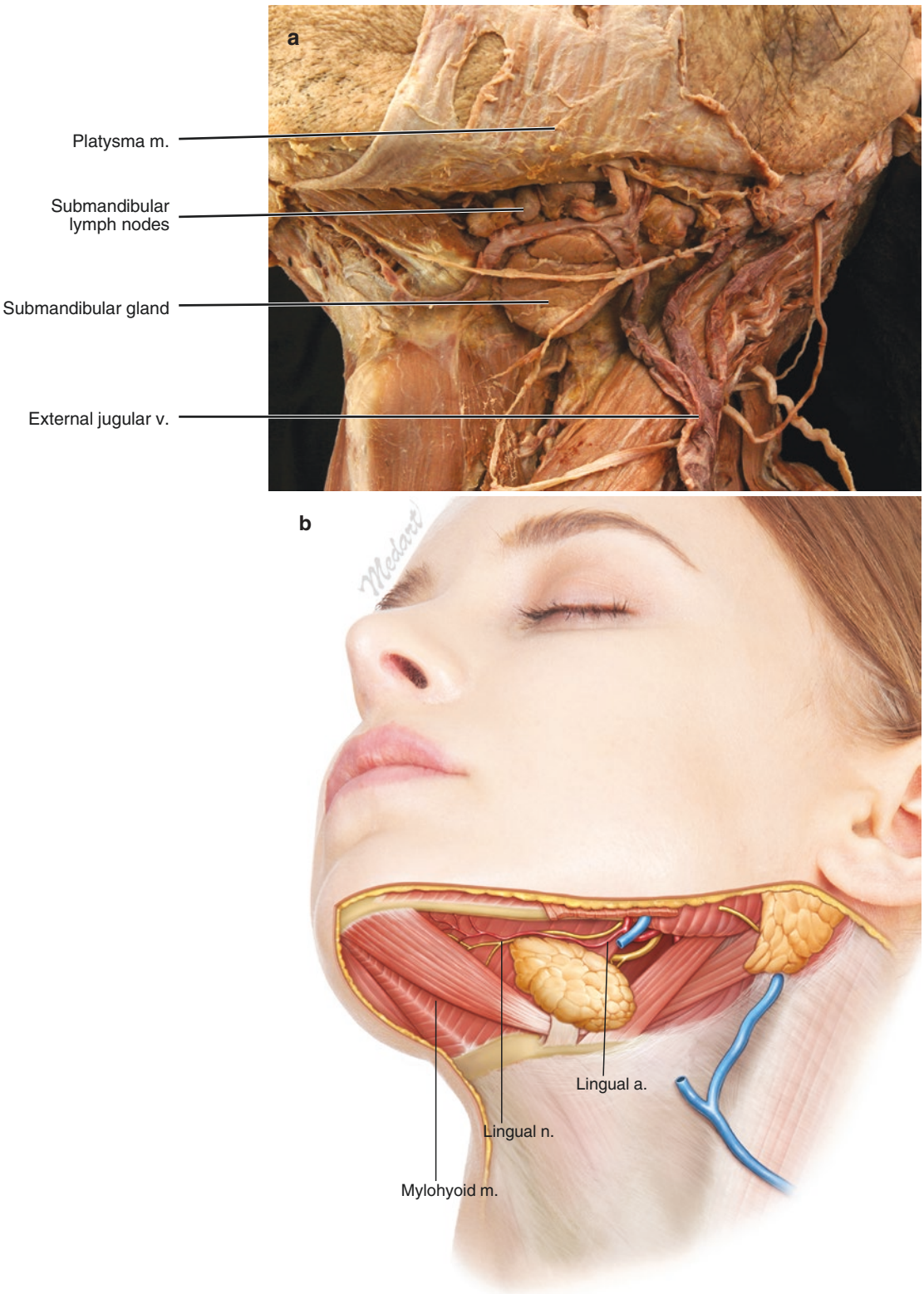

Fig. 7.8 Topography of the submandibular triangle. (**a**) dissection photograph representing the topographic anatomy of the submandibular gland and (**b**) corresponding illustration of the submandibular triangle.

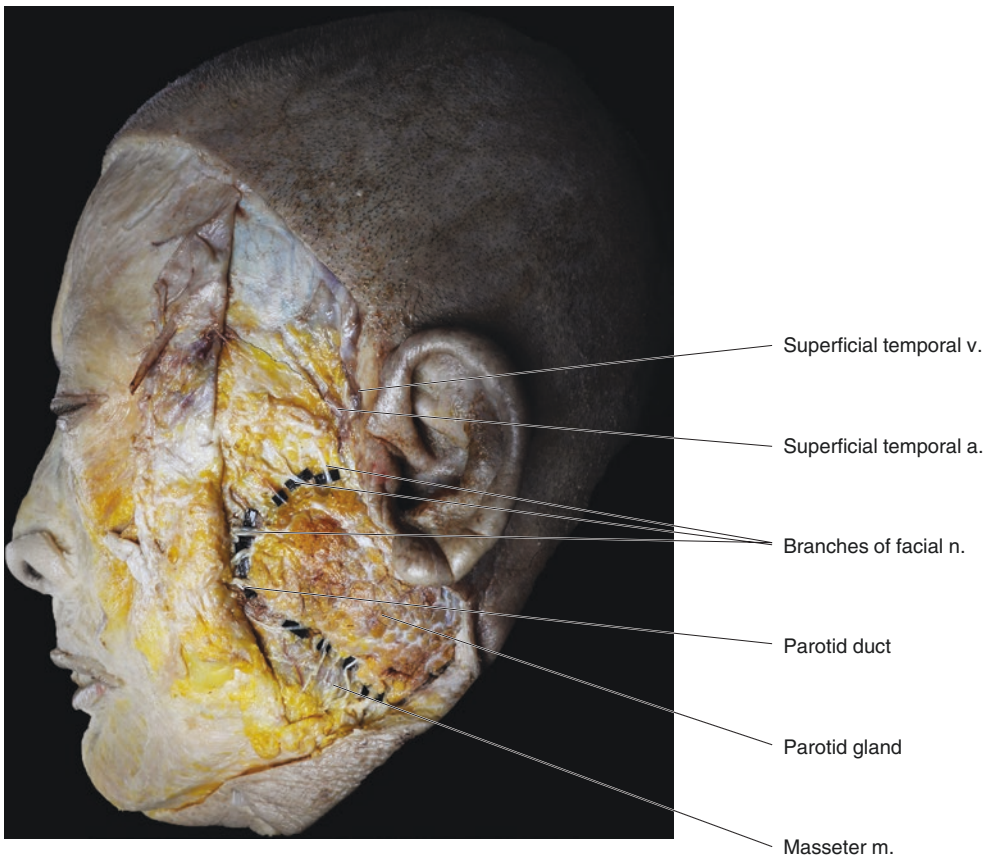

Fig. 7.9 Topography of the parotid gland. (Published with kind permission of © Hee-Jin Kim 2020. All Rights Reserved)

7.1.8 Facial Landmarks and Reference Lines for the US Examination of the Upper Superficial Cervical Region (Fig. 7.10)

Upper superficial cervical region	
C1: gnathion	**C3**: submandibular triangle
C2: point 2 cm posterior to the point C1	**C4**: mandibular angle

7.1.9 Checklists in Upper Superficial Cervical Region

Objective structures	Facial landmarks where the structures can be observed
Platysma m.	C1, C2, C3, C4
Digastric m.	C2
Mylohyoid m.	C2, C3
Genioglossus m.	C2
Geniohyoid m.	C2
Transversus menti	C1
Hyoglossus m.	C3
Sternocleidomastoid m.	C4

Objective structures	Facial landmarks where the structures can be observed
Masseter m.	C4
Submental a.	C1, C2
Anterior jugular v.	C2
Facial a.	C3
Facial v.	C3
Retromandibular v.	C4
Sublingual gland	C2
Submandibular gland	C3
Parotid gland	C4
Submandibular lymph node	C3

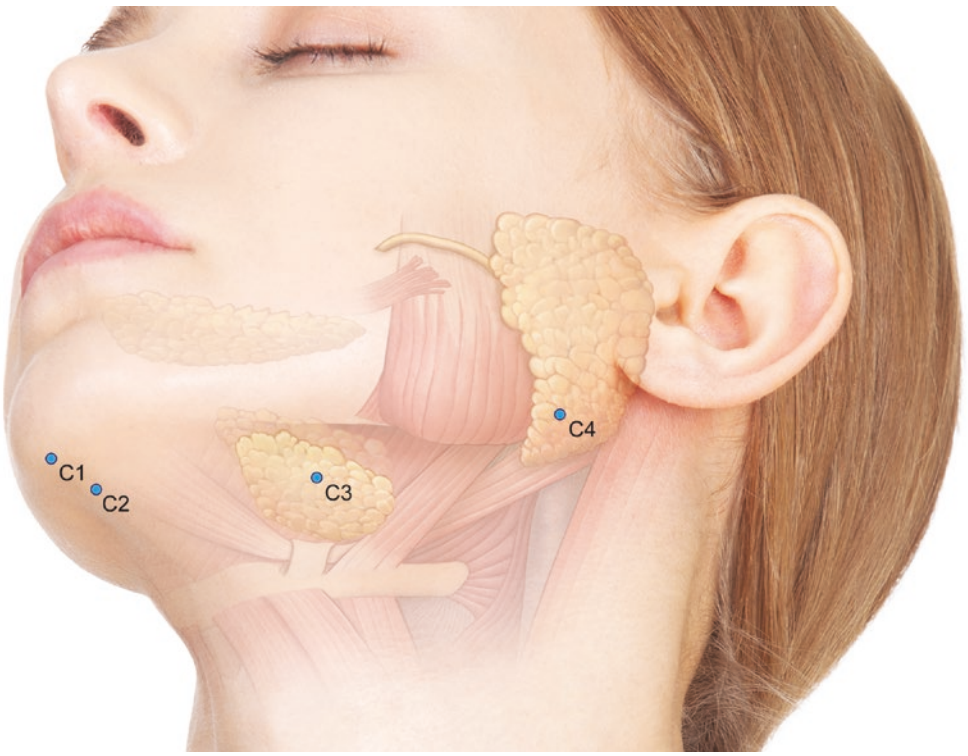

Fig. 7.10 Facial landmarks and reference lines for the ultrasonographic examination of the upper superficial cervical region. (Published with kind permission of © Kwan-Hyun Youn 2020. All Rights Reserved)

7.2 US Images of the Upper Superficial Cervical Region

7.2.1 US Anatomy Images

Generally, the skin thickness of the superficial cervical region is relatively thinner and more uniform than the facial skin. An irregular subcutaneous layer is observed deep to the hyperechoic band of the epidermis and hyperechoic dermis. The amount of the subcutaneous layer is variable depending on the region of the neck. The thickest subcutaneous layer of the neck is observed at the submental region. The thin hypoechoic platysma m. is observed from the anterior and lateral aspects of the neck.

Particularly, the hyperechoic fascial structure of the neck is clearly observed. The US images of cervical fasciae and positional relationships with the cervical mm. are straightforward. The hypoechoic suprahyoid mm. are covered by the hyperechoic superficial cervical fascia. The hypoechoic vascular structures are inside the interfascial space. The muscles are more accurately visible during the swallowing period. The submandibular gland and the tail of the parotid gland are observed in the upper superficial cervical region. These structures are visible as a homogeneous mid-gray image.

7.2.2 B Mode and Doppler Images

C1: Gnathion

The point C1, gnathion, refers to the midpoint of the inferior border of the mandible. The point is characterized by the thick hyperechoic epidermis, dermis, and subcutaneous tissue. The hypoechoic platysma m. is observed in spots underneath the subcutaneous layer. This is the area where the platysmal fibers decussated and partially insert into the inferior border of the mandible. In some cases, the superficial fibers of the DAO m. cross the midline and form the transversus menti m. The anechoic submental a. emerging into the lower face is observed within the deep subcutaneous layer (Fig. 7.11).

C2: Point 2 cm Posterior to the Point C1

The point C2 is 2 cm posterior to the point C1. The hyperechoic skin, subcutaneous tissue, and hypoechoic bands of the platysma

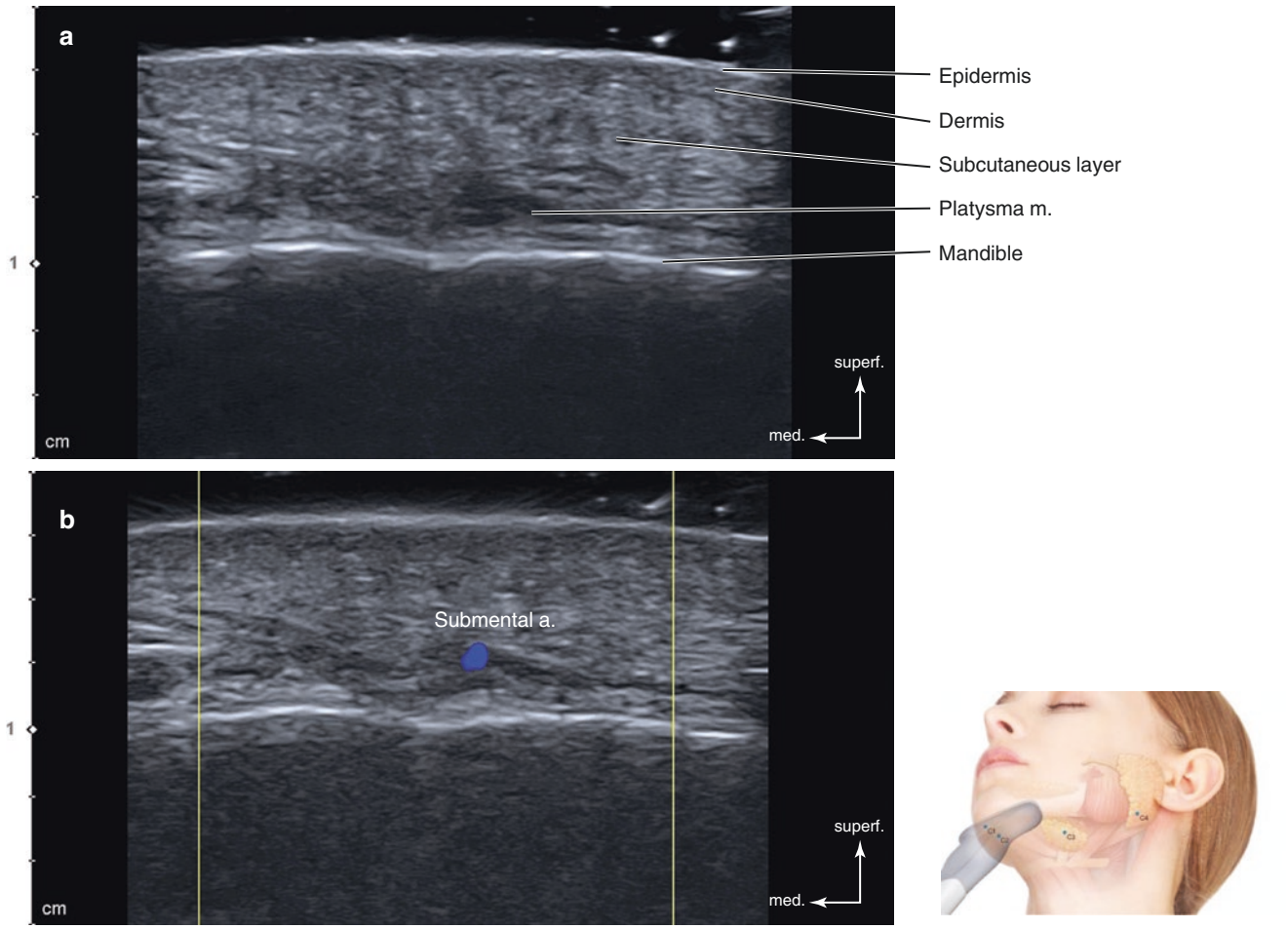

Fig. 7.11 Ultrasonography of the gnathion (C1). (**a**) B mode (transverse view, 15 MHz by linear transducer) and (**b**) Doppler mode (transverse view, 15 MHz by linear transducer). (Published with kind permission of © Hee-Jin Kim 2020. All Rights Reserved)

m. are observed. The suprahyoid mm. in the submental triangle are observed in the transverse view. The image demonstrates round-shaped hypoechoic anterior bellies of the digastric m. deep to the hypoechoic platysma m. The hypoechoic mylohyoid m. is observed as an arch across the image. The hypoechoic geniohyoid m. is located deep to the mylohyoid m. The genioglossus m. is observed in the deepest layer. These muscles are easily distinguishable while swallowing. The sublingual glands are observed in homogeneous mid-gray color lateral to the genioglossus m. The sublingual vessels are observed on the medial side of each gland. The Doppler mode image demonstrates the anterior jugular v. running underneath the platysma m. and submental vessels running superficial to the mylohyoid m. (Fig. 7.12a, b). In an aged obese patient, the saggy and volumized submental fat is visualized as a hypoechoic image with many internal septa (Fig. 7.12c).

C3: Submandibular Triangle

The point C3 is located at the submandibular triangle. The transducer was placed transversely along the inferior border of the mandible. The submandibular gland is observed as a large triangular structure of uniformly homogeneous mid-gray color. Clinicians should know that the parotid tail can be observed at the mandibular angle and should not be mistaken with the submandibular gland. The hypoechoic bands of the platysma m. are observed underneath the irregular

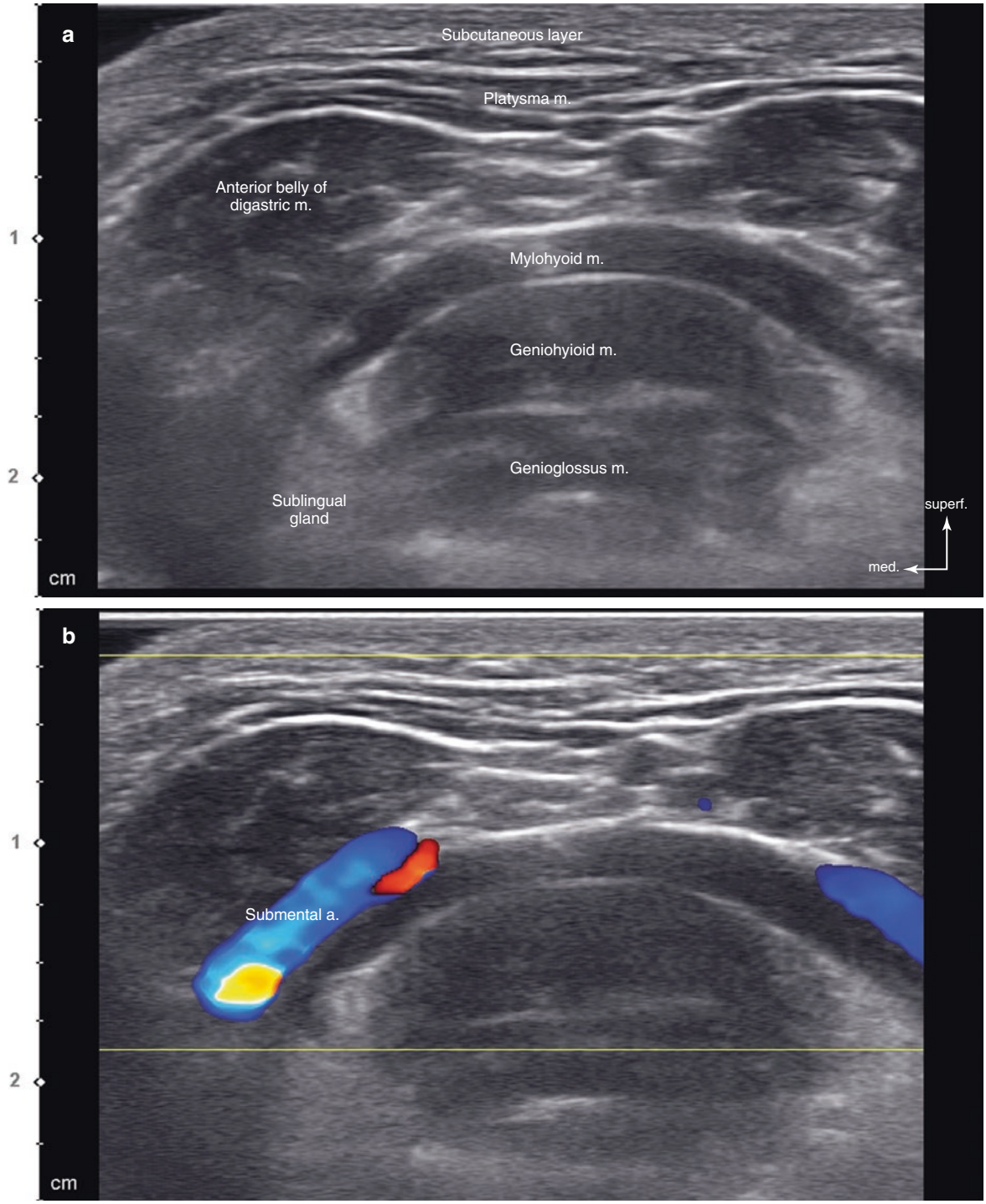

Fig. 7.12 Ultrasonography of the point at 2 cm posterior to the point C1 (C2). (**a**) B mode (transverse view, 15 MHz by linear transducer), (**b**) Doppler mode (transverse view, 15 MHz by linear transducer), and (**c**) B mode (transverse view, 15 MHz by linear transducer). (Published with kind permission of © Hee-Jin Kim 2020. All Rights Reserved)

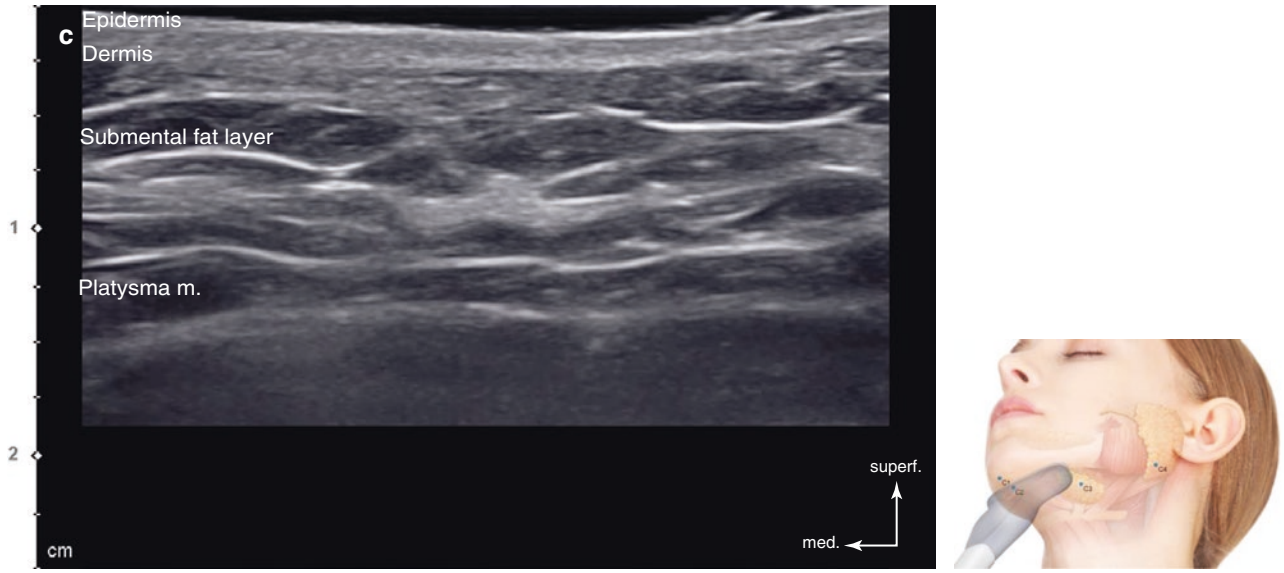

Fig. 7.12 (continued)

hyperechoic subcutaneous tissue layer. The facial a. and v. are observed medial to the submandibular gland. The submandibular lymph nodes are presented near the facial vessel. The hypoechoic bands of the anterior belly of digastric (superficial), mylohyoid (intermediate), and hyoglossus (deep) mm. are located anterior and deep to the submandibular gland. These muscles are transversely placed toward the hyoid bone. The anechoic submandibular duct runs toward the oral cavity located between the mylohyoid and hyoglossus m. The Doppler mode image is helpful in distinguishing the vessels from the duct. There are no signals from the duct compared to the vessels. The course of the facial a. and facial v. can be traced as they run superficial to the submandibular gland and toward the inferior border of the mandible (Fig. 7.13).

C4: Mandibular Angle

Point C4 is the mandibular angle. The transverse image at this point demonstrates the parotid tail extending over the inferior border of the mandible in homogeneous mid-gray color. The masseter m., parotid gland, and sternocleidomastoid m. are mainly observed. The intraparotid lymph nodes can be observed within the parotid gland as hypoechoic ovals, approximately 3–5 mm in diameter, with a central hyperechoic hilum. The Doppler mode image demonstrates the retromandibular v. and external carotid a. (deep to the vein) at the point C4. In some cases, these vessels cannot be observed due to the thick fat tissues within the gland (Fig. 7.14).

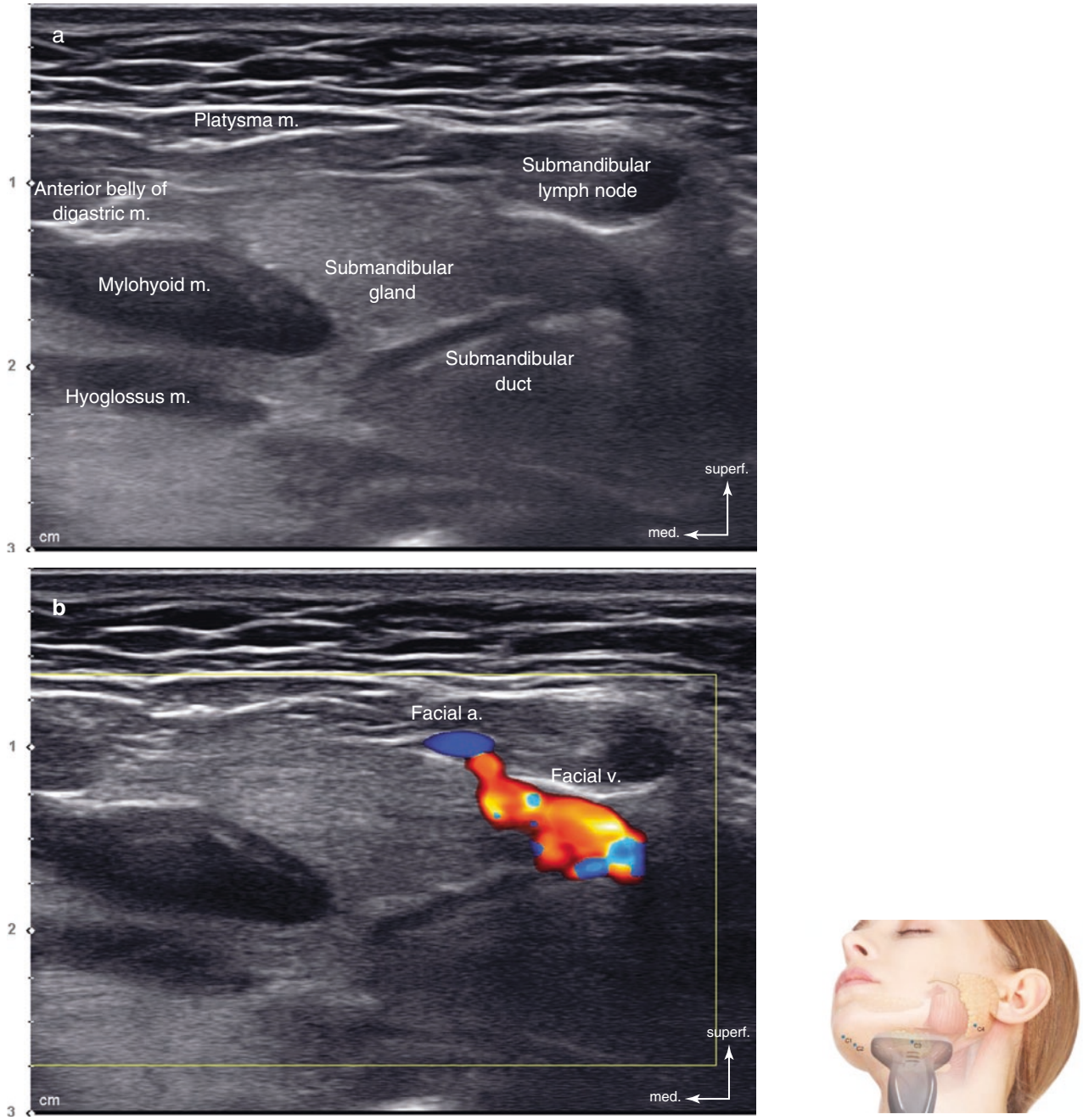

Fig. 7.13 Ultrasonography of the submandibular triangle (C3). (**a**) B mode (transverse view, 15 MHz by linear transducer) and (**b**) Doppler mode (transverse view, 15 MHz by linear transducer). (Published with kind permission of © Hee-Jin Kim 2020. All Rights Reserved)

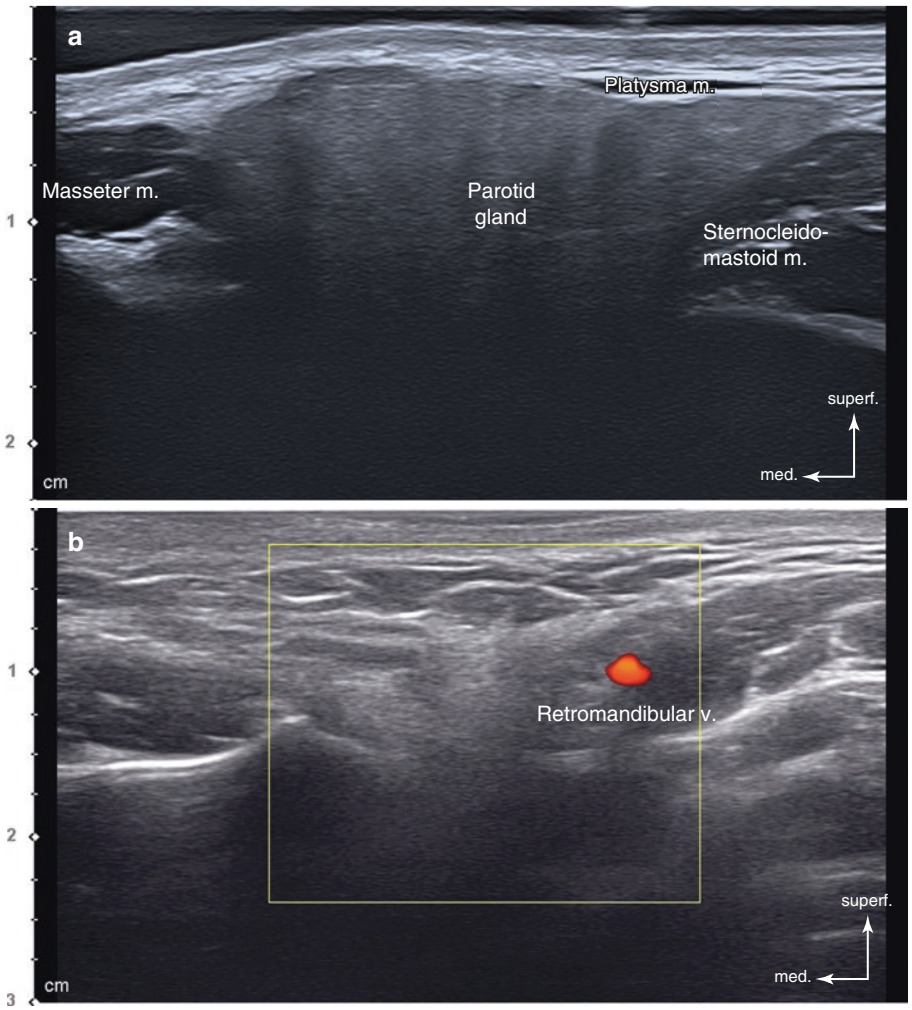

Fig. 7.14 Ultrasonography of the mandibular angle (C4). (**a**) B mode (transverse view, 15 MHz by linear transducer) and (**b**) Doppler mode (transverse view, 15 MHz by linear transducer). (Published with kind permission of © Hee-Jin Kim 2020. All Rights Reserved)

Bibliography

1. Bae JH, Youn KH, Hu KS, Lee JH, Tansatit T, Kim HJ. Clinical implications of the extension of platysmal fibers on the middle and lower faces. Plast Reconstr Surg. 2016;138(2):365–71.
2. Choi DY, Woo YJ, Won SY, Kim DH, Kim HJ, Hu KS. Topography of the lingual foramen using micro-computed tomography for improving safety during implant placement of anterior mandibular region. J Craniofac Surg. 2013;24(4):1403–7.
3. Chung IH, Hwang K, Kang MK, Hu KS, Kim HJ. Decussation patterns of the platysma in Koreans. Br J Plast Surg. 2001;54(5): 400–2.
4. Ha RY, Nojima K, Adams WP Jr, Brown SA. Analysis of facial skin thickness: defining the relative thickness index. Plast Reconstr Surg. 2005;115:1769–73.
5. Hu KS, Kang MK, Hwang K, Chung IH, KIM HJ. Decussation patterns of the platysma in Koreans. Br J Plast Surg. 2001;54: 400–2.
6. Hur MS, Bae JH, Kim HJ, Lee HB, Lee KS. Blending of the lateral deep slip of the platysma muscle into the buccinator muscle. Surg Radiol Anat. 2015;37(8):931–4.
7. Kim ST, Hu KS, Song WC, Kang MK, Park HD, Kim HJ. Location of the mandibular canal and the topography of its neurovascular structures. J Craniofac Surg. 2009;20(3):936–9.
8. Kim YS, Lee KW, Kim JS, Gil YC, Tansatit T, Shin DH, KIM HJ. Regional thickness of facial skin and superficial fat: application to the minimally invasive procedures. Clin Anat. 2020;32:1008–18.
9. Lee HJ, Choi YJ, Lee KW, Hu KS, Kim ST, Kim HJ. Ultrasonography of the internal architecture of the superficial part of the masseter muscle in vivo. Clin Anat. 2019;32(3):446–52.
10. Lee HJ, Ryu SY, Cong L, Ahn HJ, Park MK, Kim HJ, Hu KS. Anatomy of the superficial venous structures of the neck: a cadaveric study to guide superficial injections. Dermatol Surg. 2019;45(2):203–9.
11. Lee HJ, Won SY, Jehoon O, Hu KS, Mun SY, Yang HM, Kim HJ. The facial artery: a comprehensive anatomical review. Clin Anat. 2018;31:99–108.
12. Lee JH, Lee K, Jung W, Youn KH, Hu KS, Tansatit T, KIM HJ. A novel anatomical consideration on the exposed segment of the facial artery. Clin Anat. 2020;33:257–64.
13. Yang HM, Kim HJ, Park HW, Sohn HJ, Ok HT, Moon JH, Woo SH. Revisiting the topographic anatomy of the marginal mandibular branch of facial nerve relating to the surgical approach. Aesthet Surg J. 2016;36(9):977–82.
14. Yang HM, Lee JG, Hu KS, Gil YC, Choi YJ, Lee HK, Kim HJ. New anatomical insights of the course and branching patterns of the facial artery: clinical implications regarding injectable treatments to the nasolabial fold and nasojugal groove. Plast Reconstr Surg. 2014;133(5):1077–82.

US Applications in Botulinum Toxin Injection Procedures

8

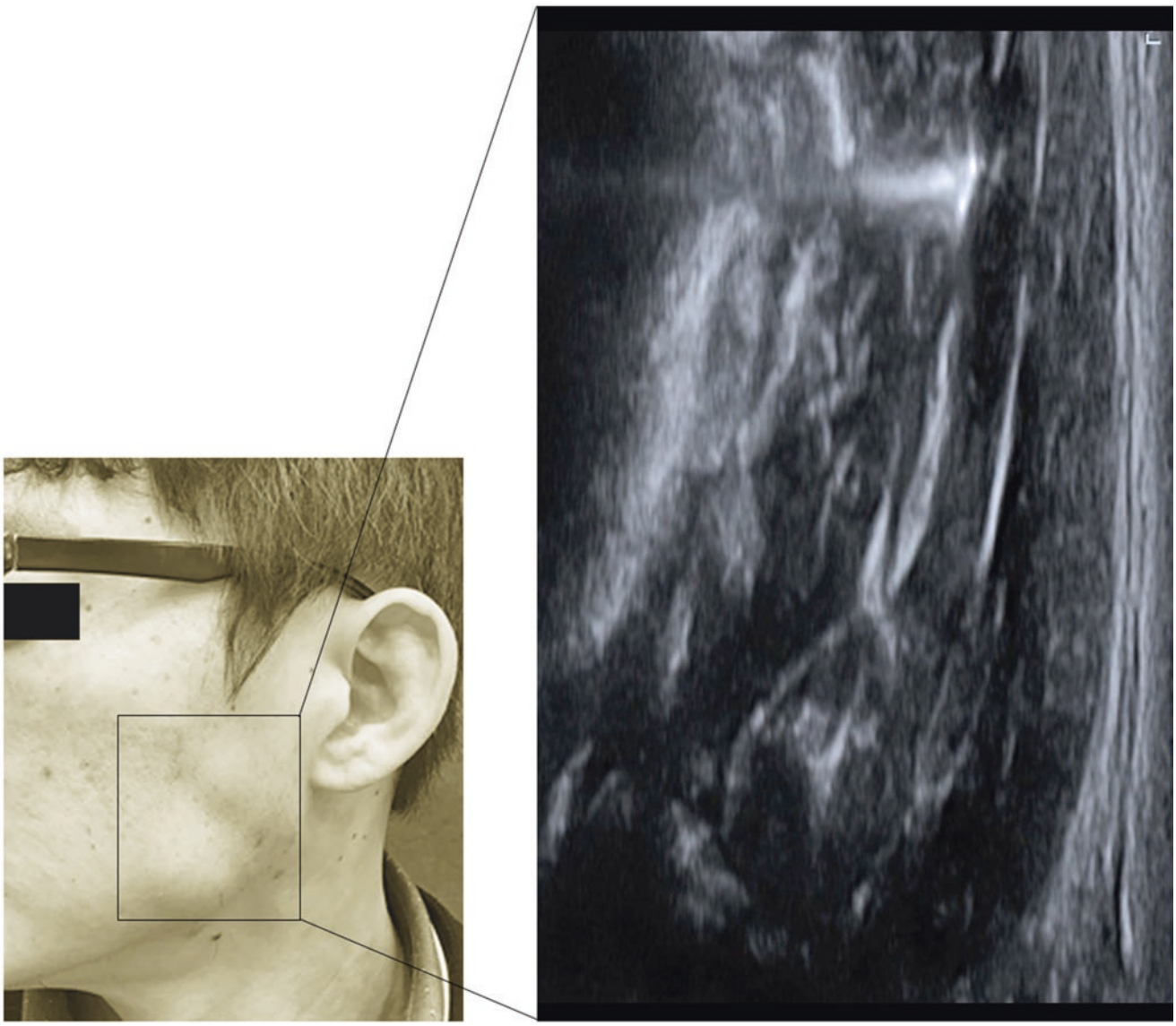

H.-J. Kim et al., *Ultrasonographic Anatomy of the Face and Neck for Minimally Invasive Procedures*,
https://doi.org/10.1007/978-981-15-6560-1_8

8.1 Backgrounds of the US-Guided Botulinum Toxin Injection Procedures

Botulinum toxin is usually injected into the muscles and glands, except intradermal injection procedures. Botulinum toxin injection requires thorough anatomical understanding because even though target muscles for each indication are specific, we can only rely on the surface anatomy when injecting. In the last 15 years, anatomical research related to minimally invasive aesthetic treatments has greatly contributed to improving the precision of blind injection techniques.

In the twenty-first century, artificial intelligence is one of the leading fields of medical interest. To depend on "palpation" and "inspection" during botulinum toxin procedures is equivalent to using solely a stethoscope in diagnosing a patient despite having MRI imaging available. However, there are a few reasons that we have relied on this technique. First, botulinum toxin injections are performed somewhat superficially, targeted 0.5–2.5 cm below the skin. Therefore, many clinicians think that palpation of the superficial facial muscles is sufficient in distinguishing anatomy, yet various depths of fat alongside diverse muscle layers make the borders ambiguous and difficult to locate. For the last 10 years, US-guided and blind injection techniques in the musculoskeletal field have been compared in many studies leading to the conclusion that blind injections are inaccurate even in the superficial muscle layer.

Also, since muscle borders can be distinguished when contracted, many clinicians tend to focus only on the superficial dermis layer, for example, diagnosing wrinkles and muscle shape, ignoring the targeted muscles that are causing the contraction. Targeting the contracting muscle is especially important since its hypertrophy and movements are the actual cause of wrinkles. Clinicians could broadly locate the area where the muscles contract, but accurately distinguishing the layer, area, border, and relationship with the adjacent anatomy is difficult. There are many anatomical variations, and anatomical alterations may occur with increases in plastic surgery or nonsurgical procedures, such as implant insertion or filler injection.

Another reason that accurate injection protocols have been overlooked is the fact that botulinum toxin has minimal complications and even if complications occur, the side effects will subside within 2–3 months. Regardless of the fact that this procedure has minimal complications and it is reversible, the practitioners must always perform accurate treatment for the patient. Treatments based on the precise diagnosis can escalate the efficacy and reduce complications, and this can be effectively acquired by an imaging tool.

When applying US imaging, botulinum injection procedures have the following advantages. First, the target structure and adjacent anatomy can be observed in real time. Second, the dynamic muscle actions can be detected simultaneously from the US image. Muscle movement during contraction cannot be captured in real time with MRIs and CTs despite their high resolution. Third, a guided injection is possible when using US. US usage is beneficial by providing reference levels for the procedures, and US-guided injection is even more reliable and safer because anatomical variations can be visualized in real time.

On the other hand, US can have some disadvantages. First, US imaging can be difficult to interpret, and manipulation of the US requires a long learning curve. The facial muscles are thin, smaller in size, and less defined when compared to other muscle layers of the body. The fat layers are divided into superficial and deep, intermingled with muscle fibers, and US may exhibit the fat tissues as different echogenicity or muscles as hypoechoic according to their thickness and density. Also, nowadays, many people undergo plastic surgery and noninvasive procedures, which can distort the normal anatomy and make interpretation difficult. Second, US-guided injection is very useful but can have a long learning curve. Unlike muscles of the body, the facial muscle size is small in aesthetic procedures require 30-gauge thin needles to be meticulously injected into a specific layer. With these reasons, approaching the target muscle with guided injection requires a very skillful injection technique to identify the needle's trajectory and to control the dosage. Third, the US transducer can hinder views during injection, such as surface wrinkles, shape, and texture, which needs to be visualized when performing aesthetic procedures. These difficulties can be somewhat resolved by using a thin and slender hockey-stick-shaped US transducer.

US-guided botulinum toxin injection requires extensive three-dimensional comprehension of the facial anatomy of the depth and layers in addition to the basic two-dimensional anatomical concept of the muscles and fat. The cross-sectional anatomy must be apprehended since US imaging captures the cross-sectional view of the structure during functional and dynamic movement.

A linear transducer can be helpful to observe the superficial area within 3 cm in depth, while a hockey-stick transducer is helpful in observing narrower areas. The frequency of the linear transducer should be 12–18 MHz for aesthetic treatment, 24–32 MHz for deep dermis and epidermis, and 3–12 MHz for deeper body muscle observation. Once an adequate transducer is selected, the depth and focus should be adjusted in relation to the target structure to obtain a clear image.

8.2 US-Guided Botulinum Toxin Injection Procedures

8.2.1 Facial Wrinkles

Facial wrinkles on the upper half of the face are frequently treated with botulinum toxin. The typical target wrinkles are the horizontal forehead lines, the glabella frown lines, and the lateral canthal lines (crow's feet).

8.2.1.1 Horizontal Forehead Lines

The frontalis m. is very thin and varies between individuals and sexes. The frontalis m. is hypoechoic and gradually appears more hyperechoic toward the upper half of the forehead under the US image. The forehead is a very thin anatomical area with the thickness of the skin to the periosteum averaging 0.5 cm. Therefore, minimal botulinum toxin injection will easily lead to diffusion to all layers, and 1–2 mm of loose connective tissue above the periosteum can also be detected by US (Figs. 3.14, 3.15, 3.18, 3.19, 3.20, and 3.21). Injection after direct touch into the periosteum will still diffuse the botulinum toxin into the frontalis m. since this layer is loose, but accurate injection into the muscle can be achieved by slightly pulling the needle 1–2 mm away after the periosteum has been contacted. To minimize muscle paralysis, the soft-tissue thickness of the forehead must be considered. The subcutaneous layer injection will diffuse the toxin and create the same intramuscular injection effect. Therefore, meticulous injection into the dermis by creating a papule will bring minimal complications.

Another factor that we need to consider is the lateral border of the frontalis m. The frontalis m. is positioned 1 cm lateral to the superior temporal line (or temporal crest), connecting to the superficial temporal fascia (Fig. 3.22). The guideline injection site for the frontalis m. is the eyebrow, but there is still the possibility of a "Spock-like" or "samurai eyebrow" appearance.

Using the out-of-plane method rather than the in-plane method is more advantageous during the US-guided injection for the frontalis m. (Fig. 8.1).

8.2.1.2 Glabellar Frown Lines

To correct the glabellar frown line, the corrugator supercilii and procerus mm. should be targeted. In the transverse US view along the eyebrow, the corrugator supercilii m. is seen as a hypoechoic image above the periosteum of the superior orbital rim near the medial end of the eyebrow. The thickness of the corrugator supercilii m. differs depending on the degree of glabellar frown lines. In Asians, the hypoechoic corrugator m. belly is shown slightly below the eyebrow line. Bone touch in this area may lead to orbital septum perforation and botulinum toxin diffusion and therefore is strictly discouraged (Figs. 4.3, 4.11, and 4.12).

The procerus m. is observed at the glabella as a hypoechoic image (Figs. 3.1, 3.10, 3.16, 3.17, 5.25, and 5.26). There is a thin deep fat layer (loose connective tissue) between the procerus m. and nasal bone. For precise targeting of the procerus m., injection should be done slightly above the periosteum.

An in-plane approach is recommended for US-guided injection for the glabellar frown lines. It should be approached from the eyebrow toward the origin of the corrugator m. belly (Fig. 8.2). When approaching the procerus m., out-of-plane is advantageous.

8.2.1.3 Lateral Canthal Lines (Crow's Feet)

The target muscle for the crow's feet injection is the lateral part of the orbital portion of the OOc m. From the US image, the hypoechoic lateral part of the OOc m. is thicker than the other area. It is observed on the lateral portion of the lateral orbital rim and continues to the thin hyperechoic superficial temporal fascia (Fig. 4.14). Meticulous dermal injection is required to avoid botulinum toxin injection into the ocular muscles. The out-of-plane approach is recommended for the OOc m. in US-guided injections (Fig. 8.3).

8.2.2 Masticatory Muscles

The most popular aesthetic botulinum toxin treatment in Asian countries is the masticatory muscle injection for the facial contouring procedure. It is also applied for functional treatments, such as bruxism and TMJ symptoms, since the masseter and temporalis mm. are the main masticatory muscle group.

8.2.2.1 Masseter Muscle

The masseter m. is a large muscle among the facial muscles that makes up the volume of the lower face and is easily visualized with US imaging. Dynamic movement of the muscle during clenching and resting can be seen using US (Fig. 2.43). The masseter m. is seen as a hypoechoic image with several hyperechoic tendons within the muscle (Figs. 6.41, 6.42, 6.43, 6.44, 6.45, and 6.46). The muscle belly lies directly above the mandibular ramus and is shown as a thick hyperechoic line. However, false-negative findings may appear in palpation when the subcutaneous fat is thick and hard to palpate or the masseter m. is weak during clenching. The masseter m. is divided into the superficial, middle, and deep layers. The superficial part can be divided

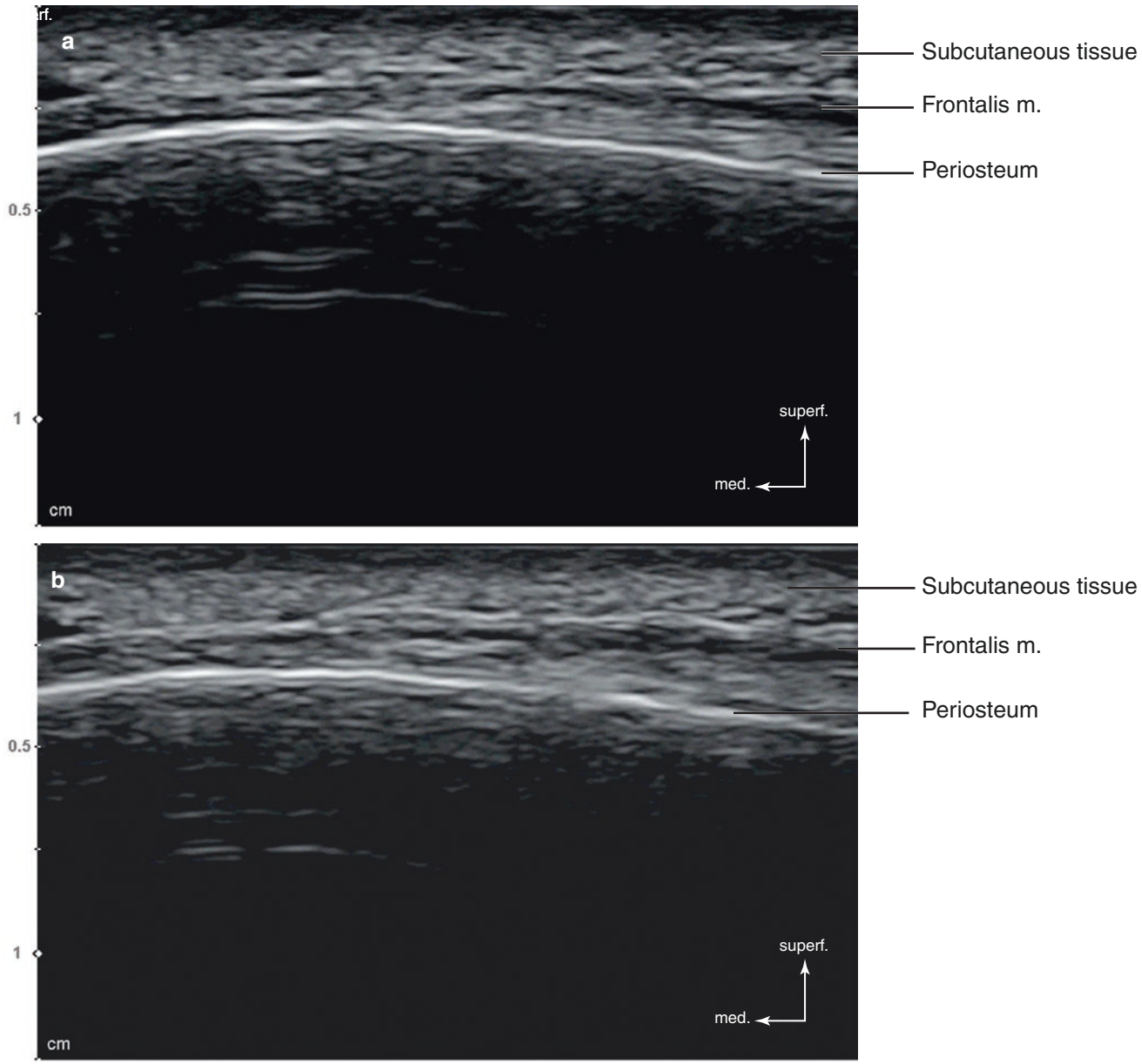

Fig. 8.1 Ultrasonography-guided botulinum toxin injection to the frontalis muscle. (**a**) Before injection, B mode (transverse view, 15 MHz by linear transducer) and (**b**) after injection, B mode (transverse view, 15 MHz by linear transducer). (Published with kind permission of © Ji-Soo Kim 2020. All Rights Reserved)

again into the superficial and deep parts or more by the DITs (deep inferior tendons) (Figs. 6.41, 6.42, 6.43, 6.45, and 6.46).

It is hypothesized that the DITs located within the superficial layer of the masseter m. may prevent the spreading of botulinum toxin into the entire layer of the superficial muscle belly. This can result in partial paralysis of superficial masseter m. fibers. In rare cases, paradoxical masseteric bulging of a part of the superficial muscle belly that is unaffected by botulinum toxin, due to the presence of the DITs, could occur (Fig. 8.4).

Therefore, classical blind injection guidelines should be changed based on new anatomical findings of the masseter m. Under the US image, DITs should be examined to prevent paradoxical bulging due to partial paralysis of the target muscle (Fig. 8.5).

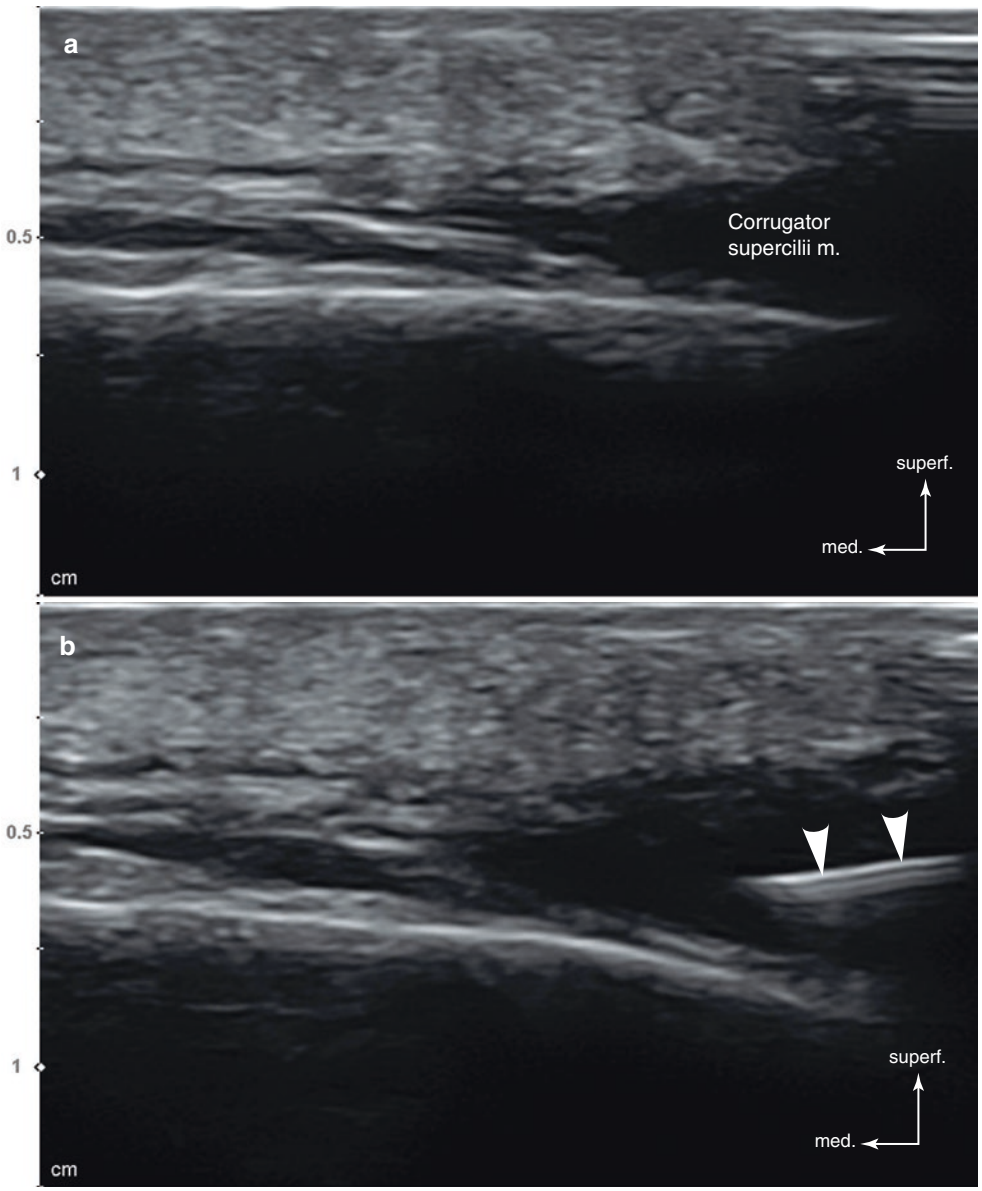

Fig. 8.2 Ultrasonography-guided botulinum toxin injection to the corrugator supercilia muscle. (**a**) Before injection, B mode (transverse view, 15 MHz by linear transducer) and (**b**) during injection (in-plane), B mode (transverse view, 15 MHz by linear transducer) (white arrowheads: injection needle). (Published with kind permission of © Ji-Soo Kim 2020. All Rights Reserved)

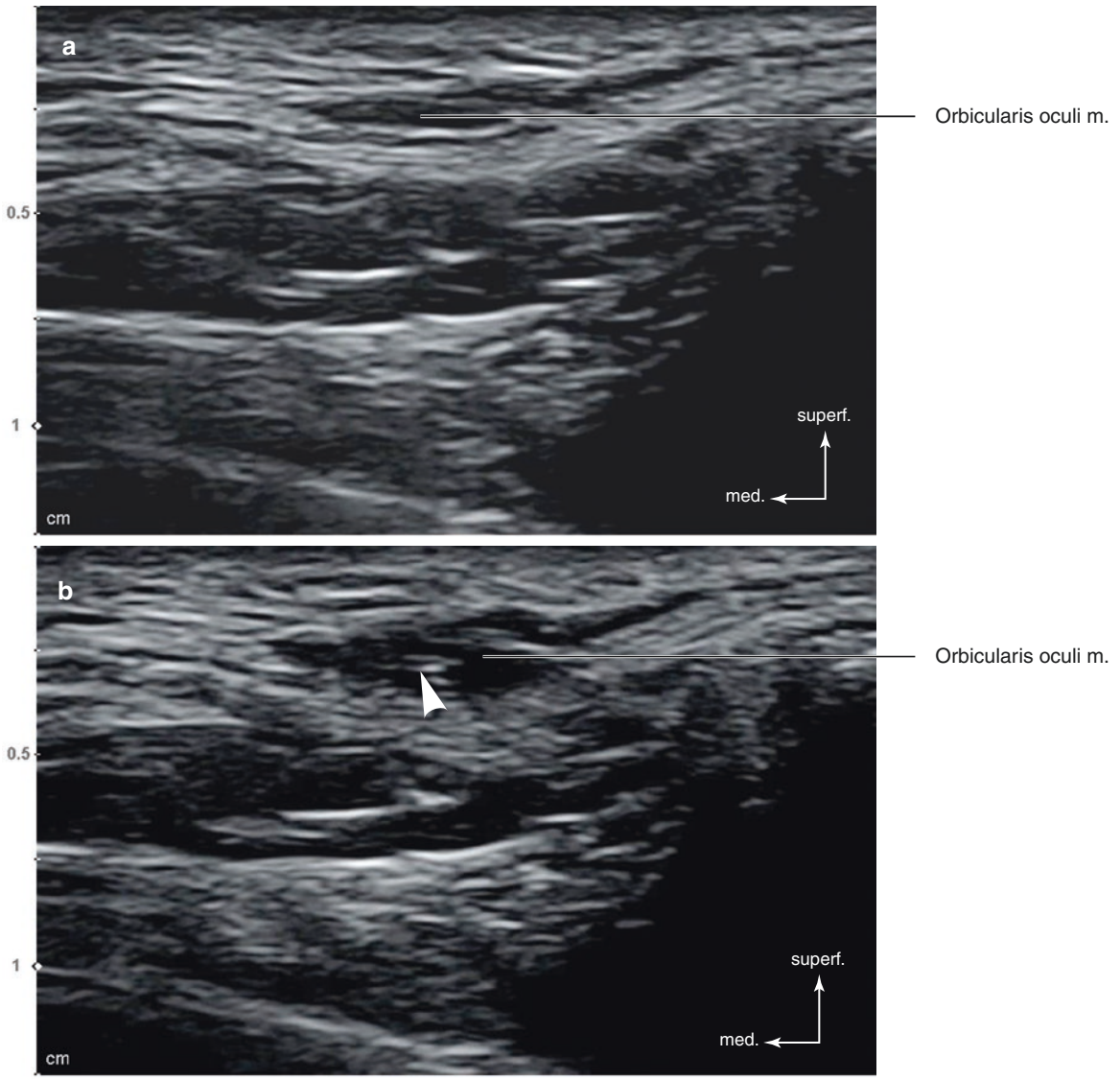

Fig. 8.3 Ultrasonography-guided botulinum toxin injection to the orbicularis oculi muscle. (**a**) Before injection, B mode (transverse view, 15 MHz by linear transducer) and (**b**) during injection (out-of-plane), B mode (transverse view, 15 MHz by linear transducer) (white arrowhead: injection needle). (Published with kind permission of © Ji-Soo Kim 2020. All Rights Reserved)

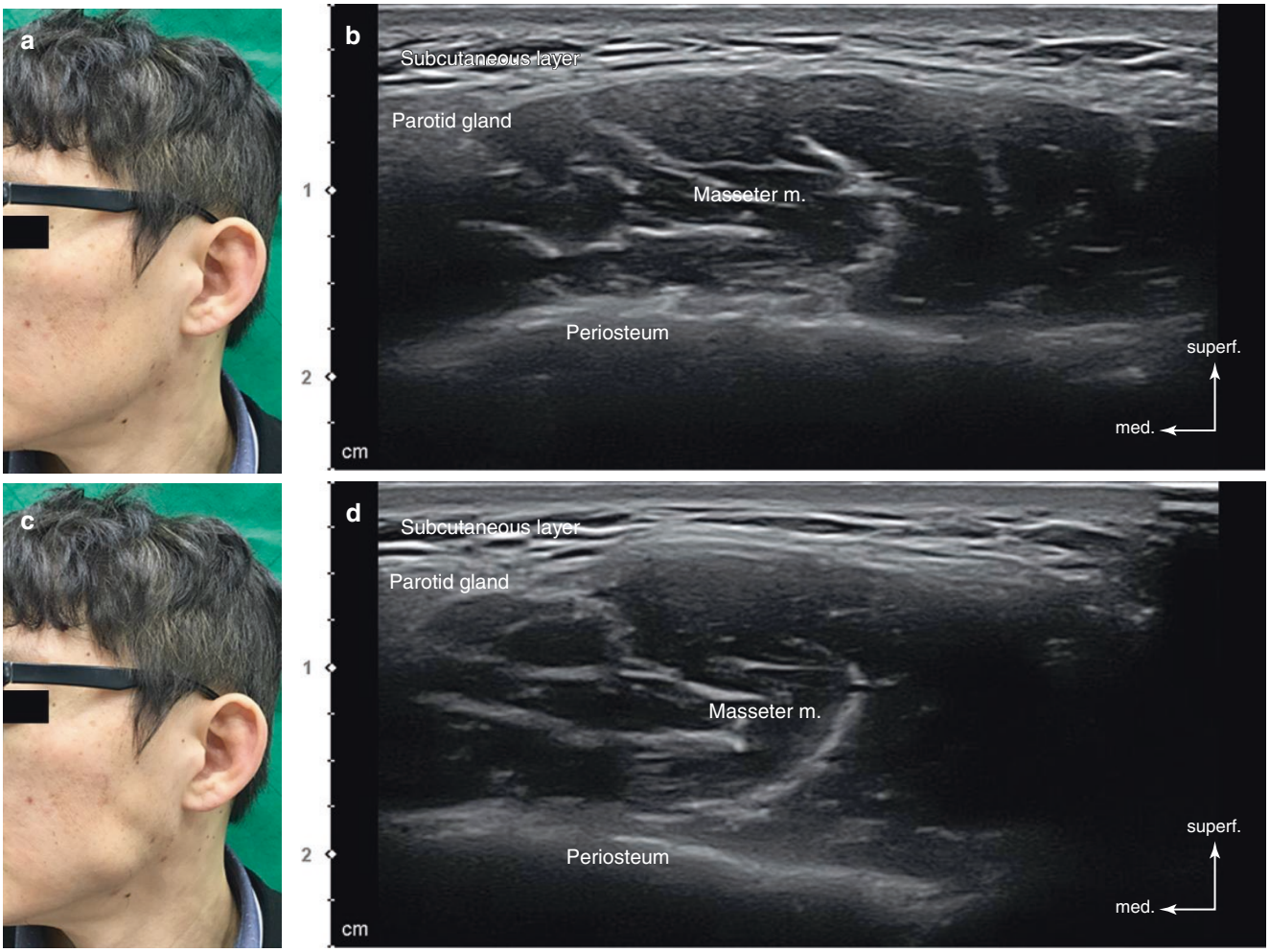

Fig. 8.4 Photograph and ultrasonography of the paradoxical masseteric bulging. (**a**) At the resting state, (**b**) at the clenching state, (**c**) at the resting state, B mode (transverse view, 15 MHz by linear transducer), and (**d**) at the clenching state, B mode (transverse view, 15 MHz by linear transducer). (Published with kind permission of © Ji-Soo Kim 2020. All Rights Reserved)

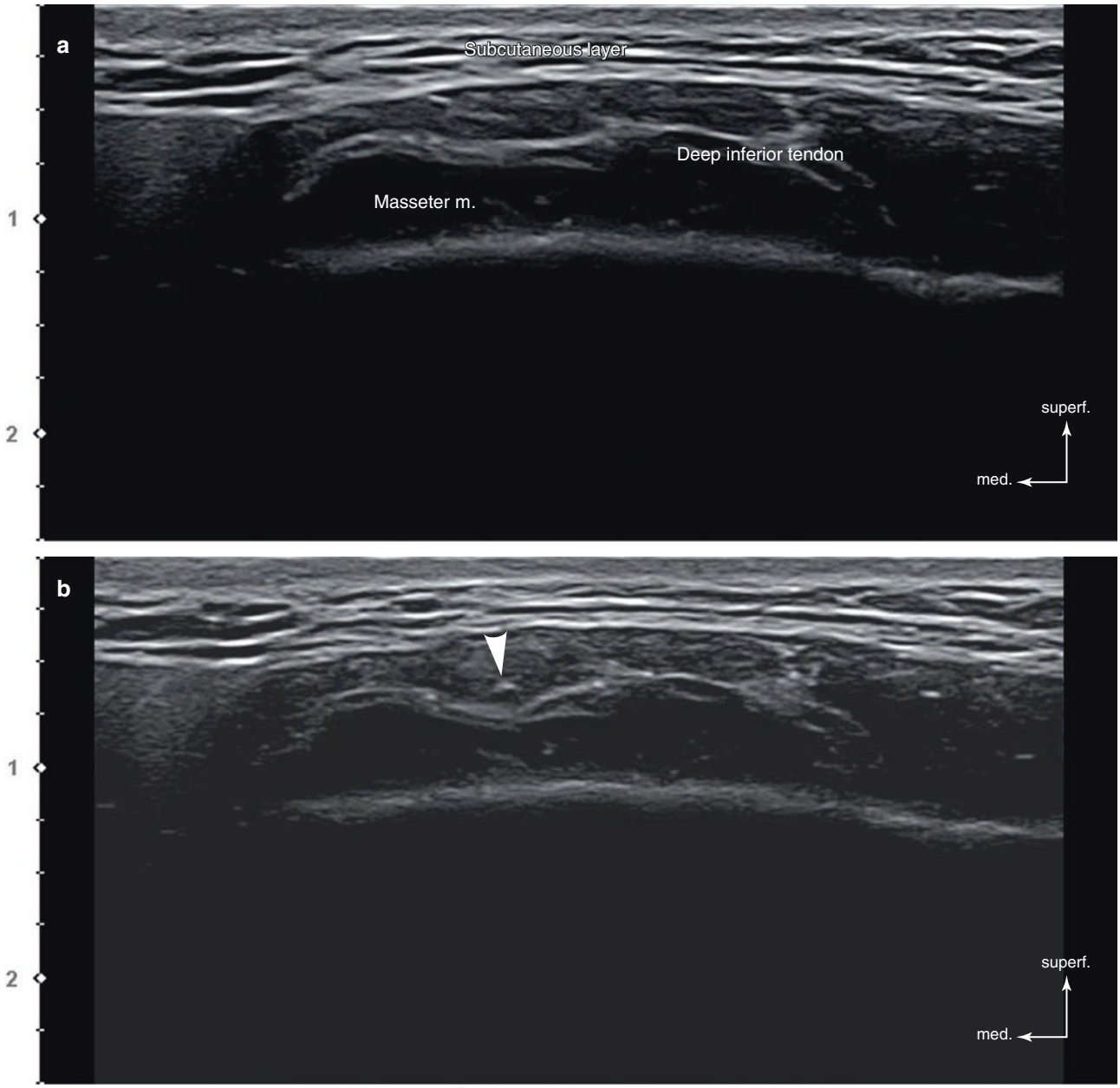

Fig. 8.5 Ultrasonography-guided botulinum toxin injection to the masseter muscle. (**a**) Before injection, B mode (transverse view, 15 MHz by linear transducer) and (**b**) during injection (out-of-plane), B mode (transverse view, 15 MHz by linear transducer) (white arrowhead: injection needle). (Published with kind permission of © Ji-Soo Kim 2020. All Rights Reserved)

The anterior and posterior portion of the masseter m. are partially covered by the origin of the risorius m. and parotid gland, respectively. These superficial structures make precise injection difficult. In addition, the main body of the buccal fat pad is anterior to the masseter m., and deep to the buccal fat pad is the buccinator m. Since diffusion into such areas can lead to unfavorable results, US-guided injections have more benefits (Figs. 6.27, 6.28, 6.29, and 8.6).

Repetitive botulinum toxin injections will reduce the masseter m. volume, and it frequently appears as hyperechoic under the US image. Usually, the inferior portion is hypoechoic, but in some cases, hyperechoic appearance can be seen throughout the entire muscle, including the superficial, deep, or both areas (Fig. 8.7).

Because the masseter m. is a thick muscle, as shown in the US image, a 1-in.-long needle is recommended to cover all the superficial and deep parts of the muscle. Layer-by-layer injec-

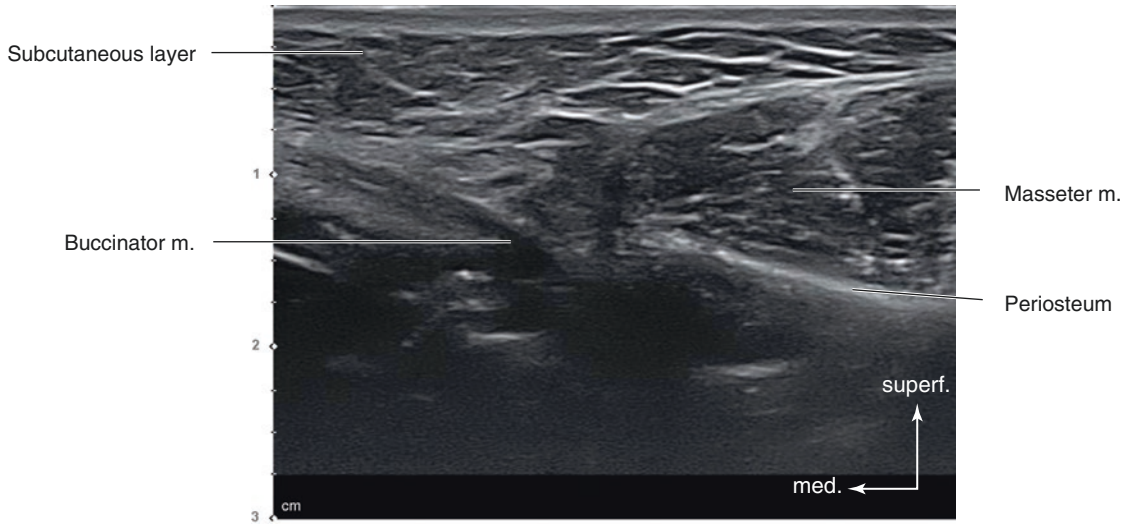

Fig. 8.6 Ultrasonography of the anterior part of the masseter muscle, B mode (transverse view, 15 MHz by linear transducer). (Published with kind permission of © Ji-Soo Kim 2020. All Rights Reserved)

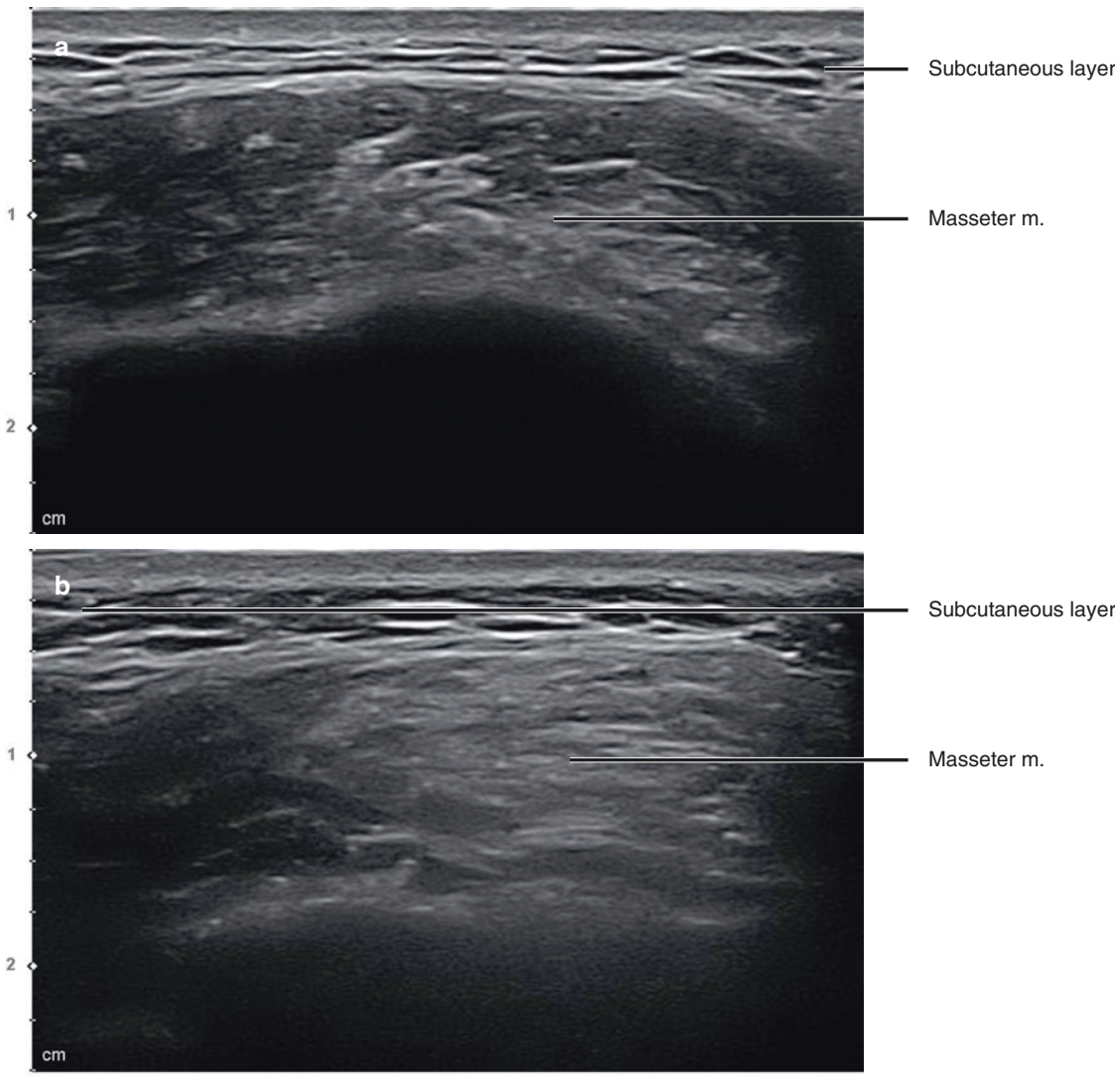

Fig. 8.7 Ultrasonography of the hyperechoic change of the masseter muscle after repetitive botulinum toxin injections. (**a**) Partial change, B mode (transverse view, 15 MHz by linear transducer) and (**b**) overall change, B mode (transverse view, 15 MHz by linear transducer). (Published with kind permission of © Ji-Soo Kim 2020. All Rights Reserved)

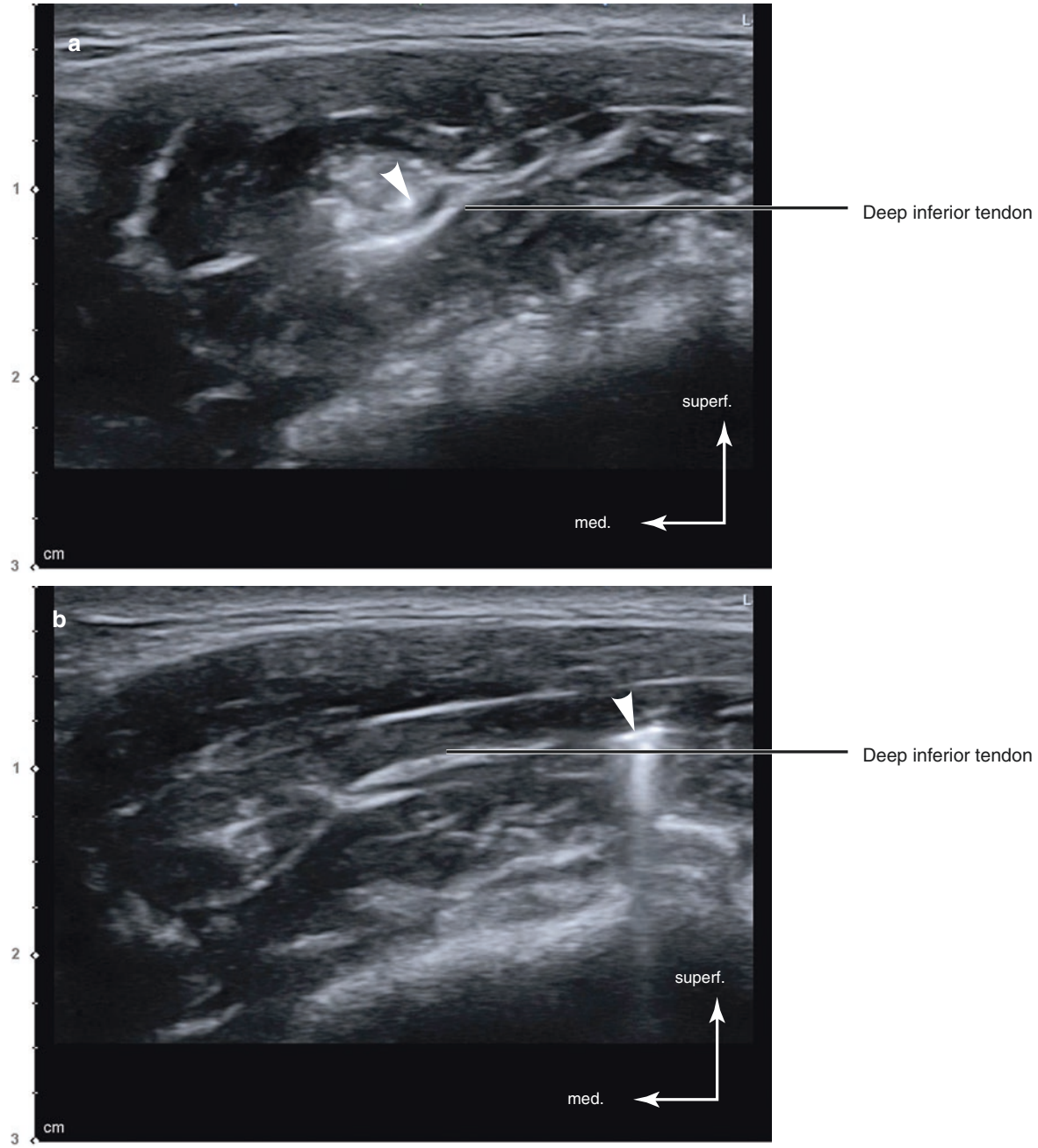

Fig. 8.8 Ultrasonography-guided dual plane botulinum toxin injection to the masseter muscle. (**a**) Superficial injection (out-of-plane), B mode (transverse view, 15 MHz by linear transducer) and (**b**) deep injection (in-plane), B mode (transverse view, 15 MHz by linear transducer) (white arrowheads: injection needle). (Published with kind permission of © Ji-Soo Kim 2020. All Rights Reserved)

tion can be done by accessing out-of-plane under a transverse US view. Once the practitioner gets accustomed, an in-plane approach and oblique plane approach (a combination of in-plane and out-of-plane) can be utilized. A longitudinal view can be employed depending on the injection point. Injection points should be confirmed under US to minimize damage to the superficial parotid duct and injecting into the risorius and zygomaticus major mm. situated near the anterior border (Fig. 8.8).

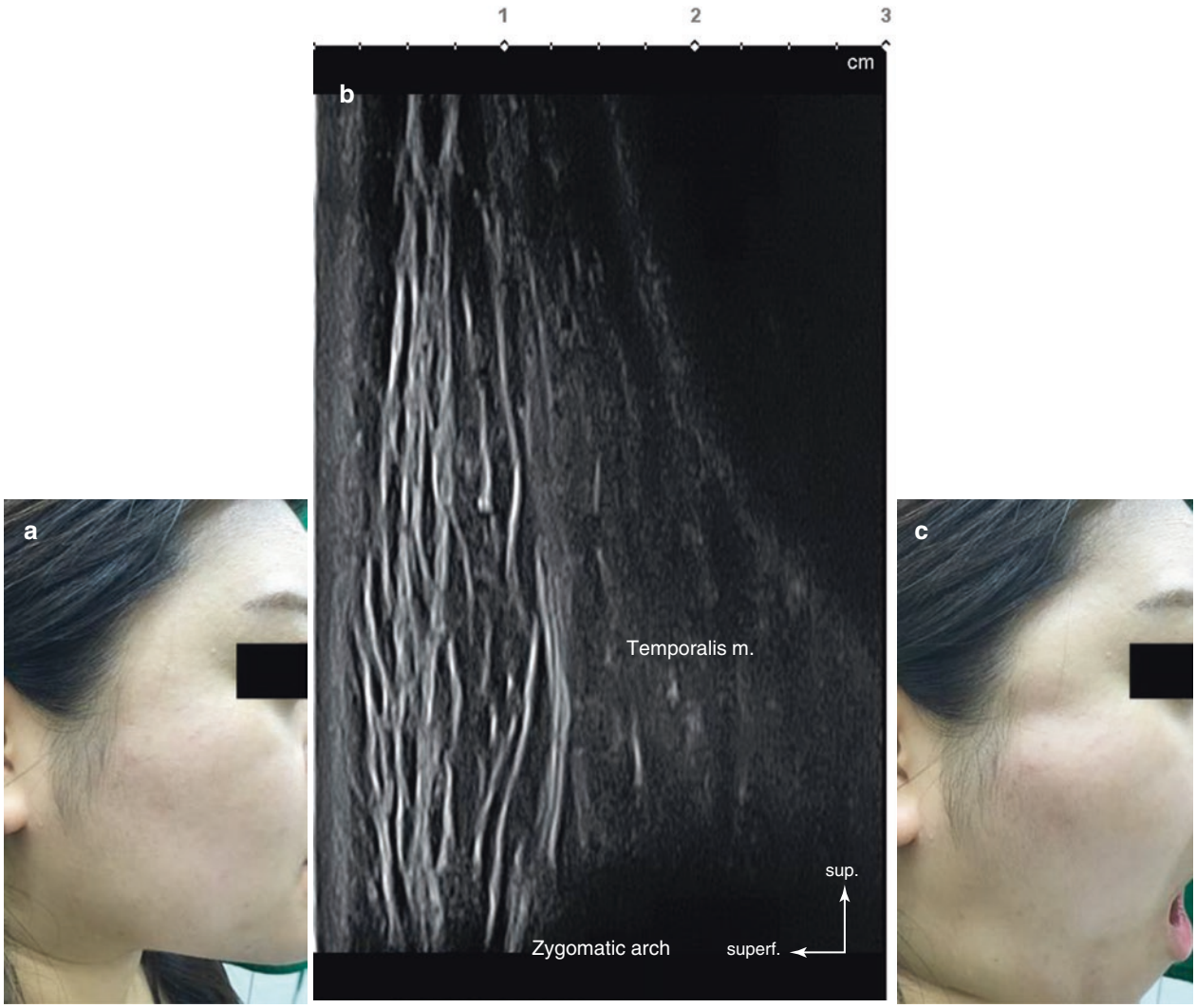

Fig. 8.9 Photograph and ultrasonography of the temporal bulging. (**a**) At the resting state, (**b**) at the clenching state, B mode (coronal view, 15 MHz by linear transducer), and (**c**) at the open mouth state. (Published with kind permission of © Hee-Jin Kim and Ji-Soo Kim 2020. All Rights Reserved)

8.2.2.2 Temporalis Muscle

The temporalis m. can also be treated using botulinum toxin. In cases where the temporalis m. is developed, the lateral sides of the head may seem wide and be an indication for aesthetic botulinum toxin treatment. The temporalis m. hypertrophy can be congenital or due to compensatory hypertrophic change after synergistic masseter m. injection of botulinum toxin. It can also be used in nonaesthetic cases such as for the treatment of migraines.

Approaching the temporalis m. is not difficult since the soft tissue is thin near the hairline area, and the muscles attach directly to the bone. US images show the muscle as a hypoechoic image above the temporal fossa. The temporalis m. is a very large muscle, which is widely distributed from the temporal area to the zygomatic arch. Injections near zygomatic arch are difficult to precisely approach since the soft tissues are thick and layers are complicated (Figs. 2.18, 2.27, and 3.13).

In specific cases, the temporalis m. and the temporal fat pad can be bulged above the zygomatic arch, and the muscle shows hyperactivity under US scanning (Fig. 8.9). Patients with previous zygomatic reduction surgical history can also show a noticeable temporalis m.

The clinical injections for the temporalis m. should be done at the territory of the temporalis m. anterior to the hairline. Using an in-plane approach under the US scan can easily access the temporalis m. The lower temporal area requires both out-of-plane and in-plane access for the precise injection (Fig. 8.10).

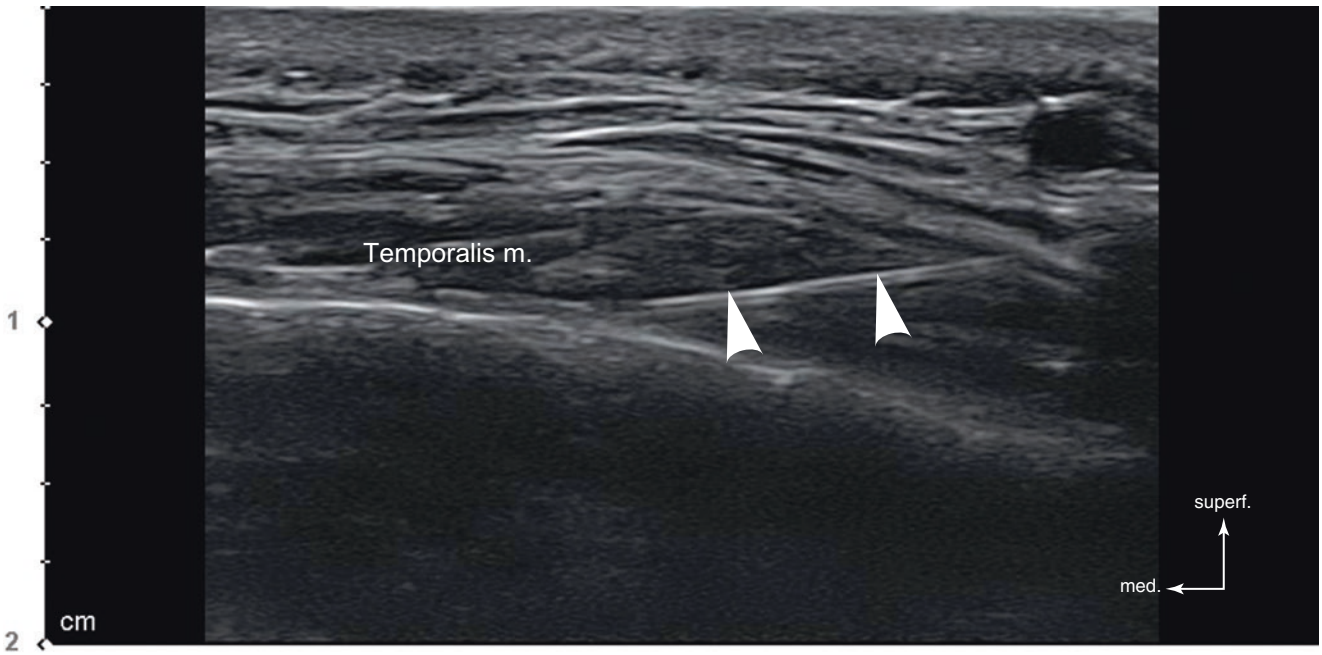

Fig. 8.10 Ultrasonography-guided botulinum toxin injection to the temporalis muscle (in-plane), B mode (transverse view, 15 MHz by linear transducer) (white arrowheads: injection needle). (Published with kind permission of © Ji-Soo Kim 2020. All Rights Reserved)

8.2.3 Salivary Gland

Botulinum injection into the salivary gland has been performed to treat sialorrhea. Recently, it has been considered for aesthetic purposes. Botulinum toxin injection in this area reduces the volume for benign hypertrophy of the salivary glands.

8.2.3.1 Parotid Glands

Botulinum toxin injection into the parotid glands is beneficial in slimming the facial contour. Congenital conditions or acquired effects such as excessive alcohol drinking can induce parotid gland hypertrophy. In such cases, the lower face looks wide, and the distal portion appears edematous with the mandible angle attenuated. Masseter m. reduction using botulinum toxin can also relatively make the parotid gland noticeable. Such cases are indications for salivary gland injection.

From the US image, the parotid gland is seen as a homogeneous hyperechoic image embracing the posterior border of the mandibular ramus and masseter m. Although the facial nerves branch within the parotid gland parenchyme, they can rarely be observed under the US image (Fig. 2.39), but some lymph nodes are frequently shown (Fig. 8.11).

In addition, the parotid duct is well identified when it is dilated by pathologic conditions, such as sialolithiasis, but normally it can be identified on US. When it is large, it is not only thickened but also covers the whole part of the masseter m. and an accessory gland may be found (Fig. 8.12).

Depending on the size, shape, and location of the gland, transverse and longitudinal view approaches using an in-plane US-guided injection can be considered. Superficial injection is suggested because injections too deep may penetrate the masseter m. or adjacent structures (Fig. 8.13).

8.2.3.2 Submandibular Gland

The submandibular gland contributes to 60–70% of unstimulated saliva secretion. Nowadays, botulinum toxin is injected into this area to aesthetically treat jawline contour and reduce double chin. Acquired conditions, such as excessive diet control, anorexia, and frequent vomiting, can lead to benign hypertrophy. An angle reduction surgery and preplatysmal fat liposuction can make submandibular gland look more noticeable, requiring botulinum toxin injection.

Anatomically, the submandibular gland is located under the platysma m. and covers several supra- and infrahyoid mm., with many blood vessels within or near the gland. From the US image, it is shown as a homogeneous hyperechoic pattern similar to the parotid gland. The gland is usually well encapsulated by the submandibular gland fascia. The hypoechoic mylohyoid m. divides the superficial and deep portions of the gland, and the deep portion is not targeted during the aesthetic botulinum toxin injection procedure. Submandibular gland ducts can be observed, and blood vessels and lymph nodes are observed (Fig. 8.14).

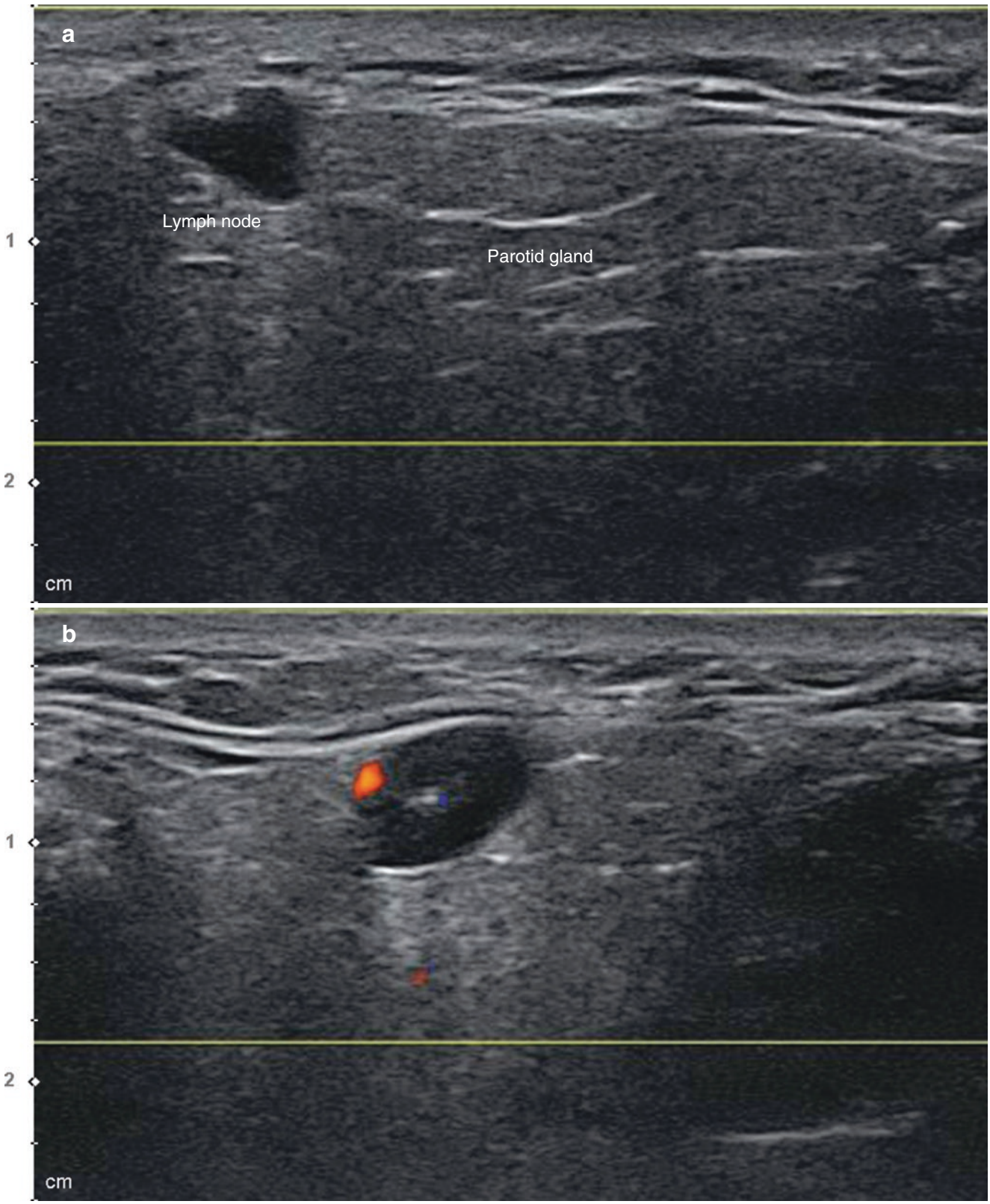

Fig. 8.11 Ultrasonography of the parotid gland and parotid lymph node. (**a**, **b**) Doppler mode (transverse view, 15 MHz by linear transducer). (Published with kind permission of © Ji-Soo Kim 2020. All Rights Reserved)

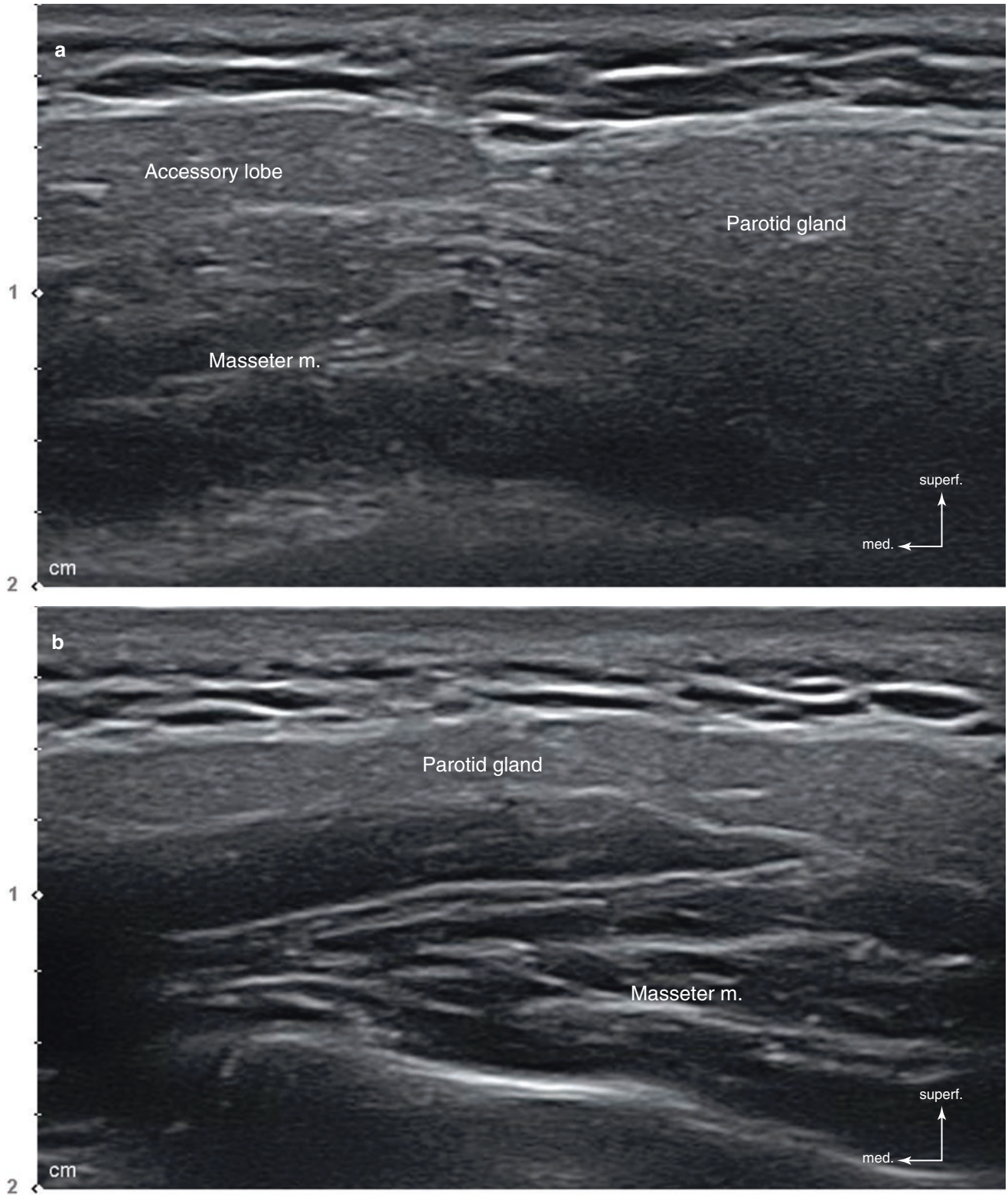

Fig. 8.12 Ultrasonography of the parotid gland. (**a**) Accessory gland covering the masseter muscle partially, B mode (transverse view, 15 MHz by linear transducer) and (**b**) parotid gland covering the whole masseter muscle, B mode (transverse view, 15 MHz by linear transducer). (Published with kind permission of © Ji-Soo Kim 2020. All Rights Reserved)

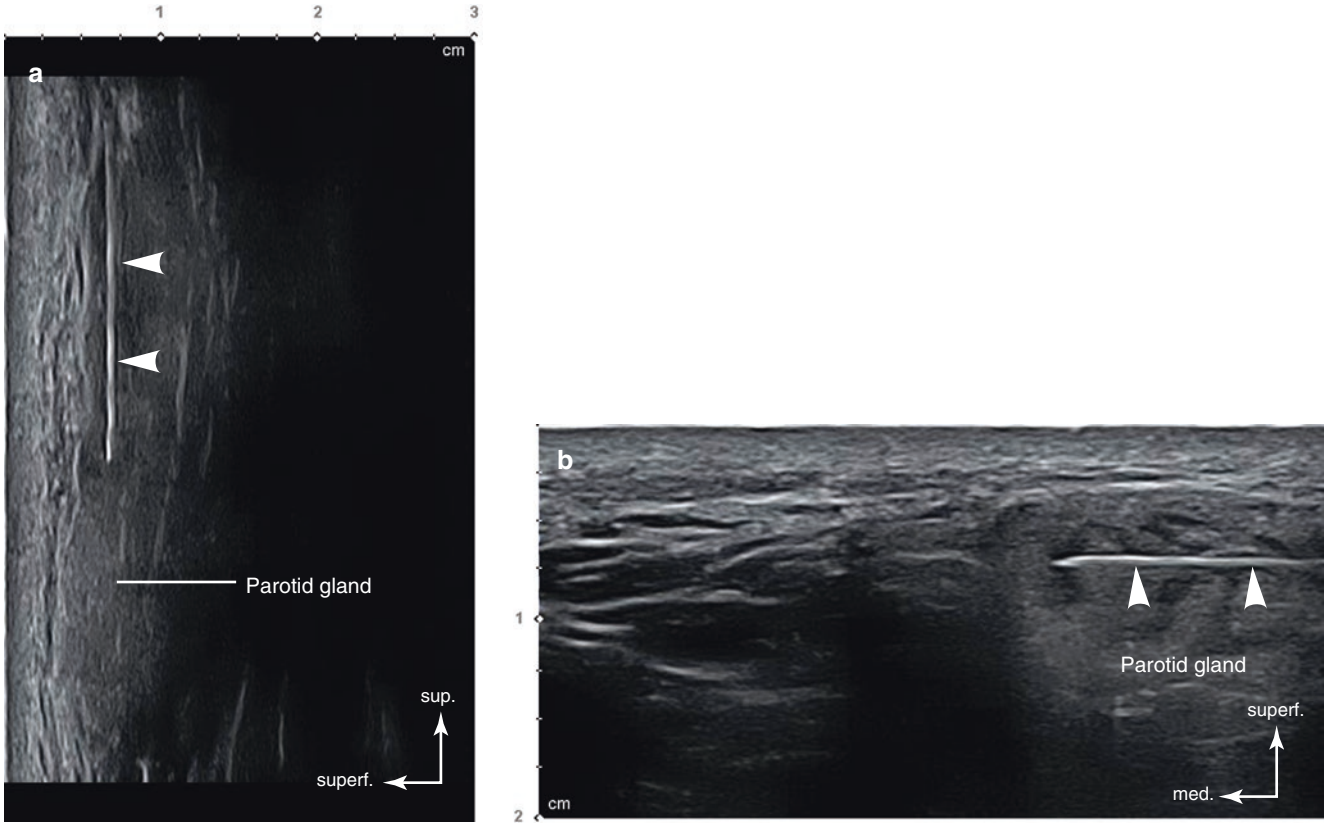

Fig. 8.13 Ultrasonography-guided botulinum toxin injection to the parotid gland. (**a**) Longitudinal approach (in-plane), B mode (transverse view, 15 MHz by linear transducer) and (**b**) transverse approach (in-plane), B mode (transverse view, 15 MHz by linear transducer) (white arrowheads: injection needle). (Published with kind permission of © Ji-Soo Kim 2020. All Rights Reserved)

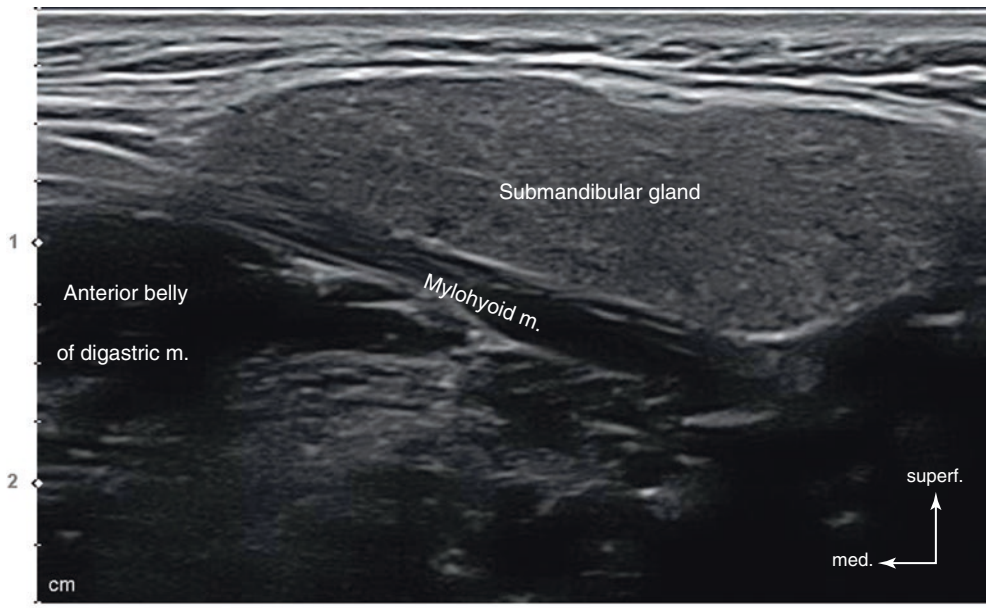

Fig. 8.14 Ultrasonography of the submandibular gland, B mode (transverse view, 15 MHz by linear transducer). (Published with kind permission of © Ji-Soo Kim 2020. All Rights Reserved)

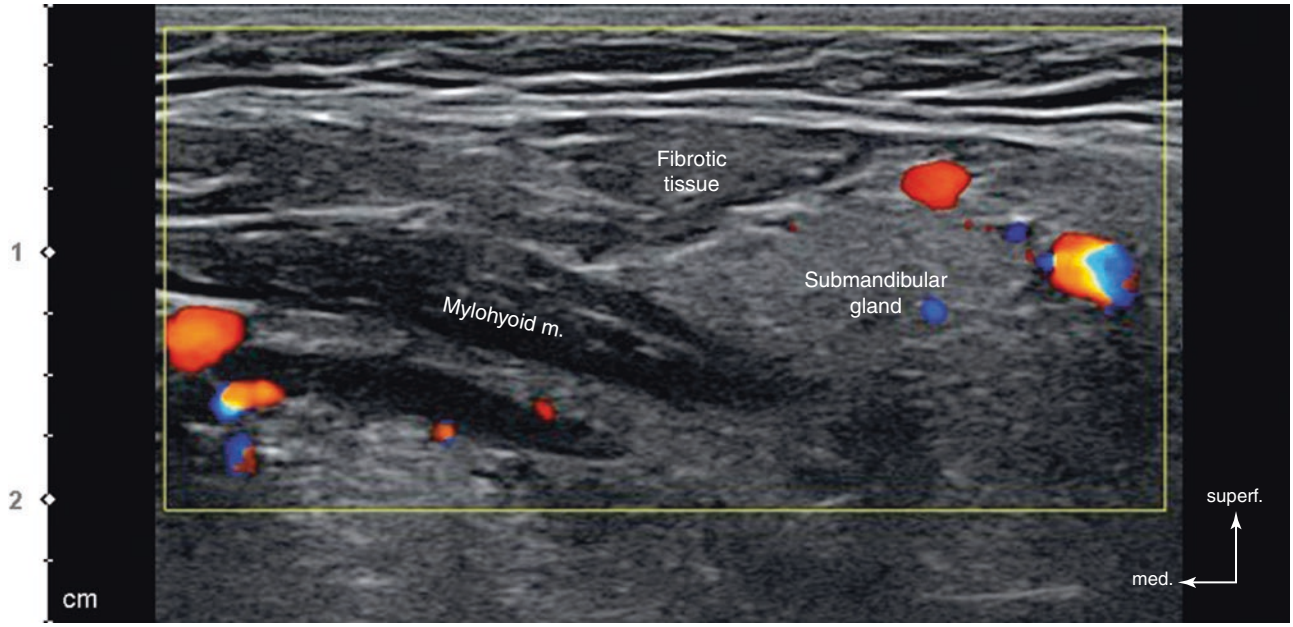

Fig. 8.15 Ultrasonography of the partial fibrosis of the submandibular gland, Doppler mode (transverse view, 15 MHz by linear transducer). (Published with kind permission of © Ji-Soo Kim 2020. All Rights Reserved)

The submandibular gland is mobile, so it is difficult to perform precise injections. Injection into the platysma m. can generate a minor restriction of neck movement, and injection into the mylohyoid m. can cause dysphagia. Thick subcutaneous layers also make it troublesome in determining the injection depth. Fibrosis in the superficial portion is occasionally observed with large vessels in the vicinity (Figs. 8.15 and 8.16).

A superficial in-plane US approach is recommended in this region to avoid vascular and inappropriate injection. For such reasons, US-guided injection is strongly advised in this area. Injection in this area requires small amounts of volume injection since glands are not dense structures and toxin can easily diffuse into other structures (Fig. 8.17).

8.2.4 Facial Asymmetry and Synkinesis

Botulinum toxin injection is very effective in treating facial asymmetry, facial synkinesis, or facial spasm. Anatomical comprehension of the facial expression muscles and the mode of action is crucially required to correlate between the dynamic muscle expressions and facial balance. Understanding the muscle imbalance in animation is also very important. Precise targeting of the facial expression muscles is the key protocol in injection procedures. However, it is not easy to precisely inject because the muscles are small and thin.

A case of congenital facial asymmetry shows the typical US-guided injection protocol (Figs. 8.18 and 8.19). The patient received the ultrasound-guided botulinum injection in each target muscle, the depressor labii inferioris (DLI), risorius, and zygomaticus major mm. using a 1-mL syringe with a 30 gauge 1-in.-long needle. The patient's smile was symmetrical 1 month after the US-guided botulinum toxin injections (Figs. 8.18 and 8.19). The symmetry was achieved by decreasing the exposure of the mandibular teeth and by elevating both mouth corners.

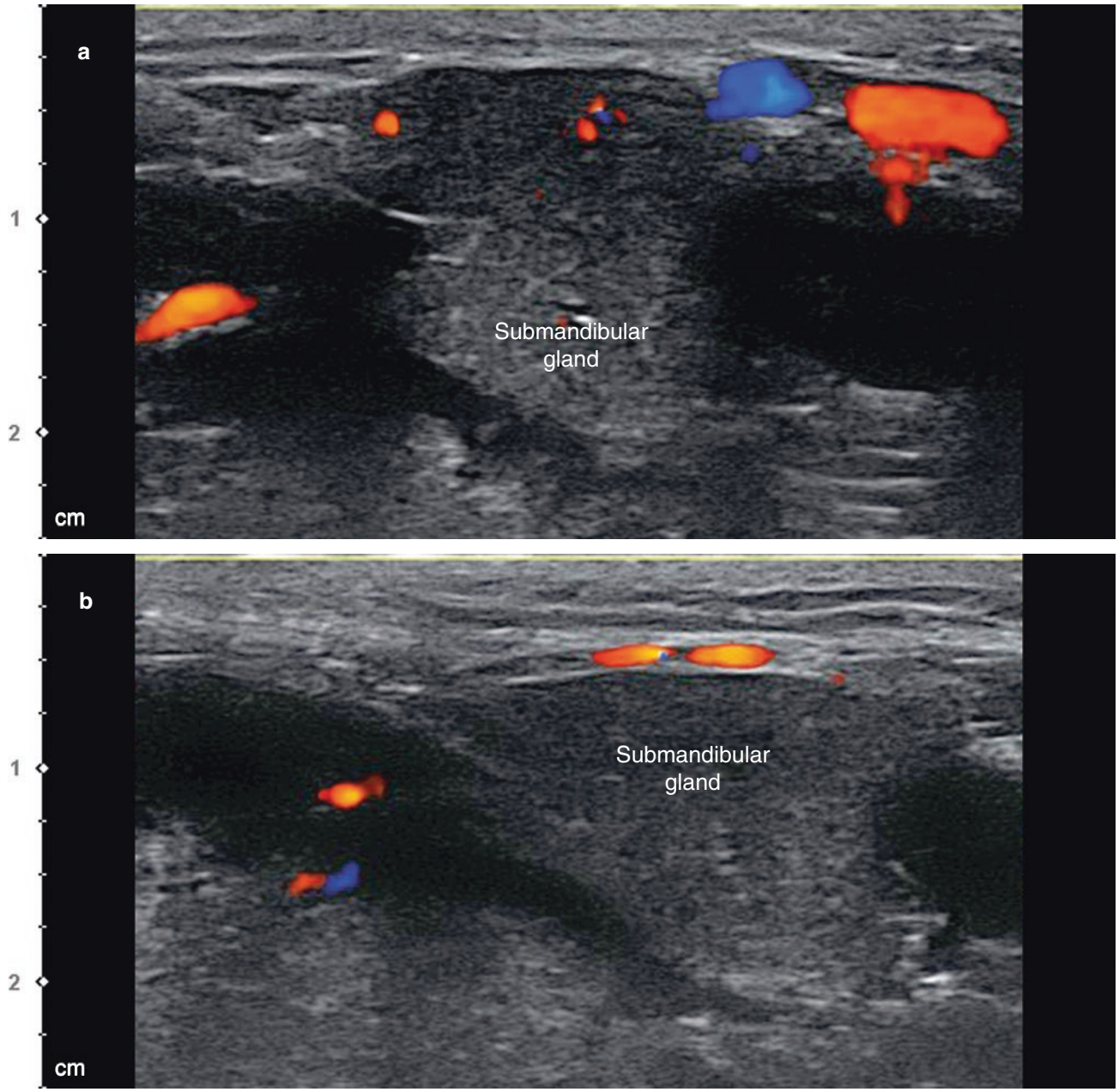

Fig. 8.16 Ultrasonography of the submandibular gland in vicinity of the large vessels. (**a**, **b**) Doppler mode (transverse view, 15 MHz by linear transducer). (Published with kind permission of © Ji-Soo Kim 2020. All Rights Reserved)

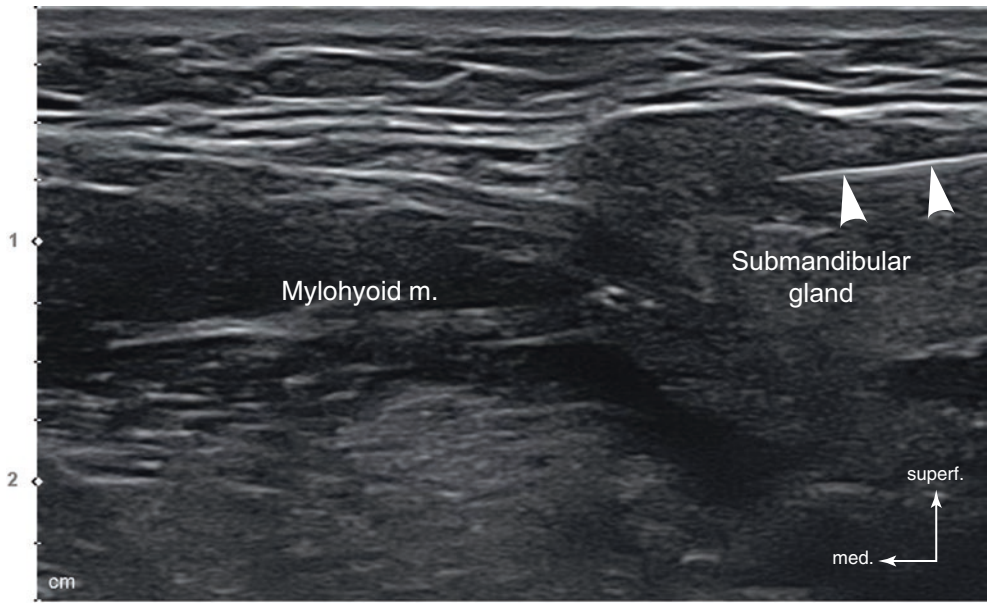

Fig. 8.17 Ultrasonography-guided botulinum toxin injection to the submandibular gland (in-plane), B mode (transverse view, 15 MHz by linear transducer) (white arrowheads: injection needle). (Published with kind permission of © Ji-Soo Kim 2020. All Rights Reserved)

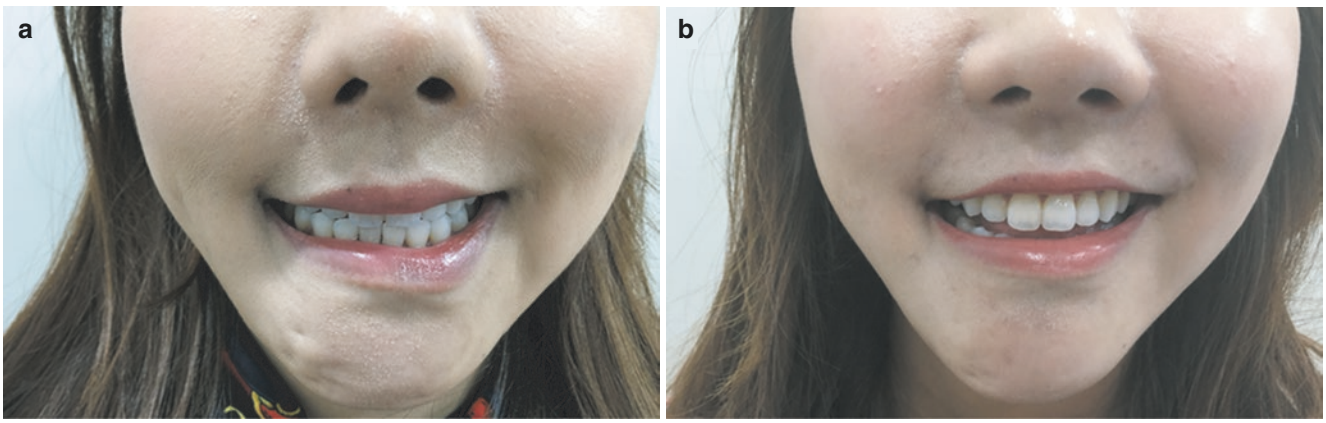

Fig. 8.18 Photographs of a case of congenital facial asymmetry correction using botulinum toxin injections. (**a**) Before the treatment and (**b**) after the treatment. (Published with kind permission of © Ji-Soo Kim 2020. All Rights Reserved)

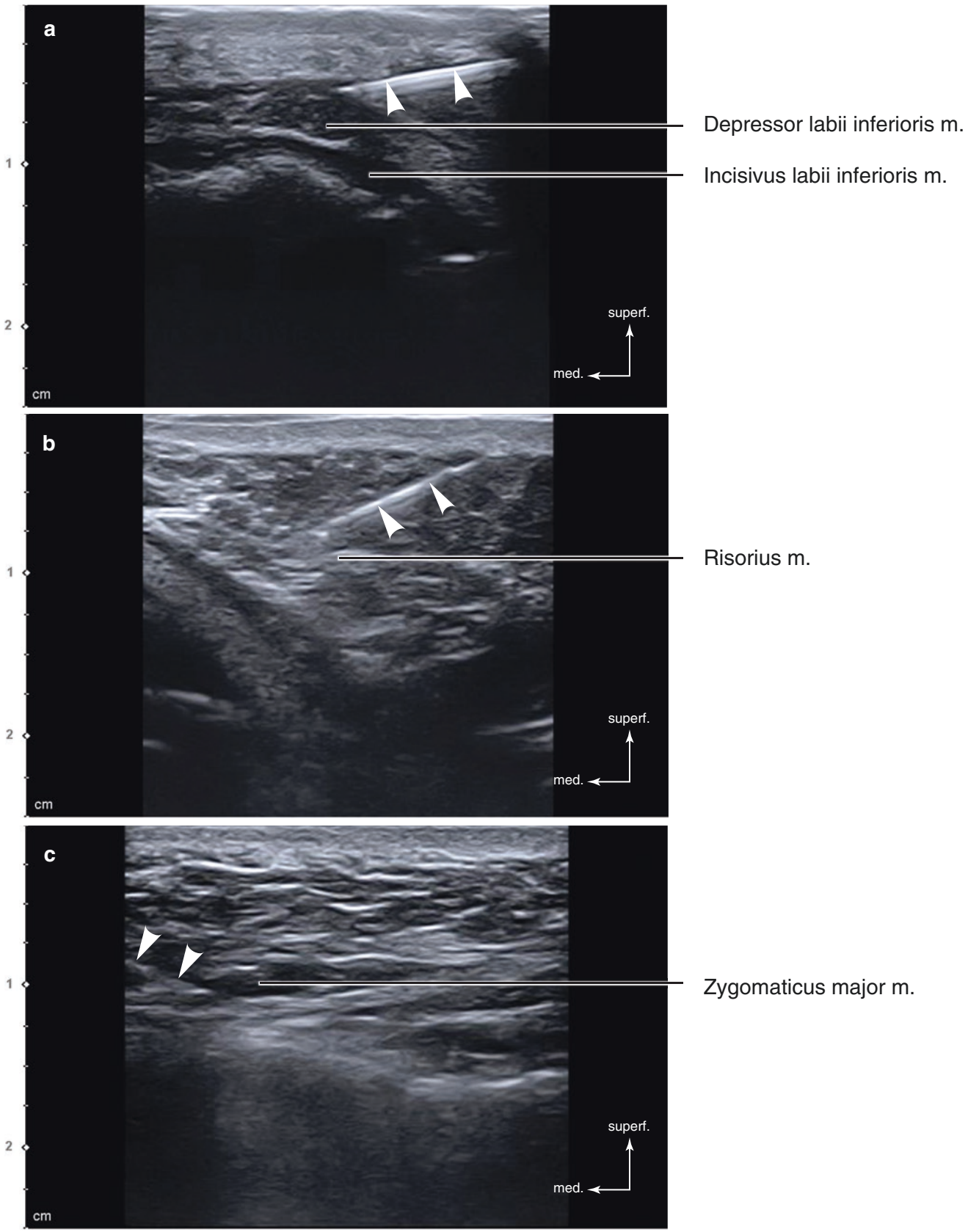

Fig. 8.19 Ultrasonography-guided botulinum toxin injection to the perioral expression muscles (in-plane). (**a**–**c**) B mode (transverse view, 15 MHz by linear transducer) (white arrowheads: injection needle). (Published with kind permission of © Ji-Soo Kim 2020. All Rights Reserved)

8.2.5 Mentalis and Platysma Muscle

Botulinum toxin injection into the lower face is advantageous in lower face remodeling, cobblestone refinement, and Nefertiti lifting. Detailed understanding of the target mentalis and platysma mm. are required.

From the transverse and longitudinal US images of the mentum, the mentalis m. is shown as a hypoechoic image above the mandible below the mandibular teeth. The mentalis m. fibers insert into the dermis (Fig. 8.20).

Only a dermal injection is insufficient in improving the cobblestone chin, and therefore deep injection into the mentalis m. should be done. Precaution is needed to not diffuse botulinum toxin into the DLI m. located lateral to the mentalis m. The injection for the mentalis m. should be approached from a lateral to medial direction when using the in-plane US technique and perpendicularly when using the out-of-plane method.

When targeting the platysma m. to improve the jaw line, the in-plane US technique is advised. Injection should approach the platysma m. and not pass the antegonial notch, which can lead to DLI m. perfusion (Fig. 8.21).

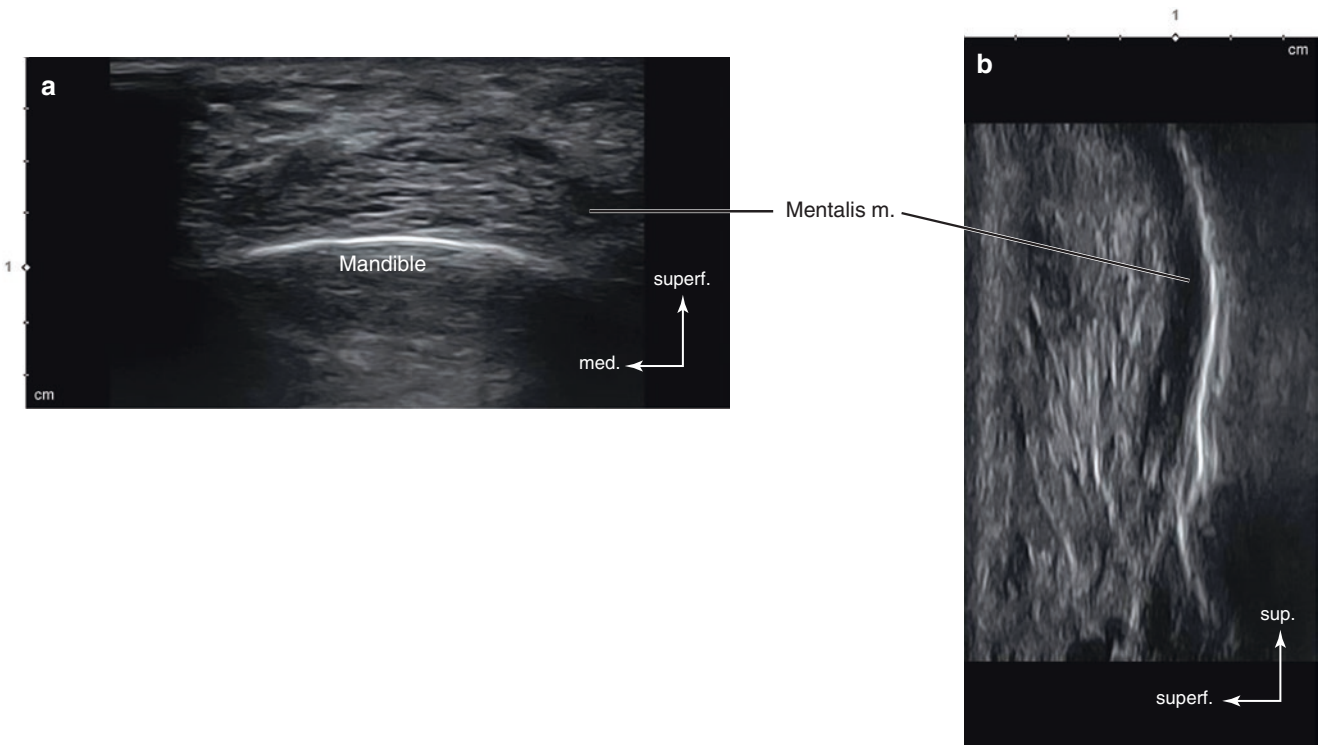

Fig. 8.20 Ultrasonography of the mentalis muscle. (**a**) B mode (transverse view, 15 MHz by linear transducer) and (**b**) B mode (sagittal view, 15 MHz by linear transducer). (Published with kind permission of © Ji-Soo Kim 2020. All Rights Reserved)

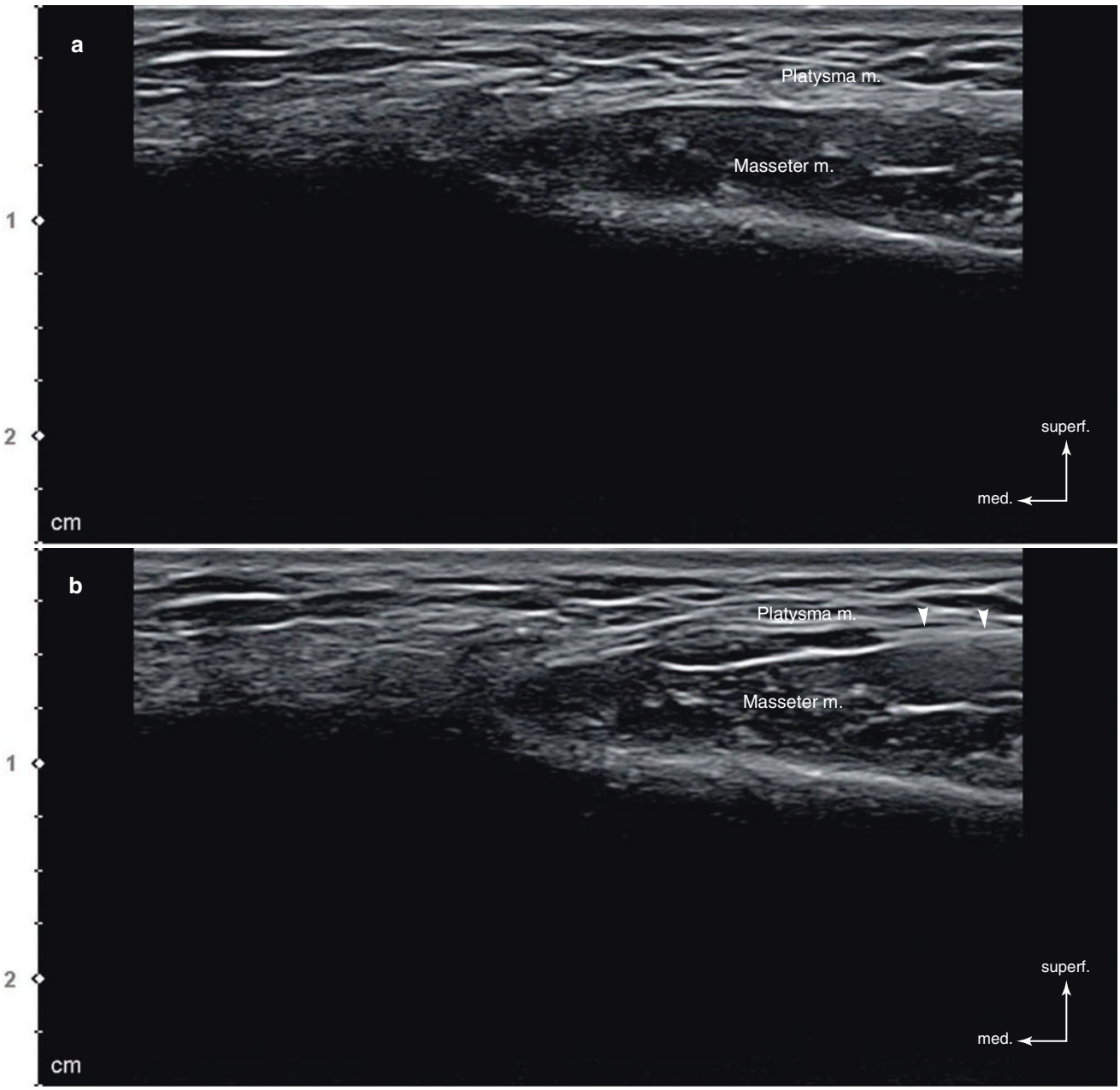

Fig. 8.21 Ultrasonography-guided botulinum toxin injection to the platysma muscle (in-plane). (**a**, **b**) B mode (transverse view, 15 MHz by linear transducer) (white arrowheads: injection needle). (Published with kind permission of © Ji-Soo Kim 2020. All Rights Reserved)

8.2.6 Body (Shoulder and Calf)

Though it is not as popular as facial botulinum toxin procedures, body contouring using toxin injection has increased. Patients who want a smooth shoulder contour and slim legs undertake this treatment. The target muscles for the shoulder and calf are the upper trapezius and the medial and lateral head of the gastrocnemius, soleus, and peroneus longus mm. (Fig. 8.22).

The trapezius m. shows a hypoechoic image from the US image. It is clearly distinguishable from the surrounding muscles. Subcutaneous fat in the shoulder area is not thick even in female patients. Nevertheless, the shoulder contours have varying individual difference of trapezius and levator scapulae mm. thickness. Since the rib and lung apex can be visualized, only the trapezius m. should be targeted. In-plane US approach is proposed for trapezius m. injections to yield safe injection into the trapezius m. Injections may be placed intramuscularly or within the fascia (Fig. 8.23).

Calf muscles can be clearly demonstrated from the US image. The main calf target muscle is the medial head of the gastrocnemius m. US images show the distinct muscle fibers and layers in this region. The medial and lateral heads of the gastrocnemius m. are evident. The soleus m. is U-shaped covering the gastrocnemius m. (Fig. 8.24a). When approaching the lateral part of the calf, US scanning is practical in differentiating the lateral head of the gastrocnemius, the lateral soleus, and the peroneus longus mm. Patients who have had repetitive gastrocnemius m. injection display hyperechoic change and is distinctly distinguishable from the soleus m. (Fig. 8.24b).

The merit of US-guided botulinum injection is that the target muscles can be easily approached regardless of fat size and position (Fig. 8.25). Blind injection involves the patient to stand in a tip-toe position to visualize the border of the medial head of the gastrocnemius m. The US allows not only the gastrocnemius m. to be identified in the relaxed position but also the observation of the medial side of the soleus m., which can be confusing when it is hypertrophied due to secondary compensation after gastrocnemius m. reduction procedures. Another advantage is the uniform injection depth of botulinum toxin injection, which can prevent irregularity of the muscles. US-guided injection is also convenient and safe for fascial layer injection, which may be required for functional purposes.

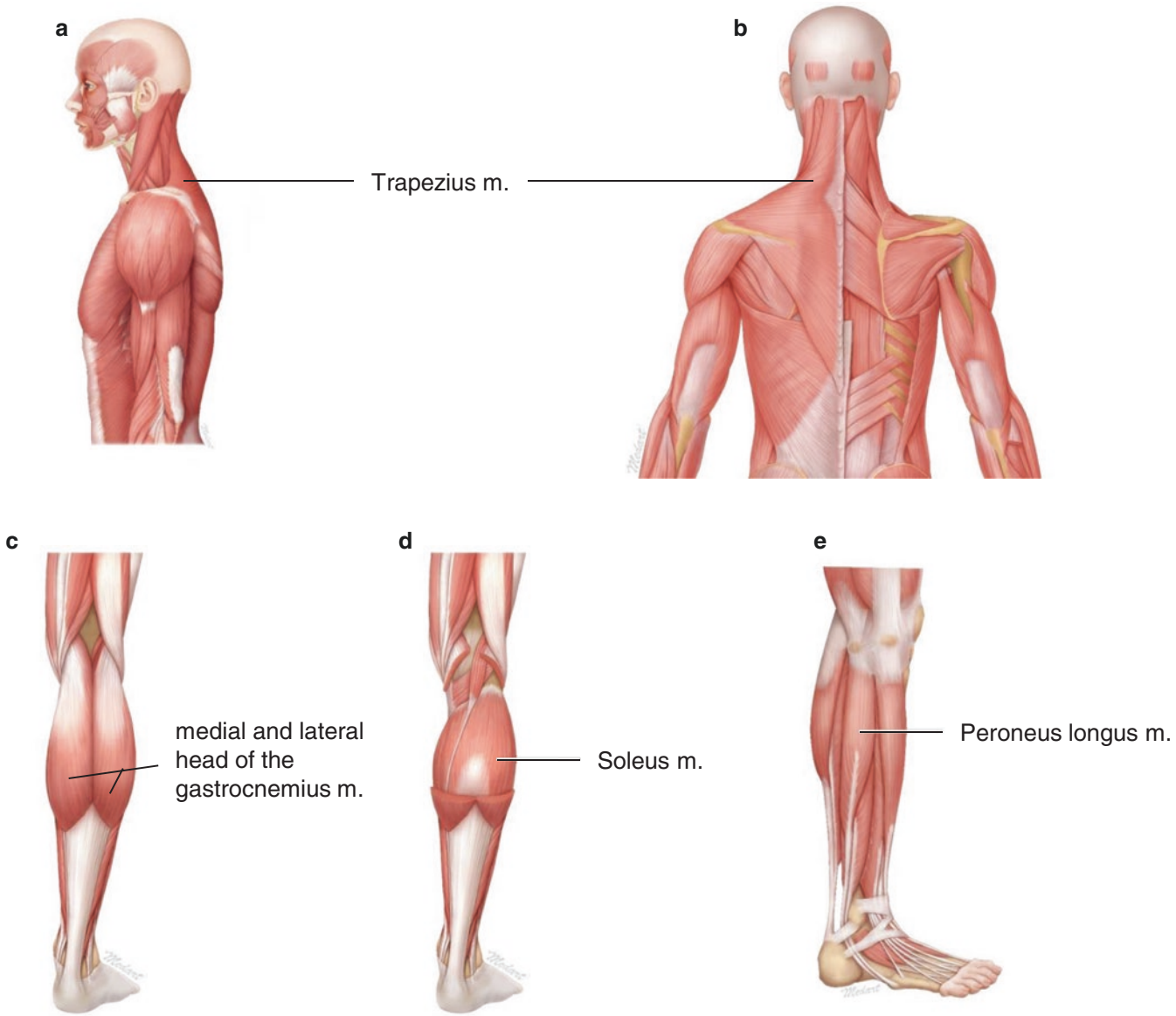

Fig. 8.22 Illustrations of the target muscles for shoulder and calf contouring using botulinum toxin. (**a**, **b**) Upper trapezius, (**c**) medial and lateral head of the gastrocnemius, (**d**) soleus, and (**e**) peroneus longus mm. (Published with kind permission of © Kwan-Hyun Youn 2020. All Rights Reserved)

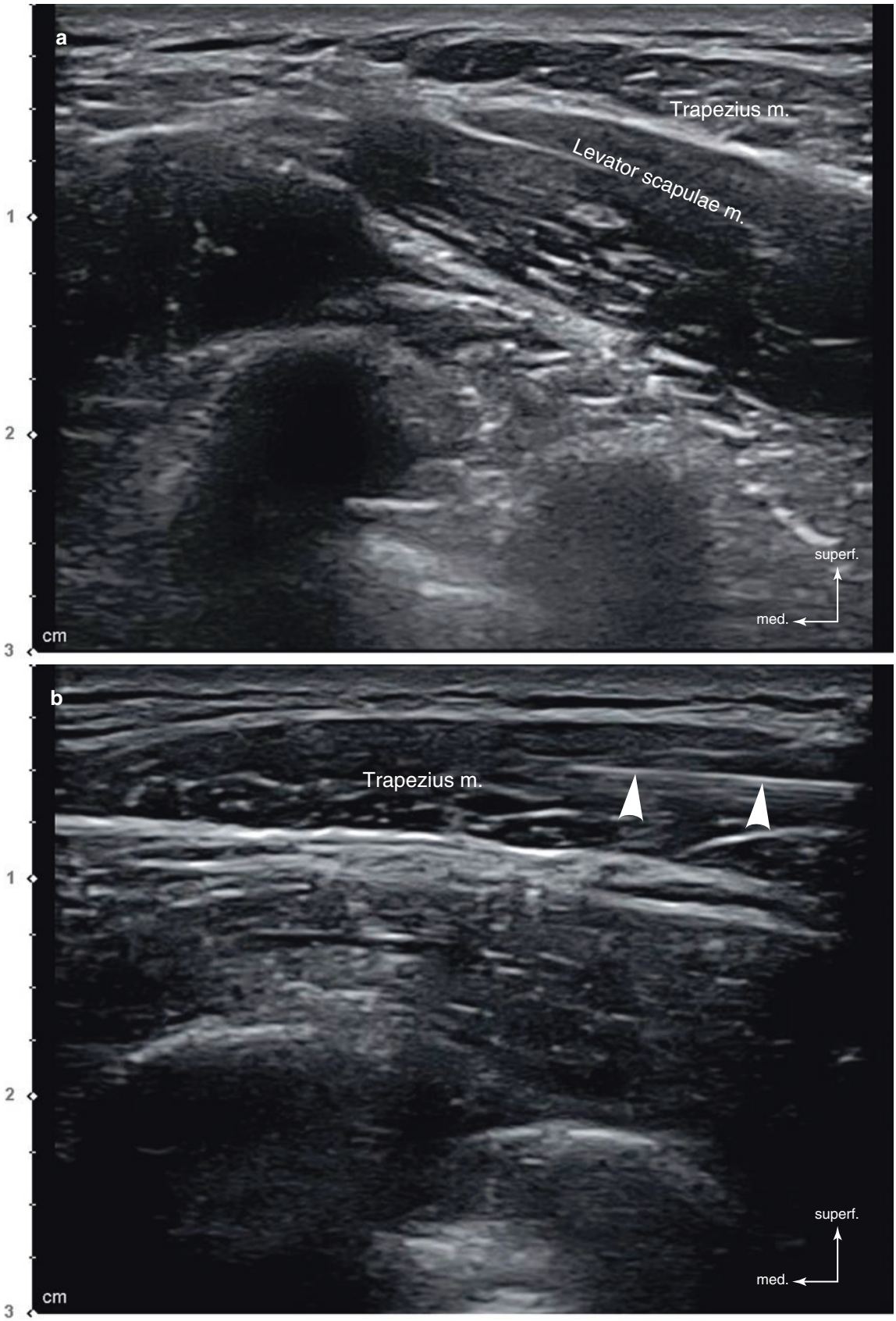

Fig. 8.23 Ultrasonography of the upper shoulder. (**a**) B mode (transverse view, 15 MHz by linear transducer) and (**b**) ultrasonography-guided botulinum toxin injection to the trapezius muscle (in-plane), B mode (transverse view, 15 MHz by linear transducer) (white arrowheads: injection needle). (Published with kind permission of © Ji-Soo Kim 2020. All Rights Reserved)

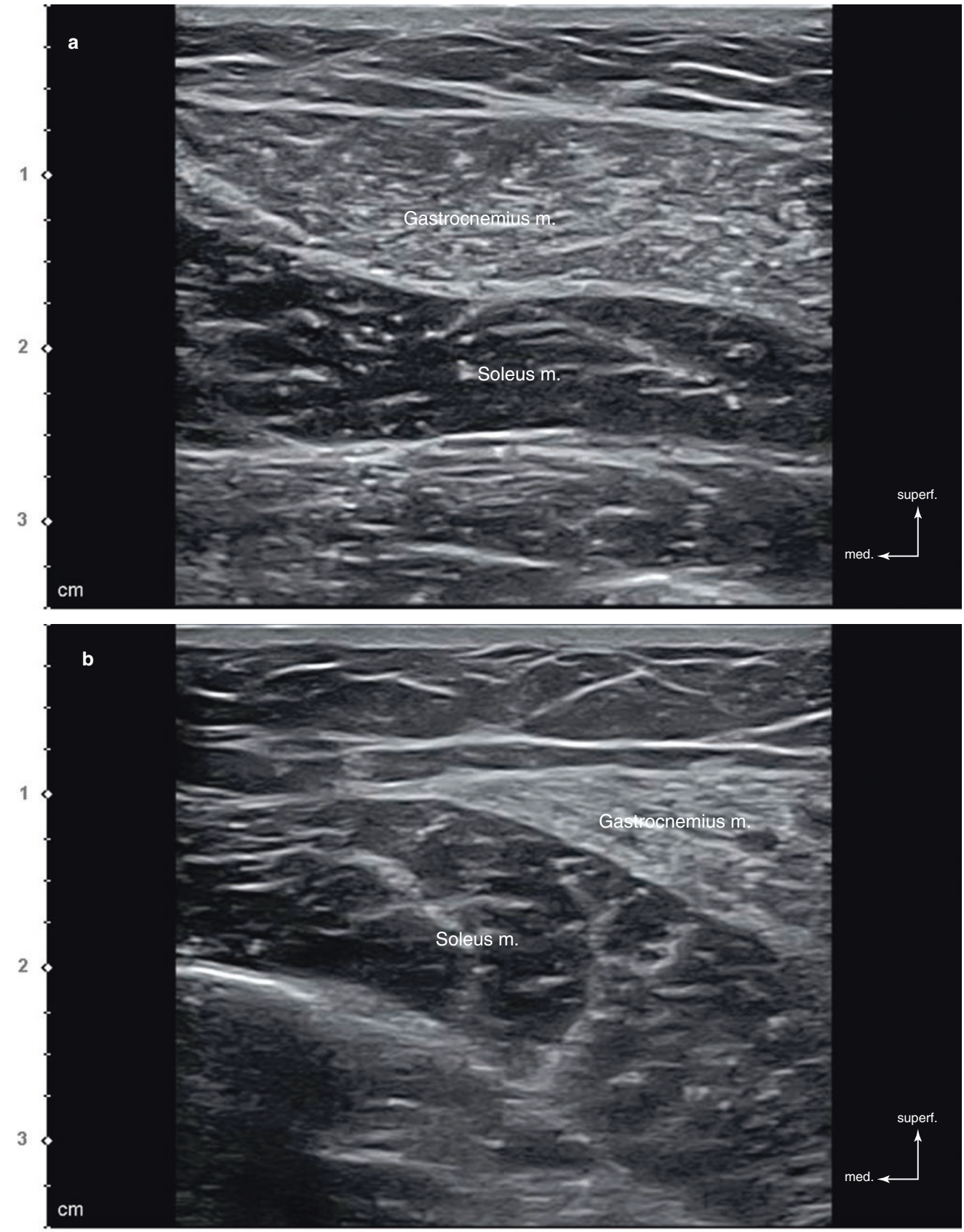

Fig. 8.24 Ultrasonography of the calf. (**a**) B mode (transverse view, 15 MHz by linear transducer) and (**b**) hyperechoic change of the gastrocnemius muscle after the repetitive botulinum toxin injections, B mode (transverse view, 15 MHz by linear transducer). (Published with kind permission of © Ji-Soo Kim 2020. All Rights Reserved)

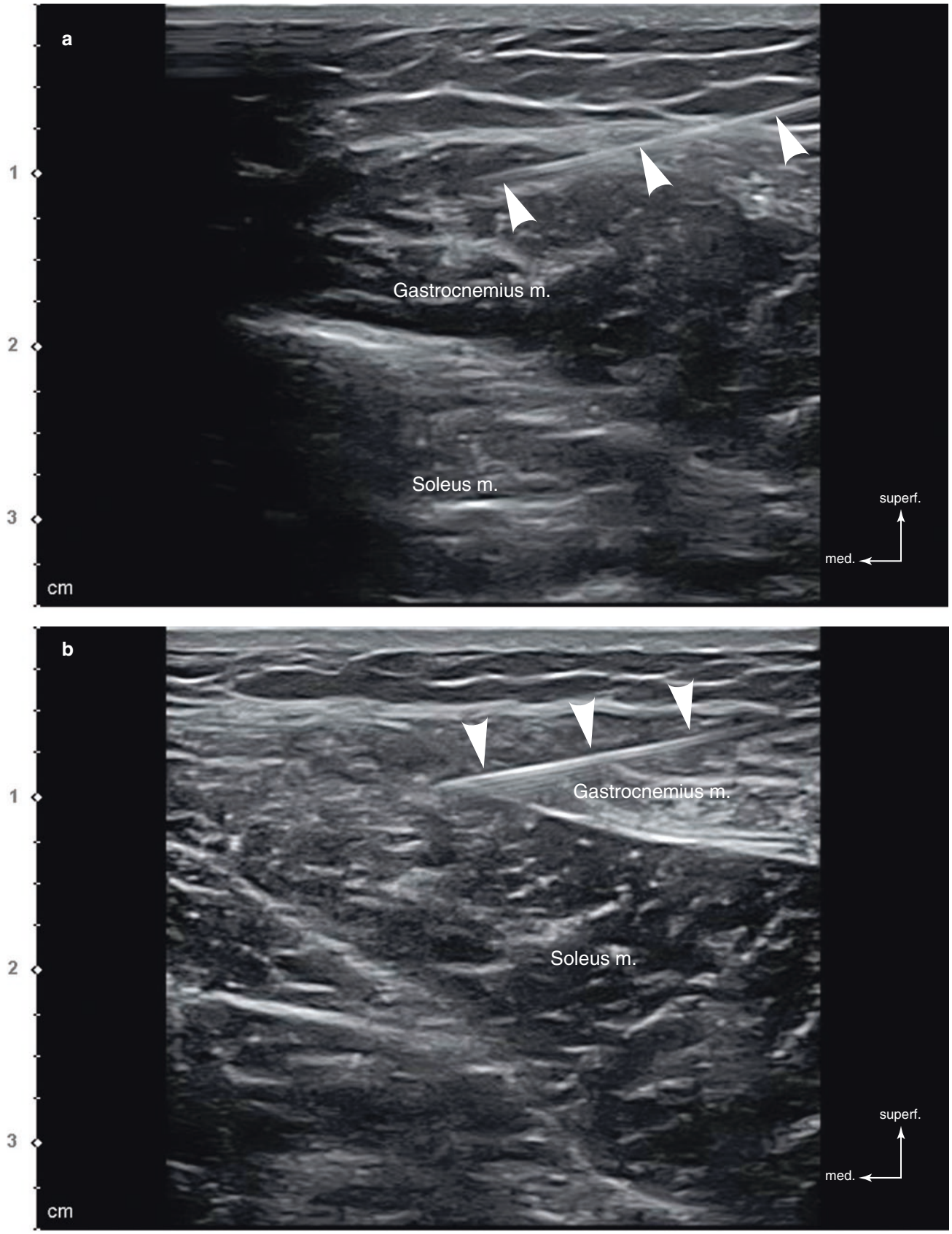

Fig. 8.25 Ultrasonography-guided botulinum toxin injection to the gastrocnemius and soleus muscle (in-plane). (**a**, **b**) B mode (transverse view, 15 MHz by linear transducer) (white arrowheads: injection needle). (Published with kind permission of © Ji-Soo Kim 2020. All Rights Reserved)

Bibliography

1. Aly AR, Rajasekaran S, Ashworth N. Ultrasound-guided shoulder girdle injections are more accurate and mor effective than landmark-guided injections: a systematic review and meta analysis. Br J Sports Med. 2015;29(16):1042–9.
2. Bae GY, Yune YM, Seo KK, Hwang SI. Botulinum toxin injection for salivary gland enlargement evaluated using computed tomographic volumetry. Dermatol Surg. 2013;39:1404–7.
3. Bae JH, Lee JS, Choi DY, Suhk JH, Kim ST. Accessory nerve distribution of aesthetic botulinum toxin injection sin to the upper trapezius muscle: anatomical study and clinical trial: reproducible BoNT injection sites for upper trapezius. Surg Radiol Anat. 2018;40(11):1253–9.
4. Cha YH, Jehoon O, Park JK, Yang HM, Kim SH. Ultrasound-guided versus blind temporomandibular joint injection: a pilot cadaveric evaluation. Int J Oral Maxillofac Surg. 2019;48(4):540–5.
5. Cunnington J, Marshall N, Hide G, Bracewell C, Isaacs J, Platt P, Kane D. A randomized, double-blind, controlled study of ultrasound-guided corticosteroid injection into the joint of patients with inflammatory arthritis. Arthritis Rheum. 2010;62(7):1862–9.
6. Gaon NQ, Wortsman X, Penaloza O, Carrasco JE. Comparison of clinical marking and ultrasound guided injection of botulinum type A toxin into the masseter muscles for treating bruxism and its cosmetic effects. J Cosmet Dermatol. 2016;15(3):238–44.
7. Hans J. Ultrasonography of the head and neck: an imaging atlas. Cham: Springer International Publishing; 2019.
8. Kim HJ, Seo KK, Lee HK, Kim JS. Clinical anatomy of the face for filler and botulinum toxin injection. New York, NY: Springer; 2016.
9. Kim YS, Lee KW, Kim JS, Gil YC, Tansatit T, Shin DH, Kim HJ. Regional thickness of facial skin and superficial fat: application to the minimally invasive procedures. Clin Anat. 2019;32:1008. https://doi.org/10.1002/ca.23331.
10. Lee HJ, Choi YJ, Lee KW, Hu KS, Kim ST, Kim HJ. Ultrasonography of the internal architecture of the superficial part of the masseter muscle in vivo. Clin Anat. 2019;32:446–52.
11. Lee HJ, Kang IW, Seo KK, Choi YJ, Kim ST, Hu KS, Kim HJ. The anatomical basis of paradoxical masseteric bulging after botulinum neurotoxin type A injection. Toxins. 2017;9:14. https://doi.org/10.3390/toxins0010014.
12. Lee HJ, Kim JS, Youn KH, Lee JW, Kim HJ. Ultrasound guided botulinum neurotoxin type A injection for correcting asymmetrical smiles. Aesthet Surg J. 2018;38(9):130–4.
13. Ahuja AT. Diagnostic ultrasound, Head and neck. Salt Lake City, UT: Amirsys; 2014.
14. Choi YJ, Won SY, Lee JG, Hu KS, Kim ST, Tansatit T, Kim HJ. Characterizing the lateral border of the frontalis for safe and effective injection of botulinum toxin. Aesthet Surg J. 2016;36(3):344–8.
15. Hur MS. Anatomical relationships of the procerus with the nasal ala and the nasal muscles: transverse part of the nasalis and levator labii superioris alaeque nasi. Surg Radiol Anat. 2017;39(8):865–9.
16. Jacobson J. Funamentals of musculoskeletal ultrasound. Philadelphia, PA: Elsevier Saunders; 2012.
17. Lee HJ, Choi KS, Won SY, Apinuntrum P, Hu KS, Kim ST, Tansatit T, Kim HJ. Topographic relationship between the supratrochlear nerve and corrugator supercilii muscle--can this anatomical knowledge improve the response to botulinum toxin injections in chronic migraine? Toxins. 2015;7(7):2629–38.
18. Lee JY, Kim JN, Kim SH, Choi HG, Hu KS, Kim HJ, Song WC, Koh KS. Anatomical verification and designation of the superficial layer of the temporalis muscle. Clin Anat. 2012;25(2):176–81.
19. Lee KL, Choi YJ, Gil YC, Hu KS, Tansatit T, Kim HJ. Locational relationship between the lateral border of the frontalis muscle and the superior temporal line. Plast Reconstr Surg. 2019;143(2):293e–8e.
20. Hur M-S, Youn K-H, Hu K-S, Song W-C, Koh K-S, Fontaine C, Kim H-J. New anatomic considerations on the levator labii superioris related with the nasal ala. J Craniofac Surg. 2010;21(1):258–60.
21. Seo KK. Botulinum toxin for Asians. Singapore: Springer; 2017.
22. Smith CF. Gray's surface anatomy and ultrasound. Amsterdam: Elsevier; 2018.
23. So JI, Song DH, Park JH, Choi ES, Yoon JY, Yoo YJ, Chung ME. Accuracy of ultrasound guided and non-ultrasound guided botulinum toxin injection into cadaver salivary glands. Ann Rehabil Med. 2017;41(1):51–7.
24. Yang HM, Kim HJ. Anatomical study of the corrugator supercilii muscle and its clinical implication with botulinum toxin A injection. Surg Radiol Anat. 2013;35(9):817–21.

US Applications in Filler Injection Procedures

9

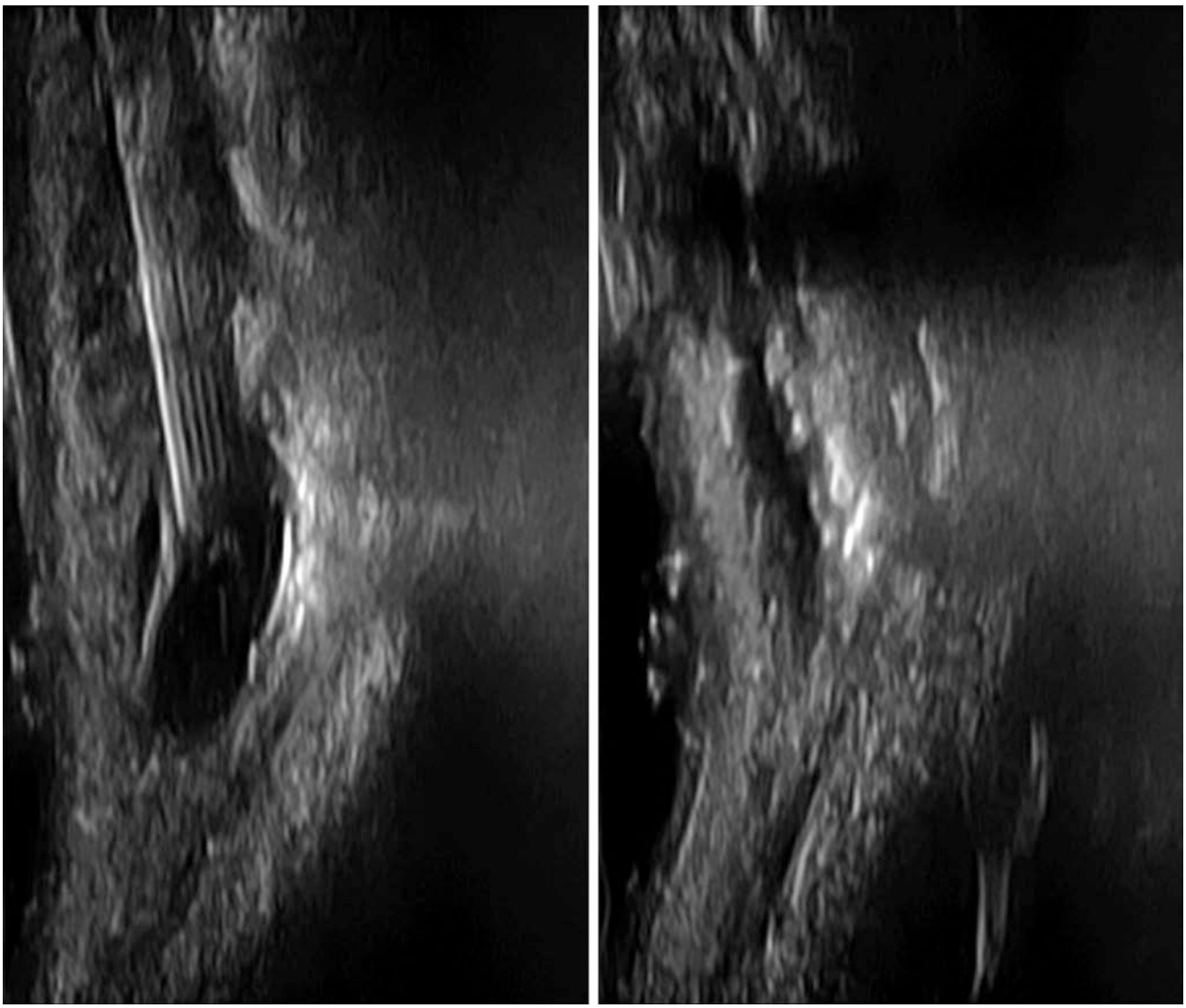

H.-J. Kim et al., *Ultrasonographic Anatomy of the Face and Neck for Minimally Invasive Procedures*,
https://doi.org/10.1007/978-981-15-6560-1_9

9.1 Backgrounds of the US-Guided Filler Injections

Since treatment indications for fillers have developed beyond past extent, a broader comprehension regarding the facial anatomy is required. Complications such as skin necrosis, blindness, and embolism can be detrimental, thus leaving practitioners wondering for a novel method that can reduce vessel-related complications. Incessant research on the vessel anatomy and distribution has been thoroughly executed, leading to fewer complications. Still, distinguishing every variation in each individual is impossible, and there will always be a limitation with blind injection. Implementing US imaging with fillers will be a revolutionary introduction to the field.

Doppler mode imaging has the advantage that allows the identification of the vessels for filler injection. Since intravascular injection of fillers can have devastating results, inspection of the vessel of each individual is necessary since vascular anatomy is varied and not one standard guideline can be used. Using US Doppler mode allows the practitioner to inspect the vessels in real time, thereby lowering the complication rates. Another advantage is that it allows the visualization of the layers below the skin. Practitioners previously defined the layers as either "deep" or "superficial" for the blind technique. However, this technique relies on tactile sensation, which is not reliable and cannot duplicate the same depth every time. The other advantage is that the location of the filler can be precisely detected and removed under US guidance. US imaging can not only locate the filler but it can also evaluate its migration, compartment formation, and granulomatous pathology. Once confirmed, US allows minimal amounts of hyaluronidase to be exactly injected into the area of interest, which is more effective than a blind technique that requires larger amounts of injection.

However, US imaging can have the disadvantage of a difficult interpretation. Unlike the body, in the face, the thin muscles and fat are entangled, and the density and thickness of muscle and fat vary making the image hypoehoic, irregular, and difficult to define. Surgical procedures generally distort the normal anatomy. Vessel images using the US Doppler scanning may exhibit false-negative images, which may rely on the US resolution or be user-dependent. Another downfall is that US cannot discover very small vessels. Regardless, the advantages of using US outweigh the risk of adverse complications using the blind technique. Therefore, we must acquaint ourselves with US imaging.

US-guided filler injections require proficiency. They can be practical in largely two clinical situations. One is when the clinicians need to inject into a precise layer, and the other is when they need to avoid vessels. Excluding treatment areas with fatal complications, US imaging should be evaluated before injection.

Using hyaluronidase injections for filler removal is considerably helpful. US imaging can be utilized to locate the filler and precisely inject the hyaluronidase. Volume reduction can be seen through real-time US imaging, resulting in less amounts of hyaluronidase used. Compare to blind injections, US-guided injections dissolves more filler after filler manipulation.

The US-guided filler removal demands detailed scanning of the area to accurately approach the filler injection site. The needle should be positioned in the filler while slowly injecting the hyaluronidase, checking that the hyaluronidase volume expands and disrupts the filler. A sufficient volume of hyaluronidase is necessary to expose all areas of the filler to the hyaluronidase. In such procedures, 23–27 gauge needles, 1–2 in. long, are usually suggested. Needles smaller than 27 gauge may not disrupt all the filler material depending on the filler cohesiveness and gel hardness; meanwhile, needles larger than 23 gauge may cause vascular injury, leading to bruising. Ultimately, selection of the needle size must take the filler shape, rheology, and extent of complications into consideration.

9.2 US-Guided Filler Injection Procedures

9.2.1 Forehead and Glabella

The forehead and glabella are one of the most common areas for filler injection with the purpose of wrinkle improvement and volume augmentation. The loose connective tissue layer above the periosteum is recommended for filler injection. For the glabella, injection into the dermal or subdermal layer or supraperiosteal layer is advised to alleviate volume depletion and glabella frown lines. A forehead augmentation case shows the hyaluronic acid (HA) filler located above the periosteum (Fig. 9.1).

Depending on the property and injection technique of the filler, and since filler injection is widely distributed in this area, it can create compartments. Fillers may also convert into a rigid granulomatous lesion revealing hypoechoic US images (Fig. 9.2). Elastography may be beneficial in comparing the stiffness between normal and adjacent tissue exhibiting a pathologic change.

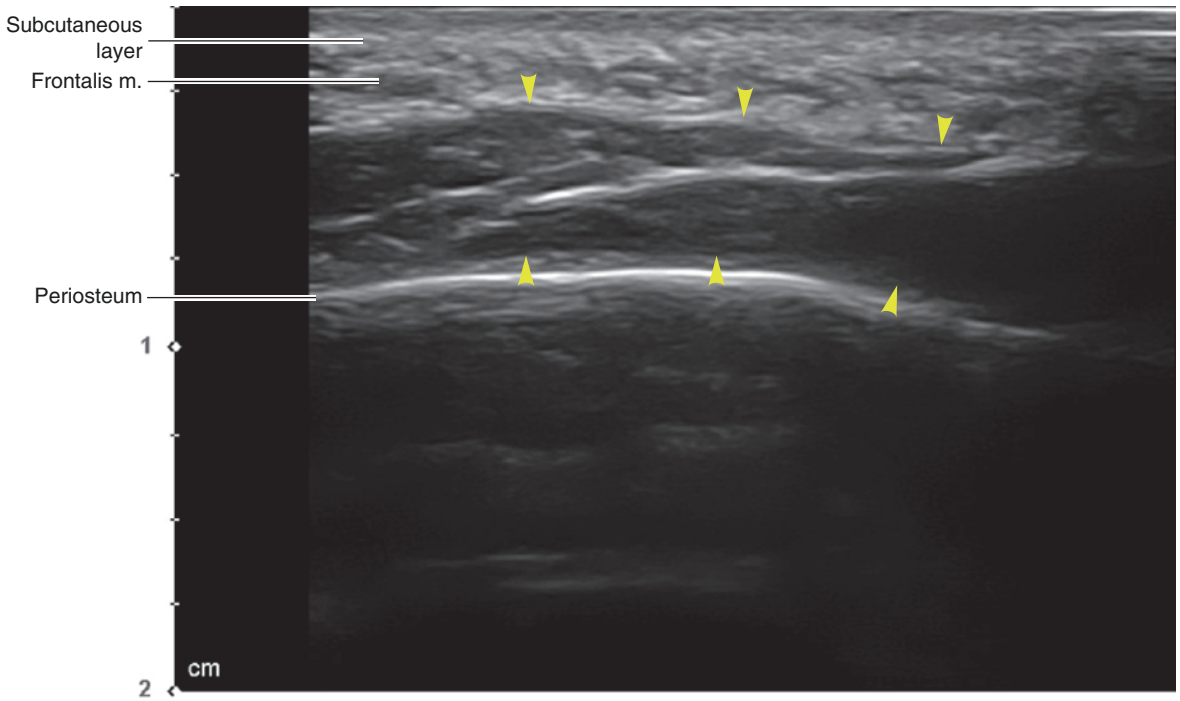

Fig. 9.1 Ultrasonography of the HA filler for the forehead augmentation, B mode (transverse view, 15 MHz by linear transducer) (yellow arrowheads: HA filler). (Published with kind permission of © Ji-Soo Kim 2020. All Rights Reserved)

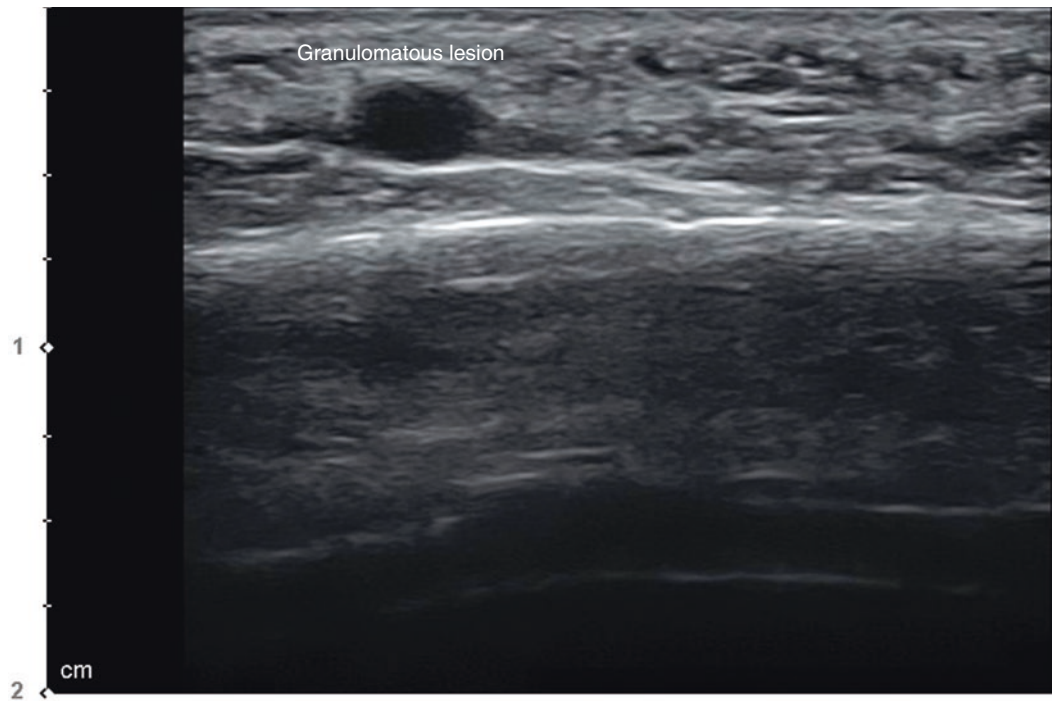

Fig. 9.2 Ultrasonography of the foreign body granuloma on the forehead after the filler injection, B mode (transverse view, 15 MHz by linear transducer). (Published with kind permission of © Ji-Soo Kim 2020. All Rights Reserved)

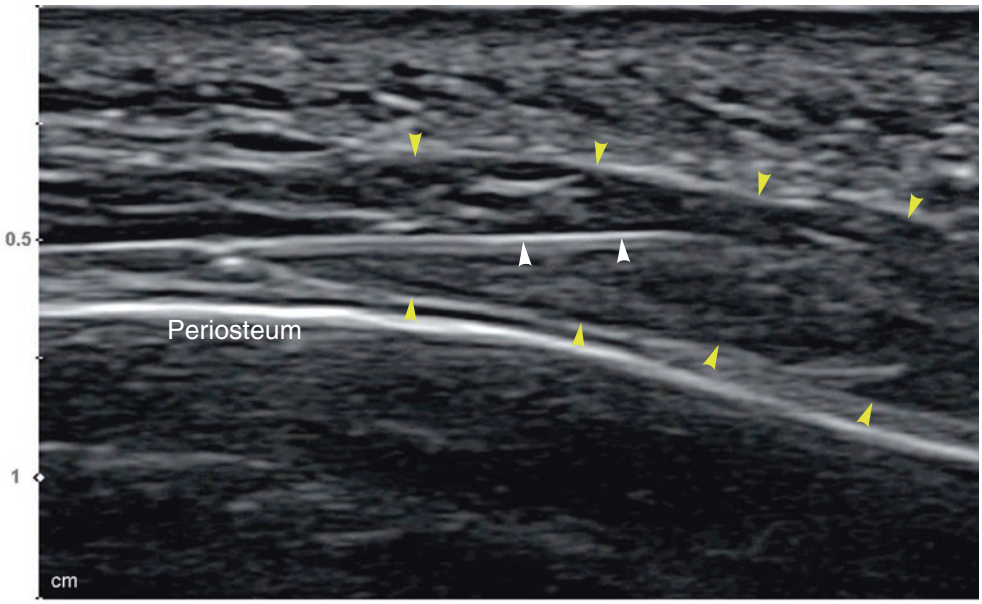

Fig. 9.3 Ultrasonography-guided filler removal on the forehead, B mode (transverse view, 15 MHz by linear transducer) (yellow arrowheads: HA filler, white arrowheads: injection needle). (Published with kind permission of © Ji-Soo Kim 2020. All Rights Reserved)

Through the Doppler image, the frontal branch of the superficial temporal a., which is lateral to the supraorbital a., should be identified and avoided during forehead augmentation procedures. Hence, the location of the supraorbital a. running within the loose connective tissue layer above the periosteum should be confirmed. At the entry point of the cannula, special concern on the exact location of the superficial temporal a. is recommended to prevent skin necrosis due to intra-arterial filler injection.

The glabella region is a highly risky area due to the presence of the supratrochlear a.; if the filler is injected intra-arterially, it could lead to skin necrosis and blindness. Vessel direction must be closely traced in the transverse and longitudinal US view modes. Recognizing the precise layer where the supratrochlear a. lies is essential since it is below the glabella wrinkles (Fig. 3.16).

When dissolving fillers in the forehead area, an in-plane approach is beneficial since this is an outspread area (Fig. 9.3). Because large amounts of the filler are usually used for forehead augmentation, a horizontal approach is recommended rather than multiple vertical injections for filler removal.

9.2.2 Temple

Fillers are injected between the lateral forehead and zygomatic arch to smoothen the curvature of the temple. In cases that younger patients who have less fat in the temple with more protruded zygoma, or aged patients who have fat atrophy in the temple, temple looks more depressed. Because thin subcutaneous fat can be seen in patients with temple depression, an excess amount of fillers in the subcutaneous layer can lead to skin irregularities. The superficial temporal a. is situated near the skin with increasing chances of vessel damage (Fig. 3.21). Injection into the temporal fat pad placed between the superficial and deep layer of the deep temporal fascia is advantageous in volumizing but carries the risk of middle temporal v. injury. Accurate injection into fat above the temporalis m. is difficult since the temporal extension of the buccal fat escalates the probability of filler migration into the lower face. Therefore, filler injection into the subSMAS fat layer or above the periosteum is desired (Fig. 9.4).

From the Doppler image, the deep temporal a. within the temporalis m. should be identified before the injection procedures (Figs. 3.23 and 3.24). The STF surrounds the superficial temporal a. (STA), which is simply observed with the Doppler image. The subSMAS fat layer usually lacks vessel distribution, being the target site for filler injection. Avoiding the STA is possible by penetrating the needle below the STF layer. A strong pinch of the soft tissue in the temple area will elevate the STF attached to the skin. The subSMAS fat layer can be easily reached by using a cannula to perforate through the skin. However, if the cannula proceeds from the zygomatic arch, it can invest into the temporal fat pad and injure the middle temporal v. and cannot advance into the upper part of the temple. Approaching from the lateral eyebrow rather than the zygomatic arch when inserting the cannula makes access to the subSMAS fat layer easier because the retro-orbicularis oculi fat (ROOF) is connected to the subSMAS fat layer (Fig. 3.22).

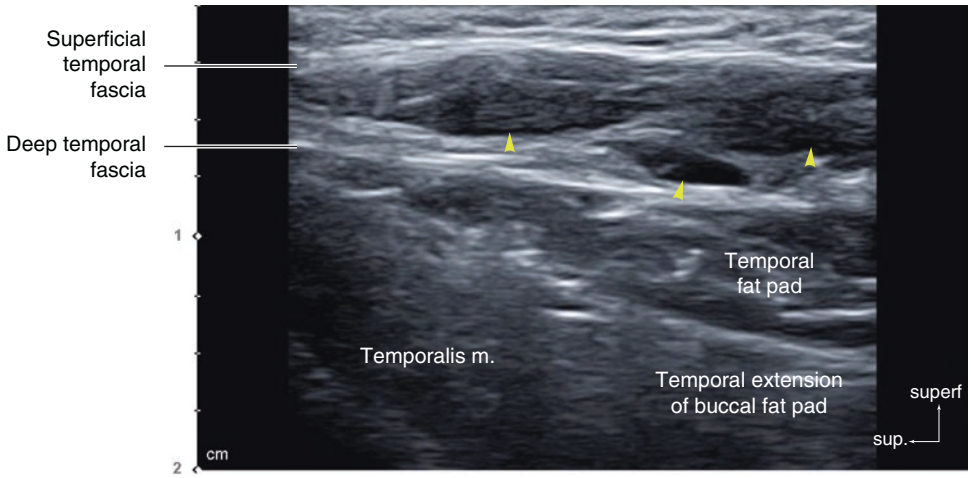

Fig. 9.4 Ultrasonography of the HA filler located between the superficial and deep temporal fascia, B mode (transverse view, 15 MHz by linear transducer) (yellow arrowheads: HA filler). (Published with kind permission of © Ji-Soo Kim 2020. All Rights Reserved)

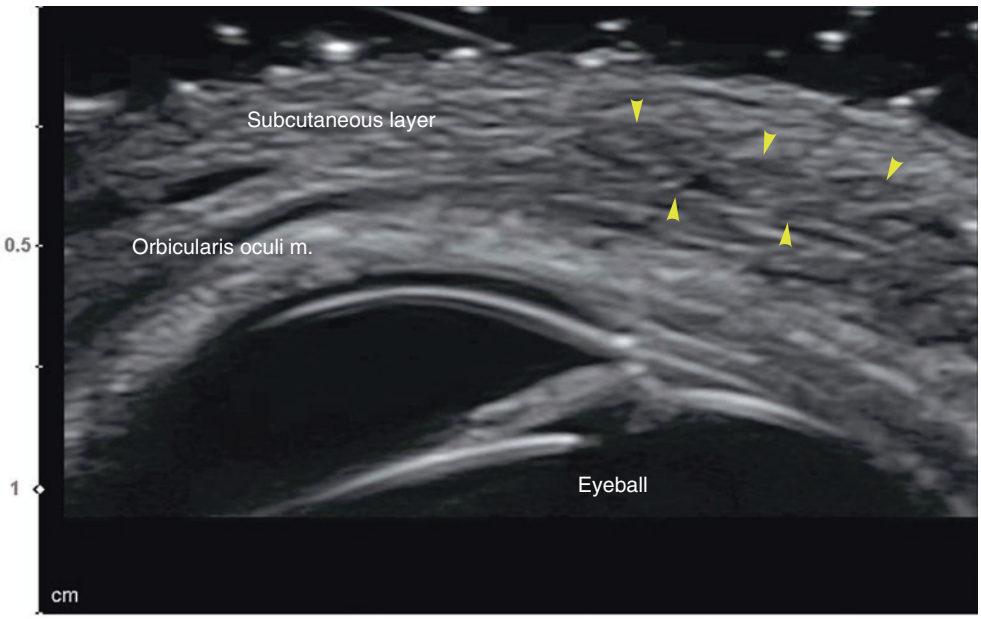

Fig. 9.5 Ultrasonography of the HA filler for the sunken eye augmentation, B mode (transverse view, 15 MHz by linear transducer) (yellow arrowheads: HA filler). (Published with kind permission of © Ji-Soo Kim 2020. All Rights Reserved)

9.2.3 Periorbital Area (Sunken Eye and Pretarsal Roll)

Generally, sunken eye enhancement requires filler injections in the subcutaneous fat layer or ROOF below the OOc m. layer (Figs. 4.13 and 4.14). The hypoechoic US image of the filler is identified in the subcutaneous layer (Fig. 9.5). For the enhancement of sunken eye appearance, injection into the subcutaneous layer will accompany irregularities unless the filler is very soft. The best injection plane is the ROOF, but the adjacent OOc m. is very thin and is approximated to the orbital septum making visualization on the US image difficult (Fig. 4.13). From the Doppler image, the supratrochlear a. passes the frontal notch toward the deep plane of the forehead, ultimately proceeding superficially (Fig. 4.11). This area coincides with the sunken eye, and a perpendicular periosteal approach must be avoided.

The target area for pretarsal roll augmentation is the subcutaneous layer superficial to the OOc m. Injections deeper to the OOc m. will compromise its shape while a superficial injection will cause the Tyndall effect. This is the hypoechoic US image of the filler lying just superficial to the OOc m. (Fig. 9.6). From the Doppler image, the vessels such as the inferior medial palpebral a. should be investigated since it runs within the pretarsal roll.

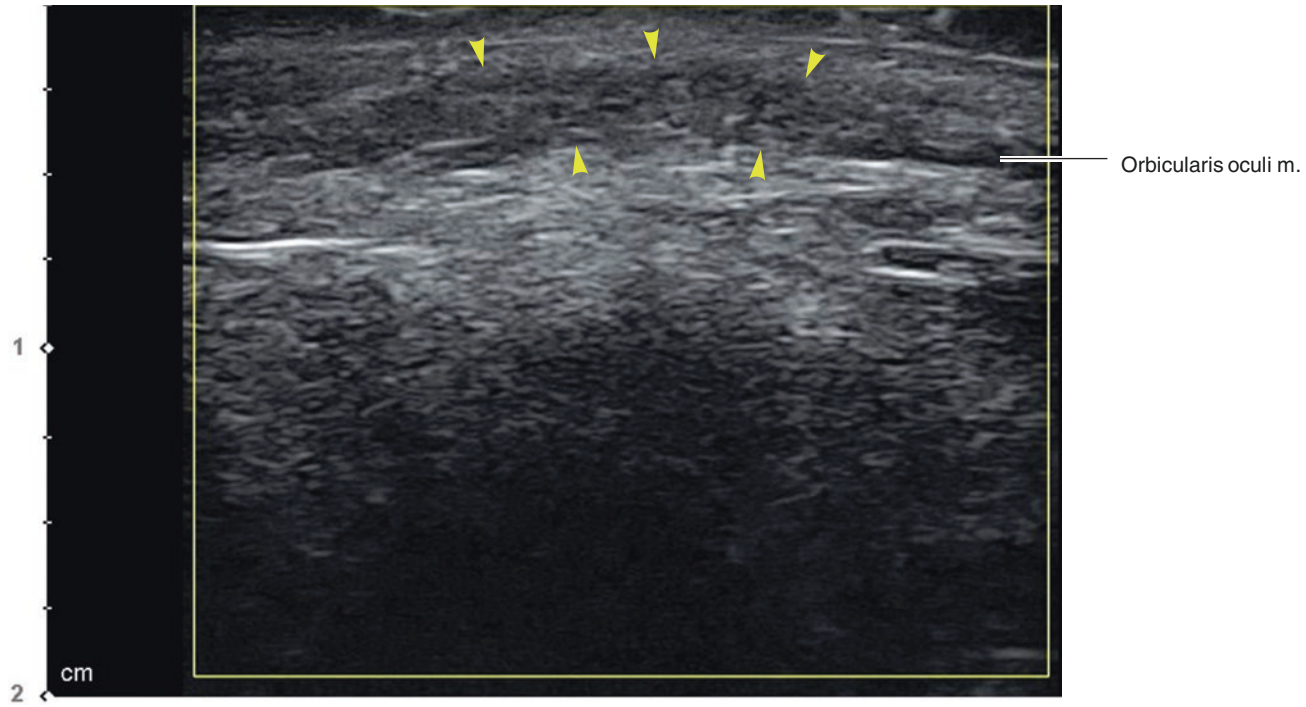

Fig. 9.6 Ultrasonography of the HA filler for the pretarsal roll augmentation, Doppler mode (transverse view, 15 MHz by linear transducer) (yellow arrowheads: HA filler). (Published with kind permission of © Ji-Soo Kim 2020. All Rights Reserved)

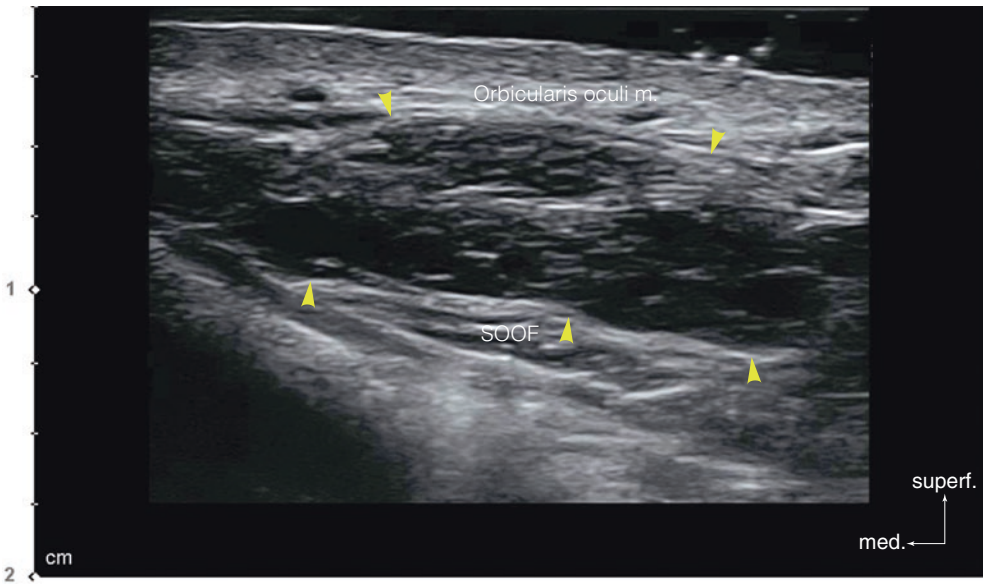

Fig. 9.7 Ultrasonography of the HA filler for the tear trough augmentation, B mode (transverse view, 15 MHz by linear transducer) (yellow arrowheads: HA filler). (Published with kind permission of © Ji-Soo Kim 2020. All Rights Reserved)

9.2.4 Tear Trough and Anterior Malar Augmentation

The ideal filler injection plane for tear trough correction is the thin subcutaneous layer or the sub orbicularis oculi fat (SOOF), which is deep to the OOc m. (Fig. 5.20). The US image shows the filler located below the OOc m. Hypoechoic filler material can be noticed medial to the tear trough above the periosteum of the inferior orbital margin. Hyperechoic filler material is also observed lateral to the tear trough in the upper layer of the SOOF (Fig. 9.7).

Enhancement of the tear trough requires a deep needle injection that pierces through the OOc m., advancing near the SOOF or prezygomatic space into the loose tissue. The cannula can comfortably approach this region or the subcutaneous layer, which is another option (Fig. 9.8). From the

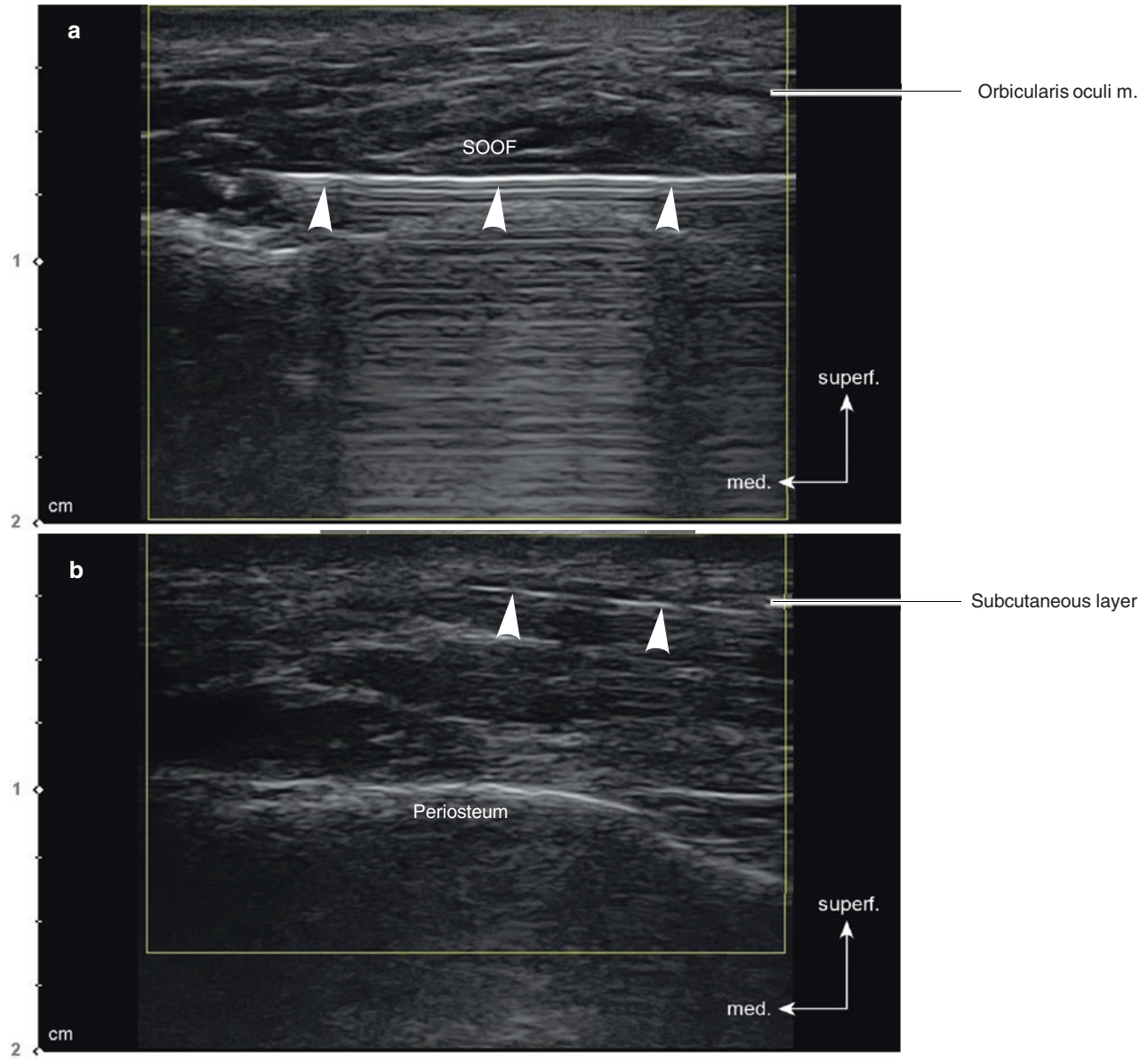

Fig. 9.8 Ultrasonography-guided HA filler injection for the tear trough augmentation. (**a**) Deep injection, B mode (transverse view, 15 MHz by linear transducer) and (**b**) superficial injection, B mode (transverse view, 15 MHz by linear transducer) (white arrowheads: injection needle). (Published with kind permission of © Ji-Soo Kim 2020. All Rights Reserved)

Doppler image, the angular and inferior palpebral aa. should be confirmed prior to injection (Figs. 4.16, 5.17, and 5.25). Subcutaneous plane injection should be implemented in select cases since fillers can cause irregularities and make the Tyndall effect.

The ideal injection plane for anterior malar augmentations is the SOOF, but the subcutaneous layer can also be addressed (Fig. 9.9). For the anterior malar augmentation procedure, the location of the infraorbital foramen must be pre-checked (Fig. 5.18). Cannula use is recommended. The cannula should slowly perforate the deep fat layer slightly above the LLS m.

Visualizing the superficial portion of the OOc m. is somewhat possible, but it is impossible to distinguish the deeper structure underneath the OOc m. Implementing US imaging to observe the hypoechoic image when removing the fillers are beneficial. Fillers injected for anterior malar augmentation should be monitored from both the superficial and deep layers. US-guided hyaluronidase injection can precisely engage into the filler and disrupt it (Figs. 9.10 and 9.11).

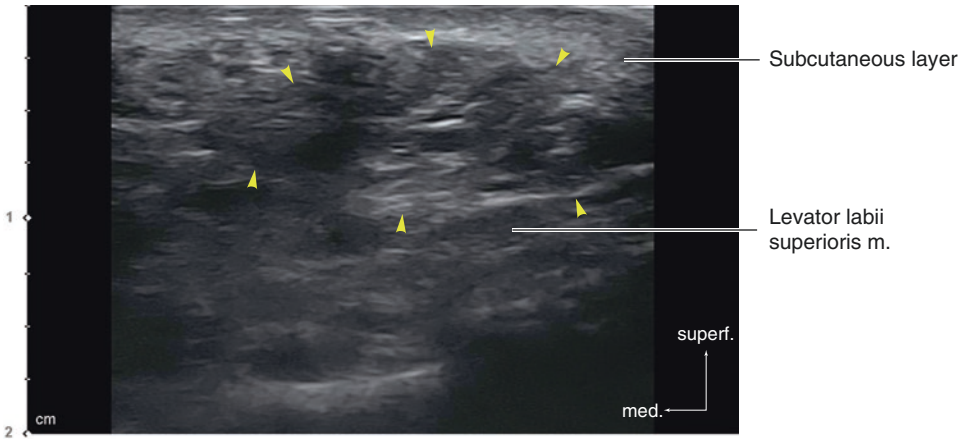

Fig. 9.9 Ultrasonography of the HA filler in the subcutaneous layer for the anterior malar augmentation, B mode (transverse view, 15 MHz by linear transducer) (yellow arrowheads: HA filler). (Published with kind permission of © Ji-Soo Kim 2020. All Rights Reserved)

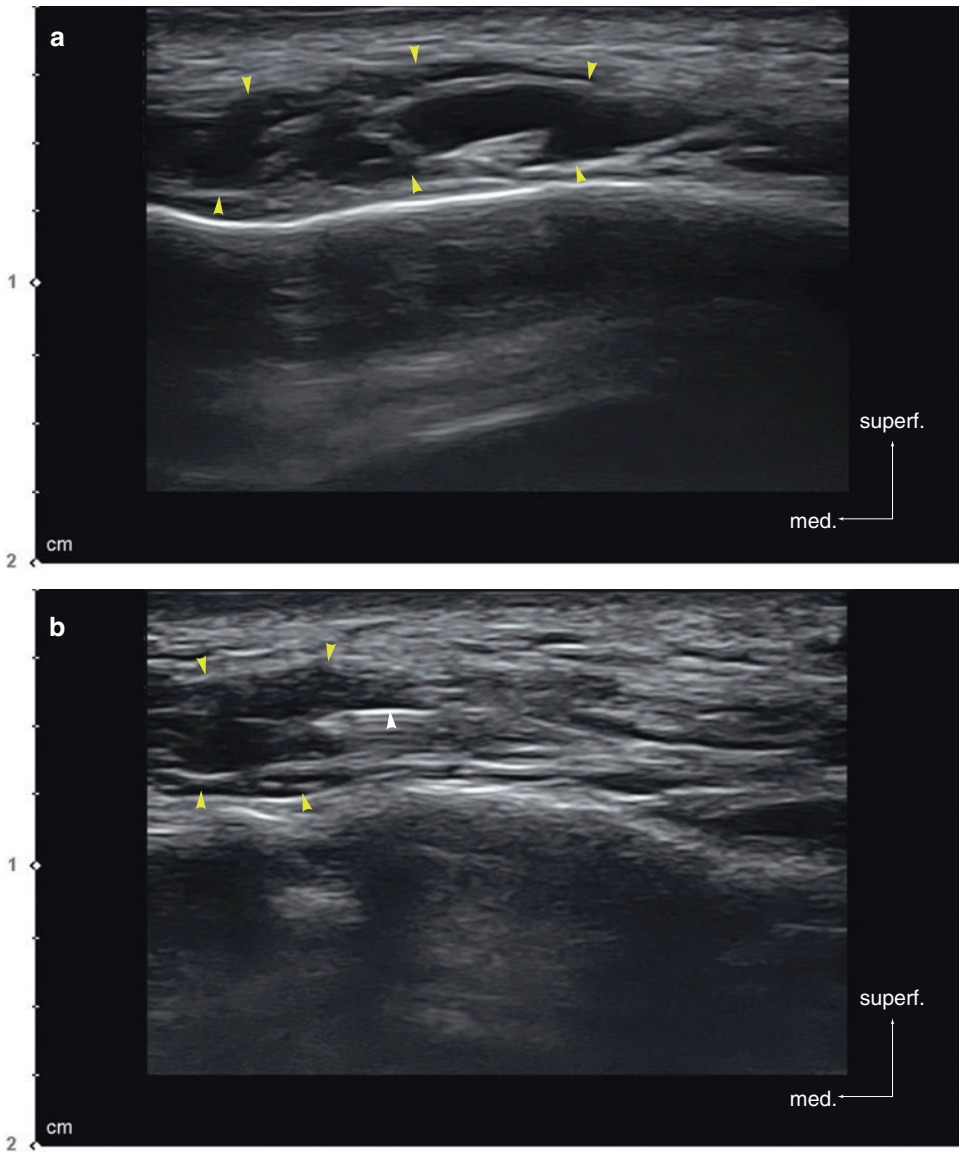

Fig. 9.10 Ultrasonography-guided filler removal on the tear trough region. (**a**) Before injection, B mode (transverse view, 15 MHz by linear transducer) and (**b**) during hyaluronidase injection, B mode (transverse view, 15 MHz by linear transducer) (yellow arrowheads: HA filler, white arrowhead: injection needle). (Published with kind permission of © Ji-Soo Kim 2020. All Rights Reserved)

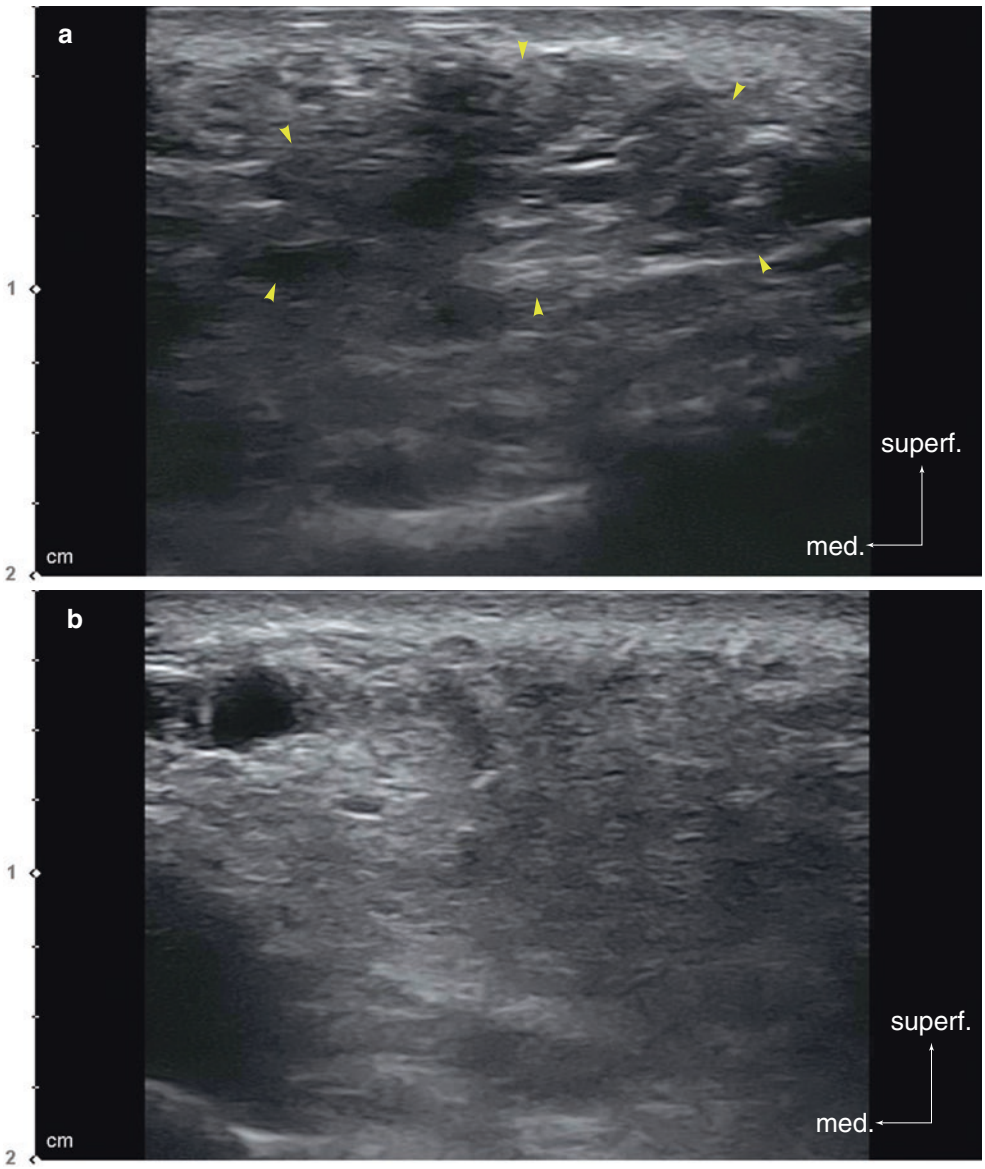

Fig. 9.11 Ultrasonography-guided filler removal on the midface. (**a**) Before injection, B mode (transverse view, 15 MHz by linear transducer) and (**b**) immediately after injection: collapsed filler, B mode (transverse view, 15 MHz by linear transducer) (yellow arrowheads: HA filler). (Published with kind permission of © Ji-Soo Kim 2020. All Rights Reserved)

9.2.5 Nose

Filler nose augmentations are one of the most highly performed procedures in Asia. The nose is also where most vascular-related complications appear. Checking the vascular anatomy of the target nasal augmentation area with US is essential to minimize complications. The US image of the transverse and longitudinal view of the nose shows moderate thickness in the soft tissue of the dorsum of the nose (Figs. 5.25, 5.26, and 5.27).

The ideal plane for filler nose augmentation is the supraperiosteal and supraperichondrial layer below the nasal mm. Superficial fatty layer (subcutaneous layer) injection is also possible, but the risks of vascular accidents are higher in this area. This US image presents the filler as hypoechoic masses in several different parts of the superficial and deep fatty layer (Fig. 9.12).

Bolus injection with hard fillers are usually applied to the nose, which increase the hypoechoicity, making it easier to differentiate with other tissues. Lateral filler migration can be observed due to the filler cohesiveness, amount, and injection site. Nasal widening cases have more retention of water within the filler and look hyperechoic (Fig. 9.13).

Filler augmentation is not recommended in patients who have had previous rhinoplasty because the implants make the supraperiosteal and supraperichondrial planes ambiguous (Fig. 9.14), and complications may arise more.

Since the nose has a high probability of complications, the transverse and longitudinal view in Doppler mode should meticulously scan and confirm the location of the dorsal nasal a. and intercanthal v. Since the nasal dorsum is a thin area, a small probe such as the hockey-stick transducer is convenient. Similar to the nasolabial fold

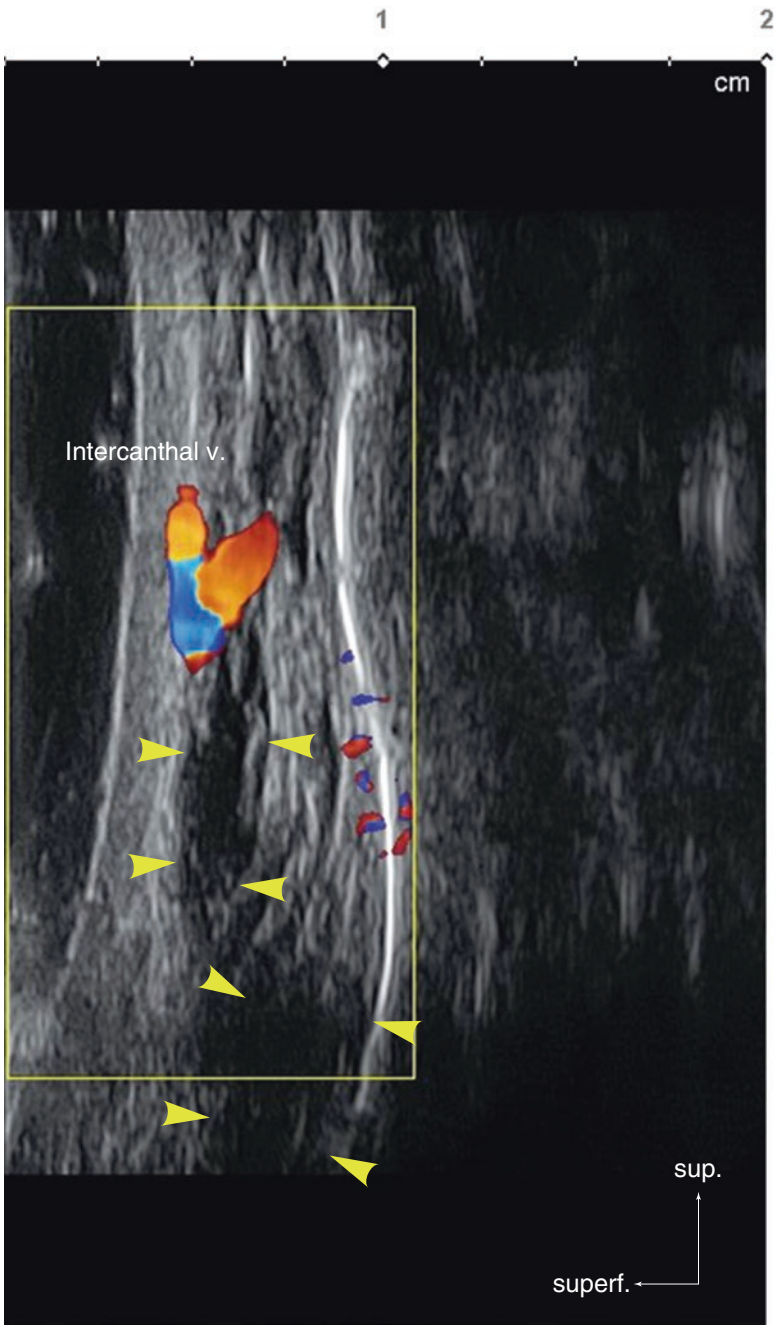

Fig. 9.12 Ultrasonography of the HA filler for the dorsum augmentation, B mode (longitudinal view, 15 MHz by linear transducer) (yellow arrowheads: HA filler). (Published with kind permission of © Ji-Soo Kim 2020. All Rights Reserved)

(NLF) case, the power Doppler mode or spectral Doppler mode can be applied for nasal US procedures. However, the vessels are more apparent under color Doppler compared to the NLF. Dorsum augmentation is typically performed in the midline of the nose. The midline and periosteal planes of the nose have been considered safe injection areas, but recent literature has reported the presence of vessels in the midline. This US image shows vessels in the midline; in these cases, the filler should be situated in the supraperiosteal plane (Fig. 5.25). Vessels are rarely seen in the deep fatty layer, but this area is not 100% safe. Vessel diameters in this area are larger than anticipated, sometimes being 1/3–1/2 thickness of the whole soft tissue and can lead to complications, especially in the nose and radix.

Clinicians have to find the safest and most aesthetically enhancing area when injecting fillers, and the Doppler mode can be very beneficial in analyzing the vascular anatomy. However, when the vascular anatomy is unfavorable, filler injection must be abandoned. It is not difficult distinguishing the filler during US-guided hyaluronidase injection in this region. US-guided injection can be attempted when the probability of vascular complications is high, but the main key in minimizing the risk is to thoroughly detect the vessel locations before an injection. US imaging can capture volume loss after accurate injection of the hyaluronidase (Fig. 9.15).

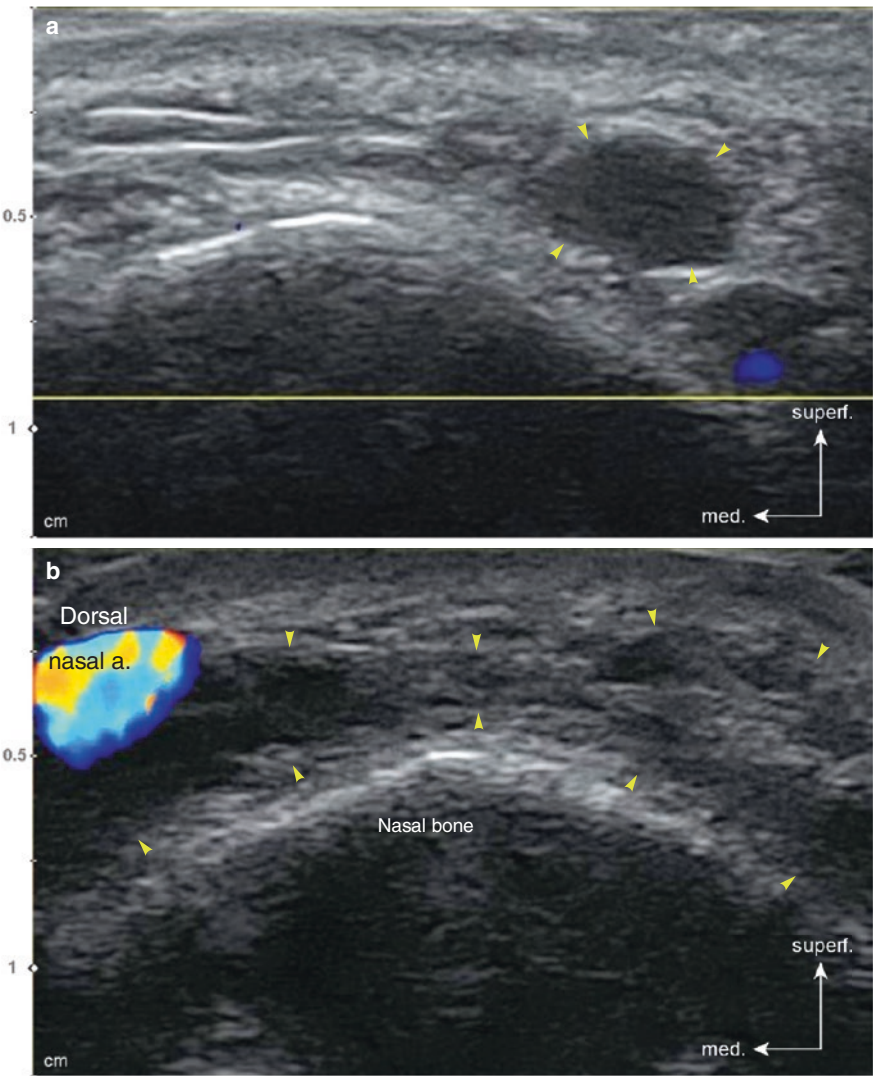

Fig. 9.13 Ultrasonography of the HA filler on the dorsum of nose. (**a**) Migrated filler, Doppler mode (transverse view, 15 MHz by linear transducer) and (**b**) widened nose, Doppler mode (transverse view, 15 MHz by linear transducer) (yellow arrowheads: HA filler). (Published with kind permission of © Ji-Soo Kim 2020. All Rights Reserved)

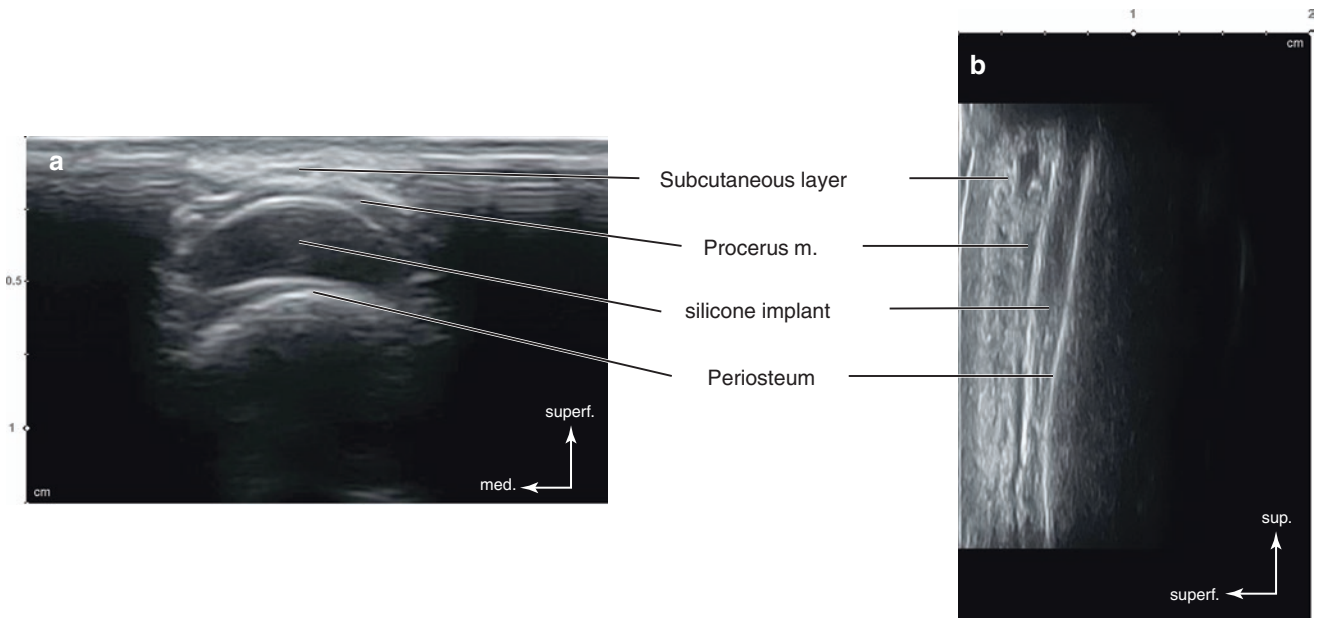

Fig. 9.14 Ultrasonography of the silicone implant on the dorsum of nose. (**a**) B mode (transverse view, 15 MHz by linear transducer) and (**b**) B mode (longitudinal view, 15 MHz by linear transducer). (Published with kind permission of © Ji-Soo Kim 2020. All Rights Reserved)

9.2.6 Nasolabial Fold

The NLF is one of the most favored filler indications while being one of the riskiest areas because of complications such as skin necrosis in the ala of the nose, blindness, and embolism. The proposed filler injection layer is the superficial dermal/subdermal layer or the deep section below the SMAS or the deep medial cheek pad above the periosteum. US interpretation is difficult in this area because the NLF is entangled with the superficial and deep fat (Figs. 6.26 and 6.28). Migration after filler injection into the NLF is often observed because the NLF area is affected by the upper lip elevators since the deep medial cheek fat pad is soft, and the fat pad is located lateral to the infraorbital space. Since the lip elevators are attached to the NLF and the OOr m. lies tightly below the skin with minimal subcutaneous fat, migration is possible if the filler is not meticulously injected into the dermal or subdermal layer (Fig. 9.16).

The facial a. located in the NLF rests in the subcutaneous layer or the muscle level. Additional precautions should be taken when the artery is positioned in the subdermal level of the superficial subcutaneous layer (Figs. 6.26, 6.28, and 6.29).

When the vascular complications are a concern, US-guided injection may be an option. Deep injection using a cannula will penetrate the deep part of the OOr m. until the deep medial cheek fat appears. This approaches below the muscle layer where the facial a. exists (Fig. 9.17a). The periosteal injection plane is advantageous in deep injections. In superficial injections, proceeding toward the dermal area is difficult with a blunt tip cannula. Even if the tip is turned up, this only sends the needle around the superficial layer of the OOr m. US-guided injection allows visualization of the advancing cannula toward the target layer and assists in avoiding the subcutaneous layer where the facial a. lies (Fig. 9.17b).

The most crucial aspect in filler removal is detecting the filler location and extent. Deep bolus injections are apt to migrate and should be closely checked. Filler compartments such as capsules and septa can be formed according to filler direction, filler injection techniques, and filler rheology. Lateral migration is common; in such cases, all compartments need to be dissolved separately using hyaluronidase (Fig. 9.18).

Implants can also be observed in this area. History taking and US imaging are beneficial in finding and removing the fillers surrounding the implant (Fig. 9.19).

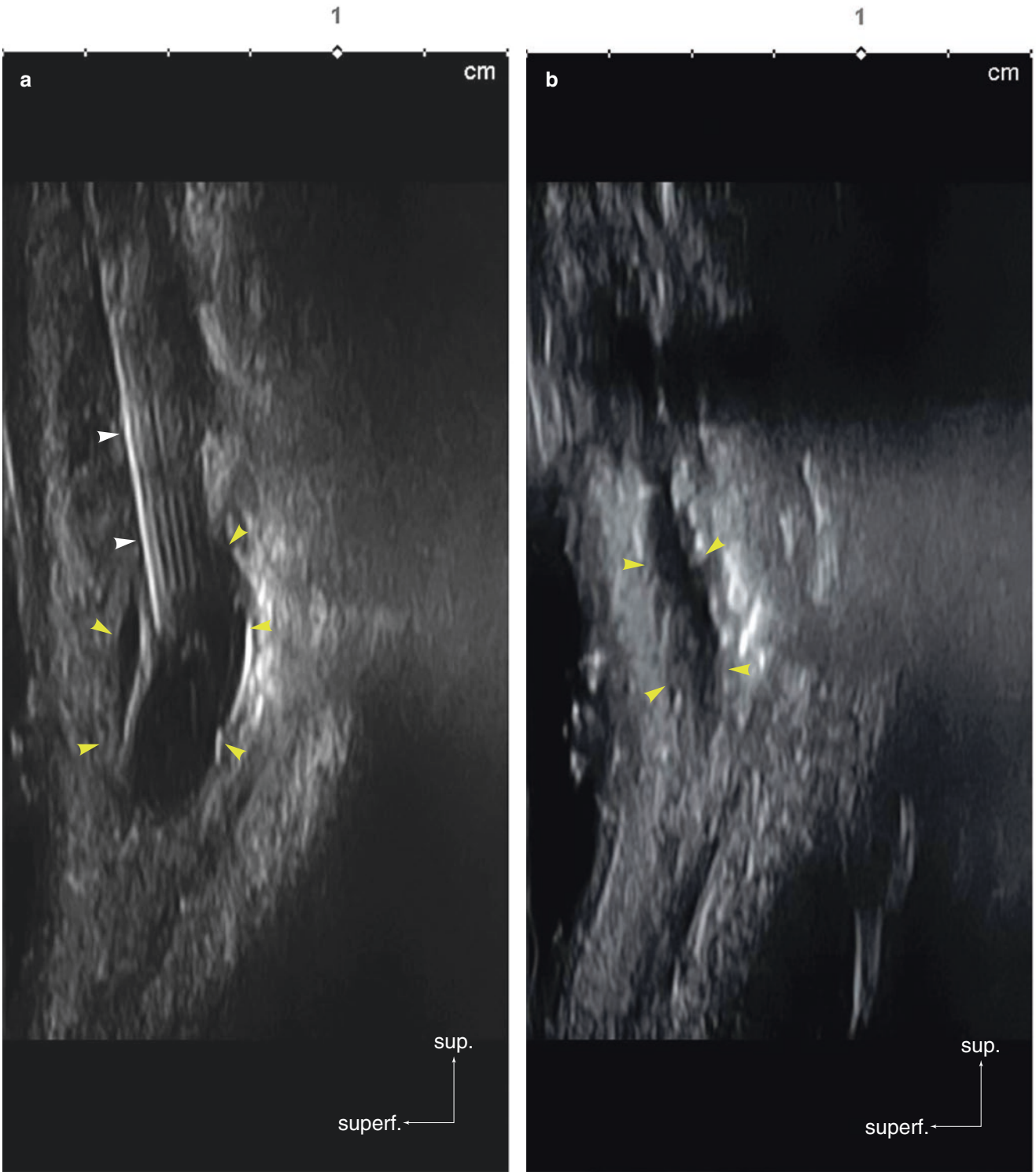

Fig. 9.15 Ultrasonography-guided filler removal on the dorsum of nose. (**a**) During injection, B mode (longitudinal view, 15 MHz by linear transducer) and (**b**) after injection, B mode (longitudinal view, 15 MHz by linear transducer) (yellow arrowheads: HA filler, white arrowheads: injection needle). (Published with kind permission of © Ji-Soo Kim 2020. All Rights Reserved)

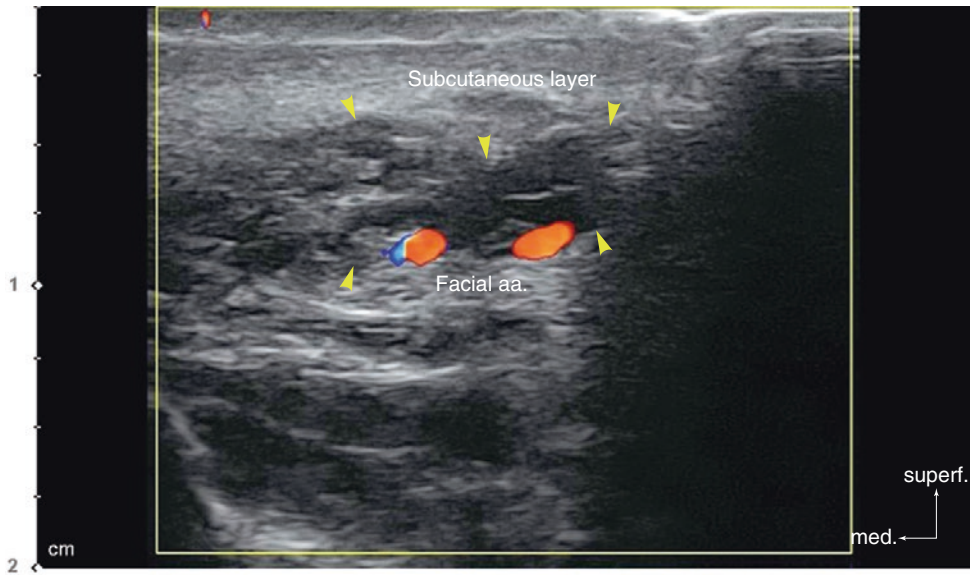

Fig. 9.16 Ultrasonography of the filler migration underneath the nasolabial fold, Doppler mode (longitudinal view, 15 MHz by linear transducer) (yellow arrowheads: HA filler). (Published with kind permission of © Ji-Soo Kim 2020. All Rights Reserved)

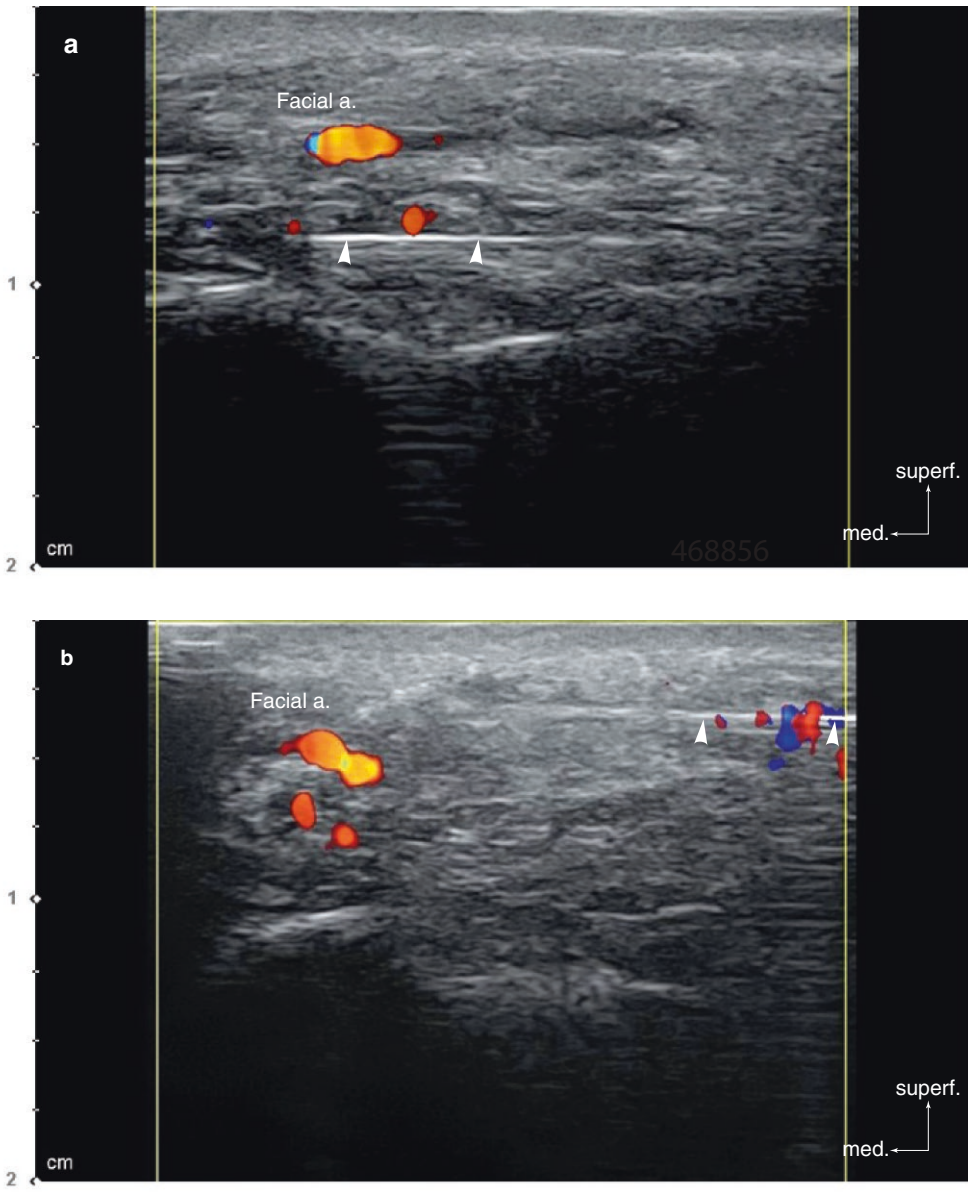

Fig. 9.17 Ultrasonography-guided filler injection for the nasolabial fold augmentation. (**a**) Deep injection, Doppler mode (transverse view, 15 MHz by linear transducer) and (**b**) superficial injection, Doppler mode (transverse view, 15 MHz by linear transducer) (white arrowheads: injection needle). (Published with kind permission of © Ji-Soo Kim 2020. All Rights Reserved)

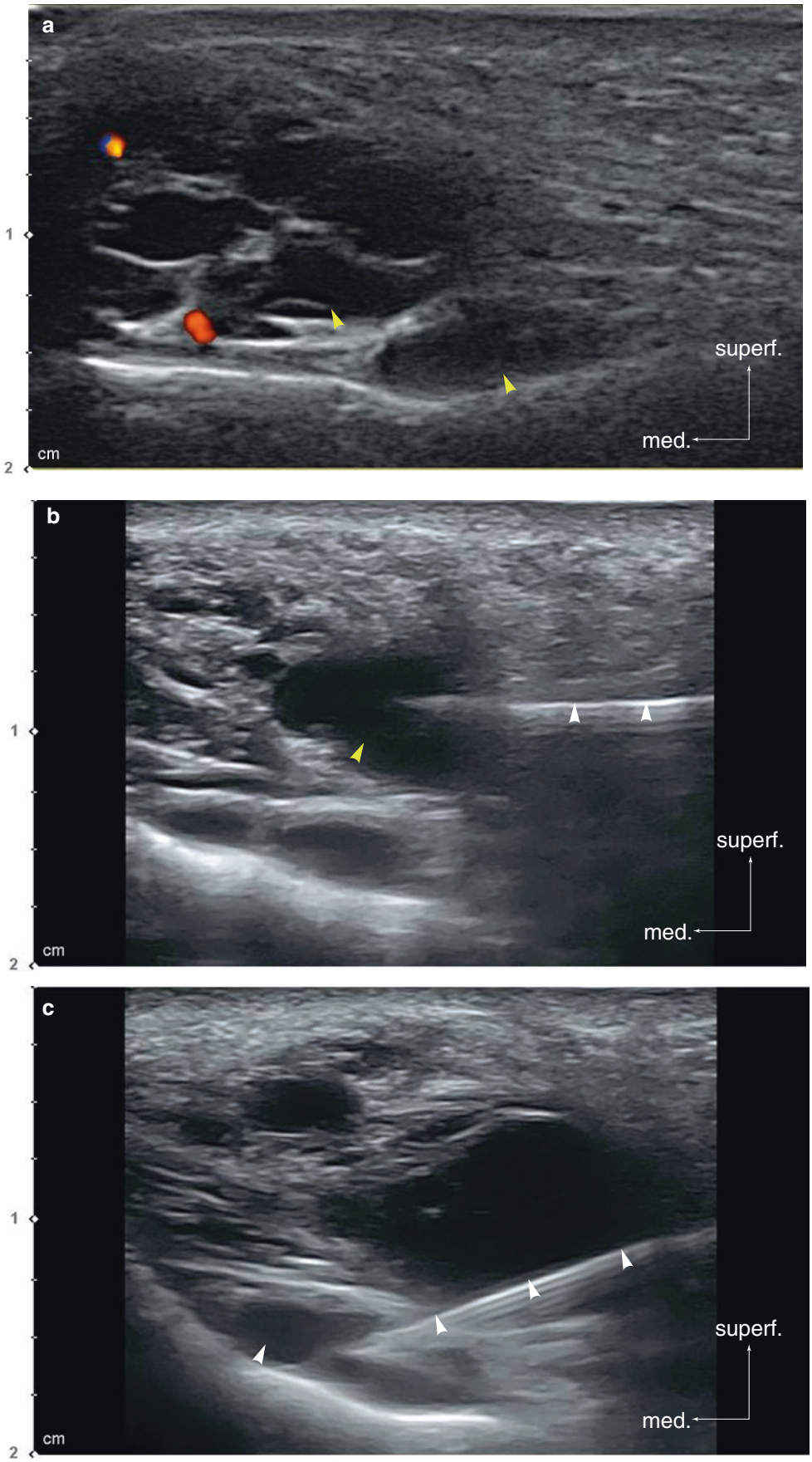

Fig. 9.18 Ultrasonography-guided HA filler removal underneath the nasolabial fold. (**a**) Compartmented filler, Doppler mode (transverse view, 15 MHz by linear transducer), (**b**) superficial part, B mode (transverse view, 15 MHz by linear transducer), and (**c**) deep part, B mode (transverse view, 15 MHz by linear transducer) (yellow arrowheads: HA filler, white arrowheads: injection needle). (Published with kind permission of © Ji-Soo Kim 2020. All Rights Reserved)

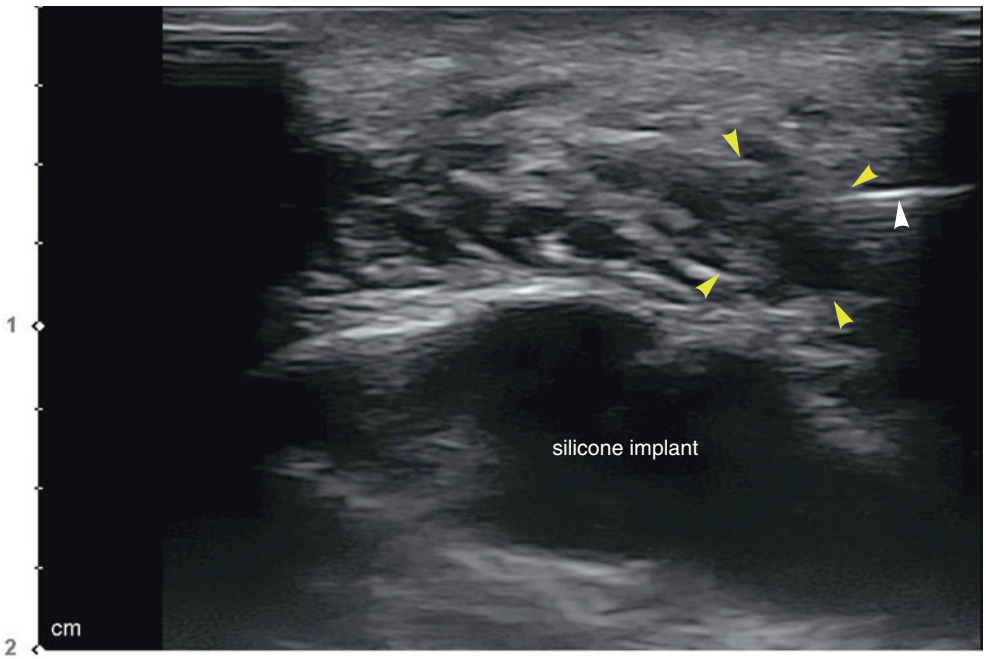

Fig. 9.19 Ultrasonography-guided HA filler removal above the silicone implant underneath the nasolabial fold, B mode (transverse view, 15 MHz by linear transducer) (yellow arrowheads: HA filler, white arrowhead: injection needle). (Published with kind permission of © Ji-Soo Kim 2020. All Rights Reserved)

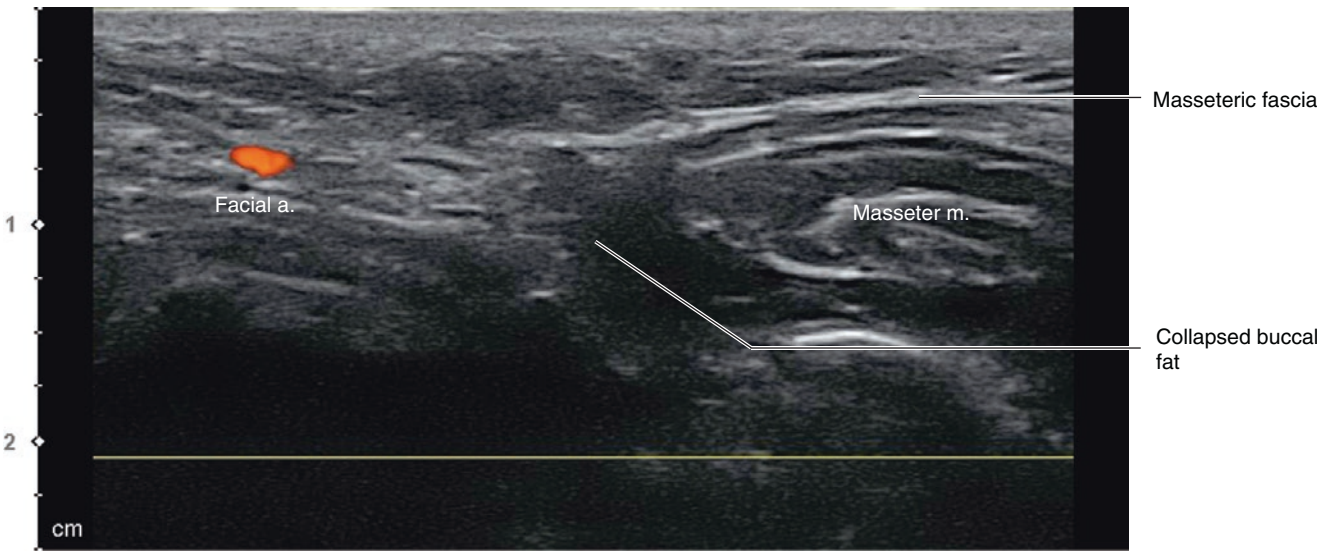

Fig. 9.20 Ultrasonography of the buccal fat collapse in a patient with sunken cheek, Doppler mode (transverse view, 15 MHz by linear transducer). (Published with kind permission of © Ji-Soo Kim 2020. All Rights Reserved)

9.2.7 Anterior Sunken Cheek and Subzygomatic Depression

The anterior sunken cheek is generally owing to atrophy after buccal fat collapse anterior to the masseter m. (Fig. 9.20).

Sunken cheek rejuvenation is done by an injection into the superficial fat of the subcutaneous layer above the SMAS or in the buccal fat pad layer below the SMAS. The SMAS layer is distinct under US imaging, and because high volume injection in the subcutaneous layer will accompany irregularities and inferior migration, buccal fat injection below the SMAS is favored. However, injection into the buccal fat pad may necessitate larger volumes of filler to achieve similar results (Fig. 9.21).

Subzygomatic depression is resolved by injecting filler into the superficial subcutaneous layer above the SMAS or in the parotid temporal fascia below the SMAS. Crucial anatomical structures lie deeply inferior to this fascia, and there are minimal chances of damage when injected above this fascia (Fig. 9.22).

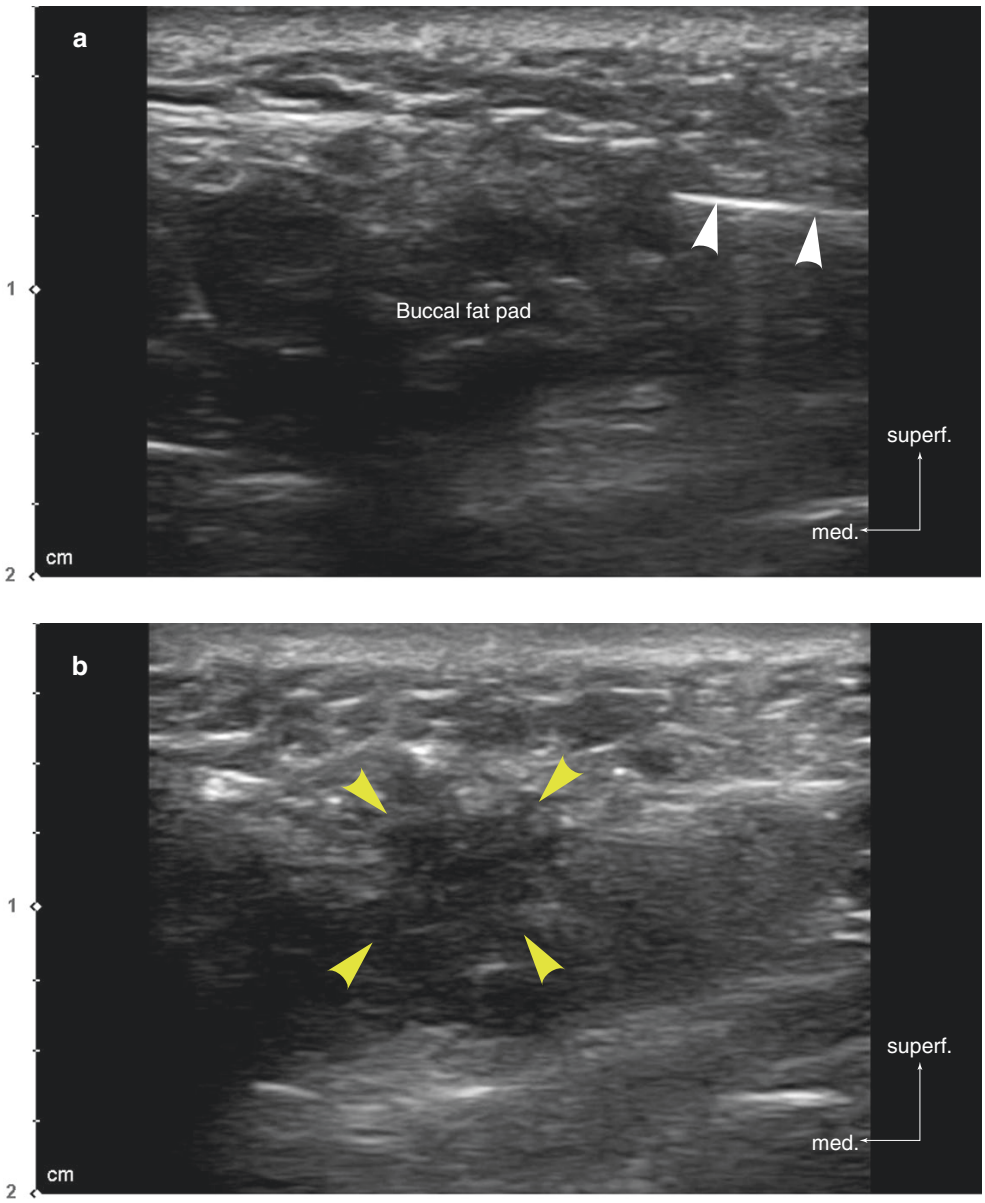

Fig. 9.21 Ultrasonography-guided filler injection into the buccal fat pad. (**a**) During injection, B mode (transverse view, 15 MHz by linear transducer) and (**b**) after injection, B mode (transverse view, 15 MHz by linear transducer) (yellow arrowheads: HA filler, white arrowheads: injection needle). (Published with kind permission of © Ji-Soo Kim 2020. All Rights Reserved)

9.2.8 Marionette Line, Prejowl Sulcus, and Perioral Area

Lower facial rejuvenation procedures demand soft filler injection into the subdermal or subcutaneous layers to alleviate wrinkles. Excess volume augmentation in the jowls may cause unfavorable aesthetic results, such as noticeable jowl. This US image shows the HA filler stable in the subcutaneous layer of the marionette line medial to the depressor anguli oris m. (Fig. 9.23). During marionette line correction, caution should be paid not to inject into the mental and inferior labial aa., which are branches of the facial a. (Fig. 9.23). A cannula injection should target the subdermal layer and focus on early detection of such vessels to avoid complications before injection.

9.2.9 Chin

When augmenting the chin, the ideal injection plane is the supraperiosteal layer of the mentum. The US transverse view of the chin reveals symmetric mentalis m. and muscle fibers attached to the dermis. Injected fillers are generally located above the periosteum (Fig. 9.24).

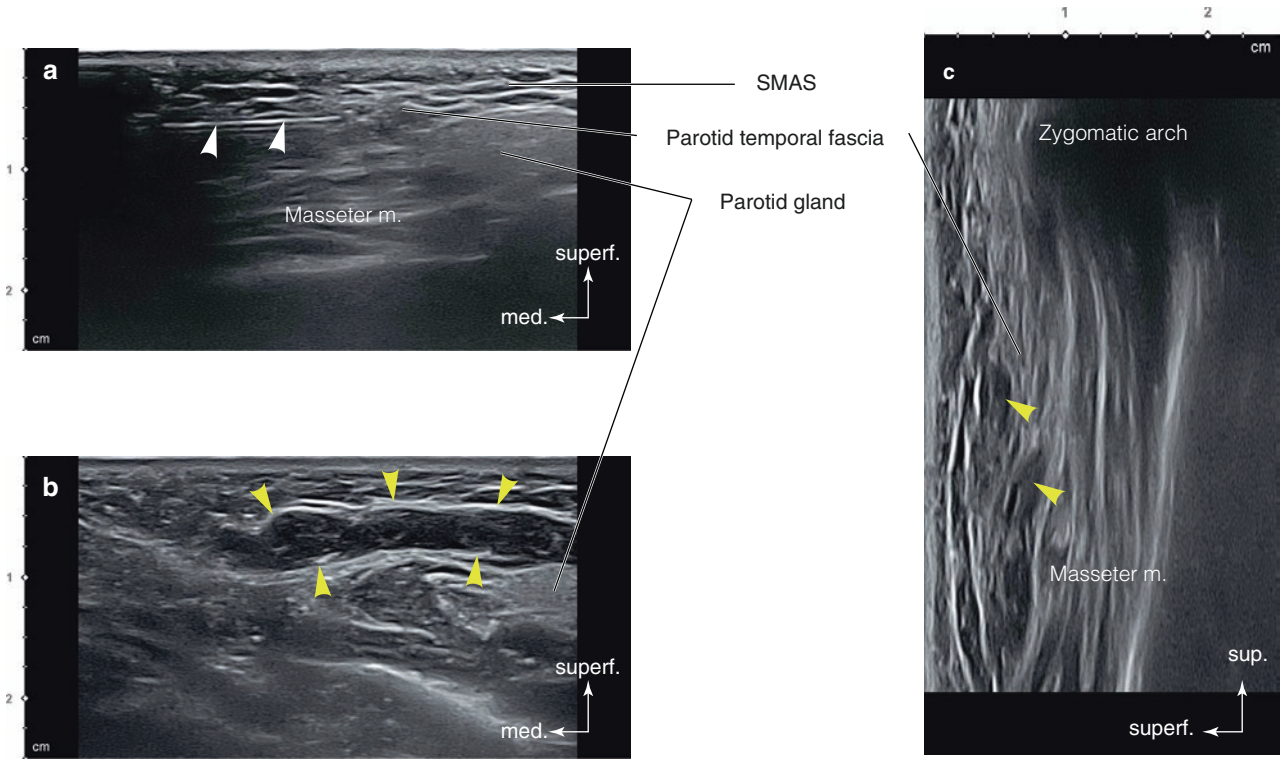

Fig. 9.22 Ultrasonography-guided filler injection for the improvement of the subzygomatic depression. (**a**) During injection, B mode (transverse view, 15 MHz by linear transducer), (**b**) filler below the SMAS, B mode (transverse view, 15 MHz by linear transducer), and (**c**) filler in the subcutaneous layer, B mode (longitudinal view, 15 MHz by linear transducer) (yellow arrowheads: HA filler, white arrowheads: injection needle). (Published with kind permission of © Ji-Soo Kim 2020. All Rights Reserved)

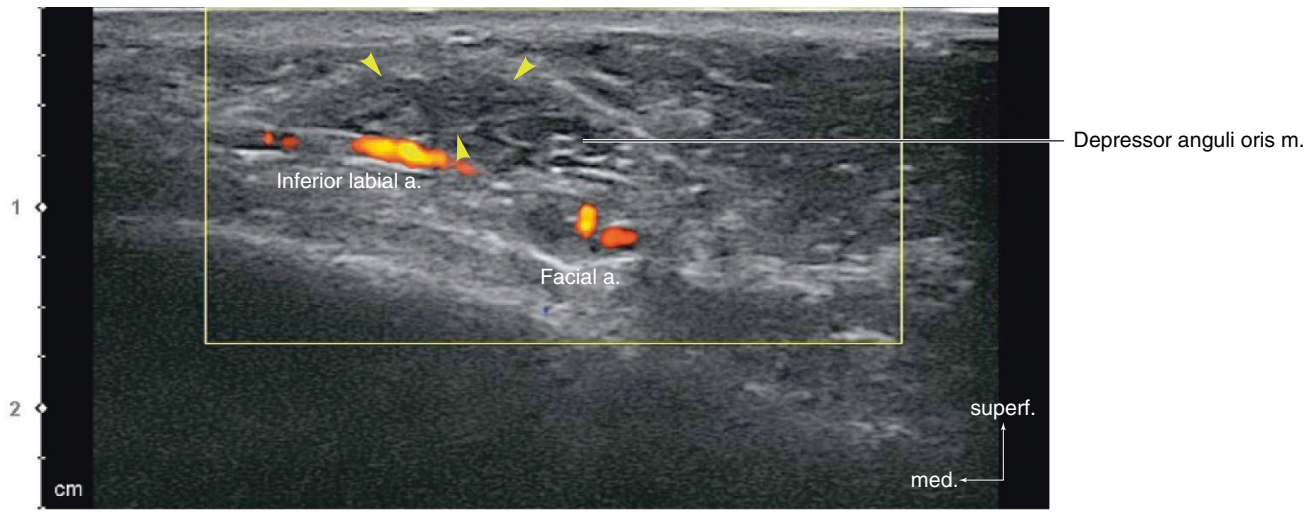

Fig. 9.23 Ultrasonography of HA filler for the marionette line improvement, Doppler mode (transverse view, 15 MHz by linear transducer) (yellow arrowheads: HA filler). (Published with kind permission of © Ji-Soo Kim 2020. All Rights Reserved)

In some cases, chin implants are usually located above the periosteum, and sometimes, granulomas may also be observed (Fig. 9.25).

This US image shows the filler as a hypoechoic solid mass immediately after chin injection, but soon it turns into a heterogeneous mass overtime. This phenomenon occurs because the mentalis m. moves more actively in this area, compared to areas such as the nose, and migration is common. A layer-by-layer technique using hyaluronidase is effective in removing injected filler materials (Fig. 9.26).

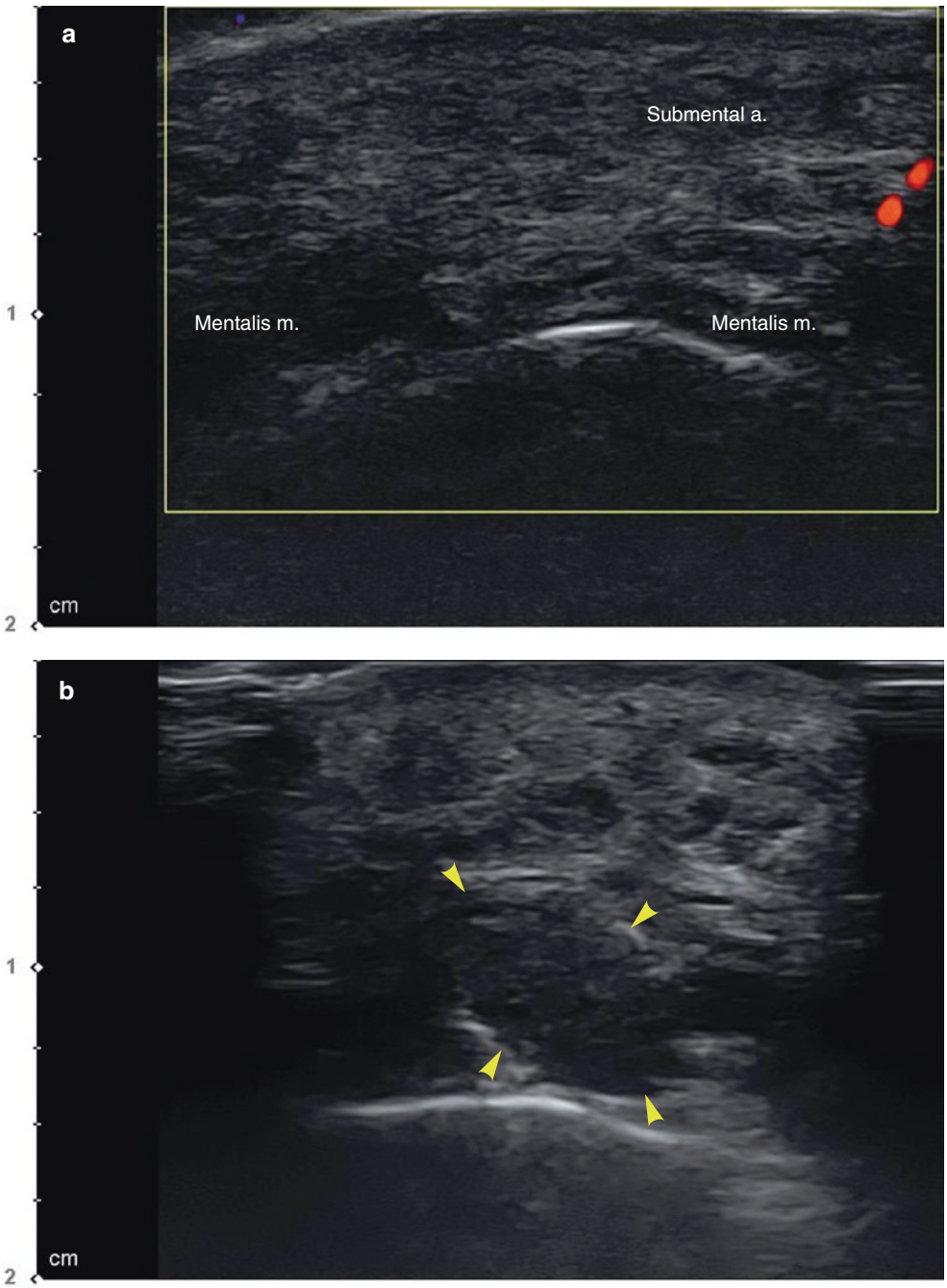

Fig. 9.24 Ultrasonography of the HA filler for the chin augmentation. (**a**) Before injection, Doppler mode (transverse view, 15 MHz by linear transducer) and (**b**) after injection, B mode (transverse view, 15 MHz by linear transducer) (yellow arrowheads: HA filler). (Published with kind permission of © Ji-Soo Kim 2020. All Rights Reserved)

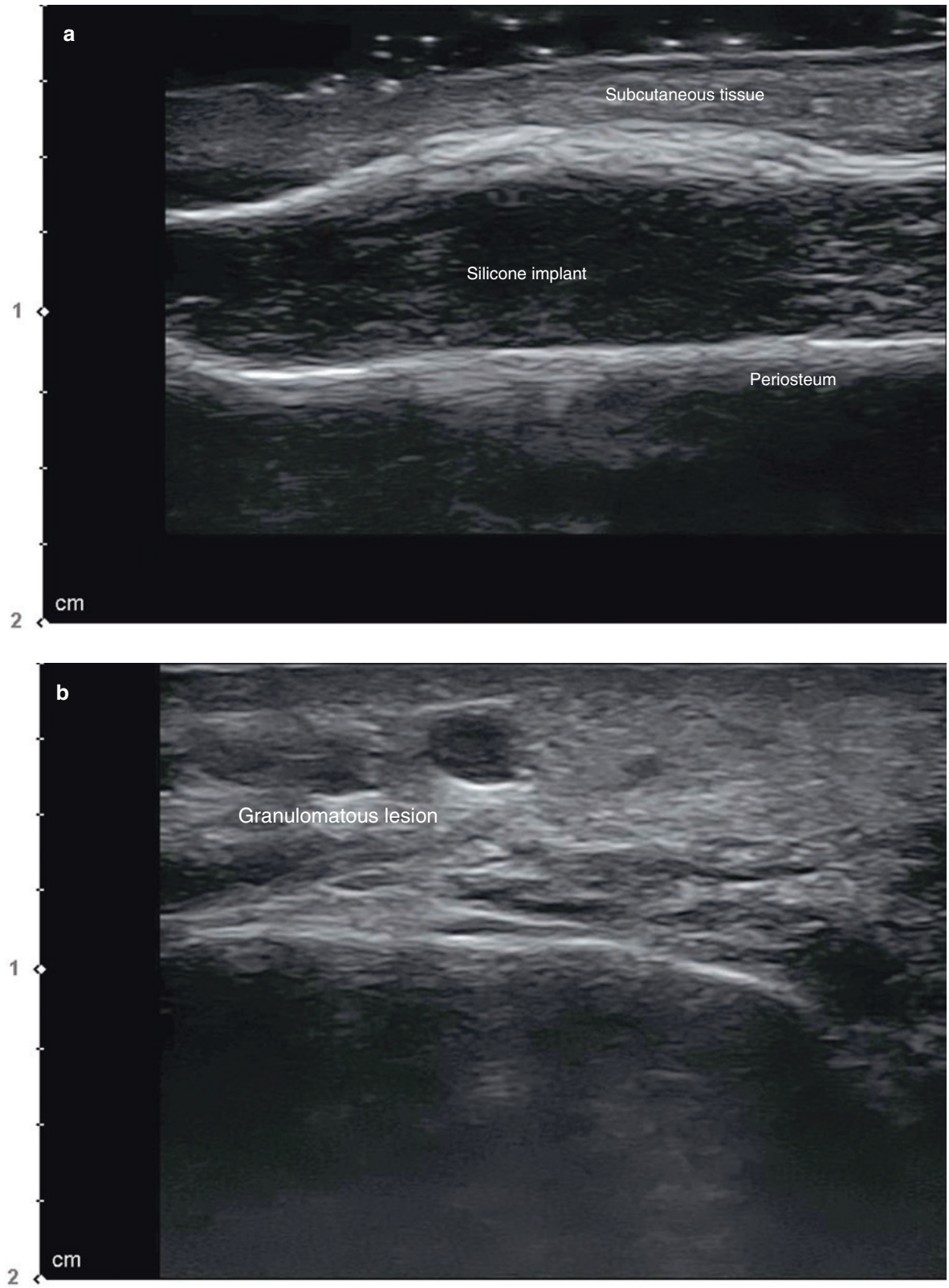

Fig. 9.25 Ultrasonography of the silicone implant on the chin. (**a**) B mode (transverse view, 15 MHz by linear transducer) and (**b**) foreign body granuloma, B mode (transverse view, 15 MHz by linear transducer). (Published with kind permission of © Ji-Soo Kim 2020. All Rights Reserved)

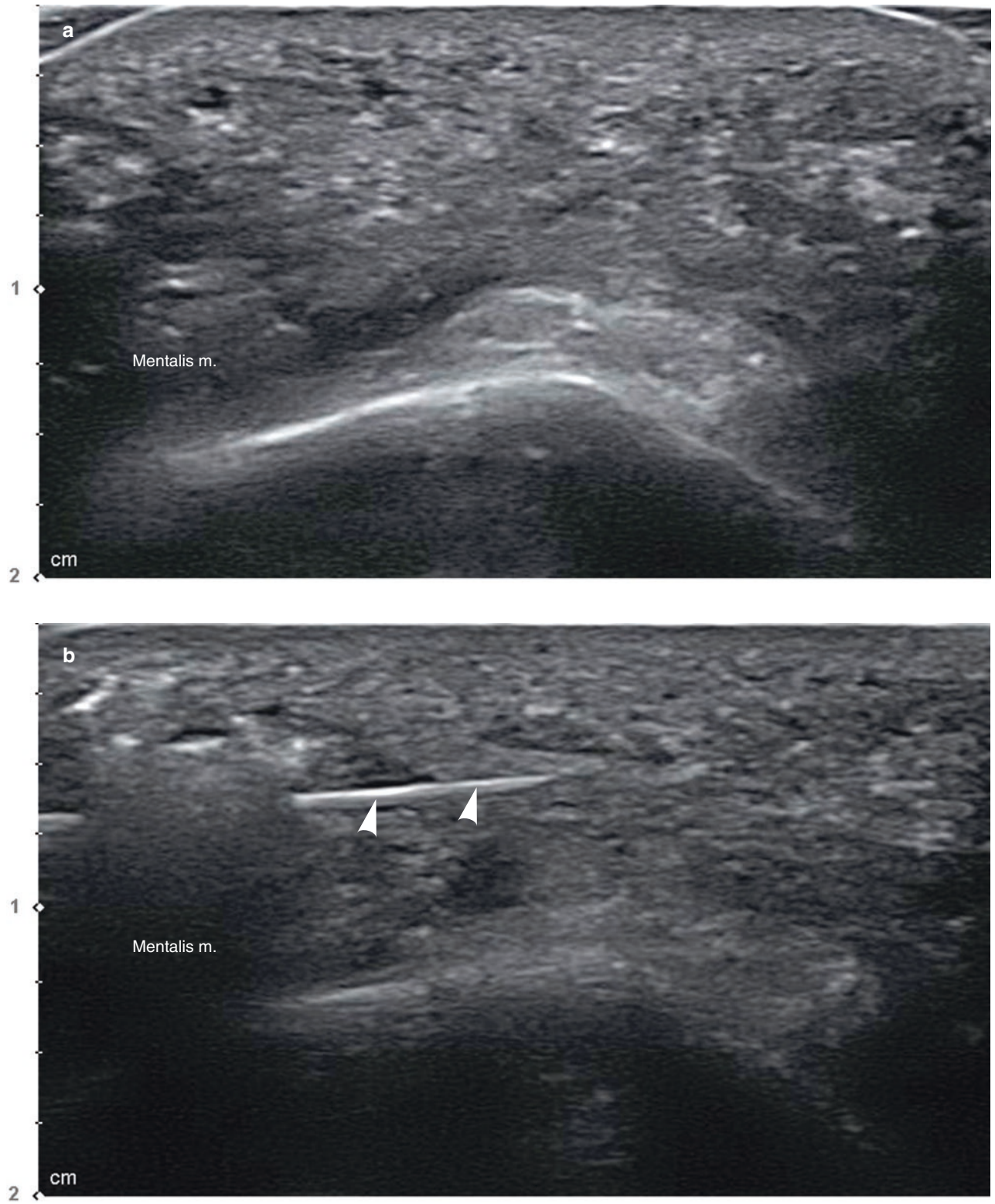

Fig. 9.26 Ultrasonography-guided HA filler removal on the chin. (**a**) Before injection, B mode (transverse view, 15 MHz by linear transducer) and (**b**) during injection, B mode (transverse view, 15 MHz by linear transducer) (while arrowheads: HA filler). (Published with kind permission of © Ji-Soo Kim 2020. All Rights Reserved)

Bibliography

1. Gerber PA, Barsch M, Filler T, Gerber AM. Identification of fascial vessels using Doppler ultrasound prior to cosmetic filler injection. J Dtsch Dermatol Ges. 2019;17(12):1281–2.
2. Hans J. Ultrasonography of the head and neck: ana imaging atlas. Cham: Springer International Publishing; 2019.
3. Koh IS, Lee W. Filler complication, filler induced hypersensitivity reactions, granuloma, necrosis and blindness. Singapore: Springer; 2019.
4. Kohn JC, Goh AS, Lin JL, Goldberg RA. Dynamic high-resolution ultrasound in vivo imaging of hyaluronic acid filler injection. Dermatol Surg. 2013;39(11):1630–6.
5. Kwon HJ, Kim BJ, Ko EJ, Choi SY. The utility of color Doppler ultrasound to explore vascular complications after filler injection. Dermatol Surg. 2017;43(12):1508–10.
6. Lee W, Kim JS, Oh W, Koh IS, Yang EJ. Nasal dorsum augmentation using soft tissue filler injection. J Cosmet Dermatol. 2019:1–7. https://doi.org/10.1111/jocd.13018.
7. Lee W, Koh IS, Oh W, Yang EJ. Ocular complications of soft tissue filler injections: a review of literature. J Cosmet Dermatol. 2019;00:1–10. https://doi.org/10.1111/jocd.13213.
8. Lee W, Oh W, Hong GW, Kim JS, Yang EJ. Novel technique of filler injection in the temple area using the vein detection device. JPRAS. 2018;6:12.
9. Lima VGF, Regattieri NAT, Pompeu MR, Costa IMC. External vascular compression by hyaluronic acid filler documented with high-frequency ultrasound. J Cosmet Dermatol. 2019;1(6):1629–31.
10. Mlosek RK, Skrzypek E, Skrzypek DM, Malinowska S. High frequency ultrasound based differentiation between nodular dermal filler deposits and foreign body granulomas. Skin Res Technol. 2018;24(3):417–22.
11. Skrzypek E, Gornicka B, Skrzypek DM, Krzysztof MR. Granuloma as complication of polycaprolactone-based dermal filler injection: ultrasound and histopathology studies. J Cosmet Laser Ther. 2019;21(2):65–8.
12. Tansatit T, Apinuntrum P, Phetudom T. Facing the worst risk: confronting the dorsal nasal artery, implication for non-surgical procedures of nasal augmentation. Aesthet Plast Surg. 2017;41:191. https://doi.org/10.1007/s00266-016-0756-0.
13. Tansatit T, Phumyoo T, Jitaree B, Sawatwong W, Rungsawang C, Jiirasutat N, et al. Ultrasound evaluation of arterial anastomosis of the forehead. J Cosmet Dermatol. 2018;17:1031–6.
14. Tansatit T, Phumyoo T, Jitaree B, Sahraoui YME, Lee JH. Anatomical and ultrasound based injections for sunken upper eyelid correction. J Cosmet Dermatol. 2019:1–7. https://doi.org/10.1111/jocd.13049.
15. Choi YJ, Lee KW, Gil YC, Hu KS, Kim HJ. Ultrasonographic analyses of the forehead region for injectable treatments. Ultrasound Med Biol. 2019;45(10):2641–8.
16. Cong LY, Lee SH, Tansatit T, Hu KS, Kim HJ. Topographic anatomy of the inferior medial palpebral artery and Its relevance to the pretarsal roll augmentation. Plast Reconstr Surg. 2016;138(3):430e–6e.
17. Kim H-S, Lee K-L, Gil Y-C, Hu K-S, Tansatit T, Kim H-J. Topographic anatomy of the infraorbital artery and its clinical implications for nasolabial fold augmentation. Plast Reconstr Surg. 2018;142(3):273e–80e.
18. Jung W, Youn KH, Won SY, Park JT, Hu KS, Kim HJ. Clinical implications of the middle temporal vein with regard to temporal fossa augmentation. Dermatol Surg. 2014;40(6):618–23.
19. Kim HJ, Seo KK, Lee HK, Kim JS. Clinical anatomy of the face for filler and botulinum toxin injection. New York, NY: Springer; 2016.
20. Kwak HH, Ko SJ, Jung HS, Park HD, Chung IH, Kim HJ. Topographic anatomy of the deep temporal nerves, with references to the superior head of lateral pterygoid. Surg Radiol Anat. 2003;25(5-6):393–6.
21. Lee HJ, Kang IW, Won SY, Lee JG, Hu KS, Tansatit T, Kim HJ. Description of a novel anatomic venous structure in the nasoglabellar area. J Craniofac Surg. 2014;25(2):633–5.
22. Lee HJ, Won SY, O J, Hu KS, Mun SY, Yang HM, Kim HJ. The facial artery: a comprehensive anatomical review. Clin Anat. 2018;31:99–108.
23. Lee JG, Yang HM, Choi YJ, Favero V, Kim YS, Hu KS, Kim HJ. Facial arterial depth and relationship with the facial musculature layer. Plast Reconstr Surg. 2015;135:437–44.
24. Lee JG, Yang HM, Hu KS, Lee YI, Lee HJ, Choi YJ, Kim HJ. Frontal branch of the superficial temporal artery: anatomical study and clinical implications regarding injectable treatments. Surg Radiol Anat. 2015;37(1):61–8.
25. Lee JH, Lee K, Jung W, Youn KH, Hu KS, Tansatit T, Park HJ, Kim HJ. A novel anatomical consideration on the exposed segment of the facial artery. Clin Anat. 2020;33:257.
26. Schelke LW, Decates TS, Velthuis PJ. Ultrasound to improve the safety of hyaluronic acid filler treatments. J Cosmet Dermatol. 2018;17(6):1019–24.
27. Smith CF. Gray's surface anatomy and ultrasound. Amsterdam: Elsevier; 2018.
28. Yang HM, Jung W, Won SY, Youn KH, Hu KS, Kim HJ. Anatomical study of medial zygomaticotemporal vein and its clinical implication regarding the injectable treatments. Surg Radiol Anat. 2015;37(2):175–80.
29. Yang HM, Lee JG, Hu KS, Gil YC, Choi YJ, Lee HK, Kim HJ. New anatomical insights on the course and branching patterns of the facial artery: clinical implications of injectable treatments to the nasolabial fold and nasojugal groove. Plast Reconstr Surg. 2014;133:1077–82.

US Applications in Thread Lifting Procedures

10

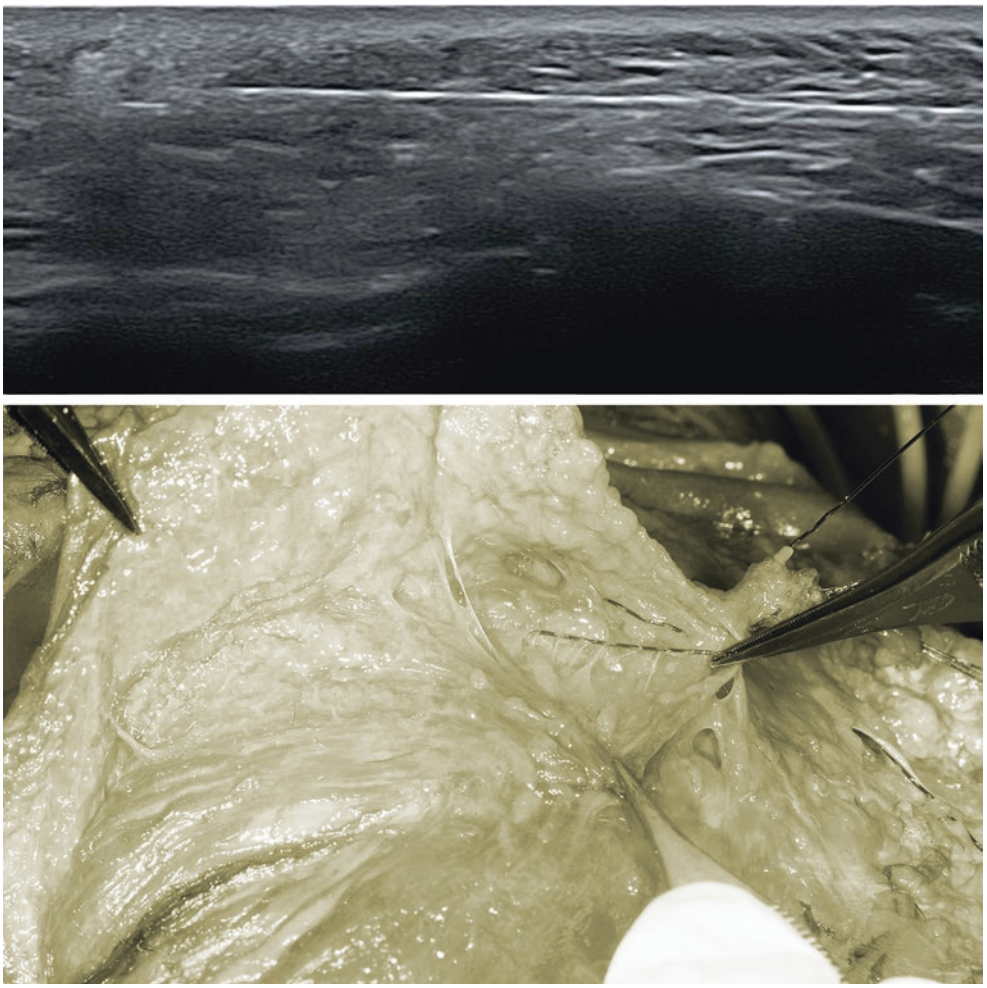

H.-J. Kim et al., *Ultrasonographic Anatomy of the Face and Neck for Minimally Invasive Procedures*,
https://doi.org/10.1007/978-981-15-6560-1_10

10.1 Backgrounds of the US-Guided Thread Lifting Procedures

Thread lifting is now widely used to improve the facial sagging and the relocation of facial fat. Recently, one of the most noticeable minimally invasive aesthetic procedures is the use of dissolving threads. As the thread manufacturing techniques develop, various thicknesses and several types of threads such as a barbed or cog thread are available for clinical uses in addition to the initial thin 6-0 monotype thread.

Currently, there are various types of dissolving threads. The most used thread is the biodegradable ingredient PDO (polydioxanone) type, which is inserted into a blunt L-type cannula about 6–10 cm long. A generalized threading technique is to have the cannula inserted into the skin and then remove it, leaving the thread in the facial tissue.

The types of threads include cutting cogs, more rigid molding cogs, monofilaments, and scaffold types braided with monofilaments (Fig. 10.1). Due to the emergence of these various types of threads, they are used extensively, either alone or in combination with botulinum toxin and filler, for face rejuvenation purposes such as skin tightening and wrinkle improvement as well as lifting.

In-office-based minimally invasive procedures differ somewhat from the surgical facelift procedures. However, these techniques are similar in that they target the SMAS layer for facelift. The problem is how to lift the sagged SMAS. In surgical cases, it is possible to check, pull, and cut the SMAS layer, contrary to the nonsurgical blind procedure. Therefore, the use of the US image can be considered to identify the correct layers during various thread lifting procedures.

During the minimally invasive thread liftings, two things should be considered. First, which layer would be appropriate for efficient results? And second is what structures should be identified for safety. The thread may cause traction injury of blood vessels and nerves, when the cannula is inserted or removed, or when the thread is excessively pulled. US-guided thread lifting procedures have advantages in that it is possible to identify the safe layer and the anatomical structures. US images demonstrate that the threads are located in various layers during blind thread insertion (Fig. 10.2). The anatomical structures such as the subcutaneous layer can be easily distinguished by US.

10.2 US-Guided Thread Lifting Procedures

An anchoring effect can be obtained by placing one end of the thread in a dense area of the facial tissue, and this is the area of the solid fascia or ligament. Generally, several sites are considered as the effective anchoring points: the deep temporal fascia (DTF), the parotid temporal fascia, and the platysma auricular fascia shown as hyperechoic images (Fig. 10.3).

10.2.1 Vertical Lifting in the Upper Face

Vertical lifting can be used for the lifting of the overall face and jowl. During the procedure, the clinical US image shows

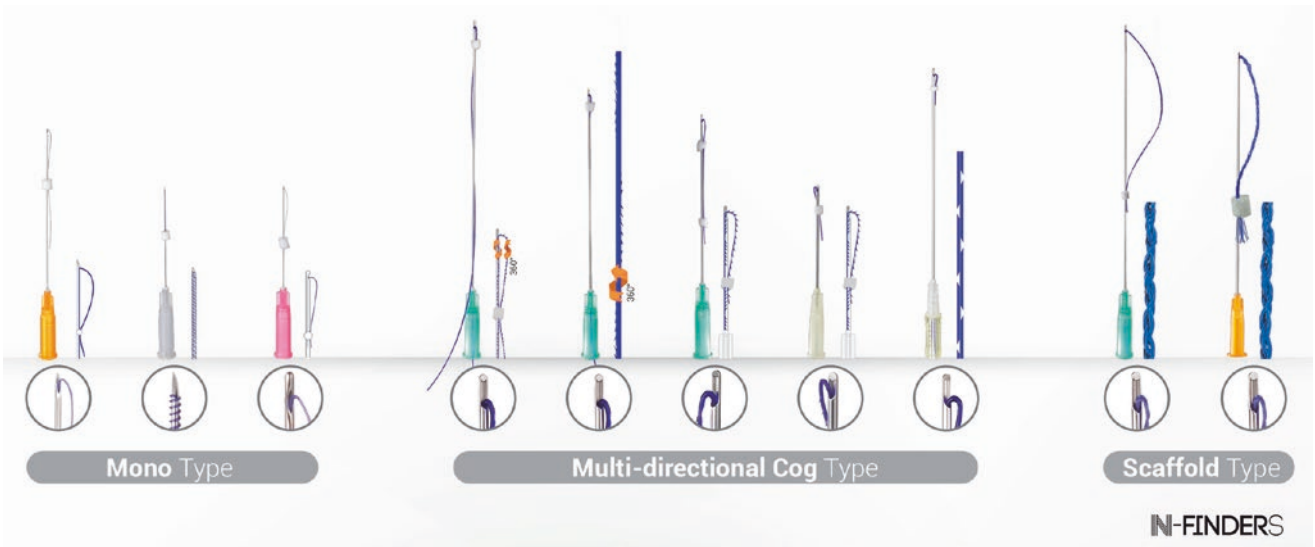

Fig. 10.1 Various types of PDO threads. (Provided by N-finders Co.)

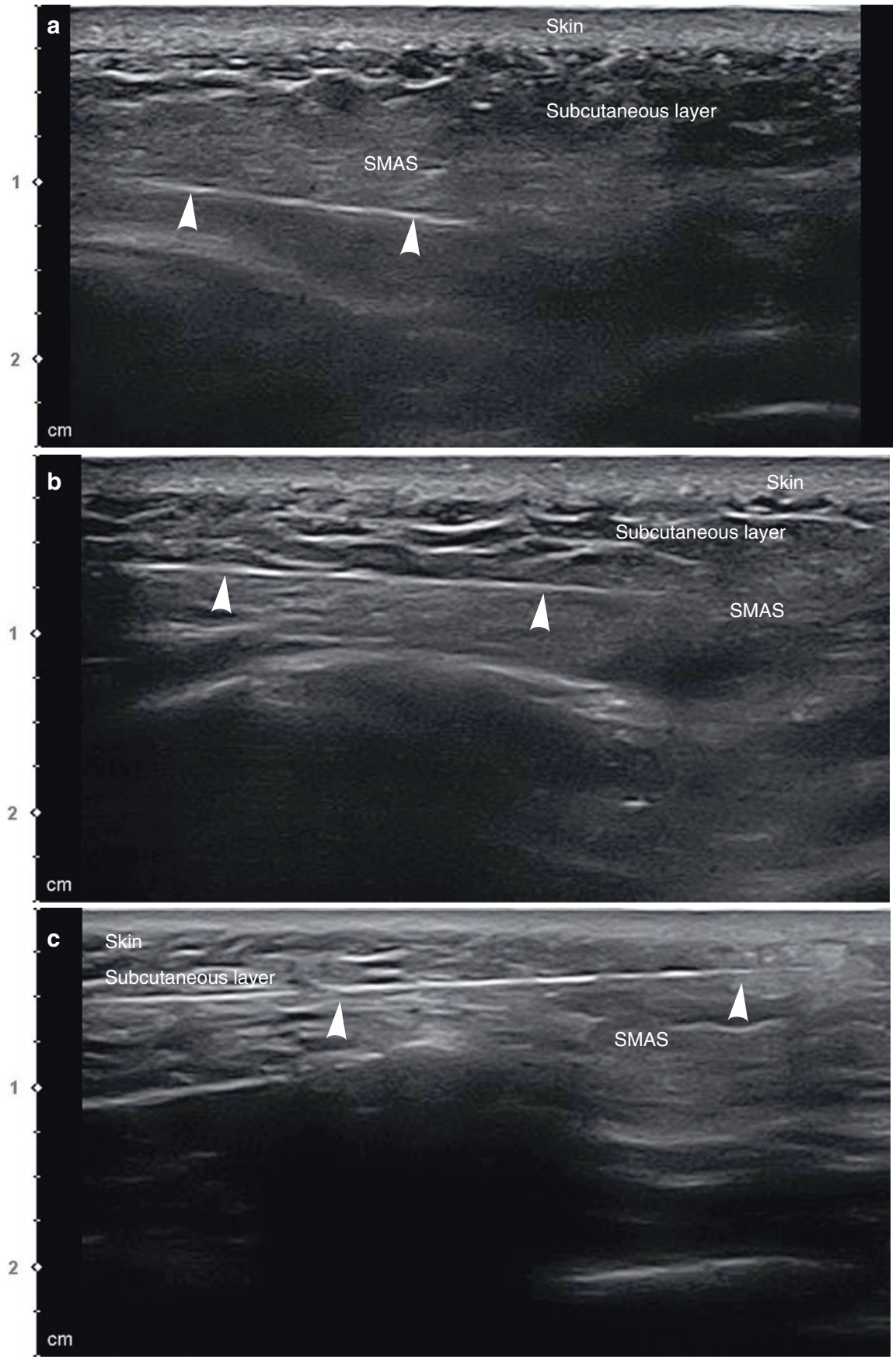

Fig. 10.2 Ultrasonography-guided multidirectional cog and scaffold type thread insertion on the midface, B mode (transverse view, 15 MHz by linear transducer). (**a**) A thread below the SMAS, (**b**) at the level of the SMAS, and (**c**) above the SMAS (arrowheads: thread cannula). (Published with kind permission of © Ji-Soo Kim 2020. All Rights Reserved)

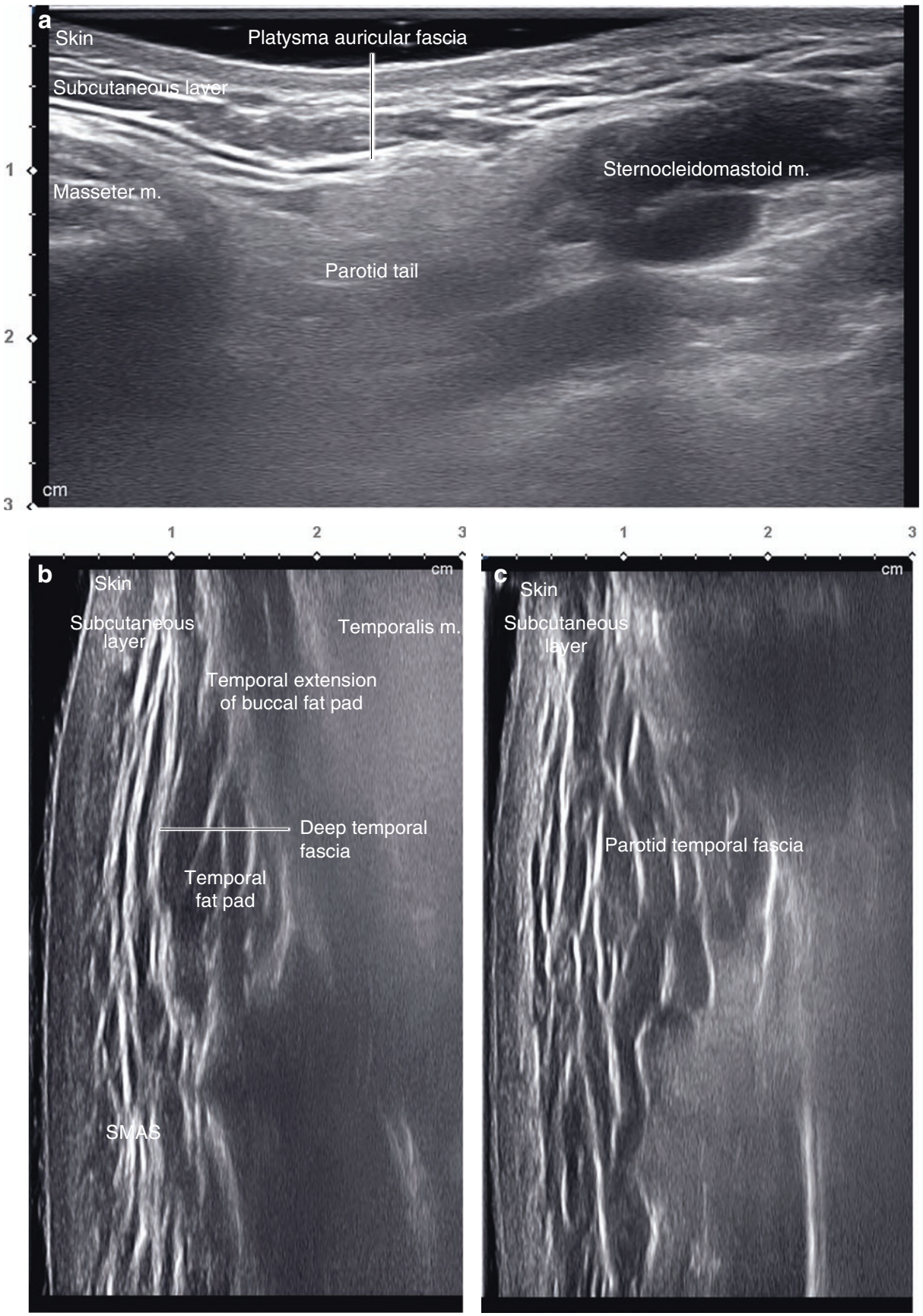

Fig. 10.3 Ultrasonography of anchoring points for lifting thread. (**a**) Platysma auricular fascia, B mode (transverse view, 15 MHz by linear transducer), (**b**) deep temporal fascia, B mode (coronal view, 15 MHz by linear transducer), and (**c**) parotid temporal fascia, B mode (coronal view, 15 MHz by linear transducer). (Published with kind permission of © Hee-Jin Kim 2020. All Rights Reserved)

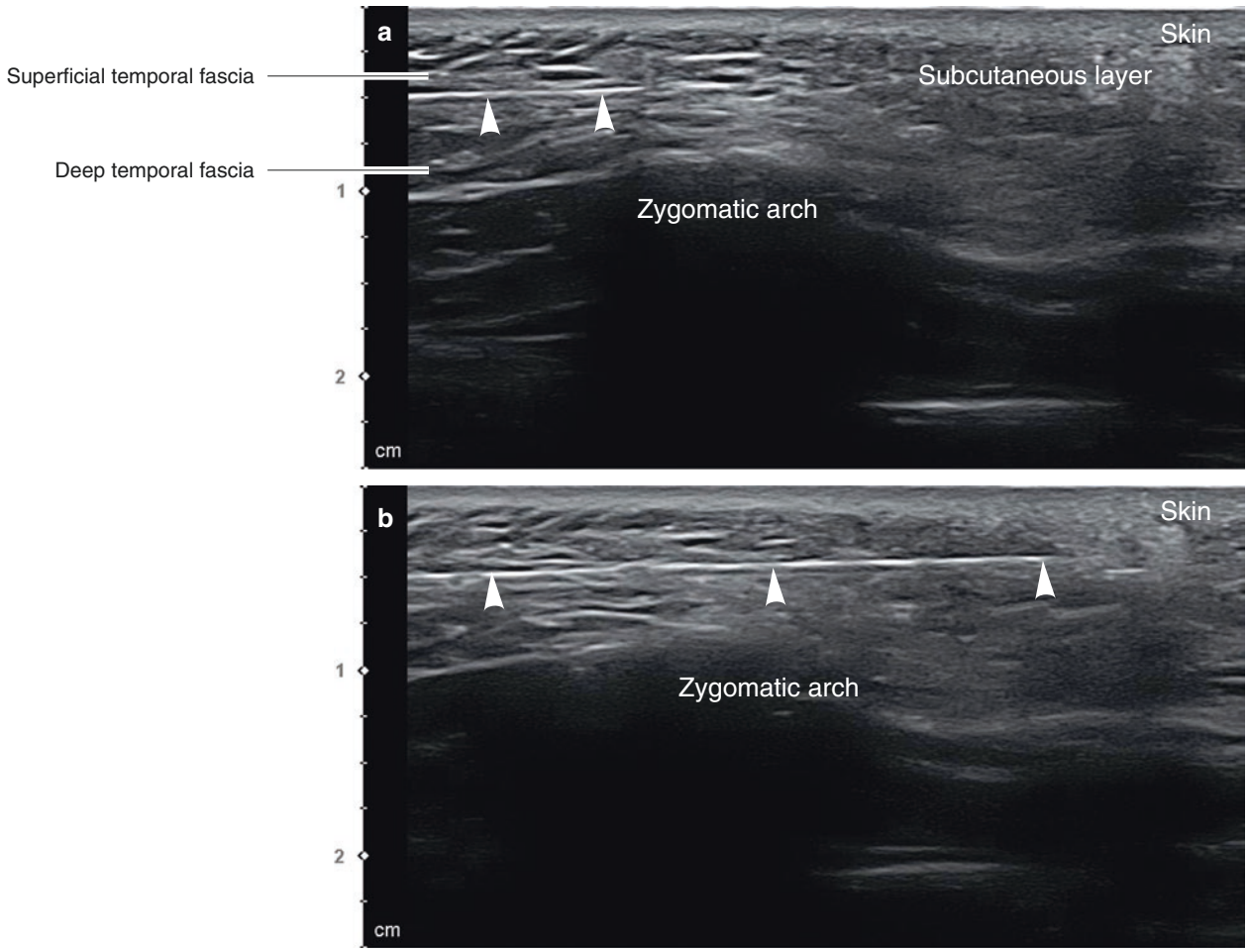

Fig. 10.4 Ultrasonography-guided multidirectional cog thread insertion for vertical lift. (**a**) Thread cannula above the zygomatic arch, B mode (coronal view, 15 MHz by linear transducer) and (**b**) at the cheek below the zygomatic arch, B mode (coronal view, 15 MHz by linear transducer) (arrowheads: thread cannula). (Published with kind permission of © Ji-Soo Kim 2020. All Rights Reserved)

that the cannula of the thread locates between the superficial and DTF. Inserting the thread downward from the temple to the buccal and cheek area is commonly performed (Fig. 10.4).

When the threads proceed beneath the SMAS, it can injure the facial n. branches, the parotid gland, and the duct. Therefore, it is recommended to pass superficial to the SMAS. From the US image of the zygomatic arch region, the cannula is located above the SMAS as it proceeds to the buccal area (Fig. 10.5).

10.2.2 Oblique/Horizontal Lifting in the Midface

For jowl or the lower facial lifting, the oblique or horizontal vector can be used in the midface. Generally, the entry point is created at the subzygomatic area in front of the tragus, and the thread is inserted obliquely to the jowl. In the buccal region, SMAS is thinner and it is apt to pass beneath the SMAS. From the US image, the tip of the thread cannula in the parotid gland area is located in the buccal fat pad space underneath the SMAS (Fig. 10.6a) and within the subcutaneous layer above the SMAS (Fig. 10.6b), respectively. If the subcutaneous fat is thin, dimples may occur, so care should be taken not to insert the thread cannula too superficial or too deep.

Alternately, a midface lifting can be done by inserting threads obliquely into the malar fat pad from the temple. In this procedure, the threads penetrate the zygomatic ligament and the ends of the threads are entrapped within the zygomatic cutaneous ligaments of the malar region (Fig. 10.7).

Also, it is possible to pull up the nasolabial fat compartment during midfacial lifting to improve the nasolabial fold. In the clinical US image, the tip of the cannula is located in the nasolabial fat compartment lateral to the nasolabial fold (Fig. 10.8).

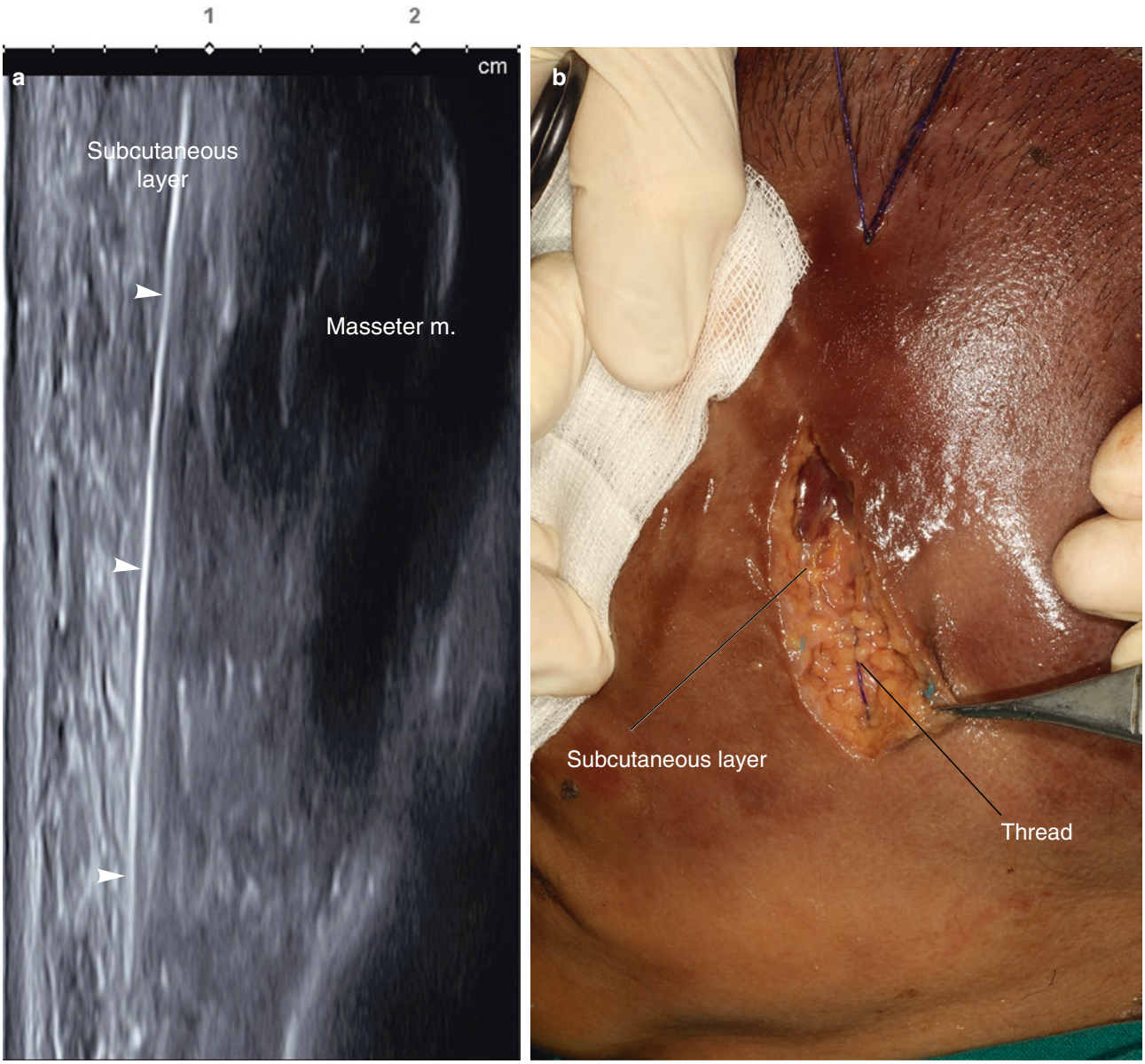

Fig. 10.5 Ultrasonography-guided multidirectional cog thread insertion for vertical lift. (**a**) B mode (coronal view, 15 MHz by linear transducer) (arrowheads: thread cannula) (published with kind permission of © Ji-Soo Kim 2020. All Rights Reserved) and (**b**) dissection photograph representing the location and layer of the inserted threads for the vertical and jowl lifting. The lifting threads are located within the subcutaneous layer above the parotid gland. (Published with kind permission of © Hee-Jin Kim 2020. All Rights Reserved)

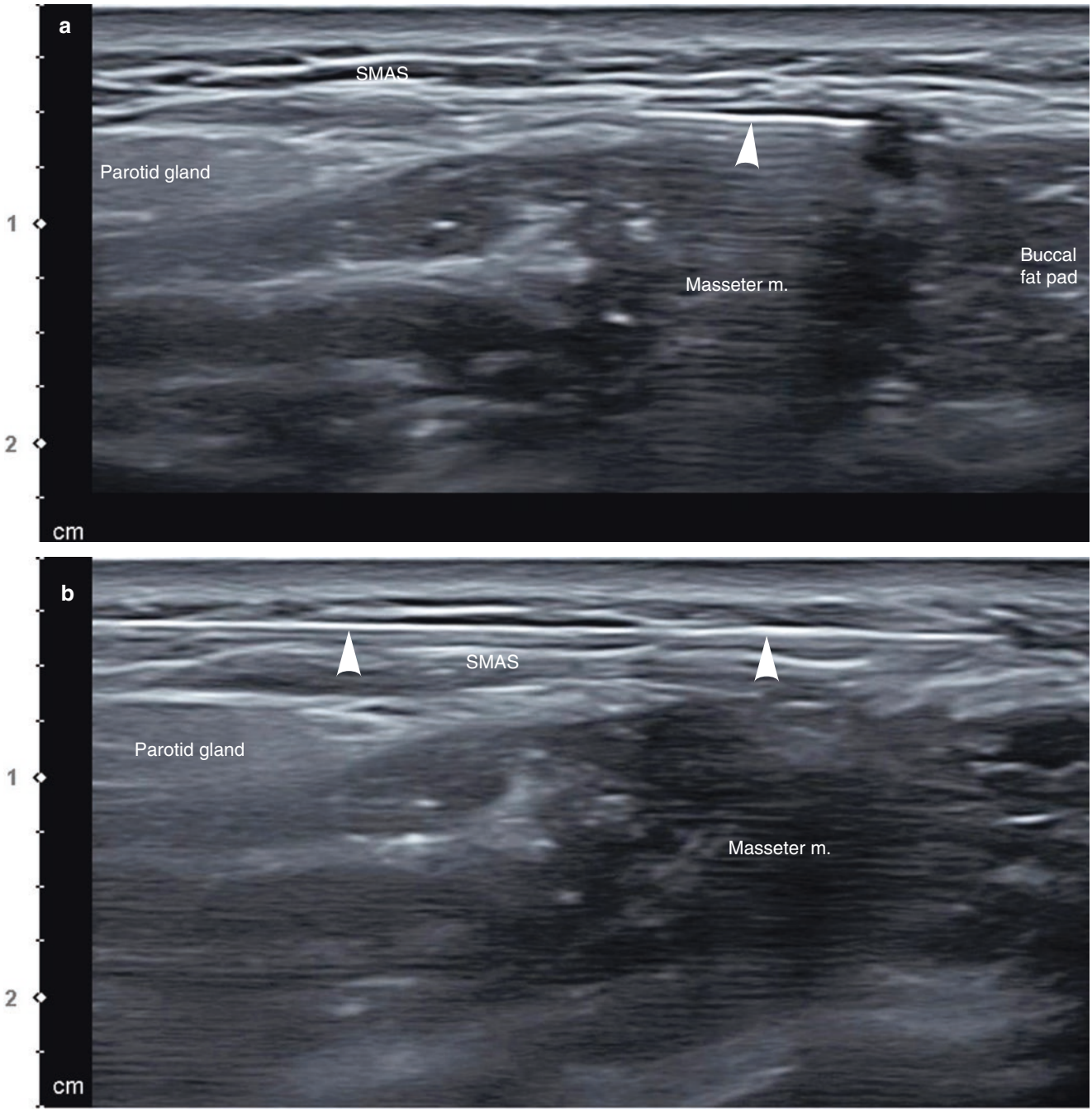

Fig. 10.6 Ultrasonography-guided multidirectional cog thread cannula insertion for oblique lift. (**a**) Below the SMAS, B mode (oblique view, 15 MHz by linear transducer) and (**b**) above the SMAS, B mode (oblique view, 15 MHz by linear transducer) (arrowheads: thread cannula). (Published with kind permission of © Ji-Soo Kim 2020. All Rights Reserved)

10.2.3 Jawline and Double Chin Lifting in the Lower Face

Threading in the lower face is often performed for jawline definement or double chin enhancement. From the clinical US image, a thick submental fat (or preplatysmal fat) is observed at the submental area. Generally, the thread should be inserted into the subcutaneous fat layer (Fig. 10.9). Since the submental region is usually formed as an arc, not a straight line, the thread cannula should be inserted three-dimensionally along the neck contour.

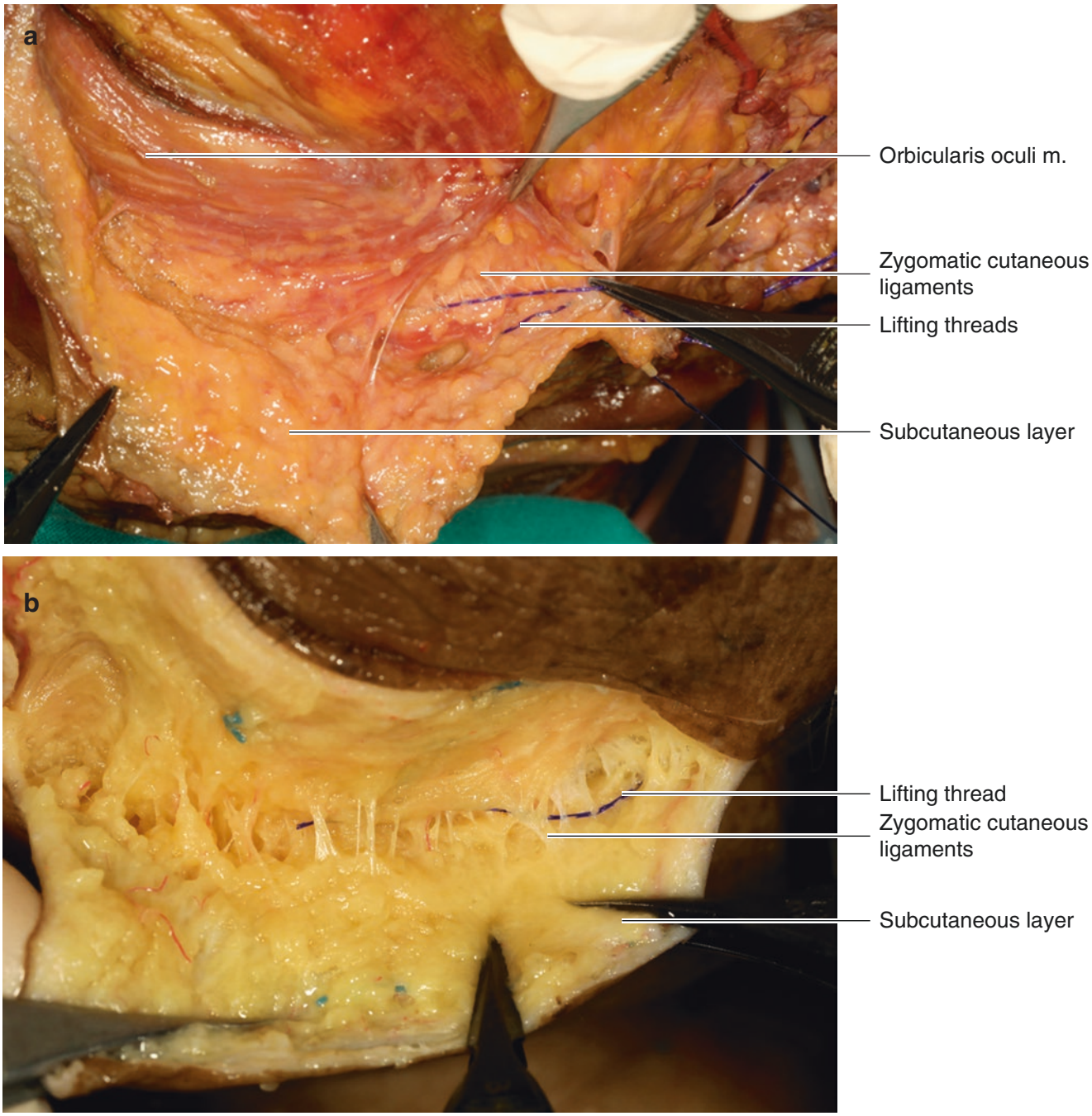

Fig. 10.7 Dissection photographs representing the location and layer of the inserted threads for the midface lifting. (**a**) Lifting threads penetrate the zygomatic ligament region and approach to the SMAS plane at the zygomatic region, and (**b**) a thread is located at the SMAS plane and entrapped with the zygomatic cutaneous ligaments. (Published with kind permission of © Hee-Jin Kim 2020. All Rights Reserved)

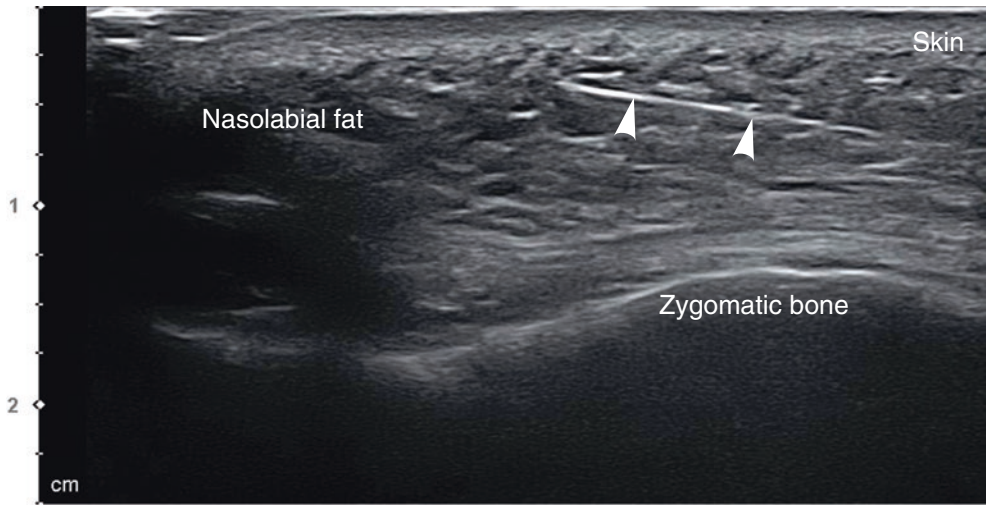

Fig. 10.8 Ultrasonography-guided multidirectional cog thread insertion for improvement of the nasolabial fold, B mode (oblique view, 15 MHz by linear transducer) (arrowheads: thread cannula). (Published with kind permission of © Ji-Soo Kim 2020. All Rights Reserved)

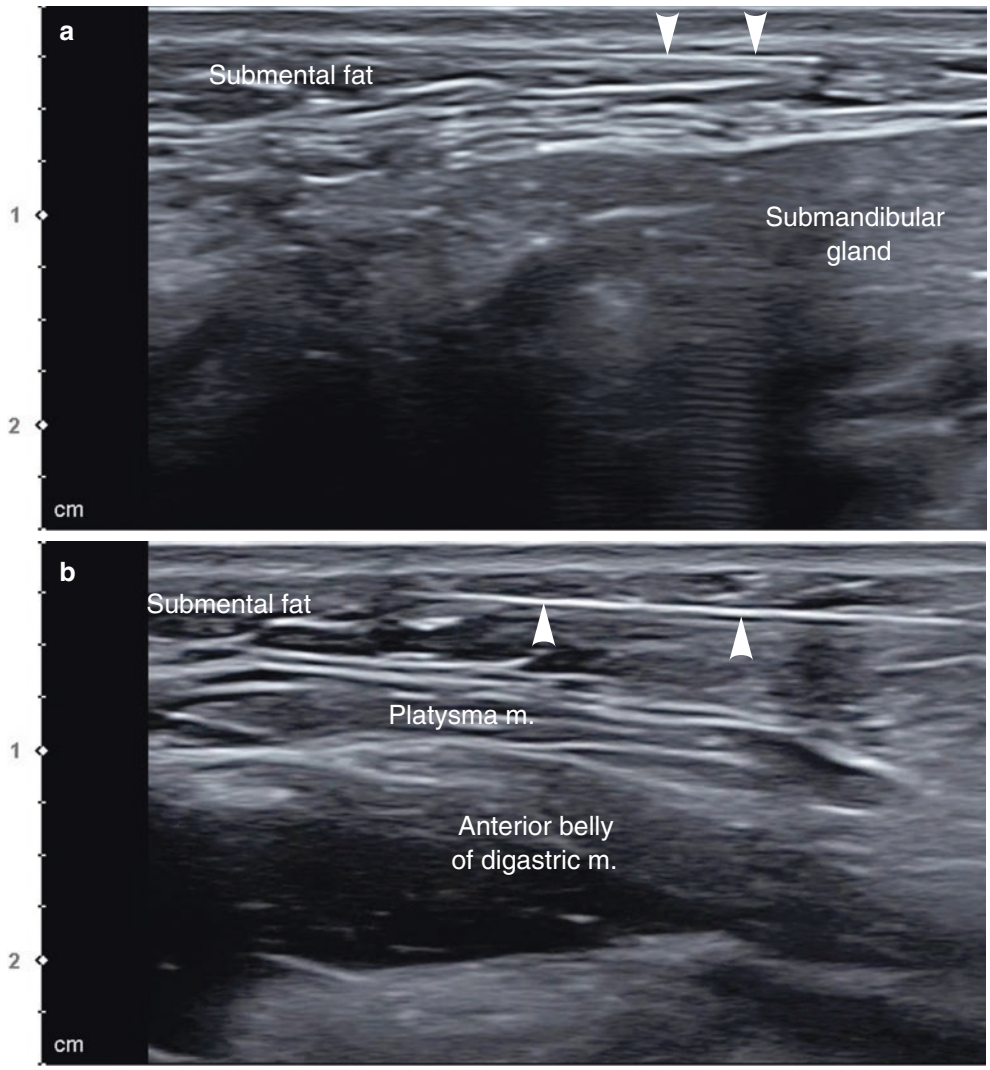

Fig. 10.9 Ultrasonography-guided multidirectional cog thread insertion for neck lift. (**a**) Above the submandibular gland, B mode (transverse view, 15 MHz by linear transducer) and (**b**) within the submental fat above the platysma muscle, B mode (transverse view, 15 MHz by linear transducer) (arrowheads: thread cannula). (Published with kind permission of © Ji-Soo Kim 2020. All Rights Reserved)

Bibliography

1. Kim BC, Oh SM, Jung WS. The art and science of thread lifting. New York, NY: Springer; 2019.
2. Lee W, Moon HJ, Kim JS, Chan BL, Yang EJ. Doppler ultrasound guided thread lifting. J Comest Dermatol. 2019;00:1–7. https://doi.org/10.1111/jocd.13240.
3. Suh DH, Jang HW, Lee AJ, Lee WS, Ryu HJ. Outcome of polydioxanone knotless thread lifting for fascial rejuvenation. Dermatol Surg. 2015;41:720–5.
4. Yoon JH, Kim SS, Oh SM, Kim BC, Jung WS. Tissue changes over time after polydioxanone thread insertion: an animal study with pigs. J Cosmet Dermatol. 2019;18:885–91. https://doi.org/10.1111/jocd.12718.